

Mid-Late Miocene climate constrained by a new  
Laser Ablation ICP-MS set up



**Michael Grahame Nairn**

School of Earth and Ocean Sciences

Cardiff University

Thesis submitted in partial fulfilment of the requirements for the degree of

*Doctor of Philosophy*

September 2018

BLANK PAGE

## Declaration

This work has not been submitted in substance for any other degree or award at this or any other university or place of learning, nor is being submitted concurrently in candidature for any degree or other award.

**Signed** \_\_\_\_\_(candidate) Date

### Statement 1

This thesis is being submitted in partial fulfilment of the requirements for the degree of PhD.

**Signed** \_\_\_\_\_(candidate) Date

### Statement 2

This thesis is the result of my own independent work/investigation, except where otherwise stated, and the thesis has not been edited by a third party beyond what is permitted by Cardiff University's Policy on the Use of Third Party Editors by Research Degree Students. Other sources are acknowledged by explicit references. The views expressed are my own.

**Signed** \_\_\_\_\_(candidate) Date

### Statement 3

I hereby give consent for my thesis, if accepted, to be available online in the University's Open Access repository and for inter-library loan, and for the title and summary to be made available to outside organisations.

**Signed** \_\_\_\_\_(candidate) Date

### Statement 4

I hereby give consent for my thesis, if accepted, to be available online in the University's Open Access repository and for inter-library loans *after expiry of a bar on access previously approved by the Academic Standards and Quality Committee*

**Signed** \_\_\_\_\_(candidate) Date

## Abstract

The unipolar icehouse world of the mid-late Miocene is a poorly understood interval in the evolution of Cenozoic climate. Widespread dissolution and poor preservation of carbonates in deep marine settings has resulted in large uncertainties in proxy-based climate reconstructions through the interval. Furthermore, models struggle to simulate the decoupling of low atmospheric CO<sub>2</sub> (~250-350ppm) forcing in a warmer than modern world. This thesis uses the Sunbird-1 core, a clay-dominated sedimentary sequence from offshore East Africa, to improve the constraints on the global climate state of the mid-late Miocene.

Prior to ~12 Ma, the Sunbird-1 site lay in a region of high productivity, with restricted, surface waters and an elevated supply of detrital organic matter invigorating carbon remineralisation in the water column. The redox environments associated with this high productivity setting resulted in the precipitation of diagenetic outer coatings on foraminifera, overprinting the primary Mg/Ca signal required for palaeotemperature reconstructions. The influence of these coatings decreased up-section, as the site subsided and experienced more open ocean conditions.

This thesis develops and optimises a series of ablation parameters on the new Laser Ablation (LA-) ICP-MS system at Cardiff University. Employing medium to low fluences and repetition rates (3.5 Jcm<sup>-2</sup> and 2.0 Hz) enables the collection of highly spatially resolved foraminiferal depth profiles suitable for assessing intra-test trace metal variability. By implementing the optimised LA-ICP-MS system this thesis reconstructs absolute sea surface temperature (SST) from Sunbird-1, indicating that applying a careful microanalytical approach can reconstruct

palaeotemperatures from diagenetically altered foraminifera. This record suggests that tropical sea surface temperature remained relatively stable at 27-29°C from 13.3-9.4 Ma, presenting the mid-late Miocene as a key interval of increasing latitudinal temperature gradients towards that of the modern day climate state.

These improved absolute sea surface temperature estimates, and the planktic foraminifera  $\delta^{18}\text{O}$  record, suggest a 39-48 m sea level equivalent increase in global ice volume through this interval. Furthermore, the planktic foraminiferal seawater  $\delta^{18}\text{O}$  record indicates that similar amplitude, short duration, fluctuations in global ice volume persisted through the mid-late Miocene. This implies that the East Antarctic Ice Sheet behaved dynamically following its expansion to a dry, land-based ice sheet during the Mid Miocene Climate Transition.

## Acknowledgements

First of all I would like to thank my primary supervisor Carrie Lear for her continuous support and guidance throughout the last four years. Your all round expertise and knowledge of inorganic geochemistry and the wider climate system are an inspiration. I know I have been frustrating at times, but your patience with me, allied with the constant encouragement to pursue my personal scientific interests, has made this PhD a thoroughly enjoyable and fulfilling experience. I am extremely fortunate to have had the opportunity to work so closely with you Carrie, and I cannot thank you enough for everything over the course of my PhD.

I must also show my gratitude to Simon Beavington-Penney, my co-supervisor. Thank you Simon for always being supportive of the PhD, and more generally me as a scientist, especially when the direction of the project changed. Your wealth of knowledge in relation to the study site, and carbonate geology as a whole, has made this PhD a reality.

Thank you to everyone who has been involved with the 'Changing Earth and Ocean' research group. For all the feedback on aspects of this work, whether at internal talks or within your always open offices, thank you. The research group goes far beyond scientific excellence, and has been a fantastic, friendly, and welcoming group to be a part of.

I would like to thank everyone who I have relied on for laboratory training and support. Your work and expertise has often gone unappreciated, but without you this thesis would not have been possible. To Elaine Mawbey for teaching me how to process foraminiferal samples, to

Sandra Nederbragt for all the isotope measurements, and especially to Anabel Morte-Ródenas for the numerous hours of training and assistance analysing samples on the ICP-MS. Further thanks must go to Mike Hamel and Ashley Norris of ASI for the training and guidance with the RESOlution Laser-Ablation facility.

Thank you to the entire School of Earth and Ocean Science PhD community. To those that I have shared the 'Palaeo-office' with: Amy, Anna, Chris, Dhobby, Emanuela, Ewa, Freya, Hennie, James, Matt, and Sophie, thank you for the discussions (both scientific and not), the cakes, and the friendship over the years. Special thanks must go to Amy and Hennie. We have been through this together from day one, and I could not have wished for better office/lab/conference mates. I hope that we will become lifelong colleagues, whereas I know we have become lifelong friends. To those members of the wider PhD community who I am now lucky enough to regard as close friends, thank you for the highs, and the support through the lows. In particular, Bob, George, Henry, Josh, Matt, Michael, and Nick, thank you for the ongoing friendships and I know we will continue to share laughter together, even if only at the World T-Ball Championships each year.

Thank you to my family for your constant support throughout my life. Your encouragement to pursue my interests, scientifically and personally means so much to me.

Finally, I would like to thank Emma. Your unwavering love and support, especially over the last few months, have really pulled me through. You will never know how appreciated you are, and I can only hope to afford you the same in the future.

## List of Commonly Used Symbols and Abbreviations

[CO <sub>3</sub> <sup>2-</sup> ]	Carbonate ion concentration
[O <sub>2</sub> ]	Oxygen concentration
BWT	Bottom water temperature
CM	Carbon maxima
CO <sub>2</sub>	Carbon dioxide
C <sub>org</sub>	Organic carbon
DIC	Dissolved inorganic carbon
EAIS	East Antarctic Ice Sheet
HR	High resolution mode
ICP-MS	Inductively coupled plasma mass spectrometry
IODP	Integrated Ocean Drilling Program, International Ocean Discovery Program
kyr	Thousand years
LA-ICP-MS	Laser ablation inductively coupled plasma mass spectrometry
LOD	Limit of detection
LR	Low resolution mode
Ma	Million years ago
MBSF	Metres below sea floor
MBSL	Metres below sea level
MCO	Miocene Climatic Optimum
Mg/Ca <sub>sw</sub>	Mg/Ca composition of seawater
MMCT	Middle Miocene Climate Transition
myr	Million years
ODP	Ocean Drilling Program
OM	Organic matter
OMZ	Oxygen minimum zone
PSU	Practical salinity unit
RSD	Relative standard deviation
SD	Standard deviation
SE	Standard error of the mean
SEM	Scanning electron microscope

SMOW	Standard Mean Ocean Water
SST	Sea surface temperature
VPDB	Vienna Pee Dee Belemnite
$\Delta[\text{CO}_3^{2-}]$	Carbonate saturation state
$\delta^{11}\text{B}$	Boron isotope composition
$\delta^{13}\text{C}$	Carbon isotope composition
$\delta^{13}\text{C}_{\text{BF}}$	Carbon isotope composition of benthic foraminifera
$\delta^{13}\text{C}_{\text{DIC}}$	Carbon isotope composition of dissolved inorganic carbon
$\delta^{13}\text{C}_{\text{PF}}$	Carbon isotope composition of planktic foraminifera
$\delta^{13}\text{C}_{\text{SW}}$	Carbon isotope composition of sea water
$\delta^{18}\text{O}$	Oxygen isotope composition
$\delta^{18}\text{O}_{\text{BF}}$	Oxygen isotope composition of benthic foraminifera
$\delta^{18}\text{O}_{\text{PF}}$	Oxygen isotope composition of planktic foraminifera
$\delta^{18}\text{O}_{\text{SW}}$	Oxygen isotope composition of sea water
$\Delta\delta^{13}\text{C}$	Benthic-planktic carbon isotope gradient
$\Delta\delta^{18}\text{O}$	Benthic-planktic oxygen isotope gradient

# Table of Contents

1	Introduction.....	1
1.1	Climate of the Cenozoic .....	1
1.2	Climate of the mid-late Miocene .....	3
1.2.1	The Miocene Climatic Optimum and Mid Miocene Climate Transition .....	3
1.2.2	Post MMCT climate.....	4
1.2.3	The extent and stability of continental ice during the mid-late Miocene.....	8
1.3	Advantages and applications of laser-ablation ICP-MS .....	8
1.4	Aims of the study .....	9
2	Materials and methods.....	11
2.1	Geological setting and lithostratigraphy.....	11
2.1.1	Site location .....	11
2.1.2	Middle Miocene change of depositional environment .....	12
2.1.3	Biostratigraphic age model.....	17
2.2	Geochemical proxies in foraminifera .....	21
2.2.1	Stable isotopes.....	22
2.2.1.1	Oxygen isotopes.....	22
2.2.1.2	Carbon isotopes.....	26
2.2.2	Trace element/calcium ratios .....	27
2.2.2.1	Mg/Ca .....	27

2.2.2.2	Benthic foraminiferal Sr/Ca .....	30
2.2.2.3	Benthic foraminiferal B/Ca .....	30
2.3	Sample collection and processing .....	32
2.4	Stable isotope analysis .....	32
2.5	Trace element analysis via solution ICP-MS.....	33
2.6	Trace element analysis via laser ablation ICP-MS.....	34
3	Changing redox conditions at Sunbird-1 and its influence on benthic foraminiferal Mg/Ca	37
3.1	Introduction.....	37
3.2	Materials and methods .....	40
3.2.1	Species selection .....	40
3.2.2	Trace metal analysis.....	42
3.3	Results .....	44
3.3.1	<i>Cibicidoides wuellerstorfi</i> and <i>Uvigerina peregrina</i> Mg/Ca .....	44
3.3.2	<i>Hoeglundina elegans</i> Sr/Ca.....	44
3.3.3	Downcore records of contaminant indicators.....	48
3.3.4	Downcore B/Ca .....	49
3.4	Discussion.....	50
3.4.1	Redox changes at Sunbird-1 .....	50
3.4.2	Characterisation of the contaminant phase .....	56

3.4.3	Potential influence of detrital silicates at Sunbird-1 .....	57
3.4.4	Assessing the impact of authigenic coatings on foraminiferal Mg/Ca and Sr/Ca records 63	
3.4.5	A potential novel way to correct for contaminant coatings.....	69
3.4.6	An assessment of the impact of the coatings on other trace metal records ....	73
3.5	Conclusions.....	74
4	Optimising LA-ICP-MS ablation parameters to assess the impact of identifying the primary test of Mn-rich foraminifera on Mg/Ca palaeothermometry .....	77
4.1	Introduction.....	77
4.2	Laser ablation instrumentation and method development .....	81
4.2.1	General laboratory setup.....	81
4.2.2	Methodology to determine optimal operating parameters for the analysis of the NIST 610 glass standard .....	85
4.2.3	Methodology to determine optimal operating parameters for the analysis of foraminiferal tests.....	86
4.2.4	Determination of the number of profiles required for a representative sample Mg/Ca: 89	
4.3	Results .....	90
4.3.1	Signal acquisition .....	90
4.3.2	Optimal operating parameters for NIST 610 glass standard .....	93
4.3.3	Optimal operating parameters for foraminiferal calcite .....	99

4.3.4	Acquiring a consistent foraminiferal Mg/Ca ratio .....	108
4.4	Discussion.....	112
4.4.1	Determining the cause of Mg/Ca-Mn/Ca correlation in downcore records ...	112
4.4.2	Characterising the contaminant phase.....	117
4.4.3	Potential impact on palaeotemperature reconstruction .....	121
4.5	Conclusions.....	124
5	Sea surface and bottom water temperature at Sunbird-1 using Mg/Ca thermometry of primary foraminiferal calcite identified with laser ablation ICP-MS.....	127
5.1	Introduction.....	127
5.2	Methods .....	129
5.2.1	Sample selection and preparation .....	129
5.2.2	LA-ICP-MS analysis .....	130
5.2.3	Data processing and screening .....	131
5.2.4	Calculating mean Mg/Ca values and propagation of uncertainty .....	136
5.3	Converting raw Mg/Ca ratios to estimates of seawater temperature .....	137
5.3.1	Accounting for the influence of the carbonate system on Mg/Ca: .....	138
5.3.1.1	Benthic foraminifera .....	138
5.3.1.2	Planktic foraminifera .....	138
5.3.2	Accounting for changes in seawater Mg/Ca .....	140
5.3.3	Accounting for changes in salinity .....	145

5.3.4	Quantifying uncertainties of reconstructed temperatures .....	146
5.4	Results .....	146
5.4.1	Effect of screening for contamination .....	146
5.4.2	Influence of identifying the primary test on temperature reconstructions....	152
5.4.3	Intra- and Inter-specimen variability in Mg/Ca .....	153
5.4.4	Sample mean Mg/Ca ratios .....	157
5.4.5	Calculating bottom water and sea surface temperature at Sunbird-1 .....	165
5.5	Discussion.....	169
5.5.1	Controls on intra- and inter-specimen variability.....	169
5.5.1.1	Intra-specimen.....	170
5.5.1.2	Inter-specimen.....	173
5.5.2	Evolution of bottom water temperature at Sunbird-1.....	177
5.5.3	Mid-late Miocene sea surface temperatures in the equatorial Indian Ocean	180
5.5.4	Short lived decreases in temperature at Sunbird-1.....	187
5.6	Conclusions.....	189
6	Unravelling the influence of Temperature, Ice Volume, Sedimentation, and Subsidence on Sunbird-1 .....	191
6.1	Introduction.....	191
6.2	Materials and methods .....	193
6.2.1	Sample selection .....	193

6.2.2	Calculating $\delta^{18}\text{O}_{\text{SW}}$ independently using Mg/Ca temperatures.....	194
6.2.3	Bottom water and sea surface temperature reconstructions.....	196
6.3	Results .....	199
6.3.1	$\delta^{13}\text{C}$ .....	199
6.3.2	$\delta^{18}\text{O}$ .....	201
6.3.3	$\Delta\delta^{13}\text{C}$ and $\Delta\delta^{18}\text{O}$ .....	204
6.3.4	$\delta^{18}\text{O}$ SST and BWT records.....	207
6.3.5	Surface and bottom water calculated $\delta^{18}\text{O}_{\text{SW}}$ .....	209
6.4	Discussion.....	212
6.4.1	Sunbird-1 planktic foraminiferal Mg/Ca and $\delta^{18}\text{O}$ : towards reliable absolute SST reconstructions for the Miocene .....	212
6.4.2	Dissimilar Mg/Ca and $\delta^{18}\text{O}$ BWT reconstructions.....	217
6.4.3	Sunbird-1 $\delta^{13}\text{C}$ as a recorder of global carbon cycling and local subsidence ..	218
6.4.4	Global ice volume and local oceanographic controls on Sunbird-1 $\delta^{18}\text{O}_{\text{SW}}$ .....	232
6.4.4.1	Local oceanographic control on Sunbird-1 benthic foraminiferal $\delta^{18}\text{O}_{\text{SW}}$ 233	
6.4.4.2	Long term evolution of global ice volume.....	240
6.4.4.3	A dynamic Antarctic ice sheet following the MMCT? .....	243
6.5	Conclusions.....	244
7	Synthesis.....	247

7.1	Conclusions.....	247
7.2	Limitations of the LA-ICP-MS analysis in this thesis.....	250
7.3	Future research directions .....	251
8	References.....	256
9	Appendices.....	277

# 1 Introduction

## 1.1 Climate of the Cenozoic

The Earth's climate system has undergone a nonlinear transition through the Cenozoic from a greenhouse state to the modern day icehouse state. This has been revealed by the compilation of oxygen isotope records recorded from benthic foraminifera across all ocean basins (Shackleton and Kennett, 1975, Miller et al., 1991, Zachos et al., 2001, Zachos et al., 2008, Cramer et al., 2009) (Figure 1.1). The benthic foraminiferal  $\delta^{18}\text{O}$  record reveals the development of deep ocean temperature and global ice volume, two environmental parameters that do not show a linear relationship. Deep ocean temperature has cooled gradually by  $\sim 12^\circ\text{C}$  through the Cenozoic, controlled primarily by long term  $\text{CO}_2$  concentrations (Cramer et al., 2011, Zhang et al., 2013). This observed gradual cooling trend is punctuated by episodes of increased  $\delta^{18}\text{O}_{\text{BF}}$  values, interpreted as stepwise transitions in the expansion of continental ice sheets, primarily over Antarctica (Lear et al., 2000, Zachos et al., 2001, Mudelsee et al., 2014).

Continental ice sheets grew in large amplitude, short intervals through the Cenozoic indicating their dynamic response to climate thresholds, and the non-linearity that exists within the climate system (DeConto and Pollard, 2003, DeConto et al., 2008). Cenozoic continental ice growth occurred in three main, geologically abrupt steps; the Eocene-Oligocene Transition, the Mid Miocene Climate Transition, and the Pliocene-Pleistocene Transition (Shackleton and Kennett, 1975, Zachos et al., 2001, Cramer et al., 2011). These three events are interpreted as the onset of Antarctic glaciation (Lear et al., 2000, Coxall et al., 2005), the expansion of the land based East Antarctic Ice Sheet (EAIS) to its continental

margins (Flower and Kennett, 1994, Holbourn et al., 2005, Lewis et al., 2007), and the intensification of glaciation across the northern hemisphere ice sheets (Sosdian and Rosenthal, 2009).

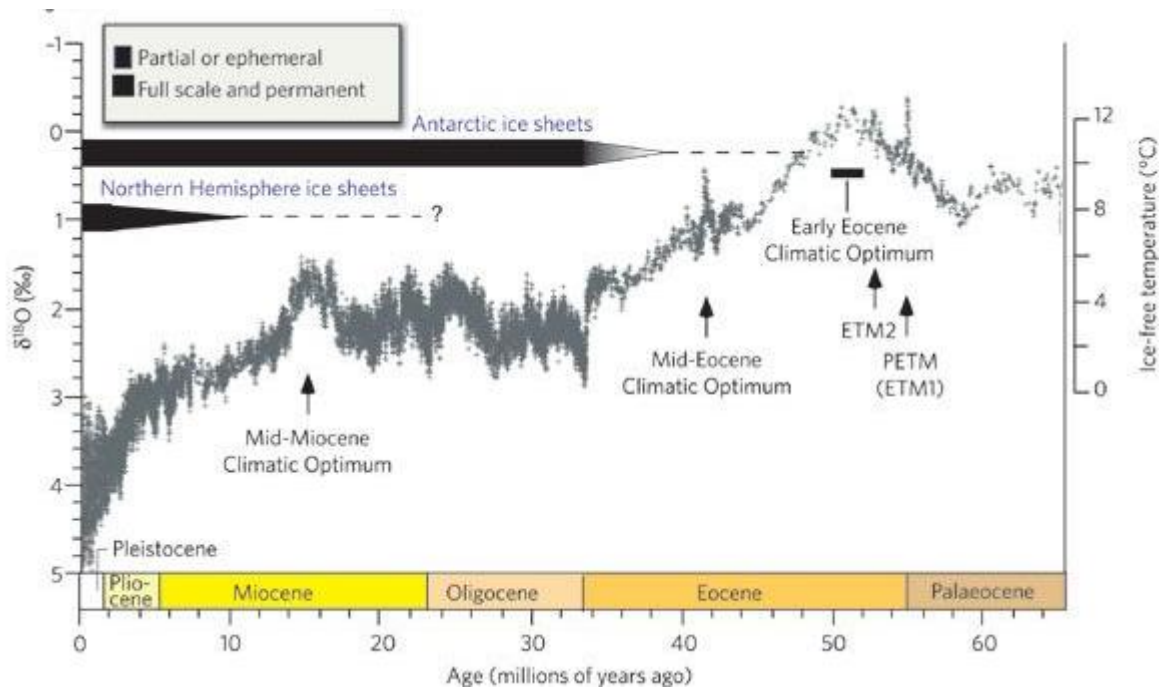


Figure 1.1: Global Cenozoic climate inferred from a deep-sea benthic foraminiferal oxygen isotope stack. Figure adapted from Zachos et al. (2008).

Strong hysteresis of the Antarctic Ice Sheet in ice sheet models arises from the strong positive feedbacks linked to its growth. Therefore, elevated boundary conditions relative to those required for Antarctic Ice Sheet growth are required for an equal magnitude of retreat, making it inherently stable (Pollard and DeConto, 2005, Gasson et al., 2014). Inclusion of new physical mechanisms for ice sheet retreat has demonstrated that ice loss from subglacial basins of East Antarctica equating to ~17m of sea level equivalent could be achieved on millennial year timescales (Pollard et al., 2015). Applying the new physical mechanisms for ice sheet retreat of Pollard et al. (2015) to the early-mid Miocene (23-14 Ma), Antarctic Ice Sheet variability equivalent to a 30-36m change in sea level has been simulated (Gasson et al., 2016).

Geochemical provenance studies suggest the EAIS behaved dynamically during the Pliocene (Cook et al., 2013). Furthermore, direct geological evidence from the ANDRILL-2A drill core in the Western Ross Sea, also spanning the 23-14 Ma time interval, also suggests there was a highly variable and dynamic EAIS despite minimal atmospheric CO<sub>2</sub> variability (Levy et al., 2016).

## 1.2 Climate of the mid-late Miocene

### 1.2.1 The Miocene Climatic Optimum and Mid Miocene Climate Transition

The Miocene Climatic Optimum, or MCO (~17 – 15 Ma), was an interval of global warmth and high amplitude climate variability (Foster et al., 2012, Greenop et al., 2014, Holbourn et al., 2014). The Miocene Climatic Optimum also had distinctive repeated perturbations of the global carbon cycle, observed as carbon maxima events, linked to the episodic drawdown of atmospheric CO<sub>2</sub> (Woodruff and Savin, 1991, Flower and Kennett, 1995, Shevenell et al., 2008), perturbations not observed following the Mid Miocene Climate Transition. These carbon maxima events of the Monterey excursion are identifiable by their elevated seawater  $\delta^{13}\text{C}$  values recorded in foraminifera, resulting from the enhanced sequestration of organic carbon on continental shelves (Flower and Kennett, 1993, Holbourn et al., 2007). The final recovery, identified by a ~0.8‰ negative  $\delta^{13}\text{C}$  excursion followed the expansion of the East Antarctic Ice Sheet, suggesting that global climate and the global carbon cycle were both dynamic and intrinsically linked through the mid-late Miocene (Holbourn et al., 2013).

The Mid Miocene Climate Transition is the most notable climatic event of the Neogene, as seen by the increase in the global benthic foraminiferal  $\delta^{18}\text{O}$  compilation following the

Miocene Climatic Optimum (Zachos et al., 2008, Cramer et al., 2009) (Figure 1.1). The mean increase from a globally distributed stack of 17  $\delta^{18}\text{O}_{\text{BF}}$  records was  $0.88 \pm 0.04 \text{ ‰}$  (Mudelsee et al., 2014). This positive  $\delta^{18}\text{O}$  excursion is coeval with the Langhian-Serravalian boundary at 13.82 Ma (Hilgen et al., 2009). Through this interval the planet underwent a deep-sea cooling of  $\sim 1 - 4^\circ\text{C}$  out of the warm climate of the Miocene Climatic Optimum leading to the expansion of the Antarctic Ice Sheet to approximately modern day volumes (Miller et al., 1991, Woodruff and Savin, 1991, Flower and Kennett, 1994, Holbourn et al., 2005, Lewis et al., 2007, Shevenell et al., 2008, Lear et al., 2010, Holbourn et al., 2013, Holbourn et al., 2014, Lear et al., 2015). The ice volume increase was associated with a  $\sim 54\text{-}69\text{m}$  sea level fall, as determined from backstripping estimates from the Marion Plateau, a carbonate platform offshore North East Australia (John et al., 2004, John et al., 2011). A change from an eccentricity (100kyr) paced climate system to one predominantly forced by obliquity (41kyr) at  $\sim 14.7$  Ma reduced seasonality at high latitudes, producing favourable conditions for large ice growth at the poles (Holbourn et al., 2013, Holbourn et al., 2014). When combined with enhanced drawdown of  $\text{CO}_2$  across the MMCT (Foster et al., 2012, Zhang et al., 2013, Sosdian et al., 2018) the climate system was primed for the expansion of the Antarctic Ice Sheet.

### 1.2.2 Post MMCT climate

Intervals through the Neogene, away from these distinct threshold events are vastly underrepresented by geochemical records. This is particularly true for the interval directly following the MMCT, the mid-late Miocene (Lunt et al., 2008). A lack of well-preserved, globally distributed successions has prevented the investigation into the evolution of global ice volume and ocean temperature during this interval. There are no distinctive long term

trends in the current benthic foraminiferal  $\delta^{18}\text{O}$  compilation (Cramer et al., 2011, Zachos et al., 2008) or atmospheric  $\text{CO}_2$  reconstructions (Beerling and Royer, 2011, Zhang et al., 2013, Sossdian et al., 2018) for the mid-late Miocene. Therefore, the interval has long been regarded as a relatively stable period of Cenozoic climate, devoid of any major shifts or transitions. This is in contrast to the highly dynamic climate inferred for the preceding Miocene climatic optimum.

The mid-late Miocene is an enigmatic interval for general circulation models (von der Heydt and Dijkstra, 2006, Knorr et al., 2011) which struggle to simulate the climate reconstructed by geochemical proxies. The lower than modern day atmospheric  $\text{CO}_2$  (Foster et al., 2012, Sossdian et al., 2018) and temperatures warmer than the modern day (Pound et al., 2011, Rousselet et al., 2013) suggest that global temperature and atmospheric  $\text{CO}_2$  forcing were decoupled through the interval (Pagani et al., 1999a, Pagani et al., 1999b, LaRiviere et al., 2012). This is in stark contrast to the long-term Neogene trend through which low pH, and therefore high  $\text{pCO}_2$ , derived from  $\delta^{11}\text{B}$  records of planktic foraminifera are associated with high SST derived from Mg/Ca records of planktic foraminifera and low continental ice volume derived from  $\delta^{18}\text{O}$  records of benthic foraminifera. This is particularly noticeable for the interval between 11.6 and 5.3 Ma, through which changes in reconstructed  $\text{pCO}_2$  do not correspond to changes in benthic foraminiferal  $\delta^{18}\text{O}$  (Sossdian et al., 2018), reinforcing the notion of a decoupling of climate and  $\text{CO}_2$  through the late Miocene.

A major, interhemispheric and interoceanic cooling of sea surface temperature (SST) through the mid-late Miocene has been recorded, averaging  $6^\circ\text{C}$  globally (Herbert et al., 2016). These

authors therefore propose the mid-late Miocene as the key interval in the intensification of the latitudinal temperature gradient. However, the tropical SST estimates may be recording cooler temperatures due to saturation of the alkenone proxy above 28°C (Müller et al., 1998) meaning better constrained tropical SST records are required to determine whether the mid-late Miocene is an important interval of change in the global climate state. The mid-late Miocene represents a key interval in terms of the transition out of the warm, dynamic climate state of the MCO into a more stable unipolar icehouse world. These changes appear not to be associated with any permanent increase in continental ice volume based on data from the benthic foraminiferal stack, but are likely to have been part of a dynamic climate system with major ice sheet-ocean interactions.

Deep marine sediments from the mid-late Miocene are characterised by their poor preservation of carbonate microfossils, including foraminifera. The dramatic reduction in sediment carbonate content and preservation quality is termed the middle-late Miocene carbonate crash (Keller and Barron, 1987, Lyle et al., 1995, Farrell et al., 1995). Although the primary cause of the carbonate crash is not fully understood, the primary mechanism is generally considered to be low fertility in the surface oceans reducing productivity, and hence the abundance of calcareous plankton (Jiang et al., 2007). In turn this caused a reduction in carbonate supply to depth prompting a shoaling of the calcite compensation depth and carbonate dissolution (Jiang et al., 2007). Other mechanisms for the carbonate crash have been proposed, for example basin wide dissolution of CaCO<sub>3</sub> (Farrell et al., 1995, Lyle et al., 1995, Lyle, 2003). However, compilations of reconstructed CO<sub>2</sub> do not support there being increased atmospheric CO<sub>2</sub> through this interval (Foster et al., 2012, Zhang et al., 2013, Bolton

et al., 2016, Super et al., 2018). Some authors have proposed that the carbonate crash is merely an artefact of increased terrigenous, non-carbonate sediments, in particular siliceous material (Keller and Barron, 1983, Diester-Haass et al., 2004). While these alternatives cannot be categorically ruled out, a decrease in the surface productivity due to reduced fertility is the most commonly suggested mechanism for the carbonate crash of the mid-late Miocene (Jiang et al., 2007).

Through this interval between ~11 Ma and ~9 Ma (the Carbonate Crash (Lyle et al., 1995)) it has proved challenging to recover continuous marine sequences. Consequently, reconstructions of ocean temperature, continental ice volume, atmospheric CO<sub>2</sub>, and ocean circulation based on geochemical proxies are poorly constrained as they typically rely on foraminifera recovered from deep marine sediment, with data resolution being compromised by poor recovery, hiatuses in sedimentation, and carbonate dissolution.

Global seafloor dissolution of carbonate through the mid-late Miocene interval (Lyle et al., 1995) means that relatively shallower settings dominated by hemipelagic clays have to be targeted for sampling, as opposed to the more typically used deep sea carbonate oozes, which are rich in foraminifera. However, sites dominated by hemipelagic clay sedimentation better preserve the primary geochemical signal of foraminifera despite their lower foraminiferal abundance (Pearson et al., 2001, Sexton et al., 2006, Pearson and Burgess, 2008, Sexton and Wilson, 2009).

### 1.2.3 The extent and stability of continental ice during the mid-late Miocene

Improving the constraints for projections of future climate requires a much improved understanding of how the EAIS behaves in a warmer world. In particular, whether the large EAIS behaves in a dynamic or a stable manner in response to climate variability on short timescales is vital for constraining future sea-level rise (DeConto and Pollard, 2016). Following the expansion of the land-based EAIS to its continental margins at ~13.8 Ma (Flower and Kennett, 1994, Holbourn et al., 2005, Lewis et al., 2007) a unipolar icehouse world dominated until, at least, the Pliocene and the onset of major Northern Hemisphere glaciation (Sosdian and Rosenthal, 2009, Bailey et al., 2013). This makes the mid-late Miocene an ideal interval to study the stability of the EAIS in a warmer than modern world. Accurate estimates of the extent and sensitivity of the EAIS in this warmer than modern world are nevertheless poorly constrained (Lear et al., 2015), often due to poor foraminiferal preservation in carbonate rich ODP sites which suffered from dissolution during the carbonate crash (11-9 Ma) (Lyle et al., 1995). In order to improve our understanding of the extent of global ice volume and EAIS stability in the unipolar icehouse world of the mid-late Miocene, improved proxy based reconstructions with reduced absolute uncertainties are required.

### 1.3 Advantages and applications of laser-ablation ICP-MS

Laser Ablation Inductively Coupled Plasma Mass Spectrometry (LA-ICP-MS) enables accurate quantitative measurements of solid substrates at high spatial resolution (~0.1µm) (Russo et al., 2002). This technique has been applied to determine the intra-test geochemical patterns in individual foraminifera (Wu and Hillaire-Marcel, 1995, Eggins et al., 2003, Hathorne et al., 2003, Reichart et al., 2003, Eggins et al., 2004, Sadekov et al., 2008, Dueñas-Bohórquez et al.,

2009, Sadekov et al., 2010, Raitzsch et al., 2011, Fehrenbacher et al., 2015). A big advantage of this microanalytical approach over more traditional bulk geochemical methods is the ability to identify pristine calcite within diagenetically altered tests (Pena et al., 2005, Creech et al., 2010, Hasenfratz et al., 2016). This pristine calcite can be utilised to accurately reconstruct palaeoenvironmental parameters such as temperature (Creech et al., 2010, Hollis et al., 2012, Hines et al., 2017), pH (Thil et al., 2016), and oxygenation (Petersen et al., 2018).

#### 1.4 Aims of the study

This thesis has the primary aim of improving the understanding of the global climate state through the mid-late Miocene (13.7 – 9.4 Ma). Such an aim will involve applying the Mg/Ca temperature proxy to determine absolute estimates of bottom water and sea surface temperatures from Sunbird-1, a site in the equatorial Western Indian Ocean. These absolute estimates of temperature will then be utilised to better constrain the extent and variability of the East Antarctic Ice Sheet in this unipolar icehouse world. The shallow water depth and tectonic subsidence of the Sunbird-1 site adds an extra layer of complexity to the primary aim of this thesis. Therefore, the influence of more localised controls will require isolating in order to interpret changes in the global climate state, in particular carbon cycling, ocean temperature, and continental ice volume.

To achieve the primary aim of the thesis the following three hypotheses will be tested:

- 1) Can one reconstruct palaeotemperatures using diagenetically altered foraminifera? If this is possible, the Mg/Ca ratios of planktic and benthic foraminifera using a new LA-

ICP-MS set up will reconstruct realistic and viable sea surface and bottom water temperatures respectively. If not, these LA-ICP-MS Mg/Ca ratios will be influenced by post-depositional diagenetic alteration.

- 2) Did tropical sea surface temperature remain stable during the Serravalian-Tortonian? If that is the case, the Mg/Ca ratios of planktic foraminifera throughout the record will remain stable. If not, these same ratios will demonstrate variability or trends.
- 3) Do the geochemical variations in the Sunbird-1 well reflect a dynamic East Antarctic Ice Sheet through the Serravalian-Tortonian? If that is the case, the seawater  $\delta^{18}\text{O}$  record, reconstructed by using foraminiferal Mg/Ca to account for the temperature component of the foraminiferal  $\delta^{18}\text{O}$  record, will demonstrate variability. If not, the seawater  $\delta^{18}\text{O}$  record will remain stable.

An additional aim of this thesis is to optimise the operating parameters on the new LA-ICP-MS system installed at Cardiff University. Optimising these operational parameters to collect accurate and precise data from homogenous glass standards, and then reproducible, accurate and precise measurements at the maximum possible spatial resolution through foraminiferal calcite, will allow the primary trace metal signal required for environmental interpretation to be isolated from any altered regions of the foraminiferal test.

## 2 Materials and methods

### 2.1 Geological setting and lithostratigraphy

#### 2.1.1 Site location

This thesis utilises cuttings recovered from the Sunbird-1 well drilled offshore Kenya by BG Group at a water depth of 723.3 m (04° 18' 13.268" S, 39° 58' 29.936" E) (Figure 2.1).

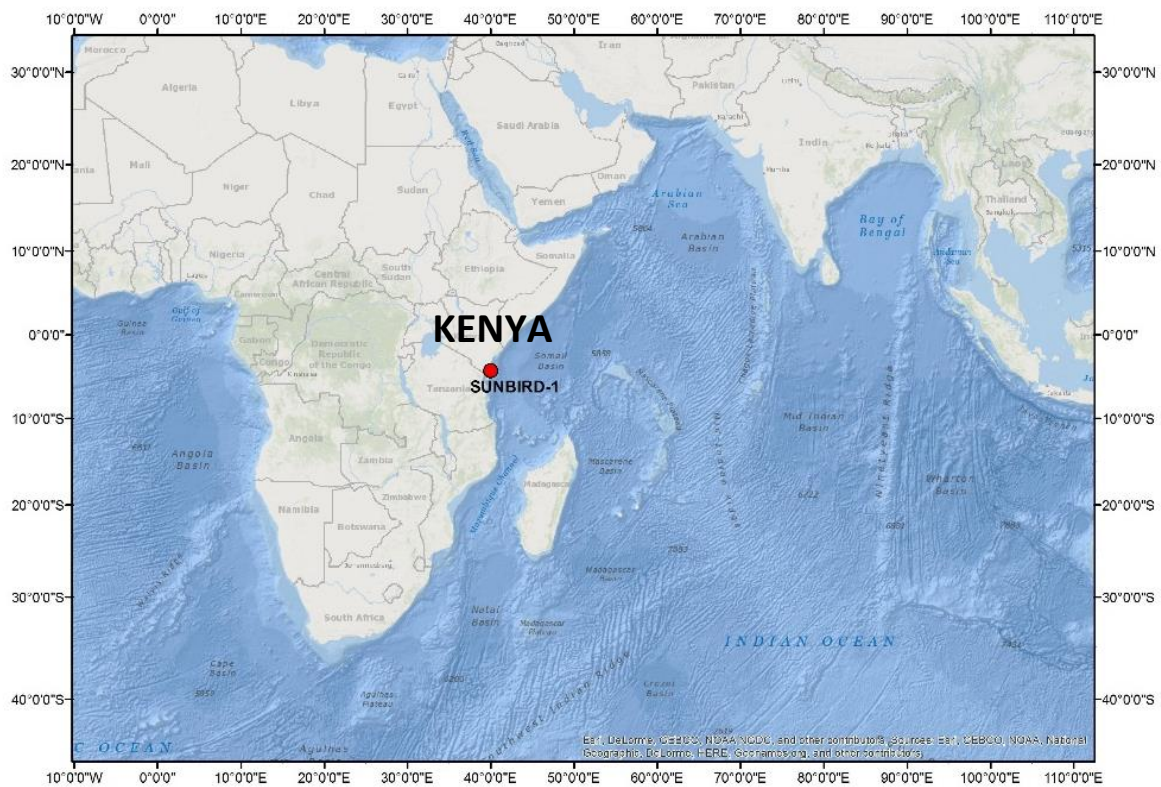


Figure 2.1: Location of the Sunbird-1 well in the Western Indian Ocean, offshore Kenya, with a modern day water depth of 723.3 m.

The Sunbird-1 carbonate build-up is situated within the Tembo Trough, an extensional graben. The extensional setting is part of the wider East African Rift System, which has had a general North-South trend since at least the Oligocene (Macgregor, 2015). The rifted region between continental crust to the west and the oceanic crust of the Simba High to the east subsided continuously through the Miocene whilst deposition was taking place (Figure 2.2).

The well penetrates through a carbonate platform and overlying pinnacle reef that built up through the early-middle Miocene (Aquitanian-Langhian), keeping pace with the subsiding basin.

### 2.1.2 Middle Miocene change of depositional environment

The stratigraphy of Sunbird-1 displays a rapid change of depositional facies in the Middle Miocene (Figure 2.3). There is evidence for the subaerial exposure of the pinnacle reef. This meteoric exposure has generated high, vuggy porosities and karstic weathering in the upper ~100 m of the carbonate platform and overlying reef, not seen in the sediments below (Figure

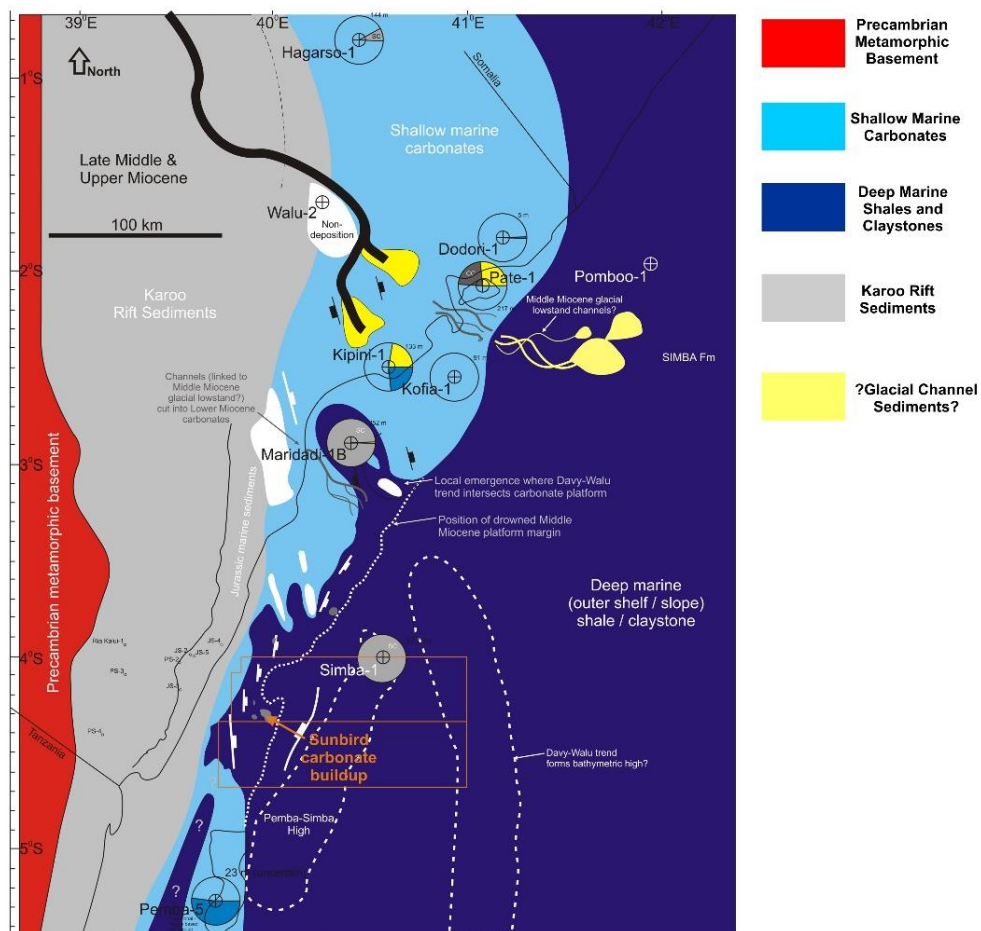


Figure 2.2: Gross depositional environment during the late Miocene. Figure after (Beavington-Penney and Rowles, 2015).

2.3). Pedogenic textures are also apparent in the pinnacle reef, a further evidence of subaerial exposure.

Following this exposure event there is a pronounced change of facies as carbonate deposition ceases and is replaced by clays (Figure 2.3). This abrupt change in facies marking the top of autochthonous carbonate is seen by the sharp decrease in limestone fraction (Figure 2.3a) and by a sharp increase in API values in the gamma ray log (Figure 2.3b). At the base of the clays, between 1626-1609 metres below sea level (MBSL)), micro to cryptocrystalline muddy limestone fragments prevail, potentially an artefact of the prior autochthonous limestone sedimentation. The abrupt lithological change from carbonates to clays at Sunbird-1 suggests that locally there was a rapid transgression. This is despite the synchronous global regression coinciding with the Mid Miocene Climate Transition, an expansion of the Antarctic Ice Sheet to a more permanent state culminating at 13.8 Ma (Holbourn et al., 2014). This paradox emphasises that deposition at Sunbird-1 took place in a complex setting, influenced by global environmental change and local tectonics. It is vital that the potential impact of these competing influences are considered when interpreting the geochemical results from the site.

This rapid meteoric exposure being synchronous with the expansion of the Antarctic Ice Sheet is likely not a coincidence; the global, ~60 metre, regression prompting the subaerial exposure of Sunbird-1. This would date the abrupt facies change at 1626 metres below sea level at the Langhian-Serravallian stratigraphic boundary (~13.8 Ma). As highlighted previously, local tectonic influence on the Sunbird-1 site could mean this is not the case, and the biostratigraphic zonations (Chapter 2.1.3) should be favoured.

Carbonate deposition never fully resumed; the Sunbird-1 platform and pinnacle reef being overlain by ~900m of clays as subsidence of the Tembo Trough accelerated. This thesis uses the cuttings from these overlying clays. The modern day water depth at Sunbird-1, within the subsiding Tembo Trough, of 723.3 m means that the deposition of the cuttings used in this thesis took place at much shallower water depths than a typical ODP or IODP site used for palaeoclimatic reconstruction. However, quantifying the absolute palaeodepth through the Sunbird-1 cuttings is challenging. Assuming a constant rate of subsidence from subaerial exposure (0 m water depth) at 13.8 Ma to 723.3 m water depth in the modern day would mean that the water depth during deposition of the Sunbird-1 cuttings utilised by this thesis was always shallower than 231 metres. This is likely a simplified assumption, and a detailed analysis of depth sensitive benthic foraminifera, combined with the planktic foraminiferal to benthic foraminiferal ratio, could improve this palaeobathymetry assessment. However, an assumption that the palaeodepth remained shallower than 300 m is likely valid, and sufficiently quantitative, for the goals of this thesis.

Sunbird-1 also differs from more typical ODP and IODP sites used for palaeoclimate reconstructions in that siliceous microfossils such as diatoms and radiolarians are present. This interpretation of sediment deposition and accumulation in a high productivity setting could be further evidenced by redox sensitive trace metal (Chapter 3) and  $\delta^{13}\text{C}$  (Chapter 6) analyses on foraminifera.

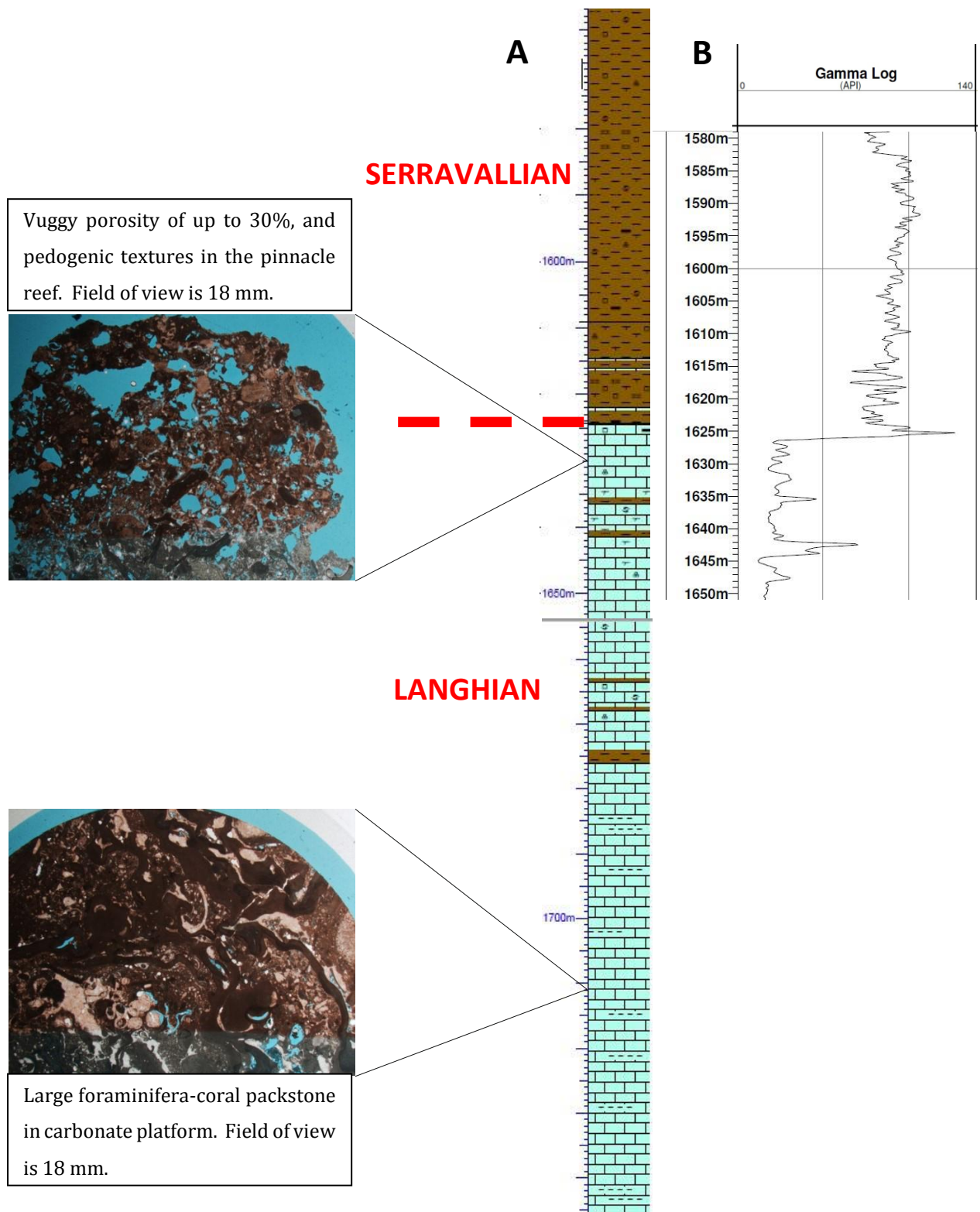


Figure 2.3: Lithological (A) and gamma ray (B) logs through the interval in which deposition at Sunbird-1 changed from autochthonous carbonate (1624m-), to pinnacle reef (1609-1624m), to clays (-1609m). The dashed horizontal line in (A) indicates the stratigraphic boundary separating the Langhian below, and the Serravallian above. Inset images of vuggy porosity in the pinnacle reef (1630m), and large foraminifera-coral packstone in the carbonate platform (1711m). Samples used in this thesis are from the 1626m cutting and above. Figure after (Beavington-Penney and Rowles, 2015).

The clay-dominated nature of the sediment means that throughout Sunbird-1 the fraction of sediment  $>63\mu\text{m}$  is low compared to an average deep-water site, ranging from 4.2%-21.1% with a mean value of 11.5% (Figure 2.4). This is most probably due to both the proximity of the site to the continent, resulting in a greater than expected input and deposition of terrestrial material. The uppermost 2 samples (1353-1356m and 1356-1359m) were rejected from the coarse fraction dataset due to the presence of concrete, emplaced by the drilling process, artificially raising the % coarse fraction. The highest percentage of coarse fraction is in the first  $\sim 500$  kyr of the record following which it fluctuates between  $\sim 5\%$  and  $\sim 15\%$  with no apparent periodicity (Figure 2.4). The higher % coarse fraction in the first  $\sim 500$ kyr of the record likely relates to the presence of limestone before the depositional environment becomes truly clay-dominated (Figure 2.3). This limestone is most probably sourced from the underlying pinnacle reef and carbonate platform, although localised regions of autochthonous carbonate cannot be ruled out. Between 11.8 Ma and 11.6 Ma there is a transient decrease in % coarse fraction. A full summary of the coarse fraction data is included in Appendix 1. To reduce the impact of diagenesis and alteration, foraminifera preserved in clay-rich sediments are preferentially used for analysis because they more likely preserve primary calcite; the impermeable nature of clays inhibiting diagenetic processes (Pearson et al., 2001, Sexton and Wilson, 2009). Tests displaying the desired exceptional preservation appear glassy and translucent under reflected light, and SEM imaging shows retention of the foraminiferal original microstructure (Pearson and Burgess, 2008). This style of preferential glassy preservation is rare to absent in published records from Miocene foraminifera.

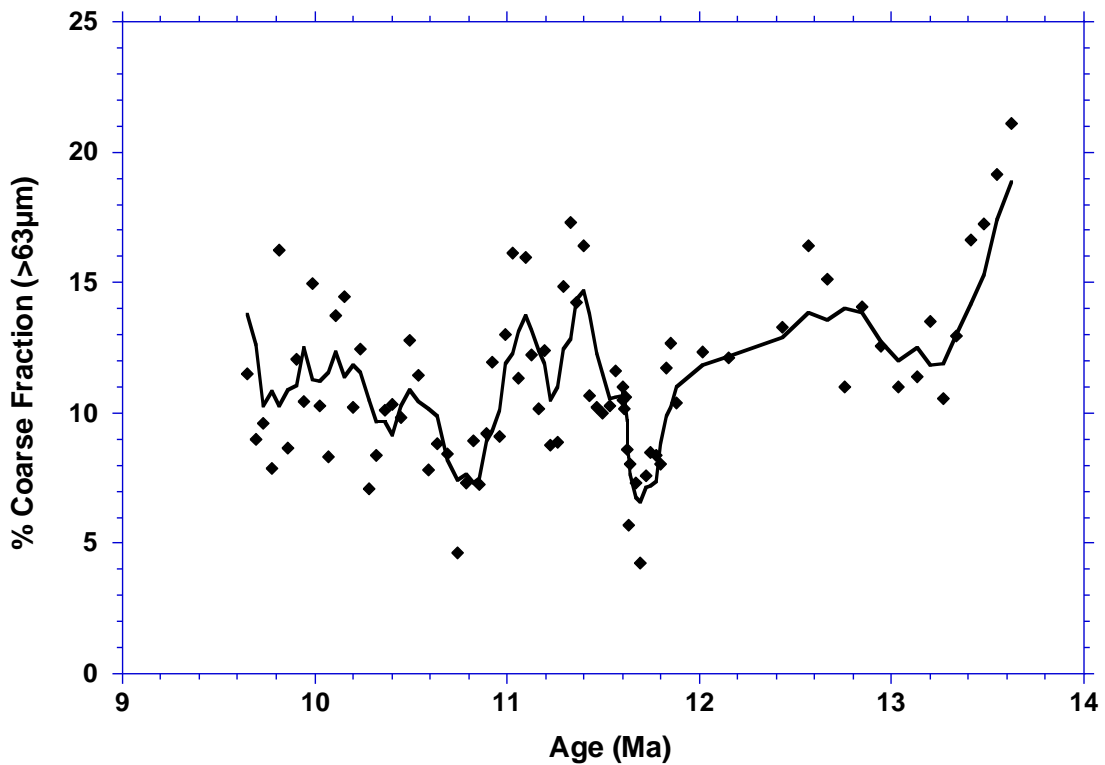


Figure 2.4: % Coarse Fraction (>63µm) in the Sunbird-1 record. Solid line denotes a 5 point moving average.

### 2.1.3 Biostratigraphic age model

Sunbird-1 recovery was continuous through the foraminifera bearing clay-rich sedimentary ooze from first returns at 1353 m until contact with the autochthonous carbonate at 1626 m (Figure 2.3). Samples were collected as cuttings at 3 m intervals, the 91 samples spanning 273 vertical metres of sediment at burial depths between 630 m and 903 metres below sea floor (mbsf). Throughout the thesis samples are generally referenced as metres below sea level (mbsl), in keeping with the original sampling during recovery. Micropalaeontological and calcareous nannoplankton assemblages for Sunbird-1 were analysed by Haydon Bailey and Liam Gallagher of Network Stratigraphic Consulting (Table 2.1). These microfossil assemblages, and the planktic foraminifera zonations of Wade et al. (2011) and calcareous

nanofossil zonations of Backman et al. (2012), were used to develop a biostratigraphic age model. Ages for reliable biostratigraphic datums were prescribed using these zonations and correlated with the Astronomical timescale of Lourens et al. (2004) included in Gradstein et al. (2004). The lowest reliable bioevent is the last downhole occurrence of *Globorotalia fohsi* in the 1611-1614 m sample, giving this depth a biostratigraphic age of 13.41 Ma. The highest bioevent is the first downhole occurrence of *Catinaster calyculus* in the 1368-1371 m sample, giving this depth a biostratigraphic age of 9.65 Ma. The 246 m of core between these reliable bioevents spans 3.76 million years (myr), yielding an average sedimentation rate of 6.5 cm/thousand years (kyr). Therefore, each sample represents 46 kyr on average.

The age-depth model was generated by linear interpolation between reliable biostratigraphic datums (Figure 2.5). The assumptions built into this age model, such as the linear interpolation, could contribute uncertainties of up to several thousands of years. However, it is the best possible age model in the absence of any magneto- or chrono-stratigraphy.

These biostratigraphic data suggest there are three distinctive periods of deposition (Figure 2.5). From the lowermost bioevent (last downhole occurrence of *Globorotalia fohsi*) at 1611-1614 m, to the last downhole occurrence of *Discoaster kugleri* at 1566-1569 m, the sedimentation rate is calculated at 2.9 cm/kyr. From this point, up to the first downhole occurrence of *Discoaster kugleri* at 1518-1521 m, the sedimentation rate is calculated at 17.1 cm/kyr, ~six times higher and being synchronous with the observed trough in % coarse fraction (Figure 2.4).

Sample Depth (MBSL)	Biostratigraphic Event		Biostratigraphic Age (Ma)
	Calcareous nannoplankton	Planktic foraminifera	
1368-1371	Top <i>C. calyculus</i>		9.65
1428-1431	Base <i>D. hamatus</i>		10.49
1446-1449	Base <i>C. coalitus</i>		10.79
1518-1521	Top <i>D. kugleri</i>		11.60
1539-1542		LDO <i>G. nepenthes</i>	11.63
1566-1569	Base <i>D. kugleri</i>		11.88
1581-1584	Top <i>C. praemacintyreii</i>		12.57
1599-1602		FDO <i>Globorotalia robusta</i>	13.13
1613-1614		LDO <i>G. foehsi</i>	13.41

Table 2.1: Biostratigraphic events used to generate the age-depth model for Sunbird-1, where FDO = First Downhole Occurrence, and LDO = Last Downhole Occurrence. The biostratigraphic datums of Wade et al., (2011) and Backman et al., (2012) are used, on the geomagnetic polarity timescale of (Gradstein et al., 2004). Sample depths are given as metres below sea level (water depth = 723 m).

Above this, until the uppermost bioevent (first downhole occurrence of *Catinaster calyculus*) at 1368-1371 m the sedimentation rate is 7.8 cm/kyr, not vastly different to the average for the whole core (6.5 cm/kyr). The lower accumulation rate of 2.9 cm/kyr prior to 11.8 Ma is surprising considering that the site of deposition would have been situated on the continental shelf where sedimentation rates are typically higher than on the continental slope. This suggests that prior to 11.8 Ma the rate of accumulation may be influenced by erosional currents or winnowing on the continental shelf and the possibility of hiatuses in deposition must be considered. This could explain the lower accumulation rate through this time interval, without having to invoke order of magnitude changes in sedimentation rate through the record of clays. This possibility must be considered in terms of its potential impact on the depositional and oceanographic environment the foraminifera used in this thesis. However, beyond the different accumulation rates of the sedimentary succession, there is no definitive evidence for hiatuses or erosional surfaces.

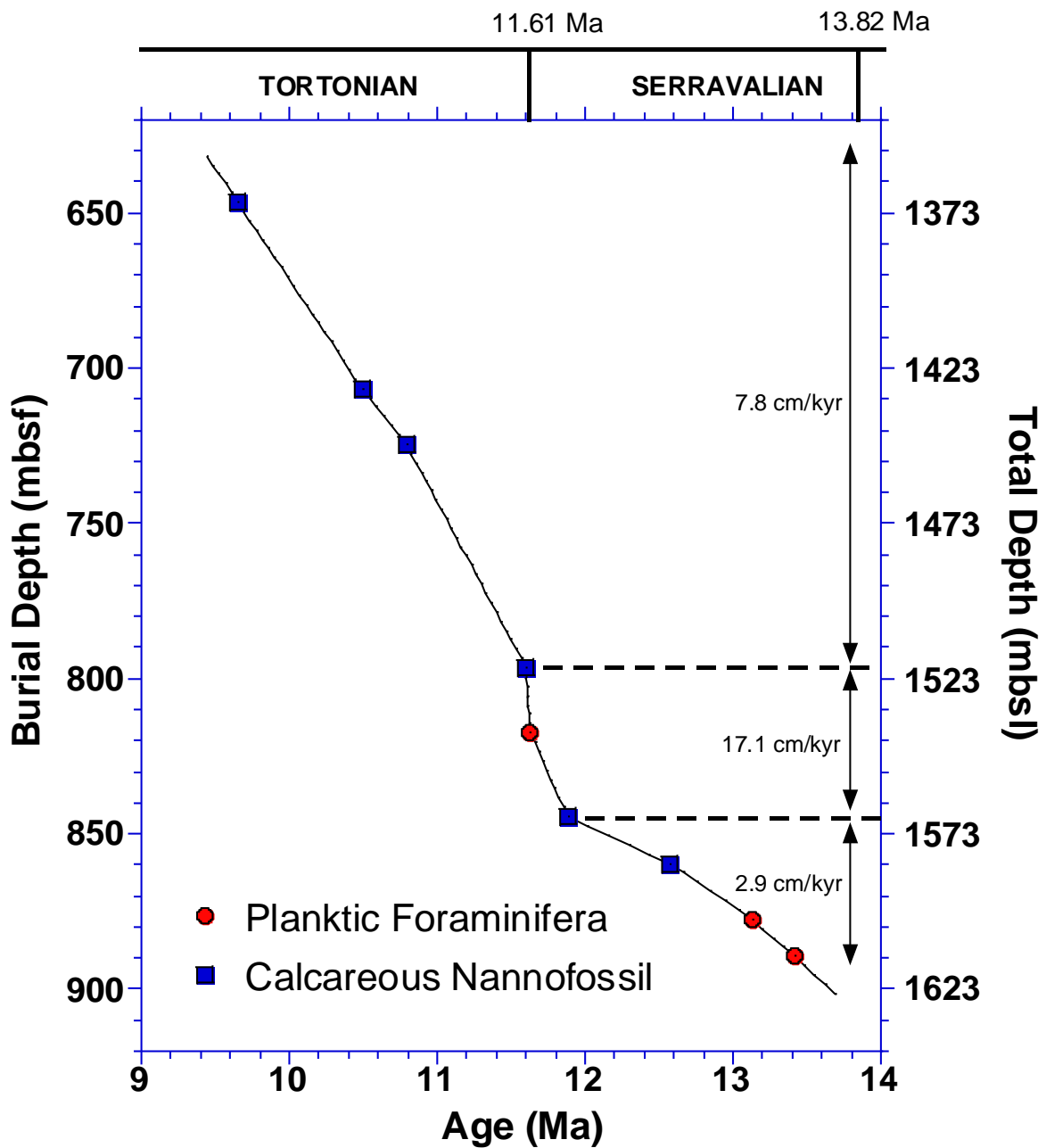


Figure 2.5: Age-depth model for Sunbird-1 using the biostratigraphic zonations of Wade et al. (2011) and Backman et al. (2012) on the geomagnetic polarity timescale of Gradstein et al. (2004) using linear interpolation between reliable biostratigraphic datums. Burial depth in the sediment and the total depth below the sea surface are given (water depth =723m). Micropalaeontological and calcareous nannoplankton assemblages for Sunbird-1 were analysed by Haydon Bailey and Liam Gallagher of Network Stratigraphic Consulting.

Taking the average sampling density of ~46 kyr and applying the Nyquist frequency ( $=1/2 \times$  sampling interval) suggests the highest frequency that can be resolved is ~92 kyr (Bendat and

Piersol, 1971). With this considered, the record is sampled at too low a resolution to adequately resolve orbital signals without potentially incorporating an aliasing effect of any precessional or obliquital periodicity into longer term eccentricity cycles (Pisias and Mix, 1988, Weedon, 2003). To interpret the shorter frequency orbital cycles sampling resolution would have to be increased 3-4 times. Therefore, to avoid any potential aliasing of orbital cyclicity only longer-term climate cycles (>100kyr) are interpreted, but note that the high sedimentation of the site would allow for this if piston coring had been utilised.

## 2.2 Geochemical proxies in foraminifera

This thesis chiefly uses foraminifera, a group of ubiquitous, single celled eukaryotes precipitating calcite tests composed of chambers, which grow successively and episodically through their lifespan, typically weeks to months. Almost all foraminifera are marine and can be either planktic or benthic. Planktic foraminifera float in the upper water column at varying depths and benthic foraminifera reside at the sea water to sediment interface. Some benthic foraminiferal species live in direct contact with bottom waters on top of the seafloor (epifaunal), whereas others inhabit the pore waters within the upper few centimetres of sediment (infaunal).

A foraminifer's calcium carbonate ( $\text{CaCO}_3$ ) test is formed from an internal calcification pool of modified ambient seawater. The chemical composition of fossil foraminiferal tests can be used to reconstruct ocean and climatic variability (e.g. temperature and salinity) through the Cenozoic and beyond, a carbonate archive of past ocean chemistry. All geochemical proxies, such as  $\delta^{18}\text{O}$  and Mg/Ca, have limitations and uncertainties inhibiting their use in isolation,

stressing the importance of utilising multiproxy approaches in palaeo-oceanographic studies. By adopting a multiproxy approach to reduce the degrees of freedom of a particular proxy it is possible to constrain the influence of the sought after palaeoenvironmental control, e.g. bottom water temperature and continental ice volume.

## 2.2.1 Stable isotopes

### 2.2.1.1 *Oxygen isotopes*

Stable oxygen isotope ratios in biogenic calcite have been used as a proxy for changes in Cenozoic climate since the original work of Harold Urey and Samuel Epstein (Urey, 1947, Urey et al., 1951, Epstein et al., 1951, Epstein et al., 1953), who determined the natural fractionation of stable isotope systems. Its use is based upon the fractionation between  $^{16}\text{O}$  and  $^{18}\text{O}$  during carbonate precipitation relative to an international reference standard (Equation 2.1). For carbonate, the standard is the Vienna Pee Dee Belemnite (VPDB), and for water the standard is Standard Mean Ocean Water (SMOW). Deviations from VPDB are customarily used with foraminiferal studies (Equation 2.1).

$$\text{Equation 2.1: } \delta^{18}\text{O} (\text{‰}) = \left( \frac{\left[ \left( \frac{^{18}\text{O}}{^{16}\text{O}} \right)_{\text{sample}} - \left( \frac{^{18}\text{O}}{^{16}\text{O}} \right)_{\text{standard}} \right]}{\left( \frac{^{18}\text{O}}{^{16}\text{O}} \right)_{\text{standard}}} \right) \times 1000$$

The  $\delta^{18}\text{O}$  of biogenic calcite varies inversely with the temperature at which it is precipitated from the water column, meaning it can be used as a palaeo-thermometer (Urey et al., 1951, Epstein et al., 1953, Emiliani, 1955). This inverse relationship between  $\delta^{18}\text{O}$  and temperature

is  $\sim 0.23\text{‰}/^{\circ}\text{C}$  (Kim and O'Neil, 1997, Bemis et al., 1998). The thermodynamic expectation is that of a quadratic fit between  $\delta^{18}\text{O}$  and temperature, but the degree of curvature to the quadratic fit is extremely slight meaning linear fits are also applicable within calibrated ranges (Shackleton, 1974, Bemis et al., 1998, Lynch-Stieglitz et al., 1999, Marchitto et al., 2014).

The other primary control on the  $\delta^{18}\text{O}$  of biogenic calcite is the  $\delta^{18}\text{O}$  of the seawater ( $\delta^{18}\text{O}_{\text{SW}}$ ). Isotopically heavier  $^{18}\text{O}$  is preferentially condensed and removed as precipitation at low latitudes due to Rayleigh Fractionation, the separation of gases during distillation. This distillation process causes precipitation to have isotopically lighter  $\delta^{18}\text{O}$  values at higher latitudes. Consequently, the  $\delta^{18}\text{O}$  of precipitation which is stored in polar ice sheets is isotopically lighter ( $-30$  to  $-50\text{‰}$ ) than seawater ( $\sim 0\text{‰}$ ). Therefore  $\delta^{18}\text{O}_{\text{SW}}$  can provide a record of global, continental ice volume due to preferential sequestration of  $^{16}\text{O}$  in polar ice sheets. The growth of continental ice sheets, such as East Antarctica and the Laurentide, equates to a  $\sim 0.011\text{‰}$  increase in  $\delta^{18}\text{O}_{\text{SW}}$  per metre fall in eustatic sea level during the cold Pleistocene world (Fairbanks, 1989). Despite the common assumption of heavier  $\delta^{18}\text{O}_{\text{ICE}}$  on Antarctica during the warmer world of the Miocene, this calibration is very similar to the  $0.0112\text{‰}$  increase in  $\delta^{18}\text{O}_{\text{SW}}$  determined using an isotope enabled model with high eccentricity, 500 ppm  $\text{CO}_2$ , and mid-Miocene topography (Gasson et al., 2016). A correction must be made to the  $\delta^{18}\text{O}_{\text{SW}}$  value due to it being measured on the SMOW scale, whereas  $\delta^{18}\text{O}_{\text{CALCITE}}$  is measured with respect to VPDB. This conversion factor is generally taken as  $-0.27\text{‰}$  (Hut, 1987).

Despite  $\delta^{18}\text{O}$  of biogenic calcite being predominantly controlled by temperature and  $\delta^{18}\text{O}_{\text{SW}}$ , some secondary effects must be considered, as outlined below.  $\delta^{18}\text{O}_{\text{SW}}$  has varied through geological time on hundred million year timescales due to chemical weathering and the alteration of seafloor basalts. However, the impact of this on  $\delta^{18}\text{O}_{\text{SW}}$  is likely negligible over the last 200 Myr (Veizer et al., 1997). Salinity effects resulting from evaporation-precipitation differences in a water masses source locality can lead to regional variations in  $\delta^{18}\text{O}_{\text{SW}}$  (LeGrande and Schmidt, 2006). Deep-water masses have differing salinities, dependent upon their source. For example North Atlantic Deep Water has a salinity of 34.9-35.0 PSU, whereas Antarctic Bottom Water has a salinity of 34.6-34.7 PSU. If unaccounted for a  $\delta^{18}\text{O}$  difference could result in misinterpretation of a temperature or ice volume signal. Carbonate ion concentration ( $[\text{CO}_3^{2-}]$ ) contributes a significant negative fractionation to the oxygen isotope ratio in planktic foraminifera (Spero et al., 1997). This  $[\text{CO}_3^{2-}]$  effect relates to pH, a -1.42‰ change in  $\delta^{18}\text{O}$  per unit pH increase (Zeebe, 2001). This offset originates from photosynthetic symbionts altering the pH of the seawater in the foraminifera's internal calcification pool. Thus, benthic foraminifera are unaffected as they reside below the photic zone, and are therefore asymbiotic. Despite being asymbiotic, changes in ocean pH will affect the  $\delta^{18}\text{O}$  of benthic foraminifera in the same direction.

Foraminifera, the carriers of the proxy signal, can calcify out of equilibrium with sea water due to vital effects during biogenic precipitation. Differences in the  $\delta^{18}\text{O}$  palaeotemperature equations of benthic foraminifera from the *Cibicidoides* and *Planulina* genera are well within analytical error and, therefore, are commonly grouped together (Lynch-Stieglitz et al., 1999, Marchitto et al., 2014). Their temperature sensitivity agrees with that of inorganic calcite,

allowing the assumption that these genera of benthic foraminifera calcify in isotopic equilibrium with sea water (Marchitto et al., 2014). Infaunal and epifaunal benthic foraminifera calcify in environments with different pH levels causing offsets between species living in the differing settings (Bemis et al., 1998). Young individuals often display a slight negative offset interpreted as an ontogenetic effect by the incorporation of oxygen from metabolic CO<sub>2</sub> (Filipsson et al., 2010). These vital, microhabitat, and ontogenetic effects can be reduced by conducting single species analyses in downcore studies.

Diagenetic overprinting of the primary calcite is a major caveat associated with foraminiferal  $\delta^{18}\text{O}$  (Schrag, 1999, Pearson et al., 2001). This can occur via dissolution on the sea floor, and within the sediment, increasing the  $\delta^{18}\text{O}_{\text{CALCITE}}$ , particularly in low pH waters. Secondary calcite cements precipitated, either into or onto the outside of the test, from pore waters during early stage burial diagenesis can also obscure any primary signal by altering the oxygen isotopic ratios. Diagenetic recrystallization is a particular caveat with planktic foraminiferal  $\delta^{18}\text{O}$  ratios from low latitude sites because it takes place in deep waters that are considerably cooler than the surface waters from which the primary calcite formed (Pearson, 2012, Edgar et al., 2013). This increases planktic foraminiferal  $\delta^{18}\text{O}$ , reconstructing artificially cooler sea surface temperatures. Diagenetic alteration of benthic foraminiferal  $\delta^{18}\text{O}$  is less of a problem due to the relative constancy of habitat. Despite significant inter-site differences in recrystallization, negligible offsets in benthic foraminiferal  $\delta^{18}\text{O}$  are observed (Edgar et al., 2013). Therefore, the benthic foraminifera preserved in deep-marine sedimentary oozes are regarded as robust recorders of primary  $\delta^{18}\text{O}$ . To reduce the impact of diagenesis and alteration, foraminifera preserved in impermeable clay rich sediments, which inhibit any

diagenetic effects, are preferentially used for analysis because they more likely preserve primary calcite (Wilson and Opdyke, 1996, Pearson et al., 2001). Tests displaying this desired exceptional preservation tend to appear glassy and translucent under reflected light and have retained their primary submicron texture (Pearson and Burgess, 2008). Unfortunately, this idealised scenario is relatively rare, recrystallization of calcite tests at the sea floor being routine.

#### 2.2.1.2 Carbon isotopes

As with  $\delta^{18}\text{O}$  the stable carbon isotope ratio ( $\delta^{13}\text{C}$ ) of carbonates is measured relative to the VPDB standard (Equation 2.2).

$$\text{Equation 2.2: } \delta^{13}\text{C} (\text{‰}) = \left( \frac{\left[ \left( \frac{^{13}\text{C}}{^{12}\text{C}} \right)_{\text{sample}} - \left( \frac{^{13}\text{C}}{^{12}\text{C}} \right)_{\text{standard}} \right]}{\left( \frac{^{13}\text{C}}{^{12}\text{C}} \right)_{\text{standard}}} \right) \times 1000$$

The  $\delta^{13}\text{C}$  of biogenic calcite is predominantly determined by the  $\delta^{13}\text{C}$  of the total dissolved inorganic carbon (DIC) of the seawater it precipitates from. Seawater  $\delta^{13}\text{C}$  ( $\delta^{13}\text{C}_{\text{sw}}$ ) varies with the global carbon cycle, because different reservoirs of carbon have different  $\delta^{13}\text{C}$  values. The relative fluxes between seawater and these reservoirs drives changes in  $\delta^{13}\text{C}_{\text{sw}}$ . In particular, the preferential uptake of  $^{12}\text{C}$  during photosynthesis results in organic carbon ( $\text{C}_{\text{org}}$ ) having isotopically lighter  $\delta^{13}\text{C}$  values. Therefore, surface waters are characterised by isotopically heavier  $\delta^{13}\text{C}$  than deeper waters. Enhanced global burial of organic carbon increases the  $\delta^{13}\text{C}$  of the whole ocean reservoir, reflected by isotopically heavier  $\delta^{13}\text{C}$  values in biogenic calcite

precipitated from seawater. A key control on the local  $\delta^{13}\text{C}_{\text{sw}}$  signature is the degree of organic matter (OM) oxidation in the upper water column. In high primary productivity regions, the enhanced biological fixation of the preferentially lighter isotope of carbon increases the  $\delta^{13}\text{C}$  of local surface waters, whilst the associated enhanced remineralisation of sinking organic matter lowers the  $\delta^{13}\text{C}$  of deeper waters.

Secondary factors have an influence on the  $\delta^{13}\text{C}$  of biogenic calcite. A number of these are due to foraminifera calcifying from an internal pool within which they biologically mediate pH, which in turn influences DIC,  $[\text{CO}_3^{2-}]$ , and  $\delta^{13}\text{C}$  levels (Spero et al., 1997, Zeebe, 1999, Evans et al., 2016, Gray et al., 2018). These secondary factors require consideration when interpreting changes in the local and global carbon cycle from foraminiferal  $\delta^{13}\text{C}$ .

## 2.2.2 Trace element/calcium ratios

### 2.2.2.1 *Mg/Ca*

The substitution of  $\text{Mg}^{2+}$  ions into the calcite lattice in place of  $\text{Ca}^{2+}$  ions is endothermic, forming the thermodynamic principle for the use of Mg/Ca ratios in calcite as a palaeotemperature proxy. The partition coefficient of  $\text{Mg}^{2+}$  into inorganic calcite has a strong positive correlation with temperature, increasing exponentially by  $3.1 \pm 0.4\%$  per  $^{\circ}\text{C}$  (Katz, 1973, Oomori et al., 1987, Burton and Walter, 1991). Initial culture studies of planktic foraminifera (Nürnberg, 1996, Nürnberg et al., 1996, Lea et al., 1999) and core top studies of benthic and planktic foraminifera (Rosenthal et al., 1997, Elderfield and Ganssen, 2000, Lear et al., 2002) support this temperature control on Mg/Ca ratios of biologically precipitated foraminiferal calcite. However, this initial work showed the incorporation of Mg into

foraminiferal calcite to be ~3 times more sensitive to temperature, showing relatively consistent sensitivities of ~9-10% per °C. This higher sensitivity suggests that there is an additional temperature effect on Mg uptake into foraminiferal tests resulting from biologically mediated processes. This “vital effect” on Mg incorporation into foraminifera is likely due to fractionation within an internal calcification pool (Elderfield et al., 1996, Bentov and Erez, 2006), but the exact process remains up for debate, necessitating the need for species-specific calibrations. Having said this, one recent calibration study suggests that planktic foraminiferal Mg/Ca-temperature sensitivity is closer to 6% per °C (Gray et al., 2018). These authors reconcile this sensitivity with previous calibrations through the temperature effect on the dissociation of water, i.e. temperature influences foraminiferal Mg/Ca both directly and indirectly via the pH effect. In the absence of high resolution pH records through the Sunbird-1 interval, the approach of Evans et al. (2016) to calculate Mg/Ca palaeotemperatures is followed (Chapter 5.3).

Whereas temperature calibrations from planktic foraminifera exhibit very good cross species agreement of ~9% per °C (Elderfield and Ganssen, 2000, Anand et al., 2003), there are significant differences between benthic foraminiferal species (Lear et al., 2002, Elderfield et al., 2006); *Uvigerina spp.* displaying much lower (~6% per °C) temperature sensitivity (Lear et al., 2002, Elderfield et al., 2006, Bryan and Marchitto, 2008). Despite these poorly understood biological (vital) effects, temperature remains the overriding control on foraminiferal Mg/Ca ratios, and studies using individual species are considered relatively robust recorders of relative changes in temperature.

The use of benthic foraminiferal Mg/Ca as an independent palaeotemperature proxy can solve the “Urey Dilemma” by providing simultaneous records of bottom water temperature and  $\delta^{18}\text{O}_{\text{sw}}$  controlled primarily by global continental ice volume (Lear et al., 2000, Billups and Schrag, 2002, Lear et al., 2015).

The influence of several secondary effects on Mg incorporation into foraminiferal calcite have been described. These include, but may not be limited to, changes in the carbonate saturation state ( $\Delta[\text{CO}_3^{2-}]$ ) (Russell et al., 2004, Elderfield et al., 2006, Rosenthal et al., 2006, Evans et al., 2016, Gray et al., 2018), salinity (Kisakürek et al., 2008, Hönisch et al., 2013, Gray et al., 2018), and seawater Mg/Ca ( $\text{Mg}/\text{Ca}_{\text{sw}}$ ) (Hasiuk and Lohmann, 2010, Evans and Müller, 2012). The potential influence of these secondary effects are considered, and accounted for, when transforming foraminiferal Mg/Ca ratios to absolute temperature estimates in Chapter 5.3. However, the shallow (723m in the modern) water depth of Sunbird-1 minimizes any effect of dissolution on planktic foraminiferal Mg/Ca (Tripathi et al., 2003), and  $\Delta[\text{CO}_3^{2-}]$  effect on benthic foraminiferal Mg/Ca (Elderfield et al., 2006). The 1-Myr residence time of Ca in seawater limits the use of trace element/calcium ratios to relative changes unless the seawater ratio can be reconstructed over longer intervals, for example  $\text{Mg}/\text{Ca}_{\text{sw}}$  when deducing absolute palaeotemperatures

Further alteration of the primary, temperature controlled, foraminiferal Mg/Ca ratio can take place post-depositionally (Edgar et al., 2015). Elevated pressures and temperatures in thick sedimentary sequences can cause recrystallization via neomorphic dissolution-precipitation processes. This can alter the primary foraminiferal calcite, elevating Mg/Ca ratios towards

those of inorganic calcite (Katz, 1973, Nurnberg et al., 1996, Pearson et al., 2001). Despite the higher partition coefficient of Mg into inorganic calcite when compared to foraminiferal calcite, Mg/Ca ratios are not affected to the same degree as  $\delta^{18}\text{O}$  by recrystallisation. This is likely due to recrystallization taking place in a relatively closed system (Elderfield et al., 1996, Bentov and Erez, 2006, Edgar et al., 2015). Conversely, dissolution lowers the Mg/Ca ratio because high Mg calcite preferentially dissolves (McCorkle et al., 1995, Brown and Elderfield, 1996, Rosenthal and Lohmann, 2002). Diagenetic overgrowths and contaminant phases, such as authigenic carbonates, oxide coatings and oxy-hydroxides, can artificially alter the primary foraminiferal Mg/Ca ratio (Pena et al., 2005, Hasenfratz et al., 2016). Ideally, studies should target foraminifera devoid of any post-depositional alteration.

#### 2.2.2.2 *Benthic foraminiferal Sr/Ca*

The Sr/Ca ratio of the aragonitic benthic foraminifera *Hoeglundina elegans* can be used to estimate bottom water temperatures (Rosenthal et al., 2006, Lear et al., 2008, Lo Giudice Cappelli et al., 2015). This is due to the  $\text{Sr}^{2+}$  cation having a better fit into the aragonitic lattice than  $\text{Mg}^{2+}$ . The Sr/Ca ratios for *H. elegans* show no covariance with the aragonite saturation state ( $\Delta[\text{CO}_3^{2-}]_{\text{aragonite}}$ ) when it is above  $\sim 15 \mu\text{mol kg}^{-1}$  (Rosenthal et al., 2006). However, the influence of  $\Delta[\text{CO}_3^{2-}]_{\text{aragonite}}$  complicates BWT reconstructions in waters undersaturated with respect to aragonite.

#### 2.2.2.3 *Benthic foraminiferal B/Ca*

Empirical core top studies show a positive, linear relationship between B/Ca ratios in benthic foraminifera and bottom water carbonate saturation state ( $\Delta[\text{CO}_3^{2-}]$ ). This correlation has

been proven to be robust at high  $\Delta[\text{CO}_3^{2-}]$  and across a wide range of ocean basins, water depths, and bottom water temperatures (Yu and Elderfield, 2007, Yu et al., 2010, Brown et al., 2011, Rae et al., 2011).

The B/Ca ratio in benthic foraminifera appears to be insensitive to any dissolution effect (Yu and Elderfield, 2007, Brown et al., 2011, Rae et al., 2011), and the long (15-20Myr) residence time of boron in seawater (Spivack and Edmond, 1987, Lemarchand et al., 2000, Lemarchand et al., 2002) means that if seawater B/Ca ( $B/Ca_{sw}$ ) can be constrained. Any variations in benthic foraminiferal B/Ca can therefore be attributed to changes in  $\Delta[\text{CO}_3^{2-}]$  obtained during biological precipitation.

There are very large interspecies differences in benthic foraminiferal B/Ca ratios. Of particular importance is that infaunal species (e.g. *Uvigerina spp.* and *Oridorsalis umbonatus*) display lower sensitivity to, and absolute values of,  $\Delta[\text{CO}_3^{2-}]$  than epifaunal species (e.g. *C. wuellerstorfi* and *C. mundulus*) (Yu and Elderfield, 2007, Rae et al., 2011, Brown et al., 2011, Mawbey, 2012). Infaunal foraminifera calcify from sedimentary pore waters as opposed to the oceanic bottom waters so are largely insensitive to deep water  $\Delta[\text{CO}_3^{2-}]$ , the effect of pore water buffering dampening any correlation (Brown et al., 2011). This notion is reinforced by the very low correlation between B/Ca and bottom water  $\Delta[\text{CO}_3^{2-}]$  in *Uvigerina spp.* ( $R^2=0.58$  (Yu and Elderfield, 2007)) and *Oridorsalis umbonatus* ( $R^2=0.31$  (Brown et al., 2011)).

## 2.3 Sample collection and processing

The Sunbird-1 well was drilled between January and March 2014 by BG Kenya, with the primary aim of sampling the mid-late Miocene carbonate platform and overlying pinnacle reef (Figure 2.3). Through the overlying clay-dominated sediment cuttings were collected at a 3 m sampling resolution, bagged, and stored for analysis.

Approximately 100 g of each sample was weighed and washed through a 63  $\mu\text{m}$  sieve using 18.2 M $\Omega$  DI water to isolate the coarse fraction for foraminiferal analyses. The <63  $\mu\text{m}$  size fraction was allowed to settle and dry before being archived. The >63  $\mu\text{m}$  fraction was dried overnight in a 40 °C oven, and weighed to determine the % coarse fraction. This coarse fraction was then dry-sieved and individual foraminiferal species were picked from the 250-355  $\mu\text{m}$  size fraction under a binocular microscope.

## 2.4 Stable isotope analysis

Picked foraminifera were crushed between two glass plates ensuring all chambers were opened. Any infill was removed as best as possible using a fine paintbrush under a binocular microscope. Fine clays and other detrital material on the outer surface of the test were removed by rinsing three times in 18.2 M $\Omega$  DI water, ultrasonicated for 5-10 seconds in methanol, and finally rinsing a further time in 18.2 M $\Omega$  DI water. Any remaining detrital particles were removed using a fine paintbrush under a binocular microscope. Once dried, samples were transferred into glass vials and analysed on a ThermoFinnigan MAT252 with online sample preparation using an automated Kiel III carbonate device. Results are reported

relative to PDB, and long-term uncertainty based on repeat analysis of NBS-19 is  $\pm 0.04$  ‰ for  $\delta^{13}\text{C}$  and  $\pm 0.08$  ‰ for  $\delta^{18}\text{O}$  ( $n=469$ , 2 standard deviations) and on repeat analysis of BCT63 is  $\pm 0.04$  ‰ for  $\delta^{13}\text{C}$  and  $\pm 0.07$  ‰ for  $\delta^{18}\text{O}$  ( $n=310$ , 2 standard deviations).

## 2.5 Trace element analysis via solution ICP-MS

As with the preparation of samples for stable isotope analysis, picked foraminifera were crushed between two glass plates ensuring all chambers were opened, and any infill was removed as best as possible using a fine paintbrush under a binocular microscope. The samples were subsequently ultrasonicated in water and methanol to remove clays and oxidized with 3%  $\text{H}_2\text{O}_2$  to remove organic matter. Any remaining detrital particles were removed using a fine paintbrush under a binocular microscope. Fragments were cleaned to remove clays, metal oxides, and organic matter following the standard protocol (Boyle and Keigwin, 1985, Barker et al., 2003) (Appendix 2). Due to the clay rich nature of the sediment the clay removal procedure was conducted twice.

Samples were dissolved in 120  $\mu\text{l}$  of trace metal pure 0.065 M  $\text{HNO}_3$  and centrifuged to assist removal of any remaining contaminant particles. This solution was then split into two aliquots of 10  $\mu\text{l}$  and 100  $\mu\text{l}$  respectively to measure calcium concentrations and trace metal ratios. The 10  $\mu\text{l}$  aliquot for measuring calcium concentrations was diluted with trace metal pure 0.5M  $\text{HNO}_3$  to a final volume of 200  $\mu\text{l}$  and the calcium concentrations of each sample were determined. This enabled standards with the same calcium concentrations as the samples to be made up to reduce matrix effects during trace element analysis (Lear et al., 2002, Lear et al., 2010). The 100  $\mu\text{l}$  aliquot for trace metal analysis was diluted with trace metal pure 0.5M

HNO<sub>3</sub> to a final volume of 350 µl. Samples were analysed at Cardiff University on a Thermo Element XR magnetic sector field HR ICP-MS against the standards with matched calcium concentration.

Samples with a boron intensity signal less than five times greater than the analytical blank were discarded. Isotope counts were blank corrected by subtracting the previous blank in the sequence, and blank corrected trace metal/calcium ratios (TM/Ca) were calculated. Together with the TM/Ca ratios of interest (B/Ca, Mg/Ca, and Sr/Ca, U/Ca), several other ratios (Al/Ca, Mn/Ca, and Fe/Ca) were analysed to screen for potential contaminant phases, in spite of the cleaning steps described above.

Two independent consistency standards (CS1 and CS2) with Mg/Ca ratios of 1.24 mmol/mol and 7.15 mmol/mol were respectively analysed at the beginning and end of every run to assess the analytical precision and long-term reproducibility. Analytical precision (2 standard deviation of the measure value/reported value) for Mg/Ca analyses throughout the study is ±1.39 % for CS1 and ±2.39 % for CS2, respectively. External reproducibility (%RSD) over the whole time period of this study is ±0.70 % and ±0.64 % respectively.

## 2.6 Trace element analysis via laser ablation ICP-MS

Laser ablation ICP-MS (LA-ICP-MS) is a microanalytical technique that allows the *in situ* geochemical analysis of individual foraminifera making it extremely useful in palaeo-oceanographic studies (Eggins et al., 2003, Hathorne et al., 2003, Reichart et al., 2003, Evans

et al., 2015a). The facilitation of highly spatially resolved analyses by LA-ICP-MS means that information about any influence of post-depositional diagenetic alteration on the foraminiferal geochemistry can be assessed (Hathorne et al., 2003, Pena et al., 2005, Creech et al., 2010, Hasenfratz et al., 2016). In December 2016, a new ArF excimer (193nm) LA-system with dual-volume laser-ablation cell (RESOLUTION S-155, Australian Scientific Instruments) was installed in the Cardiff University CELTIC laboratory. This was coupled to the Thermo Element XR magnetic sector field HR ICP-MS for LA-ICP-MS analyses. Chapter 4 provides a detailed optimisation and development of the system for the acquisition of geochemical depth profiles through foraminifera, which is then subsequently applied in Chapter 5.

National Institute of Standards and Technology (NIST) Standard Reference Material (SRM) 612 was used as the consistency standard throughout, and was calibrated for long term external accuracy and precision (reproducibility) using NIST SRM 610, the external standard. Both accuracy (Measured Value/Reported Value) and precision (2 x Standard Deviation of the Measured Values/ Reported Value) are given relative to reported values taken from the GeoRem database (<http://georem.mpch-mainz.gwdg.de/>) in January 2018 (Table 2.2). Calcium ( $^{43}\text{Ca}$ ) is used as the internal standard throughout, assuming Ca is homogenous and well characterised in both glass standards. This assumption is likely valid due to it being a major constituent of both NIST 610 and NIST 612. NIST 610-calibrated NIST 612 precision is 3.7% (n=90)). This is very low considering both glasses have been shown to contain significant Mg heterogeneity, 6.7% and 7.5% for NIST 610 and NIST 612 respectively (Jochum et al., 2011). The accuracy of the NIST 610-calibrated NIST 612 data is comparatively poor, which is

surprising considering the excellent long term calibrated precision. The Mg/Ca ratio of measured NIST 612 when calibrated to NIST 610 ranges from 7.8% to 15.8% below the reported value, with a mean offset of 12.0% (n=90) below the reported value. A similar offset has been observed over a much longer period of data collection (Evans and Müller, 2018). The NIST 610-calibrated data presented here supports the determination of Evans and Müller (2018) that the Mg values for both NIST 610 and NIST 612 require reassessment.

	<b>NIST 610</b>	<b>NIST 612</b>
<b>Mg/Ca (mmol/mol)</b>	8.75 ± 0.37	1.32 ± 0.54
<b>Al/Ca (mmol/mol)</b>	188.3 ± 2.74	187.8 ± 2.63
<b>Mn/Ca (mmol/mol)</b>	3.98 ± 0.02	0.33 ± 0.11
<b>Sr/Ca (mmol/mol)</b>	2.90 ± 0.07	0.42 ± 0.01

Table 2.2: Reported values (converted to mmol/mol) from the GeoRem database (<http://georem.mpch-mainz.gwdg.de/>) in January 2018 used in this study. Uncertainty is derived from the 95% confidence interval for each isotope. Values are corrected to NIST 610 in this thesis.

Improved accuracy and precision of Mg/Ca data may have been possible if reference materials with more homogenous Mg compositions had been used, in particular GOR128-G (Evans et al., 2015b). Unfortunately, the MPI-DING suite of glass reference materials only became available to the CELTIC Laboratory after this study. It is recommended that future analyses use MPI-DING reference glasses as a calibration standard for Mg/Ca data, instead of using NIST 610 or NIST 612.

Data processing was performed using the SILLS software (Guillong et al., 2008) following the established protocols of Longerich et al. (1996).

### **3 Changing redox conditions at Sunbird-1 and its influence on benthic foraminiferal Mg/Ca**

#### **3.1 Introduction**

The trace metal composition of benthic foraminifera has been used to reconstruct changes in many different environmental parameters through time (e.g. temperature (Mg/Ca) (Nürnberg et al., 1996, Lear et al., 2000, Sosdian and Rosenthal, 2009), carbonate saturation state (B/Ca) (Yu and Elderfield, 2007, Babila, 2014, Henehan et al., 2015), and redox conditions (U/Ca, Mn/Ca, Fe/Ca) (Boiteau et al., 2012, Koho et al., 2015, Chen et al., 2017, Petersen et al., 2018)). Changing sedimentary redox conditions are of particular interest as they can be influenced by changes in overlying primary productivity or bottom water oxygen content, and can hence offer a window into the ocean carbon cycle (Jaccard et al., 2009, Chen et al., 2017). These redox-sensitive proxies are based on the extent and composition of coatings that can form on foraminiferal tests in the sediment during early diagenesis. In many cases the Mg/Ca foraminiferal cleaning technique successfully removes such coatings (Barker et al., 2003). In some cases, however, the extent of the coatings is too severe to be completely removed by the cleaning process. In these cases, the presence of the coatings also acts as a warning flag, because the coatings may contain other elements (e.g., magnesium) that can bias downcore Mg/Ca and hence palaeotemperature records (Hasenfratz et al., 2016). Another common contaminant of foraminiferal Mg/Ca records is detrital silicates (clays), which can either be lodged inside test pores or physically bound up in such diagenetic coatings (Lea et al., 2005). Therefore, aluminium, manganese, iron, and uranium are commonly used as indicators for foraminiferal contamination. They are suggestive of the presence of non-

calcite bound phases such as detrital silicates, oxyhydroxides, ferro-manganese or oxide coatings, and secondary carbonates.

Detrital silicates, in particular clays, are characterised by elevated ( $>100 \mu\text{mol/mol}$ ) and covarying Al/Ca and Fe/Ca ratios (Barker et al., 2003, Lea et al., 2005). When foraminiferal Mn/Ca exceeds  $100 \mu\text{mol/mol}$  (Boyle, 1983), its role as a potential contaminant must be assessed (Barker et al., 2003). Phases rich in manganese are commonly Mn carbonates, Mn-Fe-oxides, and Mn-Fe-oxyhydroxides, all of which can contain magnesium from a secondary source (Boyle, 1983, Boyle and Keigwin, 1985, Pena et al., 2005, Pena et al., 2008, Hasenfratz et al., 2016). If these trace metal/calcium ratios are elevated in concert with high Mg/Ca values, the possibility of a diagenetic contribution to the Mg/Ca record, obscuring the primary palaeotemperature signal, has to be considered. Removal of any contaminant signal from the foraminiferal Mg/Ca must be achieved to successfully reconstruct bottom water temperature.

Here, a suite of trace metal records from three benthic foraminiferal species from Sunbird-1 is presented. that documents an unusually large decrease in the concentrations of redox sensitive metals in the late Miocene. While this implies a significant change in local redox conditions, it also implies that the corresponding downcore Mg/Ca records should not be interpreted solely in terms of bottom water temperature. The effectiveness of a potential new approach to correct for the diagenetic overprinting of the Mg/Ca is explored. Finally, the records are used to identify which trace metal proxies are more robust to this form of

diagenetic alteration, and an alternative approach for generating Mg/Ca-palaeotemperatures at this site is proposed.

#### Summary of Scientific Experiments:

- This chapter presents trace metal data from three species' of benthic foraminifera, *Cibicoides wuellerstorfi*, *Uvigerina peregrina*, and *Hoeglundina elegans*, from the Sunbird-1 well, analysed via solution based ICP-MS after a thorough chemical cleaning protocol.
- Both palaeotemperature proxies (Mg/Ca for the two calcite species and Sr/Ca for the aragonitic *H. elegans*) record values far greater than the expected range of bottom water temperatures.
- The Mg/Ca records demonstrate downcore point-to-point correlation with redox-sensitive trace metal proxies, Mn/Ca, U/Ca, and Fe/Ca, indicating that Mg/Ca is not recording a primary temperature signal, but is influenced by post-depositional contamination within the upper sediment.
- Attempts were made to identify and correct for the Mg-rich contaminant phase by using paired calcite-aragonite results, in particular by applying the Mg/Fe ratio of the aragonitic *H. elegans*.

## 3.2 Materials and methods

### 3.2.1 Species selection

Three species of benthic foraminifera were analysed, the calcitic *Cibicidoides wuellerstorfi* and *Uvigerina peregrina*, and the aragonitic *Hoeglundina elegans*, from up to 30 sample depths in the Sunbird-1 core. In some samples benthic foraminifera were very sparse, or even absent, so analyses were not possible in nine samples of *C. wuellerstorfi*, six samples of *U. peregrina*, and three samples of *H. elegans* (Appendix 3). This is likely due to the shallow water depth (<300 m) of Sunbird-1, in which benthic foraminifera, in particular *C. wuellerstorfi*, can be extremely rare or even absent (Lutze and Thiel, 1989).

The two calcite species were selected due to their differing life habitats, allowing for the assessment of any microhabitat effect on trace metal uptake. Variations exist in the chemistry of bottom waters and the upper few centimetres of pore waters, imparting a microhabitat effect on trace element incorporation (Tachikawa and Elderfield, 2002). Despite being only a few centimetres apart or less, these microhabitats may have very different carbonate chemistry, playing a pivotal role on foraminiferal Mg/Ca ratios widely used palaeotemperature proxy on a wide range of timescales through the Cenozoic (Rosenthal et al., 1997, Lear et al., 2000, Sosdian and Rosenthal, 2009, Elderfield et al., 2010, Lear et al., 2010, Mawbey and Lear, 2013).

*C. wuellerstorfi* lives in epifaunal environments (Lutze and Thiel, 1989), precipitating its test from the bottom water, and has been extensively used for Mg/Ca determined bottom water temperature reconstructions (Lear et al., 2002, Elderfield et al., 2006, Hillaire-Marcel and de

Vernal, 2007). However, carbonate saturation state ( $\Delta[\text{CO}_3^{2-}]$ ) impacts upon the Mg/Ca of benthic foraminifera, potentially obscuring any bottom water signal in waters with low carbonate saturation state (Chapter 2.2.2.1) (Rosenthal et al., 2006, Yu and Elderfield, 2008). This is especially noticeable with calibrations at cold bottom water temperatures  $<4^\circ\text{C}$  where there is often a strong decrease in  $\Delta[\text{CO}_3^{2-}]$  in the modern oceans (Martin et al., 2002, Healey et al., 2008). Infaunal species, such as *U. peregrina*, are potentially less susceptible to the influence of changing bottom water  $\Delta[\text{CO}_3^{2-}]$ ; a result of the pore waters they precipitate from being buffered against changes in carbonate saturation state,  $\Delta[\text{CO}_3^{2-}]$  tending to zero in the top  $\sim 10$  cm of the sediment column (Martin and Sayles, 1996, Zeebe, 2007). This buffering of  $\Delta[\text{CO}_3^{2-}]$  in pore waters means the effect of  $\Delta[\text{CO}_3^{2-}]$  in infaunal species of foraminifera should be more constant. Consequently, infaunal species calcifying from these pore waters might provide a more reliable record of bottom water temperature (Elderfield et al., 2010, Mawbey and Lear, 2013). It should be noted however that the influence of pore water buffering may not be constant (Mawbey and Lear, 2013), and infaunal foraminiferal Mg/Ca is not necessarily devoid of any influence by bottom water  $\Delta[\text{CO}_3^{2-}]$  variation (Weldeab et al., 2016).

Unlike foraminifera that secrete calcitic tests, the aragonitic *Hoeglundina elegans* shows no consistent relationship between Mg/Ca and bottom water temperature, with sensitivities ranging from 3%-16% per  $1^\circ\text{C}$  change (Rosenthal et al., 2006, Bryan and Marchitto, 2008, Ní Fhlaithearta et al., 2010, Lo Giudice Cappelli et al., 2015). Because of its aragonitic mineralogy *H. elegans* more readily accepts  $\text{Sr}^{2+}$  into its test in place of  $\text{Ca}^{2+}$ , aragonite having a partition coefficient ( $K_{\text{Sr}^{\text{arag}}}$ ) ten times that of calcite (Katz et al., 1972). Consequently, calibrations between bottom water temperature and core top *H. elegans* Sr/Ca have proven more

successful (Rosenthal et al., 2006, Lo Giudice Cappelli et al., 2015). Furthermore, *H. elegans* might be very useful for sites where contamination by high-Mg coatings may potentially cause problems with the analysis of calcitic foraminiferal tests.

### 3.2.2 Trace metal analysis

Up to 15 individuals of each species of benthic foraminifera were picked from the 250–355  $\mu\text{m}$  size fraction. In some instances sample mass was sacrificed in favour of ensuring that only foraminifera displaying well preserved tests were selected (Figure 3.1). Samples were crushed between two glass plates ensuring all chambers were opened and chemically cleaned following a published protocol that included clay removal, oxidising and reducing steps (Boyle and Keigwin, 1985, Barker et al., 2003) (Appendix 2). Each sample was analysed for trace element/calcium ratios via solution ICP-MS (Chapter 2.5).

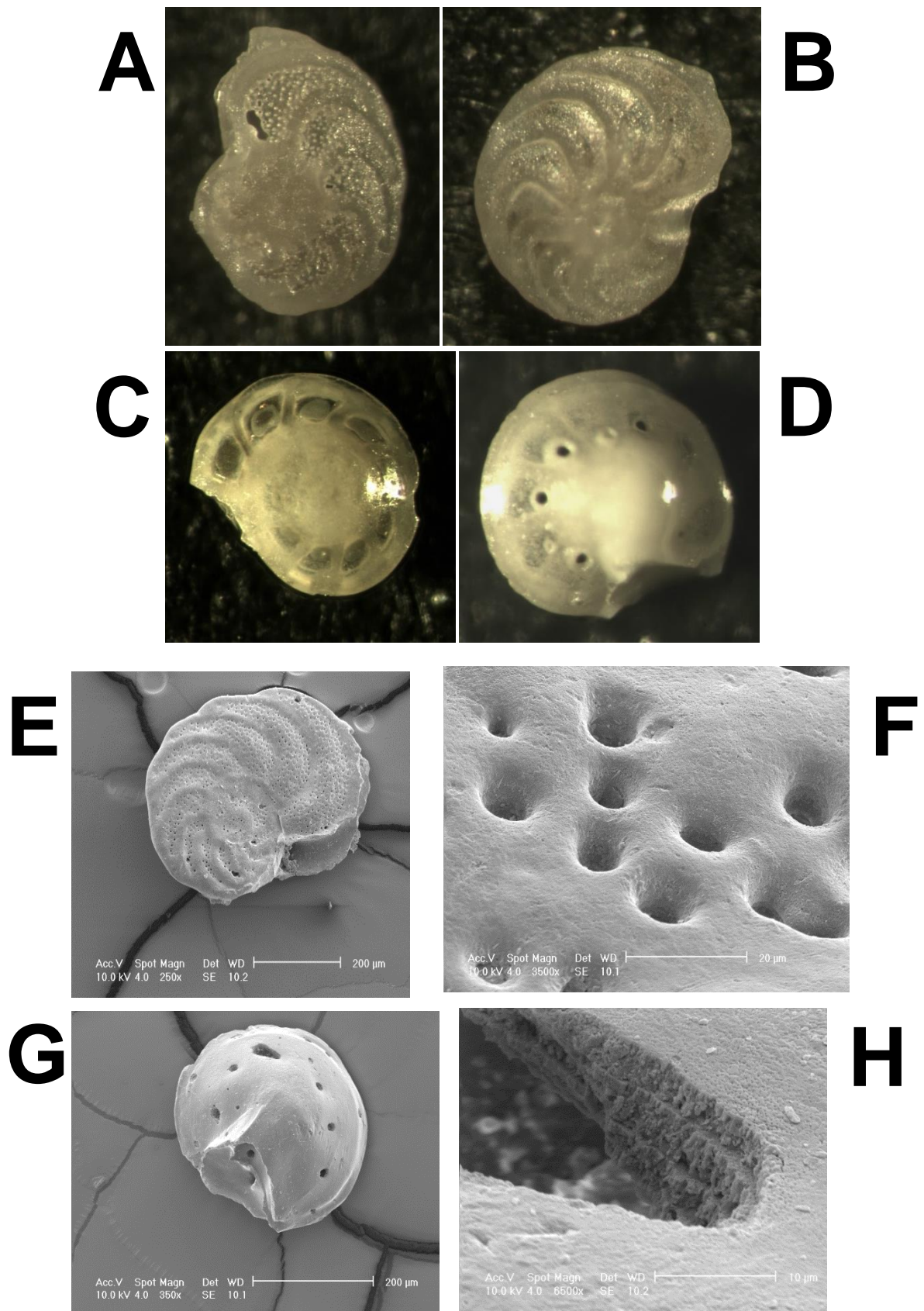


Figure 3.1: Light microscope (A-D) and SEM (E-H) images of well-preserved benthic foraminifera (*C. wuellerstorfi* (A-B, E-F) and *H. elegans* (C-D, G-H)) used for trace metal analysis from the 1368-1371m sample depth of Sunbird-1.

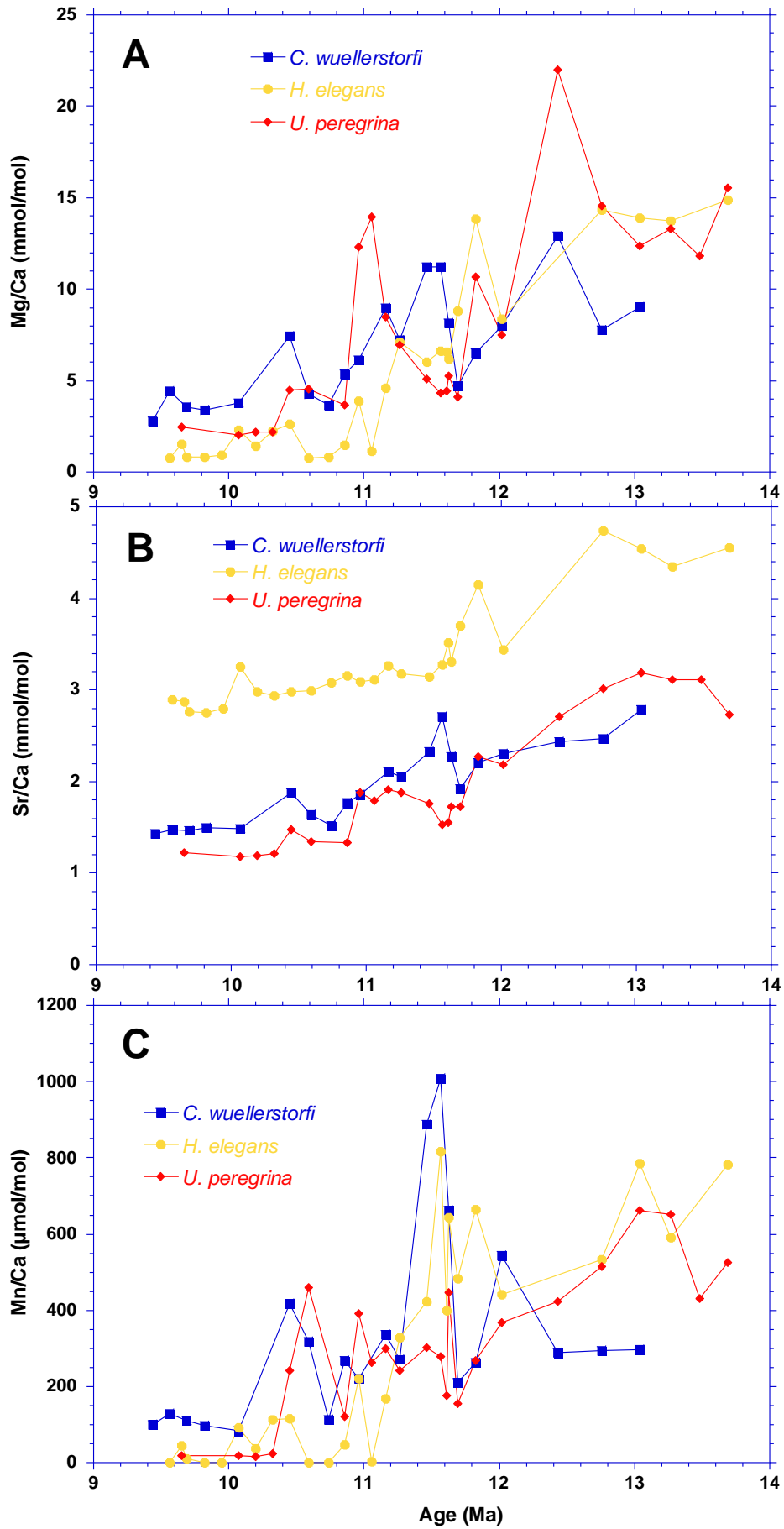
### 3.3 Results

#### 3.3.1 *Cibicidoides wuellerstorfi* and *Uvigerina peregrina* Mg/Ca

Measured *C. wuellerstorfi* Mg/Ca ranges from  $2.82 \pm 0.04$  mmol/mol to  $17.83 \pm 0.71$  mmol/mol, and measured *U. peregrina* Mg/Ca ranges from  $2.03 \pm 0.03$  mmol/mol to  $22.00 \pm 0.14$  mmol/mol (2 SD, where SD is the analytical uncertainty) (Figure 3.2a). The Mg/Ca ratios exceed the range observed in commonly applied bottom water temperature calibrations for *C. wuellerstorfi* (Lear et al., 2002, Lo Giudice Cappelli et al., 2015) and *U. peregrina* (Elderfield et al., 2010). Application of these Mg/Ca records would result in unrealistically high reconstructed bottom water temperatures (up to 24.8°C and 69.1°C for *C. wuellerstorfi* and *U. peregrina* respectively assuming modern seawater Mg/Ca). The high Mg/Ca values, and lack of the normal interspecies offset between *C. wuellerstorfi* and *U. peregrina*, strongly suggest the addition of magnesium from a secondary, post-depositional source in the early part of the record.

#### 3.3.2 *Hoeglundina elegans* Sr/Ca

*H. elegans* Sr/Ca ranges from  $2.75 \pm 0.02$  mmol/mol to  $4.74 \pm 0.10$  mmol/mol (2 SD) (Figure 3.2b). This means that all 27 values exceed the maximum value (2.72 mmol/mol) from the modern temperature calibration (Rosenthal et al., 2006). Despite our poor understanding of seawater Sr/Ca through the Cenozoic (Lear et al., 2003, Sosdian et al., 2012), applying the Rosenthal et al. (2006) core top calibration using only oversaturated waters of the Indonesian Seaway, as used by Lear et al. (2008), these Sr/Ca records would result in high reconstructed bottom water temperatures (up to 23°C) assuming modern seawater Sr/Ca (De Villiers, 1999).



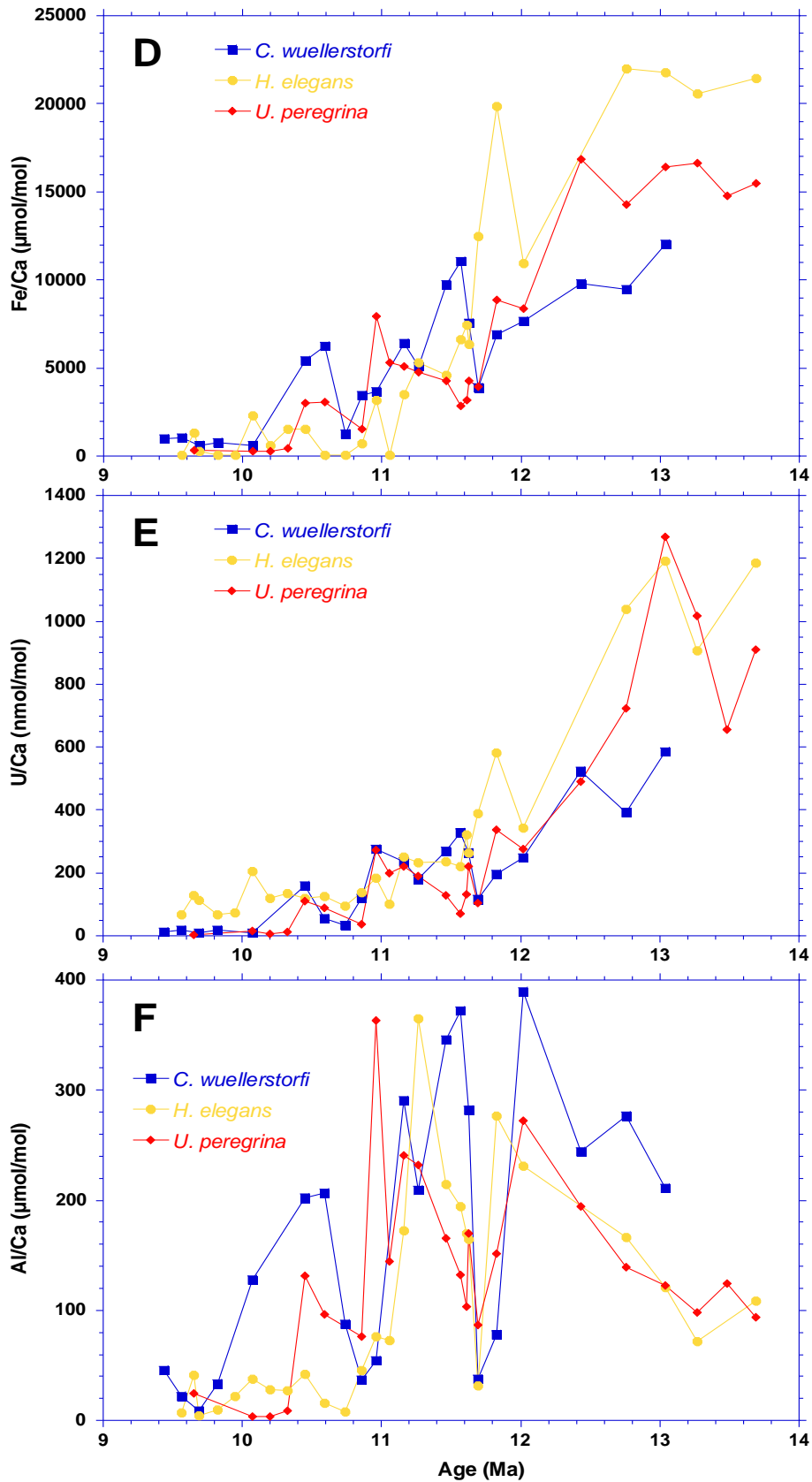


Figure 3.2: Downcore Mg/Ca (A), Sr/Ca (B), Mn/Ca (C), Fe/Ca (D), U/Ca (E), and Al/Ca (F), records for *C. wuellerstorfi* (blue squares, n=21), *U. peregrina* (red diamonds, n=24), and *H. elegans* (yellow circles, n=27) in the Sunbird-1 core.

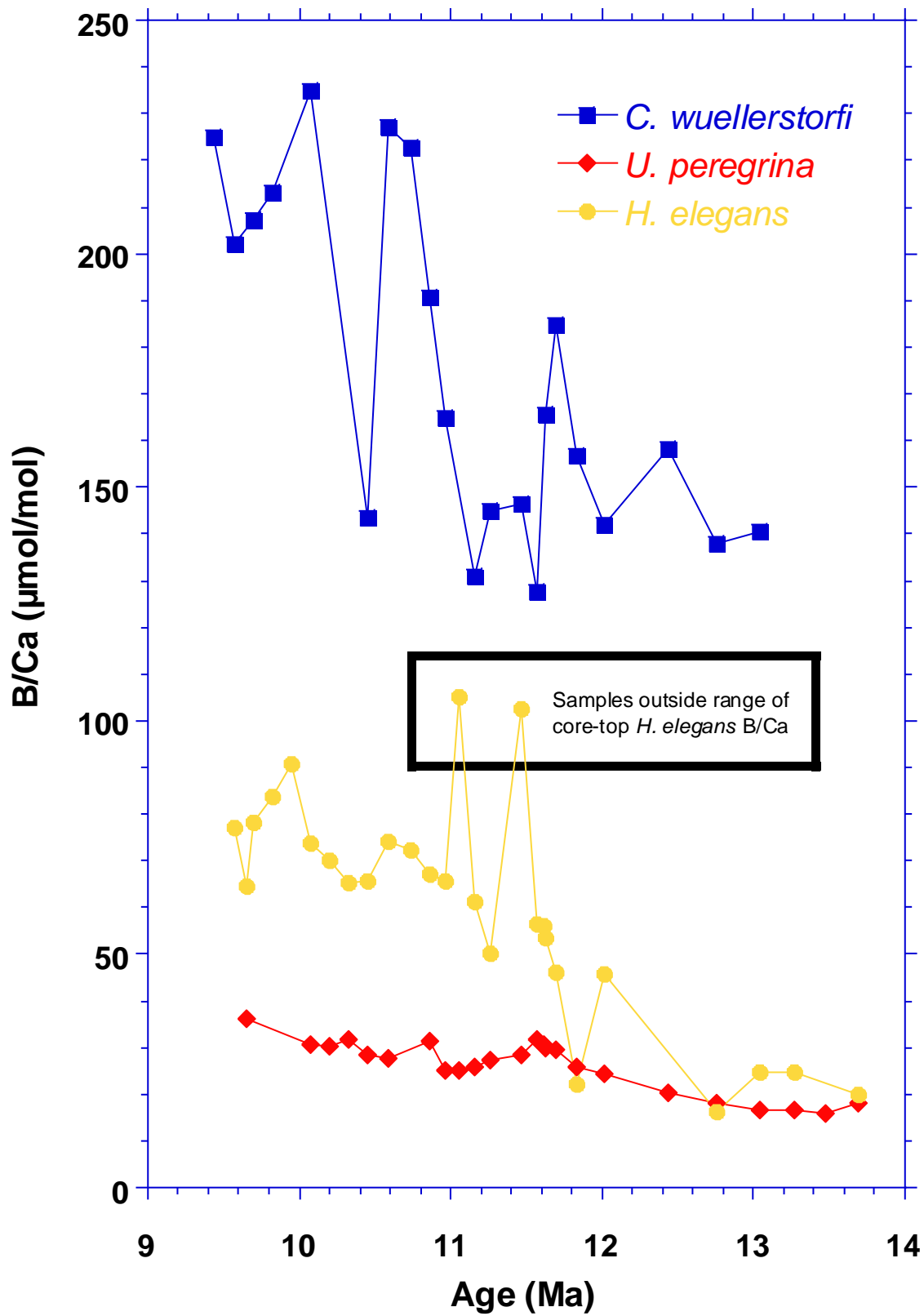


Figure 3.3: Downcore *C. wuellerstorfi* (blue squares, n=21), *U. peregrina* (red diamonds, n=24), and *H. elegans* (yellow circles, n=27) B/Ca ( $\mu\text{mol/mol}$ ) records from Sunbird-1.

### 3.3.3 Downcore records of contaminant indicators

The extremely high Mg/Ca values in both *C. wuellerstorfi* (n=21) and *U. peregrina* (n=24), and the elevated Sr/Ca values in *H. elegans* (n=27) are associated with correspondingly high Mn/Ca (Figure 3.2c), Fe/Ca (Figure 3.2d), U/Ca (Figure 3.2e), and Al/Ca (Figure 3.2f) ratios (Appendix 4). The Mn/Ca and Fe/Ca ratios are in excess of the accepted thresholds for contaminant free trace metal ratios, 100  $\mu\text{mol/mol}$  for Mn/Ca (Boyle, 1983) and Fe/Ca (Barker et al., 2003). This is particularly the case for Fe/Ca, measured values varying from 625 to 12000  $\mu\text{mol/mol}$  for *C. wuellerstorfi*, from 255 to 16400  $\mu\text{mol/mol}$  for *U. peregrina*, and from 41 to 22000  $\mu\text{mol/mol}$  for *H. elegans*. Measured *C. wuellerstorfi* Mn/Ca values vary between 85.0 and 1010  $\mu\text{mol/mol}$ , between 15.5 and 662  $\mu\text{mol/mol}$  for *U. peregrina*, and between 1.0 and 816  $\mu\text{mol/mol}$  for *H. elegans*. *C. wuellerstorfi* U/Ca values vary between 10.2 and 586 nmol/mol, *U. peregrina* U/Ca values vary between 2.70 and 1267 nmol/mol, and *H. elegans* U/Ca values vary between 67.5 and 1192 nmol/mol. These foraminiferal U/Ca ratios for Sunbird-1 are considerably higher than typical U/Ca ratios of primary foraminiferal calcite, which range from  $\sim$ 3-23 nmol/mol (Russell et al., 2004, Raitzsch et al., 2011, Chen et al., 2017). However, downcore foraminiferal U/Ca ratios of 300-700 nmol/mol have been reported (Boiteau et al., 2012, Gottschalk et al., 2016). The Al/Ca values are very similar for all three species, measured *C. wuellerstorfi* values ranging from 8.90 to 390  $\mu\text{mol/mol}$ , measured *U. peregrina* values range from 3.36 to 363  $\mu\text{mol/mol}$ , and measured *H. elegans* values range from 4.26 to 365  $\mu\text{mol/mol}$ .

### 3.3.4 Downcore B/Ca

Unlike with the Mg/Ca and Sr/Ca ratios, B/Ca ratios from all three calcite species are atypically neither high nor do they show any downcore correlation with Mg/Ca, Mn/Ca, Fe/Ca, U/Ca, or Al/Ca (Figure 3.3). Furthermore, the general decreasing trend in the redox sensitive trace metal/calcium records for all three species going up core (Figure 3.2) is reversed for B/Ca, values increasing higher up the core (Figure 3.3).

*Cibicidoides wuellerstorfi* B/Ca values range from 128  $\mu\text{mol/mol}$  to 235  $\mu\text{mol/mol}$ . This range is in agreement with previously published core top values from the same species (130-225  $\mu\text{mol/mol}$  (Yu and Elderfield, 2007), and 130-230  $\mu\text{mol/mol}$  (Rae et al., 2011)). *Uvigerina peregrina* B/Ca values range from 15.8  $\mu\text{mol/mol}$  to 36.2  $\mu\text{mol/mol}$ . These values are considerably lower than for the epifaunal *Cibicidoides wuellerstorfi*, a trend which is consistent with core top studies on the same species' (Rae et al., 2011). This trend is also seen in other infaunal species such as *Oridorsalis umbonatus* (Brown et al., 2011). The aragonitic species *Hoeglundina elegans* B/Ca values range from 16.1  $\mu\text{mol/mol}$  to 105  $\mu\text{mol/mol}$ . This is a greater range than observed in core top studies (~30-60  $\mu\text{mol/mol}$  (Yu and Elderfield, 2007), and 40-70  $\mu\text{mol/mol}$  (Rae et al., 2011)), although only two samples show significant departures from the range (Figure 3.3).

## 3.4 Discussion

### 3.4.1 Redox changes at Sunbird-1

With the exceptions of B/Ca and Al/Ca, Sunbird-1 *C. wuellerstorfi*, *U. peregrina*, and *H. elegans* trace metal/calcium ratios decrease up through the Sunbird-1 record (Figure 3.2). These include large decreases in the concentrations of redox sensitive trace metals (Mn/Ca, Fe/Ca, and U/Ca), implying significant changes in local redox conditions during the late Miocene at Sunbird-1.

Elevated concentrations of redox sensitive trace metals in the deepest part of the record suggest the early diagenetic alteration of the foraminiferal tests within the sediment column. This is likely to be Mn-, Fe-, and U-rich coatings precipitated onto the outside of the tests as a result of changing redox conditions in the sediment porewaters. Under sufficient reducing conditions, manganese and iron are released from manganese ( $Mn^{4+}$ ) and iron ( $Fe^{4+}$ ) oxyhydroxides and reduced to free aqueous  $Mn^{2+}$  and  $Fe^{2+}$  (Froelich et al., 1979). This process also leads to the reduction of uranium from uranyl ( $U^{6+}$ ) carbonate complexes to insoluble  $U^{4+}$  which can form authigenic coatings on sediment particles (Cochran et al., 1986). Hence  $Mn^{2+}$  and  $Fe^{2+}$  can diffuse through pore waters in the upper sediment, becoming oxidised when oxic conditions are re-established, precipitating as Mn-, and Fe-rich diagenetic coatings on sediments and other phases, such as foraminifera. It is therefore common to see inverse relationships between Mn/Ca and U/Ca in downcore records (e.g., (Boiteau et al., 2012)). In Sunbird-1 Mn/Ca and U/Ca both decrease up-core, although the pattern of change is not identical. The coarse, three metre, sampling resolution results in each sample incorporating precipitates formed in both reduced (U-rich) and oxic (Mn-Fe-rich) pore waters. A higher

resolution record could potentially sample these different pore water environments, and therefore display inverse relationships between Mn/Ca and U/Ca.

There are several factors that can affect the authigenic precipitation of redox sensitive metals, with the most important in typical ocean sediment cores being organic matter flux, dissolved oxygen content of the bottom waters, and sedimentation rate (Anderson, 1982, Klinkhammer, 1980). Increasing organic matter flux and decreasing bottom water [O<sub>2</sub>] lead to more reducing pore waters, which would be expected to increase the precipitation of authigenic uranium. Furthermore, more reducing conditions tends to dissolve Mn precipitates, although the dissolved Mn may diffuse into a shallower oxic zone to form new authigenic precipitates in shallower horizons. Reduced sedimentation rates provide a mechanism for increased authigenic precipitation in both reducing and oxic conditions, providing a potentially simple explanation for the decrease in both U/Ca and Mn/Ca up-section in Sunbird-1.

The early part of the Sunbird-1 record had much slower rates of sedimentation than the rest of the core (Figure 3.5). The sedimentation rate was ~2.9 cm/kyr prior to 11.8 Ma, i.e. much lower than the mean for the rest of the core (~9 cm/kyr). This would have supported the precipitation of diagenetic overgrowths in both reduced and oxic diagenetic zones (Figure 3.4), causing the concentrations of all redox sensitive trace metals to be substantially higher before 11.8 Ma because Mn-Fe-rich overgrowths, such as Mn-oxides and Mn-carbonates,

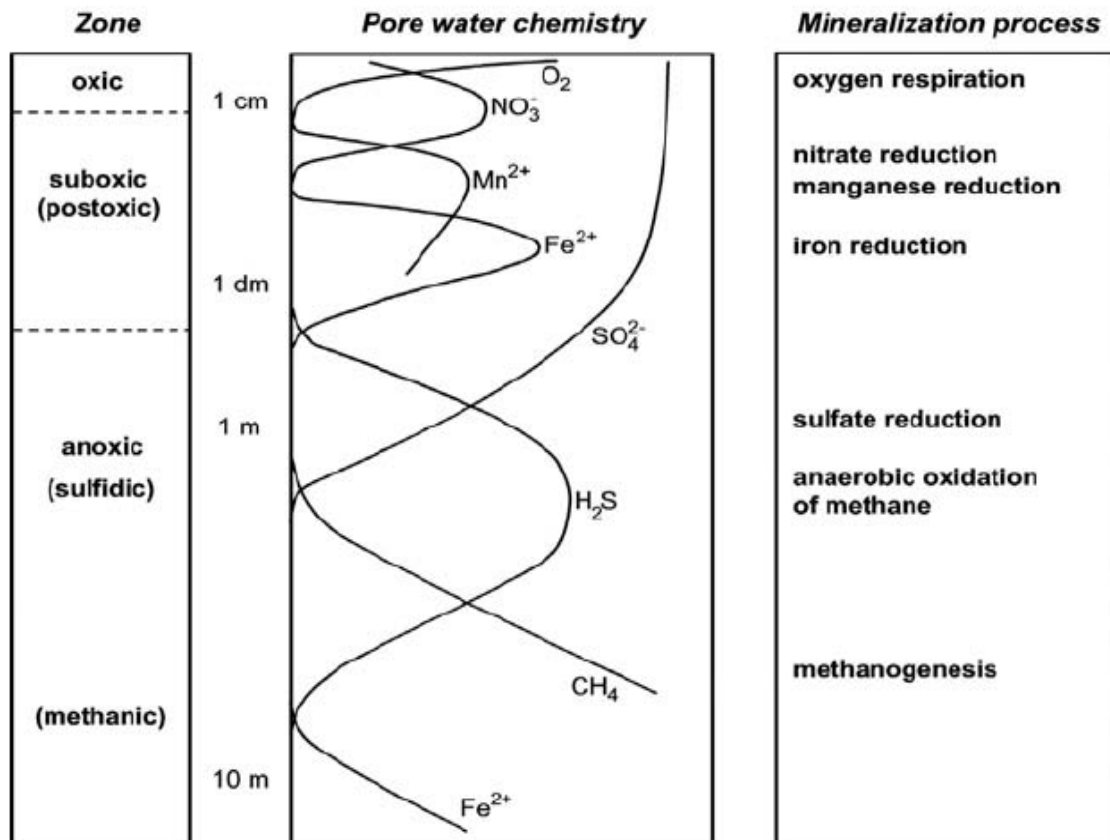


Figure 3.4: Early stage degradation of organic matter in the upper sediment column, and the associated pore water chemistry. Depths are approximate. Figure from Schulz and Zabel (2006).

slowly precipitate onto a hard substrate (Mangini et al., 1987). However, the concentrations of the redox sensitive trace metals decrease gradually over several million years, whereas the change in sedimentation rate appears to have occurred relatively abruptly around 11.8 Ma (Figure 3.5). While the lower sedimentation rates in the older part of the core would have favoured enhanced authigenic precipitation of U, Mn and Fe, it was not the only factor controlling the unusual pattern of redox sensitive metals observed in the Sunbird-1 core.

Early sedimentation at Sunbird-1 took place in shallow waters, inferred to be less than 300 metres, following subaerial exposure at the MMCT. At this time the site would have been proximal to the continent, located in a shelf environment (Figure 2.2). Furthermore, the ~60 m global sea level fall associated with the expansion of the Antarctic Ice Sheet across the

MMCT (~14 Ma) would have exposed continental shelves near Sunbird-1. Combined with localised mid-late Miocene uplift in the region, this would have increased the gradients of rivers in the Lamu basin which supply the site (Mbede, 1987, Nyagah, 1995, Mbede and Dualeh, 1997), resulting in an enhanced continental weathering flux from a vast, predominantly granitic, cratonic source area to the site of Sunbird-1. This would have supplied significant quantities of fluvial derived oxyhydroxides such as goethite together with detrital organic matter, in particular clays, via the Lamu River. Meanwhile, the substantial input of nutrients and organic matter to the Sunbird-1 site could have shoaled the oxic zone within the sediment due to available oxygen being rapidly used up via anaerobic respiration

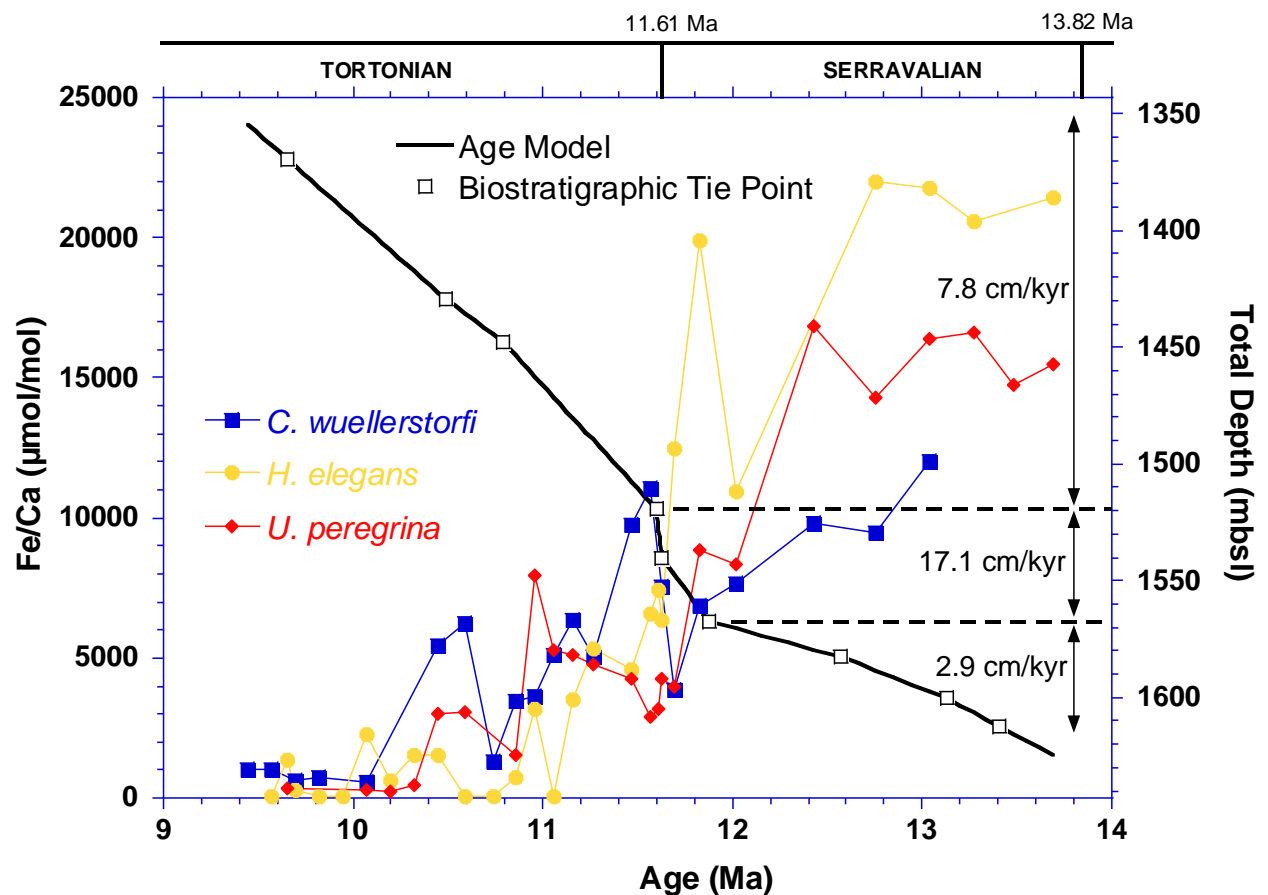


Figure 3.5: Age-depth model for Sunbird-1 using the biostratigraphic datums of Wade et al. (2011) and Backman et al. (2012) on the geomagnetic polarity timescale of Gradstein et al. (2004) using linear interpolation between reliable biostratigraphic datums. Plotted alongside are the downcore *C. wuellerstorfi* (blue squares, n=21), *U. peregrina* (red diamonds, n=24), and *H. elegans* (yellow circles, n=27) Fe/Ca ( $\mu\text{mol/mol}$ ) records from Sunbird-1.

of photosynthetic algae within the overlying euphotic zone. The degradation of organic matter can cause oxygen depletion within a few centimetres or less of the sediment-water interface, making these porewaters suboxic and favourable for authigenic uranium precipitation (Pedersen and Price, 1982, Reimers, 1987, Schulz and Zabel, 2006). Microorganisms consequently mineralise organic matter using other electron acceptors, progressively nitrate, manganese, iron, and sulfate (Froelich et al., 1979, Schulz and Zabel, 2006) (Figure 3.4). This is corroborated by the absence of *C. wuellerstorfi* in the samples prior to 13.04 Ma, potentially suggesting the oxygen concentrations in the bottom waters may have been too low for this species.

The dominant clay lithology at Sunbird-1 supports a high Fe-Mn-oxyhydroxide input associated with organic matter flux from the continent. The reduction of these Fe-Mn-oxyhydroxides due to the suboxic conditions arising from the high productivity regime' and degradation of organic matter, would have released the redox sensitive trace metals into the sediment porewaters. These redox sensitive trace metals would then have been re-precipitated as Fe-Mn-oxide foraminiferal coatings when oxic conditions were re-encountered within the sediment porewaters, causing the observed elevated ratios.

The unusual pattern of redox sensitive metals in the Sunbird-1 core likely reflects a combination of several different factors, but with a common underlying cause – the tectonic subsidence of the basin. This tectonic subsidence of the basin would have resulted in the site of deposition, of Sunbird-1 continuously changing. As well as increased water depth, Sunbird-1 would have received less sedimentary input from the continent as the site subsided.

Furthermore, as the site of deposition subsided out of the surface waters, there would likely have been an increased influence of deeper water masses, replacing the dominance of coastal waters. The potential influence of these factors, primarily controlled by basin subsidence, on the trace metal geochemistry of the bottom waters and upper sediment must be considered.

In this model, the sedimentary input of detrital Fe-Mn oxyhydroxides and organic matter both decreased gradually through time, whilst sedimentation rates increased abruptly around 11.8 Ma. Therefore, it is likely that sediment redox conditions and sedimentation rates both evolved through the Miocene at this site. It is not possible to determine whether the authigenic uranium and Fe-Mn oxyhydroxides were forming simultaneously, but this model allows for a concomitant decrease in both of their concentrations up through the core.

The decrease in redox sensitive trace metal concentration through the depositional record likely resulted from the subsidence of the site away from the surface waters characterised by high fluxes of detrital organic matter and productivity. Consequently, the supernatant bottom waters, and upper pore waters could have become more oxic; the pore waters in the upper few centimetres of the sediment column would have been less enriched in free aqueous  $\text{Mn}^{2+}$  and  $\text{Fe}^{2+}$ , which are released under reducing conditions. From  $\sim 11.5$  Ma to the end of the record there is no further decrease in the Mn/Ca, Fe/Ca, and U/Ca ratios (Figure 3.2 c, d, e), despite the likely continued tectonic subsidence of the basin. It is possible that a threshold in terms of changing redox conditions has been crossed, the environmental conditions of the site no longer promoting the formation of diagenetic coatings with elevated concentrations of these redox state sensitive trace metals.

### 3.4.2 Characterisation of the contaminant phase

Mg-Mn-rich carbonate overgrowths are a common source of contamination to foraminifera (Boyle, 1983, Pena et al., 2005, Pena et al., 2008, Hasenfratz et al., 2016). However, the elevated and co-varying Fe/Ca ratios and clay rich sediment at Sunbird-1 make this unlikely, because carbonate overgrowths tend to form in coarse grained, carbonate rich sediments (Pedersen and Price, 1982), and have low Fe/Mn ratios (Hasenfratz et al., 2016). The combined presence of Fe- and Mn-rich phases suggests the potential presence of oxides (Calvert and Pedersen, 1996).

Mg/Mn ratios in Sunbird-1, as given by the gradient of the cross plots, are 8.3 mol/mol in *C. wuellerstorfi*, 19.7 mol/mol in *U. peregrina*, and 15.3 mol/mol in *H. elegans*. The Mg/Mn ratio for *H. elegans* is likely the most realistic ratio for the contaminant coating, as there will be a temperature signal influencing the Mg/Ca ratios of the two calcite species. Average Mg/Mn ratios in Mn nodules and Mn encrustations (common forms of Mn-Fe-oxides) across a wide range of ocean basins is 0.17 – 0.32 mol/mol (De Lange et al., 1992, Baturin, 2012). The Mg/Mn ratios measured in the benthic foraminifera from Sunbird-1 are orders of magnitude different to the natural ranges for Mn-Fe-oxides, suggesting either that the contaminant is a different phase, or perhaps more likely that an unknown portion of the measured Mg/Ca decrease reflects an original temperature signal that is coincident with, but not caused by, the decrease in authigenic coatings. However, it is important to note that the application of the reductive cleaning process on these samples will have removed the vast majority of the diagenetic coatings meaning that the Mg/Mn ratios of the cleaned benthic foraminifera are not representative of the original coatings. Therefore, the disconnect between Mg/Mn ratios

in foraminifera from Sunbird-1 and the values typical of Mn-oxides does not restrict the interpretation of the foraminiferal tests having Mn-Fe-oxide coatings formed under changing redox conditions.

### 3.4.3 Potential influence of detrital silicates at Sunbird-1

The influence of detrital silicates, in particular clays, would be expected to be a major issue at Sunbird-1 due to the clay rich, low carbonate content of the sediment. Aluminium in foraminiferal tests is unambiguously considered an indicator for the presence of detrital silicate grains (Emiliani, 1955, Barker et al., 2003, Lea et al., 2005). Several samples of all three species exhibit Al/Ca ratios in excess of 100  $\mu\text{mol/mol}$ . This is the concentration below which Al incorporation is interpreted as having a negligible influence on Mg/Ca and Sr/Ca ratios. Therefore, a possible influence on trace metal/calcium ratios due to the incorporation of silicate grains into the shell digests requires investigation. Furthermore, there is covariance between *C. wuellerstorfi* and *U. peregrina* Mg/Ca and Al/Ca (Figure 3.6 d and h).

A key observation is that the *C. wuellerstorfi* and *U. peregrina* Mg/Ca and Al/Ca records show negligible point-to-point tracking downcore (Figure 3.7). Similarly, with the exception of the concomitant peak in all trace metal/calcium ratios at 11.83 Ma, Sr/Ca shows no downcore correlation with Al/Ca in *H. elegans* (Figure 3.8 e). This lack of downcore correlation with Mg/Ca or Sr/Ca, and the absence of a distinctive decrease through the record as with the redox sensitive trace metals suggests detrital silicates are not the primary cause of the signals in the trace metal/calcium records. Maximum Al/Ca values for all three species are extremely similar, ranging from 363-390  $\mu\text{mol/mol}$ . This suggests that incorporation of Al is not

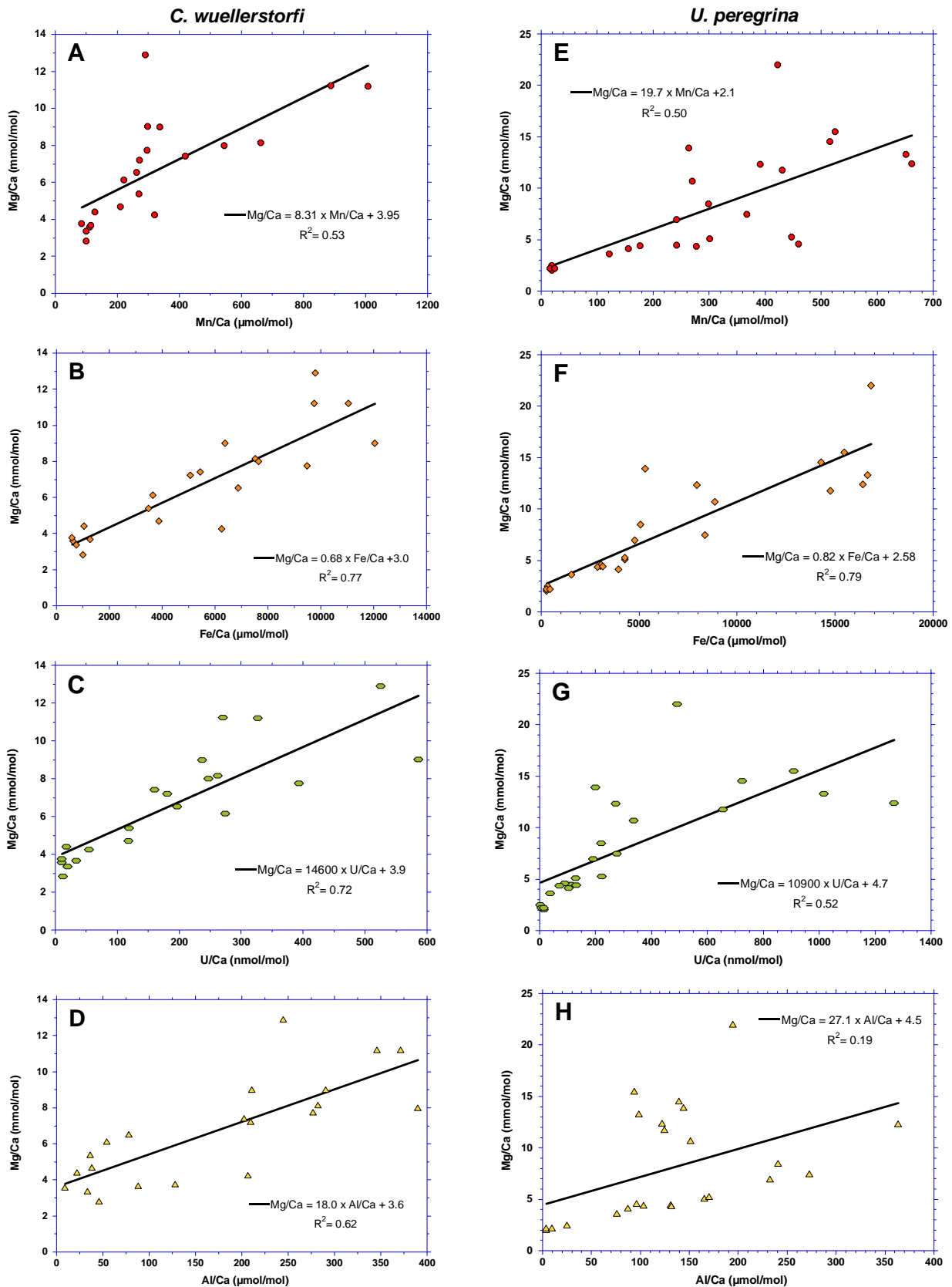


Figure 3.6: Trace metal covariance plots from Sunbird-1 for *C. wuellerstorfi* (n=21) (A-D) and *U. peregrina* (n=24) (E-H). Mg/Ca v Mn/Ca (red circles), Mg/Ca v Fe/Ca (orange diamonds), Mg/Ca v U/Ca (green hexagons), and Mg/Ca v Al/Ca (yellow triangles). R<sup>2</sup> correlations for all plots are given.

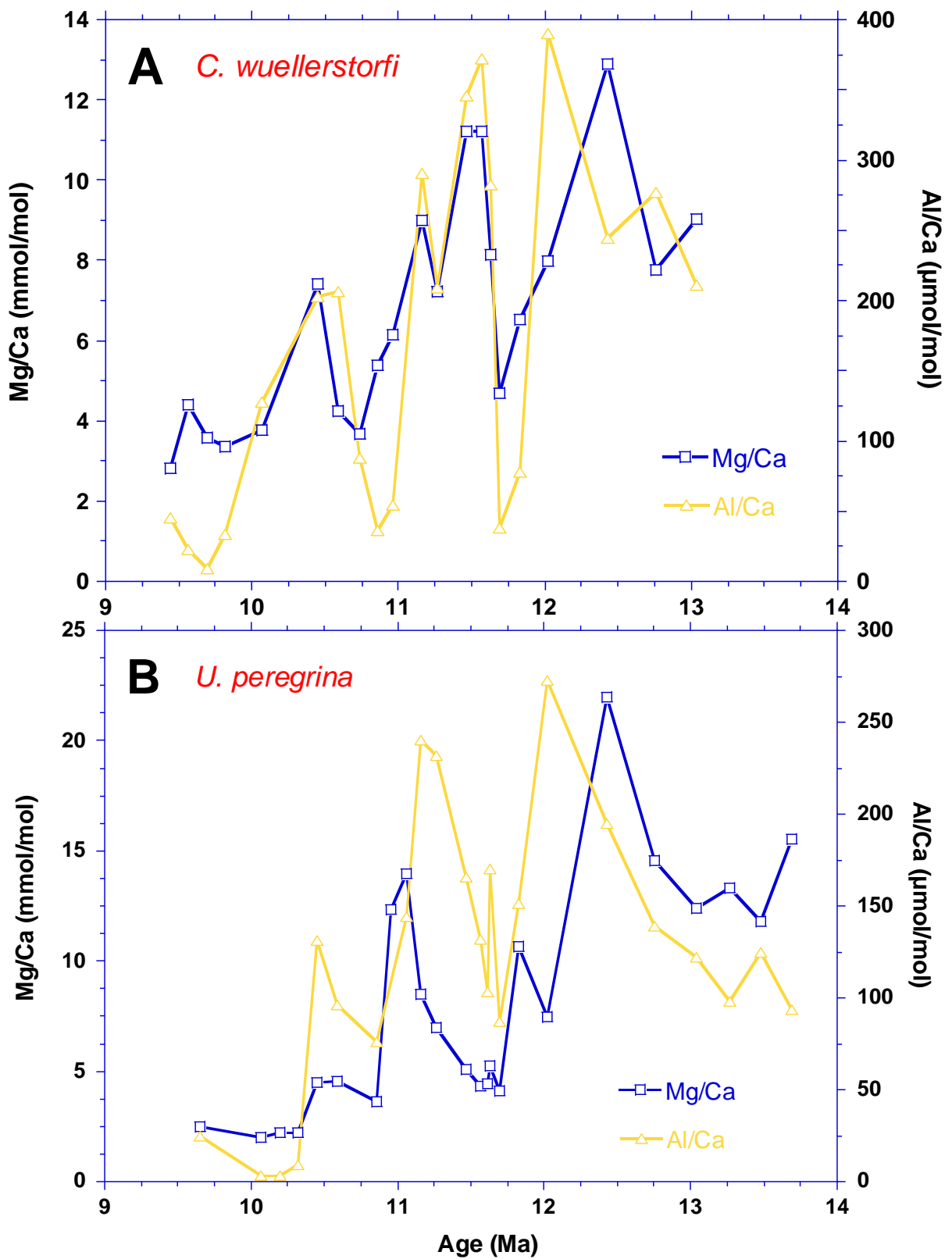


Figure 3.7: Downcore (A) *C. wuellerstorfi* (n=21) and (B) *U. peregrina* (n=24) Mg/Ca (mmol/mol) and Al/Ca ( $\mu\text{mol/mol}$ ) records from Sunbird-1.

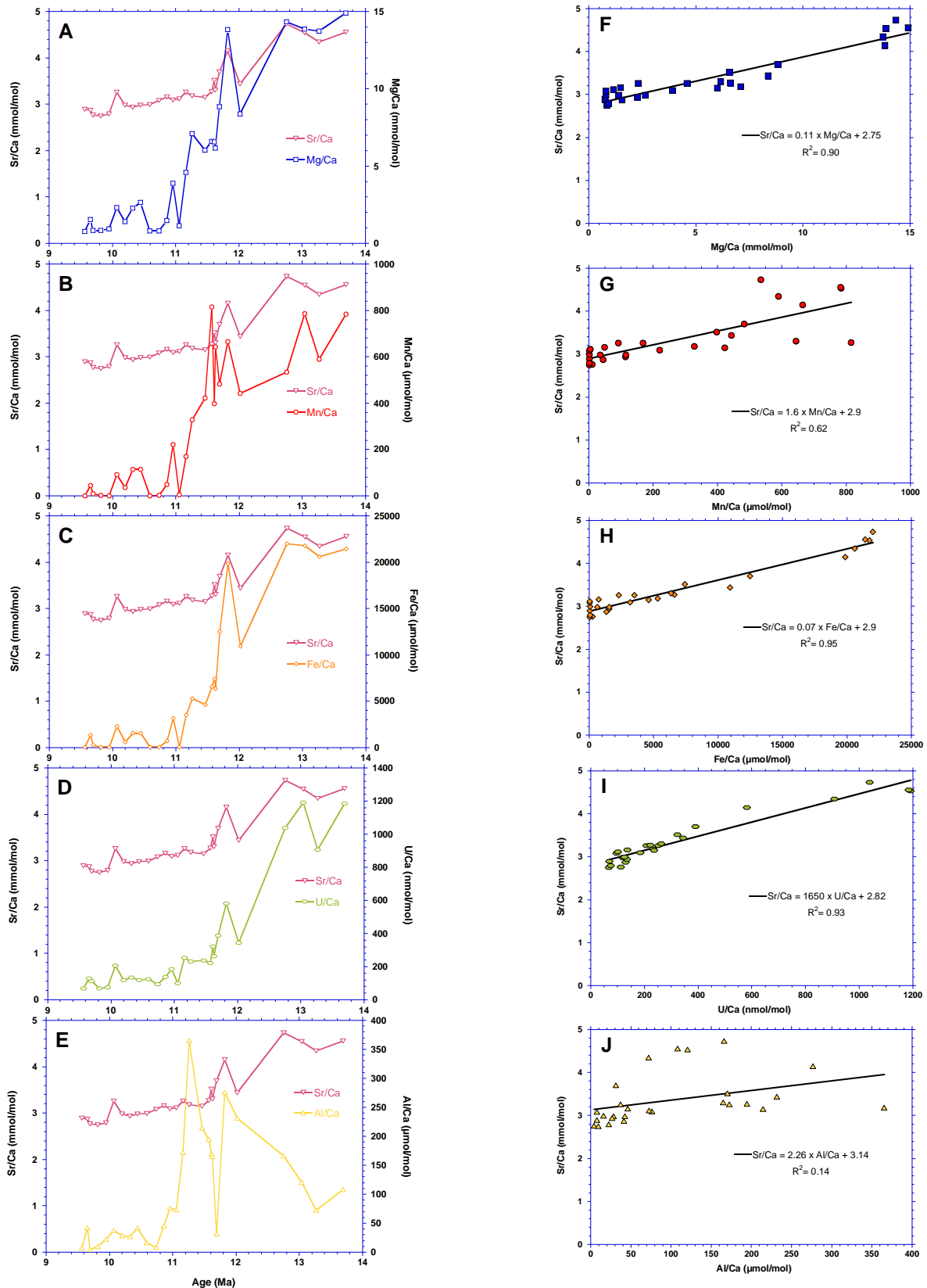


Figure 3.8: Downcore (A-E) and covariance (F-J) relationships between the *H. elegans* Sr/Ca (mmol/mol) record from Sunbird-1 and the *H. elegans* (A, F) Mg/Ca (mmol/mol), (B, G) Mn/Ca (μmol/mol), (C, H) Fe/Ca (μmol/mol), (D, I) U/Ca (nmol/mol), and (E, J) Al/Ca (μmol/mol) records.

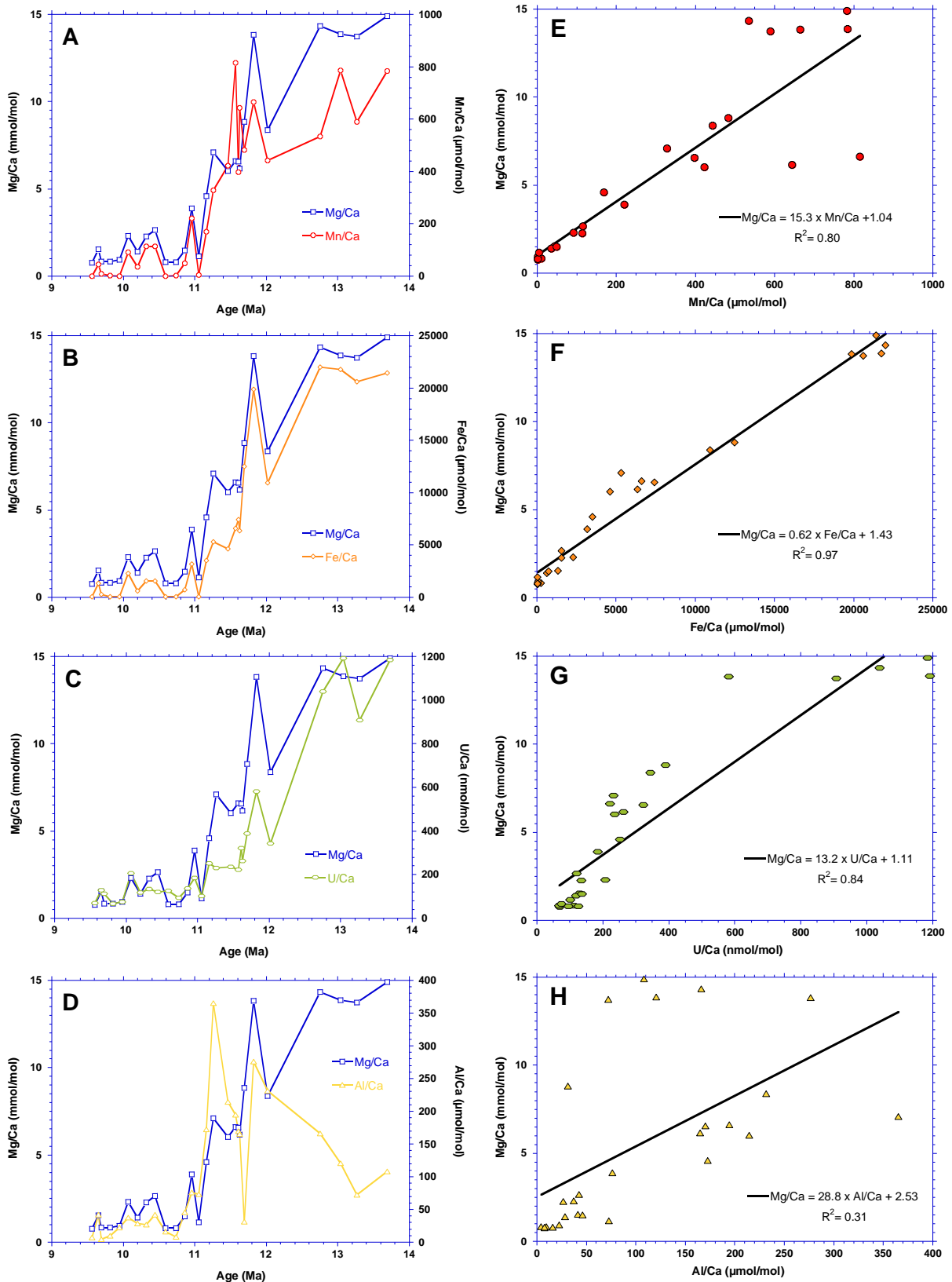


Figure 3.9: Relationship between *H. elegans* Mg/Ca (blue squares) and Mn/Ca (red circles), Fe/Ca (orange diamonds), U/Ca (green hexagons), and Al/Ca (yellow triangles) in Sunbird-1 as downcore records (A-D) and covariance plots (E-H). Note that all equations in (E) to (H) are given in mmol/mol, and for all plots n=27.

dependent upon the carbonate phase, or the microhabitat, of the foraminiferal species. However, these maximum Al/Ca values are not from the same sample (Figure 3.2 f).

This lack of Mg/Ca and Al/Ca association is further evidenced by the weak covariance between the *H. elegans* ratios ( $R^2=0.31$ ) (Figure 3.9 h). Conversely, there is striking covariance and downcore point-to-point correlation between Mg/Ca, Mn/Ca, Fe/Ca, and U/Ca in the aragonitic *H. elegans* (Figure 3.9 a-c), and cross-plots between these trace metal ratios suggest there is significant covariance between them ( $R^2>0.80$ ) (Figure 3.9 e-g). The intercept of the *H. elegans* Al/Ca v. Mg/Ca crossplot suggests samples absent of Al would have an Mg/Ca ratio of 2.53 mmol/mol, a value substantially higher than the “Al-free” Mg/Ca ratios determined from the other covariance plots (1.04 mmol/mol to 1.43 mmol/mol). Additionally, the six samples showing the highest *H. elegans* Mg/Ca ratios cover a wide range

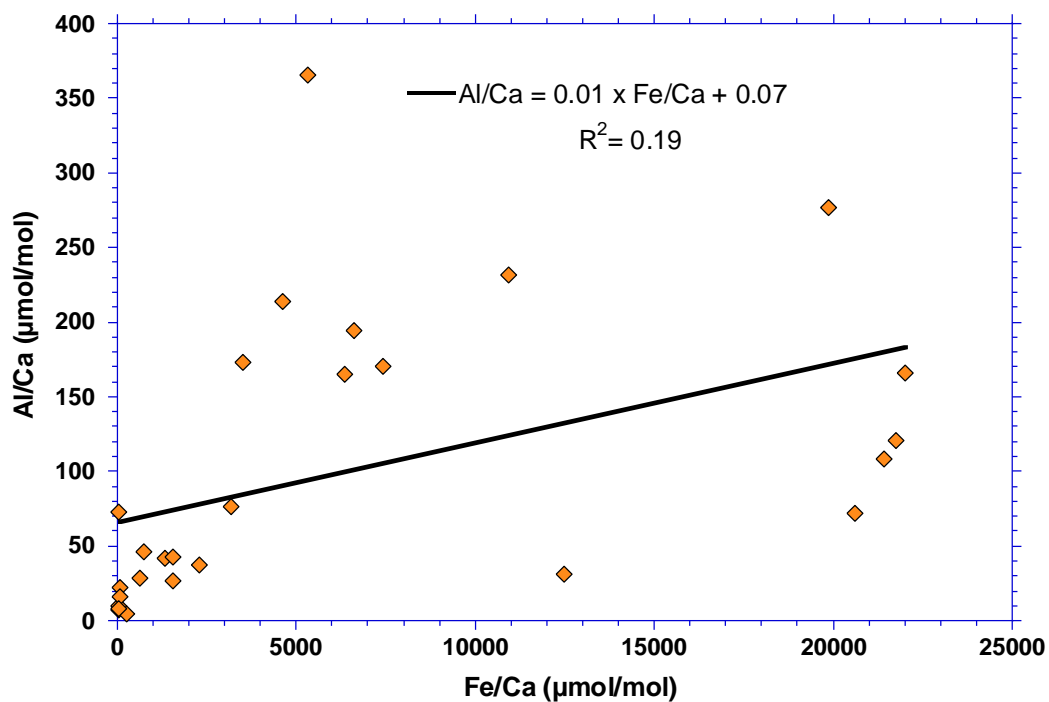


Figure 3.10: Relationship between *H. elegans* Fe/Ca and Al/Ca in Sunbird-1 (n=27). The low  $R^2$  value of 0.19 indicates a lack of correlation between Fe/Ca and Al/Ca values in *H. elegans* from Sunbird-1.

of Al/Ca ratios (Figure 3.9 h), further implying that Al/Ca is not the primary driver of increased Mg/Ca ratios at Sunbird-1. Of particular importance is the 11.26 Ma sample, which has the highest Al/Ca value in the *H. elegans* record but the Mg/Ca ratio for this sample is not substantially elevated relative to the nearby samples. Furthermore, there exists minimal covariance between *H. elegans* Fe/Ca and Al/Ca ( $R^2 = 0.19$ ) (Figure 3.10). Covariance between Fe/Ca and Al/Ca is typical of silicate contamination (Barker et al., 2003, Lea et al., 2005). With this all considered it is concluded that detrital silicate particles are not the primary driver of the elevated *C. wuellerstorfi* and *U. peregrina* Mg/Ca ratios nor the *H. elegans* Sr/Ca ratios, although due to occasional Al/Ca ratios exceeding 100  $\mu\text{mol/mol}$  their influence cannot be ruled out for individual samples.

#### 3.4.4 Assessing the impact of authigenic coatings on foraminiferal Mg/Ca and Sr/Ca records

Post-depositional alteration of primary foraminiferal calcite, and therefore their trace metal geochemistry, can have multiple causes: a) detrital silicate grains (Emiliani, 1955, Barker et al., 2003, Lea et al., 2005), b) oxyhydroxides (Boyle, 1983, Palmer, 1985), c) secondary carbonates (Boyle, 1983, Pena et al., 2005, Hasenfratz et al., 2016), and d) oxide coatings (Hasenfratz et al., 2016). These diagenetic phases have distinctive trace metal signatures which, if determined, can provide information about the post-depositional sedimentary environment and redox conditions.

Benthic foraminiferal trace metal/calcium ratios indicative of changing, post depositional sediment redox conditions (Mn/Ca, Fe/Ca, and U/Ca) are elevated throughout the Sunbird-1 record, in particular in the deepest interval. In isolation, the elevated contaminant/calcium

values are not necessarily restrictive to the application of Mg/Ca values for reconstructing bottom water temperature. If the elevated contaminant/calcium value show no relationship with Mg/Ca, then it is generally considered safe to assume that any incorporation of trace metals used as contaminant indicators are not influencing the Mg/Ca values (Lear et al., 2015). Additionally, authigenic Mn-carbonates have a Mg/Mn ratio of  $0.13 \pm 0.13$  mol/mol (Peacor et al., 1987) meaning only a minor proportion (<0.1 mmol/mol) of the measured foraminiferal Mg/Ca could originate from this contaminant coating (Schmidt et al., 2006). However, at Sunbird-1 the elevated Mg/Ca ratios demonstrate point-to-point correlation and downcore tracking with Mn/Ca, Fe/Ca, and U/Ca ratios for both *C. wuellerstorfi* and *U. peregrina* (Figure 3.11 - 3.13). This strongly suggests an association between Mg/Ca and sedimentary redox conditions, which would lead to overestimations of reconstructed bottom water temperature. In addition, the Mg/Ca ratios of the epifaunal *C. wuellerstorfi* and infaunal *U. peregrina* show significant covariance with Mn/Ca, Fe/Ca, and U/Ca ( $R^2 > 0.50$ ) (Figure 3.6 a, b, c, e, f, g). For both calcitic species this covariance is greatest between Mg/Ca and Fe/Ca. The clear downcore point-to-point correlation and significant covariance prevents the interpretation of either downcore Mg/Ca record solely in terms of bottom water temperatures.

The observed downcore point-to-point correlation and covariance between *H. elegans* Sr/Ca and trace metal ratios indicative of contamination (Mn/Ca, Fe/Ca, and U/Ca) suggests that the elevated *H. elegans* Sr/Ca values may also be compromised in terms of being used for temperature reconstruction (Figure 3.8). The downcore increase and range in absolute *H. elegans* Mg/Ca, Mn/Ca, Fe/Ca, and U/Ca values are similar to the respective trends and

absolute ranges observed for *C. wuellerstorfi* and *U. peregrina* (Figure 3.2 a, c, d, e). This suggests these trace metal/calcium ratios have a common primary control, which is independent of foraminiferal species. However, in contrast to the downcore Mg/Ca records from the two species of calcite foraminifera the *H. elegans* Sr/Ca is relatively stable, on a point-to-point basis. The main departure from this stability is the Sr/Ca peak at 11.82 Ma, which is associated with peaks in all the other trace metal/calcium records (Figure 3.8). This suggests that Sr/Ca ratios are less influenced by contaminant oxide coatings, and that in regions with changing sedimentary redox conditions *H. elegans* Sr/Ca ratios may be a more resilient palaeotemperature proxy than the more commonly applied Mg/Ca ratio of calcitic foraminifera.

In summary, the proposed mechanism for the decrease in redox sensitive trace metal concentration through the Sunbird-1 record is subsidence away from the euphotic zone with high detrital organic matter input, coupled with increasing sedimentation rates and decreasing input of fluvially derived detrital oxyhydroxides. As well as influencing pore water redox conditions, this subsidence would have also decreased bottom water temperatures; these two environmental conditions likely varying in tandem. Without an independent quantitative proxy for redox conditions it is therefore extremely challenging to deconvolve the temperature versus contaminant contributions to the foraminiferal Mg/Ca records.

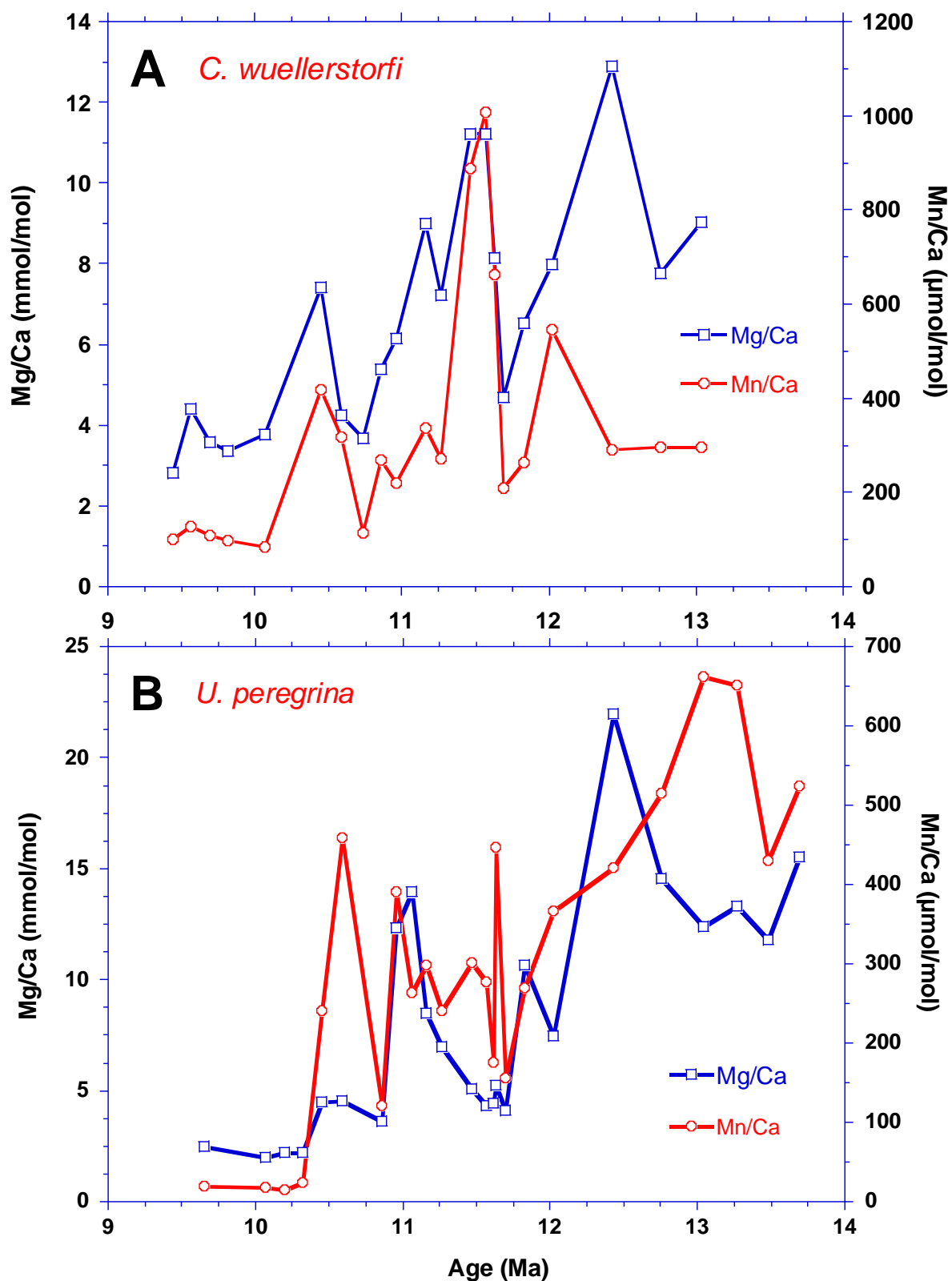


Figure 3.11: Downcore *C. wuellerstorfi* (n=21) and *U. peregrina* (n=24) Mg/Ca (mmol/mol) and Mn/Ca ( $\mu\text{mol/mol}$ ) records from Sunbird-1. All records demonstrate an overall decreasing trend, and point-to-point correlation between Mg/Ca and Mn/Ca is apparent in both species.

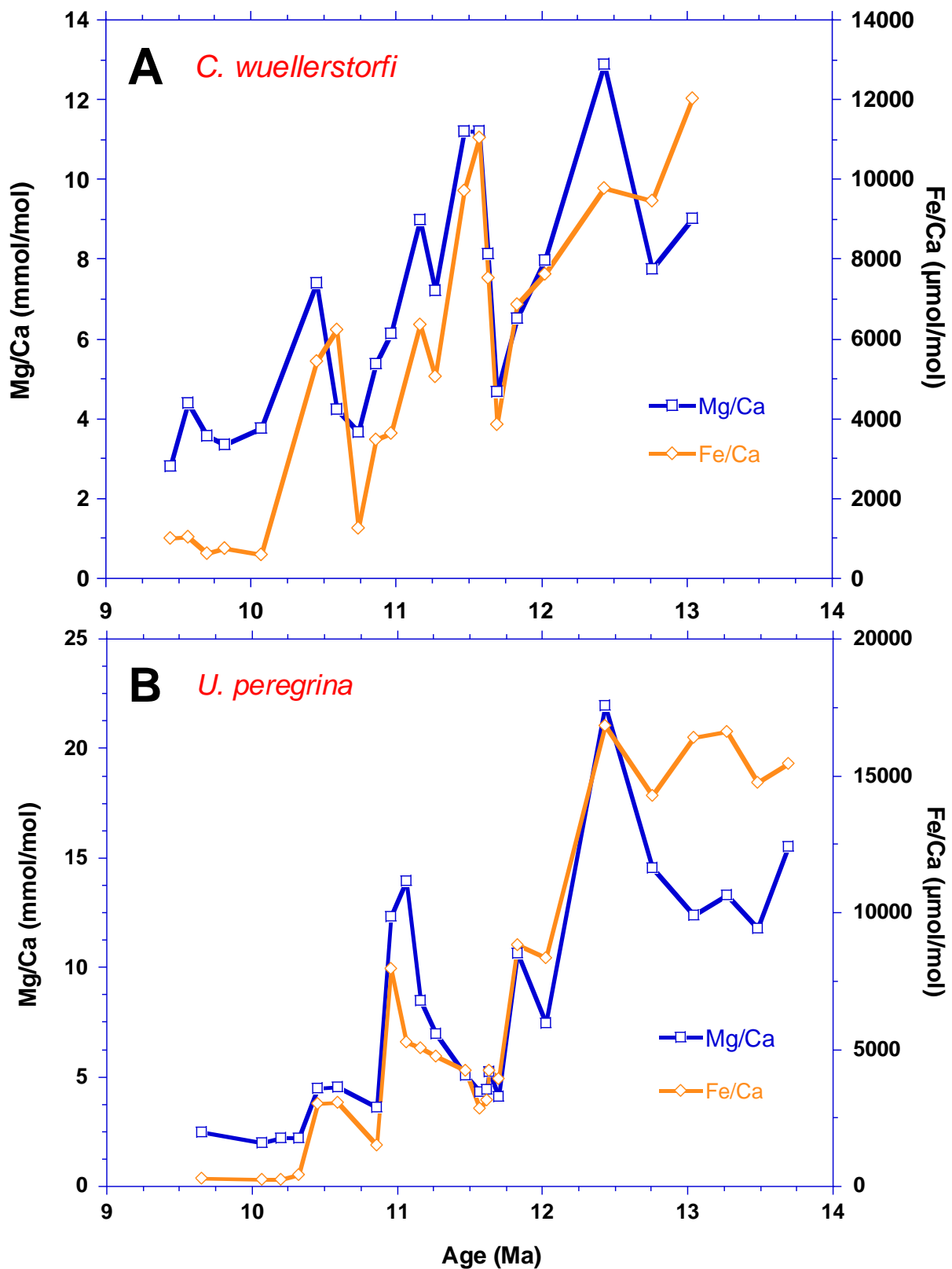


Figure 3.12: Downcore *C. wuellerstorfi* (n=21) and *U. peregrina* (n=24) Mg/Ca (mmol/mol) and Fe/Ca ( $\mu\text{mol/mol}$ ) records from Sunbird-1. All records demonstrate an overall decreasing trend, and point-to-point correlation between Mg/Ca and Fe/Ca is apparent in both species.

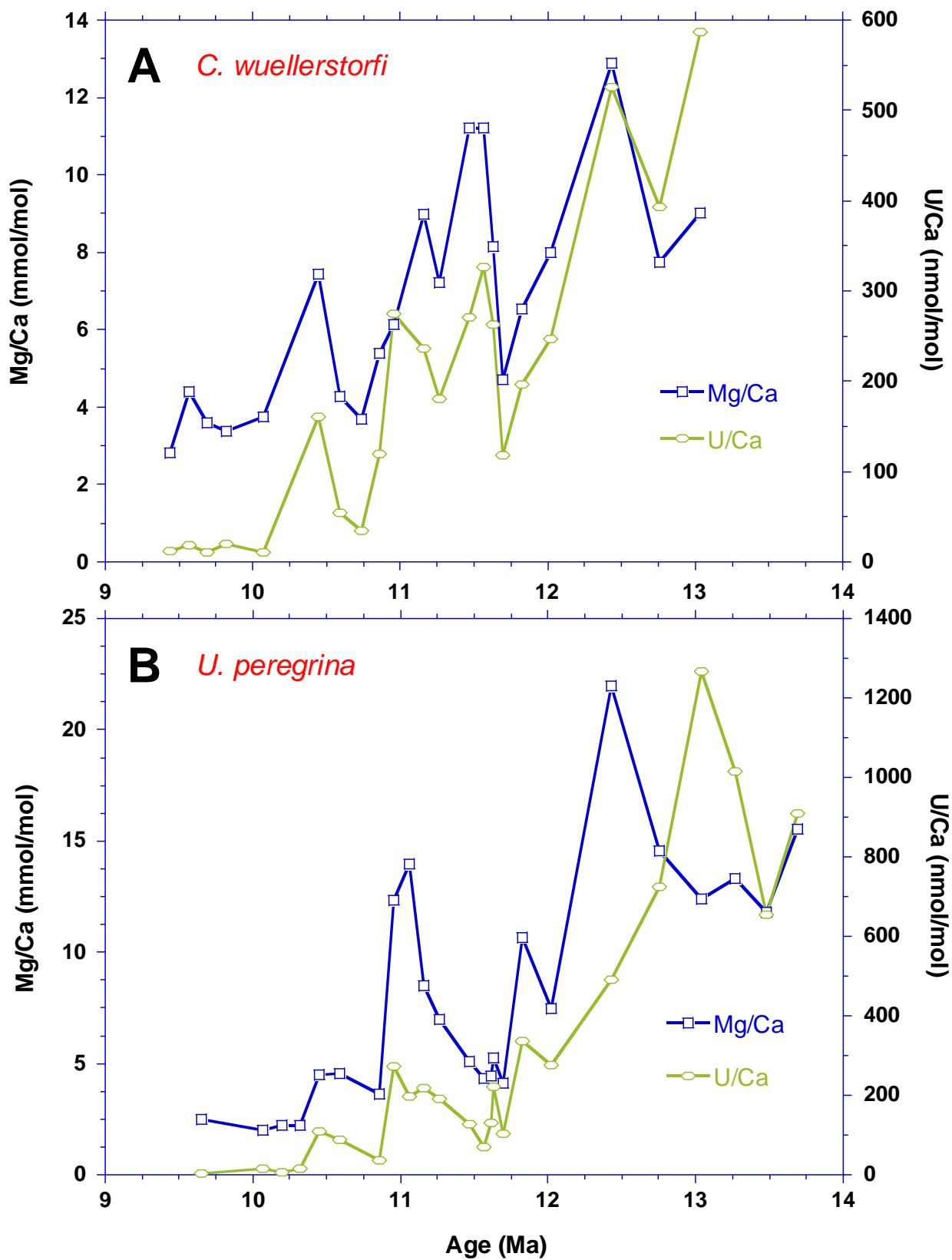


Figure 3.13: Downcore *C. wuellerstorfi* (n=21) and *U. peregrina* (n=24) Mg/Ca (mmol/mol) and U/Ca (nmol/mol) records from Sunbird-1. All records demonstrate an overall decreasing trend, and point-to-point correlation between Mg/Ca and U/Ca is apparent in both species.

### 3.4.5 A potential novel way to correct for contaminant coatings

The application of foraminiferal Mg/Ca ratios to reconstruct palaeotemperature requires the complete removal of magnesium in secondary contaminant phases, leaving only the magnesium bound in primary calcite to record the true palaeotemperature signal. Despite employing a thorough chemical cleaning protocol, which was enhanced by performing the clay removal step twice and picking out visible detrital material, excess non-calcite bound Mg appears to be present in benthic foraminiferal samples from Sunbird-1. Therefore, the possibility of obtaining more representative Mg/Ca values for the primary shell by employing a correction factor to remove the contaminant component of the Mg/Ca signal was explored. Previous work shows that whenever Mn- or Fe-rich contaminant coatings are prevalent paired measurements of the same sample, with and without the reductive step, allows the determination of the Mg/Mn or Mg/Fe of the contaminant phase (Barker et al., 2003, Lea et al., 2005). This technique has proved successful in correcting for the influence of either carbonate or oxide coatings on foraminiferal Mg/Ca ratios (Pena et al., 2005, Pena et al., 2008, Hasenfratz et al., 2016). Applying a more generic correction for the incorporation of magnesium into secondary phases bypasses this assumption that the contaminant phase is diagenetic oxide or carbonate (Equation 3.1 where X is the relevant contaminant trace metal).

$$\text{Equation 3. 1: } \frac{\text{Mg}}{\text{Ca}_{\text{CORRECTED}}} = \frac{\text{Mg}}{\text{Ca}} - \left( \frac{\text{X}}{\text{Ca}} \times \frac{\text{Mg}}{\text{X}} \right)$$

To determine the Mg/Mn, Mg/Fe, and Mg/U ratios of the contaminant phase, the paired calcitic-aragonitic trace metal ratios were utilised. Because *H. elegans* precipitates an

aragonitic test, temperature has a negligible control on the Mg/Ca ratio (Rosenthal et al., 2006, Lo Giudice Cappelli et al., 2015). Consequently, all Mg is assumed to be contained in the contaminant phase, none being incorporated into the orthorhombic aragonite lattice (a useful over-simplification). Therefore, the Mg/Mn, Mg/Fe, and Mg/U ratios of *H. elegans* are inferred as reflecting solely a contaminant signal, uncompromised by any primary temperature-controlled Mg/Ca incorporation. Incorporating these ratios with equation 3.1 corrects the downcore *C. wuellerstorfi* and *U. peregrina* Mg/Ca ratios for the presence of an Mg-rich contaminant phase (Figure 3.14).

Applying the correction factors produces a visual lowering of the downcore Mg/Ca records for both calcite species (Figure 3.14). The significance of the lowering was tested by using a two-sample paired t-test for means (RStudio, 2015). For all six scenarios the contaminant-corrected Mg/Ca data is significantly ( $P \ll 0.001$ , degrees of freedom  $\geq 20$ ) lower than the original Mg/Ca data (Table 3.1). Therefore, the use of Mg/X correction factor significantly changes the Mg/Ca data in all scenarios.

	<b>Mn-corrected</b>	<b>Fe-corrected</b>	<b>U-corrected</b>
<b><i>C. wuellerstorfi</i> (n=21)</b>	4.94 mmol/mol	3.33 mmol/mol	2.52 mmol/mol
<b><i>U. peregrina</i> (n=24)</b>	4.64 mmol/mol	4.17 mmol/mol	4.11 mmol/mol

Table 3.1: Mean lowering of the Mg/Ca value when applying the contaminant correction factor. Use of a two sample paired t-test (RStudio, 2015) shows the corrected Mg/Ca data is significantly lower than the original Mg/Ca data for all 6 scenarios ( $P \ll 0.001$ , degrees of freedom  $\geq 20$ ).

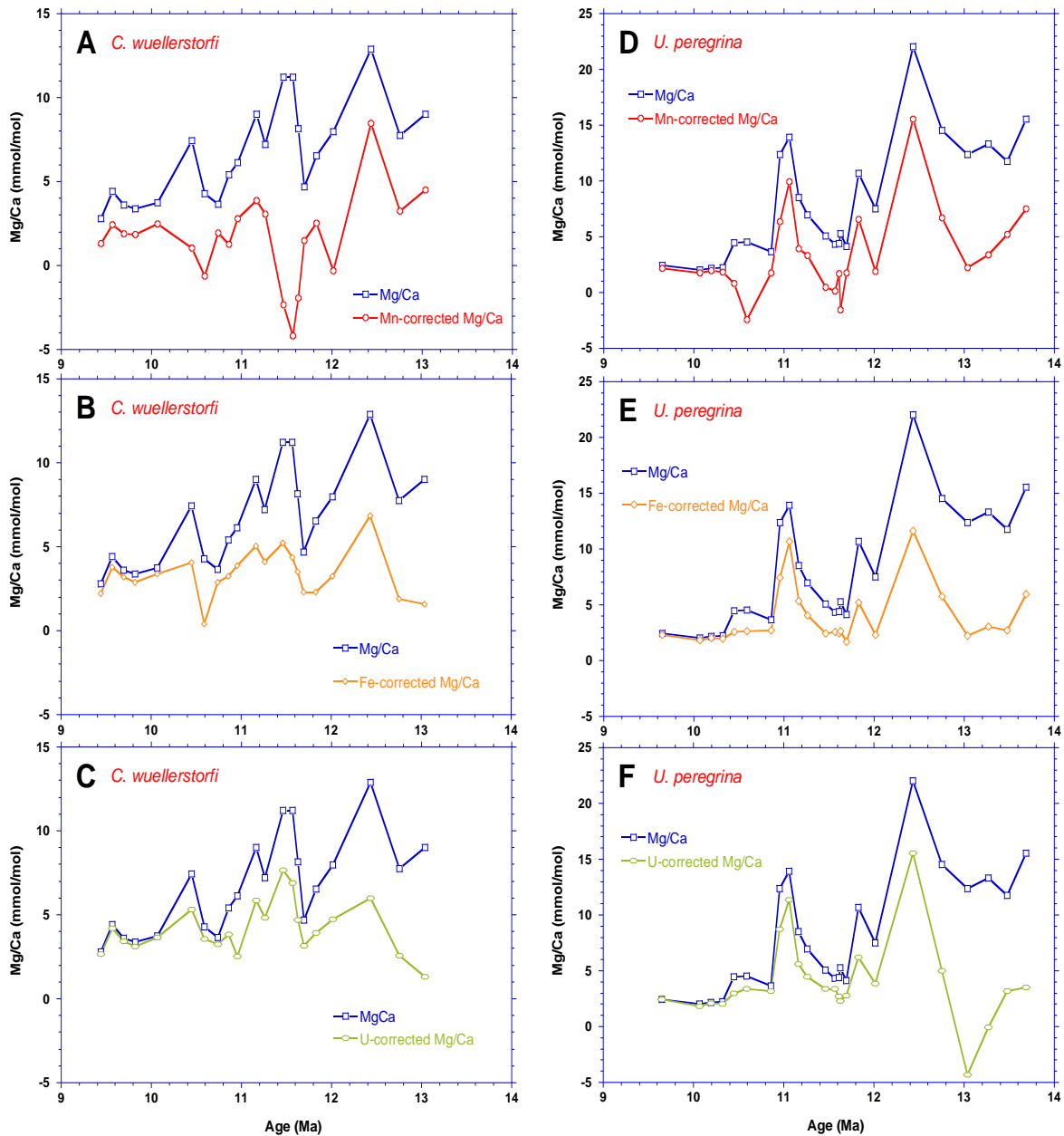


Figure 3.14: Contaminant corrected downcore *C. wuellerstorfi* (n=21) (A-C) and *U. peregrina* (n=24) (D-F) Mg/Ca (mmol/mol) records from Sunbird-1. Corrected Mg/Ca is calculated using Equation 3.1 and using the *H. elegans* Mg/X molar ratio, where X is Mn (A, D), Fe (B, E), or U (C, F). In all cases the contaminant correction lowers the Mg/Ca record, however, the corrected records show downcore point-to-point correlation with the original, contaminated Mg/Ca record.

Despite the significant lowering the application of the *H. elegans* Mg/X molar ratios does not satisfactorily correct for the contaminant phase. For all six scenarios, the contaminant corrected record shows downcore point-to-point correlation with the original Mg/Ca record

(Figure 3.14). This suggests the influence of contamination on the Mg/Ca records has not been fully accounted for. Furthermore, three of the six scenarios have corrected Mg/Ca values less than zero, which cannot be correct. The unrealistic nature of the Fe-corrected Mg/Ca records are most surprising because of the clear peak-to-peak correlation in the depth domain between *H. elegans* Mg/Ca and Fe/Ca (Figure 3.9 b), and the extremely strong covariance ( $R^2 = 0.97$ ) between them (Figure 3.9 f). In addition, the slope of the Mg/Fe linear fit is constant, indicating there is a consistent molar ratio over the full range of *H. elegans* Mg/Ca and Fe/Ca ratios. This suggests a uniform composition of contaminant through the core, independent upon Fe abundance.

A possible reason for this technique not successfully correcting for the contaminant coating is the application of a full chemical cleaning protocol. This included both the oxidative and reductive cleaning steps, which will have removed some of the contaminant coatings, but evidently not in their entirety. Pertinently, the reductive cleaning step would have reduced the Mg/Ca ratio of the primary test due to preferential dissolution of  $Mg^{2+}$  in the calcite lattice (Yu et al., 2007). Another factor could be the presence of more than contaminant phase with different compositions, e.g. one formed during reducing porewater conditions and another formed in oxic porewater conditions. This novel approach of using trace metal/calcium ratios from paired aragonitic and calcitic foraminifera to correct for contaminant coatings looks very promising, as shown by the relationship between Mg/Ca and Mn/Ca ( $R^2 = 0.80$ ), Fe/Ca ( $R^2 = 0.97$ ), and U/Ca ( $R^2 = 0.84$ ). For future studies to successfully implement this approach, they should only include the clay removal cleaning step. Unfortunately, the low abundances of benthic foraminifera in the sediment meant this experiment could not be repeated.

The failure of *H. elegans* Mg/Mn, Mg/Fe, or Mg/U ratios to satisfactorily correct for the Mg-rich contaminant phase in *C. wuellerstorfi* or *U. peregrina* means an alternative approach must be considered for determining the primary foraminiferal Mg/Ca ratio for palaeothermometry. The best way to allow for the interpretation of trace metal data with confidence is by adopting a microanalytical approach, as this allows for each sample to be individually assessed for a range of potential contaminants. This advantage is pertinent at Sunbird-1 as there is no consistent offset due to a single contaminant phase.

#### 3.4.6 An assessment of the impact of the coatings on other trace metal records

The observed impact of contamination by redox sensitive trace metals on the Mg/Ca and Sr/Ca ratios does not noticeably influence the B/Ca ratios. Whereas the redox sensitive trace metal concentrations decrease upwards in the core (Figure 3.2), the B/Ca ratios for all three species increase (Figure 3.3). This strongly suggests that B/Ca is not incorporated into the contaminant coating, and the observed trend of increasing values up through the record is likely primary.

The dampened increase in *U. peregrina* B/Ca relative to *C. wuellerstorfi* is likely due to infaunal species being less sensitive to bottom water  $\Delta[\text{CO}_3^{2-}]$ . Infaunal species of foraminifera calcify in contact with pore waters, which may be buffered against major changes in  $\Delta[\text{CO}_3^{2-}]$  (Zeebe, 2007, Mawbey and Lear, 2013, Elmore et al., 2015), as opposed to the supernatant bottom water from which epifaunal species calcify from. This dampened signal is maintained despite

the large changes in sedimentary redox conditions at the site to support the interpretation that B/Ca is unaffected by these changes.

### 3.5 Conclusions

Downcore Mn/Ca, Fe/Ca, and U/Ca from three species of benthic foraminifera indicate considerable changes in the sedimentary redox conditions at Sunbird-1 through the mid-late Miocene. These redox sensitive trace metal records demonstrate significant precipitation of authigenic uranium and Mn-Fe-oxides, during early stage diagenesis at the site. High fluxes of detrital organic matter from the proximal continent reduced oxygen concentrations in the pore waters, whilst rivers may have provided a major source for detrital Fe-Mn oxyhydroxides. Under these reducing conditions, U was precipitated and  $\text{Mn}^{2+}$ ,  $\text{Fe}^{2+}$  were released into the sedimentary porewaters where they precipitated onto the hard substrates of foraminiferal tests once they diffused into oxic regions. The concentrations of redox sensitive trace metals decreases through the record, a trend that can be explained by the tectonic subsidence of the basin. As the site subsided away from the surface waters, there was a reduction in the input of detrital organic matter and nutrients to the site of deposition.

Despite the application of a consistent and thorough cleaning protocol commonly used to remove possible contaminant phases, the Mg/Ca records from both epifaunal (*C. wuellerstorfi*) and infaunal (*U. peregrina*) benthic foraminifera at Sunbird-1 show a strong point to point downcore association with the redox sensitive trace metal ratios. This strongly suggests that the signals recorded in the foraminiferal trace metal records reflect post-depositional diagenesis. It follows that the primary geochemical signal of the foraminiferal

tests has been overprinted to some extent by the redox changes within the sediment column during early stage diagenesis. This alteration of the primary signal, by the precipitation of oxide contaminant coatings prevents the robust reconstruction of bottom water temperatures at Sunbird-1. Without an independent proxy for redox conditions, a quantitative estimate of the contaminant coatings' contribution to the foraminiferal Mg/Ca records cannot be determined. This would allow for the contribution of temperature to be isolated.

Clays dominate the sediment recovered from the Sunbird-1 well. This promotes the possibility that detrital silicates could be a primary cause of the foraminiferal Mg/Ca signals through the record. However, the foraminiferal Al/Ca records suggest this is not the case. The foraminiferal Al/Ca records do not display the decreasing trend through the record, so distinctive in the Mg/Ca, Sr/Ca, and redox-sensitive trace metal records, and also demonstrate negligible point-to-point tracking with the Mg/Ca records from the same species. Furthermore, there is a lack of correlation between *H. elegans* Al/Ca and Fe/Ca ratios, a feature typical of silicate contamination.

Using paired aragonitic-calcitic trace metal/calcium measurements to correct for the contaminant coatings has been attempted. This novel approach assumes that all Mg incorporated into the aragonitic *H. elegans* lattice is bound in the contaminant phase. However, this still results in the *C. wuellerstorfi* and *U. peregrina* Mg/Ca values being unrealistically high, likely due at least in part to the incorporation of the reductive and oxidative chemical cleaning steps. This paired aragonitic-calcitic approach showed potential,

but any future application of this technique should omit the reductive and oxidative cleaning steps.

Despite the distinctive downcore association between Mg/Ca, Sr/Ca, and the redox sensitive trace metals, it is noteworthy that the B/Ca records from all three species do not show any similar association. Furthermore, the B/Ca values are within the range of measured values from core-tops for each species. This strongly suggests that foraminiferal B/Ca ratios are unaffected by contaminant coatings which form due to changing sedimentary redox conditions, independent of microhabitat or carbonate phase.

To successfully identify the primary calcite phase from the contaminant phase, a high spatial resolution Laser Ablation (LA) ICP-MS study is required. Identifying the Mg/Ca ratios of the primary calcite using this microanalytical technique could provide a more robust quantification of absolute bottom water and sea surface temperatures from the site of Sunbird-1.

## **4 Optimising LA-ICP-MS ablation parameters to assess the impact of identifying the primary test of Mn-rich foraminifera on Mg/Ca palaeothermometry**

### **4.1 Introduction**

Sunbird-1 is a well located offshore Kenya (04° 18' 13.268" S, 39° 58' 29.936" E, 723 m water depth, Western Indian Ocean) dominated by clays reflecting high sedimentation rates (Chapter 2.1). The site provides a unique opportunity to reconstruct tropical sea surface and bottom water temperature from the mid-late Miocene using unrecrystallised foraminifera. Benthic foraminifera from Sunbird-1 have been analysed by solution based ICP-MS (Chapter 3). However, despite the glassy appearance of benthic foraminifera from Sunbird-1 under a reflecting light microscope and scanning electron microscope imagery revealing no obvious diagenetic coatings, the Mg/Ca records of both epifaunal and infaunal species show a downcore association with their respective Mn/Ca records (Figure 4.1). This association suggests diagenetic incorporation of an Mg-Mn-rich phase, inhibiting the ability of these glassy foraminifera to provide robust and reliable Mg/Ca temperatures.

By generating geochemical depth profiles through foraminiferal tests with a suitably high spatial resolution it is possible to distinguish the primary foraminiferal test from the Mg-Mn-rich contaminant phase (Creech et al., 2010), and then use the unaltered primary Mg/Ca ratio to infer the calcification temperature (Pena et al., 2005, Hasenfratz et al., 2016).

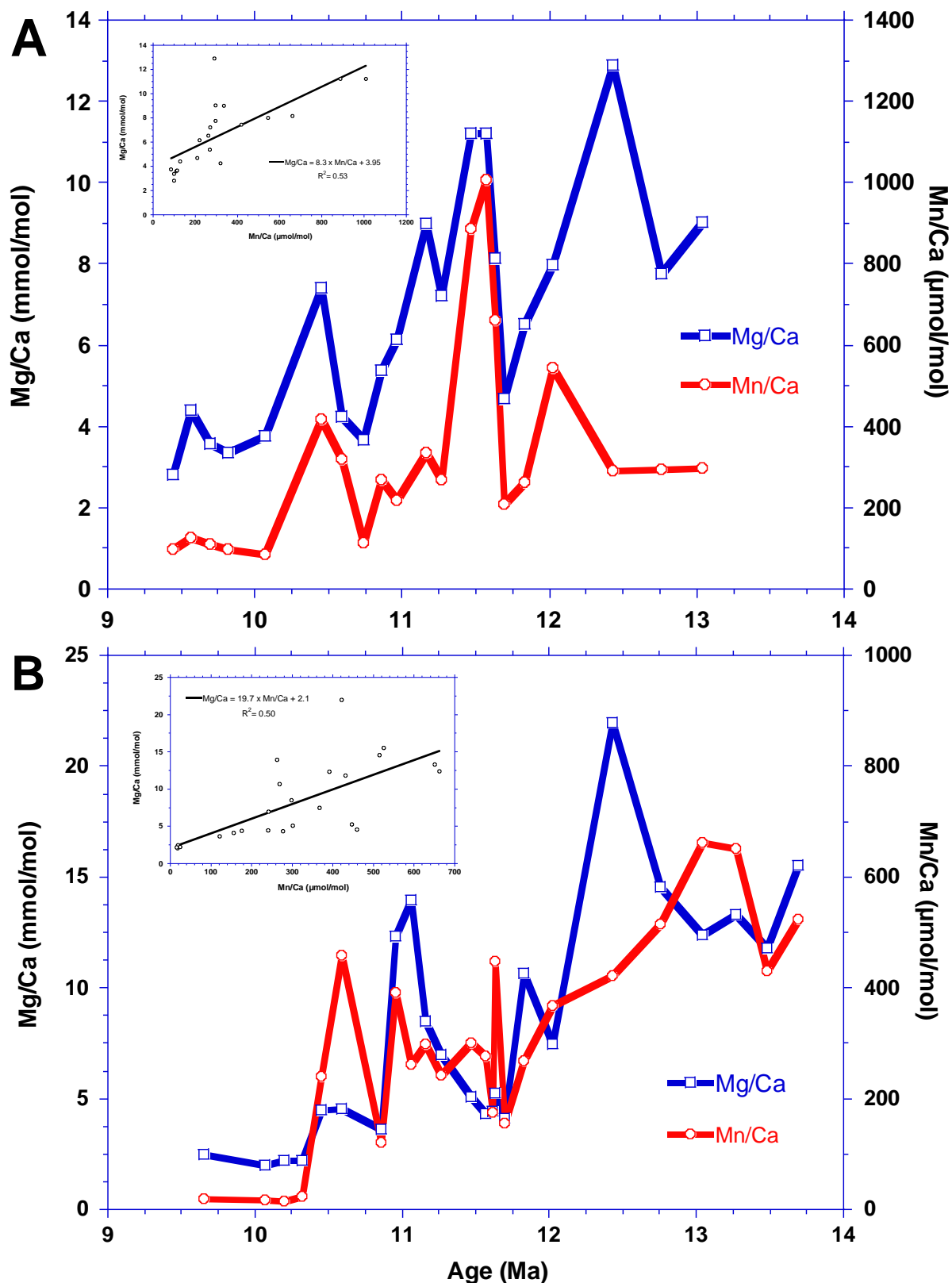


Figure 4.1: Solution based ICP-MS results from Sunbird-1. Downcore records of Mg/Ca (blue squares) and Mn/Ca (red circles) for (A) *C. wuellerstorfi* (n=21) and (B) *U. peregrina* (n=24), with insets of cross-plots between Mg/Ca and Mn/Ca for *C. wuellerstorfi* ( $R^2=0.53$ ) and *U. peregrina* ( $R^2=0.50$ ).

Direct sampling of solid phase material via Laser Ablation (LA-) allows for geochemical analyses through individual foraminiferal tests at the sub-micron scale when coupled to an inductively-coupled-plasma mass spectrometer (ICP-MS) (Wu and Hillaire-Marcel, 1995, Eggins et al., 2003, Reichart et al., 2003, Eggins et al., 2004, Evans et al., 2015a, Evans et al., 2015b, Fehrenbacher et al., 2015, Vetter et al., 2017, Petersen et al., 2018). A key advantage of analysing the trace element composition of foraminifera using LA-ICP-MS over the more traditional solution based ICP-MS is the ability to recognise the diagenetically altered portions of the tests, allowing identification of the primary calcite (Creech et al., 2010). The elemental composition of this primary calcite can provide uncompromised information about palaeotemperature (Eggins et al., 2003, Pena et al., 2005, de Nooijer et al., 2017) and other palaeo-environmental conditions such as pH (Thil et al., 2016) and oxygenation (Koho et al., 2015, Petersen et al., 2018).

This study is the first application of the RESOLUTION S-155 ArF 193nm excimer laser ablation system (Australian Scientific Instruments), when coupled to the Thermo Element XR magnetic sector field HR ICP-MS at Cardiff University. The objective of this study was to optimise the ablation parameters to collect accurate and precise data from homogenous glass standards, and then reproducible, accurate and precise measurements at the maximum possible spatial resolution through foraminiferal calcite. Optimal operating parameters for the glass standard and foraminiferal calcite had to be determined separately because they have a different matrix (Dueñas-Bohórquez et al., 2009). This was achieved by conducting extensive, systematic analyses at a range of fluences and repetition rates to determine the optimal combination of settings. Fluence is a measure of laser energy density ( $\text{Jcm}^{-2}$ ), and repetition

rate is the number of laser pulses per second (Hz). It follows that increasing these parameters increases the quantity of ablated material, and hence signal intensity, but reduces the achievable spatial resolution.

By determining optimal operating parameters, the LA-ICP-MS method has a spatial resolution that allows the primary trace metal signal to be isolated from regions of the test containing a Mg-Mn-rich diagenetic phase. This allows the primary calcite Mg/Ca to be used to calculate palaeotemperatures. Additionally, it has been possible to characterise the Mg/Mn molar ratios of the contaminant phase present in the test and assess its potential impact on Mg/Ca derived palaeotemperature estimates from traditional solution analysis.

### Summary of Scientific Experiments

- This chapter reports the first analyses using the newly installed laser ablation ICP-MS system in the School of Earth and Ocean Sciences at Cardiff University.
- The geochemical signal of the NIST 610 glass standard was measured across a range of fluences and repetition rates. Therefore the combination of these parameters that produces the most stable and intense signal, required for standardisation of geochemical analyses, could be determined.
- Test wall transects through a single *Orbulina universa* chamber were measured across a range of fluences and repetition rates. This enabled the determination of which combination of these parameters produces the most stable, intense, and reproducible signal.

- The quantity of ablation profiles required to get a consistent Mg/Ca value for a sample was determined, for both the benthic foraminifera *C. wuellerstorfi*, and the planktic foraminifera *D. altispira*. Multiple profiles from multiple specimens is required, due to the intra- and inter-specimen heterogeneity of foraminifera. A consistent Mg/Ca value for a sample is required for the determination of trends in Mg/Ca, and therefore temperature, through a record.

## 4.2 Laser ablation instrumentation and method development

### 4.2.1 General laboratory setup

Geochemical analyses were performed using an ArF excimer (193nm) LA- system with dual-volume laser-ablation cell (RESolution S-155, Australian Scientific Instruments) (Figure 4.2), installed in the Cardiff University CELTIC laboratory in December 2016, and my study is the

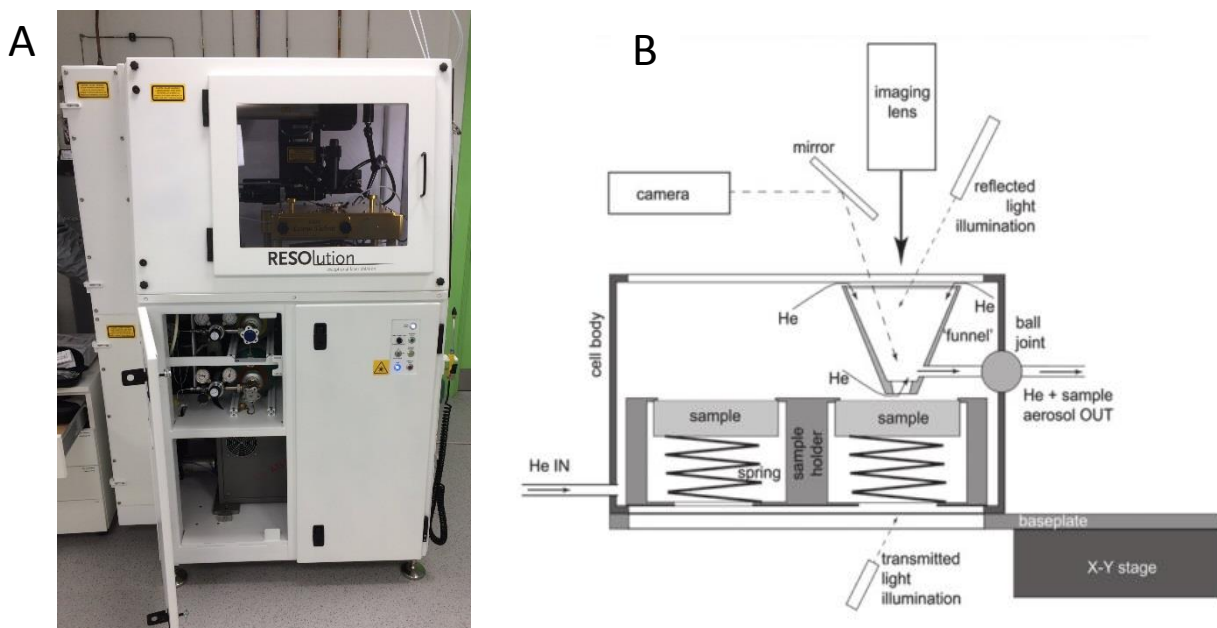


Figure 4.2: (A) RESolution ArF 193nm excimer laser ablation unit. (B) Schematic cross section adapted from Müller et al. (2009) of the Laurin dual volume S-155 laser ablation cell.

first application of the system. The dual-volume cell improves signal stability and uniformity, enabling a very short washout time. The performance and specification of the RESOLution LA-system with a smaller M-50 dual volume ablation cell has been previously described in detail (Müller et al., 2009). In the CELTIC laboratory this is coupled to a Thermo Element XR magnetic sector field HR ICP-MS. The extended range provided by the Faraday detector enables laser ablation work. Ablated sample aerosol passes through a 'squid' en route to the ICP-MS. The squid is a device which splits the aerosol into 10 differing length tubes smoothing the gas signal when they recombine (Eggins et al., 1998). This smoothing removes any spectral skew, as demonstrated by previous studies (Müller et al., 2009, Fehrenbacher et al., 2015).

Daily tuning of the system was required, as with all mass spectrometers. Daily tuning was performed on the NIST SRM 612 glass standard to ensure the sensitivity and stability of the system remained consistently high. The goal of the daily tuning procedure on the NIST SRM 612 is to ensure the signal intensity and stability of samples and standards during analysis are high enough, but oxide ratios are kept below an acceptable threshold. It is important to ensure  $U^+/Th^+$  is consistently  $\sim 1$ , and that  $ThO^+/Th^+$  remains below 0.4%. This was achieved by systematic tuning of the torch power and position, before optimising the flow of Ar (carrier, coolant, and auxiliary) to the ICP-MS. Further improvement of the signal stability was achieved by adjusting the flow rate of He and N<sub>2</sub> into the laser ablation cell. The typical operating parameters determined by this tuning are summarised in Table 4.1.

The isotopes analysed were  $^{25}\text{Mg}$ ,  $^{26}\text{Mg}$ ,  $^{43}\text{Ca}$ ,  $^{48}\text{Ca}$ ,  $^{55}\text{Mn}$ ,  $^{87}\text{Sr}$ , and  $^{88}\text{Sr}$ , each isotope having a constant dwell time of 50 milliseconds (ms), including the time devoted for sequential peak hopping. The total sweep time was therefore 350 ms allowing for 200 sweeps per peak at each repetition rate, through the 70-second method time. No spectral interference was expected on the analysed isotopes, and therefore the magnetic sector field ICP-MS was operated in low-resolution (LR) mode to maximise sensitivity. Analysing isotopes of iron with a magnetic sector field ICP-MS has to be done in medium-resolution (MR) because of spectral interference with argon in the sample gas. This applies to the interference of  $^{40}\text{Ar}^{16}\text{O}$  with  $^{56}\text{Fe}$  (May and Wiedmeyer, 1998) and  $^{40}\text{Ar}^{16}\text{O}^1\text{H}$  with  $^{57}\text{Fe}$  (Evans and Müller, 2018b). Because the acquisition of isotopes in MR follows the acquisition of isotopes in LR, it would not be possible to directly compare measurements of either  $^{56}\text{Fe}$  or  $^{57}\text{Fe}$  to the other isotopes, as they would be from spatially discrete regions of the foraminiferal test. Therefore, Fe is not analysed.

Established protocols for data reduction of time-resolved depth profiles were followed (Longerich et al., 1996). First, background count rates were subtracted from each data point to calculate the gas blank corrected element counts for both the NIST 610 reference standard and the foraminifera. Spikes, determined as values outside two standard deviations (95%) of the mean of the measurements preceding and following the proposed spike, were identified and removed. All ablation profiles were then normalised to an internal standard,  $^{43}\text{Ca}$ . Foraminiferal trace metal/Ca concentrations were calculated using the assumption of 40 wt% for  $\text{CaCO}_3$ . These background corrected ratios were then converted to mmol/mol by

normalising to the known trace metal element concentrations of the NIST SRM 610 glass standard ( $\text{Mg/Ca} = 8.75 \pm 0.37 \text{ mmol/mol}$ ) (Jochum et al., 2011).

All foraminiferal depth profiles were drift corrected by bracketing with NIST SRM 610 analyses. Due to the short timeframe of the analyses in this study, and this being the first study in the new Cardiff University CELTIC laboratory using this LA-ICPMS setup, it is not

**ICP-MS: Thermo Element XR**

RF Power	1300 Watts
Torch Position (X, Y, Z)	2.5, -0.2, -4.2 mm
Argon Carrier Flow (optimised daily)	~0.90 l/min
Argon Coolant Flow	14 l/min
Argon Auxiliary Flow	0.80 l/min
Sweep Time	350 ms
Cones	Ni

**Laser Ablation System: RESolution S-155**

Helium Flow	350 ml/min
N <sub>2</sub> Flow	4 ml/min
Spot Size	64 $\mu\text{m}$
Scan Speed	3 $\mu\text{m s}^{-1}$
Fluence (varying)	3.0-5.0 $\text{Jcm}^{-2}$
Repetition Rate (varying)	1.0-8.0 Hz
ThO <sup>+</sup> /Th <sup>+</sup>	<0.4%
U <sup>+</sup> /Th <sup>+</sup>	~1

Table 4.1: Typical LA-ICP-MS operating parameters for NIST SRM 610 and 612 glass standards.

possible to calculate long-term precision. However, an assessment of five years' worth of LA-ICPMS data, analysed on the same laser ablation system, indicates that blank corrected and calibrated measurements demonstrate no long term bias or drift (Evans and Müller, 2018b).

#### 4.2.2 Methodology to determine optimal operating parameters for the analysis of the NIST 610 glass standard

In this study NIST Standard Reference Material 610 glass is used as the external standard for calibrating the Sunbird-1 foraminiferal analyses because it is more homogenous than NIST 612 for Mg (Evans and Müller, 2018b). However, the lower elemental concentrations of the NIST Standard Reference Material 612 ( $1.32 \pm 0.54$  mmol/mol) would make it better matrix matched to foraminiferal calcite than the NIST 610 used here (Pearce et al., 1997, Jochum et al., 2011).

The optimal operating parameters for the NIST 610 glass standard in the Cardiff University CELTIC Laboratory were explored using a suite of experiments encompassing a range of fluences ( $\text{Jcm}^{-2}$ ) and repetition rates (Hz). The NIST 610 standard reference material was analysed from linear ablation paths, minimising any elemental fractionation with increasing crater depth (Eggins et al., 1998). Five ablation paths with five different energy densities (3.0, 3.5, 4.0, 4.5, and  $5.0 \text{ Jcm}^{-2}$ ) were run, all using the same operating parameters (Table 4.1) with varying repetition rates (1.0-8.0 Hz). For each repetition rate 24.5 seconds of background and 70 seconds of ablation data were collected. Data collection for each ablation path therefore totalled 756 seconds, with a total of 140 seconds of delay. The optimal operating parameters

will be the combination of fluence and repetition rate that produces an intense and stable signal, without over-compromising spatial resolution, over the 70 seconds of ablation.

#### 4.2.3 Methodology to determine optimal operating parameters for the analysis of foraminiferal tests

Different operating parameters are required for ablating foraminiferal calcite than for the glass standard because it has a different matrix. Whereas the NIST 610 standard is a homogenous glass, foraminiferal tests comprise heterogeneous, biologically precipitated calcite.

A single test of the planktic species *Orbulina universa* from the 1551-1554 m sample depth in Sunbird-1, with a biostratigraphic age of 11.74 Ma, was chosen to investigate optimal ablation parameters for foraminiferal analysis (Figure 4.3a). *Orbulina universa* was used because it has a large and all-encompassing spherical final chamber (Le Calvez, 1936, Caron et al., 1987, Lea et al., 1995,)) allowing for the maximum quantity of profiles on the same chamber of the same test to investigate reproducibility (Figure 4.3b). The test was picked from the >355 µm sediment size fraction, again to maximise the number of possible depth profiles per test. *Orbulina universa* inhabit the euphotic zone, <100 m water depth, their algal symbionts requiring light to photosynthesise (Be et al., 1973, Spero and Parker, 1985, Hemleben et al., 2012). Therefore, they precipitate their primary tests from seawater in the surface mixed layer, and their Mg/Ca ratios record sea surface temperature.

Fine clays and other detrital material on the outer surface of the test were removed by rinsing three times in 18.2 MΩ DI water, ultrasonicing for 5-10 seconds in methanol, and finally rinsing a further time in 18.2 MΩ DI water. The aggressive oxidative and reductive cleaning protocols commonly applied in the preparation of foraminifera for trace metal analysis were not included as this study was designed to distinguish between pristine test calcite and authigenic diagenetic coatings. Furthermore, these cleaning protocols were unsuccessful in removing the elevated Mg and Mn of a contaminant phase prior to solution based ICPMS from this site (Figure 4.1 and Chapter 3), and offer negligible benefit compared to that achieved by ultrasonication in 18.2 MΩ DI water and methanol (Vetter et al., 2013).

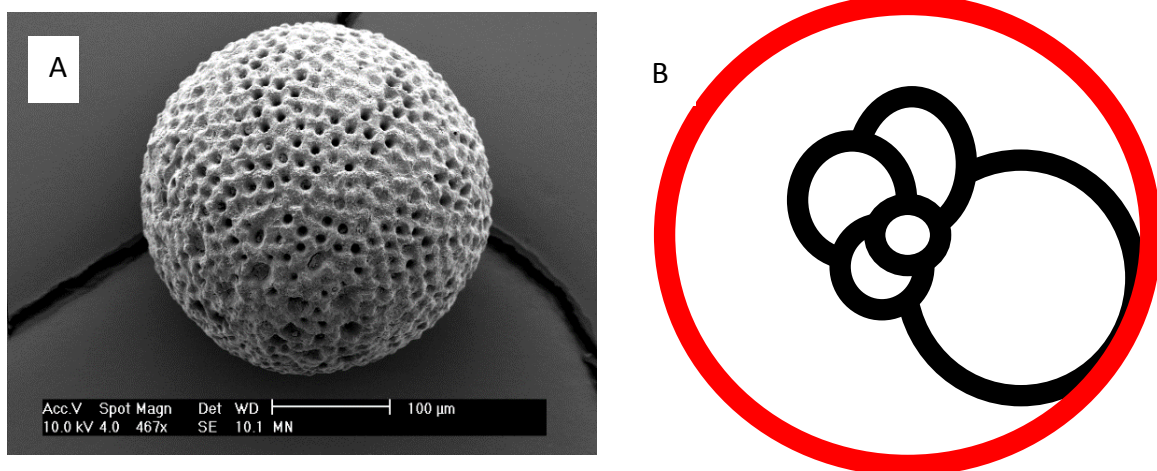


Figure 4.3: (A) SEM image of *Orbulina universa* from the 1551-1554 m depth sample in Sunbird-1, and (B) schematic cross section of *Orbulina universa* showing its all-encompassing spherical final chamber (red) and inner juvenile chambers (black).

Following the removal of any adhered clays the test was mounted onto a glass slide using double sided carbon tape and was allowed to dry before being mounted into the sample cell (Evans et al., 2015a, Fehrenbacher et al., 2015). As with the optimisation of the NIST SRM 610 glass standard a suite of experiments was conducted with different combinations of energy densities (3.0 and 3.5 Jcm<sup>-2</sup>) and repetition rates (2.0, 2.5, and 3.5 Hz) regularly

employed for ablating test wall transects through foraminifera (Table 4.2) (Creech et al., 2010, Evans et al., 2015a, Evans et al., 2015b, Holland et al., 2017). Using operational parameters for the external standard that are different to that of the foraminiferal test does not affect the accuracy of the analyte, Mg/Ca values of the foraminiferal tests being statistically identical (Dueñas-Bohórquez et al., 2009). In order to analyse intrashell variability in foraminifera it is necessary to maximise spatial resolution of depth profiles. Ideally data can be collected at the sub-micron scale by using a combination of low fluence and repetition rates so that each pulse only ablates a very thin,  $\sim 0.1 \mu\text{m}$ , layer of calcite, but enough to generate a high enough signal intensity. All depth profiles used a  $50 \mu\text{m}$  spot size to maximise spatial resolution and the number of profiles that could be obtained from the individual test, to investigate analytical reproducibility. All foraminiferal depth profiles were run on the same day to mitigate any day to day fluctuation in stability. The NIST 610 glass standard was ablated using the relevant optimised parameters (Chapter 4.3.2) to monitor and correct for its drift through the day. Despite being a synthetic glass, there is no evidence for any problems associated with matrix matching when using NIST 610 to calibrate carbonate samples (Czas et al., 2012, Evans and Müller, 2018b).

**ICPMS: Thermo Element XR**

RF Power	1300 Watts
Torch Position (X, Y, Z)	2.5, -0.2, -4.5 mm
Argon Carrier Flow (optimised daily)	~0.90 l/min
Argon Coolant Flow	14 l/min
Argon Auxiliary Flow	0.80 l/min
Sweep Time	350 ms
Cones	Ni

**Laser Ablation System: RESolution S-155**

Helium Flow	350 ml/min
N <sub>2</sub> Flow	4 ml/min
Spot Size	50 µm
Scan Speed	3 µms <sup>-1</sup>
Fluence (varying)	3.0 and 3.5 Jcm <sup>-2</sup>
Repetition Rate (varying)	2.0, 2.5, and 3.5 Hz
ThO <sup>+</sup> /Th <sup>+</sup>	<0.4%
U <sup>+</sup> /Th <sup>+</sup>	~1

Table 4.2: Operating parameters of LA-ICP-MS for *Orbulina universa* analyses.

**4.2.4 Determination of the number of profiles required for a representative sample Mg/Ca:**

Geochemical heterogeneity exists both within an individual foraminiferal test and between foraminiferal tests from the same sample (Eggins et al., 2004, Sadekov et al., 2005, Sadekov et al., 2008, Fehrenbacher and Martin, 2014). To acquire a consistent Mg/Ca ratio for temperature reconstructions the approximate total number of profiles that are required to

produce a homogenous Mg/Ca ratio for a sample, which can be deemed representative, is determined. This was conducted on individuals of *C. wuellerstorfi* and *D. altispira*, the benthic and planktic foraminiferal species used for the bottom water and sea surface temperature reconstructions in Chapter 5. A total of 10 test wall transects were conducted through each individual specimen to nullify the intra-specimen heterogeneity, and this was done for 10 specimens of each species from the 1551-1554 m sample to nullify any inter-specimen heterogeneity. This will allow determination of the number of profiles required to acquire a Mg/Ca value that is representative for the sample.

## 4.3 Results

### 4.3.1 Signal acquisition

Signal pick up is practically instantaneous, occurring within 1 second of ablation commencing (Figure 4.4). It is imperative that the intensities returned to background values before each step increase in repetition rate. This was achieved by activating the external trigger system so that data collection on the magnetic sector field ICP-MS resumed after a 20 second delay post ablation, during which the laser was turned off, allowing the intensities to return to background levels. Across the full range of fluences and repetition rates this 20 second delay was comfortably sufficient for a full washout to occur, with  $^{43}\text{Ca}$  returning to background counts before the resumption of data collection (Figure 4.4). Previous work using the same LA- and sample cell system showed signal washout over five orders of magnitude occurred within 9 seconds, and signal pick up over 5 orders of magnitude occurred within 2 seconds (Müller et al., 2009). My study demonstrates that the CELTIC laboratory instrumentation has

similarly rapid and thorough pick up and washout, confirming that the 20 second delay is appropriate.

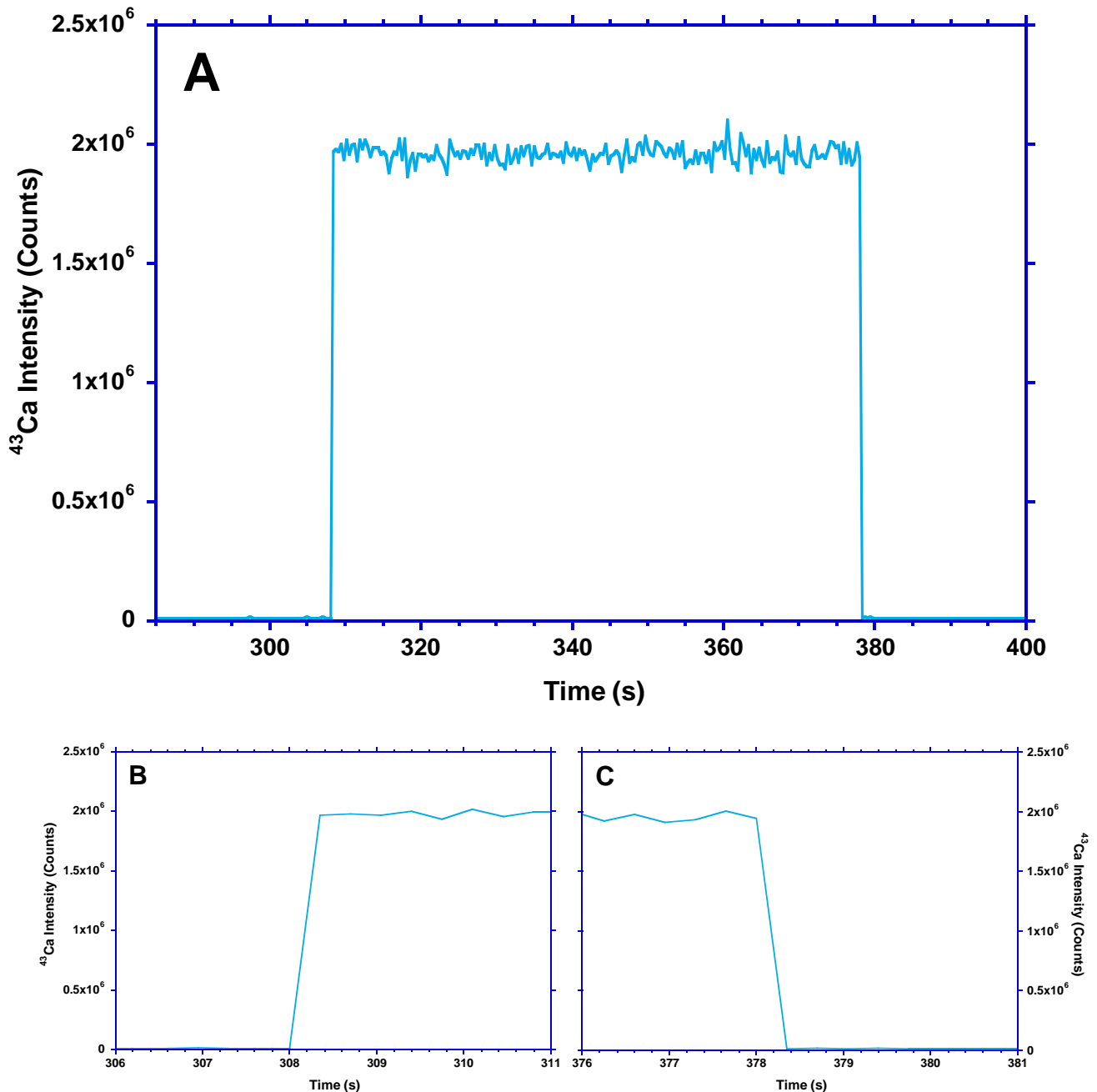


Figure 4.4: (A)  $^{43}\text{Ca}$  intensity (counts) from an example ablation path in NIST SRM 610 glass standard using the operational parameters summarised in Table 4.1, a fluence of  $4.5 \text{ Jcm}^{-2}$ , and a repetition rate of 4.0 Hz. (B) and (C) demonstrate the short (<1 second) pick-up and washout time from background to peak counts, and then back to background again.

It is vital to avoid a combination of repetition rate and sweep time that will cause harmonic oscillations in the data (Müller et al., 2009). This spectral skew is observed when the repetition rate is 3.0 Hz (1 pulse every 333 ms), the sweep time of 350 ms used here having a similar temporal beat, compared to when the repetition rate is 4.0 Hz (Figure 4.5). These observed oscillations could otherwise be erroneously interpreted as primary intrashell heterogeneity in foraminiferal depth profiles.

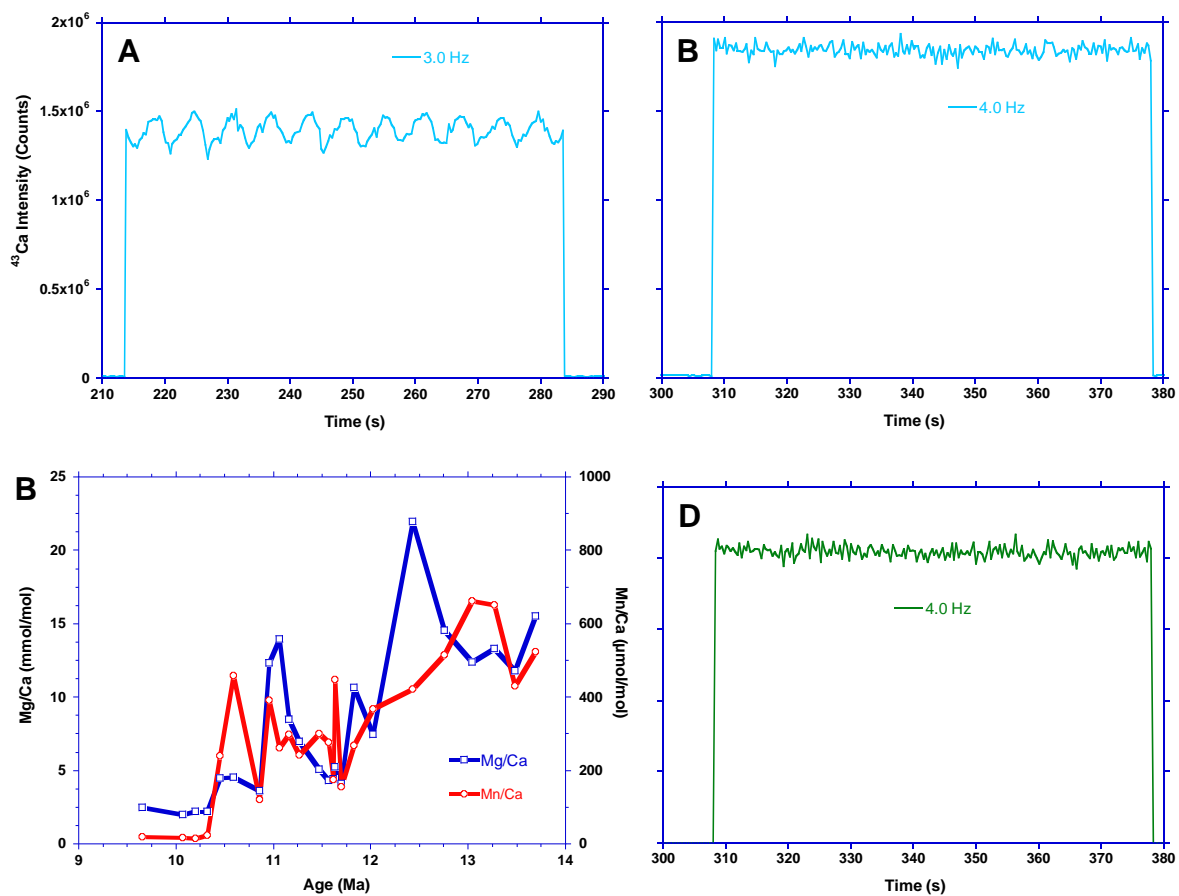


Figure 4.5: (A) Noticeable harmonic oscillation in  $^{43}\text{Ca}$  counts when the repetition rate is 3.0 Hz and the sweep time is 350 ms. (B) The 4.0 Hz segment of the ablation path with no harmonic oscillation, for comparison. (C) and (D) show the same effect for  $^{25}\text{Mg}$ . All data are from the 4.0 Jcm<sup>-2</sup> experiment on NIST SRM 610.

### 4.3.2 Optimal operating parameters for NIST 610 glass standard

Signal intensity increases at higher repetition rates, the greater number of pulses per second ablating more material. This supplies a higher quantity of analyte gas to the mass spectrometer, increasing intensities. However, higher repetition rates ablate through the test wall quicker, reducing the spatial resolution of the profiles. Therefore, a compromise regarding signal intensity will have to be accepted to increase spatial resolution within the test. The relative standard deviations (%RSD) were measured for the 70 seconds of ablation at each combination of fluence and repetition rate to quantify the stability of the signal. This signal smoothness could be further improved by increasing the dwell time at each mass of interest. However, this would also reduce the spatial resolution of the profiles through the foraminiferal test walls, potentially negating any high frequency natural intrashell variability. During the day of analysis my gas blank corrected NIST 610 ratios show a high level of stability, <3.5% RSD for Mg/Ca, <3% RSD for Mn/Ca, and <2% RSD for  $^{43}\text{Ca}/^{48}\text{Ca}$  (Table 4.3, Figure 4.6).

	Mg/Ca	$^{43}\text{Ca}/^{48}\text{Ca}$	Mn/Ca
%RSD	3.24	1.74	2.93

Table 4.3: RSDs (%) of the intensity ratios for Mg/Ca,  $^{43}\text{Ca}/^{48}\text{Ca}$ , and Mn/Ca in the NIST 610 standard from 16<sup>th</sup> June 2017, the day of the optimisation of foraminiferal calcite operating parameters experiments.

When the repetition rate is set to 1.0 Hz the intensity ratio on the mass spectrometer is extremely unstable, irrespective of the fluence, 30.3-32.2% RSD for Mg/Ca and 44.8-48.4% RSD for Mn/Ca. The RSDs decrease considerably when repetition rate is increased to 4.0 Hz, 2.5-4.1% RSD for Mg/Ca and 1.8-3.1% RSD for Mn/Ca but show minimal improvement at

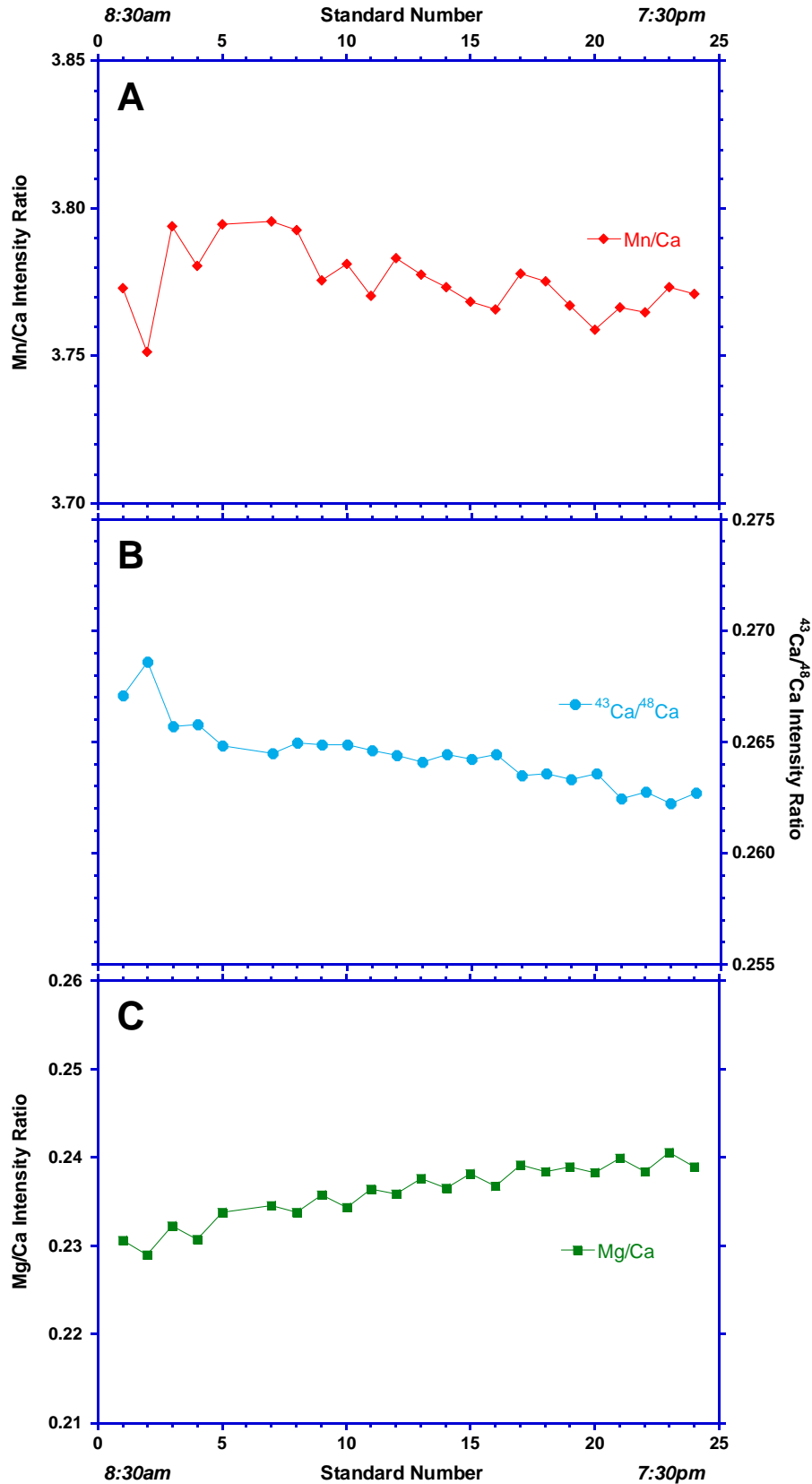


Figure 4.6: Drift in measurements ( $n=24$ ) of the gas blank corrected NIST SRM 610 glass standard for (A) Mn/Ca, (B)  $^{43}\text{Ca}/^{48}\text{Ca}$ , and (C) Mg/Ca through the course of the day on which the optimisation of foraminiferal calcite operating parameters experiments took place.

higher repetition rates (Figure 4.7, Table 4.4). When repetition rate is increased to 8.0 Hz the RSDs are lower than at 4.0 Hz, 1.3-2.2% RSD for Mg/Ca and 1.1-1.6% RSD for Mn/Ca. However, the quantity of ablated material required to achieve this slightly smoother signal is twice as high, and could potentially overload the ICP-MS, in particular for  $^{43}\text{Ca}$ . The RSDs for Mg/Ca are  $\ll 5\%$  at 4.0 Hz, which is an acceptable value to not require more material to be ablated (Figure 4.7d). These observations are consistent across all fluences used in this study, indicating that signal stability in the NIST SRM 610 glass standard is primarily controlled by repetition rate when fluence is in the range of 3.0-5.0  $\text{Jcm}^{-2}$ .

Despite this dominance of repetition rate on the signal stability the fluence does have an effect, at the preferred repetition rate of 4.0 Hz the RSDs for both Mg/Ca and Mn/Ca are  $\sim 1\%$  lower at 4.0 and 4.5  $\text{Jcm}^{-2}$  than at the other fluences tested (Figure 4.8, Table 4.4). With these experiments showing no significant difference between 4.0 and 4.5  $\text{Jcm}^{-2}$  the higher fluence of 4.5  $\text{Jcm}^{-2}$  is used, because the reported range of fluence used on NIST 610 in the literature is 4.5-5.0  $\text{Jcm}^{-2}$  (Fehrenbacher et al., 2015, Keul et al., 2017, van Dijk et al., 2017). Therefore, the optimal ablation parameters for measuring NIST 610 in the Cardiff University CELTIC Laboratory are a fluence of 4.5  $\text{Jcm}^{-2}$  and a repetition rate of 4.0 Hz.

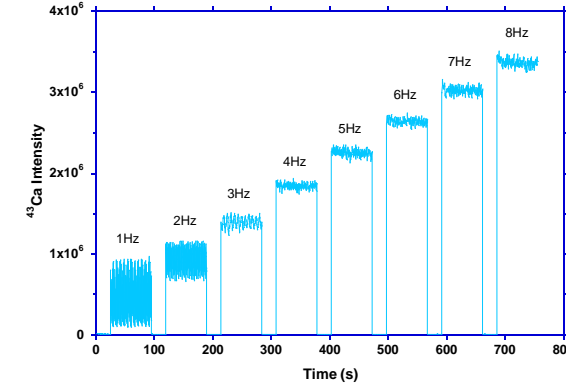
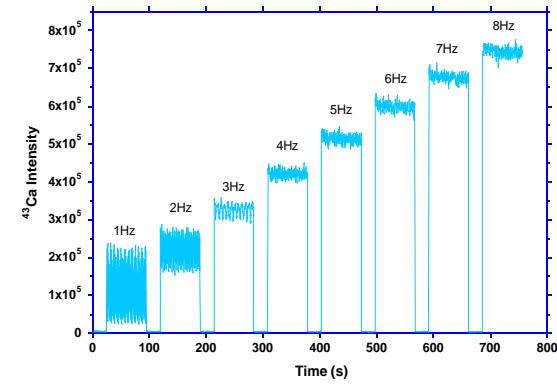
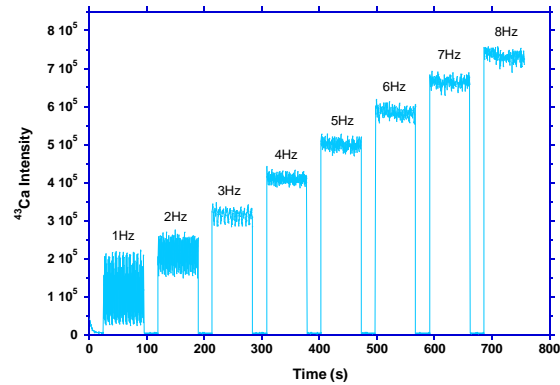
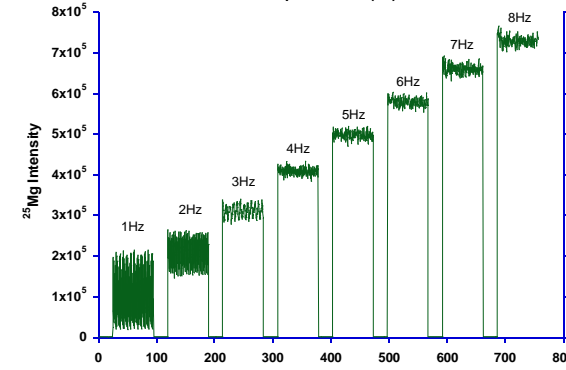
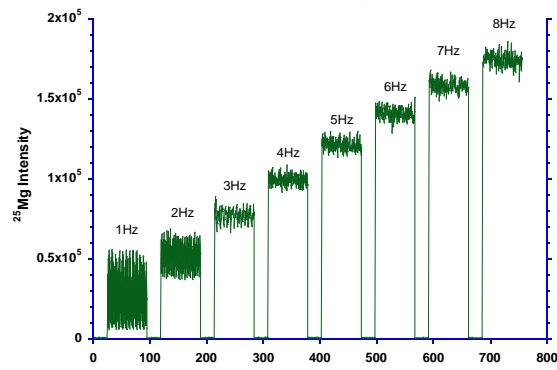
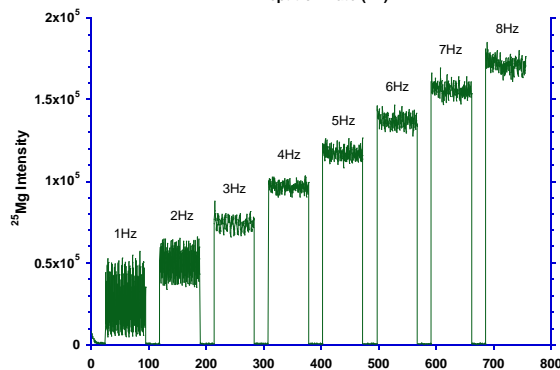
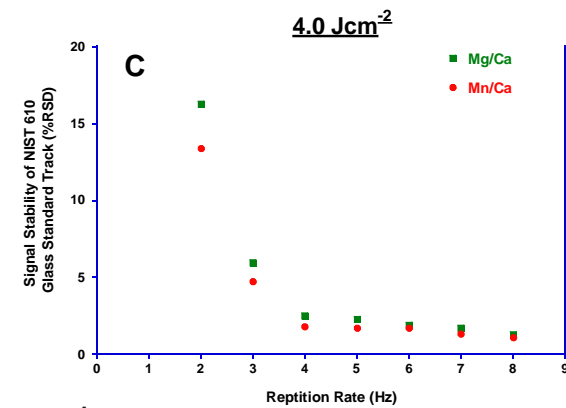
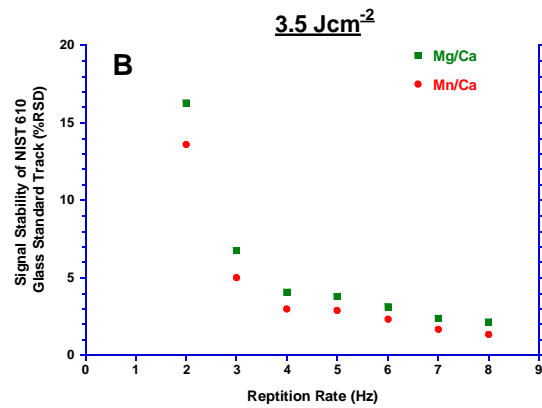
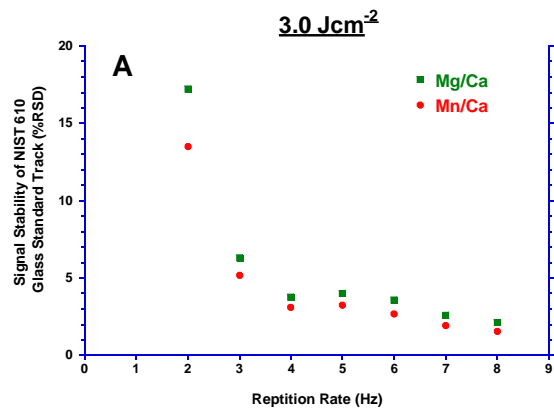
**Mg/Ca (%RSD)****Repetition Rate (Hz)**

		1	2	3	4	5	6	7	8
Fluence (Jcm <sup>-2</sup> )	3.0	31.4	17.2	6.3	3.7	4	3.6	2.6	2.1
	3.5	30.3	16.3	6.8	4.1	3.8	3.2	2.4	2.1
	4.0	32.2	16.3	6.0	2.5	2.3	1.9	1.7	1.3
	4.5	31.5	16.7	5.7	2.6	2.3	1.9	1.7	1.3
	5.0	31.4	16.6	6.6	3.8	3.5	2.6	2.2	2.1

**Mn/Ca (%RSD)****Repetition Rate (Hz)**

		1	2	3	4	5	6	7	8
Fluence (Jcm <sup>-2</sup> )	3.0	44.8	13.5	5.2	3.1	3.2	2.7	1.9	1.6
	3.5	48.4	13.6	5.0	3	2.9	2.4	1.7	1.4
	4.0	47.8	13.4	4.7	1.8	1.7	1.7	1.3	1.1
	4.5	46.6	13.8	4.4	1.9	1.8	2.1	1.5	1.1
	5.0	46.9	13.7	5.2	3.0	2.4	1.8	1.4	1.4

Table 4.4: Relative Standard Deviations (% RSDs) for Mg/Ca, and Mn/Ca measured in NIST SRM 610 for all tested combinations of fluence and repetition rate.



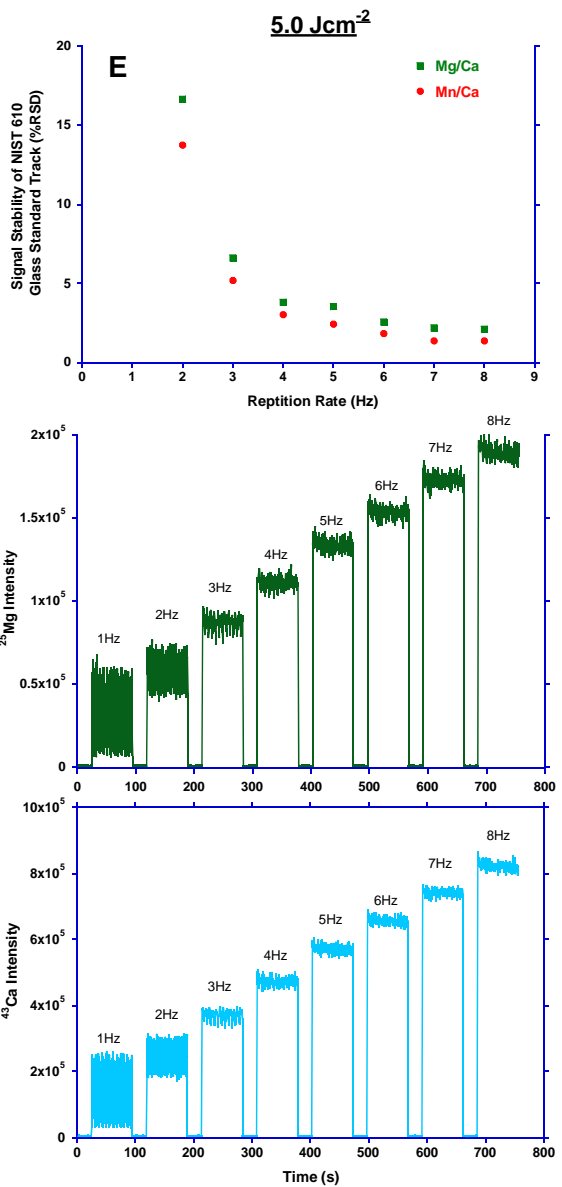
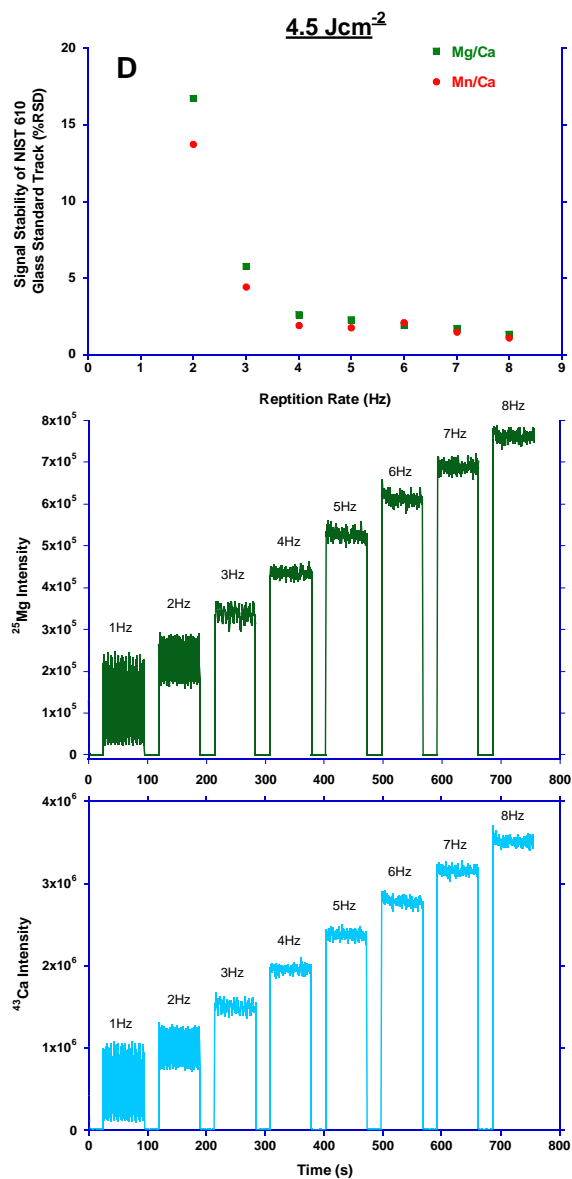


Figure 4.7: The effect of repetition rate on signal stability and sensitivity at a fluence of  $3.0 \text{ Jcm}^{-2}$  (A) to  $5.0 \text{ Jcm}^{-2}$  (E).

Top panel: Signal stability (%RSD) of Mg/Ca and Mn/Ca as a function of repetition rate.

Middle panel: Raw intensities of  $^{25}\text{Mg}$  across a range of repetition rates.

Bottom panel: Raw intensities of  $^{43}\text{Ca}$  across a range of repetition rates.

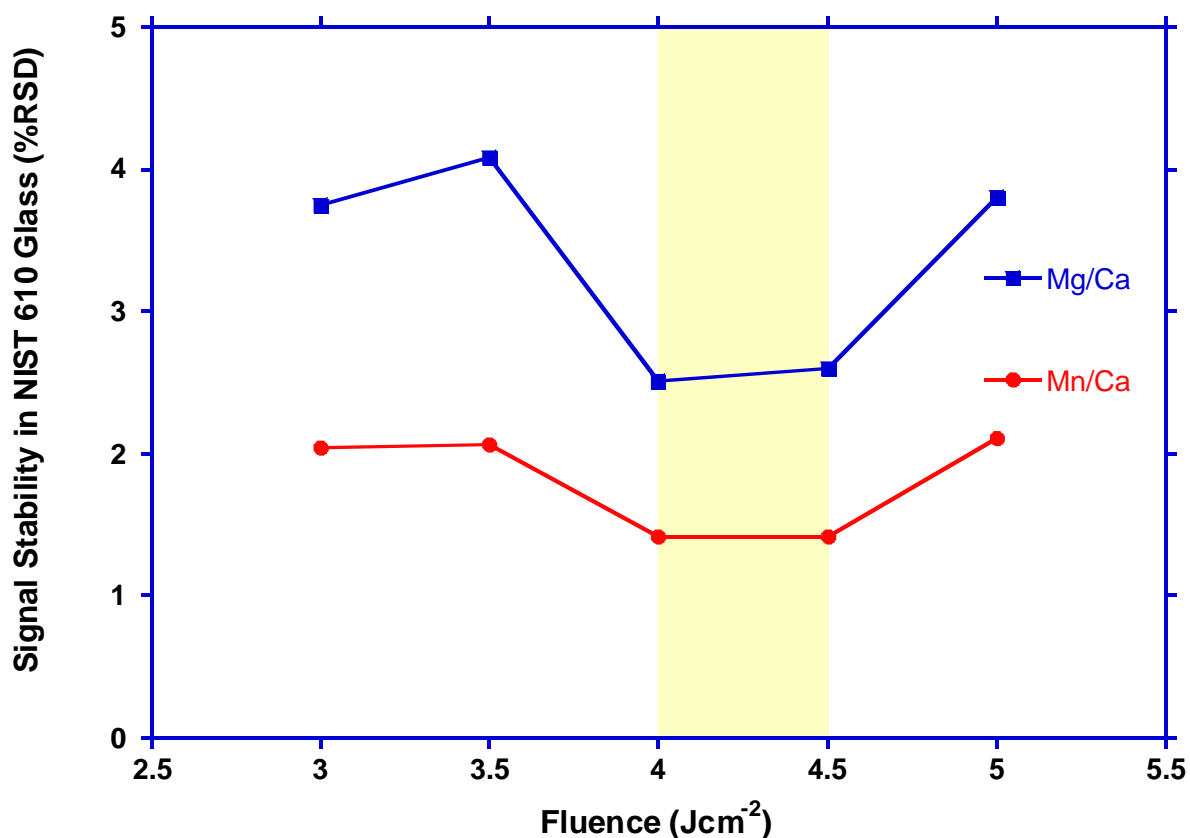


Figure 4.8: Signal stability (%RSD) for Mg/Ca (blue squares) and Mn/Ca (red circles) measured in NIST 610 at fluences ranging from 3.0 Jcm<sup>-2</sup> to 5.0 Jcm<sup>-2</sup> with a constant repetition rate of 4.0 Hz. The yellow bar shows the preferred fluences. Data are shown in Table 4.4.

#### 4.3.3 Optimal operating parameters for foraminiferal calcite

Reproducibility was used as an important criterion to determine the optimal fluence and repetition rate. For each combination of fluence and repetition rate three repeat transects through the test wall were obtained to assess analytical reproducibility. It is worth noting that no two transects will be true replicates because of the natural intrashell variability that persists through foraminifera. To minimise the impact of this unavoidable natural variability the repeat test wall transects were analysed as proximal as possible to each other, all on the same outer chamber of *O. universa*.

The first step in assessing the reproducibility for each combination of ablation parameters was simply to overlay the three Mg/Ca depth profiles (Figure 4.9). Because of the natural variability present in each profile a four point moving average is shown. Profiles are cut off at 80 seconds, beyond which all 18 show a high degree of scatter and would therefore be excluded from environmental interpretation. This may result either from the ablation breaking through the test wall, or from fractionation within a deep ablation pit (Eggins et al., 1998). The presence of elevated Mg/Ca in the outermost region of the test wall, as signified by the grey regions in Figure 4.9 and presumed to be a diagenetic coating, provides an added feature for the profiles to reproduce. This simple approach suggests that the two combinations that provide the most similar depth profiles are those with a fluence of  $3.0 \text{ Jcm}^{-2}$  and repetition rate of 2.5 Hz (Figure 4.9b), and a fluence of  $3.5 \text{ Jcm}^{-2}$  and repetition rate of 2.0 Hz (Figure 4.9d). Signal counts were high enough to deem it unnecessary to experiment with higher fluences higher than  $3.5 \text{ Jcm}^{-2}$  and repetition rates higher than 3.5 Hz as this would only reduce the spatial resolution of the depth profiles. Note that this would not be the case for analysis of isotopes with lower abundances, such as  $^{238}\text{U}$ . In light of the temporal beating previously observed at 3.0 Hz (Figure 4.5) no profiles were run with this repetition rate.

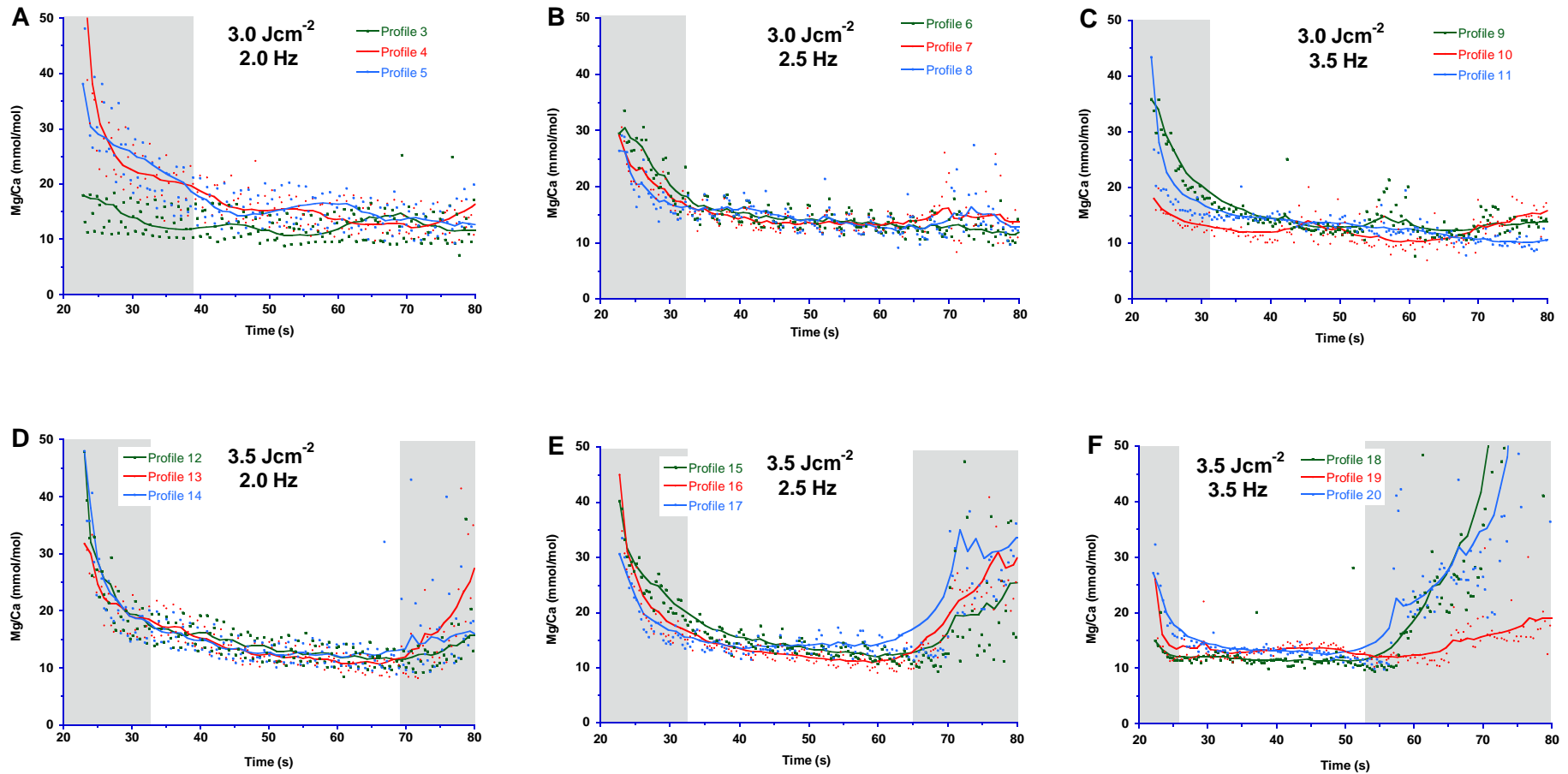


Figure 4.9: Mg/Ca variability through three repeat test wall transects for 6 combinations of ablation settings. All transects are through the single *O. universa* specimen from the 1551-1554 m depth sample in Sunbird-1. Solid lines are 4 point moving averages. Profiles are cut off at 80 seconds, beyond which all 18 show a high degree of scatter and would therefore be excluded from environmental interpretation.

In order to verify this conclusion a number of statistical measures were considered. Regions of the test which are Mg-Mn-rich are interpreted as a diagenetic coating and would be removed from further environmental consideration and palaeotemperature estimates. Therefore, for all of these statistical measures these regions of the test, the greyed out regions in Figure 4.9, are excluded. Inclusion of the Mg-Mn-rich regions of the test for these statistical measures could produce misleading results for application to future analyses, where these regions will be excluded.

First, the range in median values for the three profiles at each combination of ablation parameters were compared to assess their similarity (Table 4.5). The reason for using the median instead of the mean is to remove any skew and bias originating from inclusion of any flier data points. Fliers of high Mg/Ca values are prevalent (Figure 4.10), even within the interval determined to be primary test, and consequently mean Mg/Ca is greater than the median Mg/Ca for 17 out of 18 profiles, and for all six combined measures (Table 4.5). The smallest difference between the highest and lowest median of the three repeat depth profiles relative to the median of all the measurements combined was 4.9%, achieved when a fluence of  $3.0 \text{ Jcm}^{-2}$  and a repetition rate of 2.5 Hz was used, one of my preferred ablation settings from simple visual inspection. This supports my initial interpretation that a fluence of  $3.0 \text{ Jcm}^{-2}$  and a repetition rate of 2.5 Hz as being one of the two combinations that produces the most alike depth profiles. Comparatively, the other five combinations of fluence and repetition rate produce much larger differences, their median Mg/Ca values varying by between 8.5% and 15.7%. Median Mg/Ca values with the  $3.5 \text{ Jcm}^{-2}$  and 2.0 Hz parameters, the other preferred combination from simple visual inspection, have a difference of 8.7%.

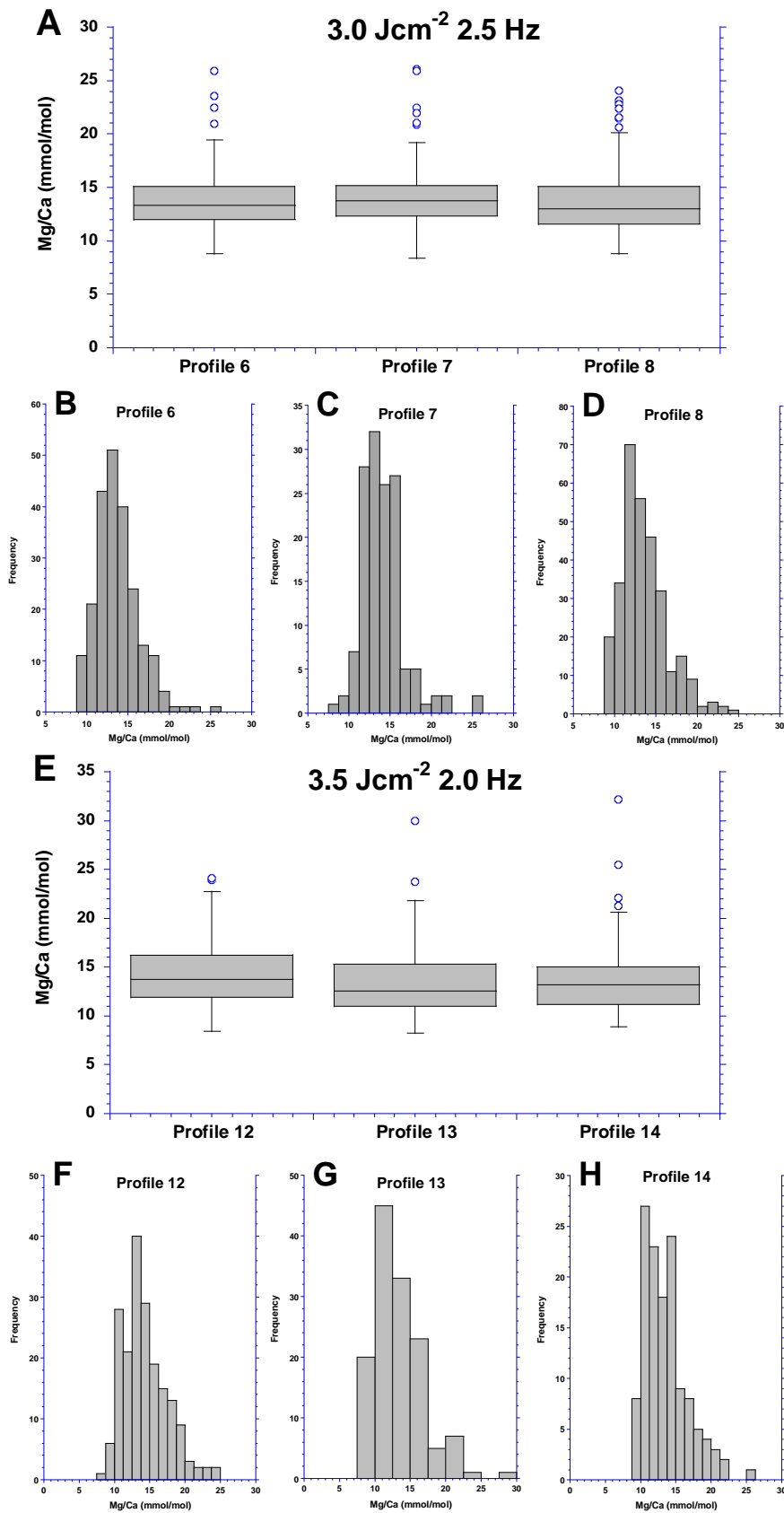


Figure 4.10: Box plots and histograms for Mg/Ca through the repeat test wall transects of *O. universa* at 3.0 Jcm<sup>-2</sup> and 2.5 Hz (A-D), and 3.5 Jcm<sup>-2</sup> and 2.0 Hz (E-H). Data do not include regions of the test determined to be influenced by an Mg-Mn-rich contaminant phase.

<u>3.0 Jcm<sup>-2</sup> 2.0 Hz</u>	Profile 3 (n=86)		Profile 4 (n=130)		Profile 5 (n=146)		Combined (n=362)	
	Mg/Ca (mmol/mol)	Mn/Ca (μmol/mol)	Mg/Ca (mmol/mol)	Mn/Ca (μmol/mol)	Mg/Ca (mmol/mol)	Mn/Ca (μmol/mol)	Mg/Ca (mmol/mol)	Mn/Ca (μmol/mol)
Mean	14.0	120	15.0	95	15.7	401	14.6	176
Median	13.5	119	14.5	92	15.2	379	14.4	118
Range	8.1	71	10.8	75	11.1	224	9.9	417
Standard Deviation	2.7	21	3.2	23	3.7	76	3.3	150
RSD (%)	19.3%	17.8%	21.6%	24.2%	23.6%	19.1%	22.4%	85.0%

<u>3.0 Jcm<sup>-2</sup> 2.5 Hz</u>	Profile 6 (n=116)		Profile 7 (n=109)		Profile 8 (n=124)		Combined (n=349)	
	Mg/Ca (mmol/mol)	Mn/Ca (μmol/mol)	Mg/Ca (mmol/mol)	Mn/Ca (μmol/mol)	Mg/Ca (mmol/mol)	Mn/Ca (μmol/mol)	Mg/Ca (mmol/mol)	Mn/Ca (μmol/mol)
Mean	13.9	460	14.2	102	14.2	100	14.1	220
Median	13.3	380	13.8	81	13.1	84	13.3	104
Range	6.7	444	6.1	180	7.5	116	9.2	599
Standard Deviation	3.3	165	2.7	70	5.7	105	4.5	210
RSD (%)	23.8%	35.9%	19.0%	69.1%	40.4%	105.5%	31.9%	95.1%

<u>3.0 Jcm<sup>-2</sup> 3.5 Hz</u>	Profile 9 (n=97)		Profile 10 (n=114)		Profile 11 (n=118)		Combined (n=329)	
	Mg/Ca (mmol/mol)	Mn/Ca (μmol/mol)	Mg/Ca (mmol/mol)	Mn/Ca (μmol/mol)	Mg/Ca (mmol/mol)	Mn/Ca (μmol/mol)	Mg/Ca (mmol/mol)	Mn/Ca (μmol/mol)
Mean	14.0	62	12.1	93	12.7	76	12.9	77
Median	13.5	61	11.5	87	12.6	76	12.6	77
Range	6.4	90	6.7	71	5.3	59	7.0	92
Standard Deviation	3.9	39	2.5	24	2.1	20	3.0	31
RSD (%)	27.9%	62.6%	20.2%	26.3%	16.3%	26.7%	23.0%	40.4%

<u>3.5 Jcm<sup>-2</sup> 2.0 Hz</u>	Profile 12 (n=100)		Profile 13 (n=114)		Profile 14 (n=118)		Combined (n=332)	
	Mg/Ca (mmol/mol)	Mn/Ca (μmol/mol)	Mg/Ca (mmol/mol)	Mn/Ca (μmol/mol)	Mg/Ca (mmol/mol)	Mn/Ca (μmol/mol)	Mg/Ca (mmol/mol)	Mn/Ca (μmol/mol)
Mean	14.5	117	13.4	101	14.0	102	14.0	107
Median	13.7	112	12.6	96	13.2	101	13.4	104
Range	7.9	83	11.3	73	9.8	60	10.8	73
Standard Deviation	4.2	33	3.5	21	4.3	18	4.0	27
RSD (%)	28.6%	28.5%	26.5%	21.2%	30.6%	17.2%	29.0%	25.6%
<u>3.5 Jcm<sup>-2</sup> 2.5 Hz</u>	Profile 15 (n=110)		Profile 16 (n=119)		Profile 17 (n=120)		Combined (n=349)	
	Mg/Ca (mmol/mol)	Mn/Ca (μmol/mol)	Mg/Ca (mmol/mol)	Mn/Ca (μmol/mol)	Mg/Ca (mmol/mol)	Mn/Ca (μmol/mol)	Mg/Ca (mmol/mol)	Mn/Ca (μmol/mol)
Mean	13.6	134	12.7	106	14.0	112	13.4	117
Median	13.4	127	12.5	103	13.7	111	13.3	111
Range	7.6	115	6.3	53	4.9	44	6.6	84
Standard Deviation	2.2	34	2.1	16	1.5	13	2.0	26
RSD (%)	16.5%	25.6%	16.3%	15.1%	10.6%	11.3%	15.0%	21.9%
<u>3.5 Jcm<sup>-2</sup> 3.5 Hz</u>	Profile 18 (n=95)		Profile 19 (n=120)		Profile 20 (n=87)		Combined (n=302)	
	Mg/Ca (mmol/mol)	Mn/Ca (μmol/mol)	Mg/Ca (mmol/mol)	Mn/Ca (μmol/mol)	Mg/Ca (mmol/mol)	Mn/Ca (μmol/mol)	Mg/Ca (mmol/mol)	Mn/Ca (μmol/mol)
Mean	11.6	100	12.7	114	12.8	98	12.4	104
Median	11.4	97	12.4	111	13.0	96	12.1	102
Range	3.0	30	3.5	49	4.0	25	4.2	43
Standard Deviation	2.1	19	1.4	16	1.2	9	1.7	17
RSD (%)	18.0%	18.6%	10.9%	14.1%	9.6%	9.3%	13.6%	16.4%

Table 4.5: Statistical summary of Mg/Ca (mmol/mol) and Mn/Ca (μmol/mol) for each of the three repeat test wall transects through *O. universa* at each combination of fluence and repetition rate. The two right hand columns document the combined statistics for each combination. The statistics were calculated only incorporating the region of the test wall transects determined to be free of contamination, i.e. without the greyed out intervals in Figure 4.9.

To assess reproducibility in a more statistically robust fashion, the variance between the three depth profiles for each combination of fluence and repetition rate was evaluated. Shapiro-Wilk Normality tests on the 18 profiles indicate that only Profile 8 ( $3.0 \text{ Jcm}^{-2}$ , 2.5 Hz) and Profile 20 ( $3.5 \text{ Jcm}^{-2}$ , 3.5 Hz) can be regarded as normally distributed populations ( $p > 0.05$ ). This non-parametric distribution of Mg/Ca values for each profile, as also seen in Figure 4.10, makes the Kruskal-Wallis test more robust than the standard ANOVA test for assessing the reproducibility between the three depth profiles for each combination of fluence and repetition rate. Furthermore, the maximum standard deviation in Mg/Ca at  $3.0 \text{ Jcm}^{-2}$ , 2.5 Hz (5.7 mmol/mol) is more than twice that of the minimum standard deviation (2.7 mmol/mol) at that combination of ablation settings, breaking another assumption of the ANOVA test. Unlike ANOVA, the Kruskal-Wallis test does not require the residuals to be normally distributed, or for the maximum standard deviation to be less than twice the minimum as it tests for differences between medians. By conducting a Kruskal-Wallis test the null hypothesis ( $p < 0.005$ ) that there is no difference between the median Mg/Ca values of each profile was unable to be rejected for two of the ablation settings tested ( $3.0 \text{ Jcm}^{-2}$ , 2.5 Hz, and  $3.5 \text{ Jcm}^{-2}$ , 2.0 Hz) (Table 4.6, highlighted).

Furthermore, the null hypothesis ( $p < 0.05$ ) that the three profiles using both of these respective ablation settings are from populations with identical distributions was also unable to be rejected by use of the Mann-Whitney-Wilcoxon test (Table 4.7, highlighted). These are also the two combinations for which the difference between the medians of the three depth profiles were lowest, lending further support to the initial conclusion.

	3.0 Jcm <sup>-2</sup>			3.5 Jcm <sup>-2</sup>		
	2.0 Hz	2.5 Hz	3.5 Hz	2.0 Hz	2.5 Hz	3.5 Hz
<b>Chi-Square (H)</b>	11.64	1.16	136.7	1.37	25.4	80.8
<b>Degrees of Freedom</b>	2	2	2	2	2	2
<b>p-value</b>	0.003	<b>0.560</b>	2.11E-30	<b>0.504</b>	3.11E-06	2.79E-18

Table 4.6: Table of results of the non-parametric Kruskal-Wallis test, for each combination of fluence and repetition rate. The null hypothesis that there is no difference between the medians of the three depth profiles can be rejected when  $H > 10.597$  ( $p < 0.005$ ). For the 3.0 Jcm<sup>-2</sup> and 2.5 Hz, and 3.5 Jcm<sup>-2</sup> and 2.0 Hz combinations, highlighted in yellow, this null hypothesis cannot be rejected.

		Profiles	W value	p-value
<b>3.0 Jcm<sup>-2</sup></b>	<b>2.0 Hz</b>	3 v 4	4664	0.040
		3 v 5	4613	0.001
		4 v 5	8472	<b>0.124</b>
	<b>2.5 Hz</b>	6 v 7	6867	<b>0.265</b>
		6 v 8	7202	<b>0.986</b>
		7 v 8	6369	<b>0.449</b>
	<b>3.5 Hz</b>	9 v 10	8412	6.96E-11
		9 v 11	5444	<b>0.227</b>
		10 v 11	3119	9.96E-14
<b>3.5 Jcm<sup>-2</sup></b>	<b>2.0 Hz</b>	12 v 13	6072	<b>0.411</b>
		12 v 14	5778	<b>0.794</b>
		13 v 14	6150	<b>0.260</b>
	<b>2.5 Hz</b>	15 v 16	8015	0.003
		15 v 17	5640	<b>0.057</b>
		16 v 17	4455	5.08E-07
	<b>3.5 Hz</b>	18 v 19	2168	6.39E-15
		18 v 20	1390	1.13E-14
		19 v 20	4552	<b>0.117</b>

Table 4.7: Table of results for the non-parametric Mann-Whitney-Wilcoxon test for each combination of fluence and repetition rate. For all of the profile comparisons using ablation setting combinations of 3.0 Jcm<sup>-2</sup> and 2.5 Hz, and 3.5 Jcm<sup>-2</sup> and 2.0 Hz, highlighted in orange, the null hypothesis that the profiles are from identical populations cannot be rejected ( $p < 0.05$ ).

Therefore, the most reproducible Mg/Ca profiles are obtained with either a combination of 3.0 Jcm<sup>-2</sup> and 2.5 Hz, or a combination of 3.5 Jcm<sup>-2</sup> and 2.0 Hz. However, the 3.0 Jcm<sup>-2</sup> and 2.5 Hz combination fails to demonstrate the full extent of the elevated Mg/Ca in the outer coating, as captured by other combinations (Figure 4.9). There is also the possibility of interaction between a repetition rate of 2.5 Hz and a sweep time of 350ms potentially leading to temporal beating, which can be seen to a minor extent (Figure 4.9b). For these reasons the analytical method which uses a fluence of 3.5 Jcm<sup>-2</sup> and a repetition rate of 2.0 Hz is preferred.

#### 4.3.4 Acquiring a consistent foraminiferal Mg/Ca ratio

There is notable spread in the measurements of Mg/Ca in *C. wuellerstorfi* (n=67) and *D. altispira* (n=72) from the 1551-1554m sample (Figure 4.11). The Mg/Ca value of single depth profiles in *C. wuellerstorfi* ranges from 1.62 mmol/mol to 3.14 mmol/mol, and from 2.67 mmol/mol to 5.23 mmol/mol in *D. altispira* (Appendix 5). This natural heterogeneity, both intra-specimen and inter-specimen, renders it challenging to acquire a reliable mean Mg/Ca for the sample, a value required for interpretation of any down record trends.

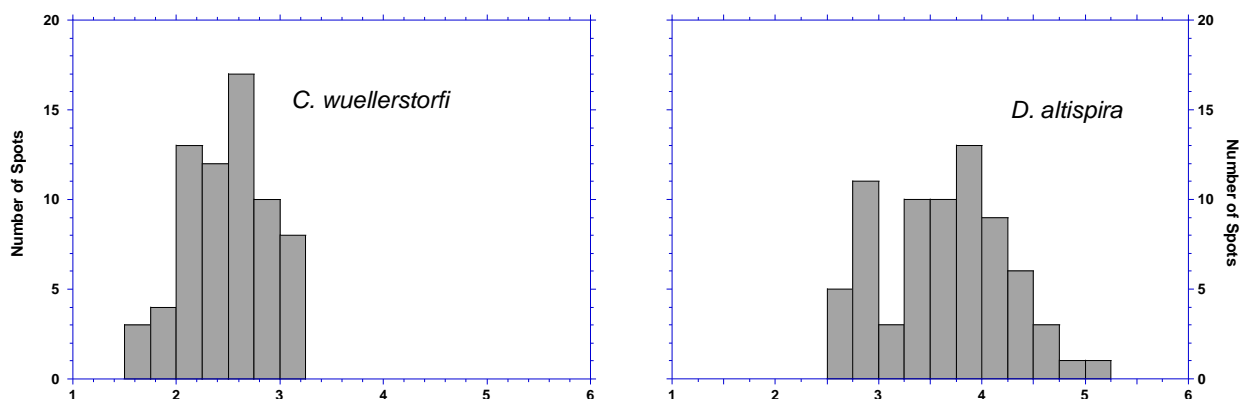


Figure 4.11: Histograms of measured Mg/Ca ratios (mmol/mol) in *C. wuellerstorfi* (n=67) and *D. altispira* (n=72) from the 1551-1554m sample.

The mean Mg/Ca value from all measurements of *C. wuellerstorfi* is  $2.48 \pm 0.09$  mmol/mol. The mean Mg/Ca value after 5 specimens, a total of 31 profiles, is well within 2 standard error of this value,  $\text{Mg/Ca} = 2.52 \pm 0.14$  mmol/mol, where errors are  $\pm 2$  SE of all the Mg/Ca measurements from that sample (Table 4.8, Figure 4.12a). Further measurements have minimal influence on the mean sample Mg/Ca and its standard error (Figure 4.12a, c). This suggests that a total of  $\sim 31$  measurements from approximately five specimens is required to get a consistent Mg/Ca value for *C. wuellerstorfi*. The extremely low standard error after only one specimen of *C. wuellerstorfi* is an artefact of there being only two depth profiles that passed the screening for contaminants, and these having Mg/Ca ratios of 2.57 and 2.58 mmol/mol.

<i>C. wuellerstorfi</i>			<i>D. altispira</i>		
Number of Spots	Sample Mean Mg/Ca (mmol/mol)	Sample 2 SE (mmol/mol)	Number of Spots	Sample Mean Mg/Ca (mmol/mol)	Sample 2 SE (mmol/mol)
2	2.57	0.00	4	3.25	0.45
4	2.46	0.20	12	3.69	0.24
12	2.80	0.17	20	3.58	0.19
21	2.64	0.16	28	3.41	0.18
31	2.52	0.14	34	3.42	0.22
38	2.48	0.12	41	3.44	0.19
45	2.52	0.11	46	3.41	0.17
54	2.53	0.09	55	3.46	0.15
59	2.55	0.09	63	3.63	0.15
67	2.48	0.09	72	3.57	0.14

Table 4.8: One example of the evolution of the mean Mg/Ca ratio and 2 SE with increased number of profiles in *C. wuellerstorfi* and *D. altispira* from the 1551-1554m sample.

The mean Mg/Ca value from all measurements of *D. altispira* is  $3.63 \pm 0.14$  mmol/mol. However, this mean Mg/Ca value is elevated by specimen 9, which has a much higher Mg/Ca ratio (4.33 mmol/mol) than any of the nine other specimens. Prior to this specimen the mean Mg/Ca value for *D. altispira* from the 1551-1554m sample is  $3.46 \pm 0.15$  mmol/mol from a total of 55 measurements across eight specimens (Table 2). The mean Mg/Ca value after four specimens, a total of 28 profiles, is  $3.41 \pm 0.18$  mmol/mol showing that an approximate doubling of the number of measurements from 28 to 55, and the number of specimens from four to eight, has a negligible effect on the mean Mg/Ca value or the standard error of the sample (Table 4.8, Figure 4.12b, d). This suggests that a total of ~28 measurements from approximately four specimens is required to get a consistent Mg/Ca value for *D. altispira*, similar to the 31 measurements from approximately five specimens required for a consistent *C. wuellerstorfi* Mg/Ca measurement.

Of the 100 depth profiles measured in both species approximately one third (n=33 and n=28) were excluded during screening for elevated Al/Ca and Mn/Ca indicative of diagenetic contamination. To account for samples from the downcore record where a higher quantity of profiles will be excluded due to contamination, where possible the required number of measurements per sample was increased to 36, six depth profiles per specimen and six specimens per sample. This result is in line with other LA-ICP-MS studies (Rathmann et al., 2004, Sadekov et al., 2008).

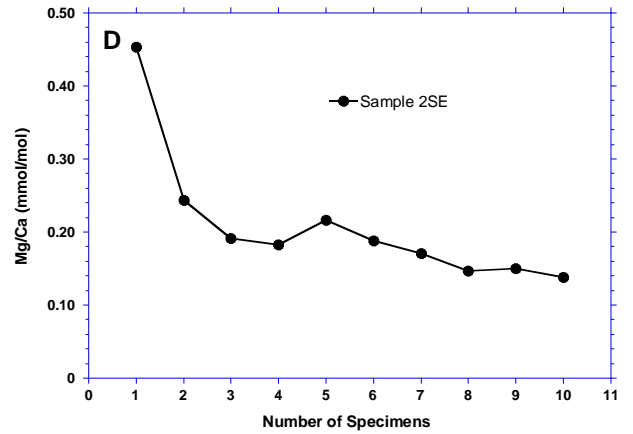
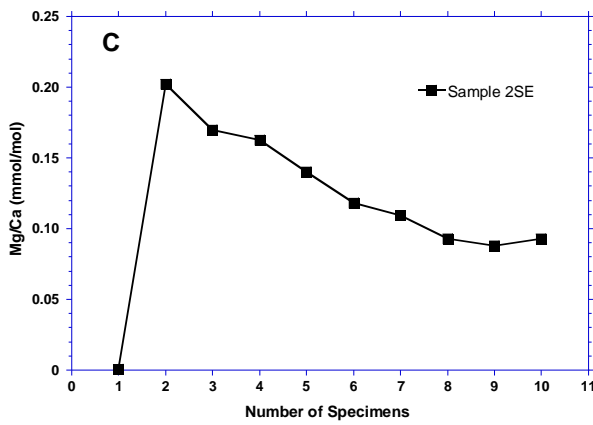
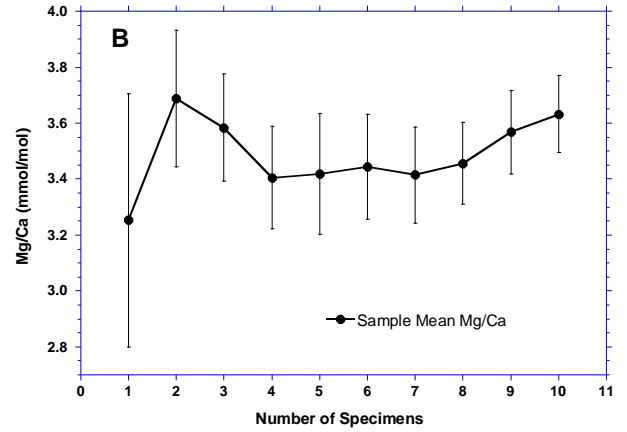
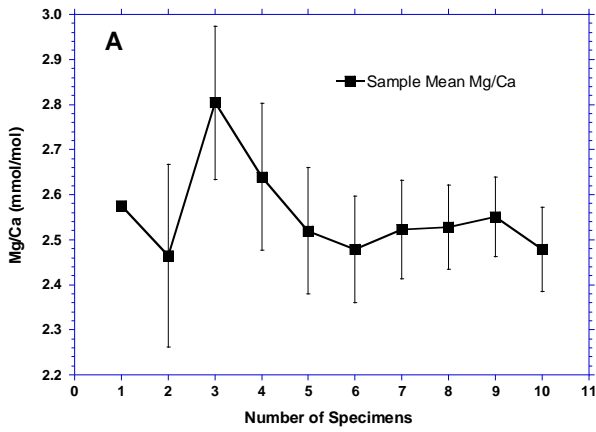


Figure 4.12: Example of the evolution of mean sample Mg/Ca with increasing specimens up to n=10 of (A) *C. wuellerstorfi* (squares), and (B) *D. altispira* (circles). Error bars are 2 SE of the sample mean, which the evolution of with increasing specimens is shown in C and D. Data is from Table 4.8.

## 4.4 Discussion

### 4.4.1 Determining the cause of Mg/Ca-Mn/Ca correlation in downcore records

The presence of concomitantly elevated Mg/Ca and Mn/Ca trace metal ratios in foraminifera from Sunbird-1 raises the possibility that the Mg/Ca ratios have been compromised by diagenetic processes, despite their glassy appearance (Figure 4.1 and Chapter 3). There are three potential causes for downcore correlations between foraminiferal Mg/Ca and Mn/Ca. The first is that the whole test is recrystallized and diagenetically altered by an Mg-Mn-rich phase throughout, fully overprinting the primary signal required for Mg/Ca palaeothermometry, as observed in Oligocene-Miocene foraminifera at ODP Site 1406 in the NW Atlantic Ocean (Richard Smith personal communication, 2017). The second possibility is that the elevated Mg/Ca in the test is not associated with the elevated Mn/Ca within the test, and the correlation observed in downcore records is a consequence of Mg/Ca and Mn/Ca independently reflecting changing environmental conditions. The third possible scenario is that the pristine primary test is coated by a Mg-Mn-rich diagenetic phase, with varying levels of contamination in downcore records (Hasenfratz et al., 2016).

Using the optimised LA-ICP-MS set-up, the intra-test variability in Mg/Ca and Mn/Ca can be compared. This allows me to determine which of the three potential causes outlined above is the primary cause for the downcore correlation between foraminiferal Mg/Ca and Mn/Ca at Sunbird-1. There are strong intra-test similarities between the Mg/Ca and Mn/Ca profiles (Figure 4.13). The most noticeable similarity is the presence of extremely elevated Mg/Ca and Mn/Ca values at the test exterior. This is interpreted as contamination by a Mg-Mn-rich diagenetic coating, likely Mn-oxyhydroxides or Mn-rich carbonates (Boyle, 1983, Barker et al.,

2003, Pena et al., 2008, Hasenfratz et al., 2016). This provides convincing evidence that the presence of a Mg-Mn-rich contaminant phase on the exterior of the test is the dominant cause of the unrealistically high Mg/Ca values from solution based ICPMS analysis. Although unnecessary for the three depth profiles shown here because of the elevated Mn/Ca values, the presence of lower  $^{43}\text{Ca}/^{48}\text{Ca}$  values could also be used as an indication of contamination by a non-primary calcite phase (Figure 4.13). It is this contaminant coating precipitated on the outer test surface with concomitantly elevated Mg/Ca and Mn/Ca ratios, that result in the elevated Mg/Ca ratios from solution based ICP-MS analyses (Chapter 3).

As well as the prominent Mg-Mn-rich contaminant coating, all profiles show elevated Mg/Ca and Mn/Ca ratios at the end of the depth profiles, beyond 70 seconds, albeit not to the same extent as the contaminant coating. Unlike the consistency at the test exterior, the raw data show significant spread about the smoothed average, most apparent in Profile 12, and the strong correspondence between the Mg/Ca and Mn/Ca trends as seen at the outermost surface is not repeated (Figure 4.13). This region of elevated Mg/Ca and Mn/Ca is most likely a result of downhole fractionation, or more likely the laser beam having broken through the test wall (Eggins et al., 1998). However, this may represent a thin layer of contaminant at the inner test wall, as reported by previous studies (Eggins et al., 2003, Pena et al., 2005, Hasenfratz et al., 2016). If this is a contaminant phase it is only prevalent in small pockets at the inner test wall, as opposed to as a consistent and ubiquitous surface. The drop off in  $^{43}\text{Ca}$  intensity further into the depth profile (Figure 4.14) suggests that the elevated Mg/Ca values result from ablation breaking through the test wall, as opposed to a highly heterogeneous inner contaminant phase.

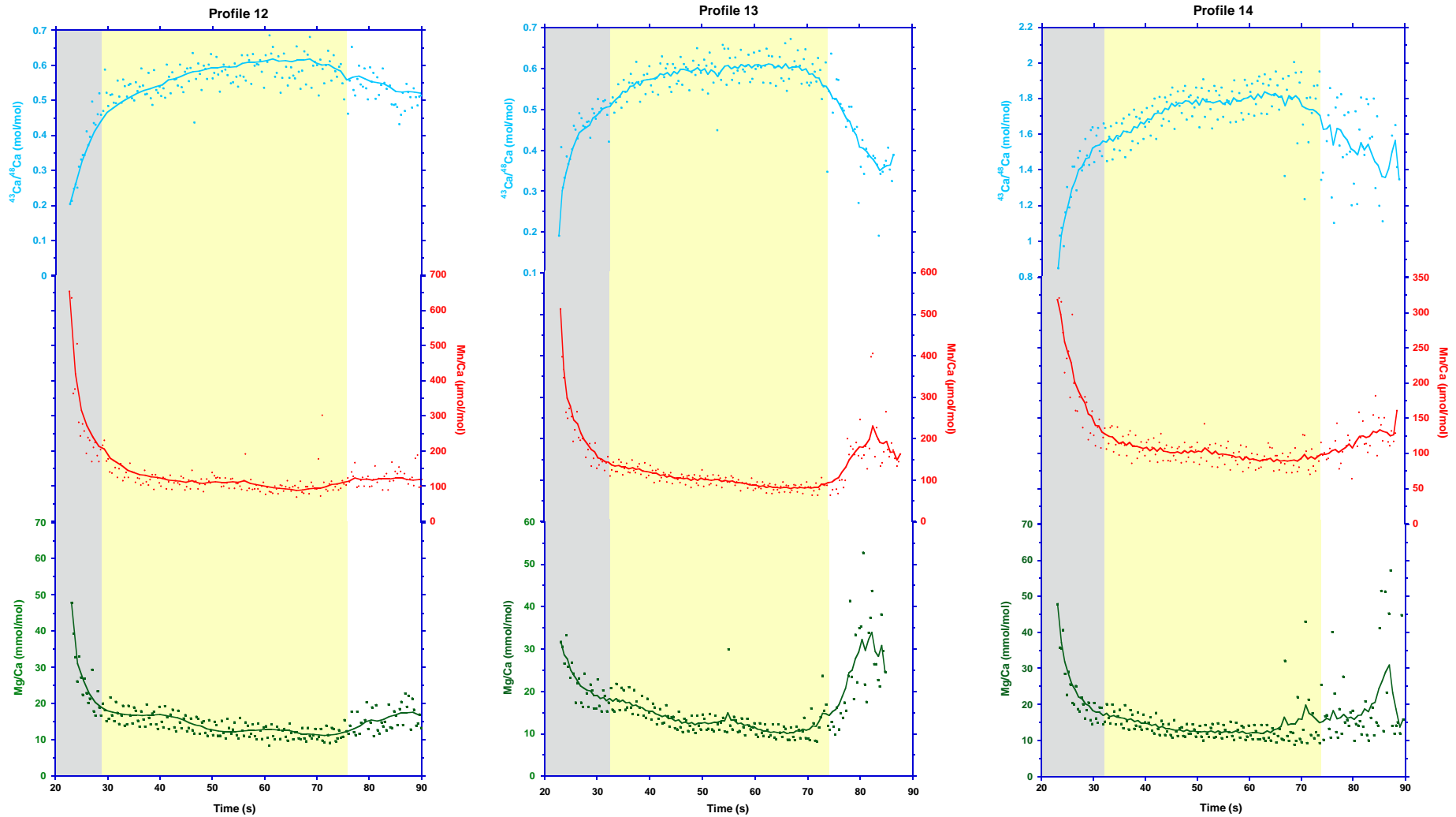


Figure 4.13:  $^{43}\text{Ca}/^{48}\text{Ca}$ , Mn/Ca, and Mg/Ca results from the three repeat test wall transects at  $3.5 \text{ Jcm}^{-2}$  and 2.0 Hz from the 1551-1554m sample of Sunbird-1, with a biostratigraphic age of 11.74 Ma. Solid lines are smoothed averages across 4 data points. Grey bars highlight the region of the profile interpreted as a diagenetically formed contaminant coating on the test exterior, and yellow bars highlight the region of the profile interpreted as primary test.

In the test interior, away from the contaminant coating and prior to ablation breaking through the test wall, the Mg/Ca profiles remain flat at ~13-14 mmol/mol. Critically in this region of the test where the Mg/Ca profiles are flat Mn/Ca ratios are also at their lowest, <200  $\mu\text{mol/mol}$ , and the foraminiferal calcite is therefore suggested to be free of significant Mn-rich contamination (Figure 4.15). This is consistent with the glassy appearance and retention of biogenic calcite seen under SEM imaging (Figure 3.1), as opposed to wholesale recrystallisation of the test. The combination of stable Mg/Ca values and low Mn/Ca values suggests this region of the test may be used for Mg/Ca palaeothermometry. This is further supported by the lack of correlation between Mg/Ca and Mn/Ca in this interior region of the test (Figure 4.16a). The absence of any correlation between Mg/Ca and Mn/Ca in the primary shell likely results from the lack of any major trends or variance in the Mn/Ca ratios through this region of the test because it does not contain the Mg-Mn rich contaminant phase. Mg/Ca

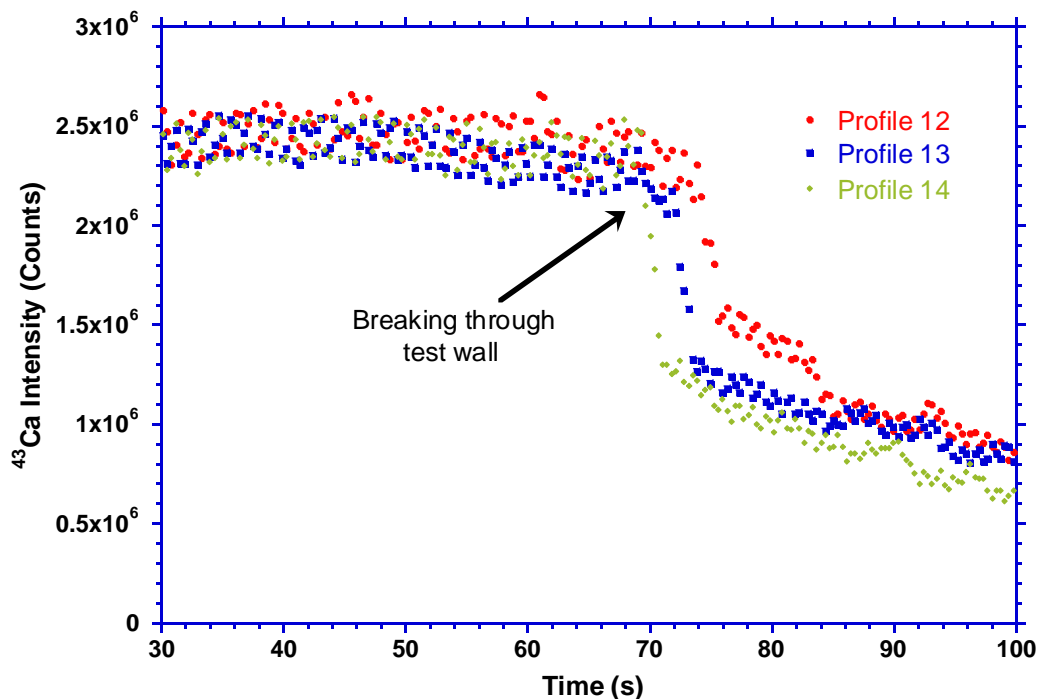


Figure 4.14: Gas blank corrected  $^{43}\text{Ca}$  intensity decrease when the laser beam breaks through the test wall. Data from the three repeat profiles through *O. universa* using the preferred ablation parameters.

within the test interior primarily reflects the temperature control on Mg uptake into the calcite lattice.

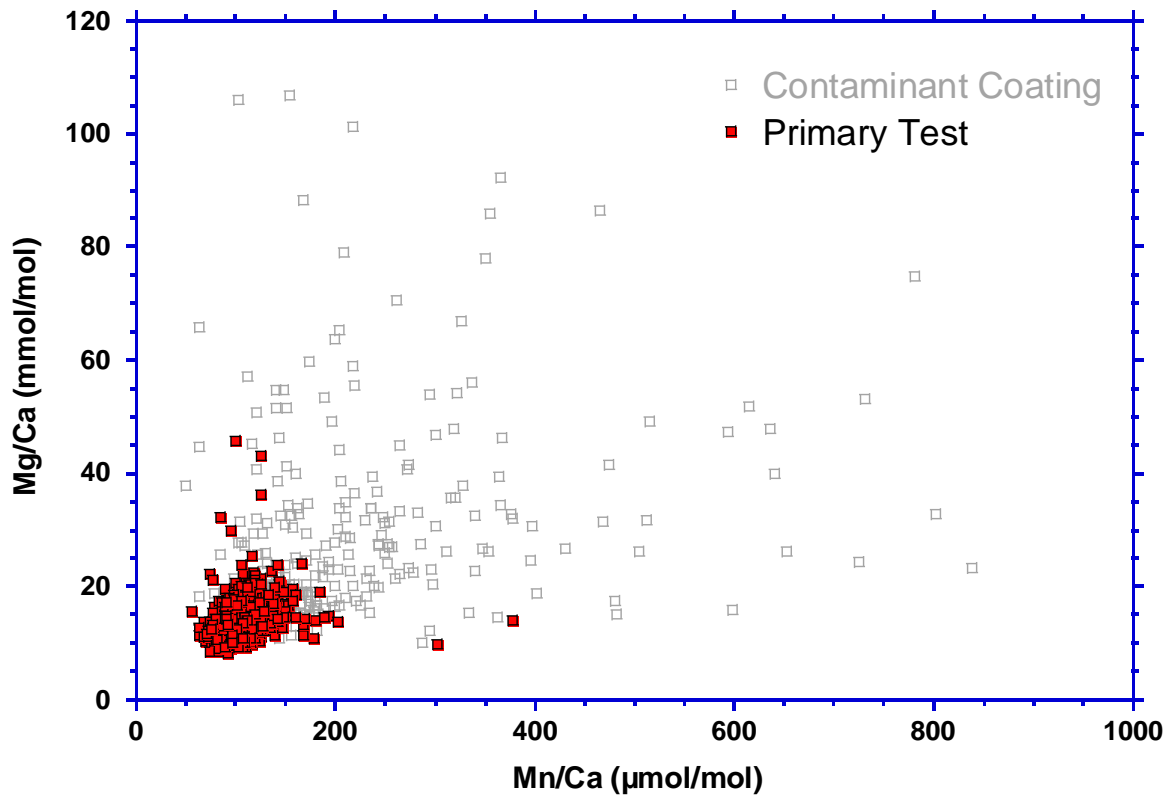


Figure 4.15: Crossplot of Mg/Ca versus Mn/Ca for the three repeat test wall transects through the test of *Orbulina universa* from the 1551-1554m depth sample in Sunbird-1 using the preferred ablation parameters of 3.5 Jcm<sup>-2</sup> and 2.0 Hz. Filled red squares are the primary calcite test (n=332), and open grey squares are regions of the test determined to be a contaminant phase (n=445).

#### 4.4.2 Characterising the contaminant phase

By combining the data from the three test wall transects using the preferred ablation parameters through the single *O. universa* test, the relationship between Mg/Ca and Mn/Ca of the contaminant coating, the primary test, and the combination of both has been characterised (Table 4.9). It is worth noting that the contaminant coating is a combination of a diagenetically precipitated coating and the primary foraminiferal calcite, coated calcite. The lack of apparent coatings under SEM imaging (Figure 2.1) and high calcium concentrations in the test wall transects strongly suggests this to be the case. When isolated from the diagenetically altered coated calcite at the outer region of the test the primary test has a mean Mg/Ca value of  $14.0 \pm 0.38$  mmol/mol. This is considerably lower than when the coated calcite, which has a mean Mg/Ca value of  $23.0$  mmol/mol  $\pm 1.72$ , is incorporated (Table 4.9). This strongly suggests that the primary test and contaminant coating are formed from different phases. The 1.24 mmol/mol lowering of Mg/Ca by identifying the primary test, isolating it from any contaminant influence of the coated calcite phase on the outer test has the potential to have a major impact on temperature estimates.

The mean Mn/Ca of the primary test,  $108 \pm 3$   $\mu$ mol/mol, is also considerably lower than it is for the Mg-Mn-rich contaminant coated calcite phase,  $235 \pm 28$   $\mu$ mol/mol, and is similar to the proposed threshold for Mn-overgrowths having a negligible influence on Mg/Ca values (Boyle, 1983). When Mg/Ca and Mn/Ca values are concomitantly high in the coated calcite region of the test, as denoted by the greyed out regions of Figure 4.13, there is a weak correlation between Mg/Ca and Mn/Ca ( $R^2=0.34$ ) (Figure 4.16b). This covariance of Mg/Ca and Mn/Ca does not propagate into the primary calcite test ( $R^2=0.04$ ) (Figure 4.16b).

	Mg/Ca (mmol/mol)	Mn/Ca ( $\mu\text{mol/mol}$ )
<b>Coated Calcite (n=74)</b>	23.0 $\pm$ 1.72	235 $\pm$ 28
<b>Primary Test (n=332)</b>	14.0 $\pm$ 0.38	108 $\pm$ 3
<b>Coating and Test (n=406)</b>	15.3 $\pm$ 0.48	126 $\pm$ 6
<b>Coating Effect</b>	1.24	17.6

Table 4.9: Mean Mg/Ca (mmol/mol) and Mn/Ca ( $\mu\text{mol/mol}$ ) ratios from a combination of the three depth profiles using the preferred ablation settings of 3.5 Jcm<sup>-2</sup> and 2.0 Hz for the contaminant coating, primary test, as well as both combined. Error estimates are  $\pm$  2 SE.

Because the contaminant coating is likely formed of a combination of diagenetic coating and primary calcite, termed coated calcite, it is not possible to determine the Mg/Mn ratio of this phase of the test by simply using a ratio of the Mg/Ca and Mn/Ca values (Table 4.9). If there was an independent estimate of the percentage contribution of contaminant material to the coated calcite then this would be possible. Instead, the gradient of the slope between Mn/Ca and Mg/Ca values of the coated calcite is used (Figure 4.17). Furthermore, the intercept (Mn/Ca = 0) provides an approximation of the “Mn-free” value, which in theory is the pristine calcite. It was ensured that all data points interpreted as coated calcite had high concentrations of <sup>43</sup>Ca [<sup>43</sup>Ca], and that the elevated Mg/Ca and Mn/Ca ratios are not an artefact of low [Ca], as interpreted for the end of the depth profile when the laser beam has broken through the test wall. Only including the three test wall transects which use the optimised ablation parameters of 3.5 Jcm<sup>-2</sup> and 2.0 Hz produces a similar Mg/Mn ratio for the coated calcite phase than when all 18 test wall transects using the six different combinations of fluence and repetition rate (Figure 4.17).

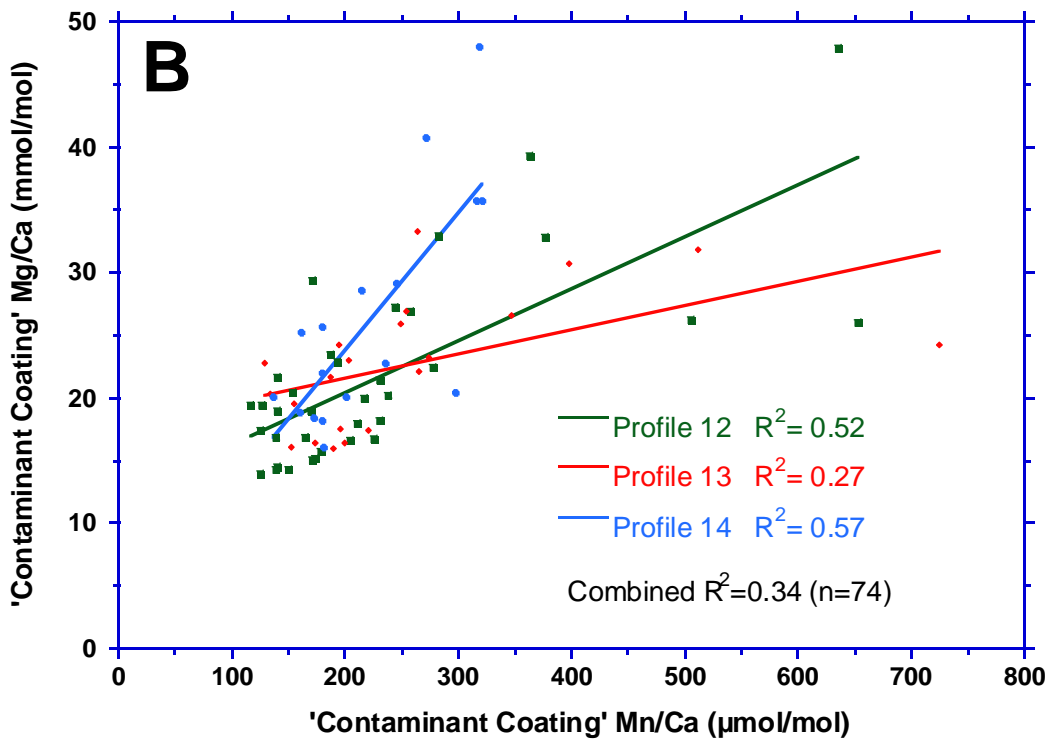
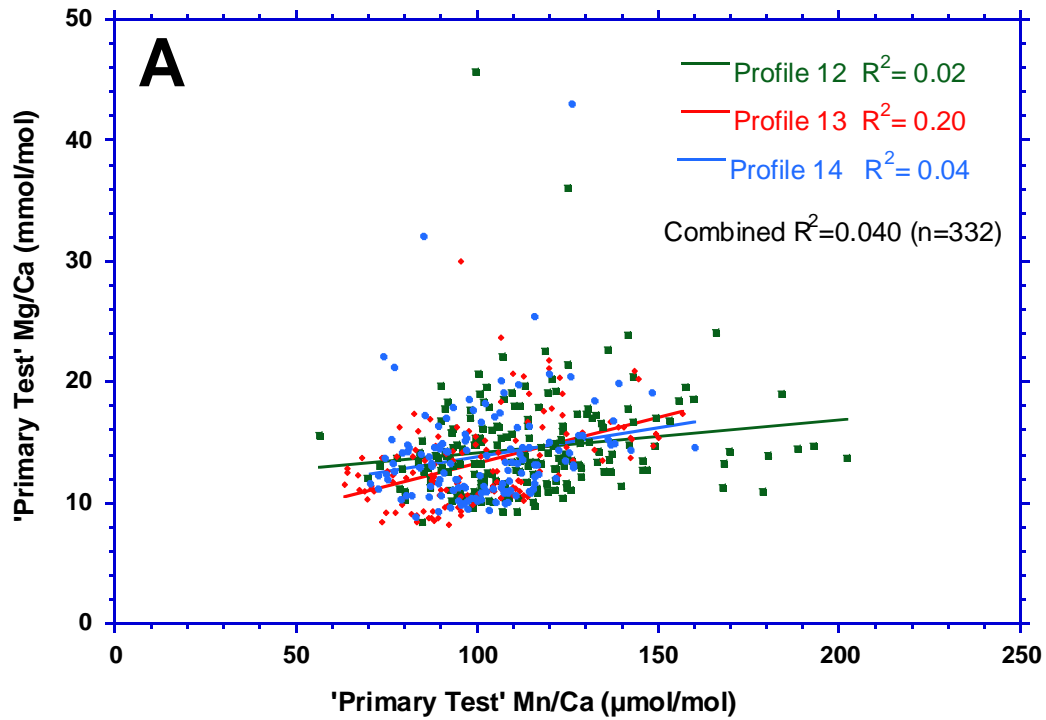


Figure 4.16: Crossplots of Mg/Ca versus Mn/Ca for the phases identified as (A) the primary test (n=332), and (B) the contaminant coating (n=74), for the repeat test wall transects through the single test of *Orbulina universa* from the 1551-1554m sample in Sunbird-1, using the optimised ablation parameters of 3.5 Jcm<sup>-2</sup> and 2.0 Hz. R<sup>2</sup> values for each transect, and for all three combined, are given. Note the different scales on the x axes.

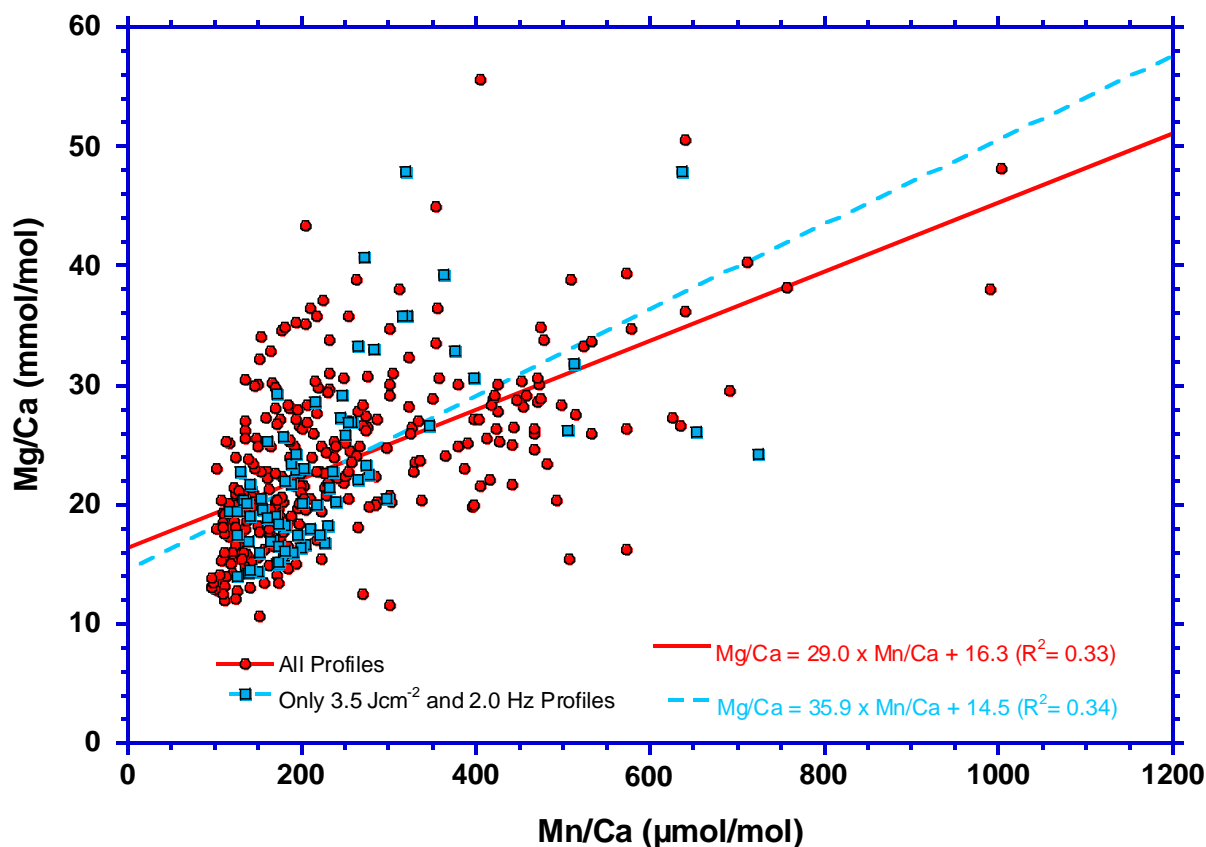


Figure 4.17: Crossplot of Mg/Ca versus Mn/Ca for the phase identified as coated calcite. Data from only the three test wall transects using the preferred ablation parameters of 3.5 Jcm<sup>-2</sup> and 2.0 Hz (blue squares, n=74) and from all 18 test wall transects (red circles, n=380) through the single test of *Orbulina universa* from the 1551-1554m sample in Sunbird-1 are given. The linear fits through both datasets have a similar Mg/Mn ratio, 35.9 mol/mol and 29.0 mol/mol respectively. The intercept with the y axis (Mn/Ca = 0) approximates the Mg/Ca ratio of contaminant free calcite.

Adopting this approach gives Mg/Mn ratios in the contaminant coated calcite of 35.9 mol/mol when using the test wall transects with ablation parameters of 3.5 Jcm<sup>-2</sup> and 2.0 Hz (n=3), and 29.0 mol/mol when using all the test wall transects through the single *O. universa* specimen, independent of ablation parameters (n=18) (Figure 4.17). That these values are close approximations to each other supports them being robust, and the coated calcite likely has an Mg/Mn molar ratio of ~30 mol/mol. This approach suggests a “Mn-free” Mg/Ca value of 14.5 mmol/mol from the three repeat test wall transects using the optimised ablation

parameters, a “Mn-free” Mg/Ca value very close to the mean Mg/Ca of the primary test from the same three test wall transects ( $14.0 \pm 0.38$ ).

Furthermore, the Mg/Mn ratio of the coated calcite enables the characterisation of the contaminant phase. Average Mg/Mn ratios in natural Ca-Mn-Mg carbonates is  $0.13 \pm 0.13$  mol/mol (Peacor et al., 1987). Additionally Mn-rich carbonates are typically low in Fe (Calvert and Pedersen, 1996, Peacor et al., 1987), whereas solution ICP-MS analysis show foraminifera from Sunbird-1 to have high Fe/Ca ratios (Chapter 3). The 30 mol/mol Mg/Mn ratio of the coated calcite contaminant phase supports the previous interpretation that the source of the Mg-Mn-rich contaminant coating influencing this sample being manganese carbonates, commonly the mineral kutnahorite, is highly unlikely (Hasenfratz et al., 2016, Pena et al., 2005). Mg/Mn ratios in Mn nodules and Mn encrustations (common forms of Mn-oxides) across a wide range of ocean basins is  $0.17 - 0.32$  mol/mol (Baturin, 2012, De Lange et al., 1992). Additionally, and in contrast to Mn-rich carbonates, high concentrations of iron are common in Mn-oxides. This corroborates the previous determination that the contaminant phase causing elevated Mg/Ca ratios is likely Mn-Fe-rich oxides precipitated during changing redox conditions onto the outer surface of the tests (Chapter 3). Unfortunately, due to the interferences described in Chapter 4.2.1 (May and Wiedmeyer, 1998, Evans and Müller, 2018a), quantitative Fe/Ca analysis by LA-ICP-MS was not possible.

#### 4.4.3 Potential impact on palaeotemperature reconstruction

Solution based ICP-MS benthic foraminiferal records from the Sunbird-1 site display unrealistically high Mg/Ca ratios inhibiting their use for palaeotemperature reconstructions

(Figure 4.1 and Chapter 3). Detailed, sub-micron scale chemical depth profiling through test walls using Laser-Ablation ICP-MS has shown the likely cause of this to be Mg-Mn-rich contaminant coating (Figure 4.10). These coatings would likely have formed post burial in the upper sediment column and the overall test geochemistry is therefore not a true reflection of the ambient seawater conditions. The LA-ICP-MS transects reveal that beyond this Mg-Mn-rich contaminant coating, Mg/Ca is stable, Mn/Ca is low ( $108 \pm 3 \mu\text{mol/mol}$ ), and the two are uncorrelated (Figure 4.16a, Table 4.9). This region of the test wall transects is interpreted to be primary, unaltered, test calcite, and therefore suitable for Mg/Ca palaeothermometry. It is therefore possible to quantify how much the contaminant coating biases Mg/Ca palaeotemperature estimates to higher values. The region of the depth profiles beyond the primary test, which may be heterogeneous contamination, or more likely is a result of downhole fractionation during ablation, or a matrix effect as ablation breaks through the test wall, is discounted.

	Temperature (°C) (Lea et al., 1999)	Temperature (°C) (Russell et al., 2004)
<b>Contaminant Coating (n=74)</b>	$33.3 \pm 0.9$	$34.3 \pm 0.8$
<b>Primary Test (n=461)</b>	$27.5 \pm 0.3$	$29.2 \pm 0.3$
<b>Coating and Test (n=535)</b>	$28.4 \pm 0.4$	$30.1 \pm 0.3$
<b>Coating Effect</b>	1.0	0.9

Table 4.10: Palaeotemperature estimates (°C) using the preferred temperature calibrations for *O. universa* (Lea et al., 1999, Russell et al., 2004). Estimates for the contaminant coating, primary test, and a combination of both are provided with errors ( $\pm 2$  SE).

*Orbulina universa* used in this study is not an ideal species to use for Mg/Ca palaeotemperature reconstructions. This is because there are few temperature calibrations,

and those available are poorly constrained (Lea et al., 1999, Russell et al., 2004). Here the available calibrations are applied to demonstrate the potential benefit of LA-ICP-MS for determining palaeotemperatures from foraminifera containing Mg-Mn-rich contaminant phases.

Using these calibrations temperature estimates for the primary test are  $\sim 1^\circ\text{C}$  lower than when the contaminant coating is included, independent of temperature calibration (Table 4.10, Figure 4.18). This suggests that the impact of identifying the primary test from any Mg-Mn-rich contaminant phase is greater than the analytical uncertainty ( $\pm 0.3^\circ\text{C}$ ). If the elevated Mg/Ca and Mn/Ca at the end of the profile was interpreted as a heterogeneous contaminant phase at the inner test wall and not a result of downhole fractionation, then the estimated

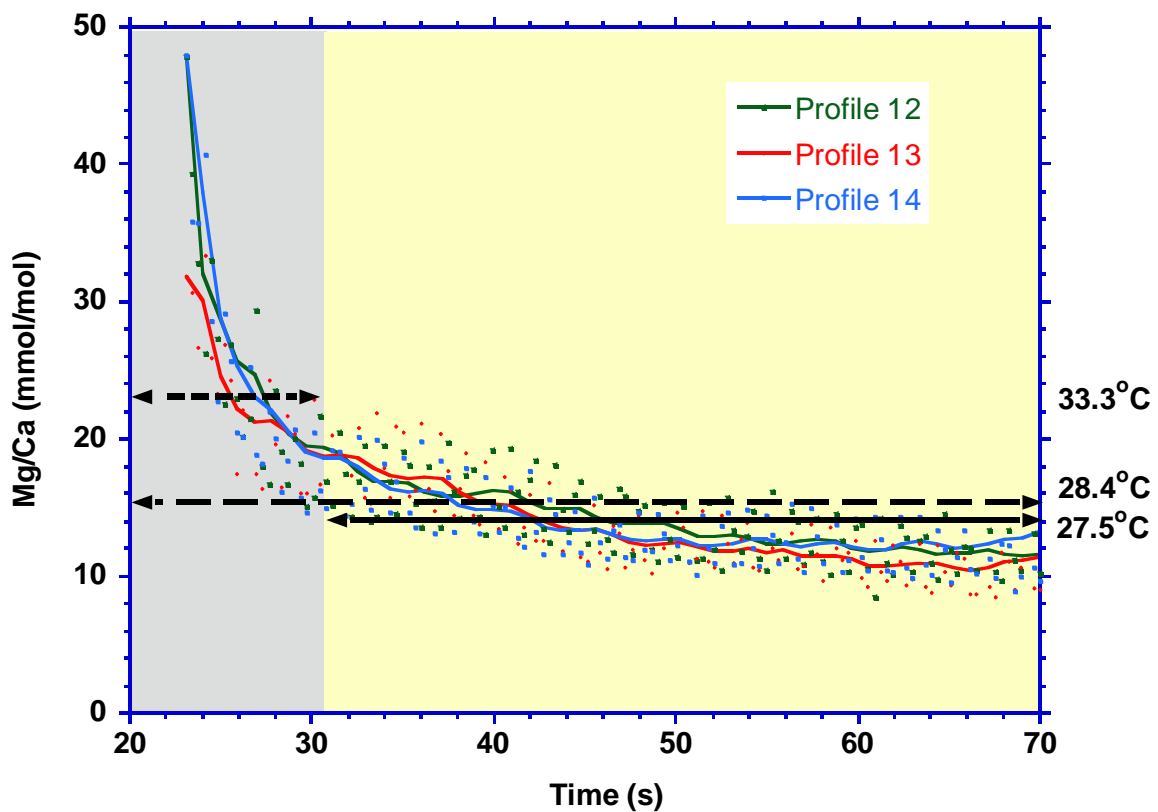


Figure 4.18: Temperature estimates for the regions of the profiles which were identified as the primary test (solid line), the primary test and contaminant coating (long dashed line), and the contaminant coating (short dashed line) using the preferred calibration for *O. universa* of Lea et al. (1999).

temperature would be  $\sim 2^{\circ}\text{C}$  higher than for the isolated primary test ( $\text{Mg}/\text{Ca}=16.6$  mmol/mol). Considering the observed 1.24 mmol/mol increase in  $\text{Mg}/\text{Ca}$  when the primary test is not isolated from the contaminant coating this would exert a much larger bias on the estimated temperature of planktic foraminifera with lower average  $\text{Mg}/\text{Ca}$  ratios. Furthermore, the expectation would be that the influence would be even greater for benthic foraminifera, such as *Cibicidoides wuellerstorfi*, one of the two calcite species which was initially analysed via solution based ICP-MS. This is investigated following the reconstruction of BWT via LA-ICP-MS measurements on *C. wuellerstorfi* in Chapter 5.5.3.1.

## 4.5 Conclusions

This study optimises the ArF 193nm excimer RESOLUTION laser ablation system (Australian Scientific Instruments) when coupled to an Element HR-ICPMS (Thermo). Analyses using a repetition rate of 3.0 Hz (1 pulse every 333 ms) demonstrate temporal beating due to interaction with the 350 ms ICP-MS sweep time. This temporal beating could be interpreted as intra-test variability, and therefore this repetition rate is not used in foraminiferal analyses. The optimal ablation parameters for producing an intense and stable signal for the NIST 610 glass standard are determined to be a fluence of  $4.5 \text{ Jcm}^{-2}$  and repetition rate of 4.0 Hz. These parameters are applied throughout the rest of the thesis, NIST 610 being used as the external standard when analysing foraminifera from Sunbird-1.

The most reproducible  $\text{Mg}/\text{Ca}$  test wall transects through foraminiferal calcite were analysed using a fluence of  $3.5 \text{ Jcm}^{-2}$  and repetition rate of 2.0 Hz. These optimised ablation parameters facilitate the acquisition of reproducible test wall transects through foraminiferal

calcite at a high enough spatial resolution to distinguish different phases of the test. This enables the identification of primary calcite in Mn-rich foraminifera, suitable for Mg/Ca palaeothermometry. To acquire a mean sample Mg/Ca for *C. wuellerstorfi* or *D. altispira*, essential for downcore temperature reconstructions, it is determined that 28-31 test wall transects from 4-5 specimens are required. This quantification of will be applied for the downcore palaeotemperature reconstructions in Chapter 5. Future studies are advised to conduct similar testing to determine the number of measurements required for a mean sample Mg/Ca to be representative, as this will likely be site dependent.

The primary calcite of an *Orbulina universa* test has been identified (Mg/Ca=14.0 ± 0.38 mmol/mol and Mn/Ca= 108 ± 3 µmol/mol). The careful LA-ICP-MS analysis isolate the primary calcite from an Mg-Mn-rich outer contaminant phase consisting of an unknown combination of coating and calcite (Mg/Ca=23.0 ± 1.72 mmol/mol and Mn/Ca= 235 ± 28 µmol/mol), and from when ablation has broken through the test wall. The contaminant coating biases the Mg/Ca ratio by 1.24 mmol/mol, equivalent to increasing sea surface temperature by approximately 1°C. This influence is greater than the analytical uncertainty through the primary test (± 0.3°C). Applying the observed Mg-Mn-rich contaminant coating to benthic foraminifera, which have lower primary Mg/Ca values, would have a much greater bias.

This study successfully sets up the first method for analysing intra-test trace metal variability of foraminifera using the new LA-ICP-MS system in the Cardiff University CELTIC Laboratory. This has allowed identification of the primary foraminiferal test required for Mg/Ca

palaeothermometry, and characterisation of the contaminant phase, which biased solution ICP-MS analyses to higher temperatures.

## **5 Sea surface and bottom water temperature at Sunbird-1 using Mg/Ca thermometry of primary foraminiferal calcite identified with laser ablation ICP-MS**

### **5.1 Introduction**

The mid-late Miocene is an important interval in the evolution of global climate through the Cenozoic. It is characterised by lower than modern day atmospheric CO<sub>2</sub> (Foster et al., 2012, Sossian et al., 2018), but temperatures were likely warmer than the modern day (Rousselle et al., 2013, Pound et al., 2011). This suggests that global temperature and atmospheric CO<sub>2</sub> forcing were decoupled through the interval (LaRiviere et al., 2012), a characteristic general circulation models struggle to simulate (Knorr et al., 2011).

Despite the significance of this climate interval, the evolution of global SST during the late Miocene is poorly constrained due to a lack of reconstructions (Lunt et al., 2008). Current proxy based reconstructions are restricted to estimates based on the unsaturated alkenone proxy (Huang et al., 2007, LaRiviere et al., 2012, Seki et al., 2012a, Zhang et al., 2014, Rousselle et al., 2013, Herbert et al., 2016) which suggests stable tropical SSTs of 28-29°C through the mid-late Miocene (Herbert et al., 2016). However, these reconstructions may be underestimating late Miocene temperatures in the tropical surface waters of the Western Indian Ocean. This is because the Uk<sub>37</sub> alkenone proxy becomes saturated above 28°C and cannot be used to calculate warmer temperatures (Müller et al., 1998).

Consequently, the use of a different proxy that is able to reconstruct warmer temperatures, such as the planktic foraminiferal Mg/Ca utilised by this study, can clarify whether tropical SST remained relatively stable at  $\sim 28^{\circ}\text{C}$  during the interval between 13.7 Ma and 9.5 Ma. This would support the mid-late Miocene as being a key interval for the development of the latitudinal temperature gradient of the modern-day ocean.

The equatorial Indian Ocean locality of Sunbird-1 means it is well-positioned for this purpose. However, foraminifera from Sunbird-1 analysed by traditional solution based ICP-MS have elevated trace element over calcium ratios as a result of diagenetic alteration, inhibiting their potential for estimating past temperatures using the Mg/Ca palaeothermometer (Chapter 3). Therefore, a laser ablation ICP-MS analytical technique in the Cardiff University CELTIC laboratory has been developed and implemented (Chapter 4). This technique produces highly spatially resolved geochemical depth profiles through individual foraminiferal tests from which the primary calcite Mg/Ca signal can be identified (Creech et al., 2010, Hollis et al., 2015, Hines et al., 2017). This primary Mg/Ca signal is then used to calculate sea surface and bottom water temperatures from Sunbird-1 and placed in context of global sea surface temperature compilations.

### Summary of Scientific Experiments

- This chapter applies the optimised ablation parameters determined in Chapter 4 to reconstruct bottom water and sea surface temperature at Sunbird-1.
- Temperatures were reconstructed by applying Mg/Ca palaeothermometry to foraminifera, bottom water temperature from the benthic species *Cibicidoides*

*wuellerstorfi*, and sea surface temperature from the planktic species *Dentoglobobadrina altispira*.

- Up to thirty-six laser ablation ICP-MS profiles, from up to six individuals, were analysed for each sample. In addition to Mg/Ca, Mn/Ca and Al/Ca were also analysed, as indicators for contamination.
- Each LA-ICP-MS depth profiles was individually inspected to identify the primary test. This was determined to be the region where Al/Ca and Mn/Ca are at their lowest, and Mg/Ca is stable. Further screening for contamination was applied after data processing, to fully remove any influence of the Mg-rich contaminant phase.

## 5.2 Methods

### 5.2.1 Sample selection and preparation

Up to six specimens of *D. altispira* and *C. wuellerstorfi* were selected from 44 depth intervals through the Sunbird-1 core for LA-ICP-MS Mg/Ca and Mn/Ca analysis (Chapter 4.3.4). However, fewer tests were available in eight samples of *D. altispira*, and in 20 samples of *C. wuellerstorfi* (Appendix 6). Foraminiferal sample preparation included the removal of fine clays and other detrital material on the outer surface of the test using DI water and methanol, but did not include the more aggressive oxidative and reductive steps (Boyle, 1983, Barker et al., 2003), as these offer negligible benefit compared to that achieved by ultrasonication in 18.2 MΩ DI water and methanol for laser ablation analysis (Vetter et al., 2013) (Chapter 4). The cleaned tests were mounted onto glass slides using double sided carbon tape and were allowed to dry before being mounted into the sample cell (Evans et al., 2015, Fehrenbacher et al., 2015).

### 5.2.2 LA-ICP-MS analysis

Analyses were performed using an ArF excimer (193nm) LA- system with dual-volume laser-ablation cell (RESOLUTION S-155, Australian Scientific Instruments) coupled to a Thermo Element XR magnetic sector field HR ICP-MS. The optimised ablation parameters and analytical settings determined for the Cardiff University CELTIC laboratory determined in Chapter 4 were used for this study, with two additions. The first attempts to remove the Mg-Mn-rich contaminant coating observed in Chapter 4 by including pre-ablation prior to analysis. This was done by applying three pulses to remove the outer  $\sim 0.5\mu\text{m}$  of the test surface, providing a simple but effective cleaning procedure. Secondly,  $^{27}\text{Al}$  was added to the analysed isotopes, elevated Al/Ca ratios being an indicator for contamination by silicates. Where possible three laser spots were analysed on each of the penultimate (f-1) and previous (f-2) chambers, however, this was not always possible meaning older chambers were frequently used to ensure 6 laser spots per specimen were analysed.

NIST SRM 610 was measured after each specimen (every six laser spots) and NIST SRM 612 was acquired at the beginning and end of every sequence (Figure 5.1). The reference values for elemental concentrations in both silicate glass standards are taken from the GEOREM website ([http://georem.mpch-mainz.gwdg.de/sample\\_query\\_pref.asp](http://georem.mpch-mainz.gwdg.de/sample_query_pref.asp)), updating from Jochum et al. (2011) (Table 2.2). NIST SRM 612 was calibrated for long term external reproducibility using NIST SRM 610. Over the duration of the study NIST 610-calibrated NIST 612 had a precision (2 SD) of 3.7% relative to the reported value. As discussed in Chapter 2.6, a more thorough assessment of accuracy cannot be made at present, as a well-characterised

calcite reference material, matrix matched to typical foraminiferal calcite, is not available (Evans et al., 2015, Fehrenbacher et al., 2015, Evans and Müller, 2018).

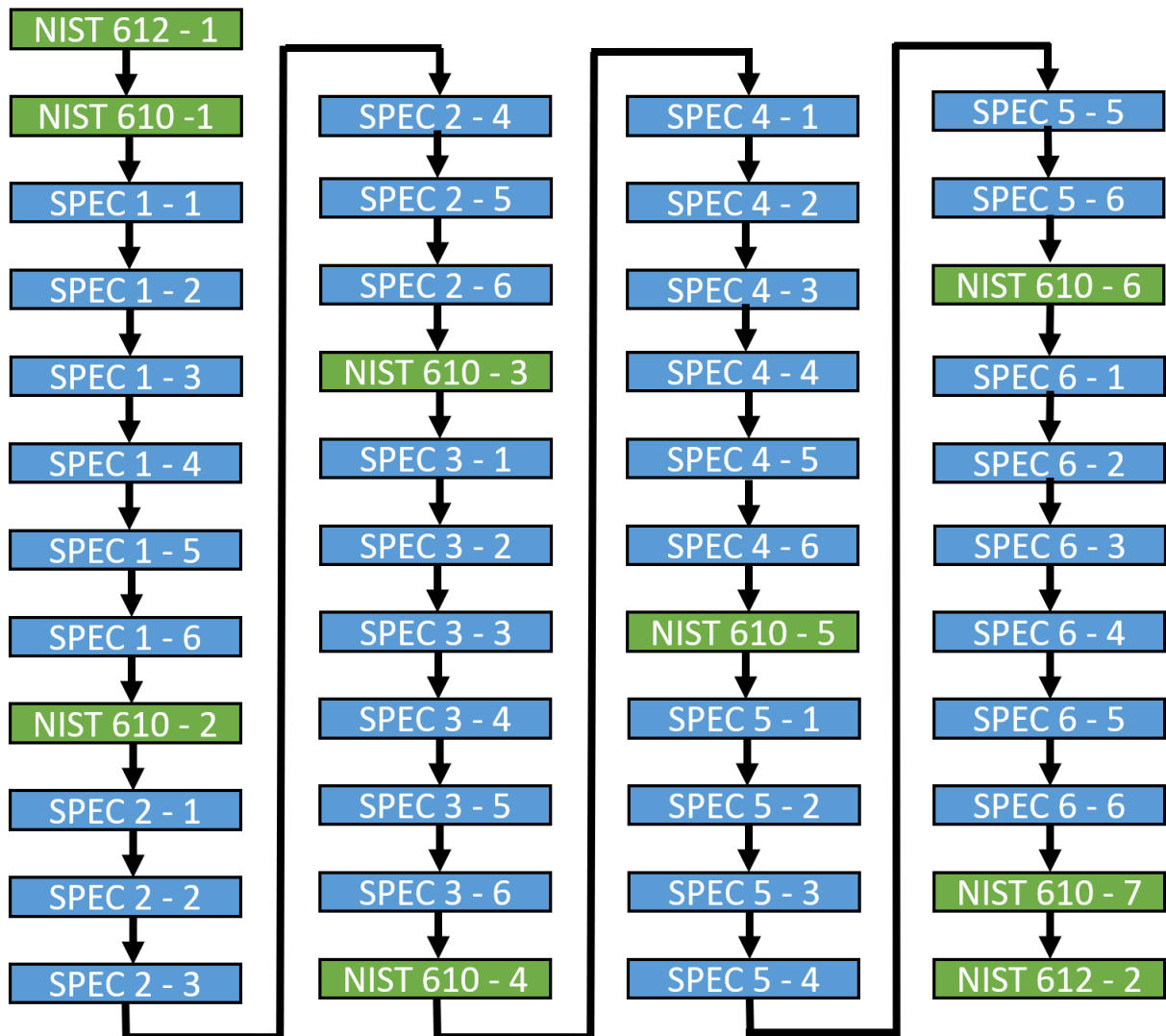


Figure 5.1: Typical LA-ICP-MS sequence composed of six depth profiles through 6 specimens, with the NIST 610 standard ablated after each specimen to enable me to calculate a linear drift correction. NIST 612 was analysed at the beginning and end of each sequence.

### 5.2.3 Data processing and screening

Each individual laser ablation profile was carefully inspected and processed using the SILLS data reduction software package (Guillong et al., 2008) following the established protocol

outlined in Longerich et al. (1996). First, a background signal of ~15 seconds, from data acquired during the period in which the laser was turned off prior to ablation, was selected for each profile. Following this the integration interval for the profile was selected based upon the following criteria:

- Stable raw  $^{43}\text{Ca}$  counts, indicating ablation of calcite,
- Stable Mg/Ca signal, indicating a consistent primary calcite phase,
- Flat Mn/Ca and Al/Ca signals, avoiding any peaks which are likely intervals of contamination.

The ratios mode feature in SILLS was regularly used in addition to the raw isotopic counts to allow an appropriate integration interval to be selected, because defining Mg/Ca, Mn/Ca, and Al/Ca is imperative for the objective of the study. An example of a typical laser ablation depth profile, with background and sample signals selected is shown below (Figure 5.2). Typically, intervals with elevated Mn and Al in concert with elevated Mg are interpreted as being contaminant phases, and are commonly found on the inner and outer test surface (Barker et al., 2003, Pena et al., 2005, de Nooijer et al., 2014, Koho et al., 2015, Hasenfratz et al., 2016). The carbon tape used to mount the foraminifera to the glass slide is greatly enriched in Al, providing a distinctive signal.

Spikes were identified using the built in software in SILLS (Guillong et al., 2008). This follows the method of Grubbs (1969) which calculates a suggested value ((mean value – suspected spike value)/ standard deviation of all samples), assuming the data is normally distributed, and compares this to a tabled value at a specified significance level, set to 5%. Identified

spikes were then inspected by myself and, if appropriate, were replaced by the suggested value, the mean of the measurements preceding and following the spike. Approximately 4 spikes, across all 8 isotopes combined, were removed per test wall transect.

Individual depth profiles were corrected by first subtracting the mean background signal. The repeated analysis of the NIST 610 standard reference material was used to linearly correct for any instrumental drift. For each sample the quality of the standard measurements was assessed in the calibration window (Figure 5.3), which allows for easy identification of any problems with the linear drift correction. A linear drift was applied because the standard measurements were equally distributed through the 36 depth profiles comprising each sample, which was always continuous without breaks between measurements (Figure 5.1). Analytical uncertainty is accounted for during this data processing step. Typically this uncertainty is small, <2% (2SE), because of the good counting statistics and stable data acquisition during ablation.

The limit of detection (LOD) of each isotope per spot was also calculated in SILLS, using the method of Longerich et al. (1996) where the LOD is the background signal + 3.3 x standard deviation on the background signal. Values that failed to meet this limit were removed by the software. Despite the high  $^{55}\text{Mn}$  gas blank due to the interference with  $^{40}\text{Ar}^{15}\text{N}$ , almost every profile exceeded the LOD for Mn/Ca measurements, an indication of the low standard deviation of the background signal.

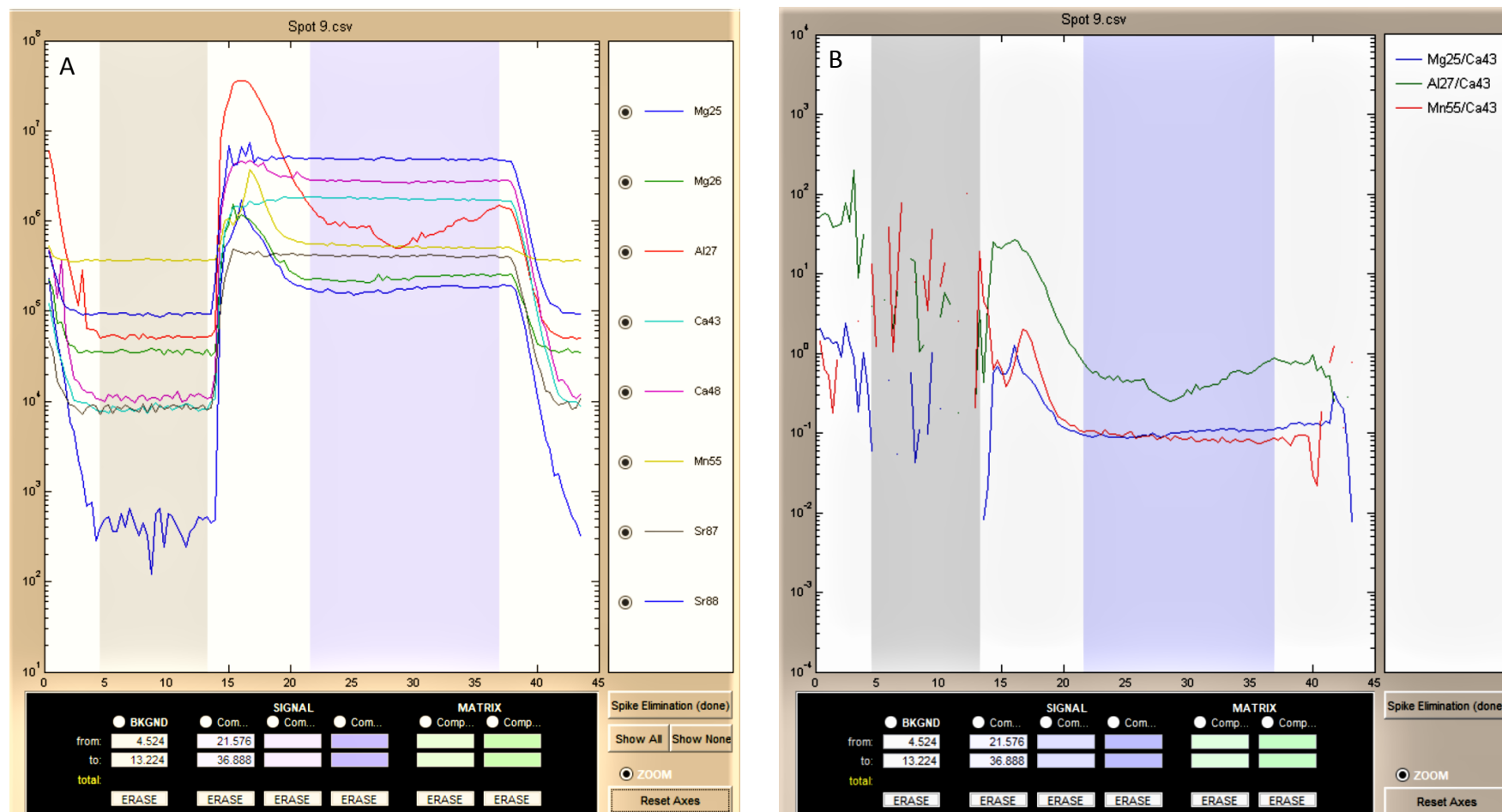


Figure 5.2: Representative LA-ICP-MS Mg, Al, and Mn profiles demonstrating the selection of background (grey panel) and sample (blue panel) signals, shown in raw isotopic counts (A), and ratios mode (B) where the isotopes of interest are relative to  $^{43}\text{Ca}$ , the internal standard. In both figures the x axis is analysis time (seconds), and the y axis is the raw intensity of the isotopes (A) or ratios (B) on a log scale. The sample interval is selected to avoid the elevated Mg/Ca, Mn/Ca, and Al/Ca at the outer surface of the test.

Further screening for contamination was conducted after data processing in the SILLS software. The ablation profiles were normalised to  $^{43}\text{Ca}$  as the internal standard and elemental concentrations (TM/Ca) were calculated, assuming 40% wt for  $\text{CaCO}_3$ . This use of  $^{43}\text{Ca}$  as an internal standard corrects for any differences in the relative yield of ablation between samples. If the assumed 40% wt is incorrect, this has no bearing on the TM/Ca ratios (e.g. Mg/Ca), only leading to possible errors in the absolute trace metal (e.g. Mg) content of the test (Rathmann et al., 2004). These ratios were then converted to mmol/mol or  $\mu\text{mol/mol}$ , the typical units used in palaeoceanographic studies. At this point integrated depth profiles which display  $\text{Mn/Ca} \gg 100 \mu\text{mol/mol}$  were excluded, as these suggest potential contamination by Mn-Fe-oxides (Chapter 3). Furthermore, integrated depth

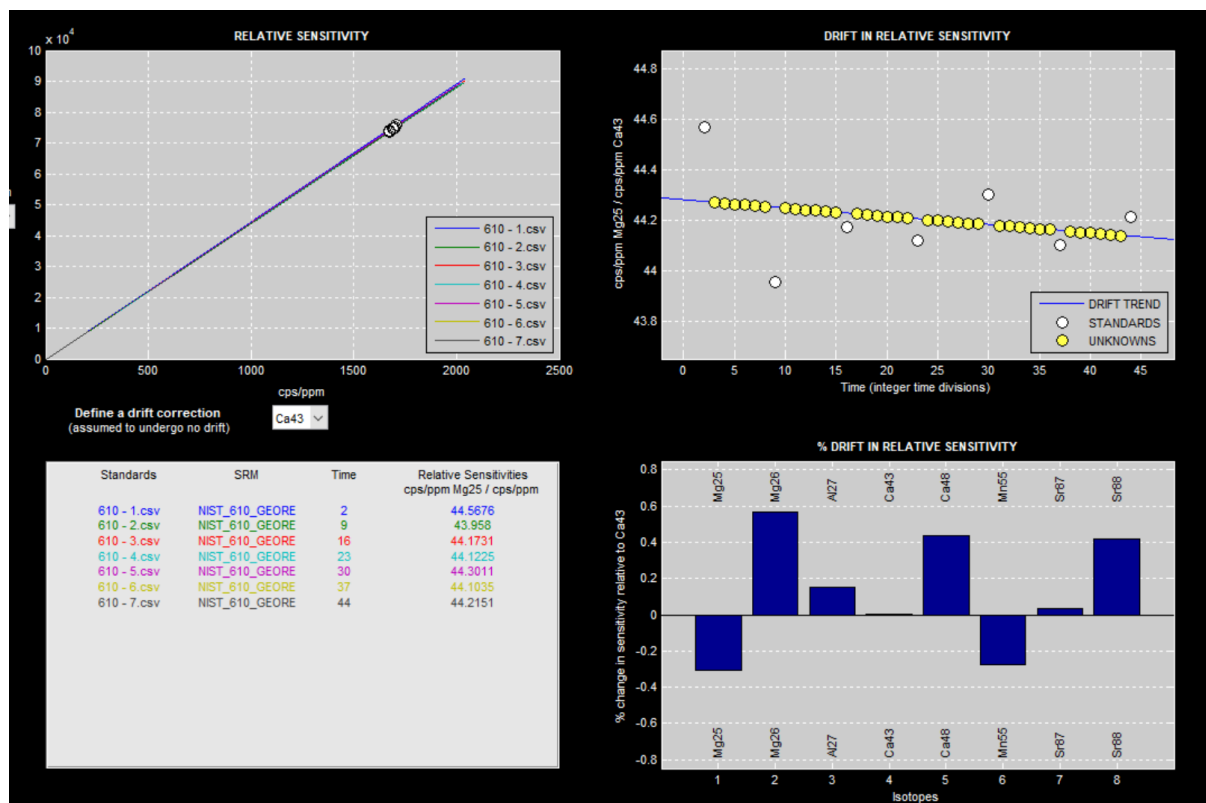


Figure 5.3: Example of the calibration window in SILLS (Guillong et al., 2008), from which the quality of the standard measurements is assessed. (A) Relative sensitivity of the chosen isotope (e.g.  $^{25}\text{Mg}$ ) versus that of the internal standard,  $^{43}\text{Ca}$ . (B) Drift in sensitivity of these isotopes through the run. The percentage drift in sensitivity of all the analysed isotopes relative to  $^{43}\text{Ca}$  as a list (C) and plot (D).

profiles with Al/Ca > 100  $\mu\text{mol/mol}$  with Mg/Ca ratios substantially higher than profiles through the same test with Al/Ca < 100  $\mu\text{mol/mol}$  were also excluded.

#### 5.2.4 Calculating mean Mg/Ca values and propagation of uncertainty

It is necessary to calculate a representative Mg/Ca value for the time interval encompassed by each sample so that long term trends in bottom water and sea surface temperature at the site of Sunbird-1 can be interpreted. Natural intra- and inter-test Mg/Ca variability within and between individual foraminifera, as revealed by microanalytical studies (Eggins et al., 2003, Eggins et al., 2004, Sadekov et al., 2005, Sadekov et al., 2008b), results in significant dispersion, as much as two to four fold (Sadekov et al., 2008b, Spero et al., 2015, Holland et al., 2017), about commonly applied palaeothermometry calibrations (Elderfield and Ganssen, 2000, Anand et al., 2003, Elderfield et al., 2006). The homogenisation of several specimens, as with bulk solution ICP-MS foraminiferal analysis, is therefore required to calculate a representative Mg/Ca for a sample, unobscured by intra- and inter-test variability, which can be used to reconstruct temperature (Chapter 4.3.4).

Each profile which passed the screening for contamination was given equal weighting, independent of the size of the integration window, to calculate the mean Mg/Ca ratio for each specimen. Errors on the single specimen Mg/Ca ratios (intra-specimen) are  $\pm 2$  Standard Error of the Mean ( $\pm 2$  SE) of all the measurements from that specimen, up to 6 depth profiles.

For the calculation of a mean sample Mg/Ca ratio, again each profile (up to a possible 36) was given equal weighting. This avoids the potential for a specimen where only 1 profile passed the screening for contamination having the same contribution to the mean Mg/Ca of the sample than a specimen where all 6 profiles passed the screening for contamination, potentially skewing the mean Mg/Ca ratio for the sample. Errors on the mean Mg/Ca ratios are  $\pm 2$  SE of all the measurements from that sample, up to 36 profiles, and is termed the sample uncertainty.

### 5.3 Converting raw Mg/Ca ratios to estimates of seawater temperature

Measurements of foraminifera from core-tops, sediment traps, and plankton tows have provided empirical calibrations between Mg/Ca and seawater temperature. This informs us that the influence of calcification temperature on the Mg/Ca ratio of foraminiferal calcite can be explained by an exponential curve of general form  $Mg/Ca = B \exp^{AT}$  where the pre-exponential constant (B) and exponential constant (A) are species specific (Nürnberg et al., 1996, Rosenthal et al., 1997, Lear et al., 2002, Anand et al., 2003). In order to convert raw Mg/Ca ratios to absolute temperatures, several secondary controls on Mg/Ca must be considered, and then accounted for where necessary. These controls may impact Mg/Ca derived temperature reconstructions on both Quaternary (Gray et al., 2018), and Cenozoic (Lear et al., 2015, Evans et al., 2018) timescales.

### 5.3.1 Accounting for the influence of the carbonate system on Mg/Ca:

Foraminiferal Mg/Ca is influenced by changes in the carbonate system (Russell et al., 2004, Elderfield et al., 2006, Yu and Elderfield, 2008, Evans et al., 2016c, Gray et al., 2018). This influence is different in benthic and planktic foraminiferal species and will therefore be discussed separately.

#### 5.3.1.1 *Benthic foraminifera*

The incorporation of  $Mg^{2+}$  into the calcite tests of benthic foraminifera is discriminated against in bottom waters with carbonate ion saturation state ( $\Delta[CO_3^{2-}]$ ) below a certain threshold, artificially lowering BWT estimates (Elderfield et al., 2006, Rosenthal et al., 2006). Therefore, infaunal foraminifera are preferred for BWT studies because the porewaters they calcify from are buffered against variations in  $\Delta[CO_3^{2-}]$  (Elderfield et al., 2010, Mawbey and Lear, 2013), although this is not always the case (Lear et al., 2015). Despite *C. wuellerstorfi* being epifaunal, the shallow water depth Sunbird-1 means that  $\Delta[CO_3^{2-}]$  is likely above the proposed threshold at which it has a significant effect of Mg/Ca (Elderfield et al., 2006).

#### 5.3.1.2 *Planktic foraminifera*

The Mg/Ca ratio in planktic foraminifera increases with decreased pH and/or  $\Delta[CO_3^{2-}]$ . However, the ultimate driver of this effect is not certain, so recent results which interpret pH, as opposed to  $\Delta[CO_3^{2-}]$  or DIC, as the parameter which controls the carbonate system's influence on Mg/Ca are followed (Evans et al., 2016c, Gray et al., 2018). Furthermore, unlike with  $\Delta[CO_3^{2-}]$ , it is possible to reconstruct pH through the Neogene using boron isotopes in

foraminifera (Foster et al., 2012, Henehan et al., 2013, Foster and Rae, 2015, Sosdian et al., 2018). The only published boron isotope pH record that spans the entire interval of Sunbird-1 is that of Sosdian et al. (2018), and this reconstructs values within error of Foster et al. (2012) when the two records overlap. To the best of my knowledge there are no other published pH records through the interval. Both records reconstruct ocean pH between 7.90 and 8.15 through the interval, which is similar to the modern day value of ~8.1 pH units (Key et al., 2015, Lauvset et al., 2016). Two scenarios to account for the influence of pH on the Mg/Ca temperature reconstructions are adopted. The first scenario uses a constant pH value of  $8.1 \pm 0.1$  pH units throughout the time interval of Sunbird-1, based on the reconstructions of (Foster et al., 2012). The second scenario uses recently published work utilising the boron isotopic composition of planktic foraminifera to reconstruct similar values of pH through this interval following the MMCT (Sosdian et al., 2018) (Figure 5.4). These authors use three  $\delta^{11}\text{B}_{\text{SW}}$  scenarios (Lemarchand et al., 2002, Raitzsch and Hönisch, 2013, Greenop et al., 2017), and their own temperature constraint on the equilibrium constant ( $K^*_B$ ). Mean pH is taken to be the average of the 50% value from the three  $\delta^{11}\text{B}_{\text{SW}}$  scenarios, and the uncertainty envelope is maximum and minimum pH at the 17% and 83% confidence interval, independent of the  $\delta^{11}\text{B}_{\text{SW}}$  scenario ( $\sim \pm 0.06$  pH units). Linear interpolation between these pH values allows me to calculate a mean pH value and associated uncertainty envelope for each Sunbird-1 sample. The higher resolution of this record reveals some variability in pH through the interval. This second scenario with varying pH to recalculate temperature, again using Equation 5.1, removing any unaccounted for influence of changing pH on the Mg/Ca derived temperature estimates is used. Measured planktic foraminiferal Mg/Ca values are corrected for using the equation of Evans et al. (2016c) (Equation 5.1).

$$\text{Equation 5.1: } \text{Mg}/\text{Ca}_{\text{CORRECTED}} = \frac{\text{Mg}/\text{Ca}_{\text{MEASURED}}}{\frac{0.66}{1 + \exp(6.9(\text{pH} - 8.0))} + 0.76}$$

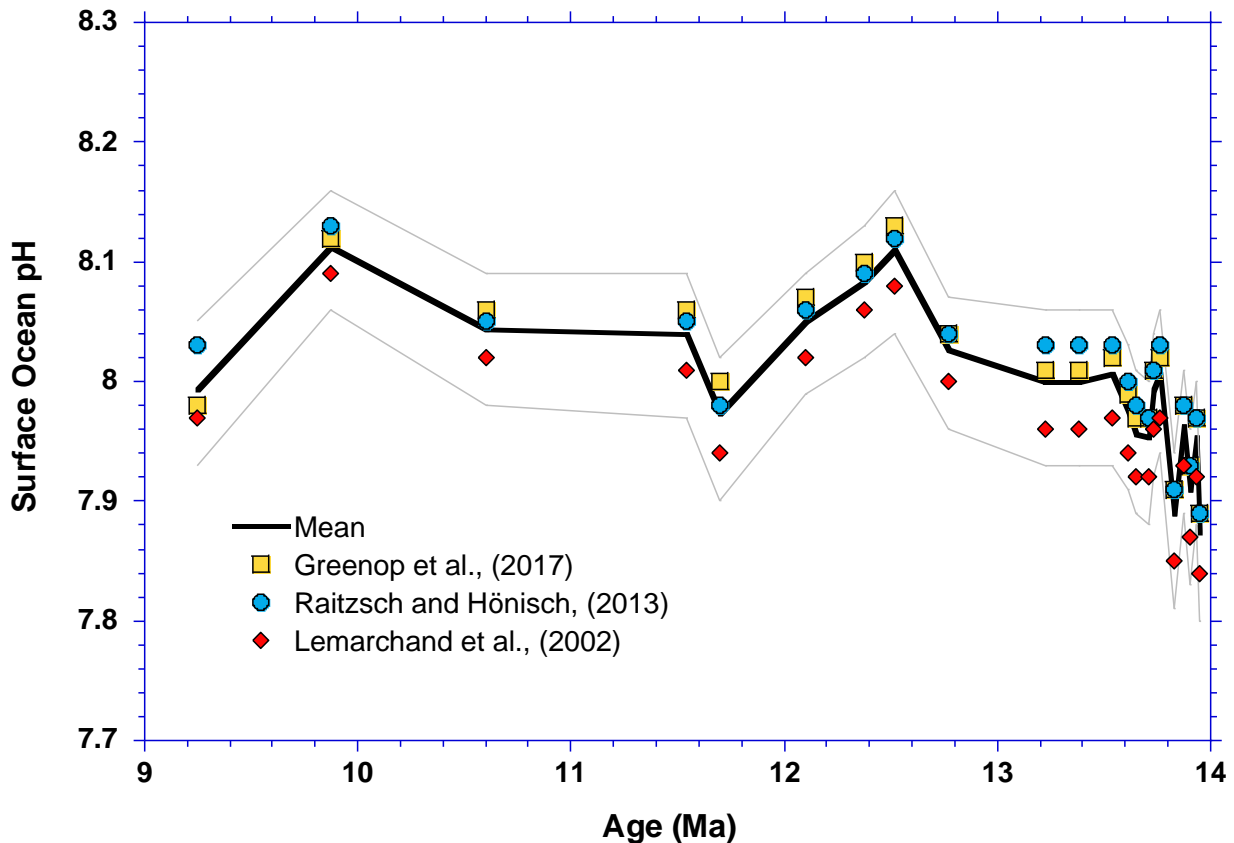


Figure 5.4: Surface ocean pH determined using  $\delta^{11}\text{B}$  measurements on planktic foraminifera from a global distribution of open ocean sites (Sosdian et al., 2018). Three  $\delta^{11}\text{B}_{\text{sw}}$  scenarios are used (Greenop et al., 2017, Lemarchand et al., 2002, Raitzsch and Hönisch, 2013). Uncertainty envelopes denote the maximum and minimum pH at the 17% and 83% confidence interval, independent of the  $\delta^{11}\text{B}_{\text{sw}}$  scenario.

### 5.3.2 Accounting for changes in seawater Mg/Ca

Fluxes of  $\text{Mg}^{2+}$  and  $\text{Ca}^{2+}$  into and out of the oceans means seawater Mg/Ca ( $\text{Mg}/\text{Ca}_{\text{sw}}$ ) experiences secular variation. This variability must be considered when determining absolute sea surface and bottom water temperatures on Cenozoic timescales. Reconstructions based

on large benthic foraminifera (Evans et al., 2018), calcite veins (Coggon et al., 2010), fluid inclusions (Horita et al., 2002), and echinoderms (Dickson, 2002) have constrained this variability through the Cenozoic (Figure 5.5). Mg/Ca<sub>SW</sub> reconstructions derived from corals show extremely large errors, in particular since the Miocene, and have therefore been omitted (Gothmann et al., 2015). Modern day Mg/Ca<sub>SW</sub> is well constrained at ~5.2 mol/mol (Broecker et al., 1982, Dickson, 2002, Horita et al., 2002, Kisakürek et al., 2008), and the Eocene-Oligocene demonstrates relatively stable values of 2-2.5 mol/mol (Coggon et al., 2010, Evans et al., 2018). However, only one data point exists from the Miocene, through which Mg/Ca<sub>SW</sub> more than doubles from ~2.2 mol/mol in the late Oligocene (Coggon et al., 2010) to 5.2 mol/mol in the modern ocean (Broecker et al., 1982). Therefore the method of Lear et al. (2015) is followed by fitting the fourth-order polynomial curve fit through the compiled seawater Mg/Ca (Mg/Ca<sub>SW</sub>) proxy records (Figure 5.5). The thin lines represent a ±0.5 mol/mol uncertainty window used in the following temperature calculations, this error envelope incorporating the majority of the spread in the proxy data. This produces the following association between Mg/Ca<sub>SW</sub> and age (Equation 5.2, R<sup>2</sup>=0.90) which has been used to approximate Mg/Ca<sub>SW</sub> for each sample at the time of calcification.

**Equation 5.2:**      
$$\text{Mg/Ca}_{\text{SW}} = 5.13 - (0.177 \times \text{Age}) + (0.00361 \times \text{Age}^2) - (2.95 \times 10^{-5} \times \text{Age}^3) + (8.08 \times 10^{-8} \times \text{Age}^4)$$

Applying the power law relationship (Equation 5.3), where H is a power law function used to describe the non-linear variation of  $Mg/Ca_{CALCITE}$  with  $Mg/Ca_{SW}$  (Hasiuk and Lohmann, 2010, Cramer et al., 2011, Evans and Müller, 2012), to the general form of the Mg/Ca palaeothermometer ( $Mg/Ca = B \exp^{AT}$ ) negates the assumption that the temperature sensitivity remains constant, independent of changing  $Mg/Ca_{SW}$  through the Cenozoic.

$$\text{Equation 5.3: } Mg/Ca = \left( \frac{B}{Mg/Ca_{SW}^{t=0H}} \right) \times Mg/Ca_{SW}^{t=H} \exp^{AT}$$

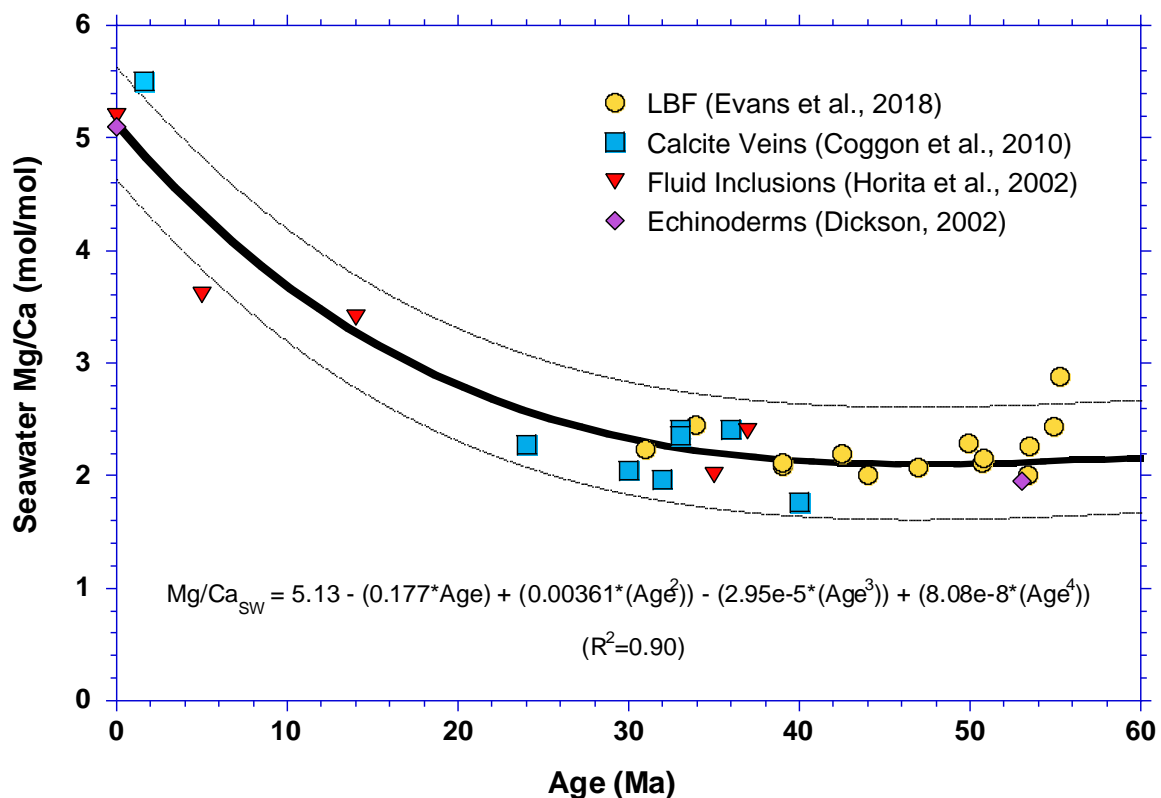


Figure 5.5: The evolution of Seawater Mg/Ca ( $Mg/Ca_{sw}$ ) through the Cenozoic from records of large benthic foraminifera (LBF) (Evans et al., 2018) (yellow circles), calcite veins (Coggon et al., 2010) (blue squares), fluid inclusions (Horita et al., 2002) (red triangles), and echinoderms (Dickson, 2002) (purple diamonds). Fourth order polynomial fit (thick black line) through the compiled data. The thin lines represent a  $\pm 0.5$  mol/mol uncertainty window used in the following temperature calculations.

Several authors have attempted to determine values of H for different species by rearranging Equation 5.3, using independently determined values for temperature, Mg/Ca<sub>SW</sub>, and A for the specific species (Evans and Müller, 2012, Lear et al., 2015, Hines et al., 2017). Temperature is determined independently using  $\delta^{18}\text{O}$  measurements of foraminiferal calcite and assuming a  $\delta^{18}\text{O}_{\text{SW}}$  for the ice-free world of the early Eocene which is commonly taken to be  $-0.89 \pm 0.02\text{‰}$  (VSMOW) (Cramer et al., 2011). Following this methodology, and using the calibrations of Lear et al. (2002) and Anand et al. (2003), H values of 0.31 and 0.20 have been calculated for *Cibicoides spp* and a mixed planktic foraminiferal assemblage respectively (Hines et al., 2017). However, these authors uses a Mg/Ca<sub>SW</sub> value of 1.6 mol/mol for the early Eocene (Evans and Müller, 2012) whereas the polynomial curve fit through the proxy records produces a Mg/Ca<sub>SW</sub> value of 2.1 mol/mol for the same interval (Figure 5.5) due to the inclusion of new proxy data from the Eocene (Evans et al., 2018). Using the same methodology and replacing Mg/Ca<sub>SW</sub> = 1.6 mol/mol with Mg/Ca<sub>SW</sub> = 2.1 mol/mol calculates an H value of 0.40 for *Cibicoides spp* and an H value of 0.26 for planktic foraminiferal species.

This correction for changing Mg/Ca<sub>SW</sub>, where modern day Mg/Ca<sub>SW</sub> = 5.2 mol/mol, is incorporated into the Mg/Ca temperature calibrations for *Cibicoides spp*. (Lear et al., 2002) (Equation 5.4) and a compilation of planktic foraminifera (Anand et al., 2003) (Equation 5.5) to calculate bottom water temperature (BWT) and sea surface temperature (SST) respectively. Note that Mg/Ca in Equation 5.5 is Mg/Ca<sub>CORRECTED</sub> from Equation 5.1. *D. altispira* is an extinct species, and therefore initially the compilation of nine modern planktic foraminifera which make up the calibration of Anand et al. (2003) is applied, as this minimises

any species-specific effects. The regressions for both calibrations have residual errors, which are accounted for in the calculation of the absolute temperature uncertainty envelopes.

$$\text{Equation 5.4: } C. wuellerstorfi \text{ Mg/Ca} = \left( \frac{0.867 \pm 0.049}{5.2^{0.40}} \right) \times \text{Mg/Ca}_{\text{sw}}^{0.40} \exp^{(0.109 \pm 0.007 \times \text{BWT})}$$

$$\text{Equation 5.5: } D. altispira \text{ Mg/Ca} = \left( \frac{0.38 \pm 0.02}{5.2^{0.26}} \right) \times \text{Mg/Ca}_{\text{sw}}^{0.26} \exp^{(0.090 \pm 0.003 \times \text{SST})}$$

The calibration of Lear et al. (2002) is from a compilation of three common species of *Cibicidoides*. Therefore a calibration specific to *C. wuellerstorfi* is used as an alternative (Equation 5.6) (Lo Giudice Cappelli et al., 2015). This has slightly higher pre-exponential and exponential coefficients, but both are well within error of the coefficients of the *Cibicidoides* spp. calibration (Lear et al., 2002).

$$\text{Equation 5.6: } C. wuellerstorfi \text{ Mg/Ca} = \left( \frac{0.91 \pm 0.10}{5.2^{0.40}} \right) \times \text{Mg/Ca}_{\text{sw}}^{0.40} \exp^{(0.120 \pm 0.01 \times \text{BWT})}$$

As an alternative SST calibration the preferred equation of (Evans et al., 2016b) is used to account for the influence of changing Mg/Ca<sub>sw</sub> when estimating SST. These authors determined that the best fit to culture-derived calibration lines is when both the pre-exponential (B) and exponential (A) coefficients vary quadratically with Mg/Ca<sub>sw</sub> (Equation 5.7 and 5.8).

**Equation 5.7:**  $B = (0.019 \times \text{Mg}/\text{Ca}_{\text{sw}}^2) - (0.16 \times \text{Mg}/\text{Ca}_{\text{sw}}) + 0.804$

**Equation 5.8:**  $A = (-0.0029 \times \text{Mg}/\text{Ca}_{\text{sw}}^2) + (0.032 \times \text{Mg}/\text{Ca}_{\text{sw}})$

These equations are substituted into A and B of the general exponential calibration,  $\text{Mg}/\text{Ca} = \text{Bexp}^{\text{AT}}$ . Although this equation is specific to *Globigerinoides ruber*, this species inhabits a shallow water depth of 0-50m (Schiebel and Hemleben, 2017) similar to the inferred habitat depth *D. altispira* (Aze et al., 2011). Furthermore, *G. ruber* is included in the multi-species compilation SST calibration regularly used for extinct species, such as *D. altispira* (Anand et al., 2003).

### 5.3.3 Accounting for changes in salinity

Salinity can exert a secondary effect on foraminiferal Mg/Ca, sensitivity measurements from culture and core-top studies show this to be ~3-5% per practical salinity unit (psu) (Kisakürek et al., 2008, Hönisch et al., 2013, Gray et al., 2018). In the absence of a robust, independent salinity proxy and the relatively minor effect of salinity on foraminiferal Mg/Ca this potential secondary control is not empirically accounted for. Sunbird-1 was located in a coastal setting and likely experienced a highly variable hydrological cycle due to changes in the position of the ITCZ making it susceptible to changes in salinity. Therefore, an error of  $\pm 0.5^\circ\text{C}$  is incorporated into the final sea surface temperature estimates, equivalent to an assumed salinity variability of  $\sim\pm 1$  PSU.

### 5.3.4 Quantifying uncertainties of reconstructed temperatures

The uncertainties ( $\pm 2SE$ ) associated with the conversion from Mg/Ca to temperature incorporates the uncertainty in the pH correction, the uncertainty on the Mg/Ca<sub>SW</sub> record, the uncertainty on the temperature calibration coefficients, and a potential uncertainty due to varying salinity. The uncertainties associated with pH and salinity are only applied to the planktic foraminiferal Mg/Ca record. This is termed the calibration uncertainty and is independent from both the analytical uncertainty described in Chapter 5.2.3, and sample uncertainty described in Chapter 5.2.4. Therefore, to determine the absolute temperature cumulative  $\pm 2SE$  uncertainty envelope all of these errors are summed. The calibration uncertainty only influences the estimates of absolute temperature and is therefore not included in the assessment of relative temperature trends (Chapter 5.5.2 and 5.5.3).

## 5.4 Results

### 5.4.1 Effect of screening for contamination

The use of LA-ICP-MS to generate simultaneous, highly spatially resolved depth profiles of Mg/Ca, Al/Ca, Mn/Ca, and others, through foraminiferal tests provides the opportunity to assess their intra-specimen preservation (Creech et al., 2010, Evans et al., 2015). This has allowed me to discount any regions of the test determined to be influenced by diagenetic features from the interval of data integration, and therefore exclude them from the primary environmental interpretation (Creech et al., 2010, Hines et al., 2017).

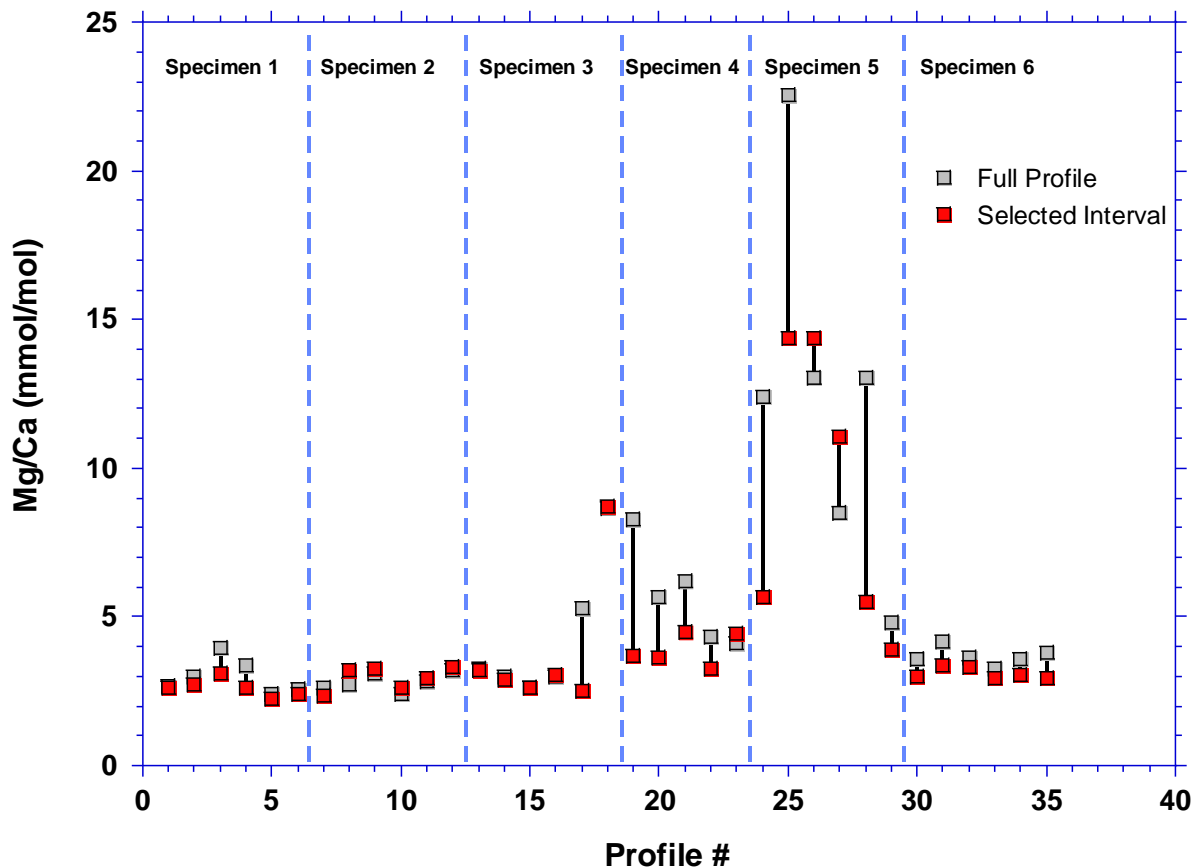


Figure 5.6: Mg/Ca ratios of all *C. wuellerstorfi* profiles from the 1473-1476m sample in Sunbird-1. Grey squares represent full geochemical profiles, and red squares represent the selected integration intervals of the profiles. Solid black lines indicate the difference between the two ratios, and dashed blue lines distinguish between the six specimens analysed.

To demonstrate the influence of selecting an interval of data integration the 1473-1476m *C. wuellerstorfi* sample was processed using the full profile from each analysis. This is, in effect, the geochemical ratios that would result from bulk analysis having omitted the thorough chemical cleaning process. Selection of a suitable interval for data integration reduces the mean Mg/Ca of the 35 profiles from 5.30 mmol/mol to 4.28 mmol/mol, mean Mn/Ca from 140  $\mu\text{mol/mol}$  to 110  $\mu\text{mol/mol}$ , and mean Al/Ca from 5060  $\mu\text{mol/mol}$  to 1330  $\mu\text{mol/mol}$  (Table 5.2). Selecting an interval for data integration has a non-uniform impact on the Mg/Ca ratio of individual profiles, some specimens showing no influence of using this technique, indicating that contamination varies between specimens from the same sample (Figure 5.6).

Despite selecting integration intervals which seem to be free from contamination many depth profiles still demonstrate elevated Mg/Ca in tandem with Mn/Ca values >150  $\mu\text{mol/mol}$ , the proposed threshold above which contamination with respect to Mg/Ca may be an issue. Therefore, all profiles with Mn/Ca values greater than 150  $\mu\text{mol/mol}$  were rejected from any environmental interpretation (Figure 5.7b). Elevated Al/Ca ratios are present, but some profiles with Al/Ca >> 100  $\mu\text{mol/mol}$  are often associated with Mg/Ca values which are the same, or lower, than profiles whose Al/Ca < 100  $\mu\text{mol/mol}$  (Figure 5.7a). This prevents the use of a threshold Al/Ca value above which samples should be discarded (Barker et al., 2003, Hollis et al., 2015). Therefore, profiles with Al/Ca >> 100  $\mu\text{mol/mol}$  and concomitantly high Mg/Ca values were also discarded using visual inspection and personal discretion.

Applying this further screening to the 1473-1476m *C. wuellerstorfi* example discards nine profiles, reducing the mean Mg/Ca from 4.28 mmol/mol to 2.96 mmol/mol, mean Mn/Ca from 110  $\mu\text{mol/mol}$  to 30  $\mu\text{mol/mol}$  and mean Al/Ca from 1330  $\mu\text{mol/mol}$  to 670  $\mu\text{mol/mol}$  (Table 5.2). This demonstrates the influence of the extra, stringent screening applied post data processing. These criteria were applied to all depth profiles, those that fail the post data processing screening being discarded from any further paleotemperature interpretation.

	Mean Mg/Ca (mmol/mol)	Mean Mn/Ca ( $\mu\text{mol/mol}$ )	Mean Al/Ca ( $\mu\text{mol/mol}$ )
Full Profile (n=35)	5.30	140	5060
All Profiles (n=35)	4.28	110	1330
Used Profiles (n=26)	2.96	30	670
Rejected Profiles (n=9)	8.06	330	3250

Table 5.2: Mean *C. wuellerstorfi* Mg/Ca, Mn/Ca, and Al/Ca from the 1473-1476m sample, which has a biostratigraphic age of 11.09Ma. Mean values for all profiles (n=35), used profiles (n=26), and rejected profiles (n=9) are given. The mean values for the full profiles, with no selection of the data integration interval are also given.

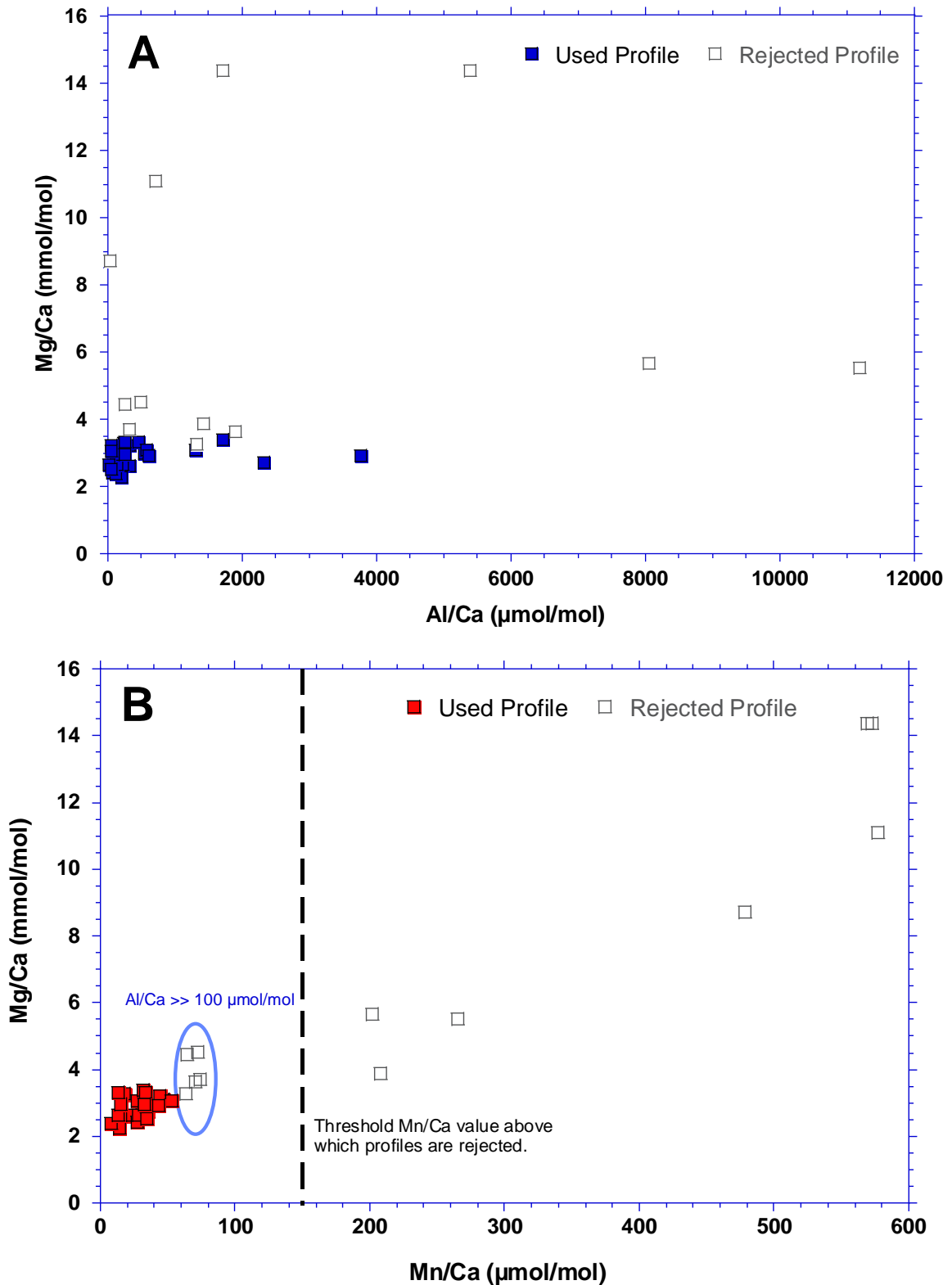


Figure 5.7: Crossplots between Mg/Ca and Al/Ca (A), and Mg/Ca and Mn/Ca (B) from measured profiles of *C. wuellerstorfi* from the 1473-1476m sample in Sunbird-1. Open squares represent rejected profiles (n=9), and closed squares represent used profiles (n=26).

Over the record as a whole 2649 analyses of foraminiferal tests from 44 samples in the Sunbird-1 core were undertaken, with 1560 analyses passing data screening for contaminant phases and therefore being used for palaeotemperature reconstruction. This consisted of 767 out of 1118 *C. wuellerstorfi* analyses (~68%) and 793 out of 1531 *D. altispira* analyses (~52%) (Table 5.3).

The rejected *C. wuellerstorfi* profiles are concentrated at either end of the record, many samples prior to 12.5 Ma and post 10.8 Ma having minimal or no profiles, which pass all the data screening criteria (Figure 5.8a). The *D. altispira* record also has very few profiles, which pass data screening at the start of the record, and has a trough in used profiles between 11.2 Ma and 10.8 Ma (Figure 5.8b). The full screening of samples with elevated Mn/Ca and/or Al/Ca ratios, post data processing, substantially reduces the mean Mg/Ca ratios of each record (Table 5.3). *C. wuellerstorfi* mean Mg/Ca is 2.87 mmol/mol, whereas without incorporating this further screening for contamination post data processing it would be 4.04 mmol/mol. *D. altispira* mean Mg/Ca is 4.14 mmol/mol, whereas without incorporating this further screening for contamination post data processing it would be 6.53 mmol/mol. The mean Mg/Ca ratios of the rejected profiles are considerably higher, 6.57 mmol/mol and 9.16 mmol/mol respectively, as are the mean Mn/Ca and Al/Ca of the rejected profiles (Table 5.3).

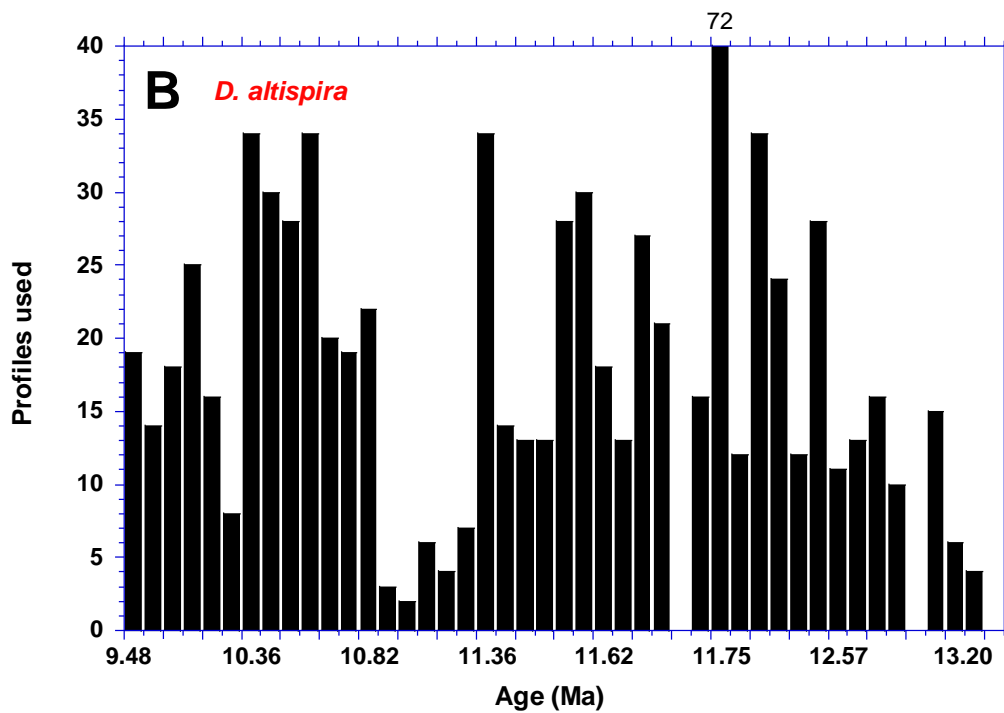
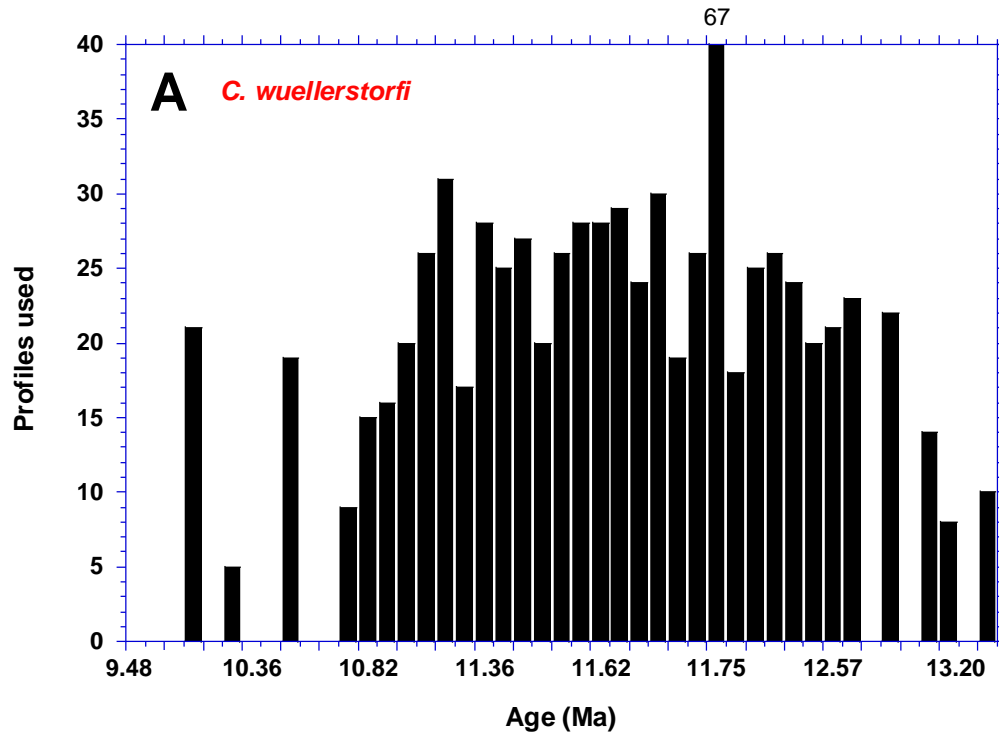


Figure 5.8: Number of profiles of (A) *C. wuellerstorfi* and (B) *D. altispira* that passed contaminant screening.

<b><i>C. wuellerstorfi</i></b>			
	Mean Mg/Ca (mmol/mol)	Mean Mn/Ca ( $\mu$ mol/mol)	Mean Al/Ca ( $\mu$ mol/mol)
All Profiles (n=1118)	4.04	140	2400
Used Profiles (n=767)	2.87	80	410
Rejected Profiles (n=351)	6.57	280	6690

<b><i>D. altispira</i></b>			
	Mean Mg/Ca (mmol/mol)	Mean Mn/Ca ( $\mu$ mol/mol)	Mean Al/Ca ( $\mu$ mol/mol)
All Profiles (n=1531)	6.53	150	3460
Used Profiles (n=793)	4.14	100	0200
Rejected Profiles (n=738)	9.16	200	7040

Table 5.3: Mean Mg/Ca, Mn/Ca, and Al/Ca *C. wuellerstorfi* and *D. altispira* in Sunbird-1. Mean values for all profiles, used profiles, and rejected profiles are given.

#### 5.4.2 Influence of identifying the primary test on temperature reconstructions

Selecting a suitable interval for data integration reduces estimated BWT for the 1473-1476m (11.09 Ma) sample from 17.7°C to 15.7°C, and further screening of profiles with Mn/Ca > 150  $\mu$ mol/mol alongside elevated Mg/Ca reduces BWT for this sample to 12.4°C. Similarly, data processing reduces mean BWT of the Sunbird-1 record from 15.5°C to 12.4°C, and mean SST from 33.3°C to 27.3°C.

It is suggested that future laser ablation analyses on foraminifera whose Mg/Ca ratios are influenced by contamination analyse twice as many depth profiles per sample than what has been determined to be required in order to obtain a mean Mg/Ca value that is representative

for the sample. This would result in a robust, reliable, and representative mean Mg/Ca being obtained for the sample even if half of the depth profiles do not pass contaminant screening. Unfortunately, this was not possible at Sunbird-1 due to the low foraminiferal abundance, less than six individual specimens being available in multiple samples.

### 5.4.3 Intra- and Inter-specimen variability in Mg/Ca

Variability in Mg/Ca ratios are reported from both within and between tests from the same sample depth. This intra- and inter-test Mg/Ca variability has a range of causes, including diurnal banding, vertical migration, and changes in calcification temperature on daily to seasonal timescales (Eggins et al., 2003, Eggins et al., 2004, Sadekov et al., 2005, Sadekov et al., 2008b, Hollis et al., 2012, Koutavas and Joanides, 2012, Fehrenbacher et al., 2015, Spero et al., 2015, Holland et al., 2017). By analysing multiple depth profiles through multiple specimens for each sample means that an assessment of both intra- and inter-test variability can be made. The 1551-1554 m sample has a greater foraminiferal abundance than the majority of the core (Chapter 4.3.4). Therefore, this sample is used as an example of the relative extent of these two sources of variability in both *C. wuellerstorfi* and *D. altispira* due to the greater number of measurements available.

The ten specimens of *C. wuellerstorfi* from the 1551-1554 m sample have a range of intra-specimen variability between 0.56 mmol/mol and 1.15 mmol/mol, with an average of 0.89 mmol/mol (Table 5.4, Figure 5.9a). This is substantially lower than for *D. altispira* from the same sample, in which intra-specimen variability ranges from 1.29 mmol/mol to 2.56 mmol/mol, with an average of 1.67 mmol/mol (Table 5.4, Figure 5.9b). This equates to an

intra-specimen variability of 1.2 to 1.7 fold for *C. wuellerstorfi*, and 1.5 to 2 fold for *D. altispira*. To my knowledge this has not previously been assessed in either species but is at the lower end of the two to four fold variability reported in cultured *O. universa* (Eggins et al., 2004, Spero et al., 2015, Holland et al., 2017). Although not specifically assessed in this study, as the primary goal was to determine mean Mg/Ca ratios for each sample to interpret downcore trends, future studies should investigate whether this intra-specimen variability is predominantly within or between different chambers. .

The inter-specimen variability is also considerably lower in *C. wuellerstorfi*, 1.03 mmol/mol, than it is in *D. altispira*, 1.38 mmol/mol. These results suggest that intra- and inter-specimen Mg/Ca variability is greater in *D. altispira* than it is in *C. wuellerstorfi* in the 1551-1554 m sample. Interestingly, for this sample, intra-specimen variability is greater than inter-specimen variability for *D. altispira* whereas the opposite is the case for *C. wuellerstorfi*. This points towards differing controls on the sample variability of the benthic and planktic foraminiferal species. One possibility is that photosymbionts regulate Mg uptake in *D. altispira*. However, *D. altispira* is an extinct species, and there is no evidence that it was symbiotic.

For *C. wuellerstorfi* the mean intra-specimen variability (2SE) across the 10 specimens is 0.15 mmol/mol, and the inter-specimen variability (2SE) between the 10 specimens is 0.18 mmol/mol (Figure 5.9a). For *D. altispira* the mean intra-specimen variability (2SE) across the 10 specimens is 0.29 mmol/mol, and the inter-specimen variability (2SE) between the 10 specimens is 0.26 mmol/mol (Figure 5.9b and Table 5.5).

	<i>C. wuellerstorfi</i>	<i>D. altispira</i>
<b>Mean Profile Mg/Ca (mmol/mol)</b>	2.48	3.63
<b>Maximum Profile Mg/Ca (mmol/mol)</b>	3.14	5.23
<b>Minimum Profile Mg/Ca (mmol/mol)</b>	1.62	2.66
<b>Mean Intra-specimen 2SE (mmol/mol)</b>	0.15	0.29
<b>Maximum Specimen Mg/Ca (mmol/mol)</b>	2.97	4.33
<b>Minimum Specimen Mg/Ca (mmol/mol)</b>	1.94	2.96
<b>Inter-specimen 2SE (mmol/mol)</b>	0.18	0.26

Table 5.4: Summary of intra- and inter-specimen variability in Mg/Ca (mmol/mol) for *C. wuellerstorfi* and *D. altispira* in the 1551-1554 m Sunbird-1 sample.

The sample uncertainty ( $\pm 2$  SE) on the mean Mg/Ca value for the 1551-1554 m sample is  $\pm 0.09$  mmol/mol for *C. wuellerstorfi* and  $\pm 0.14$  mmol/mol for *D. altispira*. Acquiring multiple LA-ICP-MS profiles through several specimens from the same sample reveals there to be substantially greater variability than this in the individual Mg/Ca ratios, as demonstrated by the scatter around the horizontal grey panel representative of the sample uncertainty (Figure 5.9). This scatter results from variability between the Mg/Ca ratios of depth profiles through the same foraminiferal test, intra-specimen variability, and between the mean Mg/Ca ratios of individual specimens from the same sample, inter-sample variability. The large number of depth profiles used to determine the mean Mg/Ca of the sample,  $n=67$  and  $n=72$  for *C. wuellerstorfi* and *D. altispira* respectively, homogenises the intra- and inter-specimen variability to estimate a mean sample Mg/Ca for the sample, used for the interpretation of long-term climatic trends (Chapter 5.4.4).

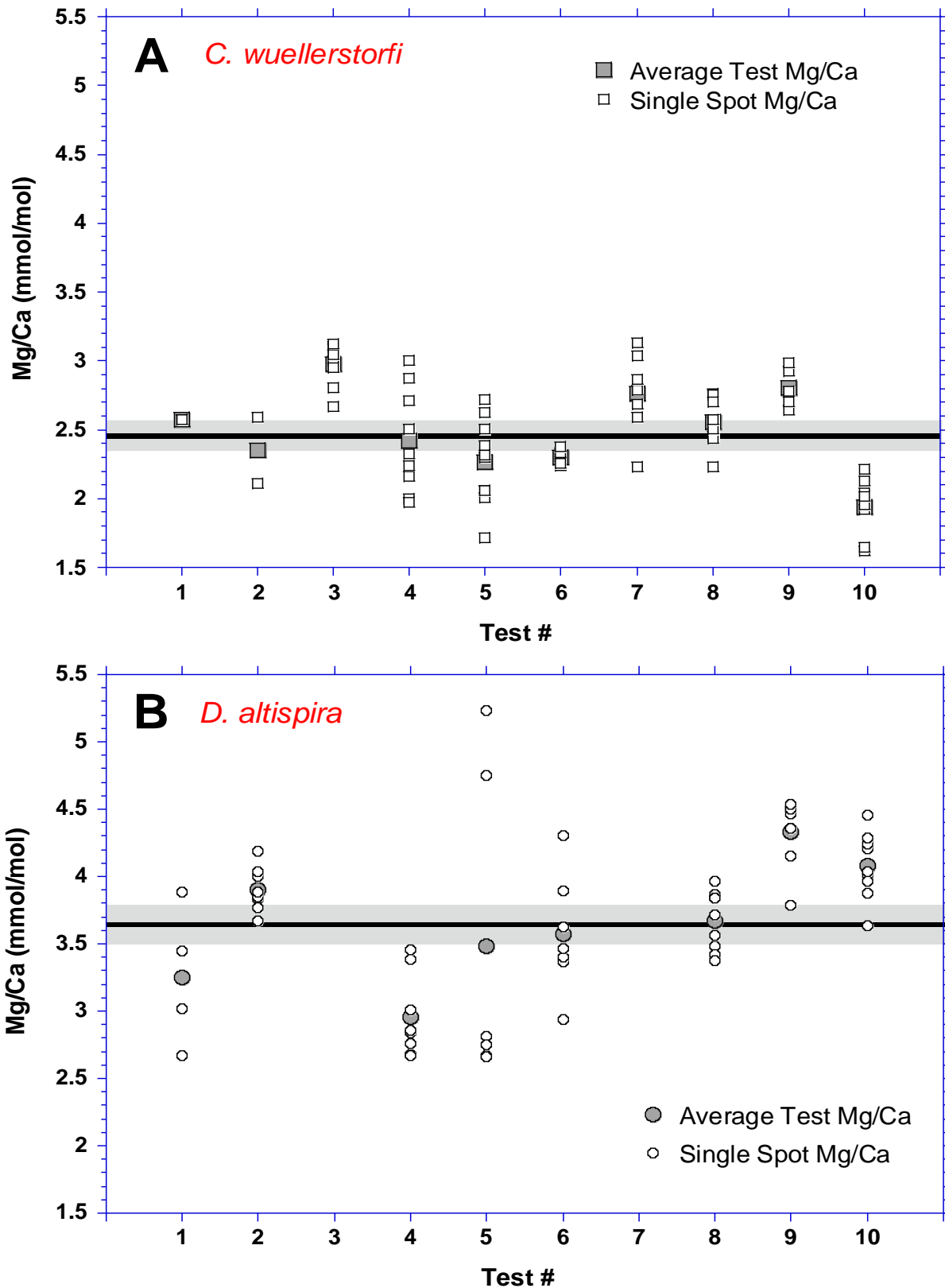


Figure 5.9: Mg/Ca of *C. wuellerstorfi* (A, squares) and *D. altispira* (B, circles) from the 1551-1554 m Sunbird-1 sample. Open symbols denote individual measurements, and filled symbols denote mean Mg/Ca values for each specimen. Horizontal black lines are the means of all depth profiles from the sample, and the grey bars the  $\pm 2$  SE sample uncertainty.

#### 5.4.4 Sample mean Mg/Ca ratios

The interpretation of temperature trends in downcore records requires the mean Mg/Ca ratio determined for a sample to be representative. For this to be the case the mean Mg/Ca of the sample must be unbiased by the natural intra- and inter-test variability observed in foraminiferal calcite.

Sample mean Mg/Ca for *C. wuellerstorfi* ranges from 2.19 to 3.60 mmol/mol, with an average value of  $2.85 \pm 0.22$  mmol/mol, and errors ( $\pm 2SE$ ) range from 0.09 to 0.53 mmol/mol (Table 5.5 and Figure 5.10a). Sample mean Mg/Ca for *D. altispira* ranges from 3.03 to 5.07 mmol/mol, with an average value of  $4.18 \pm 0.40$  mmol/mol, and errors ( $\pm 2SE$ ) range from 0.10 to 1.04 mmol/mol (Table 5.5 and Figure 5.10b). However, this assumes that the mean Mg/Ca value for each sample is representative, irrespective of the number of depth profiles and specimens averaged.

	<i>C. wuellerstorfi</i>		<i>D. altispira</i>	
	Full dataset (n=34)	Representative Samples (n=15)	Full dataset (n=43)	Representative Samples (n=14)
<b>Spots Ablated</b>	1118	598	1531	562
<b>Spots Used</b>	767	446	793	450
<b>Mean (mmol/mol)</b>	$2.85 \pm 0.22$	$2.85 \pm 0.19$	$4.18 \pm 0.40$	$3.81 \pm 0.26$
<b>Maximum (mmol/mol)</b>	3.60	3.21	5.07	4.42
<b>Minimum (mmol/mol)</b>	2.19	2.44	3.03	3.08
<b>Maximum 2SE (mmol/mol)</b>	0.53	0.29	1.04	0.40
<b>Minimum 2SE (mmol/mol)</b>	0.09	0.09	0.10	0.14

Table 5.5: Number of spots ablated, spots that passed contaminant screening, and Mg/Ca (mmol/mol) distribution statistics and 2 standard errors for *C. wuellerstorfi* and *D. altispira*. Values for the full dataset and for the representative samples, those that satisfy the requirements determined in Chapter 4.3.4, are given.

For the mean Mg/Ca value of a sample to be considered representative of mean conditions approximately 28 depth profiles from a minimum of five specimens is required (Chapter 4.3.4). Following data screening, and the exclusion of any depth profiles which have elevated Mg/Ca concomitantly with Mn/Ca > 150  $\mu\text{mol/mol}$  or Al/Ca >> 100  $\mu\text{mol/mol}$ , several samples have fewer depth profiles from fewer specimens than are required for a representative mean Mg/Ca value (Chapter 4.3.4), which is necessary for interpreting temperature trends through the record. If overlooked there is the potential to interpret spurious trends in Mg/Ca, and for any genuine long-term temperature trends to be masked by large uncertainties (Figure 5.11).

Of the 45 samples analysed only 14 samples of *D. altispira* and 15 samples of *C. wuellerstorfi* satisfy the requirements for them being representative. The representative sample means for *C. wuellerstorfi* Mg/Ca range from 2.44 mmol/mol to 3.21 mmol/mol, with an average value of  $2.85 \pm 0.19$  mmol/mol, and errors ( $\pm 2\text{SE}$ ) range from 0.09 mmol/mol to 0.29 mmol/mol (Table 5.5 and Figure 5.11). Representative sample means for *D. altispira* Mg/Ca range from 3.08 mmol/mol to 4.42 mmol/mol, with an average value of  $3.81 \pm 0.26$  mmol/mol, and errors ( $\pm 2\text{SE}$ ) range from 0.14 mmol/mol to 0.40 mmol/mol (Table 5.5 and Figure 5.11). It is notable that the range in Mg/Ca values is substantially reduced when only representative samples are considered while the record average is not significantly changed. This suggests that the more extreme values from samples not considered representative are

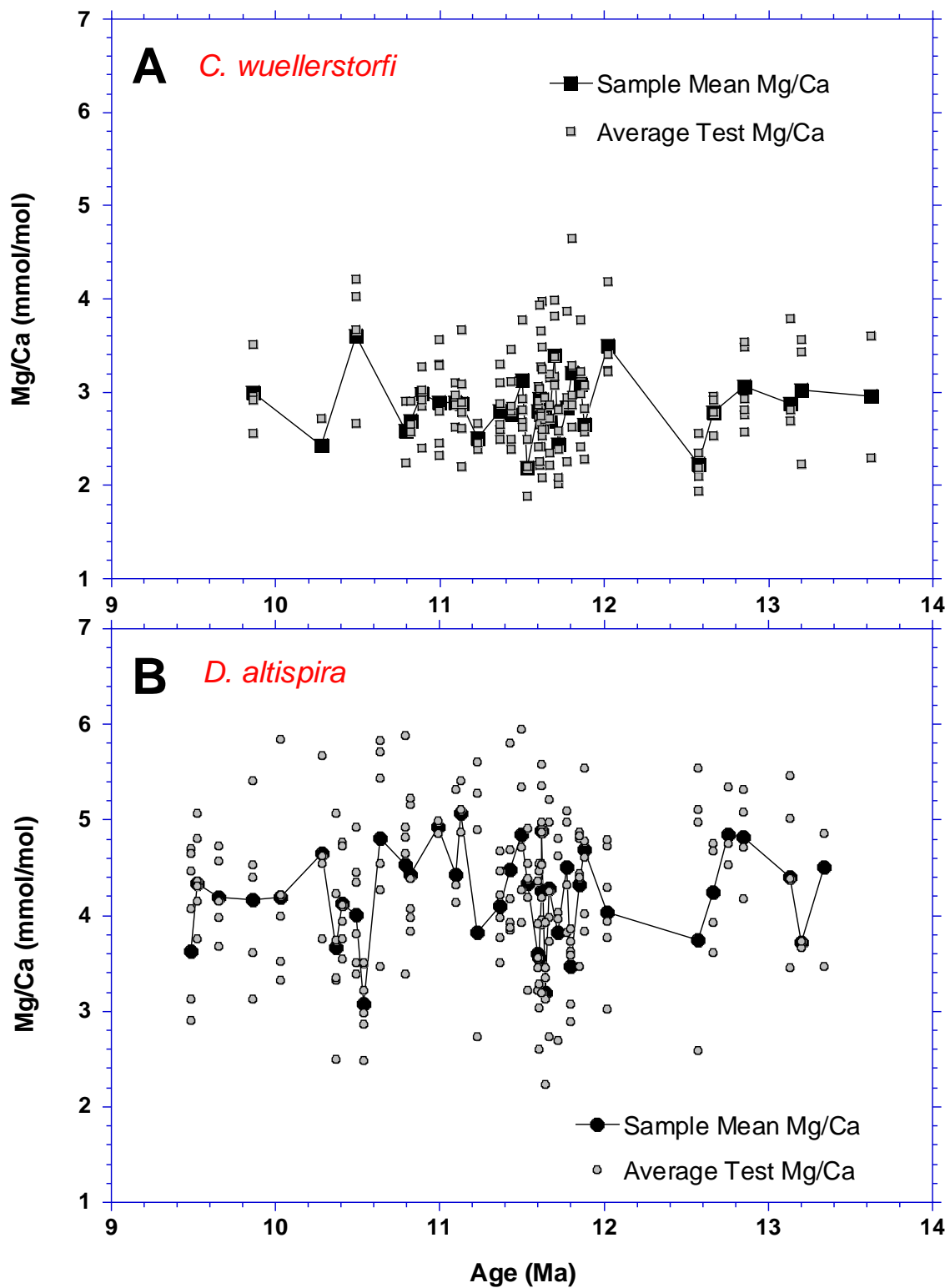


Figure 5.10: Average Mg/Ca (mmol/mol) for all tests (small grey symbols) and all samples (large black symbols) of (A) *C. wuellerstorfi* (squares), and (B) *D. altispira* (circles).

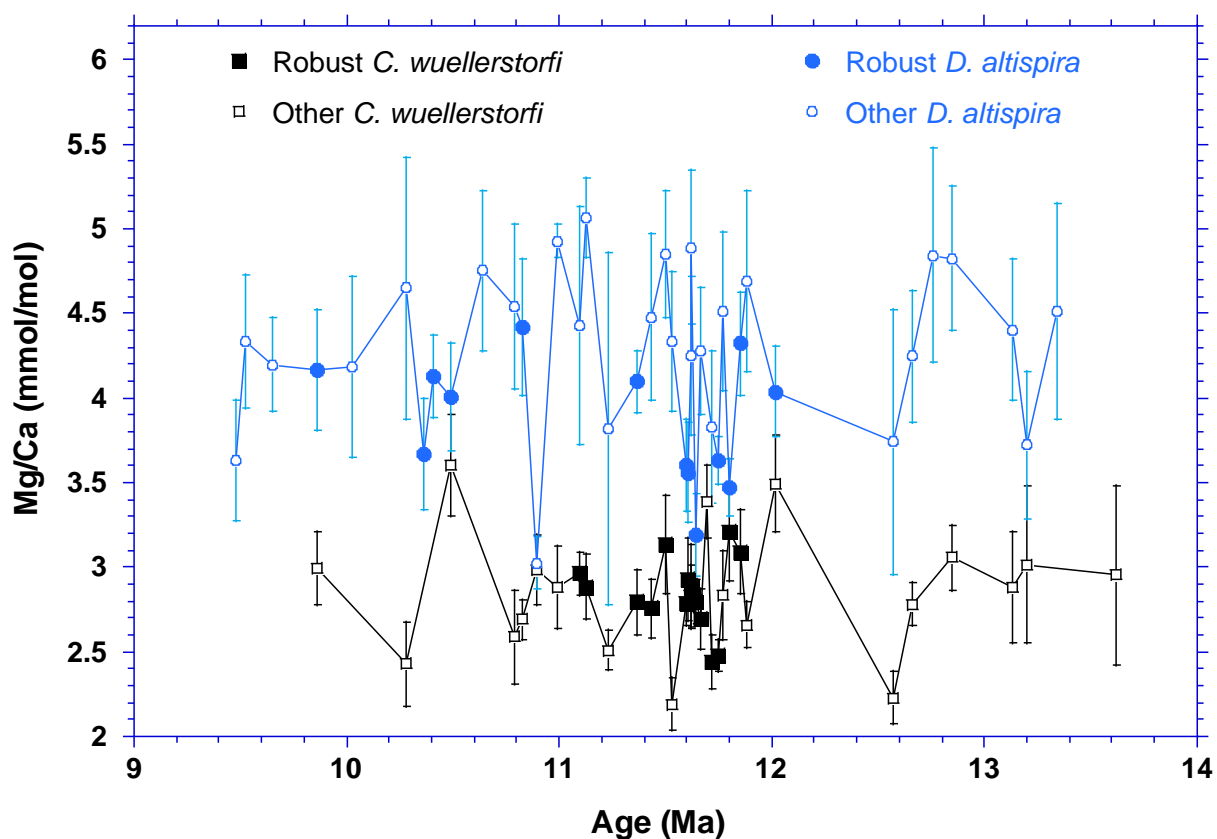


Figure 5.11: Mean *C. wuellerstorfi* (black squares) and *D. altispira* (blue circles) Mg/Ca ratios (mmol/mol) for samples considered representative of mean Mg/Ca laser ablation analyses (filled symbols) and samples also reflecting natural inter-test Mg/Ca variability (open symbols) samples.

likely not representative means for the sample, and should not be considered as such. This supports the argument of only incorporating representative samples, because the reduction in natural variability of the downcore record is likely due to the intra- and inter-test variability not being homogenised out in these samples. Additionally, that the mean Mg/Ca value for each record is the same, or within error, when the full dataset is considered suggests that the unrepresentative samples are sometimes warmer and sometimes colder than what a representative sample would be. Therefore, these samples deemed to be unrepresentative, due to the large number of profiles not passing the screening for contaminants, are not influenced by the Mg-rich contaminant coating. If they were the average Mg/Ca of the record

would be significantly reduced by excluding them. However, that that it is within error means that samples with only a few profiles determined to be contaminant free still contain useful information.

Discarding samples that do not satisfy the requirements for numbers of specimen and depth profiles substantially shortens the two records. This is particularly the case with *C. wuellerstorfi* with all representative sample means falling between 12 Ma and 11 Ma. Furthermore, there are no *D. altispira* representative sample mean values prior to 12 Ma. To alleviate this problem, adjacent samples have been combined into longer time slices so that they satisfy the requirements in terms of the number of specimens and total number of depth profiles (Table 5.6, Figure 5.12 and Appendix 7). It is acknowledged that by combining adjacent samples, which span up to 420 kyr, could incorporate orbital scale climatic variability into the binned samples. However, the individual samples that have been combined into a single binned sample do not show significant offsets to other samples they have been combined with in a bin (Figure 5.12). In addition, due to the coarse sampling resolution of the record, orbital climatic variability is not inferred because this could introduce sample aliasing over these timescales anyway. In fact, by binning adjacent samples to generate a representative mean Mg/Ca for a longer timeslice could in fact average out orbital scale variability, reducing uncertainty and assisting the interpretation of longer term climatic trends. Incorporating the six binned *C. wuellerstorfi* and the nine binned *D. altispira* Mg/Ca samples with the robust samples makes minimal difference to the overall statistics, the average Mg/Ca values for each record being well within error to when binned samples are not included.

***C. wuellerstorfi***

Average Age (Ma)	Minimum Age (Ma)	Maximum Age (Ma)	# Samples Binned	# Specimens Used	# Profiles used	Sample Mean Mg/Ca (mmol/mol)	Sample 2 SE
10.07	9.86	10.28	2	4	26	2.89	0.20
10.64	10.49	10.79	2	6	28	3.28	0.28
10.91	10.82	10.99	3	12	51	2.86	0.12
11.95	11.88	12.02	2	9	44	3.04	0.20
12.62	12.57	12.66	2	10	44	2.52	0.13
13.03	12.85	13.20	3	12	44	2.99	0.17

***D. altispira***

Average Age (Ma)	Minimum Age (Ma)	Maximum Age (Ma)	# Samples Binned	# Specimens Used	# Profiles used	Sample Mean Mg/Ca (mmol/mol)	Sample 2 SE
9.57	9.48	9.65	3	13	51	4.02	0.21
10.15	10.03	10.28	2	8	24	4.70	0.48
10.72	10.64	10.79	2	9	39	4.65	0.34
11.06	10.89	11.23	5	11	22	4.20	0.48
11.48	11.43	11.53	3	13	40	4.55	0.26
11.70	11.67	11.72	2	9	35	4.09	0.31
12.71	12.57	12.85	4	12	50	4.40	0.31
13.24	13.13	13.34	3	7	25	4.26	0.31

Table 5.6: Details about the age range and the number of samples, specimens, and profiles combined for each binned sample of *C. wuellerstorfi* and *D. altispira*.

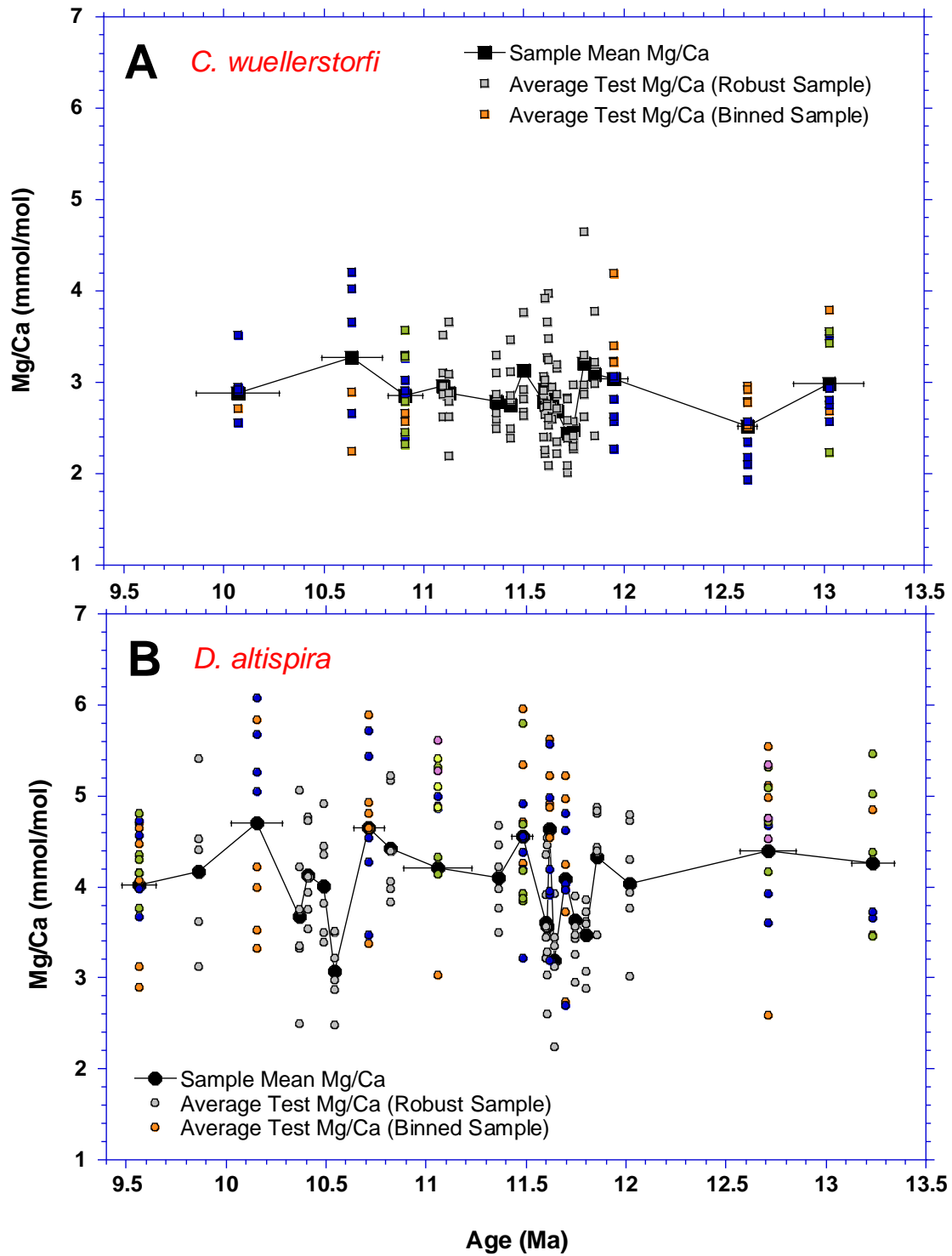


Figure 5.12: Average Mg/Ca (mmol/mol) for each sample (large black symbols), and each test of robust samples (small grey symbols) and binned samples (small coloured symbols) of (A) *C.wuellerstorfi* (squares), and (B) *D. altispira* (circles). Average Mg/Ca (mmol/mol) of tests from different individual samples combined within a binned sample are denoted by different colours.

Both the benthic *C. wuellerstorfi* and planktic *D. altispira* Mg/Ca records at Sunbird-1 display no obvious general long term trend through the interval (Figure 5.13). There is a 0.7-0.8 mmol/mol decrease in both records at 11.8-11.7 Ma. This is followed by a recovery to approximately previous values at 11.5-11.4 Ma. *D. altispira* Mg/Ca decreases by a similar magnitude from ~4.4 mmol/mol to ~3.7 mmol/mol between 10.7 Ma and 10.36 Ma, before again recovering to ~4.2 mmol/mol at 9.85 Ma. There is insufficient *C. wuellerstorfi* data through this interval, even incorporating the binned samples, to discern whether there is a similar decrease. Furthermore, the coarse sampling frequency and the requirement to combine samples in order for an Mg/Ca value to be representative could be obscuring similar variability through the rest of the record.

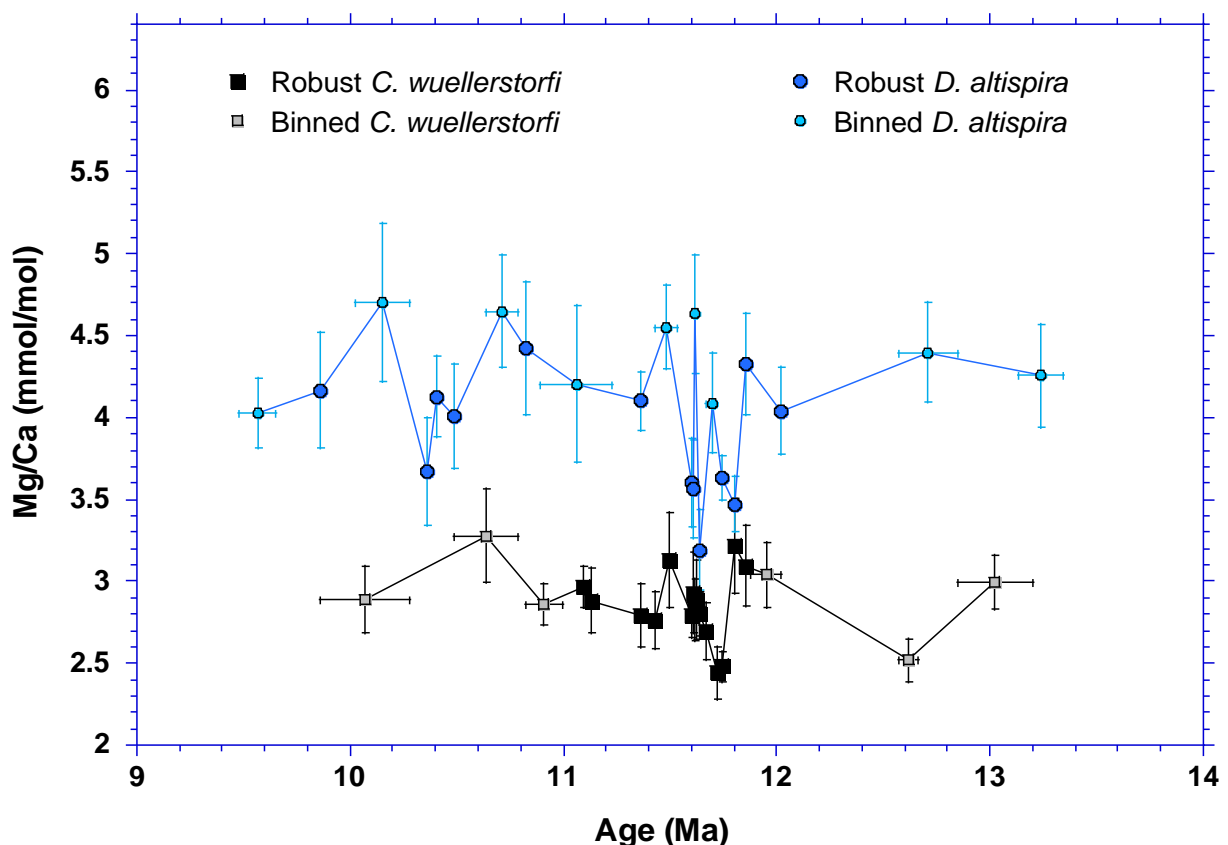


Figure 5.13: Mean *C. wuellerstorfi* (black squares) and *D. altispira* (blue circles) Mg/Ca ratios (mmol/mol) for robust (dark symbols) and binned (pale symbols) samples. See text for details on sample binning. Error bars denote the age range for binned samples and the  $\pm 2SE$  of Mg/Ca from all depth profiles in the sample.

#### 5.4.5 Calculating bottom water and sea surface temperature at Sunbird-1

A suite of bottom water temperature (Figure 5.14) and sea surface temperature (Figure 5.15) records have been calculated using the range of scenarios outlined in Section 5.4. These ranges incorporate both H values from the different estimates of Eocene Mg/Ca<sub>sw</sub> (1.6 mol/mol and 2.1 mol/mol), and the differing temperature calibrations used (Lear et al., 2002, Anand et al., 2003, Lo Giudice Cappelli et al., 2015, Evans et al., 2016a). For SST scenarios when surface pH is considered stable (Figure 5.15a), and when surface pH varies in accordance with Sossian et al. (2018), are shown (Figure 5.15b).

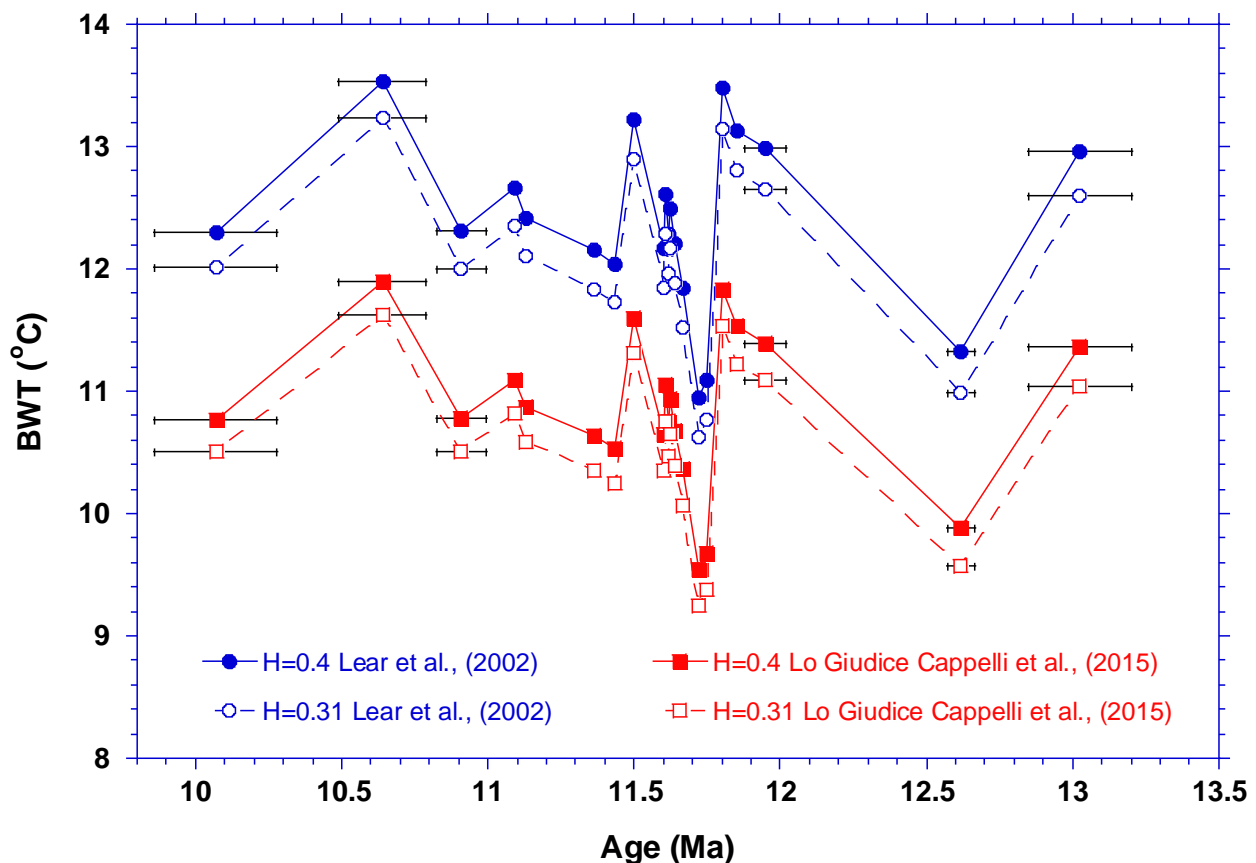


Figure 5.14: Mean absolute bottom water temperature (BWT) at Sunbird-1 using robust and binned samples. Temperatures based on Lear et al. (2002) (Equation 5.4) are blue circles, and temperatures based on Lo Giudice Cappelli et al. (2015) (Equation 5.6) are red squares. Filled symbols joined by solid lines correspond to an H value of 0.4, and open symbols joined by dashed lines correspond to an H value of 0.31 calculated assuming Eocene Mg/Ca<sub>sw</sub> values of 2.1 mol/mol and 1.6 mol/mol respectively. Error bars signify the age range of binned samples.

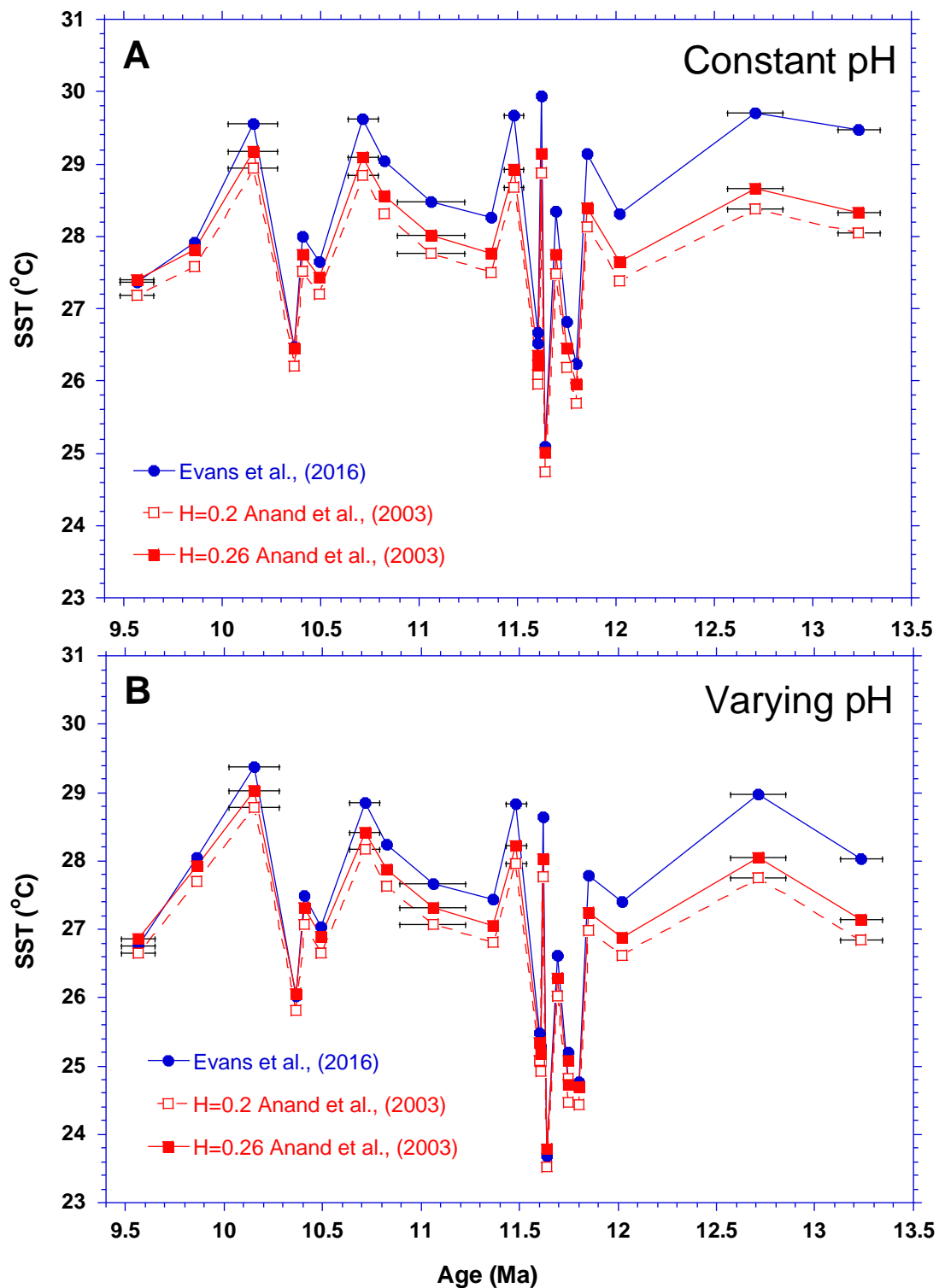


Figure 5.15: Absolute sea surface temperature (SST) at Sunbird-1 using robust and binned samples and (A) a constant pH of 8.1, or (B) varying pH of Sosdian et al. (2018). Temperatures based on Evans et al. (2016b) (Equations 5.7 and 5.8) are blue circles, and temperatures based on Anand et al. (2003) (Equation 5.5) are red squares. Filled symbols joined by solid lines correspond to an H value of 0.26, and open symbols joined by dashed lines corresponds to an H value of 0.2 calculated assuming Eocene Mg/Ca<sub>sw</sub> values of 2.1 mol/mol and 1.6 mol/mol respectively (Figure 5.5, Equation 5.3).

From this range of scenarios those which use an Eocene Mg/Ca<sub>sw</sub> value of 2.1 mol/mol as calculated using the polynomial association between Mg/Ca<sub>sw</sub> and age are preferred (Equation 5.2), as are the SST scenarios which incorporate the effect of changing pH on the Mg/Ca value used to determine temperature (Figure 5.15b). Despite being species-specific for *C. wuellerstorfi* the calibration of Lo Giudice Cappelli et al. (2015) (Equation 5.6) only covers a bottom water temperature range from 0 to 10°C meaning BWT at Sunbird-1 extends outside this calibration range. The general *Cibicidoides* calibration of Lear et al. (2002) goes up to 18°C, encompassing the full range of BWT from the Sunbird-1 record, and therefore this BWT calibration is preferred (Equation 5.4) (Figure 5.16b and Appendix 8a). Despite being widely applied to extinct planktic foraminifera species such as *D. altispira* the multi-species SST calibration of Anand et al. (2003) has a considerably higher temperature sensitivity than recent work which incorporates the influence of the carbonate system (Evans et al., 2016a). Therefore, the SST calibration of Evans et al. (2016a) is preferred (Figure 5.16a and Appendix 8b), despite it being species-specific to *G. ruber*.

For these preferred scenarios the sample and analytical uncertainties, and the calibration uncertainty are distinguished between (Figure 5.16). This is because the calibration uncertainty only influences the absolute temperature values, and can be discounted for assessing any trends in relative BWT and SST.

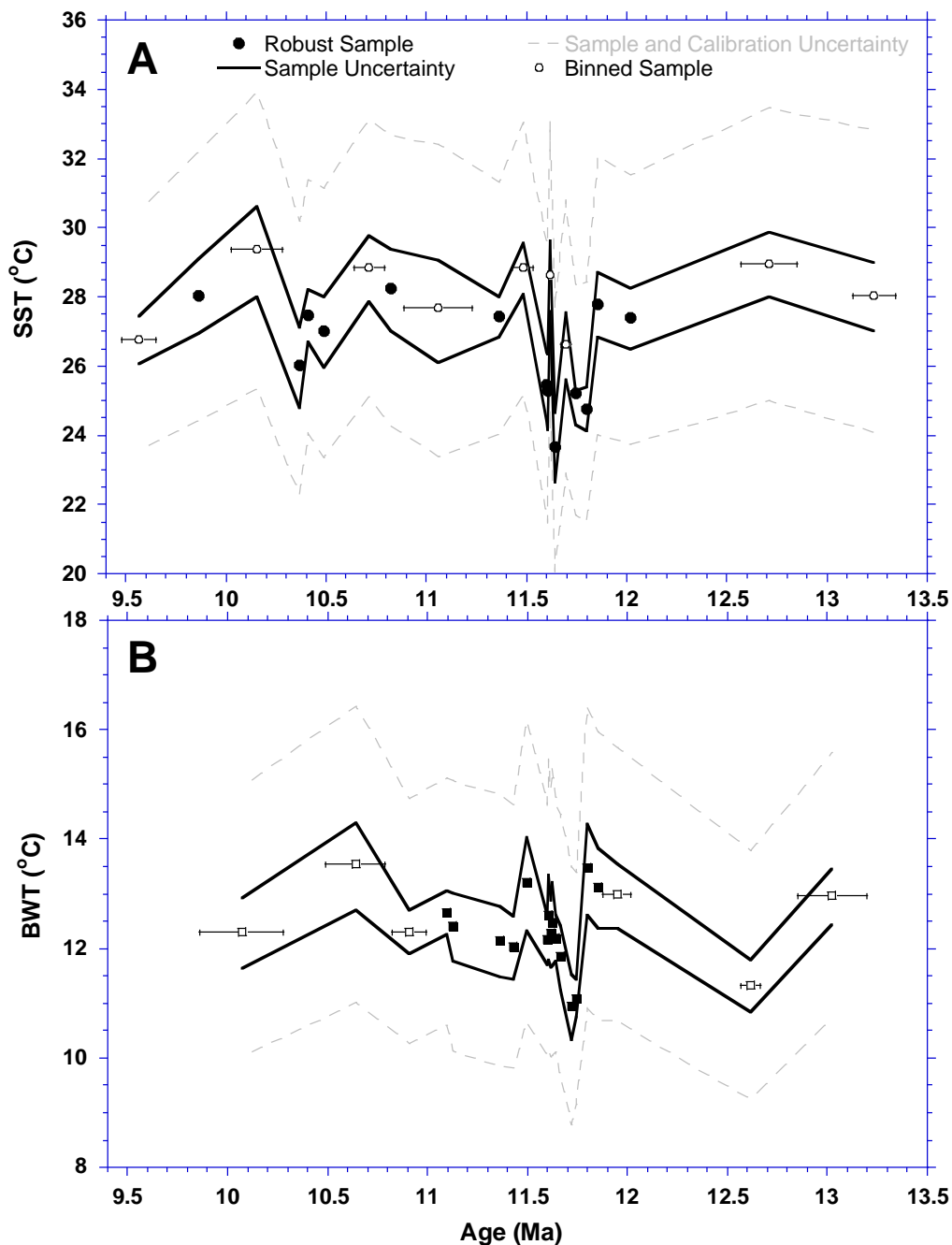


Figure 5.16: Evolution of (A) SST (circles) using the temperature calibration of Evans et al. (2016a) (Equations 5.7 and 5.8), and (B) BWT (squares) using the exponential equation of Lear et al. (2002) (Equation 5.4) at Sunbird-1. Both records include robust (filled symbols) and binned (open symbols) Mg/Ca samples and use an Eocene Mg/Ca<sub>sw</sub> of 2.1 mol/mol (Figure 5.5). Error bars show the age range of the binned samples. Two uncertainty envelopes are provided, one incorporating only the sample and analytical error (solid black lines), and one which also includes the calibration uncertainty (dashed grey lines). The calibration uncertainty on the BWT record is derived from the envelope on the Mg/Ca<sub>sw</sub> curve ( $\pm 0.5$  mol/mol) and the range in the coefficients of the temperature calibration. Additional uncertainty on the SST record is due to uncertainty ( $\sim \pm 0.06$  pH units) in the pH reconstruction of Sosdian et al. (2018), and any salinity influence ( $\pm 0.5^\circ\text{C}$ ).

The large uncertainty associated with the absolute temperature estimates ( $\sim\pm 2.5^{\circ}\text{C}$  for BWT and  $\sim\pm 3.9^{\circ}\text{C}$  for SST (2 SE)) is due to the  $\pm 0.5$  mol/mol envelope on the Mg/Ca<sub>sw</sub> curve (Figure 5.5), the errors on the calibration coefficients (Equation 5.4), the  $\sim\pm 0.06$  envelope on the pH estimate (Figure 5.4), and any potential salinity effect on the planktic foraminiferal Mg/Ca values. This makes the interpretation of absolute temperature change challenging. Therefore interpretation of the evolution of water temperature at Sunbird-1 will focus on the relative changes which exclude this calibration uncertainty, as denoted by the solid black envelopes in Figure 5.16, reducing the uncertainty (2 SE) to  $\pm 0.6^{\circ}\text{C}$  for BWT and to  $\pm 0.9^{\circ}\text{C}$  (2SE) for SST. Both temperature records have the same general features of the respective Mg/Ca records suggesting that temporal changes in pH and Mg/Ca<sub>sw</sub> have little influence on the Mg/Ca record. BWT at Sunbird-1 remains relatively constant at  $12 \pm 3^{\circ}\text{C}$  (Figure 5.16b), and SST remains relatively stable at  $\sim 27\text{-}28^{\circ}\text{C}$  through the interval (Figure 5.16a).

## 5.5 Discussion

### 5.5.1 Controls on intra- and inter-specimen variability

The Mg/Ca ratio of foraminiferal calcite tests record brief snapshots of SST or BWT over their week to month lifespans. Acquiring multiple depth profiles through multiple tests reveals that the Mg/Ca ratios of both *C. wuellerstorfi* and *D. altispira* are not homogenous within an individual test, or between tests from the same sample (Chapter 5.4.3). Similar intra- and inter-specimen heterogeneity is observed across multiple species of foraminifera, both cultured and in core tops (Eggins et al., 2004, Anand and Elderfield, 2005, Sadekov et al., 2005, Sadekov et al., 2008a, Fehrenbacher and Martin, 2014). This intra- and inter-specimen variability is lost during traditional solution based ICP-MS analysis, which requires the pooling

and homogenisation of multiple individual tests. The sampling resolution of the record makes it impossible to quantitatively distinguish between different drivers of Mg/Ca variability acting on different timescales. Sampling at much higher resolution, over shorter time intervals, reduces the possible drivers which allows for better attribution of the observed temperature variability (Sadekov et al., 2008b, Koutavas and Joanides, 2012). Below some possible drivers of this variability are considered, and an assessment of their potential influence on the observed Mg/Ca variability within, and between, tests is made. These are merely suggestions and possible interpretations so should therefore not be considered statistically significant until much larger sample sizes at substantially higher sampling resolution can be analysed.

#### 5.5.1.1 *Intra-specimen*

Discussion of the intra-specimen variability will focus on the 10 specimens of *C. wuellerstorfi* and *D. altispira* measured from the 1551-1554m (11.74 Ma) sample (Chapter 5.4.3). Both *C. wuellerstorfi* and *D. altispira* show intra-specimen variability, indicating that there exists geochemical differences between adjacent chambers of the foraminiferal tests. This variability in Mg/Ca ratios is higher in the planktic *D. altispira* (1.5 to 2 fold) than it is in the benthic *C. wuellerstorfi* (1.2 to 1.7 fold), an observation which holds true over the record as a whole. Unlike with the all-encompassing outer chamber of *Orbulina universa* used in Chapter 4 it was not possible to ablate all spots on the same chamber of either *C. wuellerstorfi* or *D. altispira*, although to reduce this effect on Mg/Ca early, juvenile stage chambers are avoided. Foraminiferal tests grow incrementally, one chamber at a time with the layer of calcite forming each new chamber covering the previously formed chambers. Consequently, each

chamber will have calcified from seawater with differing temperatures as well as other environmental conditions, such as pH, which influence the Mg/Ca composition.

Profiles through adjacent chambers with different Mg/Ca ratios could be reflecting weekly variations in temperature (Toyofuku et al., 2000). The observed 1.5 to 2 fold intra-specimen variability would equate to an apparent change in calcification temperature of up to 14°C between chambers of *D. altispira*. This is likely unreasonable at a tropical location which demonstrates considerably less SST variability in the modern day. Vertical migration between hydrographic regimes of varying temperature during their lifespan of weeks to months could contribute to the observed intra-specimen variability of *D. altispira* Mg/Ca. However, at the modern day site of Sunbird-1 the upper water column is well mixed making this unlikely. Therefore, effects beyond calcification temperature are required to account for the observed Mg/Ca variability within individuals of *D. altispira*.

Contaminant phases with elevated Mg in the interior of the test can result in extreme Mg/Ca ratios (Rathmann et al., 2004, Hasenfratz et al., 2016, Hines et al., 2017). However, selecting integration intervals with low Al/Ca and Mn/Ca ratios, and excluding any profiles with elevated Mg/Ca associated with elevated ratios of these contaminant phases post data processing, means contamination is not expected to be the cause of high Mg/Ca ratios, amplifying the intra-test variability.

Intra-test variability observed in *D. altispira* from the 1551-1554m sample is 1.5 to 2 fold, at the lower range of the two to four fold intra-specimen variability reported previously in

planktic foraminiferal Mg/Ca (Eggins et al., 2003, Eggins et al., 2004, Sadekov et al., 2005, Fehrenbacher et al., 2015, Spero et al., 2015, Holland et al., 2017). This suggests that some of the intra-test Mg/Ca variability observed in culture experiments (Fehrenbacher et al., 2015, Spero et al., 2015, Holland et al., 2017), and core tops (Eggins et al., 2004, Sadekov et al., 2005) is translated into downcore records. Despite being extinct, *D. altispira* was similar to the extant *O. universa* in that it had symbionts (Aze et al., 2011) which regulate foraminiferal calcification. Therefore, the observed intra-test Mg/Ca variability is suspected to be a result of diurnal changes in the pH of the microenvironment from which the foraminiferal calcite precipitates caused by photosynthesis and respiration of algal symbionts. Invoking symbiont driven biological effects as the principle cause of intra-specimen variability is consistent with the higher intra-specimen variability observed in *D. altispira* than in *C. wuellerstorfi*.

A caveat of this interpretation for the intra-specimen variability in Mg/Ca is that the depth profiles show no obvious evidence of the diurnal banding typical of Mg/Ca in cultured, symbiont bearing, planktic foraminifera (Eggins et al., 2004, Fehrenbacher et al., 2015, Spero et al., 2015, Davis et al., 2017, Holland et al., 2017). These results suggest that despite the range of natural variability of Mg/Ca observed in live caught planktic foraminifera being translated into the fossil record, the pattern of intra-test Mg/Ca variability is not preserved in fossil foraminifera.

The diurnal modulation of Mg/Ca by algal symbionts cannot explain the similar intra-specimen variability in the symbiont free *C. wuellerstorfi*. The 1.2 to 1.7 fold intra-test variability in *C. wuellerstorfi* requires an alternative explanation. In the absence of other

definitive controls this is proposed to be a combination natural, stochastic variability in Mg uptake, and changes in calcification temperature during the foraminifera's life cycle (Sadekov et al., 2005). More detailed, in situ culturing of benthic foraminifera at high pressure are required to assess this intra-test variability (Wollenburg et al., 2015).

#### 5.5.1.2 *Inter-specimen*

The picked specimens comprising each sample provide a record of the environmental conditions from when their individual calcite test was precipitated. The average sampling resolution through the Sunbird-1 record is ~43kyr (Figure 2.5). Therefore, each sample is recording up to 6 snapshots of the ambient sea surface and bottom water conditions through a ~43kyr time interval, the temporal distribution of these snapshots being unknown. This range in Mg/Ca between specimens from the same sample allows for an estimation of the temperature variability through the sampling interval. The inter-specimen range in Mg/Ca is much higher in *D. altispira* (0.97-3.17 mmol/mol) than it is in *C. wuellerstorfi* (0.34-2.03 mmol/mol) (Figure 5.9). It is worth noting that the binned samples do not have significantly higher inter-specimen variability than the samples that are robust, without the need to combine adjacent samples.

This inter-specimen heterogeneity could have many causes, including natural variability and changes in temperature on seasonal, inter-annual, decadal, millennial, and orbital timescales. These possible causes are not an exhaustive list. Previous studies assessing inter-specimen variability have been on a Holocene-Last Glacial Maximum timescale (Koutavas and Joanides, 2012) or from core-tops (Sadekov et al., 2008b) meaning the temperature differences could

be interpreted solely in terms of seasonal and inter-annual variability. The coarser sampling resolution of Sunbird-1 means longer timescale drivers of temperature variability must be considered, most importantly orbital forcing.

Inter-specimen variability of  $\pm 5-6\%$  in Mg/Ca exists in culture experiments of *O. universa* where temperature is held constant (Holland et al., 2017, Spero et al., 2015). This is translated into core top measurements (Sadekov et al., 2005) demonstrating that Mg/Ca differences between specimens occur naturally, with no influence of the environmental conditions during calcification. Although it is not possible to assess directly whether this is translated into downcore records, as absolute temperature is unknown, it would be unreasonable to not incorporate this natural variability between specimens at constant temperature. This natural inter-specimen variability, unrelated to calcification temperature, coupled with the fact *D. altispira* is extinct hinders any direct conversion of planktic foraminiferal Mg/Ca variability between specimens into temperature variability through the sampling interval. However, some suggestions can be made.

Seasonal differences in sea surface temperature may be recorded by the single specimen LA-ICP-MS analyses, variability which is lost when specimens are broken open and homogenised prior to solution based ICP-MS analysis. To investigate whether local temperature variations can explain the observed magnitude of inter-specimen Mg/Ca variability it was compared to the range of modern day temperature measurements near the site of Sunbird-1. Weekly resolved satellite measurements between 1997 and 2010 from the nearby Mozambique Channel demonstrates that modern day SST varies between 25.0°C and 30.2°C, an inter-

annual variability of 5.2°C (Fallet et al., 2011) similar to that recorded by meteorological observations (McClanahan, 1988). No equivalent time series of BWT measurements is available for comparison to the *C. wuellerstorfi* Mg/Ca inter-specimen variability. Using the preferred palaeotemperature equation of Evans et al. (2016a) (Equations 5.7 and 5.8), an average Mg/Ca<sub>sw</sub> through the interval of 3.55 mol/mol, an average seawater pH through the interval of 8.03, and incorporating the pH correction (Equation 5.1) this equates to a planktic foraminiferal Mg/Ca range of 3.44 mmol/mol to 4.64 mmol/mol. This suggests that tests precipitated in the same year could have Mg/Ca ratios that differ by ~1.2 mmol/mol, assuming an inter-annual variability in SST of 5.2°C. This is less than the average inter-specimen Mg/Ca range for *D. altispira* of 2.01 mmol/mol, and considerably less than the maximum inter-specimen range of 3.17 mmol/mol (Figure 5.17). Therefore, assuming modern day measurements, inter-annual SST variability cannot fully explain the inter-specimen variability of *D. altispira*, accounting for 59% on average, and only 38% of the maximum *D. altispira* inter-specimen Mg/Ca range.

Incorporating the observed 5-6% natural variability between tests cultured at constant temperatures (Spero et al., 2015) to the measured ~5.2°C inter-annual variability observed at the modern day site of Sunbird-1 (Fallet et al., 2011, McClanahan, 1988) accounts for approximately 2/3 of the mean inter-specimen Mg/Ca variability in *D. altispira*. The remaining ~3-4°C inter-specimen variability observed in SST at Sunbird-1 could be attributed to a heightened seasonal or inter-annual cycle during the mid-late Miocene. However, it is more likely that SST variability on orbital timescales causes this remaining SST variability between specimens from the same sample.

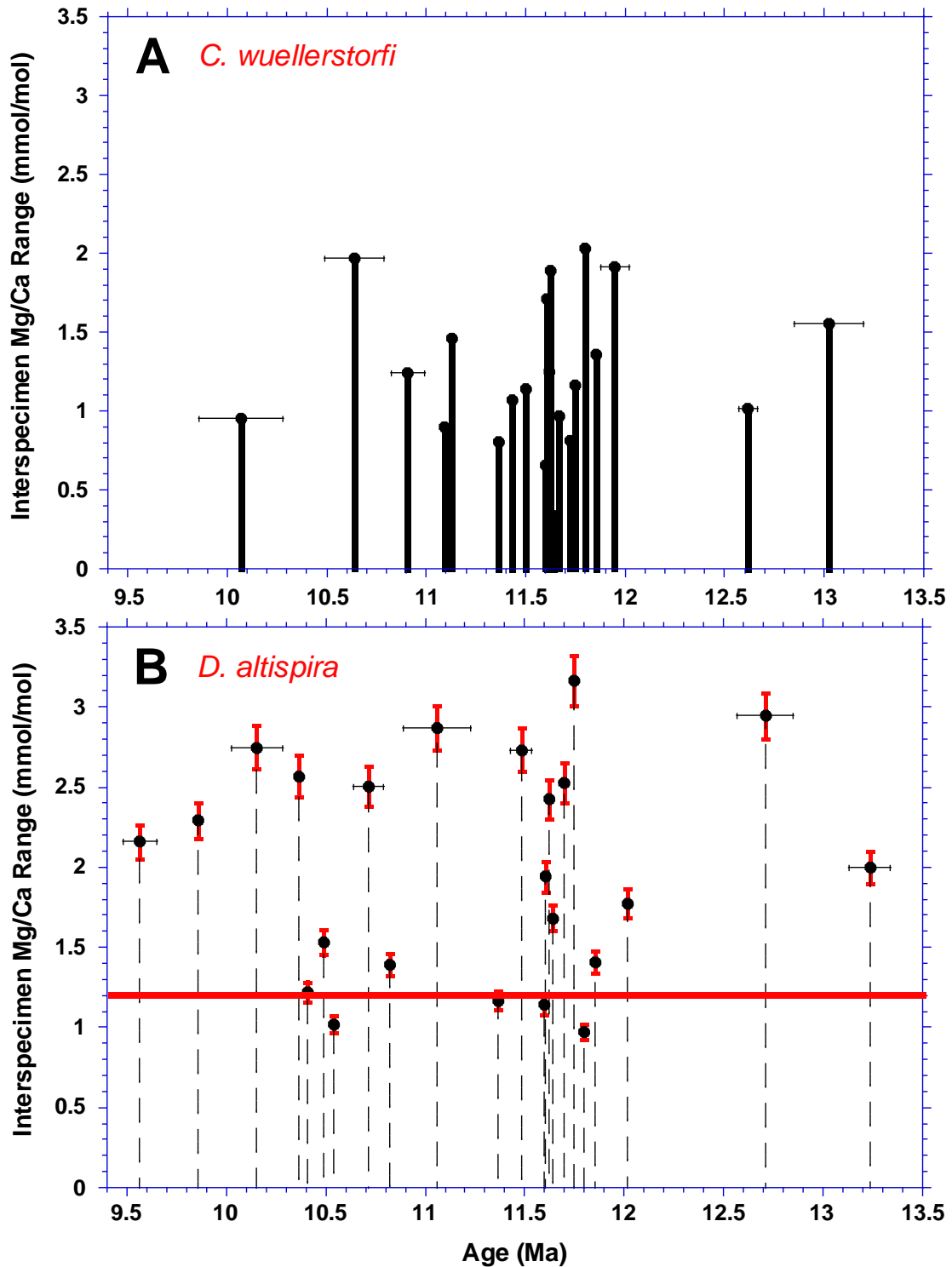


Figure 5.17: The maximum range in (A) *C. wuellerstorfi* and (B) *D. altispira* Mg/Ca between specimens from the same sample. Horizontal error bars denote the age range of binned samples. The vertical, red error bars in (B) represent the 5-6% natural variability observed in planktic foraminifera cultured at the same temperature. The horizontal red line in (B) denotes the 5.2°C inter-annual SST variability from satellite measurements taken between 1997 and 2010 (Fallet et al., 2011), samples above this line displaying greater than modern day inter-annual variability.

Global climate through this time interval shows a response to obliquity (41kyr) and eccentricity (100kyr) forcing (Holbourn et al., 2013). For a more quantitative attribution of inter-test variability, resulting from temperature variability on seasonal to orbital timescales a larger dataset is required. Unfortunately, due to the low foraminiferal abundance, this was not possible at Sunbird-1. Furthermore, in order to deconvolve the influence of temperature variability across multiple timescales a higher resolution record is needed.

A combination of biological effects causing Mg variability within specimens, and differences in calcification temperature between specimens on seasonal to orbital timescales causes the observed Mg/Ca variability within samples. However, the different contributions of the multiple possible drivers of temperature variability between specimens cannot be accurately quantified. This corroborates previous findings pertaining to the variability in SST estimates using foraminiferal Mg/Ca thermometry (Sadekov et al., 2008b). Although not currently possible, if the variability resulting from biological effects could be reliably quantified, then the contribution of seasonal, and in particular orbital scale, variability in temperature to the Mg/Ca variability within samples could be reconstructed.

### 5.5.2 Evolution of bottom water temperature at Sunbird-1

The BWT at Sunbird-1 is substantially warmer than other mid-late Miocene records from deep water open ocean sites (Lear et al., 2015) including a global compilation of sites (Cramer et al., 2011) (Figure 5.18). This is probably a result of the shallow water depth of Sunbird-1, meaning BWT is not recording a true deep water signal. Sunbird-1 was certainly not at abyssal depths through the mid-late Miocene, the pinnacle reef underlying the hemipelagic clays

containing vuggy porosity, indicating meteoric exposure, at ~13.8 Ma. The shallow water depth of Sunbird-1 is further supported by the similar features in the planktic and benthic foraminiferal Mg/Ca temperature records (Figure 5.15). Temporal variations in, and the influence of subsidence on, BWT will be further discussed in Chapter 6.

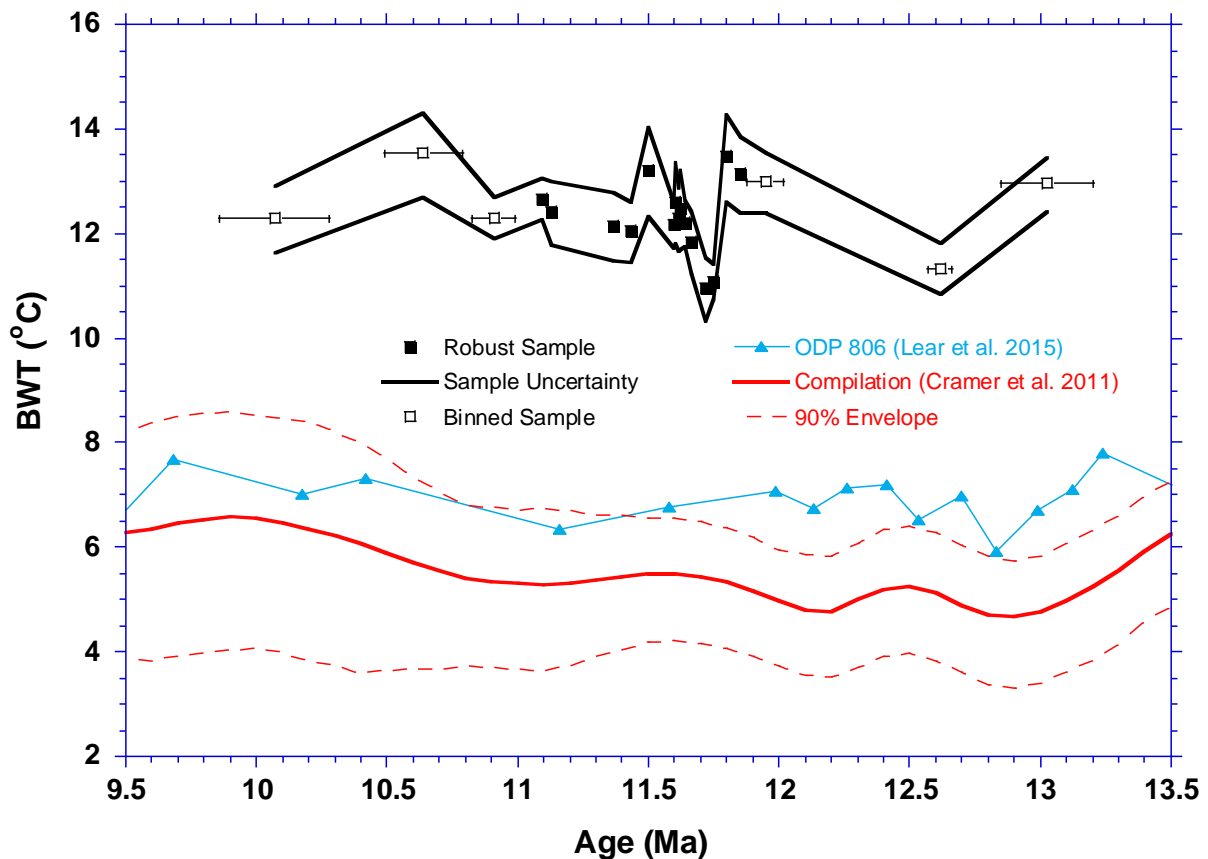


Figure 5.18: Sunbird-1 BWT (black squares) compared to ODP Site 806 in the Western Pacific (blue triangles) (Lear et al., 2015), and a compilation of Pacific deep water sites (red line) (Cramer et al., 2011).

Here the impact of adopting this microanalytical approach, incorporating the careful identification of contaminant free regions of multiple foraminiferal depth profiles and the post data processing screening for elevated concentrations of contaminant indicators, is assessed. The Mg/Ca data acquired via solution based ICP-MS analysis (Appendix 4) has been

translated to bottom water temperature (Appendix 9), using the same favoured scenario as with the Mg/Ca data acquired via laser ablation ICP-MS. The BWT reconstruction from the solution based ICP-MS Mg/Ca record (Figure 5.19) is consistently higher than that reconstructed using the microanalytical approach (Figure 5.17 b). The offset (~2-10 °C) is likely dampened by the fact that the measured Mg/Ca values above 6.2 mmol/mol (18°C) exceed the range of the preferred exponential calibration of Lear et al., (2002). However, similarities between the two BWT records exist supporting there being a temperature influence on the solution-based *C. wuellerstorfi* Mg/Ca record (Chapter 3). For example, the temperature decrease recorded at 11.8 Ma is present in both records. Therefore, this supports the suggestion that the solution-based Mg/Ca record is recording temperature variability and changing redox conditions. The dominant decreasing trend in the solution-based Mg/Ca record, attributed to changing redox conditions as the site subsided reducing the concentration of secondary Mg incorporation in diagenetic foraminiferal coatings, is not present in the LA-ICP-MS BWT reconstruction. This strongly suggests that the influence of major changes in sedimentary redox conditions on the bulk trace metal concentrations can be eliminated by the careful microanalytical approach implemented by this study. Along with stringent contaminant screening during data processing this approach has successfully isolated a more robust and reliable downcore benthic foraminiferal Mg/Ca record of primary bottom water temperature. This assumes the microanalytical approach has not introduced a

sampling bias which favours colder bottom water temperatures, although this possibility will be discussed in Chapter 6.

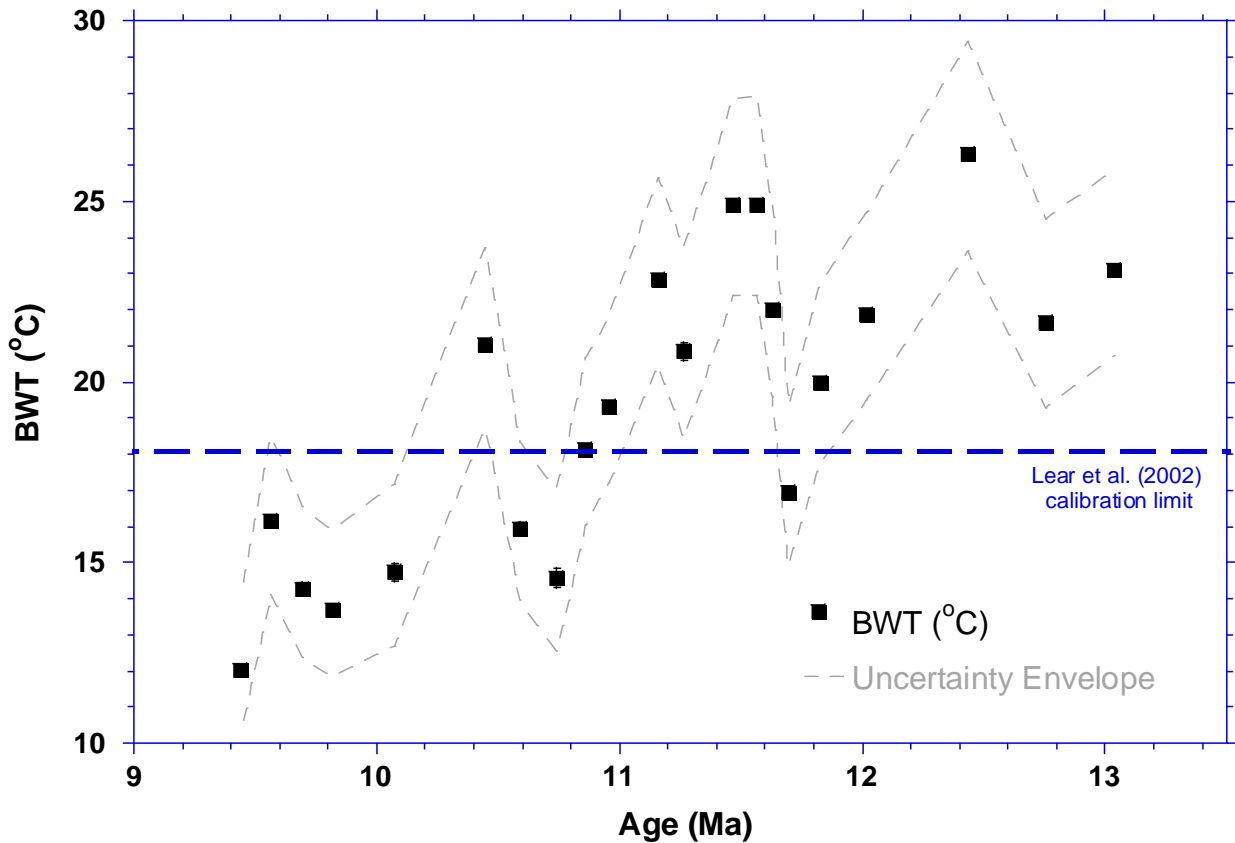


Figure 5.19: Sunbird-1 BWT record (squares) reconstructed by applying the exponential equation of Lear et al. (2002) (Equation 5.4) and an Eocene Mg/Casw of 2.1 mol/mol (Figure 5.5) to the solution-based ICP-MS Mg/Ca data. The uncertainty envelope incorporates the analytical uncertainty on the Mg/Ca measurements, the envelope on the Mg/Casw curve ( $\pm 0.5$  mol/mol), and the range in the coefficients of the temperature calibration.

### 5.5.3 Mid-late Miocene sea surface temperatures in the equatorial Indian Ocean

The Mid Miocene Climate Transition (MMCT) marks the transition from the relatively warm, high CO<sub>2</sub>, dynamic climate state of the Miocene Climatic Optimum (MCO) to a more stable climatic state no longer characterised by large fluctuations in atmospheric CO<sub>2</sub> (Foster et al., 2012, Badger et al., 2013, Sossian et al., 2018). This coincided with the expansion of the Antarctic Ice Sheet to approximately modern day volume ~13.8 Ma. Despite the lower

atmospheric CO<sub>2</sub> following this climate transition (Foster et al., 2012, Sosdian et al., 2018) temperatures were likely warmer than the modern day (Pound et al., 2011, Rousselle et al., 2013), suggesting a decoupling of global temperature and atmospheric CO<sub>2</sub> forcing (Knorr et al., 2011, LaRiviere et al., 2012). Currently, general circulation models struggle to simulate the warmer than modern day temperatures as well as the global distribution of SST from the alkenone proxy (LaRiviere et al., 2012, Rousselle et al., 2013, Herbert et al., 2016) without forcing atmospheric CO<sub>2</sub> to levels much higher than what proxies reconstruct (von der Heydt and Dijkstra, 2006), or significantly altering climate forcings other than CO<sub>2</sub> (Knorr et al., 2011). This decoupling of temperature and CO<sub>2</sub> is unlike the majority of the Cenozoic, through which these two environmental parameters are closely linked (Zachos et al., 2001, Zhang et al., 2013).

Despite the significance of this climate transition remarkably few records of SST following the MMCT exist, leaving a hole in our understanding of how surface ocean temperatures evolved through this interval (Lunt et al., 2008). Furthermore, the records that do exist are based on the Mg/Ca ratios of frosty planktic foraminifera (Sosdian et al., 2018) or unsaturated alkenones (Huang et al., 2007, LaRiviere et al., 2012, Seki et al., 2012a, Rousselle et al., 2013, Zhang et al., 2014, Herbert et al., 2016), which may be influenced by recrystallisation or limited by proxy saturation respectively. The analytical approach employed here, identification of the primary Mg/Ca signal and stringent contaminant screening, provides the accurate and reliable absolute tropical SST estimates previously lacking from this time interval.

The record of Herbert et al. (2016) reveals significant interhemispheric cooling of  $\sim 6^{\circ}\text{C}$  across all major ocean basins and latitudinal ranges between 12Ma and 5.4Ma. This late Miocene cooling of SST is latitudinally heterogeneous, with the pole-to-equator temperature gradient steepening to near-modern values through this interval. These studies may have underestimated tropical SST, and therefore latitudinal temperature gradients, between 12 Ma and 8 Ma because of the  $\text{Uk}_{37}$  proxy reaching its limit. If this was the case, and tropical SSTs through this interval were  $>28\text{-}29^{\circ}\text{C}$ , the magnitude of the following cooling would be greater, reducing the increase in latitudinal temperature gradient.

The relatively constant surface temperature through the 4.5 Myr Sunbird-1 record suggests that tropical climate was relatively stable following the global cooling associated with the expansion of the East Antarctic Ice Sheet across the MMCT. The Sunbird-1 late Miocene SST estimates are similar to the modern day measurements from the 17 CTD profiles which provide sea surface temperature measurements in a  $0.75^{\circ} \times 0.75^{\circ}$  grid square around the modern day site of Sunbird-1 (Boyer et al., 2013). These CTD profiles indicate that the modern day mixed layer is  $\sim 50\text{m}$  water depth, in which temperature varies between  $26.5^{\circ}\text{C}$  and  $28.5^{\circ}\text{C}$ . This is consistent with more recent CTD data from the nearby GLOW sites (Birch et al., 2013) and the average mean satellite sea surface temperature of  $27.6^{\circ}\text{C}$  in the nearby Mozambique Channel (Fallet et al., 2011). Notably the CTD data does not reflect the  $5.2^{\circ}\text{C}$  inter-annual variability of the satellite and meteorological observations (McClanahan, 1988, Fallet et al., 2011). That these Sunbird-1 SST estimates from LA-ICP-MS analyses are comparative with SST at the modern day study site supports the validity of LA-ICP-MS micro-analysis of Mg/Ca from multiple profiles in multiple specimens for reconstructing palaeo-SST.

Furthermore, SST estimates using the  $\delta^{18}\text{O}$  palaeo-thermometer are extremely similar (Chapter 6). This is despite the substantial intra- and inter- specimen variability in *D. altispira* Mg/Ca, which likely exceeds the range in calcification temperature through the samples. Furthermore, this study indicates that LA-ICP-MS analyses of poorly preserved foraminifera can provide reliable Mg/Ca SST's, as long as thorough data screening is conducted.

The results from Sunbird-1 indicate that SST in the equatorial Indian Ocean remained stable at temperatures of  $\sim 27^{\circ}\text{C}$ - $29^{\circ}\text{C}$  through the 13.3 Ma to 9.5 Ma interval. Other data from the  $\text{Uk}_{37}$  proxy show there to be a substantial cooling of sea surface temperature at mid-to-high latitudes in both hemispheres through this interval (LaRiviere et al., 2012, Herbert et al., 2016). Combined the stable tropical sea surface temperatures with the interhemispheric sea surface temperature decrease at mid-to-high latitudes suggests there was an increasing latitudinal temperature gradient through the mid-late Miocene. The increase in latitudinal temperature gradient is decoupled from any substantial change in atmospheric  $\text{CO}_2$  (Foster et al., 2012, Zhang et al., 2013, Sossian et al., 2018). This is unlike the majority of the Cenozoic, through which the two environmental parameters are closely linked. Therefore, an alternative mechanism for the increased equator to pole temperature gradient is required. Oceanographic reorganisation could act as a primary control through this interval, redistributing heat from the equator, to depth, instead of to surface waters at higher latitudes.

This record from Sunbird-1 supports the robustness of contemporaneous alkenone based studies which exhibit similar absolute tropical SST estimates (Huang et al., 2007, Seki et al., 2012a, Rousselle et al., 2013, Zhang et al., 2014, Herbert et al., 2016) (Figure 5.20). The  $U_{37}^k$  SST calibration fails to reconstruct  $SST > 29^\circ\text{C}$  (Müller et al., 1998) but these results using

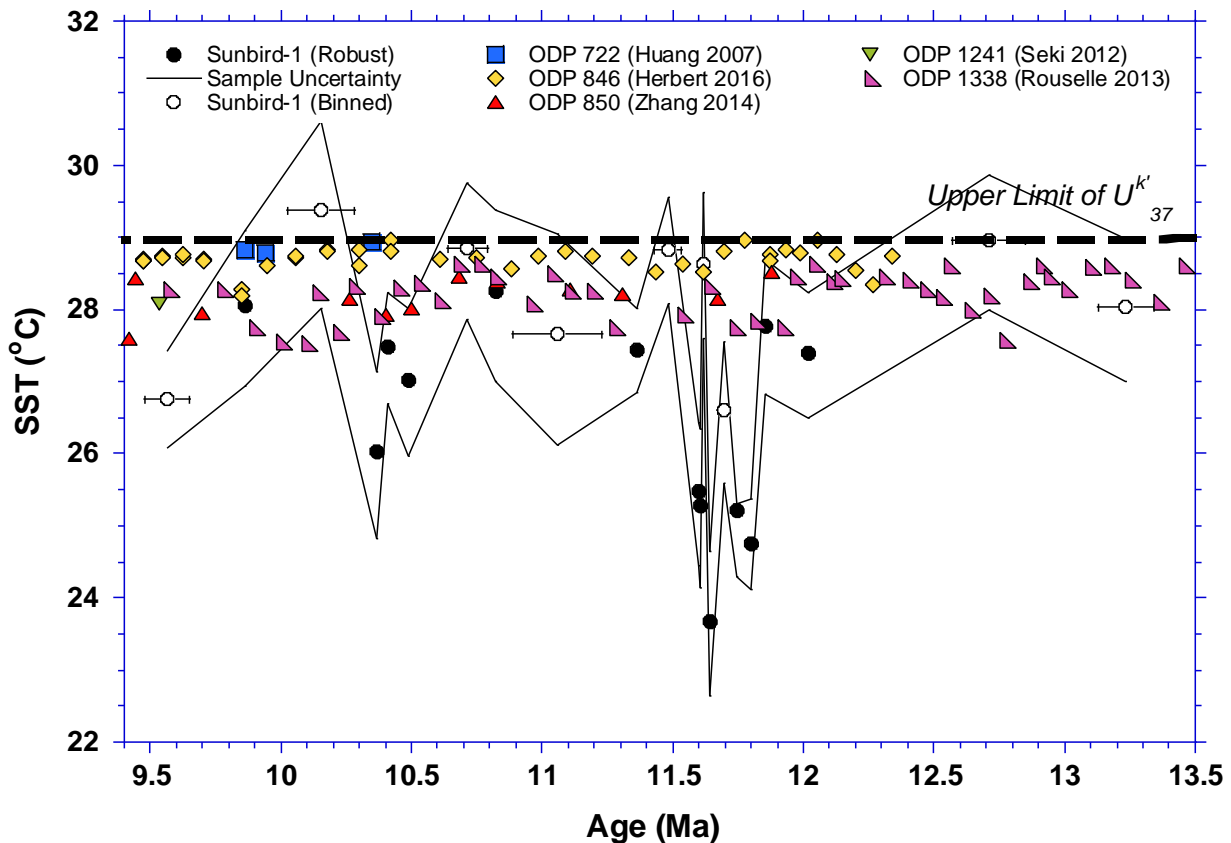


Figure 5.20: SST at Sunbird-1 compared to  $U_{37}^k$  SST estimates at contemporaneous sites. ODP Site 722 (Huang et al., 2007) in the Arabian Sea, and ODP & IODP Sites 846 (Herbert et al., 2016), 850 (Zhang et al., 2014), 1241 (Seki et al., 2012a), and U1338 (Rousselle et al., 2013) in the Eastern Equatorial Pacific. The upper limit for the  $U_{37}^k$  proxy ( $29^\circ\text{C}$ ) is shown by the thick dashed black line. All previously published records used for comparison are kept on their original age models.

Mg/Ca palaeo-thermometry suggest that this major restriction does not apply to this time interval, unlike with the preceding Miocene Climatic Optimum (MMCO) where Mg/Ca temperature estimates are higher than those estimated with the  $U_{37}^k$  proxy (Badger et al., 2013).

Although not a true tropical location, and only 2 data points, the Badger et al. (2013) Mg/Ca record from the Mediterranean estimates SST of  $\sim 27.5^{\circ}\text{C}$  at  $\sim 13\text{Ma}$ , both within the Sunbird-1 SST uncertainty envelope (Figure 5.22). Mg/Ca-SST records based on frosty planktic foraminifera also suggest stable tropical SST of  $27\text{-}29^{\circ}\text{C}$  between 13-8 and 11.4Ma (Sosdian et al., 2018) (Figure 5.21). This suggests that Mg/Ca may be significantly less influenced by diagenetic recrystallization processes than previously thought. The study of Sosdian et al. (2018) derives SST from ODP Sites 761, 872, 926, and 1000 using Mg/Ca measurements of the planktic foraminifera *Trilobatus trilobus*. *T. trilobus* is an extant species of planktic foraminifera which lives in the upper water column and, similarly to the extinct *D. altispira* used in this study, has photosymbionts. Unlike this study all the sites used by Sosdian et al. (2018) are distal to any coastline, and are therefore assumed to be representative of the open ocean. Furthermore, well preserved planktic foraminifera from clay-rich sediments of coastal Tanzania yield Indian Ocean sea surface temperatures of  $27^{\circ}\text{C}$  at 12.2 Ma and  $29^{\circ}\text{C}$  at 11.55 Ma using the  $\delta^{18}\text{O}$  palaeo-thermometer (Stewart et al., 2004), again in agreement with the Sunbird-1 temperature estimates. Although sparse in number, that previous absolute tropical SST estimates are in agreement with those reconstructed from Sunbird-1 using a very strict and stringent microanalytical approach supports their reliability (Figure 5.20 and 5.21), despite the potential caveats noted by these studies.

It is worth noting that the tropical SST records of Herbert et al. (2016), references therein, and this SST record do not sample the warm pool of the Western Pacific, where we would expect SST to be greater than 29°C, temperatures which unsaturated alkenones cannot reconstruct. The technique used in this study could be applied to palaeo-warm pool sites which recover sediment from the mid-late Miocene. These SST reconstructions will allow a more complete assessment as to whether there really was a true steepening of the latitudinal temperature gradient, which is a vital component of ocean circulation, transporting heat around the planet.

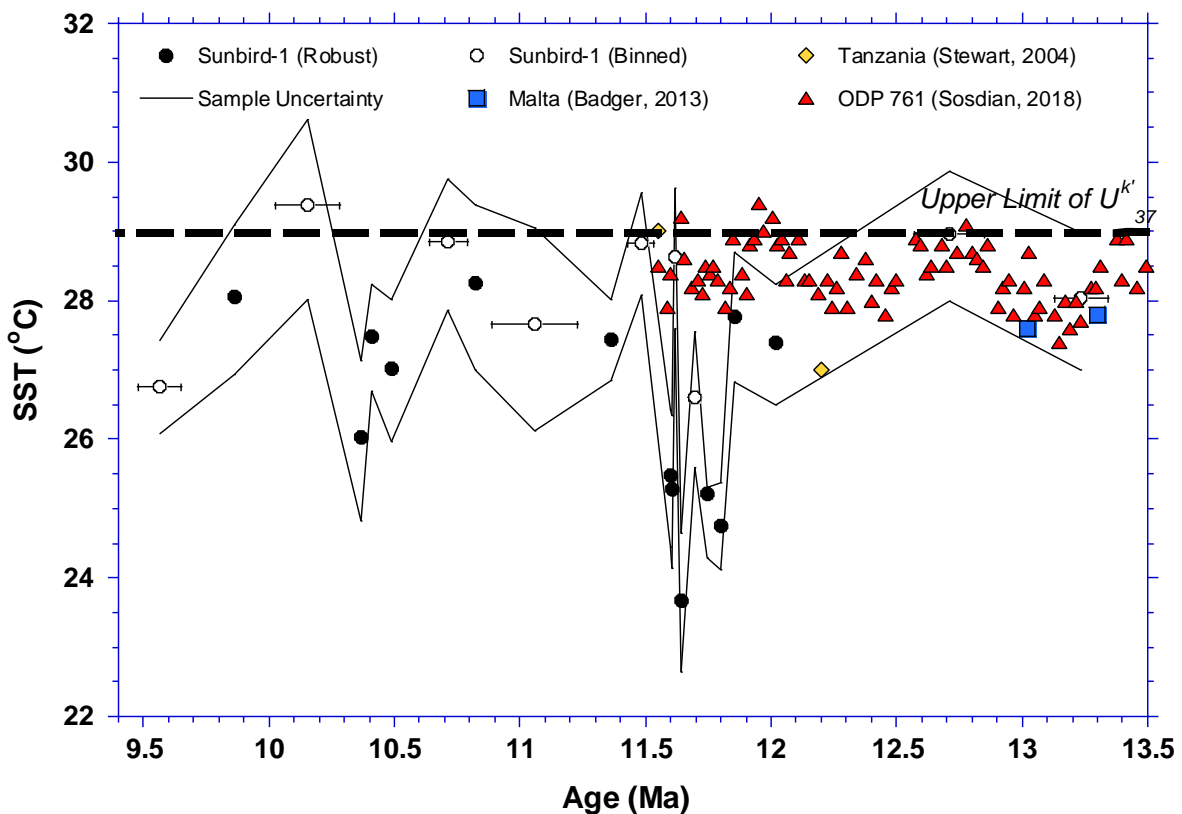


Figure 5.21: Estimated SST at Sunbird-1 compared to other Mg/Ca derived SST estimates from ODP Sites 761 (Sosdian et al., 2018), and terrestrial outcrops in Malta (Badger et al., 2013). Two temperature estimates using the  $\delta^{18}\text{O}$  of exceptionally preserved foraminifera from Tanzania are also shown (Stewart et al., 2004).

#### 5.5.4 Short lived decreases in temperature at Sunbird-1

Although the improved estimates provided by the Sunbird-1 record suggest absolute tropical sea surface temperatures remained relatively stable through the mid-late Miocene some temporal variability does persist. A distinctive feature of both records is the temperature decrease between 12.0 Ma and 11.5 Ma. The BWT record shows a  $\sim 2.5^{\circ}\text{C}$  transient decrease in temperature at 11.8-11.75 Ma, followed by a recovery over the next  $\sim 200$  kyrs. Between 11.85 Ma and 11.8 Ma SST drops sharply by  $\sim 3^{\circ}\text{C}$ , the magnitude of this temperature decrease being within error of the concomitant drop in BWT. SST remains at  $\sim 24\text{-}25^{\circ}\text{C}$  (excluding one SST value of  $28.6^{\circ}\text{C}$  at 11.62 Ma) before recovering to pre excursion values by 11.48 Ma. The similarity in duration, timing, and magnitude of the BWT and SST decrease between 11.8 Ma and 11.5 Ma suggests a single controlling mechanism, potentially a global or regional driver.

However, this transient temperature drop is not seen in BWT records from deep water, open ocean sites (Lear et al., 2010, Cramer et al., 2011, Lear et al., 2015) (Figure 5.18). No transient decrease in sea surface temperature is recorded from contemporaneous alkenone based estimates of tropical SST utilising the  $U_{37}^k$  proxy from the Arabian Sea (Huang et al., 2007), and the Eastern Equatorial Pacific (Seki et al., 2012b, Rousselle et al., 2013, Zhang et al., 2014, Herbert et al., 2016) (Figure 5.20). That this transient decrease in SST and BWT is not identified at other tropical sites suggests it is not the result of a global driver, and supports a mechanism causing local ocean cooling of the full water column at Sunbird-1.

One possibility is unaccounted for changes in either salinity or pH on the foraminiferal Mg/Ca ratios. An unaccounted for local salinity increase would decrease foraminiferal Mg/Ca, a

temporal trend inferred as decreasing BWT and SST. The lack of a robust and quantifiable proxy for salinity means a  $\pm 0.5^{\circ}\text{C}$  uncertainty was added to the temperature estimates, which does not account for any possible temporal changes in the salinity at Sunbird-1. This could be influenced by the influx of open ocean waters from the Indian Ocean gyre to the site. Despite incorporating varying pH from a globally distributed set of open ocean sites (Sosdian et al., 2018), any localised changes in pH at Sunbird-1 cannot be accounted for. An increase in pH locally would cause a decrease in Mg/Ca, and result in an artificial lowering of reconstructed temperatures through this interval. The influence of these potential local processes on the temperature record will be discussed in detail, with particular reference to the tectonic subsidence of the site in Chapter 6.

This 2-3 $^{\circ}\text{C}$  negative SST excursion between 10.7 Ma and 10.36 Ma is considerably less abrupt than the  $\sim 3^{\circ}\text{C}$  drop in  $\sim 50$  kyrs from 11.85 Ma, happening over a 300-400 kyr interval. This SST decrease is similar in timing and magnitude to the ocean cooling associated with the onset of monsoonal upwelling at ODP Sites 722 and 730 in the Western Arabian Sea (Zhuang et al., 2017). However, at ODP Sites 722 and 730 this is a permanent shift in SST as opposed to the transient 300-400 kyr excursion observed in the Sunbird-1 SST record. Pertinently, unlike the first transient temperature decrease, this event is only identified in the SST record, and not the BWT record. Therefore, unlike the 3-4 $^{\circ}\text{C}$  decrease at  $\sim 11.8$  Ma any interpretation cannot invoke the full water column. The increased palaeo-water depth at Sunbird-1 between 11.8 Ma and 10.7 Ma produced a decoupling of SST and BWT. By 10.7 Ma the surface and bottom waters are recording different transient temperature trends, indicating that they are two

distinct water masses. This interpretation, and the influence of local oceanography and seawater chemistry, will be explored further in Chapter 6.

## 5.6 Conclusions

The use of LA-ICP-MS, and rigorous screening criteria for contamination, provides new, robust, absolute temperature records from foraminiferal Mg/Ca data for the South West Indian Ocean between 13.5 Ma and 9.5 Ma. Absolute estimates of 27-29°C suggest that sea surface temperature was relatively constant through the interval. This supports the mid-late Miocene as a key transition in the Earth's climate state, represented by the development of stronger latitudinal temperature gradients. Recently published solution based foraminiferal Mg/Ca record based on frosty foraminifera reconstruct similar tropical SST's (Sosdian et al., 2018). This adds support to the suggestion that Mg/Ca may be significantly less affected by diagenetic recrystallization processes than  $\delta^{18}\text{O}$  (Edgar et al., 2015). Estimated BWT of ~12°C through the record is warmer than estimates from open ocean sites, reflecting the shallow palaeo-water depth of the site.

The acquisition of multiple depth profiles through multiple specimens reveals substantial intra- and inter-specimen Mg/Ca variability. This is likely recording primary temperature variability, that is nullified by traditional solution based ICP-MS analysis of bulk foraminiferal samples. Although further consideration of the biological precipitation of foraminiferal calcite is required these results suggest that temperature variability on both inter-annual and orbital timescales is recorded.

As well as reconstructing the poorly understood climate of the late Miocene, this analytical technique has allowed the reconstruction of reliable Mg/Ca derived palaeotemperatures using foraminifera whose bulk trace element ratios demonstrate diagenetic alteration by an Mg-Mn-rich phase. This opens up the potential for Mg/Ca palaeothermometry on other challenging time intervals, and locations, where contaminant coatings inhibit the geochemical analysis of primary foraminiferal calcite.

A limitation of the palaeotemperature records presented here is their reduced resolution due to the grouping of adjacent samples to ensure the mean Mg/Ca is representative. This limitation resulted from a substantial quantity of depth profiles failing to pass the strict contaminant screening. To alleviate this problem it is strongly suggested that future LA-ICP-MS studies aiming to reconstruct palaeotemperature from contaminated foraminifera analyse twice as many depth profiles as was required in order to obtain a mean Mg/Ca value that is representative for the sample. Unfortunately, this was not possible at Sunbird-1 due to the low foraminiferal abundance.

## 6 Unravelling the influence of Temperature, Ice Volume, Sedimentation, and Subsidence on Sunbird-1

### 6.1 Introduction

The dry, land-based East Antarctic Ice Sheet (EAIS) expanded to its continental margins at ~13.8 Ma (Flower and Kennett, 1994, Holbourn et al., 2005, Lewis et al., 2007), and the onset of major Northern Hemisphere glaciation likely did not take place until at least the Pliocene (Sosdian and Rosenthal, 2009, Bailey et al., 2013). Therefore, the intervening mid-late Miocene interval provides an opportunity to study the stability of the EAIS in a warmer than modern world.

Compilations of benthic foraminiferal  $\delta^{18}\text{O}$  imply that the extent of continental ice following this EAIS expansion remains relatively stable (Zachos et al., 2001, Zachos et al., 2008, Cramer et al., 2009). However, current estimates of global ice volume in this unipolar icehouse world have several complications meaning it is poorly understood (Lear et al., 2015). One of these major complications is the poor preservation of foraminifera through the mid-late Miocene (Lyle et al., 1995), resulting in large uncertainties in proxy based reconstructions, in particular with Mg/Ca palaeotemperatures (Lear et al., 2015). Foraminifera from Sunbird-1 demonstrate glassy preservation, potentially providing a new insight into this critical time interval in terms of our understanding of EAIS volume and dynamics.

However, the evolution of Sunbird-1 is also influenced by local tectonics, the site of deposition subsiding continuously through the mid-late Miocene. In this chapter attempts are made to

unravel these different controls on the Sunbird-1 geochemical records, teasing apart the influence of subsidence, sedimentation, temperature, and global ice volume. To aid this stable isotope ( $\delta^{13}\text{C}$  and  $\delta^{18}\text{O}$ ) and trace metal records from benthic and planktic foraminifera have been generated. Changes in the extent of continental ice volume will equally impact the benthic and planktic foraminiferal  $\delta^{18}\text{O}$  records, whereas subsidence will influence benthic environmental conditions and hence  $\delta^{13}\text{C}$  and  $\delta^{18}\text{O}$  records to a much greater than extent than surface water conditions, and hence the planktic foraminiferal  $\delta^{13}\text{C}$  and  $\delta^{18}\text{O}$  records.

This approach, supplementing the geochemical records previously discussed, has enabled me to unravel the competing controls on the evolution of Sunbird-1 and draw inferences about the global climate state, in particular the stability of the EAIS, through the mid-late Miocene.

### Summary of Scientific Experiments

- In this chapter stable carbon ( $\delta^{13}\text{C}$ ) and oxygen ( $\delta^{18}\text{O}$ ) isotope analyses of planktic and benthic foraminifera from the Sunbird-1 well are reported.
- The benthic foraminifera *Cibicidoides mundulus* and the planktic foraminifera *Globigerinoides obliquus* were used for these stable isotope analyses.
- The influence of temperature on the  $\delta^{18}\text{O}$  values was independently constrained using the LA-ICP-MS temperature records reported in Chapter 5. This has allowed the determination of the planktic and benthic foraminiferal  $\delta^{18}\text{O}_{\text{SW}}$  records.

## 6.2 Materials and methods

### 6.2.1 Sample selection

In order to generate paired benthic and planktic foraminiferal geochemical records between 6 and 10 individuals of the benthic foraminifera *Cibicidoides mundulus*, and up to 15 individuals of the planktic foraminifera *Globigerinoides obliquus* were used (Appendix 3). Foraminifera showing glassy preservation were used (Figure 2.1). Despite 6-15 specimens being used for analysis, the possibility of seasonal bias impacting the isotopic results cannot be ruled out. Planktic foraminiferal specimens from the intermediate 250-355  $\mu\text{m}$  size fraction were used because they best estimate  $\delta^{13}\text{C}$  values of dissolved inorganic carbon (Birch et al., 2013, John et al., 2014). This avoids the bias towards lower values when respired carbon is incorporated into smaller or juvenile species (Spero et al., 1997, Schmidt et al., 2008) and the photosymbiont fractionation that affects larger foraminiferal tests (Birch et al., 2013). The same is true for  $\delta^{18}\text{O}$ , young individuals often display a slight negative offset interpreted as an ontogenetic effect caused by the incorporation of oxygen from metabolic  $\text{CO}_2$  (Filipsson et al., 2010). *G. obliquus* is an extinct, symbiont bearing species with a tropical to subtropical palaeogeographical distribution, and is interpreted as being a surface mixed-layer dweller (Keller, 1985, Aze et al., 2011). The assertion that *G. obliquus* inhabits and calcifies in the surface mixed layer (Keller, 1985, Aze et al., 2011) is supported by multispecies analyses from a synchronous time slice in the Indian Ocean offshore Tanzania showing *G. obliquus* to have the most negative  $\delta^{18}\text{O}$  (-2.5‰) of all species (Paul Pearson, personal communication 2018). Additionally, *G. obliquus* has not been observed to have any gametogenic overgrowths, associated with precipitation of calcite during or post sinking. Therefore, the *G. obliquus*

records are a genuine surface water mixed layer signal and can be used to reconstruct sea surface conditions.

Samples were analysed for their  $\delta^{18}\text{O}$  and  $\delta^{13}\text{C}$  isotopic composition using the method detailed in Chapter 2.4. The long term analytical precision, based on repeat analysis of NBS-19 is  $\pm 0.042\text{‰}$  for  $\delta^{13}\text{C}$  and  $\pm 0.076\text{‰}$  for  $\delta^{18}\text{O}$  ( $n=469$ , 2 standard deviations) and on repeat analysis of BCT63 is  $\pm 0.040\text{‰}$  for  $\delta^{13}\text{C}$  and  $\pm 0.066\text{‰}$  for  $\delta^{18}\text{O}$  ( $n=310$ , 2 standard deviations). *C. mundulus*  $\delta^{18}\text{O}$  and  $\delta^{13}\text{C}$  results from the following three depths (1389-1392m, 1410-1413m, and 1461-1464m) and *G. obliquus*  $\delta^{18}\text{O}$  and  $\delta^{13}\text{C}$  results from a depth of 1503-1506m, where m is metres below sea level, were rejected due to them being low sample aliquots with poor precision, and their values being anomalous to nearby samples.

## 6.2.2 Calculating $\delta^{18}\text{O}_{\text{SW}}$ independently using Mg/Ca temperatures

Foraminiferal  $\delta^{18}\text{O}$  is primarily controlled by calcification temperature and  $\delta^{18}\text{O}_{\text{SW}}$  (Chapter 2.2.1.1). The use of an independent palaeotemperature proxy, such as Mg/Ca, can deconvolve these two primary controls, providing simultaneous records of temperature and  $\delta^{18}\text{O}_{\text{SW}}$  (Lear et al., 2000, Billups and Schrag, 2002). For the planktic foraminiferal  $\delta^{18}\text{O}_{\text{SW}}$  record the palaeotemperature equation of Bemis et al. (1998) generated using planktic foraminifera over a calibration range of 15-25°C is used (Equation 6.1), and for the benthic foraminiferal  $\delta^{18}\text{O}_{\text{SW}}$  record the  $\delta^{18}\text{O}_{\text{SW}}$  equation based on *Cibicidoides* and *Planulina* of Lynch-Stieglitz et al. (1999) generated using in-situ benthic foraminifera of the genera *Cibicidoides* and *Planulina* over a calibration range of 4-26°C is used (Equation 6.2), where 'T' is

temperature in °C in both equations. The Sunbird-1 Mg/Ca temperatures are used to calculate  $\delta^{18}\text{O}_{\text{sw}}$ .

$$\text{Equation 6.1: } (\delta^{18}\text{O}_{\text{Calcite}} - \delta^{18}\text{O}_{\text{Seawater}} + 0.27) = -0.21 \pm 0.003 T + 3.10 \pm 0.07$$

$$\text{Equation 6.2: } (\delta^{18}\text{O}_{\text{Calcite}} - \delta^{18}\text{O}_{\text{Seawater}} + 0.27) = -0.21 \pm 0.002 T + 3.38 \pm 0.03$$

For Mg/Ca palaeotemperatures where adjacent samples have been combined to ensure the mean Mg/Ca of the sample is representative, the same has been done with the corresponding  $\delta^{18}\text{O}$  samples when calculating  $\delta^{18}\text{O}_{\text{sw}}$ .

Due to the low foraminiferal abundances throughout Sunbird-1 it was not possible to conduct trace metal and stable isotope analyses on the same species of planktonic or benthic foraminifera, which would have been preferable. *D. altispira* and *G. obliquus* were selected for reconstructing surface water conditions because they were present throughout the core, allowing for single species trace metal and stable isotope records. Having to use different planktic foraminiferal species for the Mg/Ca temperature record and the  $\delta^{18}\text{O}$  record could lead to limitations when reconstructing planktic foraminiferal  $\delta^{18}\text{O}_{\text{sw}}$ . In particular, if *D. altispira* reconstructs subsurface water conditions this limitation to planktic foraminiferal  $\delta^{18}\text{O}_{\text{sw}}$  will need serious consideration. Whether this is the case is assessed by comparing the absolute sea surface temperatures recorded by each species (Chapter 6.4.1).

### 6.2.3 Bottom water and sea surface temperature reconstructions

Due to the limited sample size of, and complications with, the trace metal data described in Chapter 5 two approaches to calculate both bottom water and sea surface temperatures are employed. The first uses the salinity independent Mg/Ca palaeo-thermometer (Chapter 5), and the second assumes  $\delta^{18}\text{O}_{\text{SW}}$  using the compilation of Cramer et al. (2011) to calculate temperature using  $\delta^{18}\text{O}$ .

In order to convert the foraminiferal  $\delta^{18}\text{O}$  values to temperature any changes in ice volume require correcting for. For this the  $\delta^{18}\text{O}_{\text{SW}}$  value from the nearest 0.1 Myr time interval in the compilation of Cramer et al. (2011) (Figure 6.1) is applied, isolating the temperature control on the  $\delta^{18}\text{O}$  records. This ice volume corrected  $\delta^{18}\text{O}$  data is then converted to temperature. For *G. obliquus* the palaeotemperature equation of Bemis et al. (1998) (Equation 6.1) is applied, and for *C. mundulus* the palaeotemperature equation of Lynch-Stieglitz et al. (1999) (Equation 6.2) is applied. The palaeotemperature equations used incorporate the necessary -0.27‰ correction when converting from SMOW to VPDB (Hut, 1987).

The influence of Rayleigh distillation and the atmospheric transport of vapour means that the  $\delta^{18}\text{O}_{\text{SW}}$  of surface waters can vary by as much as 1.5‰ depending on their latitude (Broecker, 1989, Zachos et al., 1994). If unaccounted for this could bias reconstructions of sea surface temperature or continental ice volume. Using the latitudinal correction of Zachos et al. (1994) gives a  $\delta^{18}\text{O}_{\text{SW}}$  of 0.1‰ for the modern day study site of Sunbird-1. The absence of a significant offset from ‰SMOW (0‰) suggests that this will have a negligible influence on the isotopic SST reconstructions.

Furthermore, any uncertainty in the planktic foraminiferal  $\delta^{18}\text{O}$  ratios originating from the influence of salinity needs accounting for. The absence of a robust, independent salinity proxy makes any quantitative attribution of this uncertainty challenging, and therefore  $\delta^{18}\text{O}$  variability due to changes in salinity is incorporated into any temperature estimate uncertainty. Available data from the 17 CTD profiles in a  $0.75^\circ \times 0.75^\circ$  grid square around the modern day study site show salinity varies between 34.9 and 35.4 PSU in the upper 200m of the water column (Boyer et al., 2013). Using the  $\delta^{18}\text{O}_{\text{sw}}$ -salinity relationship of LeGrande and Schmidt (2006) (Equation 6.3) this range of 0.5 PSU results in a maximum  $\delta^{18}\text{O}_{\text{sw}}$  uncertainty of  $\pm 0.091\%$  based on 332 modern day measurements in the Indian Ocean. Using the palaeotemperature equation for planktic foraminifera of Bemis et al. (1998) (Equation 6.1)

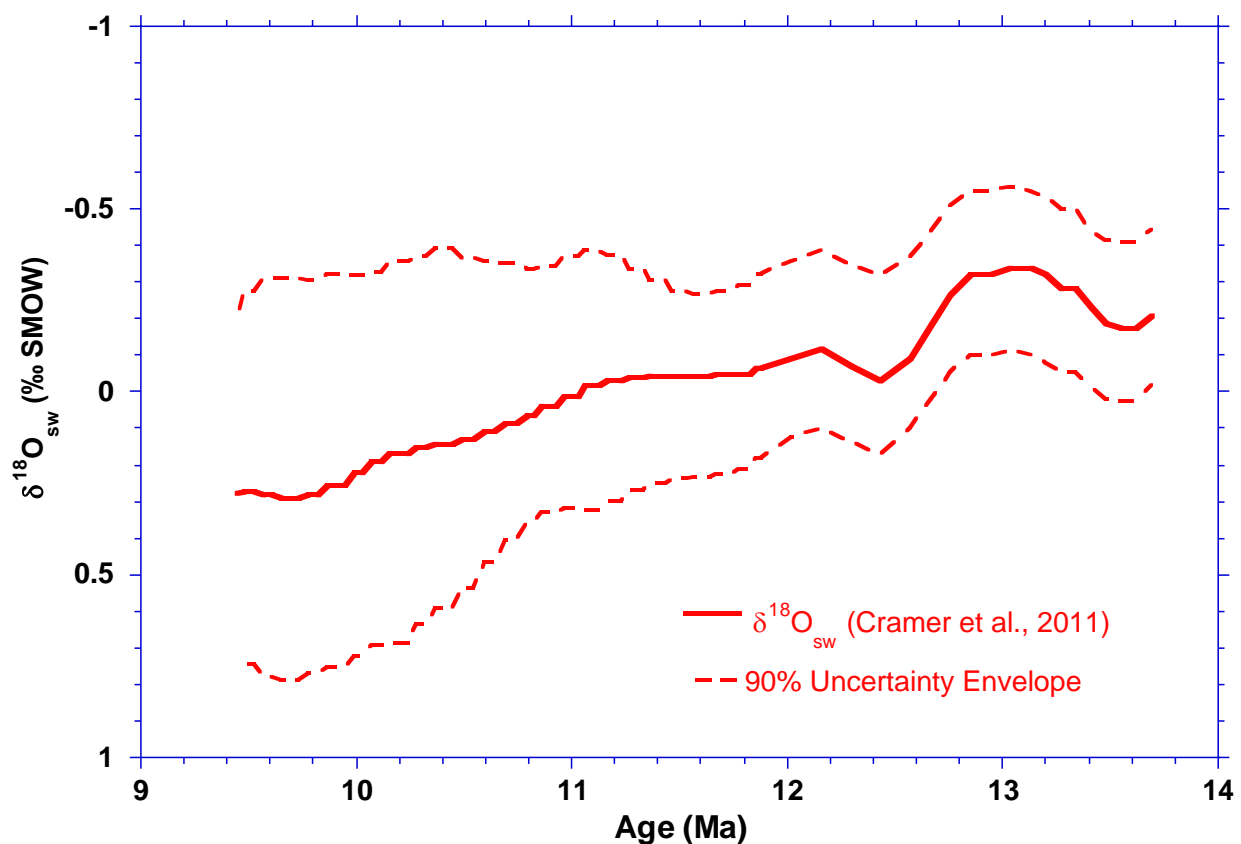


Figure 6.1:  $\delta^{18}\text{O}_{\text{sw}}$  (solid red line) and 90% confidence envelope (dashed red lines) from the Pacific Ocean compilation of Cramer et al. (2011).

this equates to a 0.4°C uncertainty in the calculated surface temperature from *G. obliquus*  $\delta^{18}\text{O}$ , an uncertainty significantly lower than that from the Cramer et al. (2011)  $\delta^{18}\text{O}_{\text{sw}}$  compilation (Figure 6.1).

$$\text{Equation 6.3: } \delta^{18}\text{O}_{\text{sw}}(\text{SMOW}) = (0.16 \pm 0.004 \times \text{Salinity}) - 5.31 \pm 0.135$$

As with the temperature estimates from the downcore LA-ICP-MS Mg/Ca record (Chapter 5) the analytical uncertainty (2 SD), and the  $\delta^{18}\text{O}_{\text{sw}}$  uncertainty in the temperature calibration originating from salinity variability and the global Cramer et al. (2011) compilation are distinguished between. This is because the calibration uncertainty does not influence any relative temperature trends.

## 6.3 Results

### 6.3.1 $\delta^{13}\text{C}$

*C. mundulus*  $\delta^{13}\text{C}$  ( $\delta^{13}\text{C}_{\text{BF}}$ ) ranges from +0.20 ‰ to +3.49 ‰ with a mean value of 1.30 ‰, and *G. obliquus*  $\delta^{13}\text{C}$  ( $\delta^{13}\text{C}_{\text{PF}}$ ) ranges from +1.15 ‰ to +4.26 ‰ with a mean value of 1.93 ‰. Both records exhibit a similar range of values (Table 6.1, Appendix 10), and there is a strong similarity between the benthic and planktic foraminiferal  $\delta^{13}\text{C}$  downcore records (Figure 6.2). This is reinforced by their significant positive correlation ( $R^2=0.59$ ) (Figure 6.3). Both records are dominated by a pronounced negative shift of  $\sim 2$  ‰ through the early part of the record (Figure 6.2). *C. mundulus*  $\delta^{13}\text{C}$  is initially  $\sim 3$  ‰ but decreases to  $\sim 1.5$  ‰ by 13 Ma and then  $\sim 1$  ‰ at 12 Ma, after which it remains relatively stable. The  $\sim 2$  ‰ negative shift in the *G.*

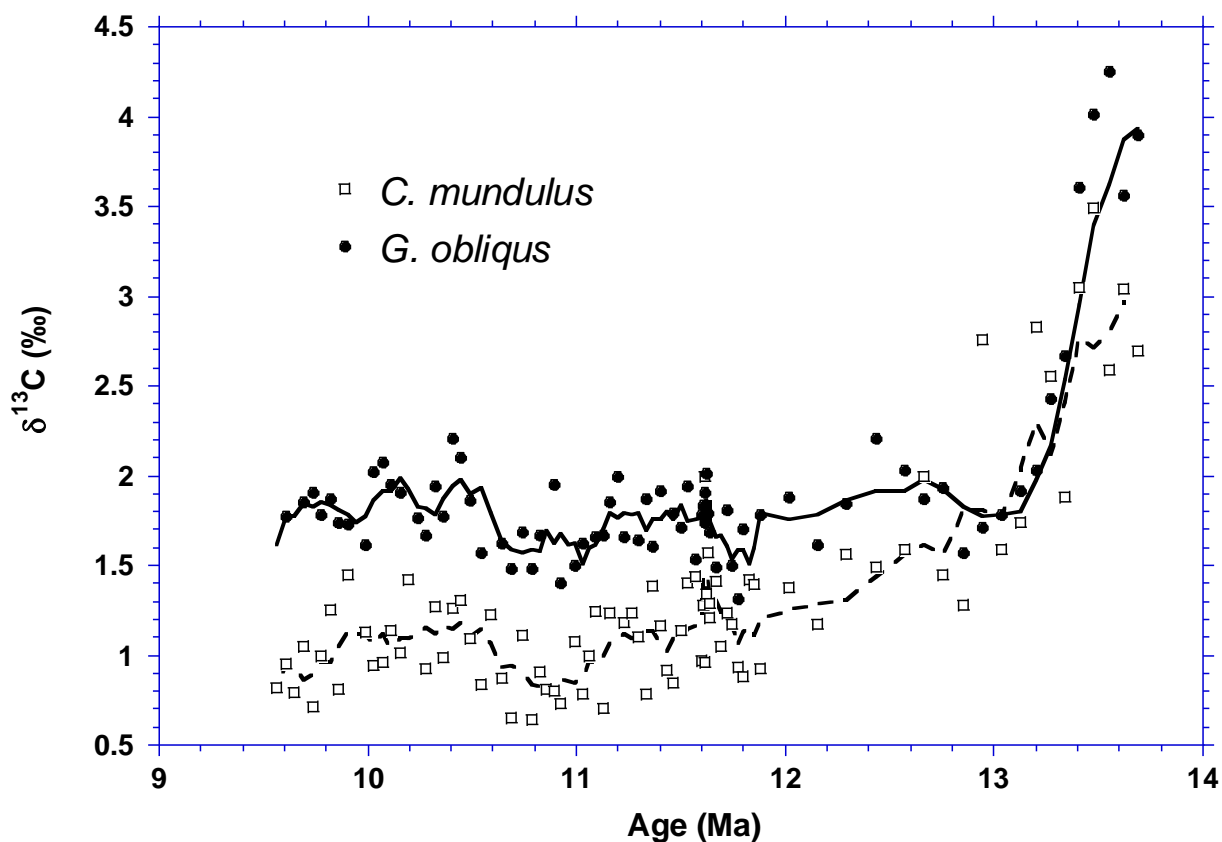


Figure 6.2: Sunbird-1  $\delta^{13}\text{C}$  records for *C. mundulus* (open squares) and *G. obliquus* (filled circles). 5 point moving averages are plotted, *C. mundulus* as a dashed line and *G. obliquus* as a solid line.

*obliquus*  $\delta^{13}\text{C}$  record is even more striking, isotopic values decreasing sharply from an initial 4‰ to ~1.7‰ in ~500 kyr, after which  $\delta^{13}\text{C}$  remains relatively stable (Figure 6.2). Despite the long-term stability in both  $\delta^{13}\text{C}$  records from 12 Ma to 9.5 Ma both demonstrate variability following the pronounced initial excursion, but without any obvious periodicity, likely due to the sampling resolution. The covariance of benthic and planktic foraminiferal  $\delta^{13}\text{C}$  is also apparent through this younger interval, the two records broadly tracking each other from 12 Ma onwards.

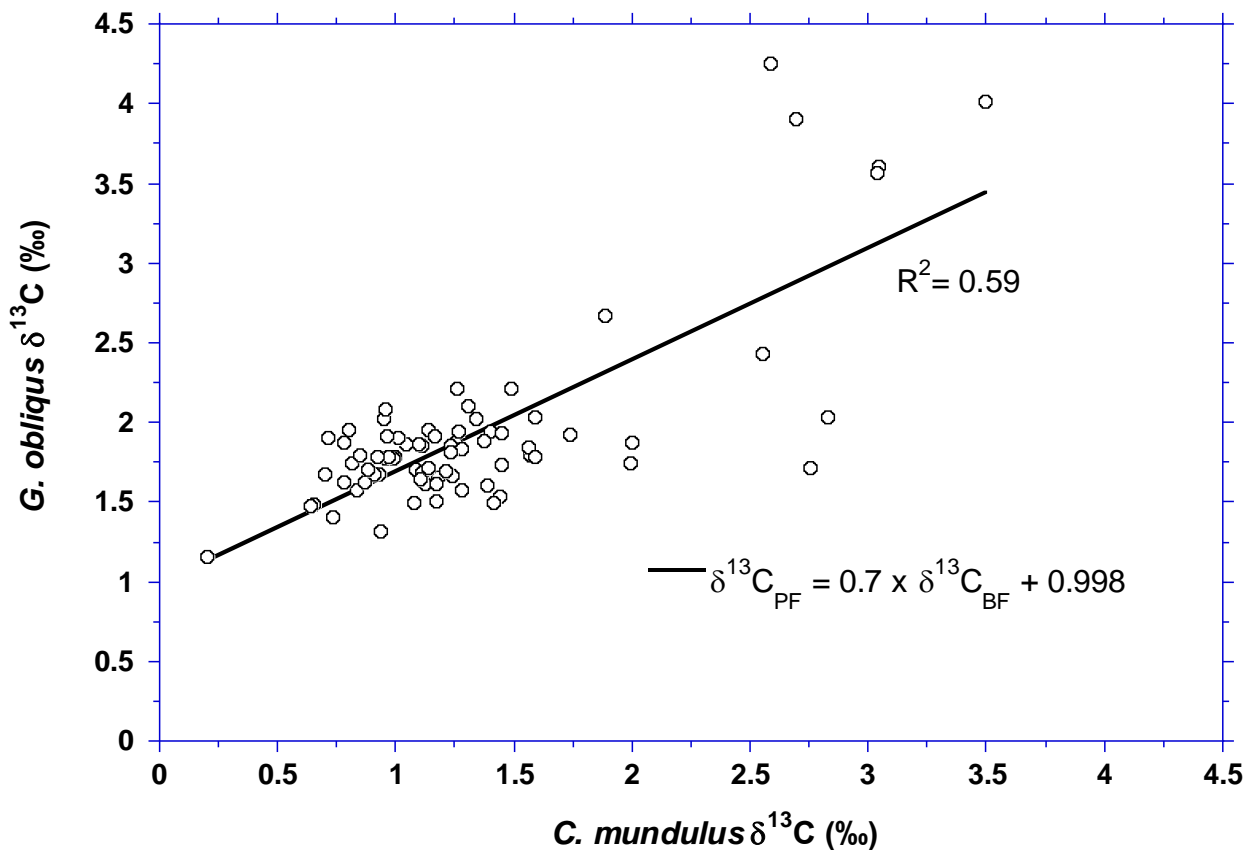


Figure 6.3: Covariance between *C. mundulus*  $\delta^{13}\text{C}$  and *G. obliquus*  $\delta^{13}\text{C}$  ( $R^2=0.59$ ,  $n=74$ ).

### 6.3.2 $\delta^{18}\text{O}$

*C. mundulus*  $\delta^{18}\text{O}$  ( $\delta^{18}\text{O}_{\text{BF}}$ ) ranges from -1.68 ‰ to +1.78 ‰ with a mean value of 0.02 ‰, and *G. obliquus*  $\delta^{18}\text{O}$  ( $\delta^{18}\text{O}_{\text{PF}}$ ) ranges from -3.63 ‰ to -2.34 ‰ with a mean value of -2.92‰. *C. mundulus*  $\delta^{18}\text{O}$  exhibits a much larger range (3.46 ‰) than *G. obliquus*  $\delta^{18}\text{O}$  (1.29 ‰) (Table 6.1, Appendix 10). The  $\delta^{18}\text{O}_{\text{BF}}$  and  $\delta^{18}\text{O}_{\text{PF}}$  records share some features, notably the  $\sim 0.6\text{‰}$  positive shift at 12.5 Ma (Figure 6.4, blue panel), similar to the shared negative shifts of the respective  $\delta^{13}\text{C}$  records. Through this interval, prior to  $\sim 12.0$  Ma, benthic foraminiferal  $\delta^{18}\text{O}$  values are initially isotopically light,  $\sim -1.5\text{‰}$ , becoming  $\sim -0.8\text{‰}$  by 12.4 Ma. This positive shift of  $\sim 0.6\text{‰}$  matches that of the  $\delta^{18}\text{O}_{\text{PF}}$  record, which shifts from  $\sim -3.4\text{‰}$  to  $\sim -2.7\text{‰}$ , albeit the  $\delta^{18}\text{O}_{\text{BF}}$  record has greater variability. However, from  $\sim 12$  Ma onwards the two records diverge

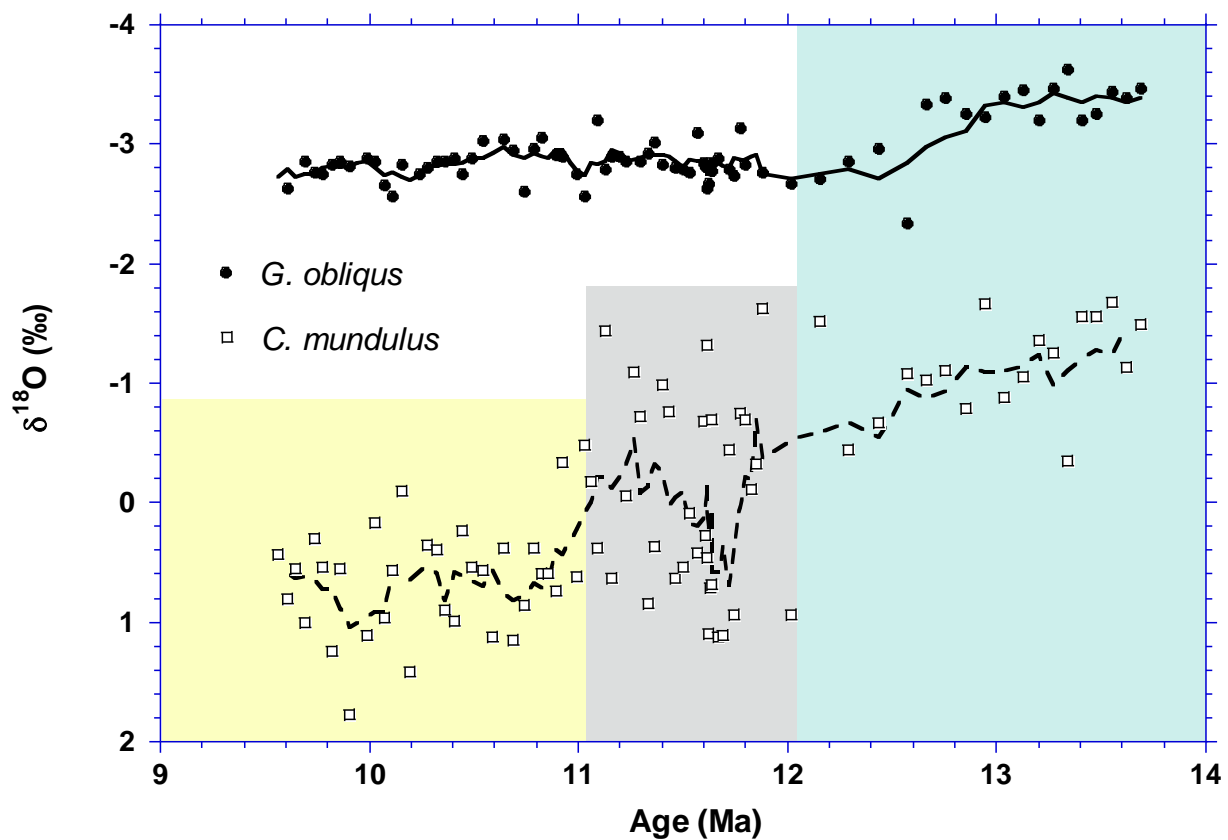


Figure 6.4: Sunbird-1  $\delta^{18}\text{O}$  records for *C. mundulus* (open squares) and *G. obliquus* (filled circles). Five point moving averages are plotted, *C. mundulus* as a dashed line and *G. obliquus* as a solid line.

greatly. Therefore, there is weaker covariance between the benthic and planktic foraminiferal  $\delta^{18}\text{O}$  records ( $R^2=0.20$ ) (Figure 6.5). This suggests that there is a lack of any significant benthic imprint on the  $\delta^{18}\text{O}_{\text{PF}}$  record, supporting the fidelity of the planktic signal.

Prior to, and following, the positive 0.6‰ shift at ~12.5 Ma, the  $\delta^{18}\text{O}_{\text{PF}}$  record remains remarkably stable, values averaging -3.4‰ prior to 12.5 Ma and -2.7‰ afterwards, with very little variability (Figure 6.4). While the  $\delta^{18}\text{O}_{\text{PF}}$  record remains stable at ~-2.7‰ there is a further positive shift in the  $\delta^{18}\text{O}_{\text{BF}}$  record, accompanied by extreme point-to-point variability of up to 2‰ between 12 Ma and 11 Ma (Figure 6.4, grey panel). Through this interval  $\delta^{18}\text{O}_{\text{BF}}$  fluctuates dramatically between the comparatively stable intervals before and after, values ranging from -1.4‰ to 1.2‰ over ~1 Myr. From 11 Ma-9.5 Ma, the variability in the  $\delta^{18}\text{O}_{\text{BF}}$

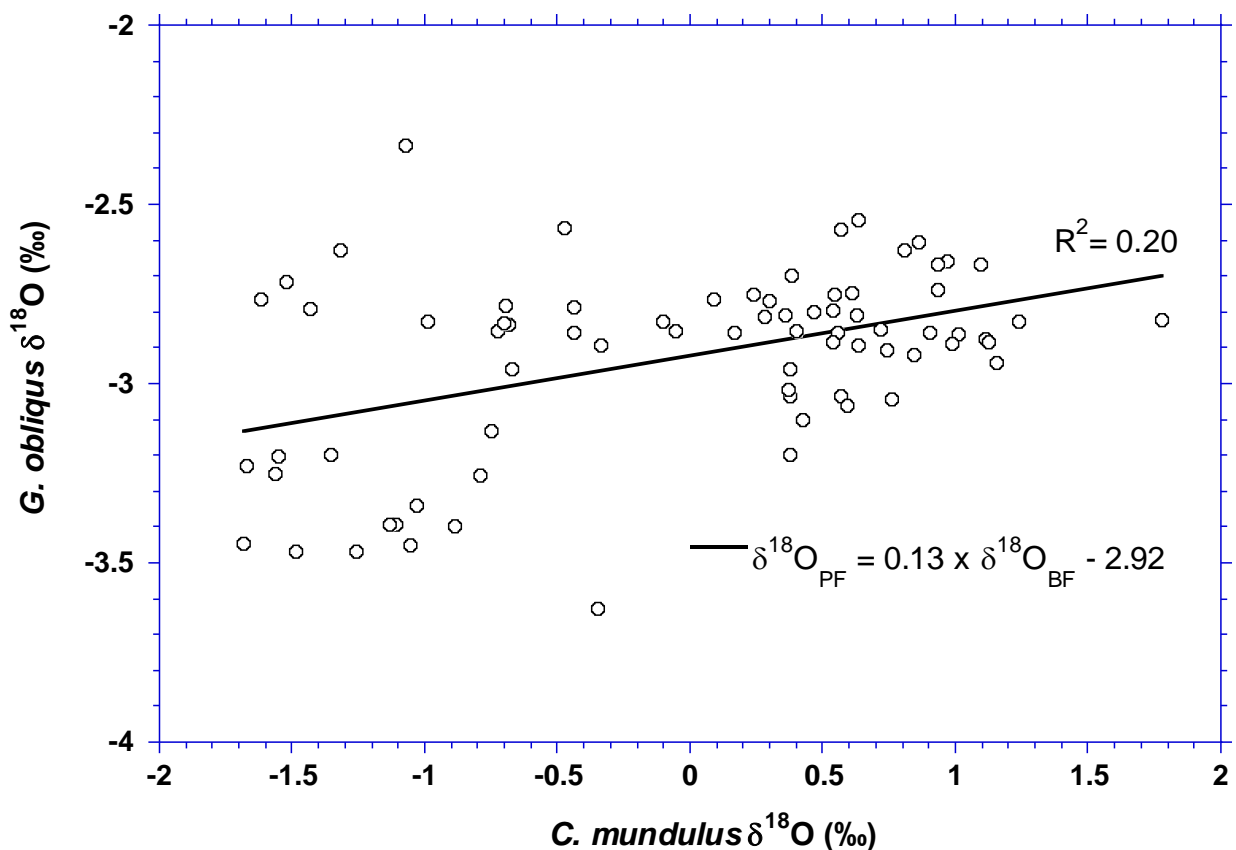


Figure 6.5: Covariance between *C. mundulus*  $\delta^{18}\text{O}$  and *G. obliquus*  $\delta^{18}\text{O}$  ( $R^2=0.20$ ,  $n=74$ ).

record decreases, varying between -0.10 ‰ and 1.78 ‰ (Figure 6.4, yellow panel). This youngest interval of the  $\delta^{18}\text{O}_{\text{BF}}$  record has reduced variability compared to between 12 Ma and 11 Ma, but it still remains considerably greater than  $\delta^{18}\text{O}_{\text{PF}}$ , which remains extremely stable.

The lack of high magnitude point-to-point variability of the Sunbird-1  $\delta^{18}\text{O}_{\text{PF}}$  record, in particular between 12 Ma and 11 Ma suggests it is likely a more robust and reliable surface mixed layer signal uninhibited by any significant secondary alteration of the foraminiferal calcite on the seafloor. Furthermore, the differences in style, magnitude, and timing of the benthic and planktic foraminiferal  $\delta^{18}\text{O}$  records following the initial  $\sim 0.6\text{‰}$  shift centred at 12.5 Ma suggests they have different primary controls.

	Mean (‰)	Median (‰)	Max (‰)	Min (‰)	Range (‰)	5-95% Range (‰)
<b><i>C. mundulus</i> <math>\delta^{13}\text{C}</math> (n=87)</b>	1.30	1.17	3.49	0.20	3.29	2.09
<b><i>G. obliquus</i> <math>\delta^{13}\text{C}</math> (n=77)</b>	1.93	1.79	4.26	1.15	3.11	2.16
<b><i>C. mundulus</i> <math>\delta^{18}\text{O}</math> (n=87)</b>	0.02	0.37	1.78	-1.68	3.46	2.70
<b><i>G. obliquus</i> <math>\delta^{18}\text{O}</math> (n=77)</b>	-2.92	-2.86	-2.34	-3.63	1.29	0.88

Table 6.1: Distribution statistics for *C. mundulus* and *G. obliquus*  $\delta^{13}\text{C}$  and  $\delta^{18}\text{O}$  in the Sunbird-1 record.

### 6.3.3 $\Delta\delta^{13}\text{C}$ and $\Delta\delta^{18}\text{O}$

The difference between the benthic and planktic foraminiferal records gives information about changes in the bottom water to surface water stable isotope gradient. The benthic-planktic gradients are calculated from the same sample, as opposed to the smoothed curves in Figure 6.2 and Figure 6.4. The benthic-planktic foraminiferal  $\delta^{13}\text{C}$  ( $\Delta\delta^{13}\text{C}$ ) record exhibits minimal variability post  $\sim 12$  Ma, *G. obliquus*  $\delta^{13}\text{C}$  being consistently 0.5‰-1‰ heavier than *C. mundulus*  $\delta^{13}\text{C}$  (Figure 6.6). This relatively constant surface to bottom water  $\delta^{13}\text{C}$  gradient is expected because the two records track each other (Figure 6.2) and demonstrate a strong covariance (Figure 6.3). Prior to 12.5 Ma, when both  $\delta^{13}\text{C}$  records are dominated by steep  $\sim 2$ ‰ negative excursions, there is very large, stochastic variability in  $\Delta\delta^{13}\text{C}$  suggesting a highly

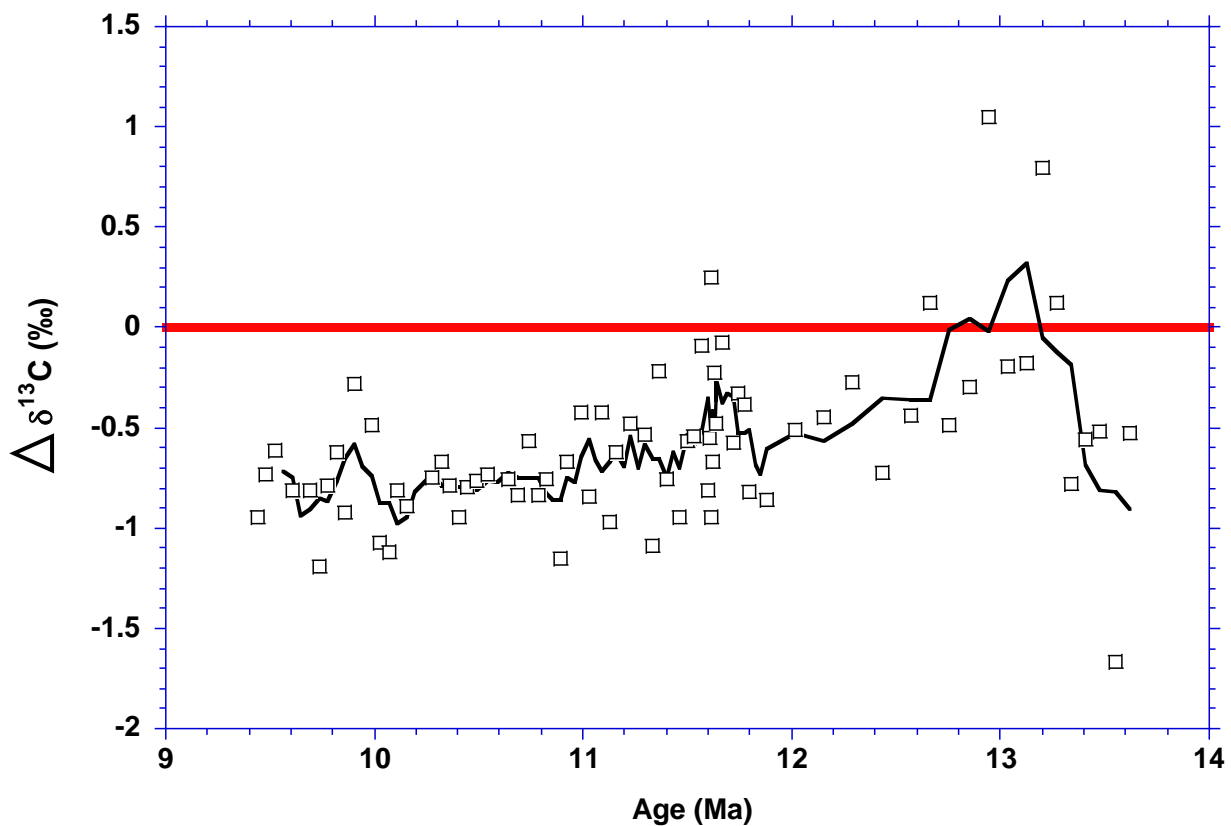


Figure 6.6: Sunbird-1 benthic-planktic foraminiferal  $\Delta\delta^{13}\text{C}$  (open squares) record. The solid line represents 5 point moving averaged data and the red horizontal line signifies equivalent values ( $\Delta\delta^{13}\text{C}$

dynamic water column. There is a slight bump towards  $\Delta\delta^{13}\text{C}=0$  at 11.8 Ma to 11.5 Ma, owing to slightly heavier benthic foraminiferal  $\delta^{13}\text{C}$  through this interval.

Due to the much larger range in  $\delta^{18}\text{O}_{\text{BF}}$  relative to  $\delta^{18}\text{O}_{\text{PF}}$  (3.46‰ versus 1.29‰) the difference between the two is dominated by changes in the benthic foraminiferal record. Therefore, the benthic-planktic foraminiferal  $\delta^{18}\text{O}$  ( $\Delta\delta^{18}\text{O}$ ) record can be split into three intervals, separated at  $\sim 12.0$  Ma and at  $\sim 11.0$  Ma, in exactly the same way as the  $\delta^{18}\text{O}_{\text{BF}}$  record (Figure 6.7). Prior to 12.0 Ma  $\Delta\delta^{18}\text{O}$  is  $\sim 2\text{‰}$  and after 11 Ma it is  $\sim 3.5\text{‰}$ , but with significant scatter about these average values. In the transition interval between 12.0 Ma and 11.0 Ma the  $\Delta\delta^{18}\text{O}$  record shows extremely high magnitude variability on  $10^4$  year timescales, values ranging from 1.2‰ to 4.0‰. The differing downcore trends (Figure 6.4) and lack of any significant covariance

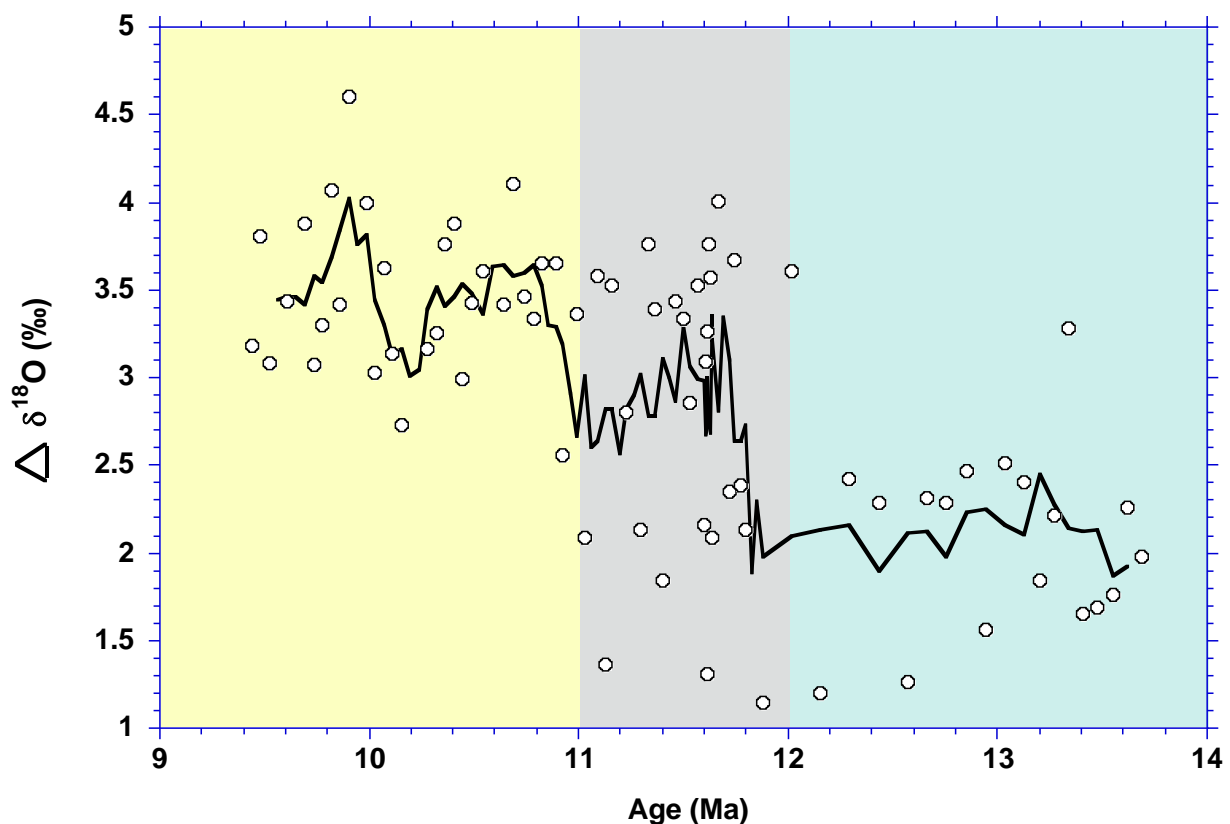


Figure 6.7: Sunbird-1 benthic-planktic foraminiferal  $\Delta\delta^{18}\text{O}$  (open squares) record. The solid line represents 5 point moving averaged data.

(Figure 6.5) between *C. mundulus*  $\delta^{18}\text{O}$  and *G. obliquus*  $\delta^{18}\text{O}$  explains why there is significant scatter in the  $\Delta\delta^{18}\text{O}$  record.

There is no correlation between the respective benthic-planktic gradients ( $R^2=0.02$ ) (Figure 6.8) suggesting  $\Delta\delta^{13}\text{C}$  and  $\Delta\delta^{18}\text{O}$  through the Sunbird-1 record have differing primary controls, or threshold responses to gradual climatic or tectonic change.

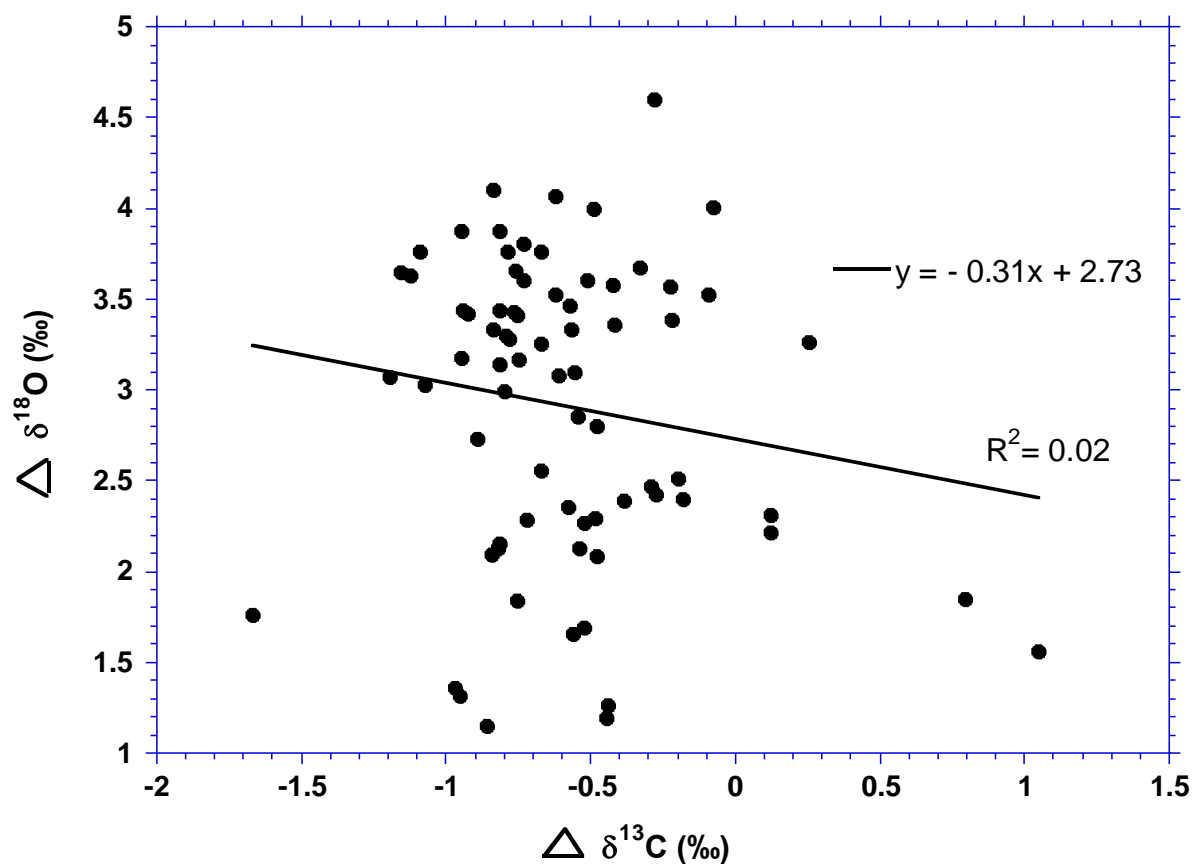


Figure 6.8: Crossplot of  $\Delta\delta^{13}\text{C}$  and  $\Delta\delta^{18}\text{O}$  values through the Sunbird-1 record. There is no significant correlation ( $R^2=0.02$ ,  $n=74$ ).

#### 6.3.4 $\delta^{18}\text{O}$ SST and BWT records

The  $\delta^{18}\text{O}$  values were converted to temperature accounting for  $\delta^{18}\text{O}_{\text{SW}}$ , and propagated the analytical and calibration uncertainty, following the method outlined in Section 6.2.2. SST ranges from 27°C - 31°C, with a mean temperature of 29°C (Figure 6.9a), and BWT ranges from 9°C – 23°C, with a mean temperature of 16°C (Figure 6.9c) (Appendix 11). Sea surface temperature for the anomalously high  $\delta^{18}\text{O}_{\text{PF}}$  value at 12.57 Ma (Figure 6.4) is not calculated. For comparison the Mg/Ca SST (Figure 6.9b) and BWT (Figure 6.9d) records generated in Chapter 5 are shown. As explained in detail in Chapter 5.3, these were determined using the calibrations of Evans et al. (2016a) and Lear et al. (2002) respectively, both including a correction for Mg/Ca<sub>SW</sub> using an Eocene Mg/Ca<sub>SW</sub> of 2.1 mol/mol. The planktic foraminiferal Mg/Ca is further corrected for the influence of changing pH using the relationship of Evans et al. (2016b) and the surface ocean pH record of Sostdian et al. (2018).

The  $\delta^{18}\text{O}$  SST record remains relatively stable between 27°C and 31°C, the only distinctive trend being a ~3°C decrease between ~12.7 Ma and 12.0 Ma (Figure 6.9a), a decrease not seen in the Mg/Ca SST record (Figure 6.9b). The  $\delta^{18}\text{O}$  BWT record is completely different, displaying point to point variability of up to 10°C (Figure 6.9c). This variability in  $\delta^{18}\text{O}$  reconstructed BWT is largest between 12 Ma and 11 Ma, BWT fluctuating between ~20°C, which dominates prior to 12.0 Ma, and ~10°C, which dominates after 11.0 Ma. As with the  $\Delta\delta^{18}\text{O}$  record (Figure 6.7), the large variability and range of  $\delta^{18}\text{O}_{\text{BF}}$  values dominates the BWT-SST temperature gradient record (Figure 6.10). The Sunbird-1  $\delta^{18}\text{O}$  derived temperature gradient increases from <10°C prior to 12.0 Ma to ~15°C after 11.0 Ma, via a 1 Myr interval of highly variable temperature gradient (Figure 6.9c). In both Figure 6.9 and 6.10 the analytical

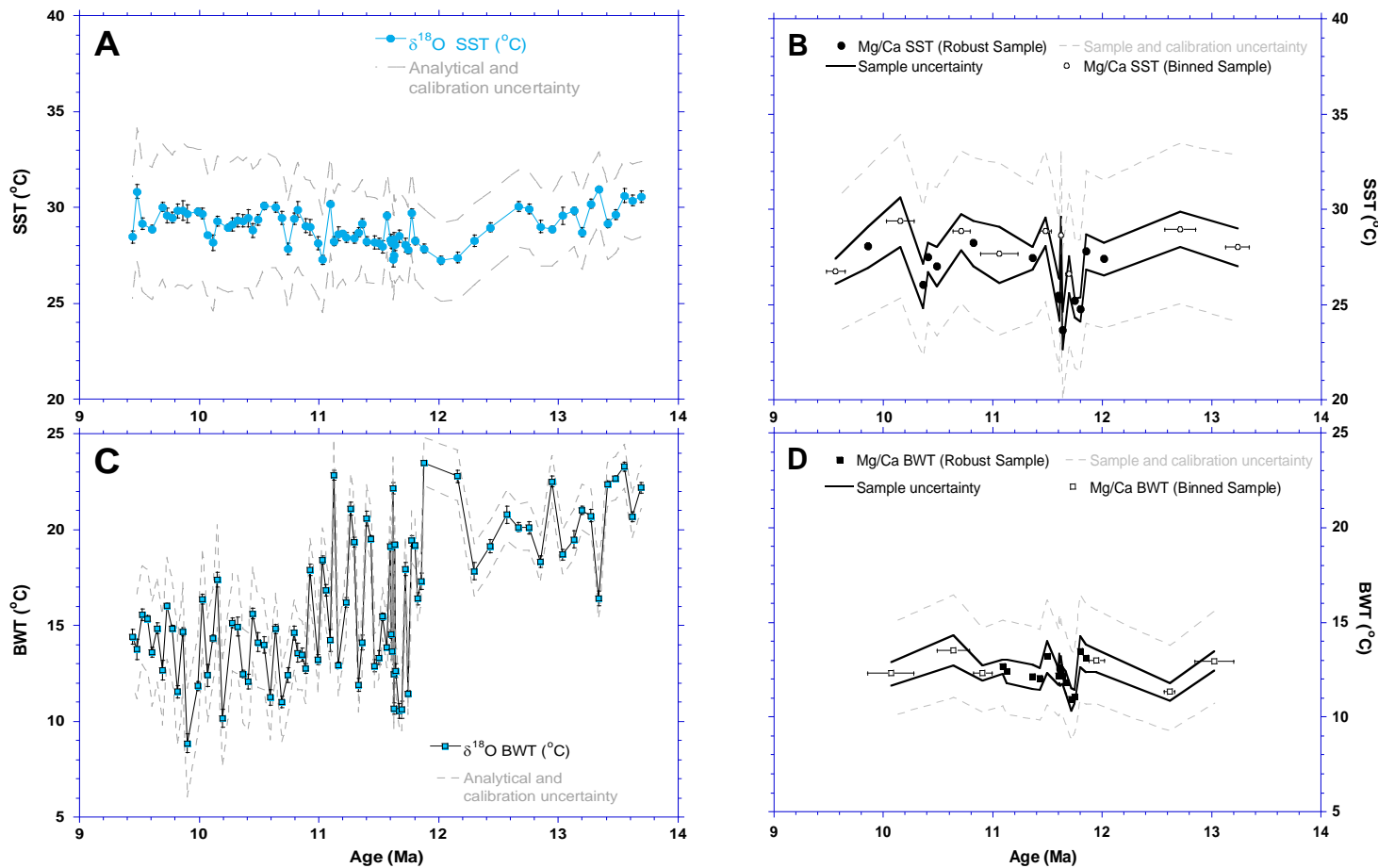


Figure 6.9: (a) Sea Surface Temperature (blue circles) and (c) Bottom Water Temperature (blue squares) records generated by applying Equation 6.2 and 6.3 respectively to the  $\delta^{18}\text{O}$  data displayed in Figure 6.2. Seawater  $\delta^{18}\text{O}$  ( $\delta^{18}\text{O}_{\text{sw}}$ ) is from the Cramer et al. (2011) compilation. Error bars denote the analytical uncertainty ( $\pm 2\text{SD}$ ), and the grey dashed lines denote the uncertainty envelope resulting from the cumulative analytical and calibration uncertainty. The calibration uncertainty incorporates the 90% confidence envelope on the  $\delta^{18}\text{O}_{\text{sw}}$  compilation (Figure 6.3), and the estimated 0.091‰ salinity influence on planktic foraminiferal  $\delta^{18}\text{O}$ . Mg/Ca SST (b) and BWT (d) records from Chapter 5 are given for comparison.

error associated with the  $\delta^{18}\text{O}$  measurements is shown as error bars. The uncertainty envelopes in Figure 6.9a and Figure 6.9c incorporates this analytical uncertainty of the  $\delta^{18}\text{O}$  measurements as well as uncertainties within the salinity and temperature calibrations, and the uncertainty associated with the  $\delta^{18}\text{O}_{\text{SW}}$  compilation.

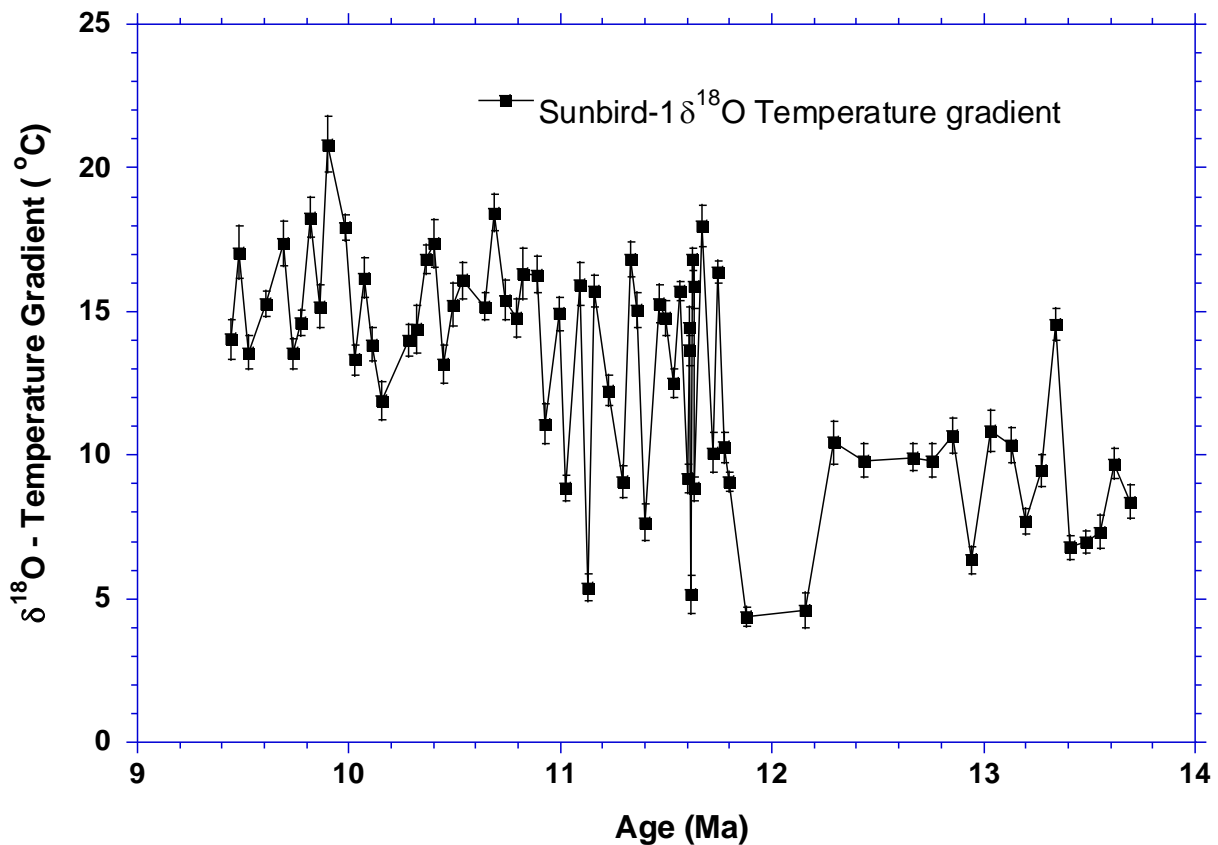


Figure 6.10: Record of the bottom water to surface water temperature gradient generated by applying Equations 6.1 and 6.2 to the  $\delta^{18}\text{O}$  data displayed in Figure 6.7. Error bars denote the analytical uncertainty ( $\pm 2\text{SD}$ ).

### 6.3.5 Surface and bottom water calculated $\delta^{18}\text{O}_{\text{SW}}$

Using the method outlined in Section 6.2.3 the LA-ICP-MS Mg/Ca records (Chapter 5) are used as independent palaeotemperature values to account for the temperature control on  $\delta^{18}\text{O}$ . This allows both surface and bottom water  $\delta^{18}\text{O}_{\text{SW}}$  records at Sunbird-1 to be calculated (Figure 6.11) (Appendix 12). Due to binning of samples with very different  $\delta^{18}\text{O}$  values the

sample uncertainty (2 SD) of the 1570.5 m (11.95 Ma) benthic foraminiferal  $\delta^{18}\text{O}_{\text{sw}}$  is extremely high ( $\pm 2.67\text{‰}$ ). Therefore, it is not included in Figure 6.11b.

Planktic foraminiferal  $\delta^{18}\text{O}_{\text{sw}}$  has a total range of  $1\text{‰}$ , values ranging from  $-0.46\text{‰}$  to  $0.54\text{‰}$  with a mean of  $0.01\text{‰}$ . Benthic foraminiferal  $\delta^{18}\text{O}_{\text{sw}}$  has a much larger range of  $2.54\text{‰}$ , values ranging from  $-1.94\text{‰}$  to  $0.61\text{‰}$  with a mean of  $-0.55\text{‰}$ . Having accounted for the influence of temperature, both  $\delta^{18}\text{O}_{\text{sw}}$  records (Figure 6.11) are very similar to their respective  $\delta^{18}\text{O}$  records (Figure 6.4). This is unsurprisingly considering the overall stability of the LA-ICP-MS temperature records (Chapter 5.4.5).

Despite the large envelopes on absolute values, as denoted by the grey dashed lines in Figure 6.11, this is predominantly a result of the calibration uncertainties. By considering the uncertainty relating to the analysis and sampling, as denoted by the vertical error bars in Figure 6.11, relative shifts within both records can be discussed. Planktic foraminiferal  $\delta^{18}\text{O}_{\text{sw}}$  increases by  $\sim 0.5\text{‰}$  through the record (Figure 6.11a). The magnitude of this  $\delta^{18}\text{O}_{\text{sw}}$  increase is the same as the increase in both  $\delta^{18}\text{O}$  records at  $\sim 12.5$  Ma (Figure 6.4). Between 12.0 Ma and 11.4 Ma there are two distinctive excursions in the planktic foraminiferal  $\delta^{18}\text{O}_{\text{sw}}$  record of  $\sim 0.8\text{‰}$  amplitude, and durations of 400 kyr and  $150 \pm 50$  kyr respectively. These cycles are poorly defined, due to the low sampling resolution, which also hinders interpretation due to possible aliasing of any orbital frequency variability. The most distinctive feature of the benthic foraminiferal  $\delta^{18}\text{O}_{\text{sw}}$  record is the extremely high point to point variability of up to  $2.5\text{‰}$  between 11.8 Ma and 11.0 Ma (Figure 6.11b). This overprints a general increasing trend,  $\delta^{18}\text{O}_{\text{sw}}$  values post 11.0 Ma approximately  $1.5\text{‰}$  heavier than prior to 11.8 Ma.

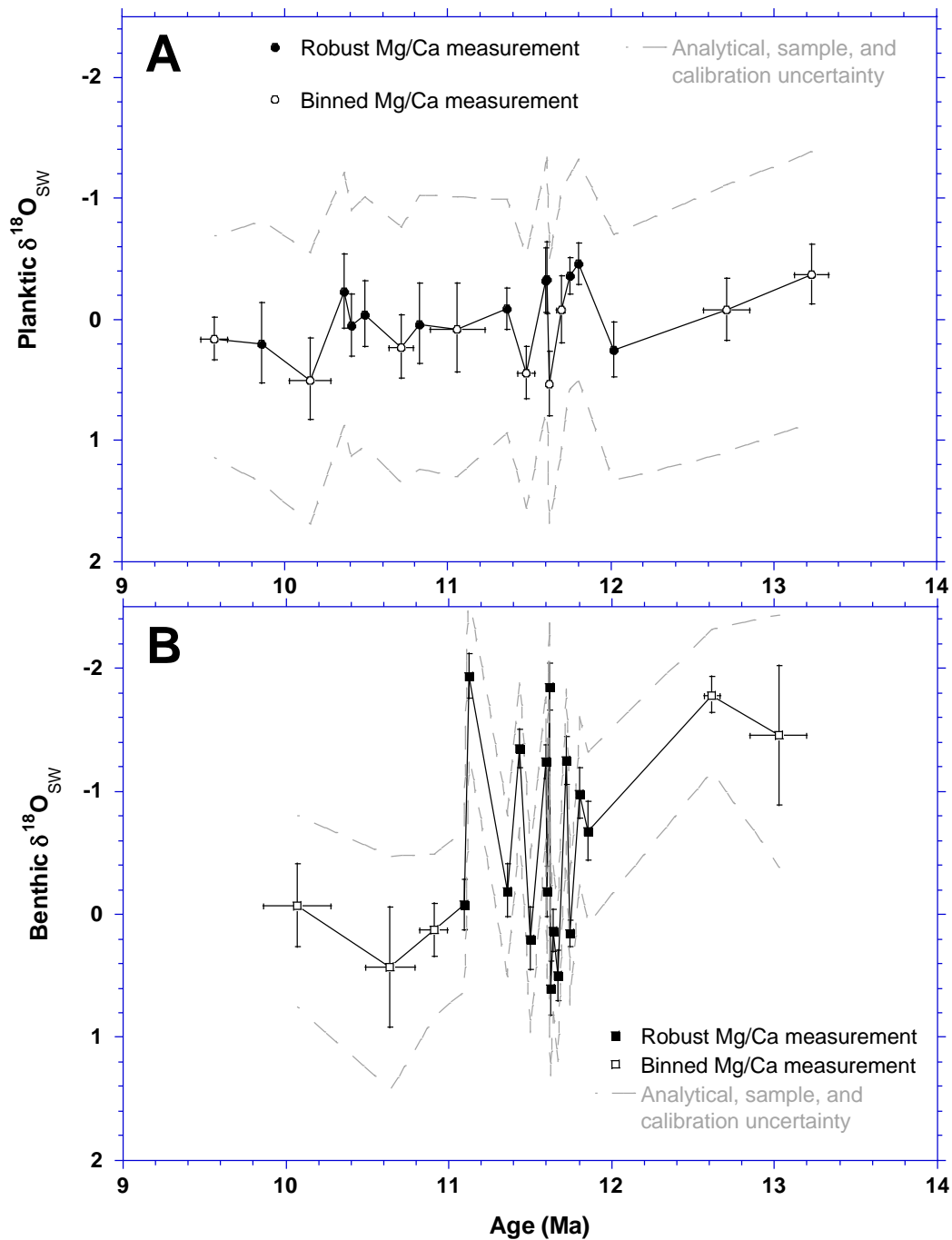


Figure 6.11: Surface water (A) and bottom water (B)  $\delta^{18}\text{O}_{\text{sw}}$  records from Sunbird-1. Planktic foraminiferal  $\delta^{18}\text{O}_{\text{sw}}$  is calculated using the  $\delta^{18}\text{O}$  equation of Bemis et al. (1998) (Equation 6.1), and benthic foraminiferal  $\delta^{18}\text{O}_{\text{sw}}$  is calculated using the  $\delta^{18}\text{O}$  equation of Lynch-Stieglitz et al. (1999) (Equation 6.2). Temperatures from Mg/Ca samples regarded as robust (filled symbols) and binned (open symbols) are distinguished between (see Chapter 5.4.4 for details). Binned samples have horizontal error bars denoting the age range the sample incorporates. Vertical error bars denote the cumulative analytical and sample uncertainty of the  $\delta^{18}\text{O}$  and Mg/Ca values ( $\pm 2\text{SD}$ ). The uncertainty envelope (grey dashed lines) denotes the full uncertainty, incorporating the analytical and sample uncertainty, and the full calibration uncertainty from the calculation of temperature from Mg/Ca and in the  $\delta^{18}\text{O}_{\text{sw}}$  calibration equations.

## 6.4 Discussion

### 6.4.1 Sunbird-1 planktic foraminiferal Mg/Ca and $\delta^{18}\text{O}$ : towards reliable absolute SST reconstructions for the Miocene

The Sunbird-1  $\delta^{18}\text{O}_{\text{PF}}$  SST record reconstructs very similar absolute temperatures to the planktic foraminiferal Mg/Ca SST record reconstructed using LA-ICP-MS (Figure 6.12). Mean SST from the Sunbird-1  $\delta^{18}\text{O}_{\text{PF}}$  record (29°C) is 2°C higher than mean SST from the Mg/Ca record (27°C), although with the exception of the two transient decreases in Mg/Ca

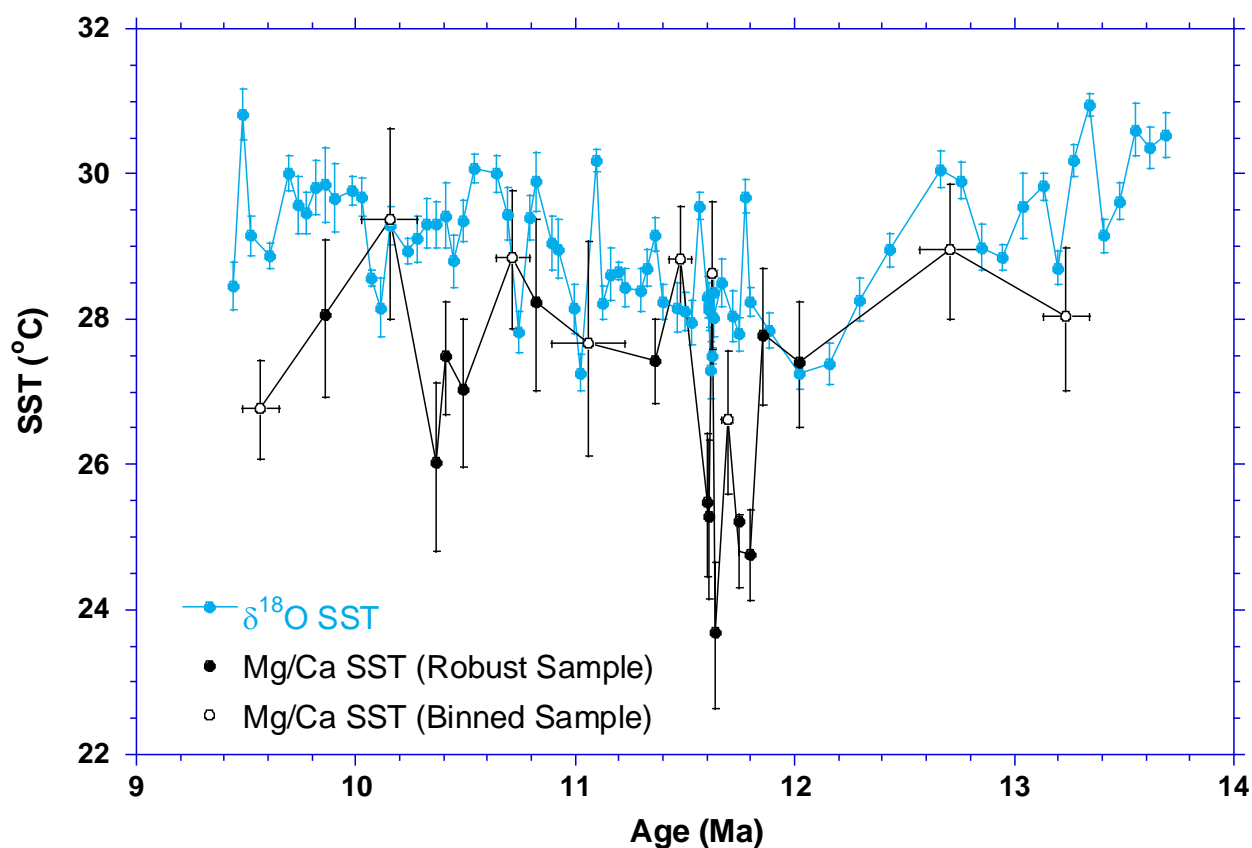


Figure 6.12: Sea surface temperature records at Sunbird-1 from planktic foraminiferal  $\delta^{18}\text{O}$  (blue) and Mg/Ca (black). The Mg/Ca record distinguishes between robust (filled symbols) and binned (open symbols) samples (see Chapter 5.4.4 for details). Error bars on the  $\delta^{18}\text{O}$  record denote the analytical uncertainty ( $\pm 2\text{SD}$ ), and error bars on the Mg/Ca record denote the sample uncertainty ( $\pm 2\text{SE}$ ). Binned Mg/Ca samples also have horizontal error bars denoting the age range the sample incorporates.

reconstructed SST initiating at 11.8 Ma and 10.7 Ma (Chapter 6.4.3) the records are within error of each other.

The similarity of the absolute SSTs reconstructed by the two proxies supports their robustness. This strengthens the argument that the LA-ICP-MS Mg/Ca SST record is recording a primary temperature signal and that the absolute sea surface temperatures at Sunbird-1 should be considered primary. Further evidence for the robustness of the  $\delta^{18}\text{O}_{\text{PF}}$  record is that it is isotopically offset by  $\sim -2\text{‰}$  from the  $\delta^{18}\text{O}$  record reconstructed using *Globigerinoides quadrilobatus* at ODP site 758 on the 90°East ridge (Banerjee et al., 2017) (Figure 6.13). Additionally, the Sunbird-1  $\delta^{18}\text{O}_{\text{PF}}$  record displays very strong point to point stability, unlike

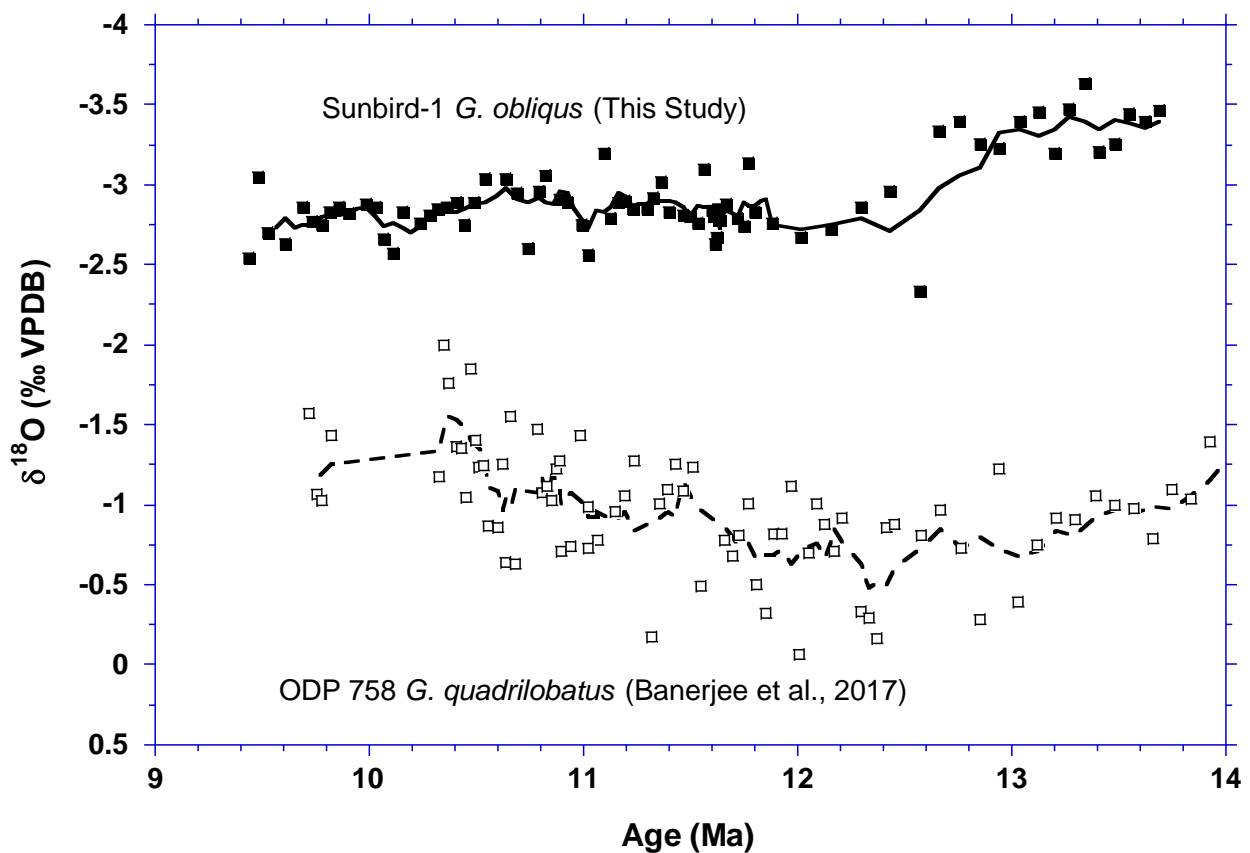


Figure 6.13: Planktic foraminiferal  $\delta^{18}\text{O}$  from Sunbird-1 (filled squares) and ODP Site 758 on the ninety-east ridge (open squares) (Banerjee et al., 2017). Five point moving averages are represented by solid and dashed lines respectively.

the record from ODP site 758 in the North-Eastern Indian Ocean (Banerjee et al., 2017) (Figure 6.13). Both planktic foraminiferal species are inferred as being surface mixed layer dwellers (Keller, 1985) so water depth of calcification cannot account for this offset. If this 2‰ offset was to be interpreted solely in terms of temperature this would equate to ~9°C (Bemis et al., 1998), whereas the modern day difference is ~2°C (Boyer et al., 2013). ODP site 758, located on the ninety-east ridge, is dominated by carbonate ooze (Banerjee et al., 2017) making it more susceptible to post depositional alteration overprinting the oxygen isotopic signature of the primary surface water conditions (Pearson et al., 2001, Sexton et al., 2006, Pearson and Burgess, 2008). This potential diagenetic influence towards isotopically heavier  $\delta^{18}\text{O}$  in the planktic foraminifera at ODP site 758 likely explains the remaining ~1.6‰ offset between the

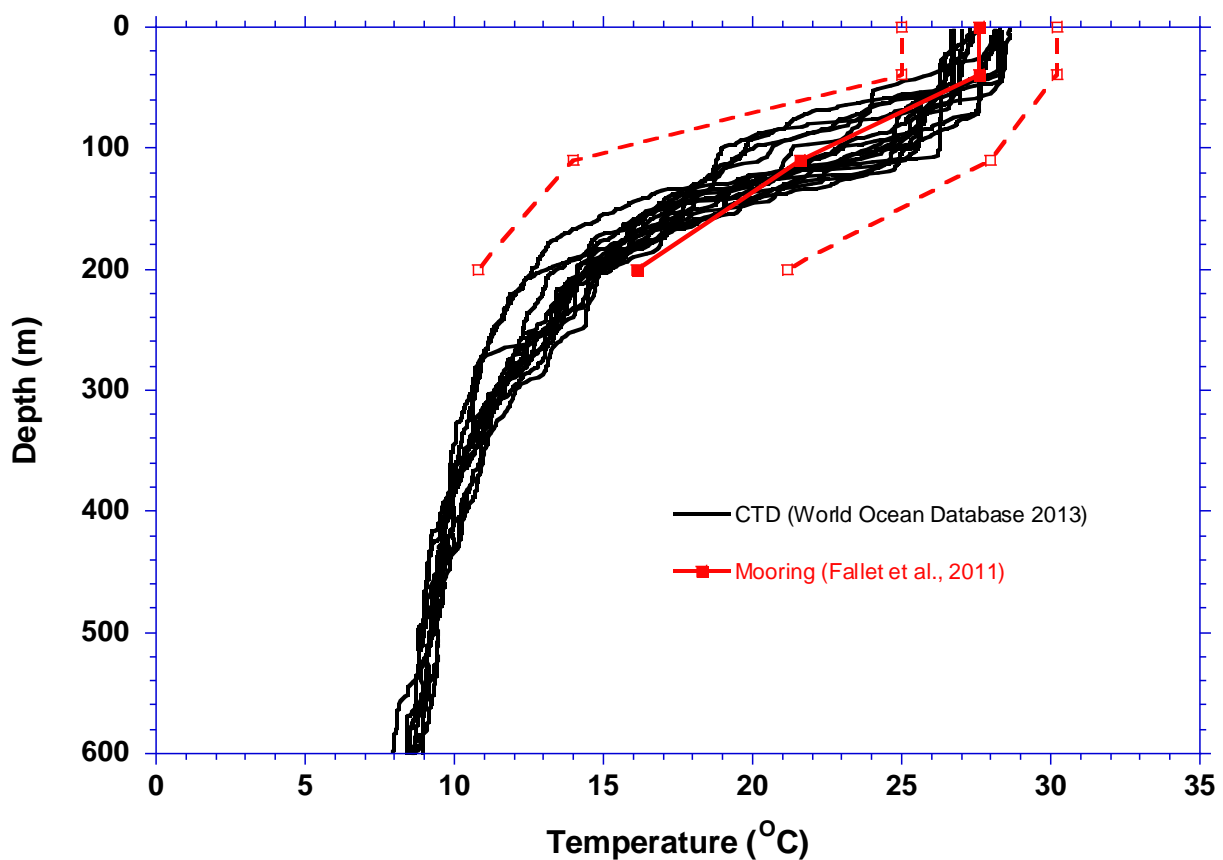


Figure 6.14: Temperature profiles down through the water column around the modern day position of Sunbird-1 generated from CTD measurements (Boyer et al., 2013), satellite data (Fallet et al., 2011).

two  $\delta^{18}\text{O}_{\text{PF}}$  records and strongly supports the fidelity and reliability of the Sunbird-1 planktic foraminiferal  $\delta^{18}\text{O}$  record.

Furthermore, both Sunbird-1 SST records are similar to modern day SST in the region, as indicated by CTD data from the same 17 CTD profiles from the  $0.75^\circ \times 0.75^\circ$  grid square around the modern day study site that were used to determine the seasonal variability in salinity (Boyer et al., 2013) (Figure 6.14). That both of the Sunbird-1 Miocene SST records are much more in line with modern SST than those from ODP Site 758 (Banerjee et al., 2017), also supports their robustness. These CTD profiles indicate that the modern day mixed layer is ~50m water depth, in which temperature varies between  $26.5^\circ\text{C}$  and  $28.5^\circ\text{C}$ . This is consistent with more recent CTD data from the nearby GLOW sites (Birch et al., 2013) and the average mean satellite sea surface temperature of  $27.6^\circ\text{C}$  in the nearby Mozambique Channel (Fallet et al., 2011) (Figure 6.14). However, it is worth noting that the CTD data fail to reflect the  $\sim 5^\circ\text{C}$  seasonal variability recorded by satellite data (Fallet et al., 2011) and meteorological observations (McClanahan, 1988), likely due to lower sampling density of the CTD measurements.

Due to it being extinct the paleoecology of *D. altispira* is poorly understood, and cannot be groundtruthed. However, the similarity in SST reconstructions strongly suggests that *D. altispira* and *G. obliquus* record the same conditions. *G. obliquus* is interpreted as recording a surface water mixed layer signal (Keller and Barron, 1985, Aze et al, 2011), and these results therefore suggest that *D. altispira* resided in the same depth habitat.

Despite reconstructing similar absolute temperatures, the  $\delta^{18}\text{O}$  SST record doesn't have the two distinct transient decreases in temperature seen in the Mg/Ca SST record. This suggests that a secondary influence on at least one of the proxies has not been properly accounted for, causing the discrepancy. This could be an increase in global or local  $\delta^{18}\text{O}_{\text{SW}}$  masking a genuine transient SST decrease in the  $\delta^{18}\text{O}$  record, a local decrease in pH or  $[\text{CO}_3^{2-}]$  causing an artificial transient SST or BWT decrease in the Mg/Ca record, or a combination of both. This could be explained by two intervals of expanding continental ice volume. Although not incorporated into the Cramer et al. (2011) compilation recent studies have proposed continued ice growth following the MMCT (Holbourn et al., 2013, Lear et al., 2015, Kominz et al., 2016). A second possibility is that the secondary influence is local, the complex continental shelf locality influencing the local seawater chemistry. The divergence in the SST records could be explained by two transient intervals of colder, fresher surface waters at 11.8 Ma and 10.7 Ma. There could be several possible mechanisms to explain the synchronous cooling and freshening of the surface waters. One mechanism is the upwelling of colder water from depth, however, deeper waters are typically denser as a result of being more saline than the surface waters above. The proximity to the continent means increased surface run off from rivers must be considered as a possible mechanism of cold, fresh water input. However, a significant increase in siliciclastic riverine input would be expected to be associated with a distinct change in lithology or grain size, neither of which are observed for either interval (Figure 2.3 and 2.4).

#### 6.4.2 Dissimilar Mg/Ca and $\delta^{18}\text{O}$ BWT reconstructions

In stark contrast to the planktic foraminiferal LA-ICP-MS Mg/Ca and planktic foraminiferal  $\delta^{18}\text{O}$  records which reconstruct similar SSTs, the respective benthic foraminiferal records are extremely dissimilar (Figure 6.15). The Mg/Ca reconstructed BWT record is very stable, remaining  $\sim 12^\circ\text{C}$  to  $13^\circ\text{C}$  through the interval, whereas the  $\delta^{18}\text{O}$  reconstructs BWT of  $\sim 20^\circ\text{C}$  from 13.8 Ma to 12.0 Ma, displays point to point variability of up to  $10^\circ\text{C}$  between 12.0 Ma and 11.0 Ma, before then stabilising at  $\sim 11^\circ\text{C}$  to  $\sim 16^\circ\text{C}$  for the rest of the record. The difference likely originates from a secondary control on one of the proxies being unaccounted for. Due to its high variability this likely influences the  $\delta^{18}\text{O}$  BWT record. That  $\delta^{18}\text{O}$  was measured on homogenised samples of 6-10 foraminifera makes it unlikely that the observed variability is due to the seasonal and inter-annual temperature variability inferred between individuals analysed by LA-ICP-MS (Chapter 5.5.2.2). Therefore, in addition to the Cramer et al. (2011) global  $\delta^{18}\text{O}_{\text{SW}}$  compilation, there are likely other controls influencing the benthic foraminiferal  $\delta^{18}\text{O}_{\text{SW}}$ , and therefore  $\delta^{18}\text{O}_{\text{BF}}$  at Sunbird-1. Possible causes could be local salinity changes, changing bottom water mass (Broecker et al., 1982), influence of coastal water, the input of river waters (Rohling and Cooke, 1999), and changing water depth, or more likely a combination of these drivers. These possible controls on the benthic foraminiferal  $\delta^{18}\text{O}_{\text{SW}}$  records beyond temperature and global  $\delta^{18}\text{O}_{\text{SW}}$  compilation will be revisited in Section 6.4.4.1.

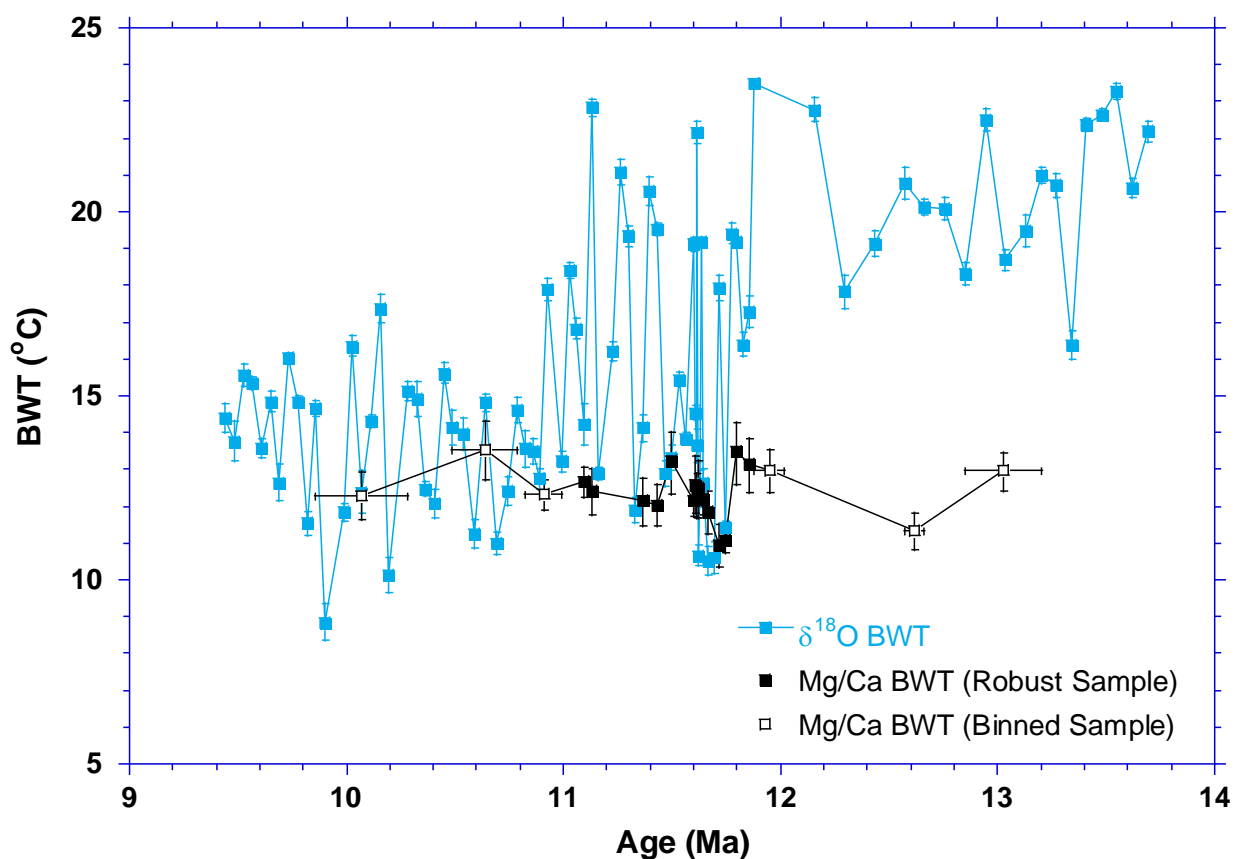


Figure 6.15: Bottom water temperature records at Sunbird-1 from benthic foraminiferal  $\delta^{18}\text{O}$  (blue) and Mg/Ca (black). The Mg/Ca record distinguishes between robust (filled symbols) and binned (open symbols) samples (see Chapter 5.4.4 for details). Error bars on the  $\delta^{18}\text{O}$  record denote the analytical uncertainty ( $\pm 2\text{SD}$ ), and error bars on the Mg/Ca record denote the sample uncertainty ( $\pm 2\text{SE}$ ). Binned Mg/Ca samples also have horizontal error bars denoting the age range the sample incorporates.

### 6.4.3 Sunbird-1 $\delta^{13}\text{C}$ as a recorder of global carbon cycling and local subsidence

Foraminiferal  $\delta^{13}\text{C}$  is primarily governed by the  $\delta^{13}\text{C}$  of the DIC of the seawater it precipitates from. The  $\delta^{13}\text{C}$  of DIC in the ocean is  $\sim 0\text{-}2\text{‰}$ , with surface enrichment of  $\delta^{13}\text{C}$  relative to the deep ocean due to the preferential utilisation of the lighter  $^{12}\text{C}$  during biological production in the euphotic zone (Zeebe and Wolf-Gladrow, 2001). The degradation of organic matter at depth releases this light carbon, lowering the  $\delta^{13}\text{C}$  of the deep ocean relative to the surface by  $\sim 1\text{‰}$  (Craig, 1970, Kroopnick, 1985). This flux of organic carbon from the surface ocean

reservoir to the deep ocean reservoir, the biological pump, is one aspect of the global carbon cycle. From 12 Ma onwards there is a consistent  $\sim 1\text{‰}$  offset between the benthic and planktic foraminiferal Sunbird-1  $\delta^{13}\text{C}$  records (Figure 6.6), variability in the two records tracking each other (Figure 6.2). This  $1\text{‰}$  offset between the two records is consistent with the expected  $\Delta\delta^{13}\text{C}$  resulting from the biological pump, the export of organic matter from the surface to deep ocean. This record of an active biological pump at the site suggests the water column was stratified at the site after 12 Ma. The corresponding decoupling of the  $\delta^{18}\text{O}$  records from this time supports the inference from the  $1\text{‰}$   $\Delta\delta^{13}\text{C}$  offset, that the Sunbird-1 ocean had thermal and chemical vertical gradients after 12 Ma. (Figure 6.4 and 6.7). Furthermore, Sunbird-1  $\delta^{13}\text{C}_{\text{BF}}$  values are relatively consistent with contemporaneous benthic

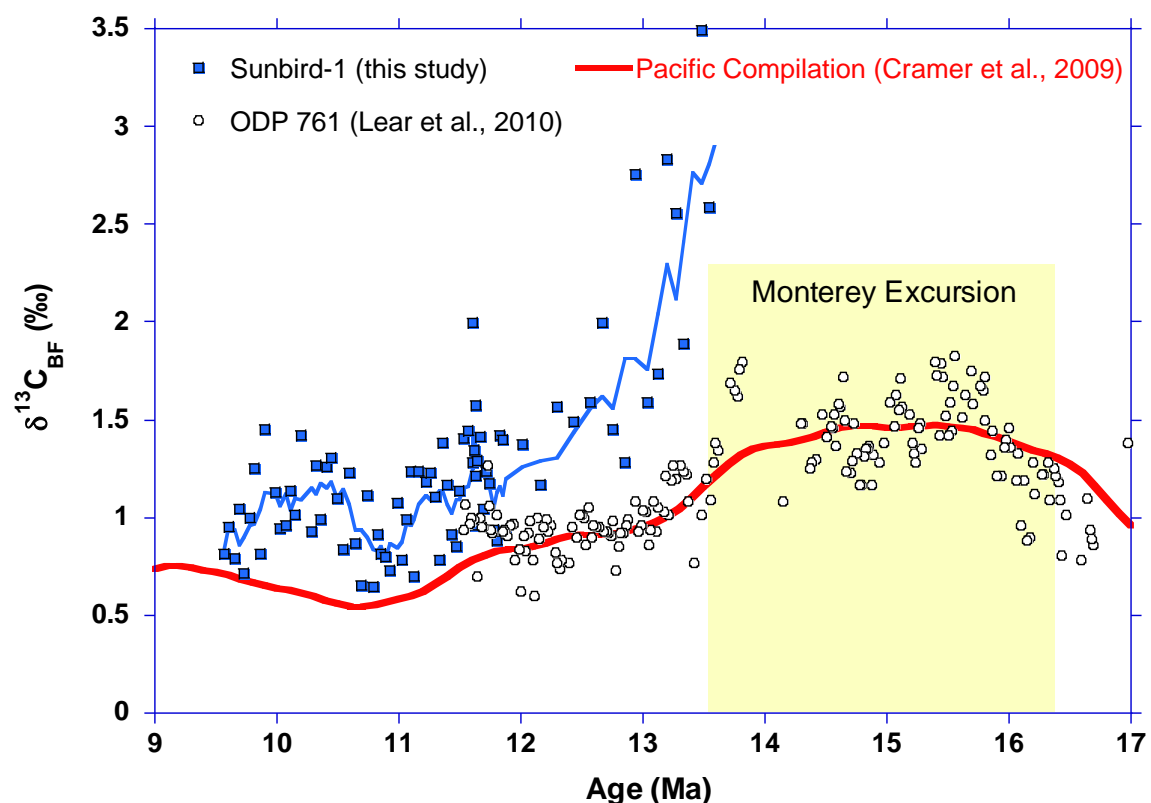


Figure 6.16: *C. mundulus*  $\delta^{13}\text{C}$  record from Sunbird-1 (filled blue squares) and its 5 point moving average (solid blue line). ODP Site 761 in the South East Indian Ocean (open circles) (Lear et al., 2010) and a Pacific compilation (red line) (Cramer et al., 2009) are shown for comparison. The positive  $\delta^{13}\text{C}$  excursion of the Monterey Excursion is highlighted by the yellow panel.

foraminiferal  $\delta^{13}\text{C}$  records from deep water sites across a range of ocean basins after 12 Ma (Lear et al., 2003, Cramer et al., 2009, Lear et al., 2010, Banerjee et al., 2017, Lear et al., 2015) (Figure 6.16). This suggests that by 12 Ma the site of deposition closely represents a deep water signal. However, prior to 12 Ma this is not the case, the standout features of the Sunbird-1  $\delta^{13}\text{C}$  records being the  $\sim 2\text{‰}$  negative shifts prior to 12 Ma. Despite their similarities in overall magnitude, the style and duration of the respective shifts differ (Figure 6.17). By investigating these shifts in the Sunbird-1  $\delta^{13}\text{C}_{\text{BF}}$  and  $\delta^{13}\text{C}_{\text{PF}}$  records prior to 12 Ma, and the differences between them, the influence of changes in the carbon cycle, both global and local, and the local subsidence at Sunbird-1, can be unravelled.

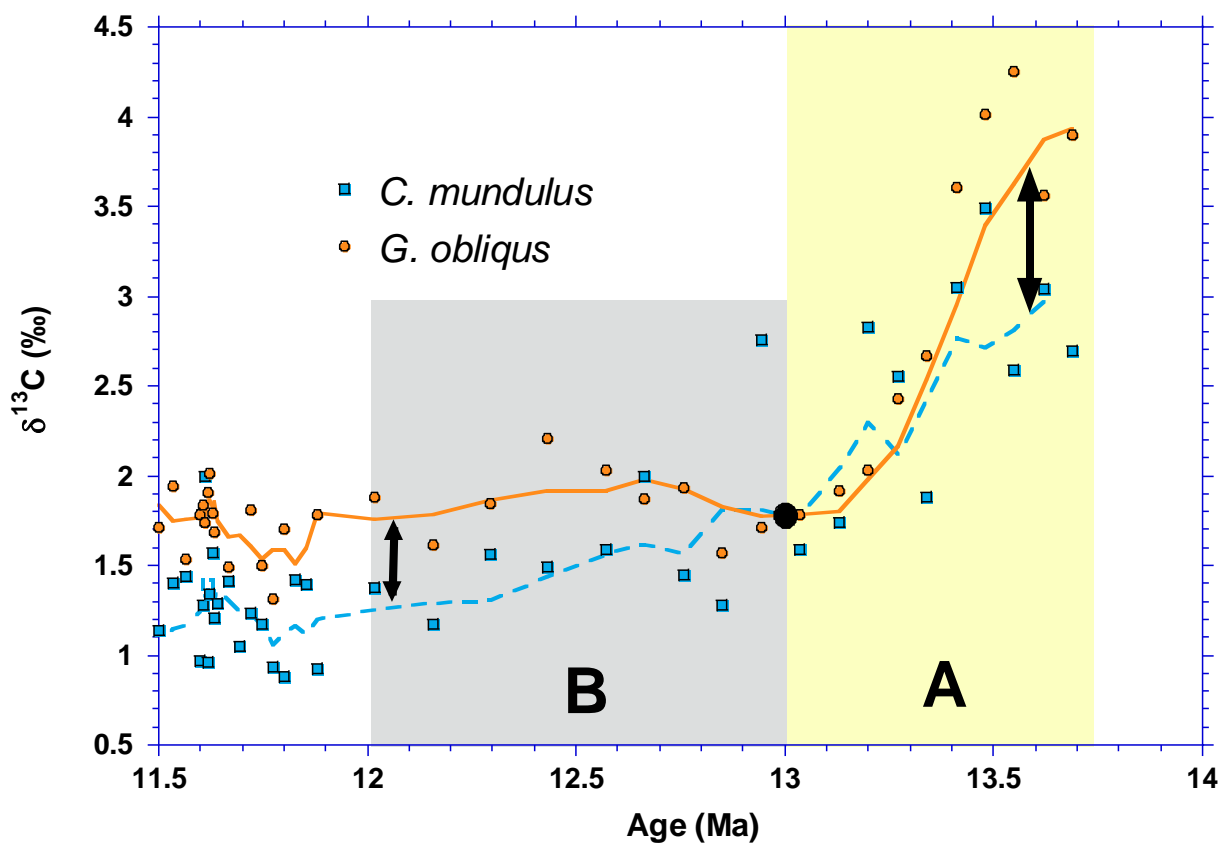


Figure 6.17:  $\delta^{13}\text{C}$  records for *C. mundulus* (blue squares) and *G. obliquus* (orange circles) from the 13.7 Ma to 11.5 Ma interval of the Sunbird-1 well. Five point moving averages are plotted, *C. mundulus* as a blue dashed line and *G. obliquus* as an orange solid line. Two intervals with different primary controls, as discussed in the text, are highlighted by the yellow (Interval A from 13.7 ma to 13.0 Ma) and grey (Interval B from 13.0 Ma to 12.0 Ma) panels. The black circle at 13.0 Ma indicates when  $\delta^{13}\text{C}_{\text{BF}} = \delta^{13}\text{C}_{\text{PF}}$ .

The majority of the  $\delta^{13}\text{C}_{\text{BF}}$  shift, and entirety of the  $\delta^{13}\text{C}_{\text{PF}}$  shift takes place between 13.7 Ma and 13.0 Ma, identified by the yellow panel (Interval A) in Figure 6.17. This coincides with the final recovery from the positive  $\delta^{13}\text{C}$  Monterey excursion (Figure 6.16). However, the magnitude of the global  $\delta^{13}\text{C}_{\text{sw}}$  signal (Cramer et al., 2009), and a record from ODP Site 761 in the South East Indian Ocean (Lear et al., 2010), between 13.7 Ma and 13.0 Ma is less than the observed signal in either Sunbird-1 record (Figure 6.16). This suggests that prior to 13 Ma benthic foraminifera from Sunbird-1 are not recording a global deep water signal, where  $\delta^{13}\text{C}$  is controlled primarily by the relative fluxes between seawater and other carbon reservoirs, and that other more localised effects also imparted an important control on the negative  $\delta^{13}\text{C}$  shifts prior to 13 Ma.

The  $\delta^{13}\text{C}$  records were adjusted for changes in seawater  $\delta^{13}\text{C}$  ( $\delta^{13}\text{C}_{\text{sw}}$ ) using the compilation of deep Pacific sites interpolated to a 0.1 Myr resolution (Cramer et al., 2009). Doing this removes the global  $\delta^{13}\text{C}_{\text{sw}}$  signal meaning any changes in  $\delta^{13}\text{C}$  seen in the Sunbird-1 record can be attributed to local effects (Figure 6.18). This allows for local geological interpretation, with particular reference to the subsidence of the site. A compilation of deep Pacific sites for this  $\delta^{13}\text{C}_{\text{sw}}$  adjustment is applied because the Pacific shows minimal changes in seawater chemistry over short timescales, the large ocean volume buffering any changes in seawater chemistry and carbon accumulation. The global signal accounts for  $\sim 0.7\%$  of the negative shift, decreasing the magnitude of the early excursion prior to 13 Ma in the  $\delta^{13}\text{C}_{\text{PF}}$  record to

~1.5‰, and in the  $\delta^{13}\text{C}_{\text{PF}}$  record to ~0.6‰ (Figure 6.18). This global signal reflects the final recovery from the positive carbon isotope excursion and associated  $\delta^{13}\text{C}$  maximum of the Monterey Excursion (CM6) resulting from increased organic carbon burial through the MCO (Vincent and Berger, 1985, Woodruff and Savin, 1991, Flower and Kennett, 1993a, Shevenell et al., 2004, Holbourn et al., 2014). Using the Pacific compilation acts to smooth the excursion that is recorded by single site records, (e.g. ODP 761 as shown in Figure 6.16) so this ~0.7‰ influence of the global signal is likely a conservative estimate. However, no single record from a deep water site displays a negative carbon isotope excursion in excess of 1‰ following the

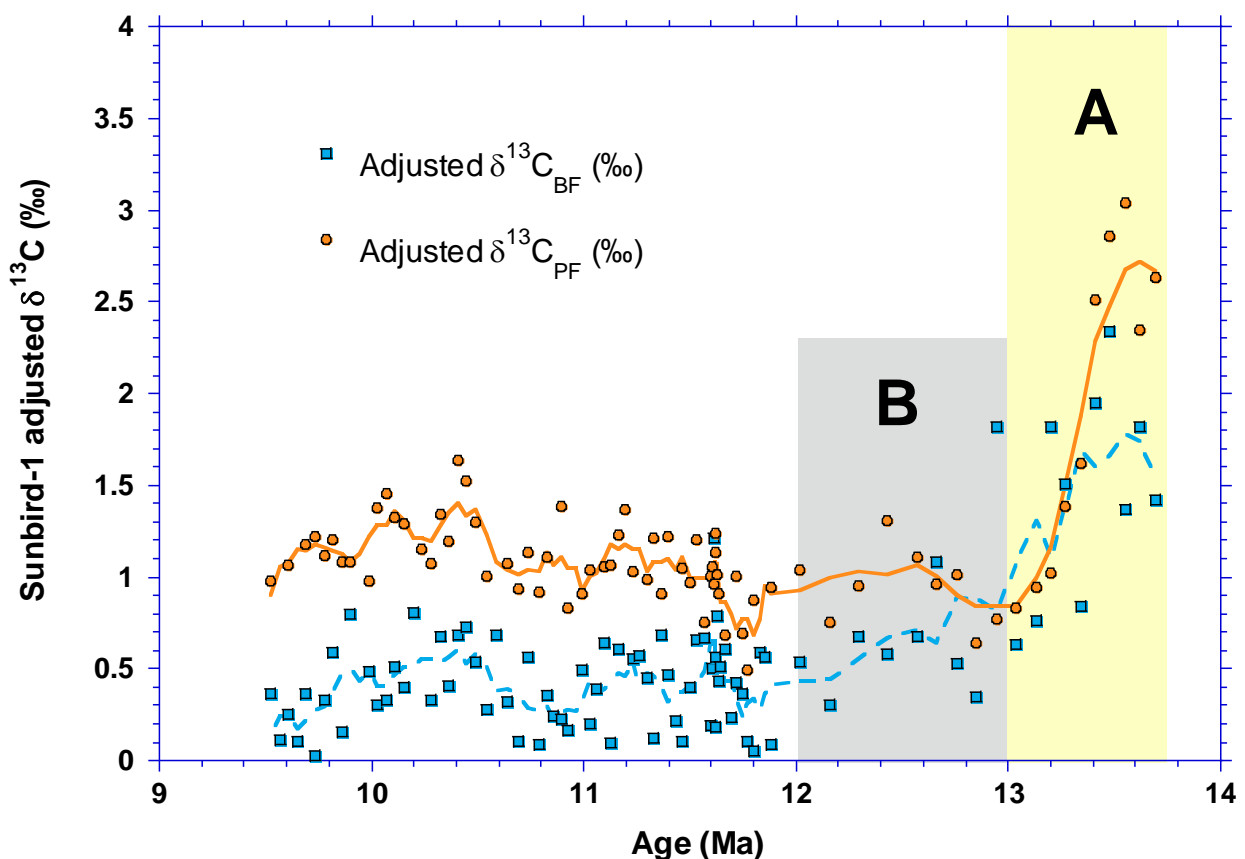


Figure 6.18: Adjusted benthic (blue squares) and planktic (orange circles) foraminiferal  $\delta^{13}\text{C}$  records from Sunbird-1 and their 5 point moving averages (dashed blue and solid orange lines respectively). The adjusted records have been corrected for the influence of the global  $\delta^{13}\text{C}_{\text{sw}}$  signal using a compilation of Pacific deep water sites (Cramer et al., 2009). Yellow (Interval A) and grey (Interval B) panels as Figure 6.17.

Monterey Excursion (Woodruff and Savin, 1991, Flower and Kennett, 1993a, Shevenell et al., 2004, Holbourn et al., 2007, Holbourn et al., 2014)

The  $\sim 0.7\text{‰}$  global  $\delta^{13}\text{C}_{\text{SW}}$  signal accounts for approximately one half of the  $\delta^{13}\text{C}_{\text{BF}}$  shift and approximately one third of the  $\delta^{13}\text{C}_{\text{PF}}$  shift prior to 13 Ma. This means that there remains a site specific negative shift which requires explaining. Because there is a larger total shift in  $\delta^{13}\text{C}_{\text{PF}}$  ( $\sim 2.2\text{‰}$ ) than there is in  $\delta^{13}\text{C}_{\text{BF}}$  ( $\sim 1.3\text{‰}$ ) through the 13.7 – 13.0 Ma interval (Figure 6.17), the shift in the  $\delta^{13}\text{C}_{\text{PF}}$  record adjusted for the global  $\delta^{13}\text{C}_{\text{SW}}$  signal ( $\sim 1.5\text{‰}$ ) is greater than the corresponding shift in the adjusted  $\delta^{13}\text{C}_{\text{BF}}$  record ( $\sim 0.6\text{‰}$ ) (Figure 6.18). Therefore, this local process has a significantly greater influence on the surface waters than the bottom waters. As discussed previously Sunbird-1 is located on a continental margin that was subsiding throughout the late Miocene having been sub-aerially exposed following the MMCT ( $\sim 13.8$  Ma). This subsidence out of the high productivity, surface water into waters with reduced primary productivity at depth could be the dominant influence on the  $\delta^{13}\text{C}_{\text{BF}}$  record prior to 13 Ma. However, this interpretation that the negative  $\delta^{13}\text{C}_{\text{BF}}$  shift prior to 13Ma reflects decreasing  $\delta^{13}\text{C}_{\text{SW}}$  values at increased water depth as the site subsides is not supported by the higher magnitude, synchronous  $\delta^{13}\text{C}_{\text{PF}}$  excursion of magnitude (Figure 6.18).

Here some potential explanations for these  $\delta^{13}\text{C}$  shifts between 13.7 Ma and 13.0 Ma from values  $>1\text{‰}$  higher than the global mean (Figure 6.16) are considered: (1) Sunbird-1 is recording the true magnitude of the global carbon isotope shift at this time, (2) Sunbird-1 is recording an amplification of the global  $\delta^{13}\text{C}$  signal, (3) Sunbird-1 was influenced by a varying

influx of waters from the Indian Ocean gyre, and (4) Sunbird-1 experienced declining local primary productivity.

One possible explanation is that the full 1.3‰ to 2.2‰ negative shift has a global cause. The Sunbird-1 record initiates within the  $\delta^{13}\text{C}$  maximum of CM6, and the Sunbird-1 negative  $\delta^{13}\text{C}$  shift is synchronous with the  $\sim 0.8\text{‰}$  shift recorded from open ocean sites during the recovery from CM6 (Holbourn et al., 2007, Lear et al., 2010, Holbourn et al., 2013). Is it possible that Sunbird-1 is recording the true magnitude of the positive  $\delta^{13}\text{C}$  excursion of CM6, and its signal is dampened in open ocean sites, as a result of bioturbation and low sedimentation rates? Using the simple model of Kump and Arthur (1999) the  $\sim 0.8\text{‰}$   $\delta^{13}\text{C}$  excursion at CM6 requires a  $\sim 70\%$  increase in burial of organic carbon globally (Badger et al., 2013). Therefore, a significantly greater, and likely unrealistic, increase in organic matter burial is required to have taken place if the 2.2‰ shift in the Sunbird-1  $\delta^{13}\text{C}_{\text{PF}}$  record represents the “true” global signal. This, in conjunction with an absence of evidence from other sites, suggests that a  $>2\text{‰}$  negative shift out of the CM6 carbon maxima is highly unlikely.

A second possibility is that shelf sites such as Sunbird-1 are more susceptible to higher magnitude changes in water mass  $\delta^{13}\text{C}$ , and hence record an amplified carbon maxima at CM6. The Monterey hypothesis states that during carbon maxima events there was lower oxygen levels and higher organic carbon within the sediment in marginal basin environments (Flower and Kennett, 1993b). This widespread sequestration of organic carbon in shallow marine basins (e.g. Sunbird-1) contributed to deep sea  $\delta^{13}\text{C}$  maxima, such as CM6 (Flower and Kennett, 1993b). Amplified sequestration, and subsequent release, of isotopically light

carbon at the site of Sunbird-1 could have locally amplified the global  $\delta^{13}\text{C}$  signal through the MCO, which Sunbird-1 records the recovery from.

Although possible, that the full shifts in the Sunbird-1  $\delta^{13}\text{C}$  records representing the true global signal, or an amplified version the global signal, is unlikely. This is because the absolute values of  $\delta^{13}\text{C}$  at Sunbird-1 are  $\sim 1.5\text{‰}$  greater than contemporaneous sites and  $>1\text{‰}$  higher than the maximum value of  $\sim 2.7\text{‰}$  in the modern open ocean (Boyer et al., 2013). Despite there being increased shallow remineralisation in a warmer world (John et al., 2014), it is more probable that a more localised process driving the surface seawater  $\delta^{13}\text{C}$  to  $>4\text{‰}$  on the Sunbird-1 continental shelf prior to  $\sim 13$  Ma is required. Early deposition at Sunbird-1 took place in a highly complex continental shelf environment proximal to the continent. The high absolute values at Sunbird-1 prior to 13 Ma could be due to Sunbird-1 being partially isolated from the open ocean. Consequently, there would have been a considerable influence from biological (e.g. primary productivity) and physical environmental (e.g. water mass mixing and riverine input) processes through the earliest interval of the record, prior to 13 Ma.

An increased influence of the nutrient poor Indian Ocean gyre would drive  $\delta^{13}\text{C}$  towards more typical values as the site subsided, the open ocean water mass having lower  $\delta^{13}\text{C}$  than the continental shelf. Physical processes such as riverine input can have a dominant influence on  $\delta^{13}\text{C}_{\text{DIC}}$  (Zeebe and Wolf-Gladrow, 2001). This can result in variability of up to  $1\text{‰}$  in  $\delta^{13}\text{C}$  on the local scale in shelf environments (Reynolds et al., 2017), supporting the potential for this being the cause of the substantially elevated Sunbird-1  $\delta^{13}\text{C}$  values prior to 13 Ma.

As well as the site of Sunbird-1 deposition, the global sea level fall of ~60 m associated with the MMCT would have subaerially exposed the proximal continental shelves, providing a source of organic carbon and nutrients. The resulting physical weathering of these exposed shelves likely delivered nutrients into the coastal waters via rivers. Enhanced supply of nutrients and organic matter from the nearby continent to the site of deposition may have resulted in extremely high primary productivity, and invigorated carbon remineralisation in the water column above Sunbird-1 deposition (John et al., 2014). This enhanced nutrient supply, increasing primary productivity, would have increased the  $\delta^{13}\text{C}_{\text{DIC}}$  of the water column (John et al., 2014) due to the preferential uptake of  $^{12}\text{C}$  by photosynthetic phytoplankton, a process commonly observed in coastal and upwelling regions characterised by high nutrient availability. This is supported by the downcore change in the concentrations of redox sensitive trace metals, which also indicate that in this early interval of the record Sunbird-1 was characterised by high primary productivity causing changeable sedimentary redox conditions (Chapter 3). Furthermore, through this interval prior to 13.0 Ma benthic foraminiferal B/Ca is at the lower limit of the reported, species-specific, range from core tops, despite the shallow water depth. It is important to note that the B/Ca records are not impacted by the contaminant coatings (Chapter 3). Therefore, it is suggested that prior to 13 Ma, invigorated remineralisation of organic matter raised  $\text{CO}_2$  and  $\Sigma\text{CO}_2$ , and hence decreased bottom water  $\Delta[\text{CO}_3^{2-}]$ .

A decrease in local primary productivity could cause a decrease in both of the benthic and planktic foraminiferal  $\delta^{13}\text{C}$  records, while also accounting for the shift in  $\delta^{13}\text{C}_{\text{PF}}$  being greater than the coeval shift in  $\delta^{13}\text{C}_{\text{BF}}$  (Figure 6.19). A decrease in productivity, and the associated

reduction in organic matter remineralisation, is again supported by the increase in between B/Ca, and therefore  $\Delta[\text{CO}_3^{2-}]$  between 13.7 Ma and 13.0 Ma (Chapter 3). Local coastal effects on  $\delta^{13}\text{C}$  have a much lower influence on  $\delta^{18}\text{O}$ , which is primarily driven by global and regional changes in temperature, salinity, and  $\delta^{18}\text{O}_{\text{sw}}$  (Emiliani, 1955, Craig and Gordon, 1965, Shackleton, 1967). Therefore, crucially, the changes in productivity inferred as having a significant influence on the  $\delta^{13}\text{C}$  records would have a negligible impact on the  $\delta^{18}\text{O}$  signal, evidenced by their lack of correlation.

The favoured explanation for the  $\delta^{13}\text{C}$  shift from exceptionally high isotopical values at 13.7 Ma is that of declining productivity from a regime with extremely high local productivity to a regime with more typical productivity for a coastal location. This explains both the simultaneous negative shift in both records, and the greater magnitude of the shift in the planktic foraminiferal  $\delta^{13}\text{C}$  record. Furthermore, this explanation agrees with the benthic foraminiferal trace metal records.

Between 13.0 Ma and 12.0 Ma the  $\delta^{13}\text{C}_{\text{PF}}$  record remains stable while the  $\delta^{13}\text{C}_{\text{BF}}$  has a further  $\sim 0.6\text{‰}$  negative shift (Interval B in Figure 6.16). This part of the record is primarily controlled by subsidence, influencing  $\delta^{13}\text{C}_{\text{BF}}$  without having any effect on the  $\delta^{13}\text{C}_{\text{PF}}$  record (Figure 6.20). Although the tectonic subsidence of the site would have had an influence between 13.7 Ma and 13.0 Ma, the shift from a higher productivity regime to a lower productivity regime is the

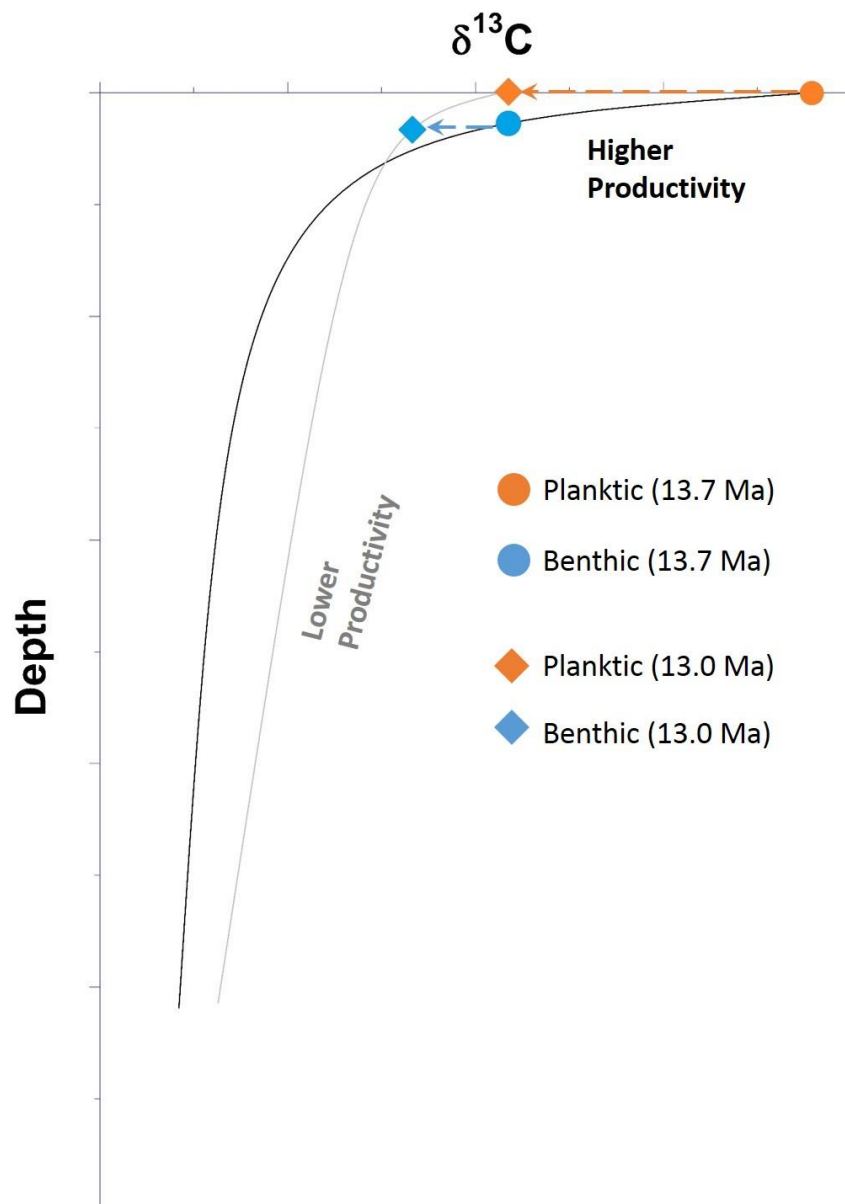


Figure 6.19: Schematic  $\delta^{13}\text{C}$  water depth profiles for a high productivity setting (black line) and a low productivity setting (grey). The impact of the proposed transition from the higher productivity setting to the lower productivity setting between 13.7 Ma (circles) and 13.0 Ma (diamonds) on the planktic (orange) and benthic (blue) foraminiferal  $\delta^{13}\text{C}$  records is shown.

dominant process on the  $\delta^{13}\text{C}$  signal through this interval. This changes between 13.0 Ma and 12.0 Ma, when the tectonic subsidence of the basin becomes the dominant process influencing the  $\delta^{13}\text{C}$  records (Figure 6.20). There is a lack of benthic foraminiferal Mg/Ca data, reconstructing BWT, through this interval identified by the shifts in the  $\delta^{13}\text{C}$  records (Figure 6.21). Unfortunately, this precludes an accurate assessment of whether BWT decreased

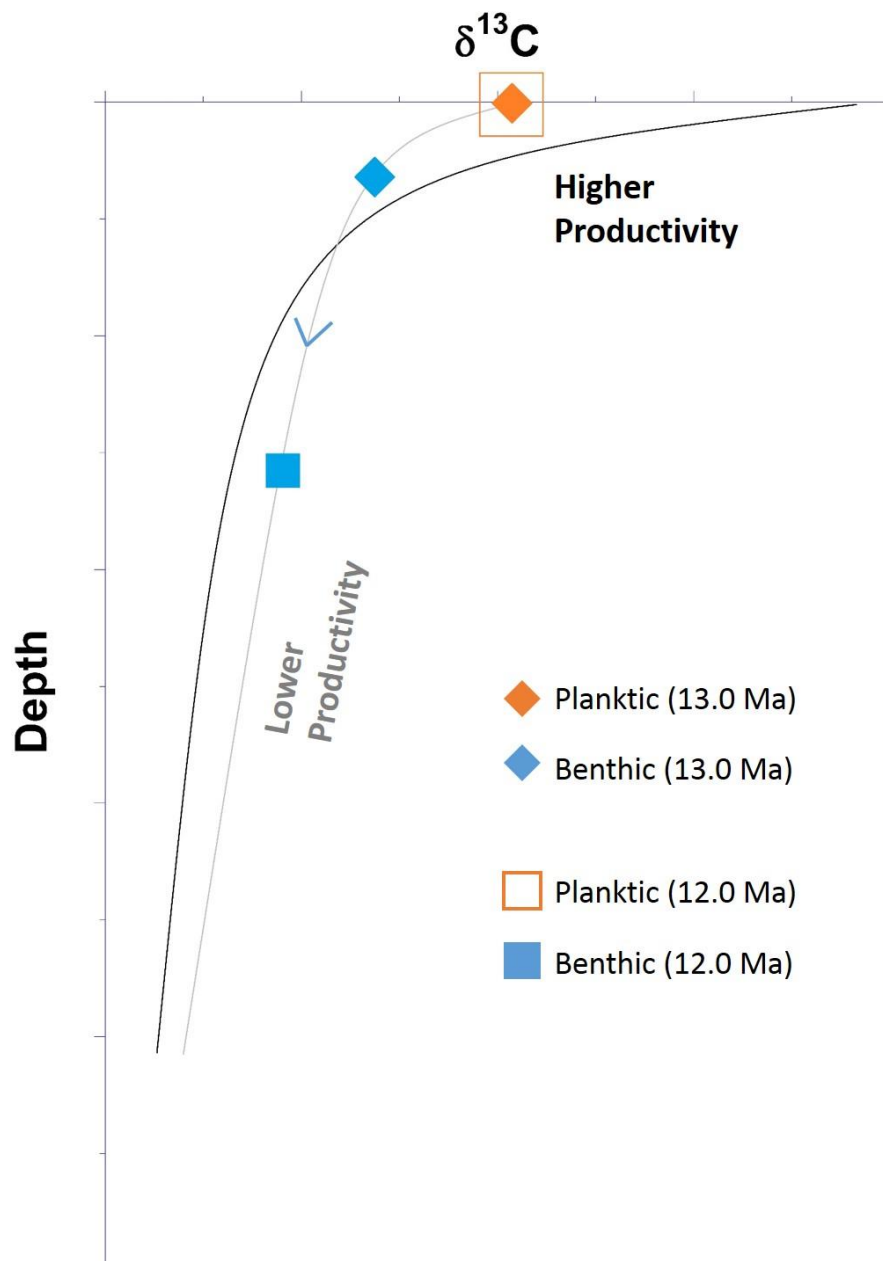


Figure 6.20: Schematic  $\delta^{13}\text{C}$  water depth profiles for a high productivity setting (black line) and a low productivity setting (grey). The impact of subsidence of the site, after the prior transition to the lower productivity setting, between 13.0 Ma (diamonds) and 12.0 Ma (squares) on the planktic (orange) and benthic (blue) foraminiferal  $\delta^{13}\text{C}$  records is shown.

between 13.0 Ma and 12.0 Ma. This would be expected if the  $\delta^{13}\text{C}$  record was recording subsidence, the chemocline and thermocline being intrinsically linked, physical mixing resulting in the upper ~50 m of the water column being characterised by relatively constant conditions, at the modern day site of Sunbird-1 (World Ocean Database, 2013) (Figure 6.22).

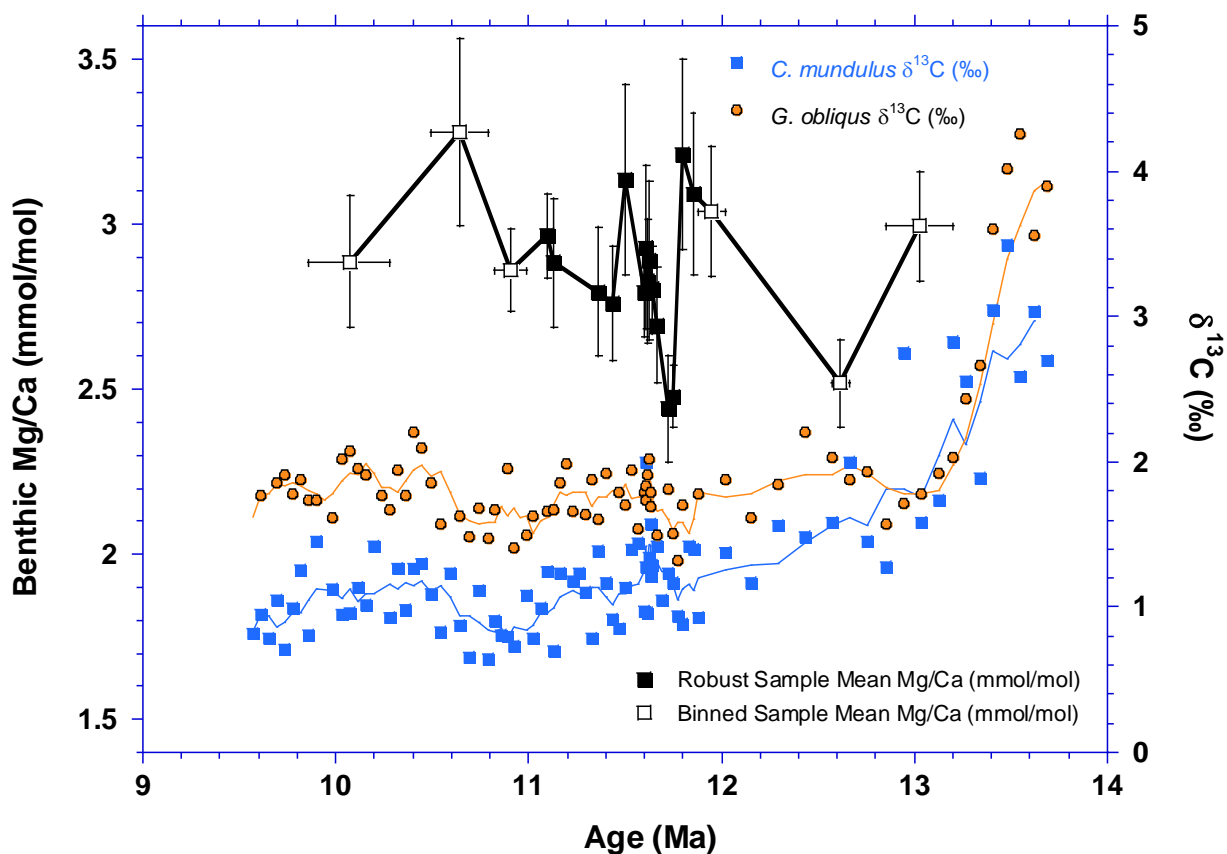


Figure 6.21: Benthic  $\delta^{13}\text{C}$  (blue squares), and planktic  $\delta^{13}\text{C}$  (orange circles) foraminiferal records from Sunbird-1 plotted alongside the benthic foraminiferal Mg/Ca (black) Sunbird-1 record.

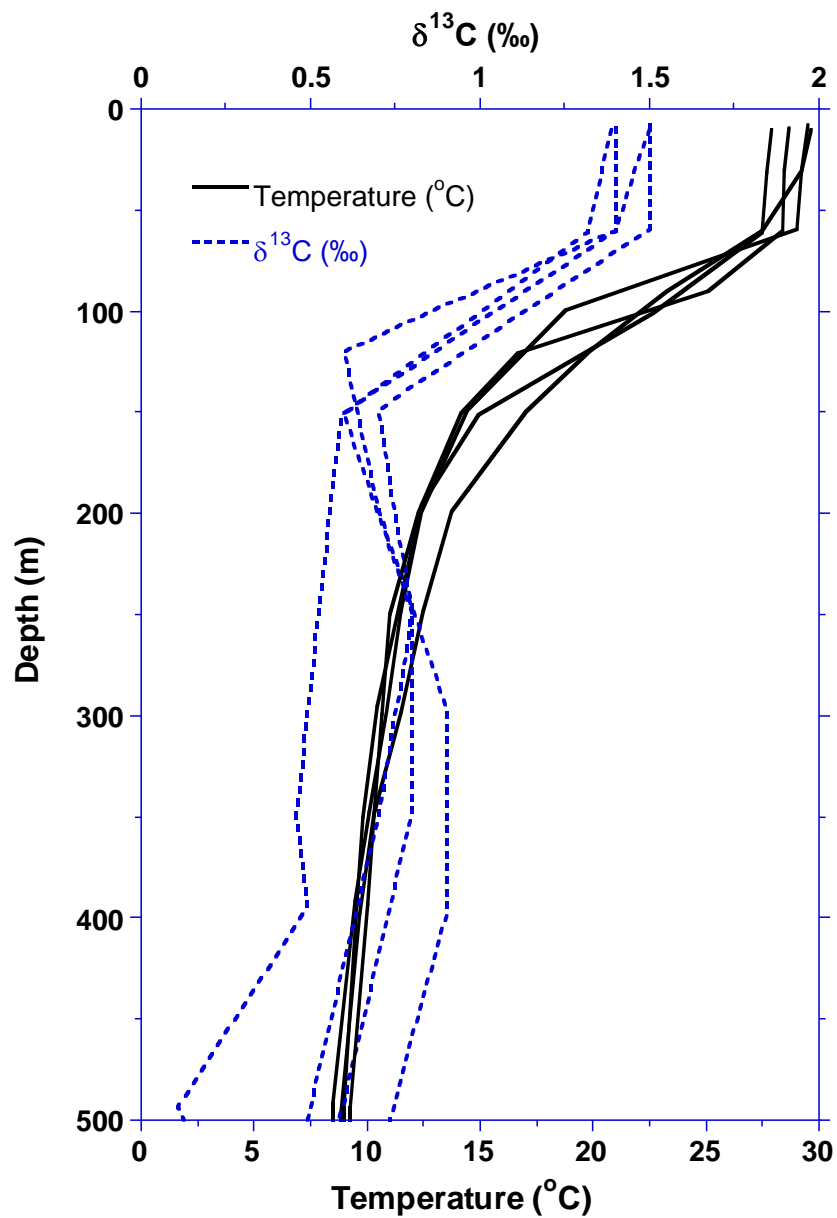


Figure 6.22:  $\delta^{13}\text{C}$  (blue dashed) and temperature (black solid) profiles for the upper 500m of the water column from the 4 CTD profiles in a  $15^\circ \times 15^\circ$  grid square around the modern day site of Sunbird-1 in the SW Indian Ocean (World Ocean Database 2013 [\(Boyer et al., 2013\)](#)).

#### 6.4.4 Global ice volume and local oceanographic controls on Sunbird-1 $\delta^{18}\text{O}_{\text{sw}}$

The oxygen isotope composition ( $\delta^{18}\text{O}$ ) of foraminiferal calcite is primarily controlled by calcification temperature and the oxygen isotope composition of the seawater ( $\delta^{18}\text{O}_{\text{sw}}$ ) it calcifies from (Emiliani, 1955, Shackleton, 1967) (Chapter 2.2.1.1). Using an independent proxy for temperature, such as Mg/Ca, can simultaneously isolate the  $\delta^{18}\text{O}_{\text{sw}}$  component of the  $\delta^{18}\text{O}$  record (Lear et al., 2000, Billups and Schrag, 2002). The  $\delta^{18}\text{O}_{\text{sw}}$  of foraminiferal calcite is principally controlled by global continental ice volume and the local evaporation-precipitation, which correlates with salinity. Further local variability resulting from advection, melting icebergs and sea ice, and freshwater input from rivers can influence the  $\delta^{18}\text{O}_{\text{sw}}$  (Rohling and Cooke, 1999, Pearson, 2012), although not all will be relevant at Sunbird-1, in particular melting icebergs and sea ice. Because the deep ocean is largely unaffected by local changes the primary driver of  $\delta^{18}\text{O}_{\text{sw}}$  change in deep water sites is global continental ice volume, the growth of ice sheets elevating  $\delta^{18}\text{O}_{\text{sw}}$ . Changes in salinity do influence deep water  $\delta^{18}\text{O}_{\text{sw}}$ , especially due to water mass changes, albeit the signals are a lot smaller than those at the surface. Global ice volume during the mid to late Miocene interval covered by Sunbird-1 is commonly regarded to be relatively stable following the expansion of the EAIS to a land-based ice sheet across the MMCT (Flower and Kennett, 1994, Lear et al., 2003, Lewis et al., 2007, John et al., 2011).

As described previously, there is very little downcore correlation (Figure 6.4) or covariance (Figure 6.5) between the benthic and planktic foraminiferal  $\delta^{18}\text{O}$  records. This lack of association between the benthic and planktic foraminiferal  $\delta^{18}\text{O}$  records cannot be explained by temperature variability, as it is still apparent in the respective  $\delta^{18}\text{O}_{\text{sw}}$  records (Figure 6.11).

Not only does this suggest they have different primary controls but also that there was significant decoupling of the planktic and benthic water masses throughout the Sunbird-1 interval.

#### 6.4.4.1 Local oceanographic control on Sunbird-1 benthic foraminiferal $\delta^{18}O_{SW}$

Sunbird-1  $\delta^{18}O_{BF}$  values are considerably lower than contemporaneous benthic foraminiferal  $\delta^{18}O$  records from a range of ocean basins (Zachos et al., 2001, Lear et al., 2003, Westerhold

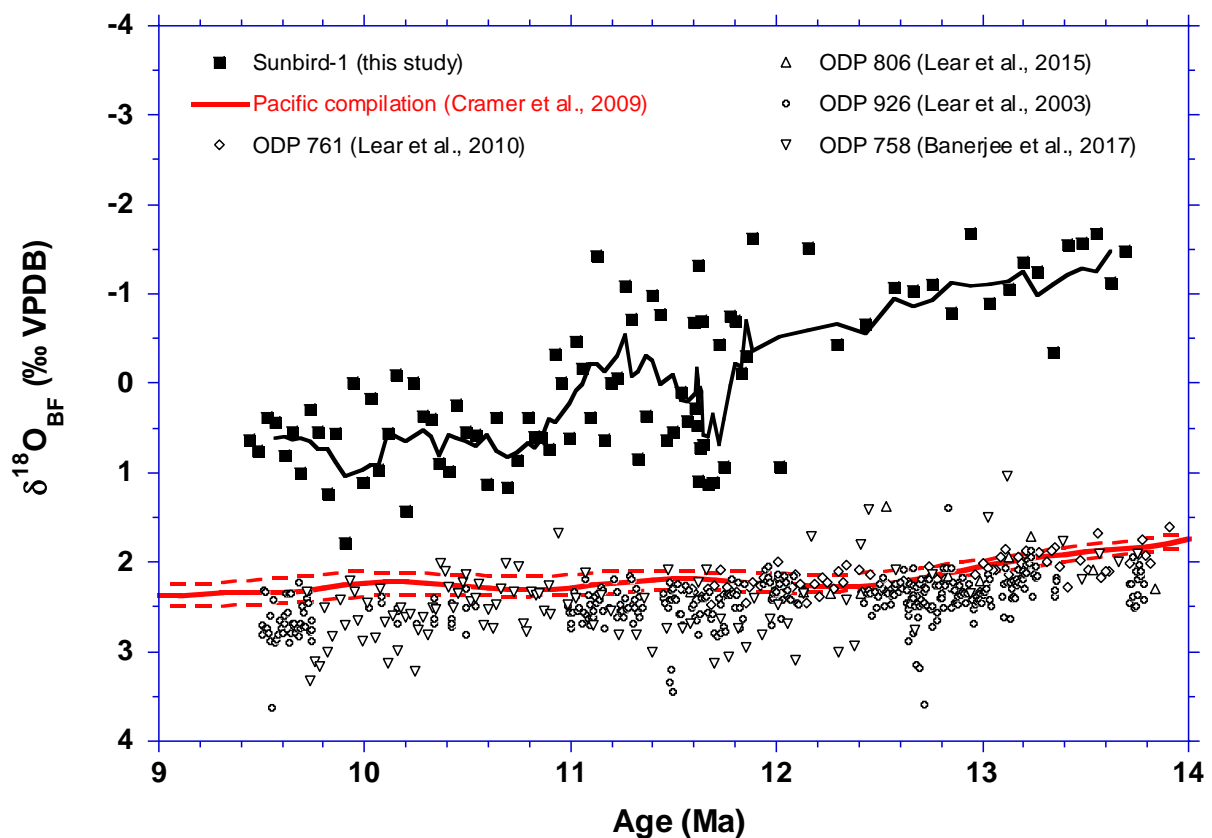


Figure 6.23: *C. mundulus*  $\delta^{18}O$  record from Sunbird-1 (filled squares) and its 5 point moving average (solid line). Previously published records from ODP Site 758 in the Indian Ocean (Banerjee et al., 2017) (open downward triangles), ODP Site 761 off North West Australia (Lear et al., 2010) (open diamonds), ODP Site 806 in the western equatorial Pacific (Lear et al., 2015) (open upward triangles), and ODP Site 926 in the western equatorial Atlantic (open circles) (Lear et al., 2003) are plotted as open symbols for comparison. The trend from a compilation of Pacific sites is shown as a red line, with dashed red lines as 95% confidence intervals (Cramer et al., 2009).

et al., 2005, Zachos et al., 2008, Cramer et al., 2009, Lear et al., 2010, Holbourn et al., 2013, Lear et al., 2015, Banerjee et al., 2017) (Figure 6.23). Using the Sunbird-1 Mg/Ca records to independently constrain temperature, isolating the  $\delta^{18}\text{O}_{\text{SW}}$  component of the Sunbird-1  $\delta^{18}\text{O}_{\text{BF}}$  record, shows that the warmer BWT at Sunbird-1 accounts for some, but not all, of this observed difference (Figure 6.24). The  $\sim 1.5\text{‰}$  increase in benthic foraminiferal  $\delta^{18}\text{O}_{\text{SW}}$  over the whole record is significantly greater than the  $\sim 0.5\text{‰}$  increase, considered to reflect Antarctic Ice Sheet expansion, at more typical open ocean benthic sites (Lear et al., 2010, Cramer et al., 2011, Lear et al., 2015). The calibration between  $\delta^{18}\text{O}_{\text{SW}}$  and ice volume, and therefore eustatic sea level, are poorly constrained beyond the Pleistocene. By assuming the maximum  $1.29\text{‰}$   $\delta^{18}\text{O}_{\text{SW}}$  change/100m of Gasson et al. (2016), determined using a cold climate, high eccentricity model scenario incorporating approximate mid-Miocene topography, solely invoking changes in global continental ice volume to explain the Sunbird-1 benthic foraminiferal  $\delta^{18}\text{O}_{\text{SW}}$  increase would require a  $\sim 120\text{m}$  sea level equivalent ice sheet expansion. This is likely a conservative estimate and would require a significant contribution of permanent Northern Hemisphere ice sheets in addition to further increase of Antarctic ice volume increase following the MMCT. This is highly unfeasible, with recent estimates of EAIS volume following the MMCT of at least 89% modern day ice volume (John et al., 2011), and greater than modern day ice volume (Lear et al., 2015). Furthermore, a significant contribution from Northern hemisphere ice sheets would be required despite major Cenozoic Northern hemisphere glaciation likely originating around 2.7 Ma (Sosdian and Rosenthal, 2009, Bailey et al., 2013), although ephemeral ice sheets and isolated glaciers on Greenland may have persisted since the late Eocene (Eldrett et al., 2007). This strongly suggests that Sunbird-1 benthic foraminiferal  $\delta^{18}\text{O}_{\text{SW}}$  is not recording a typical global deep-water signal, controlled primarily by the waxing and waning of high latitude continental ice sheets,

something which is unsurprising considering the shallow water depth of deposition. Additionally absolute benthic foraminiferal  $\delta^{18}\text{O}_{\text{sw}}$  values prior to 12.0 Ma are isotopically lighter, suggesting continental lower ice volume, than those of an ice free Eocene world, -0.89‰ (Cramer et al., 2011). Therefore, the Sunbird-1 benthic foraminiferal  $\delta^{18}\text{O}_{\text{sw}}$  record should be considered in terms of local and regional effects, these dominating over the influence of changes in continental ice volume.

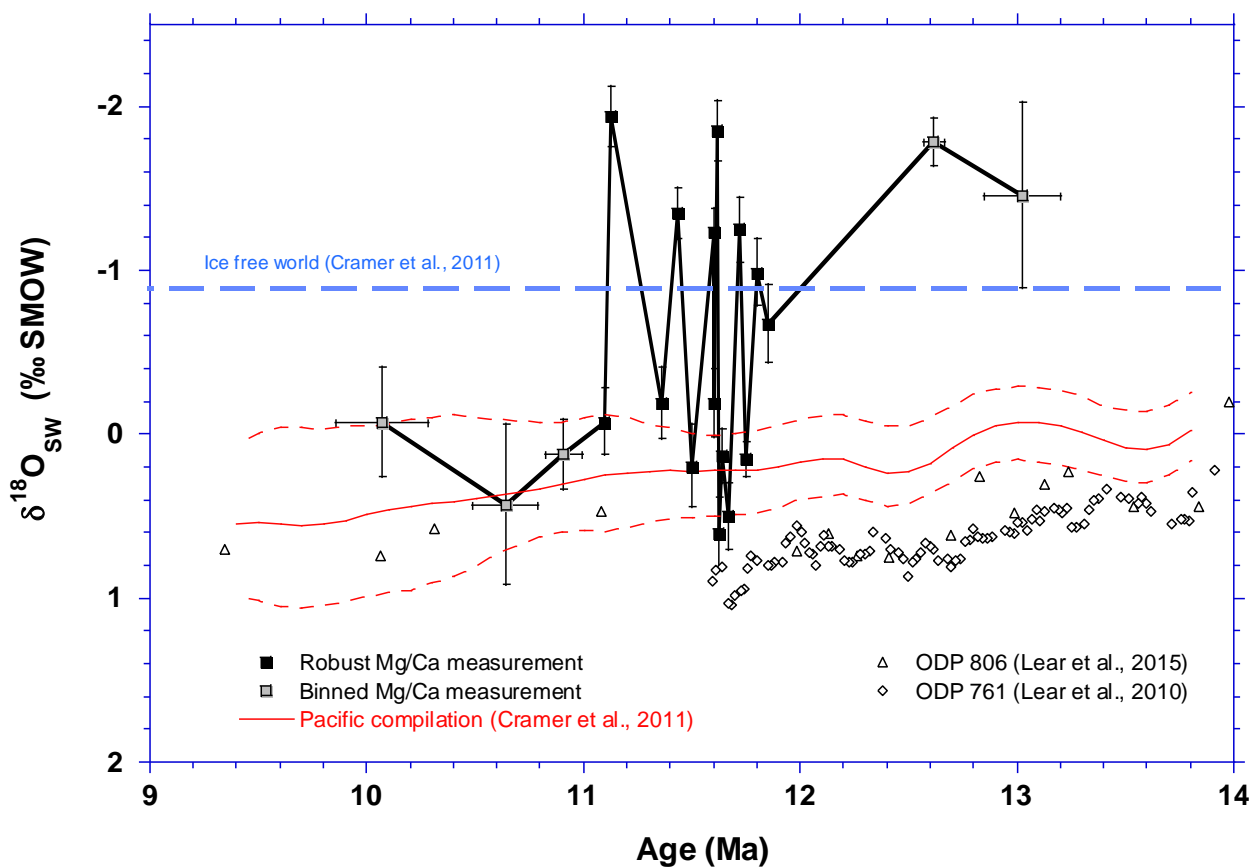


Figure 6.24: Sunbird-1 benthic foraminiferal  $\delta^{18}\text{O}_{\text{sw}}$  record as Figure 6.11b distinguishing between temperatures from Mg/Ca samples regarded as robust (black squares) and binned (grey squares) (see Chapter 5.4.4 for details). Binned samples have horizontal error bars denoting the age range the sample incorporates. Vertical error bars denote the cumulative analytical and sample uncertainty of the  $\delta^{18}\text{O}$  and Mg/Ca values ( $\pm 2\text{SD}$ ). Previously published benthic foraminiferal  $\delta^{18}\text{O}_{\text{sw}}$  records from ODP Site 761 off North West Australia (Lear et al., 2010) (open diamonds) and ODP Site 806 in the western equatorial Pacific (Lear et al., 2015) (open upward triangles) are plotted as open symbols for comparison. The trend from a compilation of Pacific sites is shown as a red line, with dashed red lines as 90% confidence intervals (Cramer et al., 2011). The ice free Eocene  $\delta^{18}\text{O}_{\text{sw}}$  value of -0.89‰ (SMOW) (Cramer et al., 2011) is shown as a horizontal blue dashed line.

The high magnitude point-to-point variability of up to 2‰ seen between 11.8 Ma and 11.0 Ma in the Sunbird-1 benthic foraminiferal  $\delta^{18}\text{O}_{\text{SW}}$  record is uncharacteristic for deep water sites (Figure 6.24). That the extremely high magnitude benthic foraminiferal  $\delta^{18}\text{O}_{\text{SW}}$  is not associated with any BWT trend (Chapter 5) makes it all the more perplexing. To be solely explained in terms of ice volume variability would require repeated growth and melting of the entire EAIS on  $10^5$  year timescales. Although likely having an influence, the 2‰ magnitude of the point-to-point variability in the benthic foraminiferal  $\delta^{18}\text{O}_{\text{SW}}$  cannot be solely explained by a dynamic East Antarctic Ice Sheet (Figure 6.24). This is similar to the  $\sim 1.5\%$  increase in benthic foraminiferal  $\delta^{18}\text{O}_{\text{SW}}$  through the interval as a whole, in that the higher magnitude point-to-point variability suggests that any influence of changing global ice volume is drowned out by another primary control. This primary control must account for a  $\sim 1\%$  increase in benthic foraminiferal  $\delta^{18}\text{O}_{\text{SW}}$  through the record as well as the majority of the up to 2‰ point to point variability, without incorporating any significant BWT variability at the site. Additionally, the respective planktic foraminiferal Mg/Ca and  $\delta^{18}\text{O}$  records show minimal variability, and therefore the surface waters at Sunbird-1 demonstrate a lack of response to this primary driver of benthic foraminiferal  $\delta^{18}\text{O}_{\text{SW}}$  change.

Only correcting for the global  $\delta^{18}\text{O}_{\text{SW}}$  compilation when calculating BWT from  $\delta^{18}\text{O}_{\text{BF}}$  reconstructs BWT on average  $8^\circ\text{C}$  warmer than the Mg/Ca BWT record prior to  $\sim 11.8$  Ma (Figure 6.15). This suggests one of two things; that benthic foraminiferal  $\delta^{18}\text{O}_{\text{SW}}$  is being driven to more negative values through this interval, or that the Mg/Ca BWT record misses a cooling trend through the record by reconstructing artificially low BWT temperatures prior to 11.8 Ma, or a combination of both. The magnitude of the variability in the  $\delta^{18}\text{O}_{\text{BF}}$  record

between 11.8 Ma and 11.0 Ma mean it is likely forced by a combination of changes in temperature and  $\delta^{18}\text{O}_{\text{SW}}$  (driven by salinity). Reconstructed BWT using both techniques are extremely similar, and the benthic foraminiferal  $\delta^{18}\text{O}_{\text{SW}}$  values are similar to those of more typical deep water sites after 11 Ma (Figure 6.24), suggesting this complicated process no longer has a significant influence on the benthic foraminiferal  $\delta^{18}\text{O}_{\text{SW}}$ .

Assuming Mg/Ca BWT is correct and there is no cooling trend through the record, the lighter  $\delta^{18}\text{O}_{\text{SW}}$  of the bottom water mass which dominates prior to  $\sim 11.8$  Ma may be influenced by fresh water input from the continent, the site being more proximal to the continent and having not subsided to deeper waters. Lower salinity water masses, such as those influenced by significant fresh water run-off, are characterised by more negative  $\delta^{18}\text{O}$  values (Craig and Gordon, 1965, Duplessy et al., 1991, Srivastava et al., 2007). By 11.0 Ma the Sunbird-1 bottom water mass is no longer influenced by this continental fresh water input, likely due to having subsided deep enough to be permanently bathed by a deep water mass. The suggestion of a change in dominant water mass from one of lower salinity influenced by fresh water input from the continent, to one more typical of an open ocean site with higher salinity waters could be investigated by foraminiferal abundance work. If this suggestion is correct, planktic foraminiferal abundance would increase at  $\sim 11.8$  Ma, because planktic foraminifera dislike shallow, low salinity waters.

From  $\sim 11.8$  Ma- 11.0 Ma the benthic foraminiferal  $\delta^{18}\text{O}_{\text{SW}}$  record fluctuates between the values of these two intervals, causing the high magnitude and high frequency oscillations in the benthic foraminiferal  $\delta^{18}\text{O}_{\text{SW}}$  record. Again, assuming that the Mg/Ca BWT record is

robust and there is no significant influence of temperature through this interval, the high magnitude and high frequency benthic foraminiferal  $\delta^{18}\text{O}_{\text{sw}}$  variability of up to 2.0‰ displayed between 11.8 Ma and 11.0 Ma is a record of fluctuations between two oceanographic regimes with contrasting water mass properties, one that prevails prior to 11.8 Ma and the other after 11.0 Ma. Through this interval of transition, the bottom water properties influencing  $\delta^{18}\text{O}_{\text{sw}}$  flip dramatically between these two end member states, recording highly dynamic and variable bottom water conditions. This emphasises that Sunbird-1 was an extremely dynamic oceanographic region.

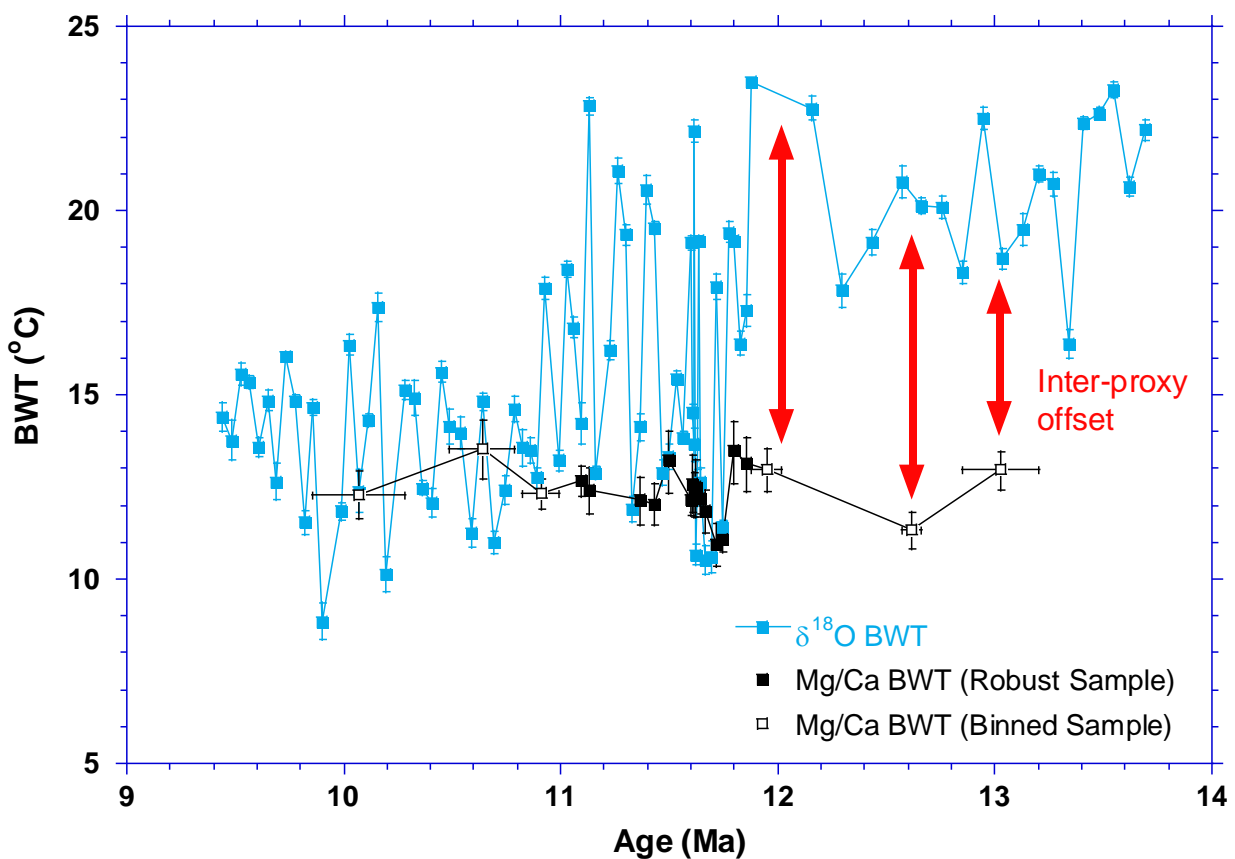


Figure 6.25: Bottom water temperature records at Sunbird-1 from benthic foraminiferal  $\delta^{18}\text{O}$  (blue) and Mg/Ca (black). The Mg/Ca record distinguishes between robust (filled symbols) and binned (open symbols) samples (see Chapter 5.4.4 for details). Error bars on the  $\delta^{18}\text{O}$  record denote the analytical uncertainty ( $\pm 2\text{SD}$ ), and error bars on the Mg/Ca record denote the sample uncertainty ( $\pm 2\text{SE}$ ). Binned Mg/Ca samples also have horizontal error bars denoting the age range the sample incorporates. The vertical red arrows indicate the 5-10°C difference between the two proxies prior to 12.0 Ma, an interval through which there are no robust Mg/Ca BWT estimates.

The possibility that the LA-ICP-MS Mg/Ca record misses a cooling trend in the bottom water temperatures has to be considered. This is particularly relevant because of the lack of robust Mg/Ca temperature data prior to 12.0 Ma, the interval where there is a 5-10°C difference between the two records of proxy reconstructed BWT (Figure 6.25). Furthermore, for the high frequency 2‰ point to point variability in the  $\delta^{18}\text{O}_{\text{BF}}$  record to be solely explained by changes in salinity would require changes of ~12 PSU using the LeGrande and Schmidt (2006) Indian Ocean calibration (Equation 6.3). This seems unrealistic. The absence of a cooling trend in the Mg/Ca BWT record and the high point to point variability in the  $\delta^{18}\text{O}$  record can be explained by the LA-ICP-MS BWT record only sampling the cool parts of the record. The strict and thorough screening criteria employed to remove LA-ICP-MS profiles with elevated Mg/Ca values resulting from contamination by a Mg-Mn-rich diagenetic outer coating has likely created a selection bias. This selection bias in the LA-ICP-MS BWT record, removing high bottom water temperatures, does not exist in the benthic foraminiferal  $\delta^{18}\text{O}$  record (Figure 6.25).

The subsidence of the basin means a cooling trend would be expected. This is supported by the trend in the *H. elegans* Sr/Ca solution ICP-MS record which demonstrates a ~7°C cooling using the BWT calibration of Rosenthal et al. (2006) incorporating only samples from the Indonesian Seaway, waters oversaturated with respect to aragonite (Lear et al., 2008). Although the absolute bottom water temperatures reconstructed by this solution ICP-MS record cannot be assumed reliable due to the large sedimentary redox signal (Chapter 3), the relative trend indicates a ~7°C cooling trend. Using the  $\delta^{18}\text{O}$  equation of Lynch-Stieglitz et al.

(1999) a 7°C cooling trend equates to a ~1.5‰ increase in  $\delta^{18}\text{O}$  meaning a much more realistic salinity variability of only ~1 PSU is required to explain the  $\delta^{18}\text{O}_{\text{BF}}$  signal.

Irrespective of the controlling factor on the complicated  $\delta^{18}\text{O}_{\text{BF}}$  record, changes in the salinity of the water mass bathing the bottom waters, a cooling trend which has been missed by the LA-ICP-MS Mg/Ca BWT record, or a combination of both, the stability of the  $\delta^{18}\text{O}_{\text{PF}}$  record indicates that this only influences the bottom waters, and not the surface waters. The clear decoupling of the benthic and planktic foraminiferal  $\delta^{18}\text{O}$  signals from 11.8 Ma onwards strongly suggests that the site has subsided sufficiently for the bottom waters to be bathed by a different water mass than the surface waters.

#### 6.4.4.2 *Long term evolution of global ice volume*

There is a general increasing trend with a total magnitude of between 0.10‰ and 0.96‰ through the Sunbird-1 planktic foraminiferal  $\delta^{18}\text{O}_{\text{SW}}$  record (Figure 6.26). The noisiness from the uncertainty in the Mg/Ca measurements causes the high degree of uncertainty in this trend. However, even incorporating this uncertainty the relative trend of increasing  $\delta^{18}\text{O}_{\text{SW}}$  through the record is robust. The approximately 0.5‰ magnitude of this  $\delta^{18}\text{O}_{\text{SW}}$  increase between 13.3 Ma and 9.5 Ma is similar to that of more typical deep water sites (Billups and Schrag, 2003, Lear et al., 2003, Lear et al., 2010, Lear et al., 2015), and the global compilation (Cramer et al., 2011). Therefore, this general long term increasing trend in planktic foraminiferal  $\delta^{18}\text{O}_{\text{SW}}$  at Sunbird-1 is recording the long term evolution of global continental ice volume. The 0.5‰ increase in  $\delta^{18}\text{O}_{\text{SW}}$  through the record corresponds to a 39-48m sea level equivalent increase in continental ice volume using the range of Miocene  $\delta^{18}\text{O}_{\text{SW}}$

sensitivities of Gasson et al. (2016). The well constrained absolute SST estimates through the mid-late Miocene (Chapter 5) mean that the absolute  $\delta^{18}\text{O}_{\text{SW}}$  values presented here are a major improvement on previous studies which are relatively poorly constrained through the interval (Lear et al., 2003, Lear et al., 2010, Lear et al., 2015). Therefore, the confidence in there being increased continental ice volume through the unipolar icehouse interval following

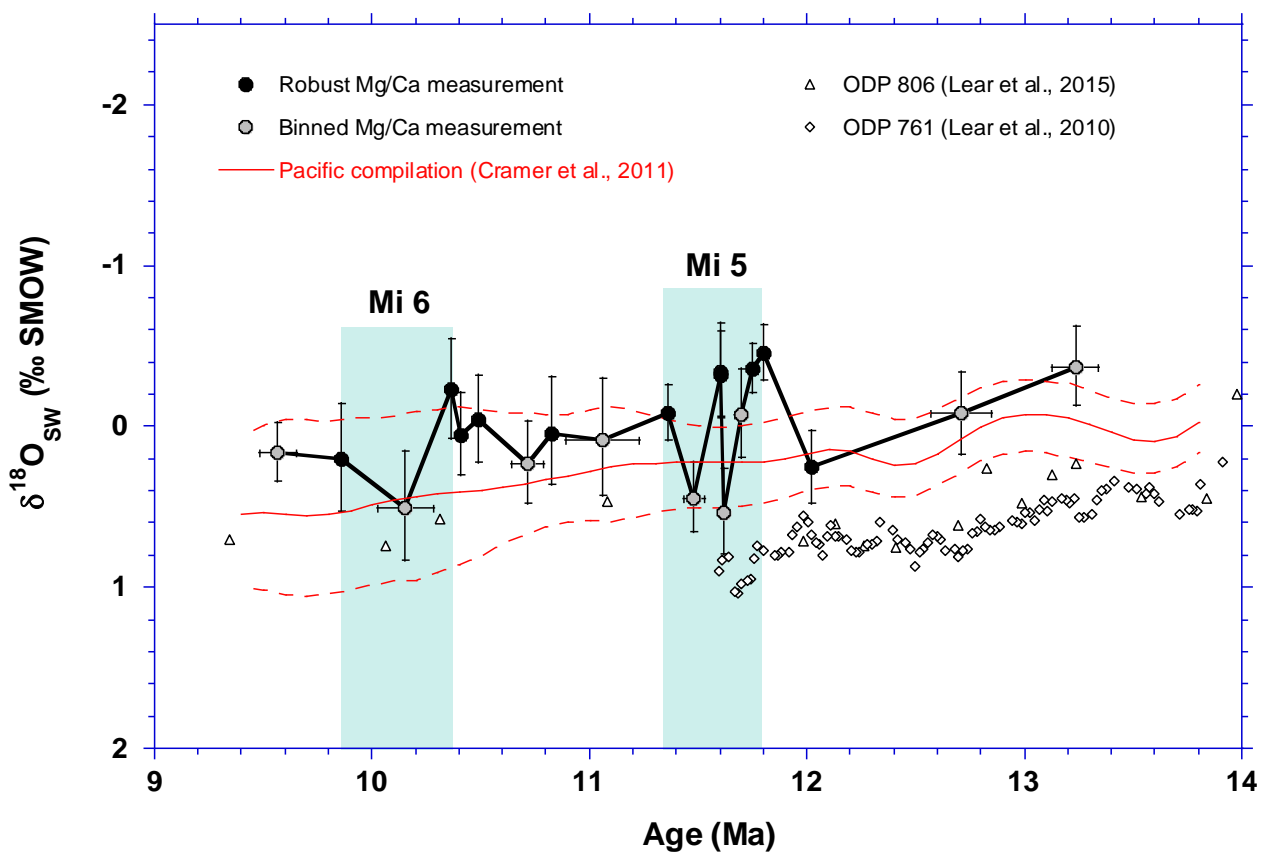


Figure 6.26: Sunbird-1 planktic foraminiferal  $\delta^{18}\text{O}_{\text{SW}}$  record as Figure 6.11a, distinguishing between temperatures from Mg/Ca samples regarded as robust (black circles) and binned (grey circles) (see Chapter 5.4.4 for details). Binned samples have horizontal error bars denoting the age range the sample incorporates. Vertical error bars denote the cumulative analytical and sample uncertainty of the  $\delta^{18}\text{O}$  and Mg/Ca values ( $\pm 2\text{SD}$ ). Previously published benthic foraminiferal  $\delta^{18}\text{O}_{\text{SW}}$  records from ODP Site 761 off North West Australia (Lear et al., 2010) (open diamonds) and ODP Site 806 in the western equatorial Pacific (Lear et al., 2015) (open upward triangles) are plotted as open symbols for comparison. The trend from a compilation of Pacific sites is shown as a red line, with dashed red lines as 90% confidence intervals (Cramer et al., 2011). Vertical blue panels indicate proposed periods of ice sheet growth, corresponding with the Mi5 and Mi6 events of (Miller et al., 1991).

the MMCT is greatly improved, the increase being approximately 39-48m sea level equivalent in magnitude.

The noisy nature of the planktic foraminiferal  $\delta^{18}\text{O}_{\text{SW}}$  record, combined with the low sampling resolution makes identifying distinct intervals of ice growth challenging. Despite this there are two apparent periods through which planktic foraminiferal  $\delta^{18}\text{O}_{\text{SW}}$  increases centred at  $\sim 11.4$  Ma and  $\sim 10.4$  Ma (signified by the vertical blue panels in Figure 6.26) which are interpreted as phases of ice sheet intensification. The two  $10^5$  year increases in the record correspond with the Mi5 and Mi6 events of Miller et al. (1991), later reported by other authors (Turco et al., 2001, Westerhold et al., 2005, Lear et al., 2010, John et al., 2011). That these intervals align with the proposed Mi5 and Mi6 continental ice sheet growth events further supports the interpretation that Sunbird-1 planktic foraminiferal  $\delta^{18}\text{O}_{\text{SW}}$  is recording a global ice volume signal (Figure 6.26). It would be expected that benthic foraminiferal  $\delta^{18}\text{O}_{\text{SW}}$  would record similar increases, ice volume change affecting both planktic and benthic foraminiferal  $\delta^{18}\text{O}_{\text{SW}}$  signatures. However, this is not the case for these two intervals in Sunbird-1, and the changing water mass properties as the site subsides drowns out the influence of the ice-sheet growth events (Chapter 6.4.4.1).

This also supports an ice volume contribution of  $\sim 0.5\%$  to the benthic foraminiferal  $\delta^{18}\text{O}_{\text{SW}}$  signal, and more typical contemporaneous deep water records (Figure 6.24). However, this leaves the further  $1\%$  increase in the Sunbird-1 benthic foraminiferal  $\delta^{18}\text{O}_{\text{SW}}$  record requiring explanation, without invoking million year timescale ice sheet evolution.

6.4.4.3 A dynamic Antarctic ice sheet following the MMCT?

The ice sheet hysteresis hypothesis of Pollard and DeConto (2005) and the thresholds for both Northern and Southern Hemisphere glaciation of DeConto et al. (2008) suggest that global ice volume was likely relatively stable between 13.8 Ma and 9.5 Ma. Additionally, due to changes in orbital configuration, the high latitudes had reduced seasonality following the MMCT meaning the Antarctic Ice Sheet is expected to have been less susceptible to dynamic changes in volume (Holbourn et al., 2013).

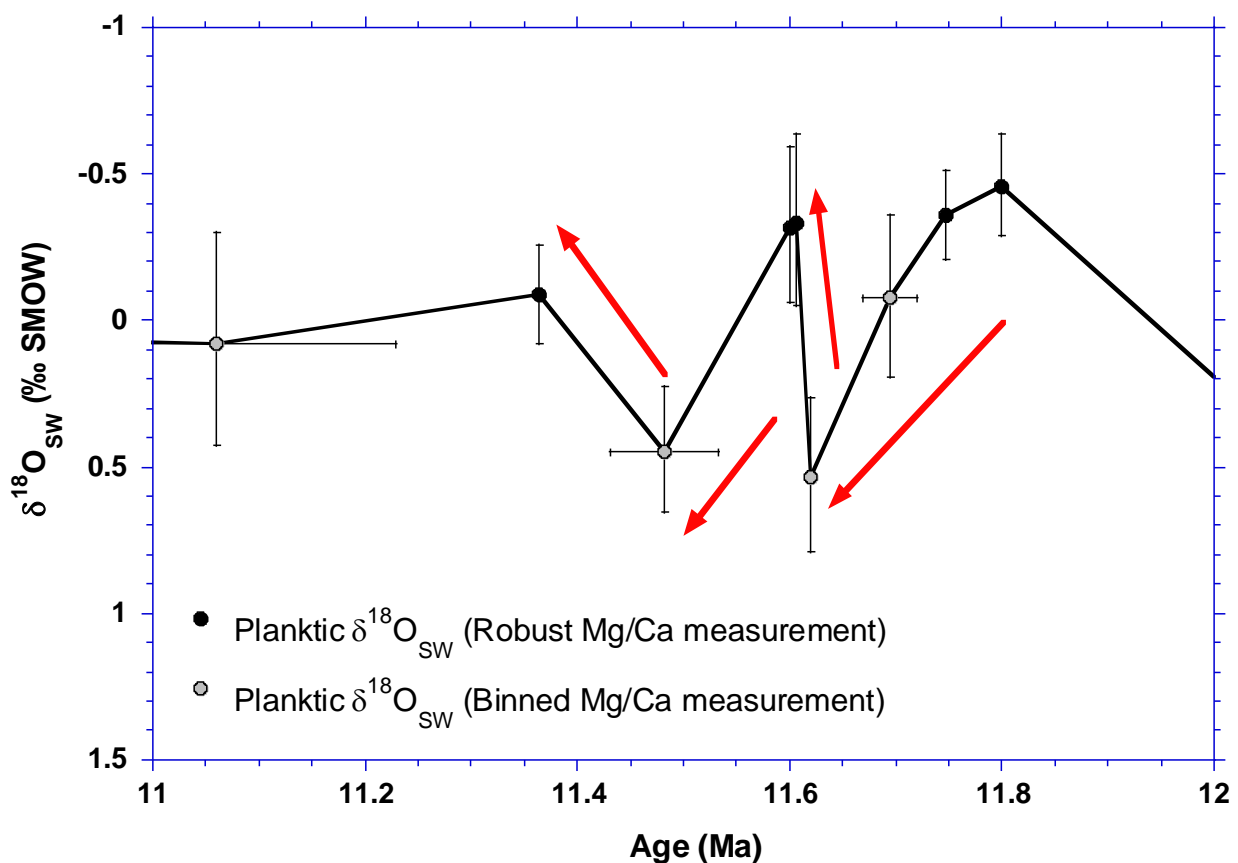


Figure 6.27: Planktic foraminiferal  $\delta^{18}\text{O}_{\text{sw}}$  record for the interval between 12 Ma and 11 Ma from Sunbird-1 distinguishing between temperatures from Mg/Ca samples regarded as robust (black circles) and binned (grey circles) (see Chapter 5.4.4 for details). Red arrows show proposed high frequency ice volume change inferred from the planktic foraminiferal  $\delta^{18}\text{O}_{\text{sw}}$  record.

Despite this, two high frequency  $\sim 0.5\text{‰}$  fluctuations between 11.8 Ma and 11.5 Ma are present in the planktic foraminiferal  $\delta^{18}\text{O}_{\text{SW}}$  record, interpreted as recording global ice volume change (Figure 6.27). This suggests that there could have been significant Antarctic ice sheet variability between 12 Ma and 11 Ma despite not being simulated by coupled climate-ice sheet models (Huybrechts, 1993, Pollard and DeConto, 2005, DeConto et al., 2008, Gasson et al., 2014). Incorporating new ice shelf hydrofracturing and ice cliff collapse mechanisms ice sheet retreat (Pollard et al., 2015) has allowed 0.52‰ to 0.66‰ variations in  $\delta^{18}\text{O}_{\text{SW}}$  (Gasson et al., 2016), although it is worth noting these simulations are for the marine based ice sheets of the early to mid-Miocene. This planktic foraminiferal  $\delta^{18}\text{O}_{\text{SW}}$  record from Sunbird-1 supports similar magnitude fluctuations resulting from a dynamic EAIS after its expansion to a dry, land-based ice sheet of approximately modern day volume across the MMCT. Although ice sheet models currently struggle to simulate it, similar large-scale variability of the East Antarctic Ice Sheet through the mid-late Miocene, inferred from high resolution  $\delta^{18}\text{O}$  records (Westerhold et al., 2005, Holbourn et al., 2013) and backstripping estimates (John et al., 2011, Kominz et al., 2016), has been inferred despite relatively stable atmospheric  $\text{CO}_2$  (Greenop et al., 2014, Sosdian et al., 2018). Additionally, provenance studies proximal to the ice margin reveal that the EAIS exhibited a dynamic response to climatic change during the Pliocene (Cook et al., 2013), behaviour which the Sunbird-1  $\delta^{18}\text{O}_{\text{SW}}$  records demonstrate to be applicable in the mid-late Miocene (Figure 6.19).

## 6.5 Conclusions

The environmental conditions at Sunbird-1 between 13.7 Ma and 9.4 Ma were influenced by multiple processes, including subsidence, primary productivity, local oceanography, ice

volume change, and the global carbon cycle. This is evidenced by the decoupling of Mg/Ca, B/Ca,  $\delta^{13}\text{C}$ , and  $\delta^{18}\text{O}$  records at the site. Foraminiferal stable isotope records are dominated by a shift from a restricted coastal environment with an extremely high supply of nutrient rich riverine waters, to a lower nutrient, higher salinity environment more typical of the open ocean. This increased influx of open ocean waters caused a decrease in primary productivity and carbon remineralisation, and an increase in salinity at Sunbird-1 through the mid-late Miocene. The primary driver of these shifts was the increasing water depth and connectivity to the Indian Ocean of Sunbird-1 as the site subsided. This variability and mixing of water masses at Sunbird-1 significantly influenced primary productivity and climate on the local scale at Sunbird-1, as seen in both the benthic and planktic foraminiferal  $\delta^{13}\text{C}$  records and the benthic foraminiferal  $\delta^{18}\text{O}$  record.

The influence of the highly changeable oceanographic regime local to Sunbird-1 is most apparent in the benthic foraminiferal  $\delta^{18}\text{O}$  record. The isolated seawater  $\delta^{18}\text{O}$  component of the signal cannot be explained solely in terms of ice volume change, as this would require repeated growth and melting of the entire East Antarctic Ice Sheet, with a further contribution from northern hemisphere ice sheets, on  $10^5$  year timescales, which is unrealistic. The dominant influence of local oceanographic and tectonic induced changes on the benthic foraminiferal  $\delta^{18}\text{O}$  record demonstrates the complexity of Sunbird-1.

The complex and unique evolution of the site makes interpretation of global changes in carbon cycling and climate challenging. However, some inferences can be drawn. The final recovery from the Monterey excursion can be easily distinguished, although constraining the

absolute magnitude of the carbon isotope excursion at the site is complicated by the concomitant decrease in productivity. An independent constraint for productivity would enable this, indicating whether there was an amplified Monterey excursion carbon isotope signal at the coastal location.

The Sunbird-1 planktic foraminiferal  $\delta^{18}\text{O}_{\text{SW}}$  record increases by  $\sim 0.5\text{‰}$  between 13.3 Ma and 9.4 Ma, implying an increase in global ice volume equivalent to a 39-48m drop in sea level. The absence of high frequency global shifts in the benthic foraminiferal  $\delta^{18}\text{O}$  record (Zachos et al., 2001, Billups and Schrag, 2002, Zachos et al., 2008, Cramer et al., 2009), and stability of coupled ice sheet climate models at mid-late Miocene  $\text{CO}_2$  concentrations (Huybrechts, 1993, Pollard and DeConto, 2005, DeConto et al., 2008, Gasson et al., 2014) has been interpreted as evidence for a stable East Antarctic Ice Sheet following its expansion to approximately its modern day volume across the MMCT (Shevenell et al., 2004, Holbourn et al., 2005, John et al., 2011, Lear et al., 2015). However, the Sunbird-1 planktic foraminiferal  $\delta^{18}\text{O}_{\text{SW}}$  record displays high frequency (100 kyr– 400 kyr) variability between 12 Ma and 11 Ma, suggesting the EAIS was more dynamic through this interval than climate models simulate. Oxygen isotope shifts of similar timing and magnitude (Westerhold et al., 2005, Holbourn et al., 2013), as well as backstripping estimates (John et al., 2011, Kominz et al., 2016), from the interval further support a dynamic EAIS as it continued to expand through the mid-late Miocene. This proposed dynamic behaviour of the ice sheet overprints the long-term trend of continued EAIS expansion after the MMCT.

## 7 Synthesis

### 7.1 Conclusions

Despite its importance, a lack of well-preserved records from either oceanic or continental drilling have been recovered from the mid-late Miocene impeding our ability to reconstruct and understand the global climate system through the interval. The Sunbird-1 core off the coast of Kenya in the South West Indian Ocean provides continuous sediment recovery from ~13.75 - ~9.42 Ma (Chapter 2). Sedimentation at Sunbird-1 is dominated by hemipelagic clays which have been shown to reduce the impact of diagenesis and geochemical alteration of foraminifera that typifies the commonly used carbonate oozes (Pearson et al., 2001, Sexton et al., 2006, Pearson and Burgess, 2008, Sexton and Wilson, 2009,).

The shallow water depth, proximity to the continent, and tectonic subsidence of Sunbird-1 complicates the local seawater chemistry and depositional conditions. A high flux of detrital organic matter from the nearby continent resulted in reduced pore water oxygen concentrations between 13.7 Ma and 12.0 Ma. This is interpreted from benthic foraminiferal redox sensitive trace metal records (U/Ca, Mn/Ca, and Fe/Ca) which indicate changing sedimentary redox conditions at the site (Chapter 3). These conditions facilitated the significant diagenetic precipitation of authigenic uranium and Mn-Fe oxides onto foraminiferal tests. These outer coatings contain elevated magnesium, overprinting the primary geochemical signal and hence hindering Mg/Ca temperature reconstruction. Attempts to correct for this using a novel technique analysing paired aragonite-calcite tests proved promising but unsuccessful, likely due to the prior application of a thorough chemical cleaning protocol.

To address this, a microanalytical approach using highly spatial resolved Laser Ablation ICP-MS depth profiles to identify the primary foraminiferal test was developed (Chapter 4). In order to successfully apply this technique the ablation parameters to collect accurate, precise, and reproducible depth profiles using the new LA-ICP-MS setup in the Cardiff University CELTIC laboratory were optimised. Using medium to low fluences and repetition rates this study successfully enables the collection, and analysis, of intra-test trace metal variability in foraminifera. As well as optimising the ablation parameters the inferred diagenetic coating overprinting the primary Mg/Ca signal can be identified. Therefore, the primary calcite required for Mg/Ca paleothermometry can be identified and used to study past ocean temperatures from challenging time intervals and localities where contaminant coatings have previously inhibited paleoenvironmental studies.

Application of the optimised ablation parameters determined in Chapter 4, combined with a rigorous screening protocol, provides a new absolute tropical sea surface temperature record through the mid-late Miocene (Chapter 5). SST estimates of 27-29°C suggest a stable tropical climate through the interval. In addition to improving estimates of absolute tropical SST through the poorly understood mid-late Miocene, this analytical technique derives robust paleotemperatures from diagenetically altered foraminifera. When combined with the interhemispheric cooling at mid-high latitudes (Herbert et al., 2016) this new record of well constrained absolute SST suggests an increased latitudinal temperature gradient, which is a key component of the modern day climate state. The increase in the equator to pole temperature gradient is decoupled from any changes in atmospheric CO<sub>2</sub>. This is unlike the

majority of the Cenozoic through which ocean temperature and atmospheric CO<sub>2</sub> are closely linked (Zachos et al., 2008, Zhang et al., 2013). The lack of any significant trend in atmospheric CO<sub>2</sub> suggests there was likely a key mechanistic control of oceanographic reorganisation on the global climate system through this interval.

Sunbird-1 had a complicated and unique evolution through the mid-late Miocene, influenced by tectonic subsidence, and changes in local productivity and oceanography. This makes interpreting global changes in carbon cycling and climate evolution challenging (Chapter 6). Between 13.7 Ma and 12.0 Ma geochemical records from the site are dominated by a shift from a restricted, high productivity, coastal environment to a lower productivity environment with reduced carbon remineralisation more typical of the open ocean. The primary driver of this shift was the increasing water depth and connectivity to the Indian Ocean of Sunbird-1 as the site subsided.

However, the planktic foraminiferal  $\delta^{18}\text{O}_{\text{sw}}$  record is not influenced by the influence of tectonic subsidence of the site. Using the improved absolute SST estimates from Mg/Ca paleothermometry (Chapter 5) to account for the temperature influence on the  $\delta^{18}\text{O}$  signal implies a 39-48m sea level equivalent increase in global ice volume between 13.3 Ma and 9.4 Ma. Furthermore, the high frequency variability between 12 Ma and 11 Ma suggests a dynamic EAIS on top of the long-term trend of continued expansion through the mid-late Miocene.

## 7.2 Limitations of the LA-ICP-MS analysis in this thesis

Mg/Ca in *U. peregrina* has been proposed as a robust palaeotemperature proxy (Elderfield et al., 2010), and may be more abundant in the deeper part of the core, where productivity was high. To improve the temporal resolution of the bottom water temperature record LA-ICP-MS analysis of *U. peregrina* should be conducted. The extent to which the screening of the LA-ICP-MS data has produced an artificial selection bias in the bottom water temperature record could also be revisited. This could, for example, involve EPMA or SEM-EDX analyses of foraminifera from different diagenetic regimes to better determine suitable Mn/Ca thresholds above which foraminiferal Mg/Ca be impacted.

Future studies which aim to determine the number of depth profiles required to acquire a Mg/Ca value that is representative for the sample should first determine the number of profiles required for a representative Mg/Ca from a single specimen, before then determining the number of specimens required for a representative Mg/Ca value for the sample. Distinguishing between these two sources of variability will also assist in deconvolving the causes of the heterogeneity, intra- and inter-specimen. This process should be performed for every species analysed, and repeated for regions with different oceanographic regimes. Although doing this at Sunbird-1 would have been helpful for a better quantitative attribution of the sources of variability, the adopted method successfully achieved its primary purpose of determining how many depth profiles were required from a sample to acquire a representative Mg/Ca value for interpreting downcore trends.

*C. wuellerstorfi* trace metal ratios from the end of the Sunbird-1 record, after 11.0 Ma, do not demonstrate the changing redox conditions of the majority of the record. That LA-ICP-MS *C. wuellerstorfi* Mg/Ca results from this same interval are extremely similar, and show no systematic offset indicating the accuracy is good. In order to better test the accuracy of the LA-ICP-MS analyses a direct comparison with solution ICP-MS analyses on the same tests could be performed. A starting point for this analysis would be to analyse the *O. universa* test used for the optimisation of ablation settings to see whether it produces similar trace metal/calcium values to the average of the full laser profile. Future studies must ensure that when conducting accuracy tests in this manner they do not apply extra chemical cleaning prior to solution ICP-MS analysis.

### 7.3 Future research directions

Using paired aragonitic-calcitic trace metal/calcium demonstrated potential as a simple, quick, and inexpensive approach to correct for the contaminant coatings. Its limitation in this study was likely the prior application of the reductive and oxidative chemical cleaning procedures. By omitting these steps future studies could more accurately use aragonitic tests to determine the Mg/Mn, Mg/Fe, and Mg/U ratios of the contaminant phase, and apply this to correct for secondary Mg incorporation into calcitic tests.

Records of redox sensitive trace metal concentrations from solution based ICP-MS analyses indicate significant changes in sedimentary redox conditions at Sunbird-1. Corresponding analyses on planktic foraminifera would be able to show whether this influence was ubiquitous, or restricted to benthic foraminiferal species within the upper sediment column.

Unfortunately, there was very low planktic foraminiferal abundance through the record, and the reconstruction of a Mg/Ca SST record by LA-ICP-MS was prioritised.

The downcore LA-ICP-MS records produced in Chapter 5 reveal there to be significant intra-specimen variability in Mg/Ca ratios. The primary focus of this research was to use a newly developed LA-ICP-MS set-up collect representative Mg/Ca values from sample depths, which could be used to reconstruct downcore palaeotemperature records. To enable this the number of foraminiferal depth profiles required for a mean Mg/Ca ratio for a sample to be representative was determined (Chapter 4.3.4). A large number of depth profiles, from multiple specimens, were required due to homogenise the intra- and inter-specimen variability. A further avenue of interesting, and important, research that this introduces is whether the variability within a specimen is intra- or inter-chamber. This was not investigated in this thesis, but an experimental set-up designed specifically to address this important question is proposed below.

An experiment testing what proportion of the intra-specimen variability can be explained by differences between chambers should be conducted on both *D. altispira* and *C. wuellerstorfi*. Furthermore, all specimens should be from the same sample depth. Therefore, the Sunbird-1 sample depth with the highest abundance of *C. wuellerstorfi* and *D. altispira* should be used for this experiment. Foraminiferal abundance work, as discussed below, will allow this to be determined. The maximum number of ablation pits from the penultimate (f-1) and previous (f-2) chambers would be analysed (Figure 7.1). For each chamber the shapiro-wilk test for normality should be applied to determine whether the Mg/Ca ratios are normally distributed.

This will decide whether the ANOVA (normally distributed) or Kruskal-Wallis (not normally distributed) test for whether the Mg/Ca ratios from each chamber originate from the same distribution. If the null hypothesis that the Mg/Ca ratios from each chamber originate from the same distribution is rejected, then there are significant heterogeneities between adjacent chambers. Therefore, intra-specimen variability would primarily result from variability between, as opposed to within, chambers. If required, this experiment can be expanded to incorporate further chambers, including the final one, allowing a full assessment of Mg/Ca ratio consistency within and between chambers throughout foraminiferal ontogeny.

The benthic foraminiferal  $\delta^{18}\text{O}$  record demonstrates large point-to-point variability, proposed to be due to changes in salinity and freshwater input. There does not currently exist a proxy

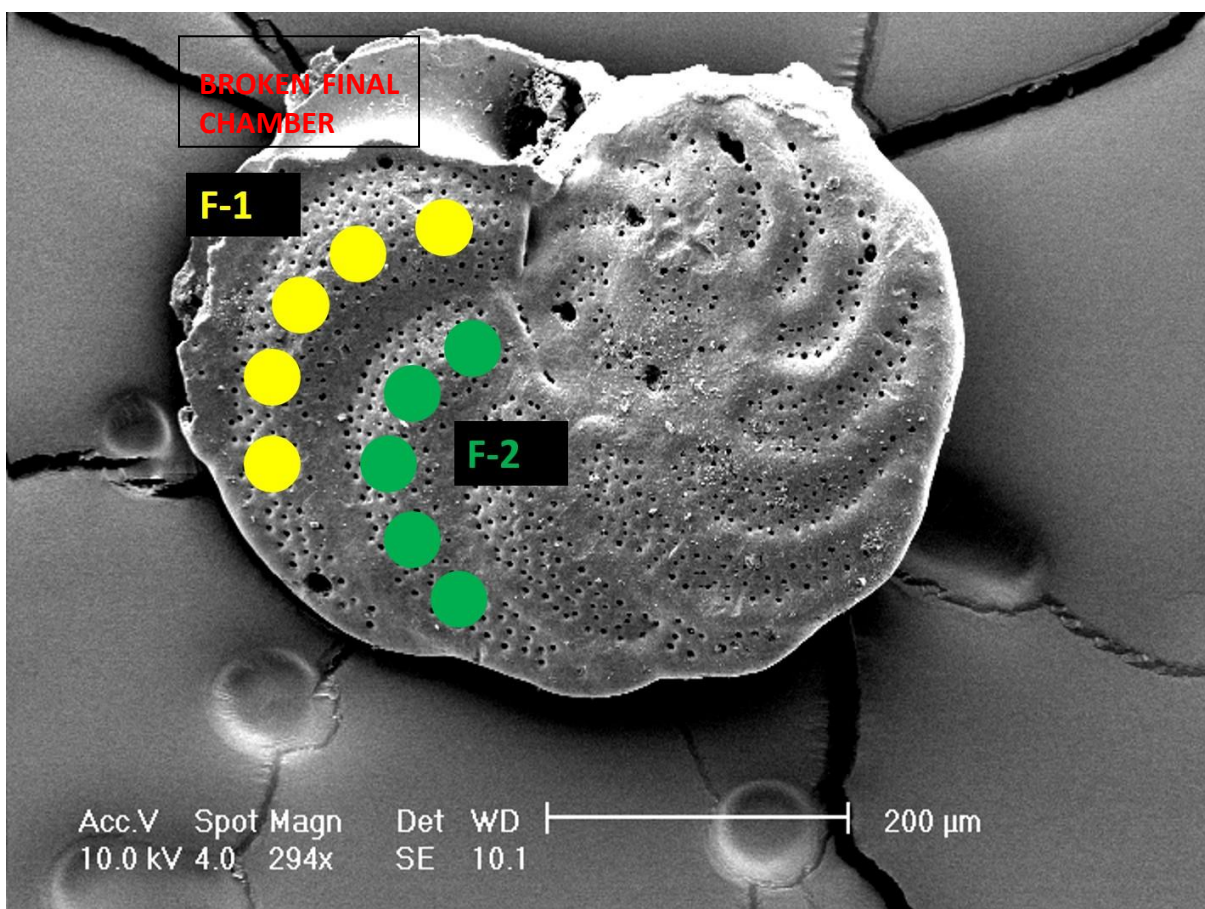


Figure 7.1: SEM image of *Cibicidoides wuellerstorfi* from the 1551-1554 m depth sample of Sunbird-1. Proposed ablation spots in the penultimate (f-1, yellow) and previous (f-2, green) chambers are annotated onto the image. Note that the final chamber of this specimen has been broken.

which independently and quantitatively reconstructs salinity. However, it would be possible through further research to investigate a possible influence of salinity changes through time at Sunbird-1. This could be achieved, albeit not quantitatively, by compiling foraminiferal abundance curves. In particular, an increase in the benthic-to-planktic foraminiferal ratio could suggest increased freshwater input, planktonic foraminifera are generally less abundant in lower salinity waters. Furthermore, the presence, or increased abundance, of freshwater foraminiferal species as well as ostracods would also support increased riverine input of lower salinity water during these intervals. The Na/Ca ratios of foraminifera have recently been proposed as a possible quantitative salinity proxy (Bertlich et al., 2018, Geerken et al., 2018). However, this potential salinity proxy is still in the development stage and requires substantial further culture and core-top studies before being quantitatively applied to downcore records such as Sunbird-1.

Although the three metre sampling interval prevented this at Sunbird-1, the high sedimentation rates, averaging 6.5 cm/kyr, would offer the opportunity to study climate at higher (orbital to sub-orbital) resolution. Therefore, the work in this thesis on Sunbird-1 could be used as a pilot study for future drilling proposals, offering an insight into the possibilities shallow water, clay-rich sites provide.

This thesis demonstrates the potential to accurately reconstruct sea surface temperature and continental ice volume from diagenetically altered foraminifera. The analytical approach developed and implemented here should be applied to more sites and time intervals where foraminiferal preservation has previously restricted our understanding of the climate system.

The mid-late Miocene is a prime example of this. Did the East Antarctic Ice Sheet behave dynamically through this unipolar icehouse world despite minimal atmospheric CO<sub>2</sub> forcing, as suggested by this study? Are the proposed Mi5 and Mi6 ice growth events observed in a global distribution of records? To answer these questions the same analytical approach developed in this study to a global distribution of high resolution sites, dominated by hemipelagic clays, including, if possible, more typical open ocean sites should be applied.

## 8 References

- ANAND, P. & ELDERFIELD, H. 2005. Variability of Mg/Ca and Sr/Ca between and within the planktonic foraminifers *Globigerina bulloides* and *Globorotalia truncatulinoides*. *Geochemistry, Geophysics, Geosystems*, 6.
- ANAND, P., ELDERFIELD, H. & CONTE, M. H. 2003. Calibration of Mg/Ca thermometry in planktonic foraminifera from a sediment trap time series. *Paleoceanography*, 18.
- ANDERSON, R. F. 1982. Concentration, vertical flux, and remineralization of particulate uranium in seawater. *Geochimica et Cosmochimica Acta*, 46, 1293-1299.
- AZE, T., EZARD, T. H., PURVIS, A., COXALL, H. K., STEWART, D. R., WADE, B. S. & PEARSON, P. N. 2011. A phylogeny of Cenozoic macroperforate planktonic foraminifera from fossil data. *Biological Reviews*, 86, 900-927.
- BABILA, T. L. 2014. *Boron/Calcium in planktonic foraminifera: proxy development and application to the Paleocene-Eocene boundary*. Rutgers University-Graduate School-New Brunswick.
- BACKMAN, J., RAFFI, I., RIO, D., FORNACIARI, E. & PÄLIKE, H. 2012. Biozonation and biochronology of Miocene through Pleistocene calcareous nannofossils from low and middle latitudes. *Newsletters on Stratigraphy*, 45, 221-244.
- BADGER, M. P., LEAR, C. H., PANCOST, R. D., FOSTER, G. L., BAILEY, T. R., LENG, M. J. & ABELS, H. A. 2013. CO<sub>2</sub> drawdown following the middle Miocene expansion of the Antarctic Ice Sheet. *Paleoceanography*, 28, 42-53.
- BAILEY, I., HOLE, G. M., FOSTER, G. L., WILSON, P. A., STOREY, C. D., TRUEMAN, C. N. & RAYMO, M. E. 2013. An alternative suggestion for the Pliocene onset of major northern hemisphere glaciation based on the geochemical provenance of North Atlantic Ocean ice-rafted debris. *Quaternary Science Reviews*, 75, 181-194.
- BANERJEE, B., AHMAD, S. M., RAZA, W. & RAZA, T. 2017. Paleoceanographic changes in the Northeast Indian Ocean during middle Miocene inferred from carbon and oxygen isotopes of foraminiferal fossil shells. *Palaeogeography, Palaeoclimatology, Palaeoecology*, 466, 166-173.
- BARKER, S., GREAVES, M. & ELDERFIELD, H. 2003. A study of cleaning procedures used for foraminiferal Mg/Ca paleothermometry. *Geochemistry, Geophysics, Geosystems*, 4.
- BATURIN, G. N. 2012. *The geochemistry of manganese and manganese nodules in the ocean*, Springer Science & Business Media.
- BE, A. W., HARRISON, S. M. & LOTT, L. 1973. *Orbulina universa* d'Orbigny in the Indian Ocean. *Micropaleontology*, 19, 150-192.
- BEAVINGTON-PENNEY, S. & ROWLES, C. 2015. Prospectivity of Miocene carbonates in the Lamu Basin, offshore Kenya: insights from the Sunbird-1 well. *Presentation at PESGB Africa E&P conference*. London.
- BEERLING, D. J. & ROYER, D. L. 2011. Convergent cenozoic CO<sub>2</sub> history. *Nature Geoscience*, 4, 418-420.

- BEMIS, B. E., SPERO, H. J., BIJMA, J. & LEA, D. W. 1998. Reevaluation of the oxygen isotopic composition of planktonic foraminifera: Experimental results and revised paleotemperature equations. *Paleoceanography*, 13, 150-160.
- BENDAT, J. S. & PIERSOL, A. G. 1971. Random data: analysis and measurement procedures, John Wiley and Sons. *New York*.
- BENTOV, S. & EREZ, J. 2006. Impact of biomineralization processes on the Mg content of foraminiferal shells: A biological perspective. *Geochemistry, Geophysics, Geosystems*, 7, n/a-n/a.
- BILLUPS, K. & SCHRAG, D. P. 2002. Paleotemperatures and ice volume of the past 27 Myr revisited with paired Mg/Ca and  $\delta^{18}O/\delta^{16}O$  measurements on benthic foraminifera. *Paleoceanography*, 17, 3-1-3-11.
- BILLUPS, K. & SCHRAG, D. P. 2003. Application of benthic foraminiferal Mg/Ca ratios to questions of Cenozoic climate change. *Earth and Planetary Science Letters*, 209, 181-195.
- BIRCH, H., COXALL, H. K., PEARSON, P. N., KROON, D. & O'REGAN, M. 2013. Planktonic foraminifera stable isotopes and water column structure: Disentangling ecological signals. *Marine Micropaleontology*, 101, 127-145.
- BOITEAU, R., GREAVES, M. & ELDERFIELD, H. 2012. Authigenic uranium in foraminiferal coatings: A proxy for ocean redox chemistry. *Paleoceanography*, 27.
- BOYER, T. P., ANTONOV, J. I., BARANOVA, O. K., COLEMAN, C., GARCIA, H. E., GRODSKY, A., JOHNSON, D. R., LOCARNINI, R. A., MISHONOV, A. V. & O'BRIEN, T. D. 2013. World Ocean Database 2013.
- BOYLE, E. & KEIGWIN, L. 1985. Comparison of Atlantic and Pacific paleochemical records for the last 215,000 years: Changes in deep ocean circulation and chemical inventories. *Earth and Planetary Science Letters*, 76, 135-150.
- BOYLE, E. A. 1983. Manganese carbonate overgrowths on foraminifera tests. *Geochimica et Cosmochimica Acta*, 47, 1815-1819.
- BROECKER, W. 1989. The salinity contrast between the Atlantic and Pacific Oceans during glacial time. *Paleoceanography and Paleoclimatology*, 4, 207-212.
- BROECKER, W. S., PENG, T.-H. & BENG, Z. 1982. *Tracers in the Sea*, Lamont-Doherty Geological Observatory, Columbia University.
- BROWN, R. E., ANDERSON, L. D., THOMAS, E. & ZACHOS, J. C. 2011. A core-top calibration of B/Ca in the benthic foraminifera *Nuttallides umbonifera* and *Oridorsalis umbonatus*: A proxy for Cenozoic bottom water carbonate saturation. *Earth and Planetary Science Letters*, 310, 360-368.
- BROWN, S. J. & ELDERFIELD, H. 1996. Variations in Mg/Ca and Sr/Ca ratios of planktonic foraminifera caused by postdepositional dissolution: Evidence of shallow Mg-dependent dissolution. *Paleoceanography*, 11, 543-551.
- BRYAN, S. P. & MARCHITTO, T. M. 2008. Mg/Ca-temperature proxy in benthic foraminifera: New calibrations from the Florida Straits and a hypothesis regarding Mg/Li. *Paleoceanography*, 23.

- BURTON, E. A. & WALTER, L. M. 1991. The effects of  $\text{CO}_2$  and temperature on magnesium incorporation in calcite in seawater and  $\text{MgCl}_2\text{-CaCl}_2$  solutions. *Geochimica et Cosmochimica Acta*, 55, 777-785.
- CALVERT, S. & PEDERSEN, T. 1996. Sedimentary geochemistry of manganese; implications for the environment of formation of manganese black shales. *Economic Geology*, 91, 36-47.
- CARON, D. A., FABER, W. W. & BÉ, A. W. 1987. Growth of the spinose planktonic foraminifer *Orbulina universa* in laboratory culture and the effect of temperature on life processes. *Journal of the marine biological association of the United Kingdom*, 67, 343-358.
- CHEN, P., YU, J. & JIN, Z. 2017. An evaluation of benthic foraminiferal U/Ca and U/Mn proxies for deep ocean carbonate chemistry and redox conditions. *Geochemistry, Geophysics, Geosystems*.
- COCHRAN, J. K., CAREY, A. E., SHOLKOVITZ, E. R. & SURPRENANT, L. D. 1986. The geochemistry of uranium and thorium in coastal marine sediments and sediment pore waters. *Geochimica et Cosmochimica Acta*, 50, 663-680.
- COGGON, R. M., TEAGLE, D. A., SMITH-DUQUE, C. E., ALT, J. C. & COOPER, M. J. 2010. Reconstructing past seawater Mg/Ca and Sr/Ca from mid-ocean ridge flank calcium carbonate veins. *Science*, 327, 1114-1117.
- COOK, C. P., VAN DE FLIERT, T., WILLIAMS, T., HEMMING, S. R., IWAI, M., KOBAYASHI, M., JIMENEZ-ESPEJO, F. J., ESCUTIA, C., GONZÁLEZ, J. J. & KHIM, B.-K. 2013. Dynamic behaviour of the East Antarctic ice sheet during Pliocene warmth. *Nature Geoscience*, 6, 765-769.
- COXALL, H. K., WILSON, P. A., PÄLIKE, H., LEAR, C. H. & BACKMAN, J. 2005. Rapid stepwise onset of Antarctic glaciation and deeper calcite compensation in the Pacific Ocean. *Nature*, 433, 53-57.
- CRAIG, H. 1970. Abyssal carbon 13 in the South Pacific. *Journal of geophysical research*, 75, 691-695.
- CRAIG, H. & GORDON, L. I. 1965. Deuterium and oxygen 18 variations in the ocean and the marine atmosphere.
- CRAMER, B., MILLER, K., BARRETT, P. & WRIGHT, J. 2011. Late Cretaceous–Neogene trends in deep ocean temperature and continental ice volume: reconciling records of benthic foraminiferal geochemistry ( $\delta^{18}\text{O}$  and Mg/Ca) with sea level history. *Journal of Geophysical Research: Oceans (1978–2012)*, 116.
- CRAMER, B., TOGGWEILER, J., WRIGHT, J., KATZ, M. & MILLER, K. 2009. Ocean overturning since the Late Cretaceous: Inferences from a new benthic foraminiferal isotope compilation. *Paleoceanography*, 24.
- CREECH, J. B., BAKER, J. A., HOLLIS, C. J., MORGANS, H. E. G. & SMITH, E. G. C. 2010. Eocene sea temperatures for the mid-latitude southwest Pacific from Mg/Ca ratios in planktonic and benthic foraminifera. *Earth and Planetary Science Letters*, 299, 483-495.

- CZAS, J., JOCHUM, K., STOLL, B., WEIS, U., YANG, Q.-C., JACOB, D. & ANDREAE, M. 2012. Investigation of matrix effects in 193 nm laser ablation-inductively coupled plasma-mass spectrometry analysis using reference glasses of different transparencies. *Spectrochimica Acta Part B: Atomic Spectroscopy*, 78, 20-28.
- DAVIS, C. V., FEHRENBACHER, J. S., HILL, T. M., RUSSELL, A. D. & SPERO, H. J. 2017. Relationships Between Temperature, pH, and Crusting on Mg/Ca Ratios in Laboratory-Grown Neogloboquadrina Foraminifera. *Paleoceanography*, 32, 1137-1152.
- DE LANGE, G., VAN OS, B. & POORTER, R. 1992. Geochemical composition and inferred accretion rates of sediments and manganese nodules from a submarine hill in the Madeira Abyssal Plain, eastern North Atlantic. *Marine geology*, 109, 171-194.
- DE NOOIJER, L. J., HATHORNE, E. C., REICHART, G.-J., LANGER, G. & BIJMA, J. 2014. Variability in calcitic Mg/Ca and Sr/Ca ratios in clones of the benthic foraminifer *Ammonia tepida*. *Marine Micropaleontology*, 107, 32-43.
- DE NOOIJER, L. J., VAN DIJK, I., TOYOFUKU, T. & REICHART, G. J. 2017. The Impacts of Seawater Mg/Ca and Temperature on Element Incorporation in Benthic Foraminiferal Calcite. *Geochemistry, Geophysics, Geosystems*, 18, 3617-3630.
- DE VILLIERS, S. 1999. Seawater strontium and Sr/Ca variability in the Atlantic and Pacific oceans. *Earth and Planetary Science Letters*, 171, 623-634.
- DECONTO, R. M. & POLLARD, D. 2003. A coupled climate–ice sheet modeling approach to the early Cenozoic history of the Antarctic ice sheet. *Palaeogeography, Palaeoclimatology, Palaeoecology*, 198, 39-52.
- DECONTO, R. M. & POLLARD, D. 2016. Contribution of Antarctica to past and future sea-level rise. *Nature*, 531, 591-597.
- DECONTO, R. M., POLLARD, D., WILSON, P. A., PÄLIKE, H., LEAR, C. H. & PAGANI, M. 2008. Thresholds for Cenozoic bipolar glaciation. *Nature*, 455, 652-656.
- DICKSON, J. 2002. Fossil echinoderms as monitor of the Mg/Ca ratio of Phanerozoic oceans. *Science*, 298, 1222-1224.
- DUEÑAS-BOHÓRQUEZ, A., DA ROCHA, R. E., KUROYANAGI, A., BIJMA, J. & REICHART, G.-J. 2009. Effect of salinity and seawater calcite saturation state on Mg and Sr incorporation in cultured planktonic foraminifera. *Marine Micropaleontology*, 73, 178-189.
- DUPLESSY, J., LABEYRIE, L., JUILLETLECLERC, A., MAITRE, F., DUPRAT, J. & SARNTHEIN, M. 1991. Surface salinity reconstruction of the North-Atlantic Ocean during the last glacial maximum. *Oceanologica Acta*, 14, 311-324.
- EDGAR, K. M., ANAGNOSTOU, E., PEARSON, P. N. & FOSTER, G. L. 2015. Assessing the impact of diagenesis on  $\delta^{11}\text{B}$ ,  $\delta^{13}\text{C}$ ,  $\delta^{18}\text{O}$ , Sr/Ca and B/Ca values in fossil planktic foraminiferal calcite. *Geochimica et Cosmochimica Acta*, 166, 189-209.
- EDGAR, K. M., PÄLIKE, H. & WILSON, P. A. 2013. Testing the impact of diagenesis on the  $\delta^{18}\text{O}$  and  $\delta^{13}\text{C}$  of benthic foraminiferal calcite from a sediment burial depth transect in the equatorial Pacific. *Paleoceanography*, 28, 468-480.

- EGGINS, S., DE DECKKER, P. & MARSHALL, J. 2003. Mg/Ca variation in planktonic foraminifera tests: implications for reconstructing palaeo-seawater temperature and habitat migration. *Earth and Planetary Science Letters*, 212, 291-306.
- EGGINS, S. M., KINSLEY, L. & SHELLEY, J. 1998. Deposition and element fractionation processes during atmospheric pressure laser sampling for analysis by ICP-MS. *Applied Surface Science*, 127, 278-286.
- EGGINS, S. M., SADEKOV, A. & DE DECKKER, P. 2004. Modulation and daily banding of Mg/Ca in *Orbulina universa* tests by symbiont photosynthesis and respiration: a complication for seawater thermometry? *Earth and Planetary Science Letters*, 225, 411-419.
- ELDERFIELD, H., BERTRAM, C. J. & EREZ, J. 1996. A biomineralization model for the incorporation of trace elements into foraminiferal calcium carbonate. *Earth and Planetary Science Letters*, 142, 409-423.
- ELDERFIELD, H. & GANSSEN, G. 2000. Past temperature and  $\delta^{18}\text{O}$  of surface ocean waters inferred from foraminiferal Mg/Ca ratios. *Nature*, 405, 442-445.
- ELDERFIELD, H., GREAVES, M., BARKER, S., HALL, I. R., TRIPATI, A., FERRETTI, P., CROWHURST, S., BOOTH, L. & DAUNT, C. 2010. A record of bottom water temperature and seawater  $\delta^{18}\text{O}$  for the Southern Ocean over the past 440kyr based on Mg/Ca of benthic foraminiferal *Uvigerina* spp. *Quaternary Science Reviews*, 29, 160-169.
- ELDERFIELD, H., YU, J., ANAND, P., KIEFER, T. & NYLAND, B. 2006. Calibrations for benthic foraminiferal Mg/Ca paleothermometry and the carbonate ion hypothesis. *Earth and Planetary Science Letters*, 250, 633-649.
- ELDRETT, J. S., HARDING, I. C., WILSON, P. A., BUTLER, E. & ROBERTS, A. P. 2007. Continental ice in Greenland during the Eocene and Oligocene. *Nature*, 446, 176-179.
- ELMORE, A. C., MCCLYMONT, E. L., ELDERFIELD, H., KENDER, S., COOK, M. R., LENG, M. J., GREAVES, M. & MISRA, S. 2015. Antarctic Intermediate Water properties since 400 ka recorded in infaunal (*Uvigerina peregrina*) and epifaunal (*Planulina wuellerstorfi*) benthic foraminifera. *Earth and Planetary Science Letters*, 428, 193-203.
- EMILIANI, C. 1955a. Pleistocene temperatures. *The Journal of Geology*, 63, 538-578.
- EMILIANI, C. 1955b. Pleistocene temperatures. *The Journal of Geology*, 538-578.
- EPSTEIN, S., BUCHSBAUM, R., LOWENSTAM, H. & UREY, H. C. 1951. Carbonate-water isotopic temperature scale. *Geological Society of America Bulletin*, 62, 417-426.
- EPSTEIN, S., BUCHSBAUM, R., LOWENSTAM, H. A. & UREY, H. C. 1953. Revised carbonate-water isotopic temperature scale. *Geological Society of America Bulletin*, 64, 1315-1326.
- EVANS, D., BHATIA, R., STOLL, H. & MÜLLER, W. 2015a. LA-ICPMS Ba/Ca analyses of planktic foraminifera from the Bay of Bengal: Implications for late Pleistocene orbital control on monsoon freshwater flux. *Geochemistry, Geophysics, Geosystems*, 16, 2598-2618.
- EVANS, D., BRIERLEY, C., RAYMO, M. E., EREZ, J. & MÜLLER, W. 2016a. Planktic foraminifera shell chemistry response to seawater chemistry: Pliocene-Pleistocene seawater Mg/Ca, temperature and sea level change. *Earth and Planetary Science Letters*.

- EVANS, D., BRIERLEY, C., RAYMO, M. E., EREZ, J. & MÜLLER, W. 2016b. Planktic foraminifera shell chemistry response to seawater chemistry: Pliocene–Pleistocene seawater Mg/Ca, temperature and sea level change. *Earth and Planetary Science Letters*, 438, 139-148.
- EVANS, D., EREZ, J., ORON, S. & MÜLLER, W. 2015b. Mg/Ca-temperature and seawater-test chemistry relationships in the shallow-dwelling large benthic foraminifera *Operculina ammonoides*. *Geochimica et Cosmochimica Acta*, 148, 325-342.
- EVANS, D. & MÜLLER, W. 2012. Deep time foraminifera Mg/Ca paleothermometry: Nonlinear correction for secular change in seawater Mg/Ca. *Paleoceanography and Paleoclimatology*, 27.
- EVANS, D. & MÜLLER, W. 2018a. Automated Extraction of a Five-Year LA-ICP-MS Trace Element Data Set of Ten Common Glass and Carbonate Reference Materials: Long-Term Data Quality, Optimisation and Laser Cell Homogeneity. *Geostandards and Geoanalytical Research*, 42, 159-188.
- EVANS, D. & MÜLLER, W. 2018b. Automated Extraction of a Five-Year LA-ICP-MS Trace Element Dataset of Ten Common Glass and Carbonate Reference Materials: Long-Term Data Quality, Optimisation and Laser Cell Homogeneity. *Geostandards and Geoanalytical Research*.
- EVANS, D., SAGOO, N., RENEMA, W., COTTON, L. J., MÜLLER, W., TODD, J. A., SARASWATI, P. K., STASSEN, P., ZIEGLER, M., PEARSON, P. N., VALDES, P. J. & AFFEK, H. P. 2018. Eocene greenhouse climate revealed by coupled clumped isotope-Mg/Ca thermometry. *Proceedings of the National Academy of Sciences of the United States of America*, 115, 1174-1179.
- EVANS, D., WADE, B. S., HENEHAN, M., EREZ, J. & MÜLLER, W. 2016c. Revisiting carbonate chemistry controls on planktic foraminifera Mg / Ca: Implications for sea surface temperature and hydrology shifts over the Paleocene-Eocene Thermal Maximum and Eocene-Oligocene transition. *Climate of the Past*, 12, 819-835.
- FAIRBANKS, R. G. 1989. A 17, 000-year glacio-eustatic sea level record: influence of glacial melting rates on the Younger Dryas event and deep-ocean circulation. *Nature*, 342, 637-642.
- FALLET, U., ULLGREN, J. E., CASTAÑEDA, I. S., VAN AKEN, H. M., SCHOUTEN, S., RIDDERINKHOF, H. & BRUMMER, G.-J. A. 2011. Contrasting variability in foraminiferal and organic paleotemperature proxies in sedimenting particles of the Mozambique Channel (SW Indian Ocean). *Geochimica et Cosmochimica Acta*, 75, 5834-5848.
- FARRELL, J. W., RAFFI, I., JANECEK, T. R., MURRAY, D. W., LEVITAN, M., DADEY, K. A., EMEIS, K.-C., LYLE, M., FLORES, J.-A. & HOVAN, S. 1995. 35. LATE NEOGENE SEDIMENTATION PATTERNS IN THE EASTERN EQUATORIAL PACIFIC OCEAN1.
- FEHRENBACHER, J. S. & MARTIN, P. A. 2014. Exploring the dissolution effect on the intrashell Mg/Ca variability of the planktic foraminifer *Globigerinoides ruber*. *Paleoceanography*, 29, 854-868.
- FEHRENBACHER, J. S., SPERO, H. J., RUSSELL, A. D., VETTER, L. & EGGINS, S. 2015. Optimizing LA-ICP-MS analytical procedures for elemental depth profiling of foraminifera shells. *Chemical Geology*, 407-408, 2-9.

- FILIPSSON, H., BERNHARD, J. M., LINCOLN, S. A. & MCCORKLE, D. C. 2010. A culture-based calibration of benthic foraminiferal paleotemperature proxies: Delta O-18 and Mg/Ca results.
- FLOWER, B. & KENNETT, J. 1993a. Middle Miocene ocean-climate transition: High-resolution oxygen and carbon isotopic records from Deep Sea Drilling Project Site 588A, southwest Pacific. *Paleoceanography*, 8, 811-843.
- FLOWER, B. P. & KENNETT, J. P. 1993b. Relations between Monterey Formation deposition and middle Miocene global cooling: Naples Beach section, California. *Geology*, 21, 877-880.
- FLOWER, B. P. & KENNETT, J. P. 1994. The middle Miocene climatic transition: East Antarctic ice sheet development, deep ocean circulation and global carbon cycling. *Palaeogeography, palaeoclimatology, palaeoecology*, 108, 537-555.
- FLOWER, B. P. & KENNETT, J. P. 1995. Middle Miocene deepwater paleoceanography in the southwest Pacific: relations with East Antarctic Ice Sheet development. *Paleoceanography*, 10, 1095-1112.
- FOSTER, G. L., LEAR, C. H. & RAE, J. W. B. 2012. The evolution of pCO<sub>2</sub>, ice volume and climate during the middle Miocene. *Earth and Planetary Science Letters*, 341–344, 243-254.
- FOSTER, G. L. & RAE, J. W. 2015. Reconstructing Ocean pH with Boron Isotopes in Foraminifera. *Annual Review of Earth and Planetary Sciences*.
- FROELICH, P. N., KLINKHAMMER, G., BENDER, M. L., LUEDTKE, N., HEATH, G. R., CULLEN, D., DAUPHIN, P., HAMMOND, D., HARTMAN, B. & MAYNARD, V. 1979. Early oxidation of organic matter in pelagic sediments of the eastern equatorial Atlantic: suboxic diagenesis. *Geochimica et Cosmochimica Acta*, 43, 1075-1090.
- GASSON, E., DECONTO, R. M., POLLARD, D. & LEVY, R. H. 2016. Dynamic Antarctic ice sheet during the early to mid-Miocene. *Proc Natl Acad Sci U S A*.
- GASSON, E., LUNT, D., DECONTO, R., GOLDNER, A., HEINEMANN, M., HUBER, M., LEGRANDE, A., POLLARD, D., SAGOO, N. & SIDDALL, M. 2014. Uncertainties in the modelled CO<sub>2</sub> threshold for Antarctic glaciation. *Climate of the Past*.
- GOTHMANN, A. M., STOLARSKI, J., ADKINS, J. F., SCHOENE, B., DENNIS, K. J., SCHRAG, D. P., MAZUR, M. & BENDER, M. L. 2015. Fossil corals as an archive of secular variations in seawater chemistry since the Mesozoic. *Geochimica et Cosmochimica Acta*, 160, 188-208.
- GOTTSCHALK, J., VÁZQUEZ RIVEIROS, N., WAELBROECK, C., SKINNER, L. C., MICHEL, E., DUPLESSY, J.-C., HODELL, D. & MACKENSEN, A. 2016. Carbon isotope offsets between benthic foraminifer species of the genus *Cibicides* (*Cibicidoides*) in the glacial sub-Antarctic Atlantic. *Paleoceanography*, n/a-n/a.
- GRADSTEIN, F. M., OGG, J. G. & SMITH, A. G. 2004. *A geologic time scale 2004*, Cambridge University Press.
- GRAY, W. R., WELDEAB, S., LEA, D. W., ROSENTHAL, Y., GRUBER, N., DONNER, B. & FISCHER, G. 2018. The effects of temperature, salinity, and the carbonate system on Mg/Ca in *Globigerinoides ruber* (white): A global sediment trap calibration. *Earth and Planetary Science Letters*, 482, 607-620.

- GREENOP, R., FOSTER, G. L., WILSON, P. A. & LEAR, C. H. 2014. Middle Miocene climate instability associated with high-amplitude CO<sub>2</sub> variability. *Paleoceanography*, 29, 845-853.
- GREENOP, R., HAIN, M. P., SOSDIAN, S. M., OLIVER, K. I. C., GOODWIN, P., CHALK, T. B., LEAR, C. H., WILSON, P. A. & FOSTER, G. L. 2017. A record of Neogene seawater  $\delta^{11}\text{B}$  reconstructed from paired  $\delta^{11}\text{B}$  analyses on benthic and planktic foraminifera. *Climate of the Past*, 13, 149-170.
- GRUBBS, F. E. 1969. Procedures for detecting outlying observations in samples. *Technometrics*, 11, 1-21.
- GUILLONG, M., MEIER, D. L., ALLAN, M. M., HEINRICH, C. A. & YARDLEY, B. W. 2008a. Appendix A6: SILLS: A MATLAB-based program for the reduction of laser ablation ICP-MS data of homogeneous materials and inclusions. *Mineralogical Association of Canada Short Course*, 40, 328-333.
- GUILLONG, M., MEIER, D. L., ALLAN, M. M., HEINRICH, C. A. & YARDLEY, B. W. 2008b. Appendix A6: SILLS: A MATLAB-based program for the reduction of laser ablation ICP-MS data of homogeneous materials and inclusions. *Mineralogical Association of Canada Short Course Series*, 40, 328-333.
- HASENFRATZ, A. P., MARTÍNEZ-GARCÍA, A., JACCARD, S. L., VANCE, D., WÄLLE, M., GREAVES, M. & HAUG, G. H. 2016. Determination of the Mg/Mn ratio in foraminiferal coatings: An approach to correct Mg/Ca temperatures for Mn-rich contaminant phases. *Earth and Planetary Science Letters*.
- HASIUK, F. J. & LOHMANN, K. C. 2010. Application of calcite Mg partitioning functions to the reconstruction of paleocean Mg/Ca. *Geochimica et Cosmochimica Acta*, 74, 6751-6763.
- HATHORNE, E., ALARD, O., JAMES, R. & ROGERS, N. 2003. Determination of intratest variability of trace elements in foraminifera by laser ablation inductively coupled plasma-mass spectrometry. *Geochemistry, Geophysics, Geosystems*, 4.
- HEALEY, S. L., THUNELL, R. C. & CORLISS, B. H. 2008. The Mg/Ca-temperature relationship of benthic foraminiferal calcite: New core-top calibrations in the < 4 C temperature range. *Earth and Planetary Science Letters*, 272, 523-530.
- HEMLEBEN, C., SPINDLER, M. & ANDERSON, O. R. 2012. *Modern planktonic foraminifera*, Springer Science & Business Media.
- HENEHAN, M. J., FOSTER, G. L., RAE, J. W. B., PRENTICE, K. C., EREZ, J., BOSTOCK, H. C., MARSHALL, B. J. & WILSON, P. A. 2015. Evaluating the utility of B/Ca ratios in planktic foraminifera as a proxy for the carbonate system: A case study of *Globigerinoides ruber*. *Geochemistry, Geophysics, Geosystems*, 16, 1052-1069.
- HENEHAN, M. J., RAE, J. W., FOSTER, G. L., EREZ, J., PRENTICE, K. C., KUCERA, M., BOSTOCK, H. C., MARTÍNEZ-BOTÍ, M. A., MILTON, J. A. & WILSON, P. A. 2013. Calibration of the boron isotope proxy in the planktonic foraminifera *Globigerinoides ruber* for use in palaeo-CO<sub>2</sub> reconstruction. *Earth and Planetary Science Letters*, 364, 111-122.

- HERBERT, T. D., LAWRENCE, K. T., TZANOVA, A., PETERSON, L. C., CABALLERO-GILL, R. & KELLY, C. S. 2016. Late Miocene global cooling and the rise of modern ecosystems. *Nature Geoscience*.
- HILGEN, F., ABELS, H., IACCARINO, S., KRIJGSMAN, W., RAFFI, I., SPROVIERI, R., TURCO, E. & ZACHARIASSE, W. 2009. The global stratotype section and point (GSSP) of the Serravallian Stage (Middle Miocene). *Episodes*, 32, 152-166.
- HILLAIRE-MARCEL, C. & DE VERNAL, A. 2007. Introduction Methods in Late Cenozoic Paleoceanography: Introduction. In: CLAUDE, H. M. & ANNE DE, V. (eds.) *Developments in Marine Geology*. Elsevier.
- HINES, B. R., HOLLIS, C. J., ATKINS, C. B., BAKER, J. A., MORGANS, H. E. & STRONG, P. C. 2017. Reduction of oceanic temperature gradients in the early Eocene Southwest Pacific Ocean. *Palaeogeography, palaeoclimatology, palaeoecology*, 475, 41-54.
- HOLBOURN, A., KUHN, W., CLEMENS, S., PRELL, W. & ANDERSEN, N. 2013. Middle to late Miocene stepwise climate cooling: Evidence from a high-resolution deep water isotope curve spanning 8 million years. *Paleoceanography*, 28, 688-699.
- HOLBOURN, A., KUHN, W., LYLE, M., SCHNEIDER, L., ROMERO, O. & ANDERSEN, N. 2014. Middle Miocene climate cooling linked to intensification of eastern equatorial Pacific upwelling. *Geology*, 42, 19-22.
- HOLBOURN, A., KUHN, W., SCHULZ, M. & ERLÉNKEUSER, H. 2005. Impacts of orbital forcing and atmospheric carbon dioxide on Miocene ice-sheet expansion. *Nature*, 438, 483-487.
- HOLBOURN, A., KUHN, W., SCHULZ, M., FLORES, J.-A. & ANDERSEN, N. 2007. Orbitally-paced climate evolution during the middle Miocene “Monterey” carbon-isotope excursion. *Earth and Planetary Science Letters*, 261, 534-550.
- HOLLAND, K., EGGINS, S. M., HÖNISCH, B., HAYNES, L. L. & BRANSON, O. 2017. Calcification rate and shell chemistry response of the planktic foraminifer *Orbulina universa* to changes in microenvironment seawater carbonate chemistry. *Earth and Planetary Science Letters*, 464, 124-134.
- HOLLIS, C., HINES, B., LITTLER, K., VILLASANTE-MARCOS, V., KULHANEK, D., STRONG, C., ZACHOS, J., EGGINS, S., NORTHCOTE, L. & PHILLIPS, A. 2015. The Paleocene–Eocene Thermal Maximum at DSDP Site 277, Campbell Plateau, southern Pacific Ocean.
- HOLLIS, C. J., TAYLOR, K. W., HANDLEY, L., PANCOST, R. D., HUBER, M., CREECH, J. B., HINES, B. R., CROUCH, E. M., MORGANS, H. E. & CRAMPTON, J. S. 2012. Early Paleogene temperature history of the Southwest Pacific Ocean: Reconciling proxies and models. *Earth and Planetary Science Letters*, 349, 53-66.
- HÖNISCH, B., ALLEN, K. A., LEA, D. W., SPERO, H. J., EGGINS, S. M., ARBUSZEWSKI, J., ROSENTHAL, Y., RUSSELL, A. D. & ELDERFIELD, H. 2013. The influence of salinity on Mg/Ca in planktic foraminifers—Evidence from cultures, core-top sediments and complementary  $\delta^{18}\text{O}$ . *Geochimica et Cosmochimica Acta*, 121, 196-213.
- HORITA, J., ZIMMERMANN, H. & HOLLAND, H. D. 2002. Chemical evolution of seawater during the Phanerozoic: Implications from the record of marine evaporites. *Geochimica et Cosmochimica Acta*, 66, 3733-3756.

- HUANG, Y., CLEMENS, S. C., LIU, W., WANG, Y. & PRELL, W. L. 2007. Large-scale hydrological change drove the late Miocene C4 plant expansion in the Himalayan foreland and Arabian Peninsula. *Geology*, 35, 531-534.
- HUT, G. 1987. Consultants' group meeting on stable isotope reference samples for geochemical and hydrological investigations.
- HUYBRECHTS, P. 1993. Glaciological modelling of the Late Cenozoic East Antarctic ice sheet: stability or dynamism? *Geografiska Annaler: Series A, Physical Geography*, 75, 221-238.
- JACCARD, S. L., GALBRAITH, E. D., SIGMAN, D. M., HAUG, G. H., FRANCOIS, R., PEDERSEN, T. F., DULSKI, P. & THIERSTEIN, H. R. 2009. Subarctic Pacific evidence for a glacial deepening of the oceanic respired carbon pool. *Earth and Planetary Science Letters*, 277, 156-165.
- JIANG, S., WISE, S. & WANG, Y. Cause of the middle/late Miocene carbonate crash: dissolution or low productivity. Proceedings of the Ocean Drilling Program. Scientific Results, 2007. Ocean Drilling Program College Station, TX, 1-24.
- JOCHUM, K. P., WEIS, U., STOLL, B., KUZMIN, D., YANG, Q., RACZEK, I., JACOB, D. E., STRACKE, A., BIRBAUM, K. & FRICK, D. A. 2011. Determination of reference values for NIST SRM 610–617 glasses following ISO guidelines. *Geostandards and Geoanalytical Research*, 35, 397-429.
- JOHN, C. M., KARNER, G. D., BROWNING, E., LECKIE, R. M., MATEO, Z., CARSON, B. & LOWERY, C. 2011. Timing and magnitude of Miocene eustasy derived from the mixed siliciclastic-carbonate stratigraphic record of the northeastern Australian margin. *Earth and Planetary Science Letters*, 304, 455-467.
- JOHN, C. M., KARNER, G. D. & MUTTI, M. 2004.  $\delta^{18}\text{O}$  and Marion Plateau backstripping: combining two approaches to constrain late middle Miocene eustatic amplitude. *Geology*, 32, 829-832.
- JOHN, E. H., WILSON, J. D., PEARSON, P. N. & RIDGWELL, A. 2014. Temperature-dependent remineralization and carbon cycling in the warm Eocene oceans. *Palaeogeography, Palaeoclimatology, Palaeoecology*, 413, 158-166.
- KATZ, A. 1973. The interaction of magnesium with calcite during crystal growth at 25–90 C and one atmosphere. *Geochimica et Cosmochimica Acta*, 37, 1563-1586.
- KATZ, A., SASS, E., STARINSKY, A. & HOLLAND, H. 1972. Strontium behavior in the aragonite-calcite transformation: An experimental study at 40–98 C. *Geochimica et Cosmochimica Acta*, 36, 481-496.
- KELLER, G. 1985. Depth stratification of planktonic foraminifers in the Miocene ocean. *The Miocene ocean: paleoceanography and biogeography*, 163, 177-196.
- KELLER, G. & BARRON, J. A. 1987. Paleodepth distribution of Neocene deep-sea hiatuses. *Paleoceanography*, 2, 697-713.
- KEUL, N., LANGER, G., THOMS, S., DE NOOIJER, L. J., REICHART, G. J. & BIJMA, J. 2017. Exploring foraminiferal Sr/Ca as a new carbonate system proxy. *Geochimica et Cosmochimica Acta*, 202, 374-386.

- KEY, R. M., OLSEN, A., VAN HEUVEN, S., LAUVSET, S. K., VELO, A., LIN, X., SCHIRNICK, C., KOZYR, A., TANHUA, T. & HOPPEMA, M. 2015. Global Ocean Data Analysis Project, Version 2 (GLODAPv2). Carbon Dioxide Information Analysis Center, Oak Ridge Nat Lab.
- KIM, S.-T. & O'NEIL, J. R. 1997. Equilibrium and nonequilibrium oxygen isotope effects in synthetic carbonates. *Geochimica et Cosmochimica Acta*, 61, 3461-3475.
- KISAKÜREK, B., EISENHAEUER, A., BÖHM, F., GARBE-SCHÖNBERG, D. & EREZ, J. 2008. Controls on shell Mg/Ca and Sr/Ca in cultured planktonic foraminiferan, *Globigerinoides ruber* (white). *Earth and Planetary Science Letters*, 273, 260-269.
- KISAKÜREK, B., EISENHAEUER, A., BÖHM, F., GARBE-SCHÖNBERG, D. & EREZ, J. 2008. Controls on shell Mg/Ca and Sr/Ca in cultured planktonic foraminiferan, *Globigerinoides ruber* (white). *Earth and Planetary Science Letters*, 273, 260-269.
- KLINKHAMMER, G. P. 1980. Early diagenesis in sediments from the eastern equatorial Pacific, II. Pore water metal results. *Earth and Planetary Science Letters*, 49, 81-101.
- KNORR, G., BUTZIN, M., MICHEELS, A. & LOHMANN, G. 2011. A warm Miocene climate at low atmospheric CO<sub>2</sub> levels. *Geophysical Research Letters*, 38.
- KOHO, K., DE NOOIJER, L. & REICHART, G. 2015. Combining benthic foraminiferal ecology and shell Mn/Ca to deconvolve past bottom water oxygenation and paleoproductivity. *Geochimica et Cosmochimica Acta*, 165, 294-306.
- KOMINZ, M. A., MILLER, K. G., BROWNING, J. V., KATZ, M. E. & MOUNTAIN, G. S. 2016. Miocene relative sea level on the New Jersey shallow continental shelf and coastal plain derived from one-dimensional backstripping: A case for both eustasy and epeirogeny. *Geosphere*, 12, 1437-1456.
- KOUTAVAS, A. & JOANIDES, S. 2012. El Niño–Southern Oscillation extrema in the Holocene and Last Glacial Maximum. *Paleoceanography and Paleoclimatology*, 27.
- KROOPNICK, P. 1985. The distribution of <sup>13</sup>C of ΣCO<sub>2</sub> in the world oceans. *Deep Sea Research Part A. Oceanographic Research Papers*, 32, 57-84.
- KUMP, L. R. & ARTHUR, M. A. 1999. Interpreting carbon-isotope excursions: carbonates and organic matter. *Chemical Geology*, 161, 181-198.
- LARIVIERE, J. P., RAVELO, A. C., CRIMMINS, A., DEKENS, P. S., FORD, H. L., LYLE, M. & WARA, M. W. 2012. Late Miocene decoupling of oceanic warmth and atmospheric carbon dioxide forcing. *Nature*, 486, 97.
- LAUVSET, S. K., KEY, R. M., OLSEN, A., VAN HEUVEN, S., VELO, A., LIN, X., SCHIRNICK, C., KOZYR, A., TANHUA, T. & HOPPEMA, M. 2016. A new global interior ocean mapped climatology: the 1°× 1° GLODAP version 2. *Earth System Science Data*, 8, 325.
- LEA, D. W., MARTIN, P. A. & SPERO, H. 1995. Calcium uptake and calcification rate in the planktonic foraminifer *Orbulina universa*. *Oceanographic Literature Review*, 10, 865-866.
- LEA, D. W., MASHIOTTA, T. A. & SPERO, H. J. 1999. Controls on magnesium and strontium uptake in planktonic foraminifera determined by live culturing. *Geochimica et Cosmochimica Acta*, 63, 2369-2379.

- LEA, D. W., PAK, D. K. & PARADIS, G. 2005. Influence of volcanic shards on foraminiferal Mg/Ca in a core from the Galápagos region. *Geochemistry, Geophysics, Geosystems*, 6.
- LEAR, C. H., BAILEY, T. R., PEARSON, P. N., COXALL, H. K. & ROSENTHAL, Y. 2008. Cooling and ice growth across the Eocene-Oligocene transition. *Geology*, 36, 251-254.
- LEAR, C. H., COXALL, H. K., FOSTER, G. L., LUNT, D. J., MAWBNEY, E. M., ROSENTHAL, Y., SOSDIAN, S. M., THOMAS, E. & WILSON, P. A. 2015. Neogene ice volume and ocean temperatures: Insights from infaunal foraminiferal Mg/Ca paleothermometry. *Paleoceanography*.
- LEAR, C. H., ELDERFIELD, H. & WILSON, P. 2000. Cenozoic deep-sea temperatures and global ice volumes from Mg/Ca in benthic foraminiferal calcite. *Science*, 287, 269-272.
- LEAR, C. H., ELDERFIELD, H. & WILSON, P. A. 2003a. A Cenozoic seawater Sr/Ca record from benthic foraminiferal calcite and its application in determining global weathering fluxes. *Earth and Planetary Science Letters*, 208, 69-84.
- LEAR, C. H., MAWBNEY, E. M. & ROSENTHAL, Y. 2010. Cenozoic benthic foraminiferal Mg/Ca and Li/Ca records: Toward unlocking temperatures and saturation states. *Paleoceanography*, 25.
- LEAR, C. H., ROSENTHAL, Y. & SLOWEY, N. 2002. Benthic foraminiferal Mg/Ca-paleothermometry: A revised core-top calibration. *Geochimica et Cosmochimica Acta*, 66, 3375-3387.
- LEAR, C. H., ROSENTHAL, Y. & WRIGHT, J. D. 2003b. The closing of a seaway: Ocean water masses and global climate change. *Earth and Planetary Science Letters*, 210, 425-436.
- LEGRANDE, A. N. & SCHMIDT, G. A. 2006. Global gridded data set of the oxygen isotopic composition in seawater. *Geophysical Research Letters*, 33.
- LEMARCHAND, D., GAILLARDET, J., LEWIN, E. & ALLEGRE, C. 2000. The influence of rivers on marine boron isotopes and implications for reconstructing past ocean pH. *Nature*, 408, 951-954.
- LEMARCHAND, D., GAILLARDET, J., LEWIN, E. & ALLEGRE, C. 2002. Boron isotope systematics in large rivers: implications for the marine boron budget and paleo-pH reconstruction over the Cenozoic. *Chemical Geology*, 190, 123-140.
- LEVY, R., HARWOOD, D., FLORINDO, F., SANGIORGI, F., TRIPATI, R., VON EYNATTEN, H., GASSON, E., KUHN, G., TRIPATI, A. & DECONTO, R. 2016. Antarctic ice sheet sensitivity to atmospheric CO<sub>2</sub> variations in the early to mid-Miocene. *Proceedings of the National Academy of Sciences*, 201516030.
- LEWIS, A., MARCHANT, D., ASHWORTH, A., HEMMING, S. & MACHLUS, M. 2007. Major middle Miocene global climate change: Evidence from East Antarctica and the Transantarctic Mountains. *Geological Society of America Bulletin*, 119, 1449-1461.
- LO GIUDICE CAPPELLI, E., REGENBERG, M., HOLBOURN, A., KUHN, W., GARBE-SCHÖNBERG, D. & ANDERSEN, N. 2015. Refining *C. wuellerstorfi* and *H. elegans* Mg/Ca temperature calibrations. *Marine Micropaleontology*, 121, 70-84.
- LONGERICH, H., JACKSON, S. & GUNTHER, D. 1996. Laser ablation inductively coupled plasma mass spectrometric transient signal data acquisition and analyte concentration

calculation (vol 11, pg 899, 1996). ROYAL SOC CHEMISTRY THOMAS GRAHAM HOUSE, SCIENCE PARK, MILTON ROAD, CAMBRIDGE, CAMBS, ENGLAND CB4 4WF.

- LUNT, D. J., FLECKER, R., VALDES, P. J., SALZMANN, U., GLADSTONE, R. & HAYWOOD, A. M. 2008. A methodology for targeting palaeo proxy data acquisition: A case study for the terrestrial late Miocene. *Earth and Planetary Science Letters*, 271, 53-62.
- LUTZE, G. F. & THIEL, H. 1989. Epibenthic foraminifera from elevated microhabitats; Cibicidoides wuellerstorfi and Planulina ariminensis. *The Journal of Foraminiferal Research*, 19, 153-158.
- LYLE, M., DADEY, K. A. & FARRELL, J. W. 1995. 42. The Late Miocene (11–8 Ma) Eastern Pacific Carbonate Crash: evidence for reorganization of deep-water Circulation by the closure of the Panama Gateway. *1995 Proceedings of the Ocean Drilling Program, Scientific Results*, 138.
- LYNCH-STIEGLITZ, J., CURRY, W. B. & SLOWEY, N. 1999. A geostrophic transport estimate for the Florida Current from the oxygen isotope composition of benthic foraminifera. *Paleoceanography*, 14, 360-373.
- MACGREGOR, D. 2015. History of the development of the East African Rift System: A series of interpreted maps through time. *Journal of African Earth Sciences*, 101, 232-252.
- MANGINI, A., HALBACH, P., PUTEANUS, D. & SEGL, M. 1987. Chemistry and growth history of central Pacific Mn-crusts and their economic importance. *Marine Minerals*. Springer.
- MARCHITTO, T. M., CURRY, W. B., LYNCH-STIEGLITZ, J., BRYAN, S. P., COBB, K. M. & LUND, D. C. 2014. Improved oxygen isotope temperature calibrations for cosmopolitan benthic foraminifera. *Geochimica et Cosmochimica Acta*, 130, 1-11.
- MARTIN, P. A., LEA, D. W., ROSENTHAL, Y., SHACKLETON, N. J., SARNTHEIN, M. & PAPENFUSS, T. 2002. Quaternary deep sea temperature histories derived from benthic foraminiferal Mg/Ca. *Earth and Planetary Science Letters*, 198, 193-209.
- MARTIN, W. & SAYLES, F. 1996. CaCO<sub>3</sub> dissolution in sediments of the Ceara Rise, western equatorial Atlantic. *Geochimica et Cosmochimica Acta*, 60, 243-263.
- MAWBAY, E. M. 2012. *Cenozoic Records of Seawater Chemistry: Chemical Proxies as Indicators of Past Climate*. Cardiff University.
- MAWBAY, E. M. & LEAR, C. H. 2013. Carbon cycle feedbacks during the Oligocene-Miocene transient glaciation. *Geology*, 41, 963-966.
- MAY, T. W. & WIEDMEYER, R. H. 1998. A table of polyatomic interferences in ICP-MS. *ATOMIC SPECTROSCOPY-NORWALK CONNECTICUT-*, 19, 150-155.
- MBEDE, E. I. 1987. A review of the hydrocarbon potential of Kenya. *Journal of African Earth Sciences (1983)*, 6, 313-322.
- MBEDE, E. I. & DUALEH, A. 1997. The coastal basins of Somalia, Kenya and Tanzania. *Sedimentary Basins of the World*. Elsevier.
- MCCLANAHAN, T. R. 1988. Seasonality in East Africa's coastal waters. *Marine Ecology Progress Series*, 191-199.

- MCCORKLE, D. C., MARTIN, P. A., LEA, D. W. & KLINKHAMMER, G. P. 1995. Evidence of a dissolution effect on benthic foraminiferal shell chemistry:  $\delta^{13}\text{C}$ , Cd/Ca, Ba/Ca, and Sr/Ca results from the Ontong Java Plateau. *Paleoceanography*, 10, 699-714.
- MILLER, K. G., WRIGHT, J. D. & FAIRBANKS, R. G. 1991. Unlocking the ice house: Oligocene-Miocene oxygen isotopes, eustasy, and margin erosion. *Journal of Geophysical Research: Solid Earth (1978–2012)*, 96, 6829-6848.
- MUDELSEE, M., BICKERT, T., LEAR, C. H. & LOHMANN, G. 2014. Cenozoic climate changes: A review based on time series analysis of marine benthic  $\delta^{18}\text{O}$  records. *Reviews of Geophysics*, 52, 333-374.
- MÜLLER, P. J., KIRST, G., RUHLAND, G., VON STORCH, I. & ROSELL-MELÉ, A. 1998. Calibration of the alkenone paleotemperature index U 37 K' based on core-tops from the eastern South Atlantic and the global ocean (60 N-60 S). *Geochimica et Cosmochimica Acta*, 62, 1757-1772.
- MÜLLER, W., SHELLEY, M., MILLER, P. & BROUDE, S. 2009. Initial performance metrics of a new custom-designed ArF excimer LA-ICPMS system coupled to a two-volume laser-ablation cell. *Journal of Analytical Atomic Spectrometry*, 24, 209-214.
- NÍ FHLAITHEARTA, S., REICHART, G. J., JORISSEN, F. J., FONTANIER, C., ROHLING, E., THOMSON, J. & DE LANGE, G. 2010. Reconstructing the seafloor environment during sapropel formation using benthic foraminiferal trace metals, stable isotopes, and sediment composition. *Paleoceanography*, 25.
- NÜRNBERG, D. 1996. Magnesium in tests of *Neogloboquadrina pachyderma* sinistral from high northern and southern latitudes. *Oceanographic Literature Review*, 43.
- NURNBERG, D., BIJMA, J. & HEMLEBEN, C. 1996. Assessing the reliability of magnesium in foraminiferal calcite as a proxy for water mass temperature. *Geochim. Cosmochim. Acta*, 60, 803-814.
- NÜRNBERG, D., BIJMA, J. & HEMLEBEN, C. 1996. Assessing the reliability of magnesium in foraminiferal calcite as a proxy for water mass temperatures. *Geochimica et Cosmochimica Acta*, 60, 803-814.
- NYAGAH, K. 1995. Stratigraphy, depositional history and environments of deposition of Cretaceous through Tertiary strata in the Lamu Basin, southeast Kenya and implications for reservoirs for hydrocarbon exploration. *Sedimentary Geology*, 96, 43-71.
- OOMORI, T., KANESHIMA, H., MAEZATO, Y. & KITANO, Y. 1987. Distribution coefficient of  $\text{Mg}^{2+}$  ions between calcite and solution at 10–50° C. *Marine Chemistry*, 20, 327-336.
- PAGANI, M., ARTHUR, M. A. & FREEMAN, K. H. 1999a. Miocene evolution of atmospheric carbon dioxide. *Paleoceanography*, 14, 273-292.
- PAGANI, M., FREEMAN, K. H. & ARTHUR, M. A. 1999b. Late Miocene atmospheric CO<sub>2</sub> concentrations and the expansion of C<sub>4</sub> grasses. *Science*, 285, 876-879.
- PALMER, M. 1985. Rare earth elements in foraminifera tests. *Earth and planetary science letters*, 73, 285-298.

- PEACOR, D. R., ESSENE, E. J. & GAINES, A. 1987. Petrologic and crystal-chemical implications of cation order-disorder in kutnahorite [CaMn (CO<sub>3</sub>)<sub>2</sub>]. *American Mineralogist*, 72, 319-328.
- PEARCE, N. J., PERKINS, W. T., WESTGATE, J. A., GORTON, M. P., JACKSON, S. E., NEAL, C. R. & CHENERY, S. P. 1997. A compilation of new and published major and trace element data for NIST SRM 610 and NIST SRM 612 glass reference materials. *Geostandards and Geoanalytical Research*, 21, 115-144.
- PEARSON, P. N. 2012. Oxygen isotopes in foraminifera: Overview and Historical review. *Paleontological Society Papers*, 18, 1-38.
- PEARSON, P. N. & BURGESS, C. E. 2008. Foraminifer test preservation and diagenesis: comparison of high latitude Eocene sites. *Geological Society, London, Special Publications*, 303, 59-72.
- PEARSON, P. N., DITCHFIELD, P. W., SINGANO, J., HARCOURT-BROWN, K. G., NICHOLAS, C. J., OLSSON, R. K., SHACKLETON, N. J. & HALL, M. A. 2001. Warm tropical sea surface temperatures in the Late Cretaceous and Eocene epochs. *Nature*, 413, 481-487.
- PEDERSEN, T. & PRICE, N. 1982. The geochemistry of manganese carbonate in Panama Basin sediments. *Geochimica et Cosmochimica Acta*, 46, 59-68.
- PENA, L., CACHO, I., CALVO, E., PELEJERO, C., EGGINS, S. & SADEKOV, A. 2008. Characterization of contaminant phases in foraminifera carbonates by electron microprobe mapping. *Geochemistry, Geophysics, Geosystems*, 9.
- PENA, L., CALVO, E., CACHO, I., EGGINS, S. & PELEJERO, C. 2005. Identification and removal of Mn-Mg-rich contaminant phases on foraminiferal tests: Implications for Mg/Ca past temperature reconstructions. *Geochemistry, Geophysics, Geosystems*, 6.
- PETERSEN, J., BARRAS, C., BÉZOS, A., LA, C., DE NOOIJER, L. J., MEYSMAN, F. J. R., MOURET, A., SLOMP, C. P. & JORISSEN, F. J. 2018. Mn/Ca intra- and inter-test variability in the benthic foraminifer *Ammonia tepida*. *Biogeosciences*, 15, 331-348.
- PISIAS, N. & MIX, A. 1988. Aliasing of the geologic record and the search for long-period Milankovitch cycles. *Paleoceanography*, 3, 613-619.
- POLLARD, D. & DECONTO, R. M. 2005. Hysteresis in Cenozoic Antarctic ice-sheet variations. *Global and Planetary Change*, 45, 9-21.
- POLLARD, D., DECONTO, R. M. & ALLEY, R. B. 2015. Potential Antarctic Ice Sheet retreat driven by hydrofracturing and ice cliff failure. *Earth and Planetary Science Letters*, 412, 112-121.
- POUND, M. J., HAYWOOD, A. M., SALZMANN, U., RIDING, J. B., LUNT, D. J. & HUNTER, S. J. 2011. A Tortonian (late Miocene, 11.61–7.25 Ma) global vegetation reconstruction. *Palaeogeography, Palaeoclimatology, Palaeoecology*, 300, 29-45.
- RAE, J. W., FOSTER, G. L., SCHMIDT, D. N. & ELLIOTT, T. 2011. Boron isotopes and B/Ca in benthic foraminifera: proxies for the deep ocean carbonate system. *Earth and Planetary Science Letters*, 302, 403-413.

- RAITZSCH, M., HATHORNE, E. C., KUHNERT, H., GROENEVELD, J. & BICKERT, T. 2011a. Modern and late Pleistocene B/Ca ratios of the benthic foraminifer *Planulina wuellerstorfi* determined with laser ablation ICP-MS. *Geology*, 39, 1039-1042.
- RAITZSCH, M. & HÖNISCH, B. 2013. Cenozoic boron isotope variations in benthic foraminifers. *Geology*, 41, 591-594.
- RAITZSCH, M., KUHNERT, H., HATHORNE, E. C., GROENEVELD, J. & BICKERT, T. 2011b. U/Ca in benthic foraminifers: A proxy for the deep-sea carbonate saturation. *Geochemistry, Geophysics, Geosystems*, 12.
- RATHMANN, S., HESS, S., KUHNERT, H. & MULITZA, S. 2004. Mg/Ca ratios of the benthic foraminifera *Oridorsalis umbonatus* obtained by laser ablation from core top sediments: Relationship to bottom water temperature. *Geochemistry, Geophysics, Geosystems*, 5.
- REICHART, G.-J., JORISSEN, F., ANSCHUTZ, P. & MASON, P. R. 2003. Single foraminiferal test chemistry records the marine environment. *Geology*, 31, 355-358.
- REIMERS, C. E. 1987. An in situ microprofiling instrument for measuring interfacial pore water gradients: methods and oxygen profiles from the North Pacific Ocean. *Deep Sea Research Part A. Oceanographic Research Papers*, 34, 2019-2035.
- REYNOLDS, D., HALL, I., SCOURSE, J., RICHARDSON, C., WANAMAKER, A. & BUTLER, P. 2017. Biological and Climate Controls on North Atlantic Marine Carbon Dynamics Over the Last Millennium: Insights From an Absolutely Dated Shell-Based Record From the North Icelandic Shelf. *Global Biogeochemical Cycles*.
- ROHLING, E. J. & COOKE, S. 1999. Stable oxygen and carbon isotopes in foraminiferal carbonate shells. *Modern foraminifera*. Springer.
- ROSENTHAL, Y., BOYLE, E. A. & SLOWEY, N. 1997. Temperature control on the incorporation of magnesium, strontium, fluorine, and cadmium into benthic foraminiferal shells from Little Bahama Bank: Prospects for thermocline paleoceanography. *Geochimica et Cosmochimica Acta*, 61, 3633-3643.
- ROSENTHAL, Y., LEAR, C. H., OPPO, D. W. & LINSLEY, B. K. 2006. Temperature and carbonate ion effects on Mg/Ca and Sr/Ca ratios in benthic foraminifera: Aragonitic species *Hoeglundina elegans*. *Paleoceanography*, 21.
- ROSENTHAL, Y. & LOHMANN, G. P. 2002. Accurate estimation of sea surface temperatures using dissolution-corrected calibrations for Mg/Ca paleothermometry. *Paleoceanography*, 17, 16-1-16-6.
- ROUSSELLE, G., BELTRAN, C., SICRE, M.-A., RAFFI, I. & DE RAFÉLIS, M. 2013. Changes in sea-surface conditions in the Equatorial Pacific during the middle Miocene–Pliocene as inferred from coccolith geochemistry. *Earth and Planetary Science Letters*, 361, 412-421.
- RSTUDIO, T. 2015. RStudio: integrated development for R. *RStudio, Inc., Boston, MA* URL <http://www.rstudio.com>, 42.
- RUSSELL, A. D., HÖNISCH, B., SPERO, H. J. & LEA, D. W. 2004. Effects of seawater carbonate ion concentration and temperature on shell U, Mg, and Sr in cultured planktonic foraminifera. *Geochimica et Cosmochimica Acta*, 68, 4347-4361.

- RUSSO, R. E., MAO, X., LIU, H., GONZALEZ, J. & MAO, S. S. 2002. Laser ablation in analytical chemistry—a review. *Talanta*, 57, 425-451.
- SADEKOV, A., EGGINS, S. M., DE DECKKER, P. & KROON, D. 2008a. Uncertainties in seawater thermometry deriving from intratest and intertest Mg/Ca variability in *Globigerinoides ruber*. *Paleoceanography*, 23.
- SADEKOV, A., EGGINS, S. M., DE DECKKER, P. & KROON, D. 2008b. Uncertainties in seawater thermometry deriving from intratest and intertest Mg/Ca variability in *Globigerinoides ruber*. *Paleoceanography and Paleoclimatology*, 23.
- SADEKOV, A. Y., EGGINS, S. M. & DE DECKKER, P. 2005. Characterization of Mg/Ca distributions in planktonic foraminifera species by electron microprobe mapping. *Geochemistry, Geophysics, Geosystems*, 6.
- SADEKOV, A. Y., EGGINS, S. M., KLINKHAMMER, G. P. & ROSENTHAL, Y. 2010. Effects of seafloor and laboratory dissolution on the Mg/Ca composition of *Globigerinoides sacculifer* and *Orbulina universa* tests—A laser ablation ICPMS microanalysis perspective. *Earth and Planetary Science Letters*, 292, 312-324.
- SCHIEBEL, R. & HEMLEBEN, C. 2017. *Planktic Foraminifers in the Modern Ocean*, Springer.
- SCHMIDT, D., ELLIOTT, T. & KASEMANN, S. 2008. The influences of growth rates on planktic foraminifers as proxies for palaeostudies—a review. *Geological Society, London, Special Publications*, 303, 73-85.
- SCHMIDT, M. W., VAUTRAVERS, M. J. & SPERO, H. J. 2006. Western Caribbean sea surface temperatures during the late Quaternary. *Geochemistry, Geophysics, Geosystems*, 7.
- SCHRAG, D. P. 1999. Effects of diagenesis on the isotopic record of late Paleogene tropical sea surface temperatures. *Chemical Geology*, 161, 215-224.
- SCHULZ, H. D. & ZABEL, M. 2006. *Marine geochemistry*, Springer.
- SEKI, O., SCHMIDT, D. N., SCHOUTEN, S., HOPMANS, E. C., SINNINGHE DAMSTÉ, J. S. & PANCOST, R. D. 2012a. Paleoceanographic changes in the Eastern Equatorial Pacific over the last 10 Myr. *Paleoceanography*, 27.
- SEKI, O., SCHMIDT, D. N., SCHOUTEN, S., HOPMANS, E. C., SINNINGHE DAMSTÉ, J. S. & PANCOST, R. D. 2012b. Paleoceanographic changes in the Eastern Equatorial Pacific over the last 10 Myr. *Paleoceanography and Paleoclimatology*, 27.
- SEXTON, P. F. & WILSON, P. A. 2009. Preservation of benthic foraminifera and reliability of deep-sea temperature records: Importance of sedimentation rates, lithology, and the need to examine test wall structure. *Paleoceanography*, 24.
- SEXTON, P. F., WILSON, P. A. & PEARSON, P. N. 2006. Microstructural and geochemical perspectives on planktic foraminiferal preservation: “Glassy” versus “Frosty”. *Geochemistry, Geophysics, Geosystems*, 7.
- SHACKLETON, N. 1967. Oxygen isotope analyses and Pleistocene temperatures re-assessed.pdf>.
- SHACKLETON, N. 1974. Attainment of isotopic equilibrium between ocean water and the benthonic foraminifera genus *Uvigerina*: isotopic changes in the ocean during the last glacial.

- SHACKLETON, N. & KENNETT, J. 1975. Paleotemperature history of the Cenozoic and the initiation of Antarctic glaciation: oxygen and carbon isotope analyses in DSDP Sites 277, 279, and 281. *Initial reports of the deep sea drilling project*, 29, 743-755.
- SHEVENELL, A. E., KENNETT, J. P. & LEA, D. W. 2004. Middle Miocene southern ocean cooling and Antarctic cryosphere expansion. *Science*, 305, 1766-1770.
- SHEVENELL, A. E., KENNETT, J. P. & LEA, D. W. 2008. Middle Miocene ice sheet dynamics, deep-sea temperatures, and carbon cycling: A Southern Ocean perspective. *Geochemistry, Geophysics, Geosystems*, 9.
- SOSDIAN, S. & ROSENTHAL, Y. 2009. Deep-sea temperature and ice volume changes across the Pliocene-Pleistocene climate transitions. *Science*, 325, 306-310.
- SOSDIAN, S. M., GREENOP, R., HAIN, M. P., FOSTER, G. L., PEARSON, P. N. & LEAR, C. H. 2018. Constraining the evolution of Neogene ocean carbonate chemistry using the boron isotope pH proxy. *Earth and Planetary Science Letters*, 498, 362-376.
- SOSDIAN, S. M., LEAR, C. H., TAO, K., GROSSMAN, E. L., O'DEA, A. & ROSENTHAL, Y. 2012. Cenozoic seawater Sr/Ca evolution. *Geochemistry, Geophysics, Geosystems*, 13, n/a-n/a.
- SPERO, H. J., BIJMA, J., LEA, D. W. & BEMIS, B. E. 1997. Effect of seawater carbonate concentration on foraminiferal carbon and oxygen isotopes. *Nature*, 390, 497-500.
- SPERO, H. J., EGGINS, S. M., RUSSELL, A. D., VETTER, L., KILBURN, M. R. & HÖNISCH, B. 2015. Timing and mechanism for intratest Mg/Ca variability in a living planktic foraminifer. *Earth and Planetary Science Letters*, 409, 32-42.
- SPERO, H. J. & PARKER, S. L. 1985. Photosynthesis in the symbiotic planktonic foraminifer *Orbulina universa*, and its potential contribution to oceanic primary productivity. *The Journal of Foraminiferal Research*, 15, 273-281.
- SPIVACK, A. & EDMOND, J. 1987. Boron isotope exchange between seawater and the oceanic crust. *Geochimica et Cosmochimica Acta*, 51, 1033-1043.
- SRIVASTAVA, R., RAMESH, R., PRAKASH, S., ANILKUMAR, N. & SUDHAKAR, M. 2007. Oxygen isotope and salinity variations in the Indian sector of the Southern Ocean. *Geophysical Research Letters*, 34.
- STEWART, D. R., PEARSON, P. N., DITCHFIELD, P. W. & SINGANO, J. M. 2004. Miocene tropical Indian Ocean temperatures: evidence from three exceptionally preserved foraminiferal assemblages from Tanzania. *Journal of African Earth Sciences*, 40, 173-189.
- TACHIKAWA, K. & ELDERFIELD, H. 2002. Microhabitat effects on Cd/Ca and  $\delta^{13}\text{C}$  of benthic foraminifera. *Earth and Planetary Science Letters*, 202, 607-624.
- THIL, F., BLAMART, D., ASSAILLY, C., LAZARETH, C. E., LEBLANC, T., BUTSHER, J. & DOUVILLE, E. 2016. Development of laser ablation multi-collector inductively coupled plasma mass spectrometry for boron isotopic measurement in marine biocarbonates: New improvements and application to a modern *Porites* coral. *Rapid Communications in Mass Spectrometry*, 30, 359-371.

- TOYOFUKU, T., KITAZATO, H., KAWAHATA, H., TSUCHIYA, M. & NOHARA, M. 2000. Evaluation of Mg/Ca thermometry in foraminifera: Comparison of experimental results and measurements in nature. *Paleoceanography*, 15, 456-464.
- TRIPATI, A. K., DELANEY, M. L., ZACHOS, J. C., ANDERSON, L. D., KELLY, D. C. & ELDERFIELD, H. 2003. Tropical sea-surface temperature reconstruction for the early Paleogene using Mg/Ca ratios of planktonic foraminifera. *Paleoceanography*, 18.
- TURCO, E., HILGEN, F., LOURENS, L., SHACKLETON, N. & ZACHARIASSE, W. 2001. Punctuated evolution of global climate cooling during the Late Middle to Early Late Miocene: High-resolution planktonic foraminiferal and oxygen isotope records from the Mediterranean. *Paleoceanography*, 16, 405-423.
- UREY, H. C. 1947. The thermodynamic properties of isotopic substances. *J. Chem. Soc.*, 562-581.
- UREY, H. C., LOWENSTAM, H. A., EPSTEIN, S. & MCKINNEY, C. R. 1951. Measurement of paleotemperatures and temperatures of the Upper Cretaceous of England, Denmark, and the southeastern United States. *Geological Society of America Bulletin*, 62, 399-416.
- VAN DIJK, I., DE NOOIJER, L. J., WOLTHERS, M. & REICHART, G. J. 2017. Impacts of pH and [CO<sub>2</sub>] on the incorporation of Zn in foraminiferal calcite. *Geochimica et Cosmochimica Acta*, 197, 263-277.
- VEIZER, J., BRUCKSCHEN, P., PAWELLEK, F., DIENER, A., PODLAHA, O. G., CARDEN, G. A., JASPER, T., KORTE, C., STRAUSS, H. & AZMY, K. 1997. Oxygen isotope evolution of Phanerozoic seawater. *Palaeogeography, Palaeoclimatology, Palaeoecology*, 132, 159-172.
- VETTER, L., SPERO, H. J., EGGINS, S. M., WILLIAMS, C. & FLOWER, B. P. 2017. Oxygen isotope geochemistry of Laurentide ice-sheet meltwater across Termination I. *Quaternary Science Reviews*, 178, 102-117.
- VETTER, L., SPERO, H. J., RUSSELL, A. D. & FEHRENBACHER, J. S. 2013. LA-ICP-MS depth profiling perspective on cleaning protocols for elemental analyses in planktic foraminifers. *Geochemistry, Geophysics, Geosystems*, 14, 2916-2931.
- VINCENT, E. & BERGER, W. H. 1985. Carbon dioxide and polar cooling in the Miocene: The Monterey hypothesis. *The Carbon Cycle and Atmospheric CO<sub>2</sub>: Natural Variations Archean to Present*, 455-468.
- VON DER HEYDT, A. & DIJKSTRA, H. A. 2006. Effect of ocean gateways on the global ocean circulation in the late Oligocene and early Miocene. *Paleoceanography*, 21.
- WADE, B. S., PEARSON, P. N., BERGGREN, W. A. & PÄLIKE, H. 2011. Review and revision of Cenozoic tropical planktonic foraminiferal biostratigraphy and calibration to the geomagnetic polarity and astronomical time scale. *Earth-Science Reviews*, 104, 111-142.
- WEEDON, G. P. 2003. *Time-series analysis and cyclostratigraphy: examining stratigraphic records of environmental cycles*, Cambridge University Press.

- WELDEAB, S., ARCE, A. & KASTEN, S. 2016. Mg/Ca- $\Delta$ CO<sub>3</sub> pore water 2--temperature calibration for Globobulimina spp.: A sensitive paleothermometer for deep-sea temperature reconstruction. *Earth and Planetary Science Letters*, 438, 95-102.
- WESTERHOLD, T., BICKERT, T. & RÖHL, U. 2005. Middle to late Miocene oxygen isotope stratigraphy of ODP site 1085 (SE Atlantic): new constraints on Miocene climate variability and sea-level fluctuations. *Palaeogeography, Palaeoclimatology, Palaeoecology*, 217, 205-222.
- WILSON, P. A. & OPDYKE, B. N. 1996. Equatorial sea-surface temperatures for the Maastrichtian revealed through remarkable preservation of metastable carbonate. *Geology*, 24, 555-558.
- WOLLENBURG, J. E., RAITZSCH, M. & TIEDEMANN, R. 2015. Novel high-pressure culture experiments on deep-sea benthic foraminifera - Evidence for methane seepage-related  $\delta^{13}\text{C}$  of Cibicides wuellerstorfi. *Marine Micropaleontology*, 117, 47-64.
- WOODRUFF, F. & SAVIN, S. 1991. Mid-Miocene isotope stratigraphy in the deep sea: High-resolution correlations, paleoclimatic cycles, and sediment preservation. *Paleoceanography*, 6, 755-806.
- WU, G. & HILLAIRE-MARCEL, C. 1995. Application of LP-ICP-MS to benthic foraminifers. *Geochimica et Cosmochimica Acta*, 59, 409-414.
- YU, J. & ELDERFIELD, H. 2007. Benthic foraminiferal B/Ca ratios reflect deep water carbonate saturation state. *Earth and Planetary Science Letters*, 258, 73-86.
- YU, J. & ELDERFIELD, H. 2008. Mg/Ca in the benthic foraminifera *Cibicidoides wuellerstorfi* and *Cibicidoides mundulus*: Temperature versus carbonate ion saturation. *Earth and Planetary Science Letters*, 276, 129-139.
- YU, J., ELDERFIELD, H., GREAVES, M. & DAY, J. 2007. Preferential dissolution of benthic foraminiferal calcite during laboratory reductive cleaning. *Geochemistry, Geophysics, Geosystems*, 8.
- YU, J., FOSTER, G. L., ELDERFIELD, H., BROECKER, W. S. & CLARK, E. 2010. An evaluation of benthic foraminiferal B/Ca and  $\delta^{11}\text{B}$  for deep ocean carbonate ion and pH reconstructions. *Earth and Planetary Science Letters*, 293, 114-120.
- ZACHOS, J., PAGANI, M., SLOAN, L., THOMAS, E. & BILLUPS, K. 2001. Trends, rhythms, and aberrations in global climate 65 Ma to present. *Science*, 292, 686-93.
- ZACHOS, J. C., DICKENS, G. R. & ZEEBE, R. E. 2008. An early Cenozoic perspective on greenhouse warming and carbon-cycle dynamics. *Nature*, 451, 279-283.
- ZACHOS, J. C., STOTT, L. D. & LOHMANN, K. C. 1994. Evolution of early Cenozoic marine temperatures. *Paleoceanography*, 9, 353-387.
- ZEEBE, R. 1999. An explanation of the effect of seawater carbonate concentration on foraminiferal oxygen isotopes.pdf>.
- ZEEBE, R. E. 2001. Seawater pH and isotopic paleotemperatures of Cretaceous oceans. *Palaeogeography, Palaeoclimatology, Palaeoecology*, 170, 49-57.

- ZEEBE, R. E. 2007. Modeling CO<sub>2</sub> chemistry,  $\delta^{13}\text{C}$ , and oxidation of organic carbon and methane in sediment porewater: Implications for paleo-proxies in benthic foraminifera. *Geochimica et Cosmochimica Acta*, 71, 3238-3256.
- ZEEBE, R. E. & WOLF-GLADROW, D. A. 2001. *CO<sub>2</sub> in seawater: equilibrium, kinetics, isotopes*, Gulf Professional Publishing.
- ZHANG, Y. G., PAGANI, M. & LIU, Z. 2014. A 12-million-year temperature history of the tropical Pacific Ocean. *Science*, 344, 84-87.
- ZHANG, Y. G., PAGANI, M., LIU, Z., BOHATY, S. M. & DECONTO, R. 2013. A 40-million-year history of atmospheric CO<sub>2</sub>. *Philosophical Transactions of the Royal Society A: Mathematical, Physical and Engineering Sciences*, 371, 20130096.
- ZHUANG, G., PAGANI, M. & ZHANG, Y. G. 2017. Monsoonal upwelling in the western Arabian Sea since the middle Miocene. *Geology*, 45, 655-658.

## 9 Appendices

**Appendix 1:** Weighed coarse fraction (% >63 $\mu\text{m}$ ) in the Sunbird-1 core. Shaded samples are discounted. See text for details.

Depth (MBSL)	Age (Ma)	Coarse Fraction (% >63 $\mu\text{m}$ )
1356	9.44	58.11
1359	9.48	60.93
1362	9.52	15.18
1365	9.57	19.84
1368	9.61	13.30
1371	9.65	11.52
1374	9.69	8.98
1377	9.73	9.58
1380	9.78	7.86
1383	9.82	16.27

1386	9.86	8.67
1389	9.90	12.07
1392	9.94	10.44
1395	9.99	14.98
1398	10.03	10.26
1401	10.07	8.32
1404	10.11	13.71
1407	10.15	14.43
1410	10.20	10.19
1413	10.24	12.43
1416	10.28	7.11
1419	10.32	8.39
1422	10.36	10.10
1425	10.41	10.30
1428	10.45	9.82
1431	10.49	12.81

1434	10.54	11.43
1437	10.59	7.80
1440	10.64	8.81
1443	10.69	8.42
1446	10.74	4.64
1449	10.79	7.34
1452	10.82	8.92
1455	10.86	7.28
1458	10.89	9.19
1461	10.93	11.97
1464	10.96	9.12
1467	10.99	12.98
1470	11.03	16.14
1473	11.06	11.31
1476	11.09	15.95
1476	11.13	12.25

1479	11.16	10.15
1482	11.20	12.37
1488	11.23	8.79
1491	11.26	8.88
1494	11.30	14.84
1497	11.33	17.32
1500	11.36	14.24
1503	11.40	16.40
1506	11.43	10.65
1509	11.47	10.19
1512	11.50	10.00
1515	11.53	10.27
1518	11.57	11.61
1521	11.60	11.00
1524	11.60	10.50
1527	11.61	10.15

1530	11.61	10.61
1533	11.62	8.60
1536	11.62	8.58
1539	11.63	5.72
1542	11.63	8.03
1545	11.66	7.33
1548	11.69	4.24
1551	11.71	7.60
1554	11.74	8.50
1557	11.77	8.36
1560	11.80	8.03
1563	11.82	11.70
1566	11.85	12.69
1569	11.88	10.36
1572	12.02	12.34
1575	12.16	12.10

1578	12.29	N/A
1581	12.43	13.29
1584	12.57	16.43
1587	12.66	15.15
1590	12.76	10.98
1593	12.85	14.08
1596	12.94	12.58
1599	13.04	10.98
1602	13.13	11.40
1605	13.20	13.50
1608	13.27	10.56
1611	13.34	12.95
1614	13.41	16.62
1617	13.48	17.23
1620	13.55	19.14
1623	13.62	21.09

1626

13.69

20.36

## **Appendix 2:** Cardiff University foraminifera cleaning procedure for trace metal analysis.

### **I. Before You Start**

- Set your tubes of crushed forams in a clean, perspex rack. Ensure samples are clearly labelled with permanent ink and record a list or diagram of samples before starting. Randomize your samples prior to cleaning.

- Locate your reagents (remake or refill as necessary). All reagents should be prepared and stored in new, acid-leached PE bottles. You will need:

10% HCl or HNO<sub>3</sub> for rinsing pipette tips (250 mL; top up bottle from labelled dewars in the flow bench each day you clean)

DI H<sub>2</sub>O for rinsing pipette tips (250 mL; rinse and refill bottle with fresh water each day you clean)

DI H<sub>2</sub>O for foram cleaning (500 mL wash bottle; rinse and refill with fresh water each day you clean)

Trace grade methanol for foram cleaning (store in a 250 mL bottle; pour off a small amount into a 125 mL spray bottle just before use)

Empty 60 mL bottle for reducing reagent

Empty 60 mL bottle for rinsing reducing reagent

Empty 60 mL bottle for oxidizing reagent

DI H<sub>2</sub>O for sample transfers (250 mL; rinse and refill bottle with fresh water each day you clean)

0.002 M HNO<sub>3</sub> for foram leaching (0.001 M for small samples) (250 mL; make fresh if old or contaminated)

- Turn on flow bench and allow to run for at least 15 minutes before using.
- Wipe down all work surfaces with DI water before starting (counter surfaces, interior of flow benches and fume cupboard, equipment surfaces).
- If floor has not been mopped recently, mop floor using DI water from the reservoir in Room 2.12.

## II. Removal of Fine Clays

1. Drain the ultrasonic bath in the flow bench and refill with fresh DI H<sub>2</sub>O. Fill to the base of your perspex rack. Use the prop provided and never fill below the minimum fill line.
2. Tap your sample rack firmly on the bench to shake forams to the base of tubes.
3. Open tube tops slowly in case forams are stuck to the sides or lids.
4. Using your DI H<sub>2</sub>O for foram cleaning, gently fill each tube most of the way.
5. If forams are visible in the tube lids, add a small amount of water to the lids as well.

Close tubes.

6. Tap rack firmly on the bench to settle forams and get rid of any air bubbles. CHL: If forams will not settle or bubbles won't rise, tap the side or corners of the rack firmly on the edge of the flow bench.
7. Turn on siphon (switch is on the rear of the pump, on the right-hand side). Always make sure the siphon tip is in the flow bench when the pump is on.
8. If siphon waste beaker is full, empty into the labelled waste container beneath the water purifier. Check the waste level throughout the cleaning process and don't let it rise above the "max fill" line.
9. Rinse siphon tip in 10% HCl (3x) and then DI H<sub>2</sub>O (3x) tip rinses. Don't siphon up too much tip rinse at once, as this can cause siphon waste to splash and contaminate the pump tubing.
10. Siphon off as much water as possible from the tubes. This works best if you avoid putting the siphon tip directly in the sample. Instead, rest the tip against the front of the tube, above water level, and siphon down gradually.
11. Open all tubes and fill ~1/3 full with water (not quite up to the rack base). Close tubes.  
CHL: The forams will agitate best in minimal H<sub>2</sub>O.
12. Tap rack as necessary to remove air bubbles.
13. Ultrasonicate for 1 minute (set the bath to "hold"). Fine clays should now be dislodged and held in suspension.
14. Turn off bath and remove rack. Open all tubes and vigorously squirt DI H<sub>2</sub>O for foram cleaning into each tube so as to agitate the sample and mix clays throughout. Close tubes.

15. Tap rack firmly on the bench, invert and shake, then wait for forams to settle. Don't wait too long, or suspended clays will also settle. If necessary, tap the rack again to encourage forams to settle.

16. Clean siphon tip (3x 10% HCl and 3x DI H<sub>2</sub>O) while waiting for forams to settle.

17. Siphon off as much water as possible. Don't siphon off your forams.

18. Repeat steps 11-17 a total of 3x with DI H<sub>2</sub>O. To avoid systematic variations in the effectiveness of clay removal: Begin siphoning at a different row and (or) side of the rack during each rinse step. Change the orientation of the rack in the sonic bath during each sonication.

19. Fill 125 mL spray bottle ~1/5 full with trace grade methanol. Loosen cap of spray bottle when not in use to keep methanol from dripping from the tip.

20. Repeat steps 11-17 1-2x with trace grade methanol, depending on the degree of clay contamination in your samples. Special instructions for methanol:

- Always wear goggles when working with methanol
- Fill tubes to the top of the rack with methanol (rather than just 1/3 full)
- Do not add additional methanol after ultrasonication; simply siphon off existing methanol
- Methanol is less viscous than water, so take special care when siphoning; don't go too quite to the bottom of the tube
- When siphoning methanol, it may work better to press siphon tip against the rear of the tube (rather than the front)

- Dispose of any leftover methanol in the labelled waste container
21. Repeat steps 11-17 an additional 2x with DI H<sub>2</sub>O.
  22. Pipette off all remaining water using a clean (3x 10% HCl and 3x DI H<sub>2</sub>O), 100 µL (yellow) pipette tip. It is not necessary to rinse the tip between samples.

### III. Removal of Metal Oxides (Reducing Step)

1. Turn on power source for hotplate in the fume cupboard and set to 300 °C.
2. Rinse and fill the glass evaporating dish in the fume cupboard with DI H<sub>2</sub>O from the ELGA tap. Fill to the base of your perspex rack. Set on hotplate.
3. Rinse and fill tall form beaker containing thermometer with DI H<sub>2</sub>O from the ELGA tap. Set on hot plate. Use this to top up the evaporating dish as water evaporates.
4. Drain the ultrasonic bath in the fume cupboard and refill with fresh DI H<sub>2</sub>O. Fill to the base of your perspex rack. Use the prop provided and never fill below the minimum fill line.
5. Prepare your reducing reagent in the labelled, empty 60 mL bottle. Please note that hydrous hydrazine is volatile, carcinogenic, and explosive. Always work in the fume cupboard and take care to minimize exposure. Dispose of all related waste (pipette tips, parafilm, gloves) in a plastic bag and seal bag before removing from fume cupboard.

- Pour 10 mLs ammonia solution and 10 mLs citric acid/ammonia solution (both stored in the fridge) into the empty bottle; pour these reagents directly from the bottles (no pipettes) and take care not to touch the lids of reagent bottles to any other surfaces.
  - Prepare a waste bag, a fresh strip of parafilm, and a clean (3x 10% HCl and 3x DI H<sub>2</sub>O) 1000 µL (blue) pipette tip
  - Remove hydrous hydrazine from fridge
  - Pipette 1200 µL hydrous hydrazine into the reducing reagent
  - Dispose of pipette tip
  - Cap reducing reagent and invert to mix
  - Re-parafilm hydrous hydrazine and return to fridge
6. Before proceeding, ensure hot water bath is hot (on verge of boiling, 80-90 °C). This can take about 30 minutes.
7. Open tubes. Using a clean (3x 10% HCl and 3x DI H<sub>2</sub>O) 100 µL pipette tip, add 100 µL reducing reagent to each tube. Be aware that the reagent has a low viscosity and tends to drip. Close tubes firmly.
8. Because ammonia has a high vapor pressure, tube caps will tend to blow open in the hot water bath. To prevent this, clamp tubes shut by screwing a perspex plate to the top of your rack. Ensure your tubes are firmly closed and that they are in good contact with the plate surface.

9. Place racks in the hot water bath for a total of 30 minutes. Calcium carbonate is slightly soluble in ammonia, so avoid letting your foram fragments sit in the reducing agent for longer than the necessary 30 minutes. Every 2 minutes:

- Remove rack
- Tighten screws on perspex clamp
- Invert, shake, and tap rack to settle forams and remove bubbles
- Ultrasonicate rack for a few seconds (this will agitate the reagent into all parts of the sample and discourage dissolved oxides from re-precipitating)
- Tap rack firmly and return to hot water bath
- Top off the water bath as necessary using hot water from the beaker

10. After 30 minutes, remove rack and clamp and carefully open and close all tubes to release gas. Keep one finger on the top of the tube and use your thumb to open the tube in a peeling motion.

11. Pipette off as much reducing reagent as possible using a clean (3x 10% HCl and 3x DI H<sub>2</sub>O) 100  $\mu$ L pipette tip. Do not use siphon. Eject waste into the reducing reagent bottle. Eject tip into waste bag.

12. Fill tube caps and tubes (to top of rack or higher) with DI H<sub>2</sub>O for foram cleaning. Close tubes. Tap rack firmly to settle forams.

13. Turn on the siphon in the fume cupboard using the labelled control knob on the left-hand panel. Rinse the siphon tip (3x 10% HCl and 3x DI H<sub>2</sub>O). Siphon caps and then siphon off as much water as possible from tubes.
14. Repeat steps 12 and 13 two more times.
15. Fill tubes half full with DI H<sub>2</sub>O for foram cleaning, close tubes, then set in the hot water bath for 5 minutes.
16. In the meantime, prepare a fresh strip of parafilm.
17. Remove hydrazine waste container (brown bottle) from fridge and place in fume cupboard.
18. Dump leftover reducing reagent into waste container.
19. Fill the empty 60 mL bottle for rinsing reducing reagent with DI H<sub>2</sub>O from the ELGA tap.
20. Rinse the reducing reagent bottle 2-3x with DI H<sub>2</sub>O, dumping rinse water into the waste container.
21. Re-parafilm waste container and return to fridge.
22. If 5 minutes have passed, remove rack from hot water bath, clean siphon tip (3x 10% HCl and 3x DI H<sub>2</sub>O), siphon caps, and then siphon off as much water as possible from tubes.
23. Repeat steps 12 and 13 two more times.
24. Repeat step 15.
25. Repeat step 22. It is now safe to remove the rack from the fume hood.

26. Turn hotplate off or down as appropriate (you will need it again in Section V). Please remember to turn off the power source as well.

#### IV. Sample Transfer

1. In the flow bench, label a new set of acid-leached tubes for your samples.
2. Using a disposable scalpel, cut off ~1/4 of a 100  $\mu$ L pipette tip.
3. Set the pipettor to 70  $\mu$ L and thoroughly clean the pipette tip (6x 10% HCl and 6x DI H<sub>2</sub>O).
4. If you have not already, rinse and refill your DI H<sub>2</sub>O for sample transfers.
5. Open an old tube. Hold pipette tip directly over foram fragments and pipette and expel fragments ( $\pm$  H<sub>2</sub>O) into the new tube of the same sample number.
6. Add a small amount of DI H<sub>2</sub>O for sample transfers to the old tube. Repeat transfer until no foram fragments are visible in the old tube and then again once more (usually 2-3x).
7. Between samples, rinse the pipette tip 2-3x in your DI H<sub>2</sub>O for sample transfers.
8. Once all samples have been transferred into new tubes, turn on the siphon, clean the siphon tip (3x 10% HCl and 3x DI H<sub>2</sub>O), and siphon off as much water as possible.

## V. Removal of Organic Matter (Oxidizing Step)

1. In the fume cupboard, ensure hot water bath is hot (on verge of boiling, 80-90 °C) and filled to the base of your perspex rack.
2. Prepare your oxidizing reagent in the labelled, empty 60 mL bottle.
  - Pour 15 mL 0.1 N NaOH (stored in the fridge) into the empty bottle; pour this reagent directly from the bottle (no pipettes) and take care not to touch the lid of the reagent bottle to any other surface
  - Using a clean (3x 10% HCl and 3x DI H<sub>2</sub>O) 100 µL pipette tip, add 50 µL H<sub>2</sub>O<sub>2</sub>; SB: please pour a small quantity of H<sub>2</sub>O<sub>2</sub> into the H<sub>2</sub>O<sub>2</sub> bottle cap, pipette from the cap, and dispose of cap contents before re-capping the bottle
  - Cap reagent bottle and invert to mix
3. Open tubes and add 250 µL oxidizing reagent to each sample. Close tubes.
4. Set rack in hot water bath for 5 minutes.
5. Remove rack and invert, shake, and tap the rack to settle forams and remove bubbles. Ultrasonicate rack for a few seconds, then tap rack firmly and return to hot water bath.
6. Repeat steps 4 and 5.
7. Open tubes and top them off with DI H<sub>2</sub>O for foram cleaning.

8. Turn on siphon, clean siphon tip (3x 10% HCl and 3x DI H<sub>2</sub>O), and siphon off oxidizing reagent.
9. Repeat steps 7 and 8 two more times.

## VI. Dilute Acid Leach

1. In the flow bench, clean a 1000  $\mu$ L pipette tip (3x 10% HCl and 3x DI H<sub>2</sub>O).
2. Add 250  $\mu$ L 0.002 N HNO<sub>3</sub> to each tube. Because HNO<sub>3</sub> will dissolve carbonate, you may wish to use 0.001 N HNO<sub>3</sub> for small samples. You may also wish to skip ultrasonication and do fewer (or no) repetitions of the leach.
3. Tap the rack firmly and check for air bubbles. If necessary, tap some more.
4. Ultrasonicate the rack for 30 seconds.
5. Remove rack from bath. Invert, shake, and tap rack firmly to settle forams.
6. Open tubes. While waiting for forams to settle, turn on siphon and clean siphon tip (3x 10% HCl and 3x DI H<sub>2</sub>O).
7. Once forams have settled, siphon off as much acid as possible.
8. Repeat steps 2-7 4x as quickly as possible to avoid dissolving your samples. To avoid systematic variations in the effectiveness of the acid leach: Begin siphoning at a different row and (or) side of the rack during each rinse step. Change the orientation of the rack in the sonic bath during each sonication.

9. Fill tubes and caps with DI H<sub>2</sub>O for foram cleaning. Close tubes.
10. Tap rack firmly, check for bubbles, and ultrasonicate for a few seconds.
11. Remove rack from bath. Invert, shake, and tap rack firmly to settle forams.
12. Turn on siphon and clean siphon tip (3x 10% HCl and 3x DI H<sub>2</sub>O). Once forams have settled, siphon caps and then siphon off as much water as possible from tubes.
13. Repeat steps 10-13.
14. Pipette off all remaining water using a clean (3x 10% HCl and 3x DI H<sub>2</sub>O), 100 µL pipette tip. It is important to remove as much water as possible. Use a new, freshly-cleaned tip for each sample.

Your samples may be stored indefinitely at this point.

**Appendix 3:** Number of foraminifera from the 250-355 µm size fraction analysed for stable isotope (*Cibicidoides mundulus* and *Globigerinoides obliquus*) and trace metal/calcium (*Cibicidoides wuellerstorfi*, *Uvigerina peregrina*, and *Hoeglundina elegans*) ratios in the Sunbird-1 core. Shaded samples are discounted. See text for details.

Depth (MBSL)	Age (Ma)	<i>Cibicidoides mundulus</i>	<i>Globigerinoides obliquus</i>	<i>Cibicidoides wuellerstorfi</i>	<i>Uvigerina peregrina</i>	<i>Hoeglundina elegans</i>
1356	9.44	5	12	9	0	7
1359	9.48	6	15			
1362	9.52	10	16			
1365	9.57	10	0	5	0	11
1368	9.61	12	15			
1371	9.65	6	0	5	3	15
1374	9.69	4	15	13	0	15
1377	9.73	10	15			
1380	9.78	8	15			
1383	9.82	5	15	6	0	9
1386	9.86	12	15			
1389	9.90	8	15			
1392	9.94	6	4	6	2	9
1395	9.99	8	15			
1398	10.03	10	15			
1401	10.07	6	16	9	13	7
1404	10.11	12	15			
1407	10.15	12	16			
1410	10.20	6	0	4	14	15
1413	10.24	12	15			
1416	10.28	12	15			
1419	10.32	5	15	7	14	15
1422	10.36	6	15			
1425	10.41	6	15			
1428	10.45	6	15	6	15	15
1431	10.49	6	15			
1434	10.54	6	15			

1437	10.59	5	0	8	14	15
1440	10.64	11	16			
1443	10.69	12	15			
1446	10.74	6	10	7	2	14
1449	10.79	6	16			
1452	10.82	6	15			
1455	10.86	5	0	9	15	15
1458	10.89	6	14			
1461	10.93	8	15			
1464	10.96	6	0	15	12	15
1467	10.99	6	13			
1470	11.03	10	15			
1473	11.06	4	0	14	13	7
1476	11.09	10	15			
1479	11.13	11	15			
1482	11.16	11	15	15	15	15
1485	11.20	9	15			
1488	11.23	6	15			
1491	11.26	0	0	15	15	14
1494	11.30	12	15			
1497	11.33	12	15			
1500	11.36	6	15			
1503	11.40	12	15			
1506	11.43	12	13			
1509	11.47	5	10	11	15	15
1512	11.50	6	12			
1515	11.53	12	15			
1518	11.57	6	15	11	15	15
1521	11.60	12	15			
1524	11.60	6	15			
1527	11.61	5	10	8	15	15
1530	11.61	12	14			
1533	11.62	6	11			
1536	11.62	6	10	14	14	15
1539	11.63	12	15			
1542	11.63	6	3			
1545	11.66	6	12			
1548	11.69	6	0	15	13	12

1551	11.71	12	14			
1554	11.74	6	12			
1557	11.77	12	8			
1560	11.80	12	13			
1563	11.82	5	0	15	15	7
1566	11.85	4	4			
1569	11.88	12	12			
1572	12.02	6	15	15	15	15
1575	12.16	12	10			
1578	12.29	12	13			
1581	12.43	5	7	10	12	3
1584	12.57	12	12			
1587	12.66	6	14			
1590	12.76	6	12	10	15	15
1593	12.85	4	13			
1596	12.94	6	15			
1599	13.04	5	10	12	15	13
1602	13.13	5	15			
1605	13.20	4	12			
1608	13.27	7	10	0	15	9
1611	13.34	5	6			
1614	13.41	12	14			
1617	13.48	10	14	0	14	0
1620	13.55	12	15			
1623	13.62	10	13			
1626	13.69	4	10	0	15	7

**Appendix 4:** Trace Metal/Calcium ratios from solution based ICP-MS analyses of benthic foraminifera (*Cibicoides wuellerstorfi*, *Uvigerina peregrina*, and *Hoeglundina elegans*) in the Sunbird-1 core.

***Cibicoides wuellerstorfi***

Depth (MBSL)	Age (Ma)	Mg/Ca (mmol/mol)	2SD	Sr/Ca (mmol/mol)	2SD	U/Ca (nmol/mol)	2SD	Al/Ca (μmol/mol)	2SD	Mn/Ca (μmol/mol)	2SD	B/Ca (μmol/mol)	2SD	Fe/Ca (μmol/mol)	2SD
1356	9.44	2.82	0.04	1.43	0.02	12.70	0.52	45.71	0.96	99.55	2.29	224.87	5.22	1011.80	16.39
1365	9.57	4.41	0.06	1.47	0.02	18.24	0.55	22.32	0.46	127.85	0.69	202.05	6.26	1033.03	15.50
1374	9.69	3.59	0.07	1.47	0.05	10.72	0.27	8.90	0.17	109.86	1.67	207.37	4.56	625.13	24.88
1383	9.82	3.37	0.04	1.49	0.02	19.86	1.02	33.63	2.64	98.65	3.41	213.12	10.74	753.61	28.64
1401	10.07	3.76	0.10	1.49	0.05	10.18	0.79	127.89	5.29	84.99	2.26	234.83	5.73	590.38	4.01
1428	10.45	7.42	0.09	1.88	0.03	160.56	2.25	202.65	0.81	417.97	6.35	143.58	1.15	5444.66	218.88
1437	10.59	4.26	0.08	1.64	0.01	54.02	1.67	206.59	7.23	319.00	8.68	227.28	5.14	6257.69	325.40
1446	10.74	3.67	0.11	1.51	0.03	34.00	1.46	87.84	2.20	113.92	3.46	222.82	8.16	1280.17	82.44
1455	10.86	5.39	0.06	1.77	0.01	118.94	2.33	36.52	1.03	268.90	2.10	190.56	2.93	3474.63	95.90
1464	10.96	6.14	0.01	1.85	0.03	274.79	4.18	53.96	0.17	220.08	2.60	165.00	7.46	3644.46	228.87
1473	11.06	17.83	0.71	1.81	0.06	155.93	1.62	57.30	1.58	191.39	2.76	170.73	4.30	5122.20	160.84
1482	11.16	9.00	0.07	2.10	0.02	236.83	0.85	290.68	6.69	336.07	2.89	130.85	2.07	6377.97	43.37
1491	11.26	7.22	0.19	2.05	0.05	180.27	2.74	209.41	3.89	270.60	2.22	145.09	3.48	5073.93	9.13
1509	11.47	11.22	0.08	2.32	0.01	271.05	8.13	345.74	2.63	888.59	4.98	146.35	1.08	9741.15	300.03
1518	11.57	11.21	0.11	2.71	0.02	326.84	5.36	371.72	4.16	1008.04	3.63	127.47	2.63	11048.34	269.58
1536	11.63	8.15	0.13	2.27	0.02	262.59	7.72	282.15	4.01	661.36	9.92	165.56	4.04	7527.38	16.56
1548	11.69	4.70	0.04	1.92	0.04	117.91	2.71	38.12	0.63	210.04	2.77	184.81	11.38	3876.54	4.65
1563	11.83	6.53	0.10	2.21	0.01	196.93	5.24	78.01	0.89	262.36	5.30	156.60	1.50	6879.71	81.18

1572	12.02	7.99	0.11	2.30	0.02	247.32	2.37	389.86	3.66	544.65	7.41	142.07	1.70	7645.52	128.44
1581	12.43	12.90	0.19	2.44	0.05	525.44	4.52	244.50	4.06	290.16	2.67	158.15	2.53	9801.74	429.32
1590	12.76	7.75	0.12	2.47	0.05	393.27	3.70	276.75	5.37	295.52	4.79	138.06	2.93	9480.37	83.43
1599	13.04	9.02	0.02	2.78	0.06	586.24	17.47	210.57	1.90	296.58	3.86	140.70	2.28	12047.17	390.33

***Uvigerina peregrina***

Depth (MBSL)	Age (Ma)	Mg/Ca (mmol/mol)	2SD	Sr/Ca (mmol/mol)	2SD	U/Ca (nmol/mol)	2SD	Al/Ca (μmol/mol)	2SD	Mn/Ca (μmol/mol)	2SD	B/Ca (μmol/mol)	2SD	Fe/Ca (μmol/mol)	2SD
1371	9.65	2.47	0.02	1.22	0.02	2.70	0.36	24.72	0.44	19.07	0.78	36.18	2.73	321.10	11.75
1401	10.07	2.03	0.03	1.18	0.03	14.63	0.49	3.36	0.18	18.31	0.42	30.67	1.20	271.73	12.28
1410	10.20	2.20	0.02	1.20	0.02	6.84	0.11	3.39	0.07	15.55	0.23	30.22	1.17	255.12	4.03
1419	10.32	2.21	0.02	1.21	0.01	13.94	0.10	9.24	0.09	24.10	0.23	31.92	0.59	438.71	6.76
1428	10.45	4.47	0.09	1.48	0.02	110.81	0.84	131.28	2.70	241.20	1.01	28.29	0.98	3024.23	66.53
1437	10.59	4.56	0.10	1.35	0.02	88.33	0.71	96.14	0.87	459.11	6.06	27.76	0.59	3060.35	36.72
1455	10.86	3.65	0.02	1.33	0.02	37.22	0.39	75.81	1.05	121.41	1.75	31.48	1.17	1529.62	50.17
1464	10.96	12.34	0.02	1.88	0.01	272.14	3.59	363.41	4.36	391.37	6.73	25.00	0.54	7956.63	74.79
1473	11.06	13.94	0.05	1.80	0.01	198.54	1.63	144.21	1.53	263.10	1.42	24.95	0.35	5292.20	93.14
1482	11.16	8.49	0.09	1.91	0.01	219.75	3.52	240.56	1.64	298.33	5.85	25.90	0.66	5078.06	145.23
1491	11.26	6.98	0.06	1.88	0.03	191.39	4.06	232.12	1.67	241.64	2.22	27.23	1.00	4759.93	33.32
1509	11.47	5.08	0.06	1.75	0.01	128.05	2.07	165.65	2.35	301.13	5.18	28.55	0.47	4261.44	17.90
1518	11.57	4.35	0.04	1.53	0.03	70.82	2.61	131.79	0.90	277.47	7.21	31.60	1.52	2869.13	66.56
1527	11.61	4.42	0.10	1.56	0.03	131.07	4.14	103.28	2.40	176.29	1.66	30.64	1.18	3156.41	2.53
1536	11.63	5.25	0.07	1.73	0.04	222.20	16.27	170.21	1.23	447.25	7.16	29.97	1.76	4264.77	7.68
1548	11.69	4.13	0.03	1.72	0.03	103.49	1.74	87.08	0.68	155.85	1.12	29.44	0.98	3957.23	5.54
1563	11.83	10.67	0.07	2.27	0.03	337.01	2.43	151.22	2.33	269.29	0.48	25.78	0.56	8853.21	42.50

1572	12.02	7.49	0.03	2.19	0.02	276.44	2.71	272.71	0.93	367.41	5.51	24.36	0.89	8355.38	170.45
1581	12.43	22.00	0.14	2.71	0.03	491.29	10.02	194.61	3.70	421.72	4.89	20.27	0.09	16839.99	299.75
1590	12.76	14.53	0.03	3.02	0.02	723.44	18.66	139.01	0.67	515.12	3.61	18.21	0.17	14268.88	65.64
1599	13.04	12.38	0.06	3.19	0.03	1267.29	46.89	122.25	1.32	662.08	6.09	16.45	0.62	16402.60	167.31
1608	13.27	13.30	0.12	3.12	0.07	1016.40	27.24	98.38	0.47	651.25	9.64	16.48	0.28	16640.78	266.25
1617	13.48	11.79	0.13	3.11	0.01	656.06	23.22	124.50	1.07	430.77	4.91	15.84	0.34	14759.56	298.14
1626	13.69	15.52	0.42	2.73	0.09	909.27	26.73	93.87	1.86	524.84	3.04	17.93	0.27	15459.23	163.87

***Hoeglundina elegans***

Depth (MBSL)	Age (Ma)	Mg/Ca (mmol/mol)	2SD	Sr/Ca (mmol/mol)	2SD	U/Ca (nmol/mol)	2SD	Al/Ca (μmol/mol)	2SD	Mn/Ca (μmol/mol)	2SD	B/Ca (μmol/mol)	2SD	Fe/Ca (μmol/mol)	2SD
1365	9.57	0.77	0.04	2.89	0.11	69.10	3.32	7.48	0.48	1.17	0.02	77.21	2.46	48.44	0.70
1371	9.65	1.55	0.01	2.87	0.03	129.72	1.32	41.61	0.20	44.23	0.50	64.60	1.78	1339.87	0.07
1374	9.69	0.84	0.02	2.77	0.05	112.18	1.66	4.26	0.17	9.75	0.06	78.05	1.17	259.55	0.05
1383	9.82	0.84	0.01	2.75	0.02	67.50	0.77	9.48	0.13	1.39	0.03	83.78	0.85	45.98	0.72
1392	9.94	0.92	0.04	2.79	0.05	74.28	5.90	22.21	0.70	1.04	0.16	90.87	5.85	63.16	0.83
1401	10.07	2.30	0.03	3.26	0.09	206.72	4.47	37.32	0.51	91.88	0.88	73.68	0.96	2289.60	0.18
1410	10.20	1.40	0.02	2.98	0.01	118.94	2.02	28.39	0.37	36.23	0.11	70.15	1.59	616.06	0.18
1419	10.32	2.26	0.01	2.94	0.08	135.22	2.38	26.83	0.58	113.74	0.55	65.19	0.73	1558.27	0.08
1422	10.36	6.57	0.06	3.52	0.02	322.12	7.67	170.02	2.99	398.18	7.41	56.17	1.43	7439.78	0.05
1428	10.45	2.65	0.02	2.98	0.02	119.91	1.82	42.40	0.71	114.96	1.15	65.54	1.02	1558.20	0.06
1437	10.59	0.79	0.01	2.99	0.04	125.67	1.28	15.81	0.31	1.26	0.01	74.30	1.23	67.64	0.13
1446	10.74	0.80	0.01	3.08	0.04	95.12	0.99	7.92	0.11	1.30	0.02	72.25	1.46	41.14	0.16
1455	10.86	1.48	0.01	3.16	0.02	136.55	0.36	45.94	0.53	48.53	0.56	67.05	1.60	736.63	0.09
1464	10.96	3.90	0.13	3.09	0.07	184.28	3.91	76.30	0.64	220.07	1.63	65.60	0.46	3175.91	0.19

1473	11.06	1.16	0.01	3.11	0.06	100.99	1.86	72.96	0.10	3.85	0.06	104.97	1.72	56.20	0.64
1482	11.16	4.60	0.07	3.26	0.03	252.06	1.71	172.67	1.04	169.18	1.96	61.30	0.82	3493.91	0.09
1491	11.26	7.10	0.07	3.18	0.04	231.53	1.57	365.39	2.85	328.04	2.03	50.24	0.20	5327.23	0.16
1509	11.47	6.02	0.02	3.15	0.02	236.32	3.88	214.25	1.80	422.09	0.42	102.60	2.22	4613.90	0.39
1518	11.57	6.61	0.04	3.27	0.06	221.33	3.19	194.30	3.03	815.67	7.99	56.38	0.15	6601.75	0.07
1536	11.63	6.16	0.07	3.31	0.06	262.75	4.89	164.89	0.59	644.03	5.67	53.32	1.38	6341.26	0.07
1548	11.69	8.83	0.15	3.70	0.08	389.20	4.98	31.23	1.31	483.00	6.76	46.06	0.97	12485.06	0.10
1563	11.83	13.84	0.33	4.15	0.09	581.68	10.82	276.37	5.14	665.16	7.05	22.05	1.45	19885.49	0.12
1572	12.02	8.37	0.11	3.44	0.03	343.39	2.68	231.54	2.87	442.57	9.91	45.57	0.62	10938.44	0.08
1590	12.76	14.33	0.20	4.74	0.10	1038.51	31.78	166.15	3.52	534.34	10.15	16.07	0.93	22001.77	0.13
1599	13.04	13.87	0.10	4.54	0.04	1191.81	20.26	120.86	1.35	784.89	13.81	24.66	0.39	21755.73	0.02
1608	13.27	13.73	0.07	4.35	0.09	907.93	15.98	71.98	1.19	589.96	5.07	24.68	0.27	20590.55	0.14
1626	13.69	14.91	0.33	4.56	0.11	1184.86	23.93	108.20	1.93	783.22	19.89	19.76	0.53	21425.63	0.10

**Appendix 5:** *Cibicoides wuellerstorfi* and *Dentogloboquadrina altispira* LA-ICP-MS Mg/Ca ratios from the 1551-1554m sample in the Sunbird-

1 core. Up to 10 profiles through 10 tests were analysed for each species. Shaded samples are discounted. See text for details.

***Cibicoides wuellerstorfi***

Specimen Number	Profile Number	Profile Mg/Ca (mmol/mol)	Profile Mn/Ca (μmol/mol)	Profile Al/Ca (μmol/mol)	Specimen Profiles Used	Total Profiles Used	Specimen Mean Mg/Ca (mmol/mol)	Intraspecimen 2 SE	Sample Mean Mg/Ca (mmol/mol)	Sample 2 SE
1	1	6.80	467.27	2654.60						
1	2	4.35	224.29	3680.80						
1	3	6.63	468.73	1365.38						

1	4	10.50	505.93	8862.24
1	5	8.70	560.47	4152.12
1	6	21.78	1285.88	23443.02
1	7	5.56	323.35	2800.42
1	8	3.19	153.21	796.48

1	9	2.58	80.51	242.79
1	10	2.57	68.17	358.13

2	2	2.57	0.00	2.57	0.00
---	---	------	------	------	------

2	1	6.61	437.54	11905.64
2	2	6.74	498.79	11212.72
2	3	4.97	135.38	6558.72
2	4	6.80	566.65	12822.73
2	5	6.77	578.77	12326.34
2	6	4.93	326.17	7190.55

2	7	2.11	36.35	354.46
2	8	2.59	51.89	201.35

2	4	2.35	0.34	2.46	0.20
---	---	------	------	------	------

3	1	3.38	157.50	301.76
3	2	3.00	111.60	116.54
3	3	3.18	173.53	384.49

3	4	3.09	123.62	92.59
3	5	3.11	101.25	70.42
3	6	2.95	96.20	125.30
3	7	3.12	123.60	124.84
3	8	3.05	102.87	131.85

3	9	2.67	59.36	109.43						
3	10	2.81	60.47	34.29	8	12	2.97	0.11	2.80	0.17
4	1	2.88	178.20	356.34						
4	2	3.00	198.13	371.91						
4	3	2.50	200.66	436.84						
4	4	2.16	158.49	186.75						
4	5	2.32	228.60	339.96						
4	6	2.24	221.92	488.08						
4	7	1.97	160.66	171.24						
4	8	2.00	172.37	281.71						
4	9	2.71	114.45	350.30						
4	10	3.08	119.63	3492.19	9	21	2.42	0.24	2.64	0.16
5	1	2.72	60.05	34.91						
5	2	2.30	32.97	BELOW LOD						
5	3	2.06	28.56	BELOW LOD						
5	4	2.50	33.55	15.53						
5	5	2.01	23.65	14.62						
5	6	2.62	59.02	24.06						
5	7	2.31	31.47	24.37						
5	8	2.39	32.26	19.22						
5	9	1.72	26.45	16.05						
5	10	2.06	43.93	8.93	10	31	2.27	0.19	2.52	0.14

6	1	2.32	58.74	234.66						
6	2	2.27	81.55	209.41						
6	3	2.29	78.96	192.51						
6	4	3.12	123.75	2323.85						
6	5	2.77	89.92	2147.52						
6	6	2.33	39.52	911.12						
6	7	2.26	63.12	545.70						
6	8	2.24	59.09	105.73						
6	9	2.37	53.84	180.70						
6	10	2.74	67.75	1736.96	7	38	2.30	0.03	2.48	0.12
7	1	2.68	49.00	20.32						
7	2	3.04	65.86	83.41						
7	3	2.23	63.72	18.44						
7	4	2.79	49.09	20.51						
7	5	3.14	76.08	55.90						
7	6	3.97	81.09	100.41						
7	7	3.79	69.12	102.21						
7	8	2.87	72.50	28.56						
7	9	2.59	71.16	43.95	7	45	2.76	0.21	2.52	0.11
8	1	2.77	39.90	49.82						
8	2	2.45	23.45	26.54						
8	3	2.44	23.93	38.50						
8	4	2.75	34.77	39.22						

8	5	2.55	28.78	50.98						
8	6	2.51	115.37	356.22						
8	7	2.71	53.24	46.47						
8	8	2.58	57.11	185.68						
8	9	2.23	35.09	34.09	9	54	2.55	0.05	2.53	0.09
9	1	2.64	64.07	216.95						
9	2	3.55	55.36	1188.61						
9	3	2.78	40.59	50.58						
9	4	6.23	124.22	15437.28						
9	5	27.34	198.22	136122.02						
9	6	2.93	48.34	102.11						
9	7	3.89	180.91	1227.04						
9	8	2.98	63.41	482.34						
9	9	3.66	85.15	2043.17						
9	10	2.70	47.27	159.02	5	59	2.81	0.12	2.55	0.09
10	1	1.62	21.53	7.20						
10	2	2.04	67.92	29.88						
10	3	2.82	107.52	2297.15						
10	4	1.92	76.33	79.46						
10	5	1.64	21.27	147.30						
10	6	2.13	74.64	903.57						
10	7	1.96	91.73	288.40						
10	8	2.22	89.34	216.43						

10 9 2.02 52.02 70.88 8 67 1.94 0.14 2.48 0.09

***Dentogloboquadrina altispira***

Specimen Number	Profile Number	Profile Mg/Ca (mmol/mol)	Profile Mn/Ca (μmol/mol)	Profile Al/Ca (μmol/mol)	Profiles Used	Total Profiles Used	Specimen Mean Mg/Ca (mmol/mol)	Intraspecimen 2 SE	Sample Mean Mg/Ca (mmol/mol)	Sample 2 SE
1	1	4.29	135.91	1051.58						
1	2	2.55	60.08	2954.85						
1	3	4.16	122.92	2145.85						
1	4	3.01	101.10	393.93						
1	5	3.99	147.10	684.97						
1	6	3.44	221.55	261.14						
1	7	3.88	123.65	86.25						
1	8	2.67	140.51	163.48	4	4	3.25	0.45	3.25	0.45
2	1	4.00	48.54	104.05						
2	2	4.39	177.82	2260.88						
2	3	3.83	134.93	108.14						
2	4	3.85	72.18	176.33						
2	5	4.19	52.21	97.48						
2	6	4.04	120.71	247.50						
2	7	3.88	46.25	152.04						
2	8	4.62	84.81	9191.57						
2	9	3.67	107.17	107.34						
2	10	3.77	127.52	134.45	8	12	3.90	0.11	3.69	0.24

3	1	2.98	38.76	174.94						
3	2	3.63	115.68	25.31						
3	3	4.01	84.68	162.80						
3	4	2.93	47.72	31.35						
3	5	3.68	49.39	298.93						
3	6	4.00	123.31	113.15						
3	7	2.97	44.74	459.94						
3	8	3.71	54.99	252.16						
3	9	3.53	71.79	42.79						
3	10	4.05	172.26	127.54	8	20	3.43	0.27	3.58	0.19
4	1	3.56	177.09	388.39						
4	2	2.68	70.66	1289.21						
4	3	2.67	72.76	446.64						
4	4	3.77	143.72	1994.85						
4	5	2.84	83.44	1341.72						
4	6	2.76	99.77	1250.12						
4	7	3.39	158.76	238.26						
4	8	2.86	93.46	84.11						
4	9	3.46	99.77	1534.95						
4	10	3.01	75.13	3649.24	8	28	2.96	0.20	3.41	0.18
5	1	3.52	175.52	390.40						
5	2	2.67	70.52	1285.17						

5	3	2.66	72.21	443.15						
5	4	3.76	143.41	2041.42						
5	5	2.81	82.64	1314.64						
5	6	2.75	99.60	1259.40						
5	7	4.75	86.39	134.06						
5	8	4.70	165.53	239.43						
5	9	5.07	155.35	184.85						
5	10	5.23	73.34	106.15	6	34	3.48	0.88	3.42	0.22
6	1	3.63	75.79	115.40						
6	2	4.37	100.23	5354.09						
6	3	3.89	40.91	4606.43						
6	4	2.94	58.76	126.24						
6	5	3.36	32.27	2572.33						
6	6	4.31	78.44	3154.13						
6	7	3.41	83.15	2001.13						
6	8	3.75	160.46	254.45						
6	9	4.19	227.45	406.01						
6	10	3.46	116.30	192.33	7	41	3.57	0.30	3.44	0.19
7	1	3.60	82.34	427.25						
7	2	9.92	144.47	32842.16						
7	3	5.13	104.01	16818.22						
7	4	4.25	80.17	8658.66						
7	5	3.11	83.02	250.86						

7	6	2.98	88.43	127.45						
7	7	3.28	89.61	160.29						
7	8	2.85	86.86	190.67						
7	9	5.07	139.49	12143.06	5	46	3.17	0.23	3.41	0.17
8	1	3.87	138.79	80.93						
8	2	3.71	80.81	73.71						
8	3	3.84	45.72	118.05						
8	4	3.48	130.95	58.55						
8	5	3.84	115.21	83.94						
8	6	4.30	133.56	316.96						
8	7	3.42	67.84	130.27						
8	8	3.37	55.20	171.26						
8	9	3.56	157.32	59.17						
8	10	3.97	127.07	57.76	9	55	3.67	0.14	3.46	0.15
9	1	4.47	180.27	162.10						
9	2	4.51	145.99	114.83						
9	3	4.50	156.87	53.55						
9	4	4.36	80.51	256.09						
9	5	3.78	114.19	67.45						
9	6	5.38	483.62	615.02						
9	7	5.21	129.74	302.94						
9	8	4.15	99.60	680.68						
9	9	4.36	161.91	287.49						

9	10	4.54	154.56	154.52	8	63	4.33	0.17	3.57	0.15
10	1	4.21	73.09	30.09						
10	2	4.46	81.03	48.76						
10	3	3.88	56.01	489.43						
10	4	4.01	57.76	30.39						
10	5	3.96	53.64	461.28						
10	6	4.03	52.55	99.54						
10	7	3.64	54.27	78.15						
10	8	4.52	182.15	24.67						
10	9	4.24	125.98	209.41						
10	10	4.29	104.37	133.39	9	72	4.08	0.16	3.63	0.14

**Appendix 6:** Summary of *Cibicoides wuellerstorfi* and *Dentogloboquadrina altispira* mean Mg/Ca ratios in the Sunbird-1 core from LA-ICP-MS analyses. Shaded samples are discounted.

See text for details.

***Cibicoides wuellerstorfi***

Depth (MBSL)	Age (Ma)	# Spots used	# Specimens Used	Sample Mean Mg/Ca (mmol/mol)	Interspecimen 2 SE	Sample 2 SE
1359	9.48	N/A	N/A	N/A	N/A	N/A
1362	9.52	N/A	N/A	N/A	N/A	N/A
1371	9.65	N/A	N/A	N/A	N/A	N/A
1386	9.86	21	4	2.99	0.39	0.22
1398	10.03	N/A	N/A	N/A	N/A	N/A
1416	10.28	5	1	2.43	N/A	0.25
1422	10.36	N/A	N/A	N/A	N/A	N/A
1425	10.41	N/A	N/A	N/A	N/A	N/A
1431	10.49	19	4	3.60	0.69	0.30
1434	10.54	N/A	N/A	N/A	N/A	N/A
1440	10.64	N/A	N/A	N/A	N/A	N/A
1449	10.79	9	2	2.59	0.65	0.28
1452	10.82	15	3	2.69	0.20	0.12
1458	10.89	16	4	2.99	0.36	0.20
1467	10.99	20	5	2.88	0.40	0.24
1476	11.09	26	5	2.96	0.30	0.13
1479	11.13	31	6	2.88	0.40	0.19
1488	11.23	17	3	2.51	0.16	0.12
1500	11.36	28	6	2.79	0.26	0.19
1506	11.43	25	5	2.76	0.35	0.17
1512	11.50	27	5	3.13	0.42	0.29
1515	11.53	20	4	2.19	0.25	0.15
1521	11.60	26	5	2.79	0.20	0.14
1524	11.61	28	5	2.93	0.56	0.25
1530	11.62	28	6	2.83	0.37	0.19
1533	11.62	29	5	2.89	0.63	0.24
1542	11.64	24	4	2.80	0.13	0.13
1545	11.67	30	6	2.69	0.33	0.17

1548	11.69	19	4	3.39	0.40	0.21
1551	11.72	26	6	2.44	0.29	0.16
1554	11.75	67	10	2.48	0.18	0.09
1557	11.77	18	4	2.84	0.58	0.26
1560	11.80	25	5	3.21	0.72	0.29
1566	11.85	26	5	3.09	0.44	0.24
1569	11.88	24	5	2.66	0.26	0.14
1572	12.02	20	4	3.50	0.46	0.29
1584	12.57	21	5	2.23	0.21	0.16
1587	12.66	23	5	2.78	0.15	0.13
1590	12.76	N/A	N/A	N/A	N/A	N/A
1593	12.85	22	6	3.06	0.33	0.19
1599	13.04	N/A	N/A	N/A	N/A	N/A
1602	13.13	14	3	2.88	0.70	0.33
1605	13.20	8	3	3.02	0.85	0.47
1611	13.34	N/A	N/A	N/A	N/A	N/A
1623	13.62	10	2	2.95	1.31	0.53

### ***Dentogloboquadrina altispira***

Depth (MBSL)	Age (Ma)	# Spots used	# Specimens Used	Sample Mean Mg/Ca (mmol/mol)	Interspecimen 2 SE	Sample 2 SE
1359	9.48	19	5	3.63	0.71	0.36
1362	9.52	14	4	4.34	0.47	0.39
1371	9.65	18	4	4.20	0.43	0.28
1386	9.86	25	5	4.17	0.79	0.35
1398	10.03	16	5	4.18	0.89	0.54
1416	10.28	8	3	4.65	0.91	0.77
1422	10.36	34	6	3.67	0.72	0.33
1425	10.41	30	6	4.13	0.41	0.25
1431	10.49	28	6	4.01	0.49	0.32
1434	10.54	34	6	3.08	0.32	0.16
1440	10.64	20	5	4.75	0.93	0.47
1449	10.79	19	4	4.54	0.90	0.49
1452	10.82	22	5	4.42	0.55	0.40
1458	10.89	3	1	3.03	N/A	0.16
1467	10.99	2	2	4.93	0.14	0.10
1476	11.09	6	2	4.43	0.90	0.71

1479	11.13	4	3	5.07	0.31	0.23
1488	11.23	7	3	3.82	1.49	1.04
1500	11.36	34	6	4.10	0.36	0.18
1506	11.43	14	4	4.48	0.76	0.49
1512	11.50	13	4	4.85	0.82	0.38
1515	11.53	13	5	4.33	0.57	0.41
1521	11.60	28	6	3.60	0.23	0.27
1524	11.61	30	6	3.56	0.67	0.30
1530	11.62	18	4	4.25	0.85	0.47
1533	11.62	13	4	4.89	0.30	0.45
1542	11.64	27	5	3.19	0.55	0.25
1545	11.67	21	4	4.28	0.90	0.37
1548	11.69	0	0	N/A	N/A	N/A
1551	11.72	16	5	3.83	0.74	0.45
1554	11.75	72	10	3.63	0.26	0.14
1557	11.77	12	4	4.51	0.42	0.47
1560	11.80	34	6	3.47	0.32	0.17
1566	11.85	24	5	4.32	0.48	0.31
1569	11.88	12	4	4.69	0.68	0.54
1572	12.02	28	6	4.04	0.54	0.27
1584	12.57	11	2	3.74	1.88	0.78
1587	12.66	13	4	4.25	0.56	0.39
1590	12.76	16	3	4.85	0.49	0.63
1593	12.85	10	3	4.83	0.58	0.43
1599	13.04	0	0	N/A	N/A	N/A
1602	13.13	15	3	4.40	1.00	0.42
1605	13.20	6	2	3.72	0.07	0.43
1611	13.34	4	2	4.51	1.38	0.64
1623	13.62	0	0	N/A	N/A	N/A

**Appendix 7:** Summary of Robust plus binned *Cibicoides wuellerstorfi* and *Dentogloboquadrina altispira* mean Mg/Ca ratios in the Sunbird-1 core from LA-ICP-MS analyses. Minimum and maximum age refer to the age range of the combined (binned) samples (Table 5.6).

***Cibicoides wuellerstorfi***

Depth (MBSL)	Age (Ma)	Minimum Age (Ma)	Maximum Age (Ma)	# Spots used	# Specimens Used	Sample Mean Mg/Ca (mmol/mol)	Interspecimen 2 SE	Sample 2 SE	Interspecimen Range
1401	10.07	9.86	10.28	26	4	2.89	0.32	0.20	0.96
1440	10.64	10.49	10.79	28	6	3.28	0.59	0.28	1.97
1459	10.91	10.82	10.99	51	12	2.86	0.21	0.12	1.25
1476	11.09	11.09	11.09	26	5	2.96	0.30	0.13	0.90
1479	11.13	11.13	11.13	31	6	2.88	0.40	0.19	1.47
1500	11.36	11.36	11.36	28	6	2.79	0.26	0.19	0.81
1506	11.43	11.43	11.43	25	5	2.76	0.35	0.17	1.07
1512	11.50	11.50	11.50	27	5	3.13	0.42	0.29	1.14
1521	11.60	11.60	11.60	26	5	2.79	0.20	0.14	0.65
1524	11.61	11.61	11.61	28	5	2.93	0.56	0.25	1.71
1530	11.62	11.62	11.62	28	6	2.83	0.37	0.19	1.25
1533	11.62	11.62	11.62	29	5	2.89	0.63	0.24	1.89
1542	11.64	11.64	11.64	24	4	2.80	0.13	0.13	0.34
1545	11.67	11.67	11.67	30	6	2.69	0.33	0.17	0.97
1551	11.72	11.72	11.72	26	6	2.44	0.29	0.16	0.81

1554	11.75	11.75	11.75	67	10	2.48	0.18	0.09	1.16
1560	11.80	11.80	11.80	25	5	3.21	0.72	0.29	2.03
1566	11.85	11.85	11.85	26	5	3.09	0.44	0.24	1.36
1570.5	11.95	11.88	12.02	44	9	3.04	0.36	0.20	1.91
1585.5	12.62	12.57	12.66	44	10	2.52	0.21	0.13	1.02
1600	13.03	12.85	13.20	44	12	2.99	0.27	0.17	1.55

***Dentogloboquadrina altispira***

Depth (MBSL)	Age (Ma)	Minimum Age (Ma)	Maximum Age (Ma)	# Spots used	# Specimens Used	Sample Mean Mg/Ca (mmol/mol)	Interspecimen 2 SE	Sample 2 SE	Interspecimen Range
1365	9.57	9.48	9.65	51	13	4.02	0.31	0.21	2.16
1386	9.86	9.86	9.86	25	5	4.17	0.79	0.35	2.29
1407	10.15	10.03	10.28	24	8	4.70	0.69	0.48	2.75
1422	10.36	10.36	10.36	34	6	3.67	0.72	0.33	2.57
1425	10.41	10.41	10.41	30	6	4.13	0.41	0.25	1.22
1431	10.49	10.49	10.49	28	6	4.01	0.49	0.32	1.53
1434	10.54	10.54	10.54	34	6	3.08	0.32	0.16	1.02
1444.5	10.72	10.64	10.79	39	9	4.65	0.54	0.34	2.50
1452	10.82	10.82	10.82	22	5	4.42	0.55	0.40	1.39
1463	11.06	10.89	11.23	22	11	4.20	0.51	0.48	2.87
1500	11.36	11.36	11.36	34	6	4.10	0.36	0.18	1.17
1510.5	11.48	11.43	11.53	40	13	4.55	0.40	0.26	2.73
1521	11.60	11.60	11.60	28	6	3.60	0.23	0.27	1.14

1524	11.61	11.61	11.61	30	6	3.56	0.67	0.30	1.94
1531.5	11.62	11.62	11.62	31	8	4.63	0.49	0.36	2.42
1542	11.64	11.64	11.64	27	5	3.19	0.55	0.25	1.68
1548	11.70	11.67	11.72	35	9	4.09	0.53	0.31	2.53
1554	11.75	11.75	11.75	72	10	3.63	0.26	0.14	3.17
1560	11.80	11.80	11.80	34	6	3.47	0.32	0.17	0.97
1566	11.85	11.85	11.85	24	5	4.32	0.48	0.31	1.41
1572	12.02	12.02	12.02	28	6	4.04	0.54	0.27	1.78
1588.5	12.71	12.57	12.85	50	12	4.40	0.43	0.31	2.94
1606.5	13.24	13.13	13.34	25	7	4.26	0.55	0.31	2.00

**Appendix 8a:** Bottom Water Temperatures calculated from the robust plus binned *Cibicidoides wuellerstorfi* mean Mg/Ca ratios in the Sunbird-1 core from LA-ICP-MS analyses (Appendix 7). Minimum and maximum age refer to the age range of the combined (binned) samples (Table 5.6). Seawater Mg/Ca is calculated from this study using Equation 5.2, the polynomial fit through the proxy data in Figure 5.5. Temperature is calculated using the calibration of Lear et al. (2002) assuming an Eocene seawater Mg/Ca of 2.1 mol/mol (H=0.4) (Equation 5.4). Maximum and Minimum temperatures refer to the full range of absolute temperatures derived incorporating the analytical, sample, and calibration

uncertainty. Spl Error Only Maximum and Minimum temperatures refer to the range of temperatures derived from the analytical and sample uncertainty only. Shaded samples are discounted. See text for details.

### Bottom Water Temperature

Depth (MBSL)	Age (Ma)	Minimum Age (Ma)	Maximum Age (Ma)	Sample Mean Mg/Ca (mmol/mol)	Seawater Mg/Ca (mol/mol)	Temperature (°C)	Maximum Temperature (°C)	Minimum Temperature (°C)	Spl Error Only Max Temperature (°C)	Spl Error Only Min Temperature (°C)
1401	10.07	9.86	10.28	2.89	3.68	12.30	14.95	10.03	12.92	11.64
1440	10.64	10.49	10.79	3.28	3.62	13.54	16.44	11.02	14.30	12.70
1459	10.91	10.82	10.99	2.86	3.59	12.31	14.73	10.26	12.70	11.90
1476	11.09	11.09	11.09	2.96	3.57	12.66	15.11	10.59	13.05	12.26
1479	11.13	11.13	11.13	2.88	3.56	12.41	15.07	10.14	13.01	11.77
1500	11.36	11.36	11.36	2.79	3.54	12.15	14.81	9.87	12.77	11.49
1506	11.43	11.43	11.43	2.76	3.53	12.04	14.63	9.83	12.60	11.45
1512	11.50	11.50	11.50	3.13	3.52	13.22	16.16	10.65	14.03	12.33
1521	11.60	11.60	11.60	2.79	3.51	12.17	14.64	10.07	12.60	11.71
1524	11.61	11.61	11.61	2.93	3.51	12.61	15.44	10.16	13.35	11.80
1530	11.62	11.62	11.62	2.83	3.51	12.29	14.93	10.03	12.87	11.66
1533	11.62	11.62	11.62	2.89	3.51	12.49	15.30	10.05	13.22	11.69
1542	11.64	11.64	11.64	2.80	3.51	12.20	14.66	10.12	12.62	11.76
1545	11.67	11.67	11.67	2.69	3.51	11.85	14.45	9.62	12.42	11.23
1551	11.72	11.72	11.72	2.44	3.50	10.95	13.50	8.77	11.53	10.33
1554	11.75	11.75	11.75	2.48	3.50	11.09	13.39	9.16	11.43	10.74

1560	11.80	11.80	11.80	3.21	3.49	13.48	16.42	10.91	14.27	12.61
1566	11.85	11.85	11.85	3.09	3.49	13.13	15.96	10.69	13.83	12.38
1570.5	11.95	11.88	12.02	3.04	3.48	12.98	15.66	10.69	13.56	12.37
1585.5	12.62	12.57	12.66	2.52	3.41	11.33	13.80	9.24	11.80	10.84
1600	13.03	12.85	13.20	2.99	3.37	12.96	15.58	10.73	13.46	12.43

**Appendix 8b:** Sea Surface Temperatures calculated from the robust plus binned *Dentogloboquadrina altispira* mean Mg/Ca ratios in the Sunbird-1 core from LA-ICP-MS analyses (Appendix 7). Minimum and maximum age refer to the age range of the combined (binned) samples (Table 5.6). pH is calculated by linear interpolation between the pH measurements of Sossian et al. (2018). pH corrected Mg/Ca is calculated using the multi-species calibration of Evans et al. (2016b) (Equation 5.2). Seawater Mg/Ca is calculated from this study using Equation 5.2, the polynomial fit through the proxy data in Figure 5.5. The pre-exponential (B) and exponential (A) constants of the Mg/Ca-temperature calibration are calculated using the calibration of Evans et al. (2016a), (Equation 5.7 and 5.8). Temperature is calculated as  $\ln((\text{Mg/Ca})/B)/A$ , using the values of B and A calculated in the previous columns. Maximum and Minimum temperatures refer to the full range of absolute temperatures derived incorporating the analytical, sample, and calibration uncertainty. Spl Error Only Maximum and Minimum temperatures refer to the range of temperatures derived from the analytical and sample uncertainty only.

## Sea Surface Temperature

Depth (MBSL)	Age (Ma)	Minimum Age (Ma)	Maximum Age (Ma)	Sample Mean Mg/Ca (mmol/mol)	pH	pH Corrected Mg/Ca (mmol/mol)	Seawater Mg/Ca (mol/mol)	Pre-exponential Constant (B)	Exponential Constant (A)
1365	9.57	9.48	9.65	4.02	8.05	3.91	3.74	0.4714	0.0791
1386	9.86	9.86	9.86	4.17	8.11	4.30	3.70	0.4721	0.0787
1407	10.15	10.03	10.28	4.70	8.09	4.73	3.67	0.4727	0.0784
1422	10.36	10.36	10.36	3.67	8.07	3.61	3.65	0.4732	0.0781
1425	10.41	10.41	10.41	4.13	8.06	4.05	3.64	0.4733	0.0781
1431	10.49	10.49	10.49	4.01	8.05	3.90	3.63	0.4735	0.0780
1434	10.54	10.54	10.54	3.08	8.05	2.97	3.63	0.4736	0.0779
1444.5	10.72	10.64	10.79	4.65	8.04	4.46	3.61	0.4741	0.0777
1452	10.82	10.82	10.82	4.42	8.04	4.24	3.60	0.4743	0.0776
1463	11.06	10.89	11.23	4.20	8.04	4.03	3.57	0.4750	0.0773
1500	11.36	11.36	11.36	4.10	8.04	3.93	3.54	0.4758	0.0769
1510.5	11.48	11.43	11.53	4.55	8.04	4.36	3.53	0.4761	0.0768
1521	11.60	11.60	11.60	3.60	8.01	3.36	3.51	0.4764	0.0766
1524	11.61	11.61	11.61	3.56	8.01	3.31	3.51	0.4764	0.0766
1531.5	11.62	11.62	11.62	4.63	8.01	4.27	3.51	0.4765	0.0766
1542	11.64	11.64	11.64	3.19	8.00	2.92	3.51	0.4765	0.0766
1548	11.70	11.67	11.72	4.09	7.97	3.65	3.50	0.4767	0.0765
1554	11.75	11.75	11.75	3.63	7.95	3.18	3.50	0.4768	0.0764
1560	11.80	11.80	11.80	3.47	7.99	3.16	3.49	0.4770	0.0764
1566	11.85	11.85	11.85	4.32	8.00	3.98	3.49	0.4771	0.0763
1572	12.02	12.02	12.02	4.04	8.03	3.84	3.47	0.4776	0.0761

1588.5	12.71	12.57	12.85	4.40	8.05	4.24	3.40	0.4797	0.0753
1606.5	13.24	13.13	13.34	4.26	8.00	3.90	3.35	0.4813	0.0746

### Sea Surface Temperature (cont)

Depth (MBSL)	Age (Ma)	Minimum Age (Ma)	Maximum Age (Ma)	Temperature (°C)	Maximum Temperature (°C)	Minimum Temperature (°C)	Spl Error Only Max Temperature (°C)	Spl Error Only Min Temperature (°C)
1365	9.57	9.48	9.65	26.77	30.47	23.55	27.42	26.07
1386	9.86	9.86	9.86	28.05	32.19	24.40	29.09	26.93
1407	10.15	10.03	10.28	29.38	33.92	25.35	30.62	28.01
1422	10.36	10.36	10.36	26.02	30.18	22.29	27.13	24.81
1425	10.41	10.41	10.41	27.48	31.38	24.05	28.23	26.69
1431	10.49	10.49	10.49	27.03	31.15	23.35	28.01	25.97
1434	10.54	10.54	10.54	23.58	27.04	20.46	24.22	22.92
1444.5	10.72	10.64	10.79	28.85	33.10	25.10	29.76	27.86
1452	10.82	10.82	10.82	28.25	32.71	24.28	29.38	27.01
1463	11.06	10.89	11.23	27.67	32.41	23.40	29.06	26.11
1500	11.36	11.36	11.36	27.44	31.31	24.04	28.00	26.85
1510.5	11.48	11.43	11.53	28.84	33.03	25.17	29.56	28.08
1521	11.60	11.60	11.60	25.48	29.60	21.77	26.43	24.45
1524	11.61	11.61	11.61	25.29	29.51	21.48	26.34	24.15
1531.5	11.62	11.62	11.62	28.64	33.08	24.71	29.62	27.59
1542	11.64	11.64	11.64	23.68	27.64	20.07	24.65	22.63
1548	11.70	11.67	11.72	26.61	30.80	22.88	27.56	25.60

1554	11.75	11.75	11.75	24.81	28.30	21.69	25.30	24.30
1560	11.80	11.80	11.80	24.76	28.42	21.48	25.38	24.12
1566	11.85	11.85	11.85	27.79	32.05	24.02	28.69	26.82
1572	12.02	12.02	12.02	27.40	31.53	23.73	28.24	26.50
1588.5	12.71	12.57	12.85	28.97	33.46	25.01	29.87	28.00
1606.5	13.24	13.13	13.34	28.03	32.82	24.08	28.98	27.01

**Appendix 9:** Bottom Water Temperatures calculated from the *Cibicidoides wuellerstorfi* solution based ICP-MS Mg/Ca ratios in the Sunbird-1 core (Appendix 4) and corrected for seawater Mg/Ca. Seawater Mg/Ca is calculated from this study using Equation 5.2, the polynomial fit through the proxy data in Figure 5.5. Temperature is calculated using the calibration of Lear et al. (2002) assuming an Eocene seawater Mg/Ca of 2.1 mol/mol (H=0.4) (Equation 5.4). Maximum and Minimum temperatures refer to the full range of absolute temperatures derived incorporating the analytical and calibration uncertainty. Spl Error Only Maximum and Minimum temperatures refer to the range of temperatures derived from the analytical uncertainty only.

### Bottom Water Temperature

Depth (MBSL)	Age (Ma)	Mg/Ca (mmol/mol)	Seawater Mg/Ca (mol/mol)	Temperature (°C)	Maximum Temperature (°C)	Minimum Temperature (°C)	Spl Error Only Max Temperature (°C)	Spl Error Only Min Temperature (°C)
1356	9.44	2.82	3.75	12.01	14.11	10.26	12.14	11.88
1365	9.57	4.41	3.74	16.14	18.50	14.14	16.25	16.02
1374	9.69	3.59	3.72	14.25	16.55	12.31	14.42	14.07
1383	9.82	3.37	3.71	13.70	15.89	11.85	13.81	13.58
1401	10.07	3.76	3.68	14.74	17.15	12.70	14.98	14.49
1428	10.45	7.42	3.64	21.01	23.73	18.72	21.13	20.90
1437	10.59	4.26	3.62	15.94	18.36	13.89	16.11	15.76
1446	10.74	3.67	3.60	14.59	17.02	12.53	14.85	14.32
1455	10.86	5.39	3.59	18.12	20.62	16.01	18.21	18.02
1464	10.96	6.14	3.58	19.33	21.84	17.22	19.35	19.31
1482	11.16	9.00	3.56	22.85	25.66	20.48	22.92	22.79
1491	11.26	7.22	3.55	20.84	23.70	18.42	21.09	20.59
1509	11.47	11.22	3.53	24.91	27.86	22.42	24.98	24.85
1518	11.57	11.21	3.52	24.92	27.90	22.39	25.01	24.82
1536	11.63	8.15	3.51	22.00	24.84	19.61	22.15	21.86

1548	11.69	4.70	3.50	16.95	19.37	14.92	17.03	16.87
1563	11.83	6.53	3.49	19.99	22.69	17.73	20.13	19.86
1572	12.02	7.99	3.47	21.86	24.67	19.48	21.98	21.73
1581	12.43	12.90	3.43	26.30	29.43	23.64	26.43	26.16
1590	12.76	7.75	3.39	21.67	24.49	19.28	21.80	21.52
1599	13.04	9.02	3.37	23.08	25.89	20.72	23.10	23.07

**Appendix 10:** Stable Isotope ratios of the benthic foraminifera (*Cibicoides mundulus*) and the planktic foraminifera (*Globigerinoides obliquus*) in the Sunbird-1 core. Shaded samples are discounted. See text for details.

***Cibicoides mundulus***

Depth (MBSL)	Age (Ma)	$\delta^{13}\text{C}$ (‰ VPDB)	$\delta^{13}\text{C}$ 1 SD	$\delta^{18}\text{O}$ (‰ VPDB)	$\delta^{18}\text{O}$ 1 SD
1356	9.44	0.203	0.017	0.633	0.039
1359	9.48	1.115	0.042	0.763	0.057
1362	9.52	1.086	0.029	0.383	0.031
1365	9.57	0.816	0.019	0.437	0.019
1368	9.61	0.956	0.012	0.807	0.027
1371	9.65	0.789	0.019	0.550	0.03
1374	9.69	1.047	0.028	1.012	0.054
1377	9.73	0.714	0.014	0.301	0.014
1380	9.78	0.995	0.012	0.545	0.017
1383	9.82	1.253	0.018	1.238	0.034
1386	9.86	0.813	0.018	0.558	0.024
1389	9.90	1.45	0.032	1.779	0.053
1392	9.94	0.655	0.092	0.256	0.087
1395	9.99	1.127	0.014	1.114	0.024
1398	10.03	0.947	0.014	0.166	0.027
1401	10.07	0.958	0.031	0.969	0.062
1404	10.11	1.137	0.024	0.567	0.018
1407	10.15	1.014	0.017	-0.101	0.041
1410	10.20	1.422	0.024	1.421	0.049
1413	10.24	1.731	0.087	-0.192	0.102
1416	10.28	0.927	0.012	0.358	0.026
1419	10.32	1.269	0.019	0.400	0.051
1422	10.36	0.988	0.02	0.903	0.021
1425	10.41	1.263	0.016	0.988	0.041
1428	10.45	1.305	0.016	0.241	0.03
1431	10.49	1.097	0.015	0.540	0.049
1434	10.54	0.835	0.018	0.572	0.046
1437	10.59	1.23	0.017	1.128	0.041

1440	10.64	0.87	0.018	0.376	0.024
1443	10.69	0.651	0.022	1.158	0.03
1446	10.74	1.113	0.027	0.862	0.041
1449	10.79	0.642	0.03	0.375	0.038
1452	10.82	0.912	0.022	0.595	0.051
1455	10.86	0.813	0.025	0.588	0.036
1458	10.89	0.8	0.007	0.742	0.028
1461	10.93	0.733	0.016	-0.335	0.032
1464	10.96	0.809	0.027	1.712	0.065
1467	10.99	1.078	0.013	0.614	0.028
1470	11.03	0.784	0.019	-0.475	0.021
1473	11.06	0.994	0.018	-0.171	0.029
1476	11.09	1.113	0.033	2.737	0.06
1476	11.13	1.24	0.032	0.377	0.026
1479	11.16	0.701	0.015	-1.432	0.018
1482	11.20	1.236	0.03	0.637	0.045
1488	11.23	1.179	0.026	-0.052	0.027
1491	11.26	1.231	0.023	-1.089	0.037
1494	11.30	1.106	0.019	-0.723	0.028
1497	11.33	0.783	0.015	0.843	0.036
1500	11.36	1.385	0.018	0.370	0.04
1503	11.40	1.164	0.027	-0.987	0.041
1506	11.43	0.915	0.027	-0.765	0.018
1509	11.47	0.85	0.022	0.629	0.035
1512	11.50	1.14	0.028	0.538	0.037
1515	11.53	1.402	0.023	0.092	0.021
1518	11.57	1.443	0.015	0.424	0.015
1521	11.60	0.972	0.016	-0.681	0.022
1524	11.60	1.281	0.014	0.280	0.022
1527	11.61	1.994	0.024	0.466	0.047
1530	11.61	0.962	0.021	-1.317	0.03
1533	11.62	1.344	0.019	1.095	0.03
1536	11.62	1.571	0.028	0.717	0.051
1539	11.63	1.212	0.012	-0.697	0.014
1542	11.63	1.292	0.024	0.682	0.039
1545	11.66	1.415	0.015	1.124	0.04
1548	11.69	1.045	0.024	1.107	0.046
1551	11.71	1.236	0.018	-0.436	0.036

1554	11.74	1.174	0.014	0.935	0.017
1557	11.77	0.935	0.021	-0.747	0.03
1560	11.80	0.88	0.018	-0.699	0.015
1563	11.82	1.419	0.017	-0.112	0.034
1566	11.85	1.398	0.013	-0.318	0.044
1569	11.88	0.925	0.008	-1.618	0.011
1572	12.02	1.374	0.028	0.935	0.051
1575	12.16	1.171	0.017	-1.522	0.034
1578	12.29	1.565	0.021	-0.435	0.046
1581	12.43	1.489	0.023	-0.672	0.036
1584	12.57	1.587	0.022	-1.073	0.046
1587	12.66	1.999	0.023	-1.028	0.023
1590	12.76	1.449	0.017	-1.106	0.032
1593	12.85	1.28	0.034	-0.791	0.031
1596	12.94	2.756	0.019	-1.669	0.03
1599	13.04	1.588	0.018	-0.886	0.029
1602	13.13	1.738	0.029	-1.051	0.046
1605	13.20	2.831	0.013	-1.353	0.022
1608	13.27	2.554	0.026	-1.255	0.033
1611	13.34	1.885	0.024	-0.347	0.041
1614	13.41	3.046	0.021	-1.550	0.019
1617	13.48	3.494	0.017	-1.563	0.017
1620	13.55	2.588	0.013	-1.682	0.024
1623	13.62	3.039	0.012	-1.132	0.026
1626	13.69	2.696	0.019	-1.487	0.03

***Globigerinoides obliquus***

Depth (MBSL)	Age (Ma)	$\delta^{13}\text{C}$ (‰ VPDB)	$\delta^{13}\text{C}$ 1 SD	$\delta^{18}\text{O}$ (‰ VPDB)	$\delta^{18}\text{O}$ 1 SD
1356	9.44	1.151	0.031	-2.546	0.034
1359	9.48	1.848	0.024	-3.045	0.038
1362	9.52	1.699	0.015	-2.697	0.029
1365	9.57	N/A	N/A	N/A	N/A
1368	9.61	1.771	0.036	-2.630	0.019
1371	9.65	N/A	N/A	N/A	N/A

1374	9.69	1.859	0.025	-2.863	0.025
1377	9.73	1.907	0.014	-2.768	0.041
1380	9.78	1.785	0.013	-2.752	0.029
1383	9.82	1.874	0.015	-2.828	0.039
1386	9.86	1.738	0.015	-2.858	0.053
1389	9.90	1.732	0.021	-2.822	0.049
1392	9.94	N/A	N/A	N/A	N/A
1395	9.99	1.617	0.018	-2.878	0.021
1398	10.03	2.021	0.025	-2.860	0.028
1401	10.07	2.08	0.03	-2.657	0.011
1404	10.11	1.951	0.023	-2.572	0.042
1407	10.15	1.906	0.019	-2.829	0.027
1410	10.20	N/A	N/A	N/A	N/A
1413	10.24	1.767	0.011	-2.757	0.019
1416	10.28	1.673	0.02	-2.809	0.033
1419	10.32	1.939	0.016	-2.852	0.035
1422	10.36	1.773	0.019	-2.860	0.032
1425	10.41	2.211	0.019	-2.887	0.047
1428	10.45	2.102	0.013	-2.754	0.038
1431	10.49	1.86	0.009	-2.886	0.029
1434	10.54	1.569	0.022	-3.034	0.021
1437	10.59	N/A	N/A	N/A	N/A
1440	10.64	1.623	0.025	-3.037	0.026
1443	10.69	1.485	0.02	-2.944	0.037
1446	10.74	1.683	0.022	-2.604	0.03
1449	10.79	1.479	0.013	-2.958	0.032
1452	10.82	1.67	0.035	-3.060	0.043
1455	10.86	N/A	N/A	N/A	N/A
1458	10.89	1.956	0.029	-2.906	0.039
1461	10.93	1.406	0.02	-2.893	0.042
1464	10.96	N/A	N/A	N/A	N/A
1467	10.99	1.498	0.021	-2.748	0.035
1470	11.03	1.628	0.013	-2.564	0.026
1473	11.06	N/A	N/A	N/A	N/A
1476	11.09	1.661	0.02	-3.201	0.016
1476	11.13	1.671	0.02	-2.793	0.024
1479	11.16	1.855	0.029	-2.892	0.038
1482	11.20	1.992	0.014	-2.900	0.012

1488	11.23	1.658	0.021	-2.852	0.027
1491	11.26	N/A	N/A	N/A	N/A
1494	11.30	1.643	0.022	-2.854	0.03
1497	11.33	1.875	0.027	-2.918	0.026
1500	11.36	1.605	0.017	-3.018	0.024
1503	11.40	1.917	0.027	-2.825	0.025
1506	11.43	1.521	0.070	-2.421	0.096
1509	11.47	1.793	0.015	-2.808	0.035
1512	11.50	1.709	0.02	-2.797	0.027
1515	11.53	1.945	0.029	-2.764	0.032
1518	11.57	1.536	0.021	-3.100	0.02
1521	11.60	1.786	0.025	-2.838	0.029
1524	11.60	1.835	0.022	-2.815	0.032
1527	11.61	1.741	0.007	-2.800	0.028
1530	11.61	1.912	0.015	-2.629	0.041
1533	11.62	2.017	0.017	-2.669	0.011
1536	11.62	1.796	0.023	-2.850	0.032
1539	11.63	1.69	0.024	-2.782	0.029
1542	11.63	N/A	N/A	N/A	N/A
1545	11.66	1.493	0.022	-2.883	0.034
1548	11.69	N/A	N/A	N/A	N/A
1551	11.71	1.814	0.017	-2.786	0.038
1554	11.74	1.503	0.012	-2.737	0.024
1557	11.77	1.319	0.02	-3.133	0.024
1560	11.80	1.702	0.018	-2.830	0.02
1563	11.82	N/A	N/A	N/A	N/A
1566	11.85	N/A	N/A	N/A	N/A
1569	11.88	1.783	0.023	-2.764	0.025
1572	12.02	1.883	0.019	-2.668	0.022
1575	12.16	1.618	0.033	-2.718	0.03
1578	12.29	1.842	0.019	-2.857	0.031
1581	12.43	2.211	0.02	-2.959	0.024
1584	12.57	2.028	0.025	-2.338	0.072
1587	12.66	1.875	0.018	-3.340	0.026
1590	12.76	1.933	0.023	-3.395	0.027
1593	12.85	1.573	0.03	-3.258	0.033
1596	12.94	1.71	0.031	-3.229	0.019
1599	13.04	1.783	0.018	-3.396	0.046

1602	13.13	1.919	0.011	-3.450	0.02
1605	13.20	2.034	0.014	-3.197	0.024
1608	13.27	2.434	0.017	-3.470	0.023
1611	13.34	2.666	0.012	-3.629	0.017
1614	13.41	3.605	0.013	-3.202	0.024
1617	13.48	4.016	0.014	-3.254	0.026
1620	13.55	4.256	0.017	-3.446	0.037
1623	13.62	3.563	0.022	-3.395	0.029
1626	13.69	3.903	0.034	-3.468	0.031

**Appendix 11:** Bottom Water Temperatures calculated from *Cibicidoides mundulus*  $\delta^{18}\text{O}$  ratios in the Sunbird-1 core (Appendix 10) using the calibration of Lynch-Stieglitz et al. (1999) (Equation 6.3). Seawater  $\delta^{18}\text{O}$  ( $\delta^{18}\text{O}_{\text{sw}}$ ) is from Cramer et al. (2011), with a 90% confidence envelope (Figure 6.3). This  $\delta^{18}\text{O}_{\text{sw}}$  was converted from VSMOW to VPDB by incorporating a  $-0.27\text{‰}$  correction (Hut, 1987). Maximum and Minimum temperatures refer to the full range of absolute temperatures derived incorporating the analytical and calibration uncertainty. Spl Error Only Maximum and Minimum temperatures refer to the range of temperatures derived from the analytical uncertainty only. Shaded samples are discounted. See text for details.

Sea Surface Temperatures calculated from *Globigerinoides obliquus*  $\delta^{18}\text{O}$  ratios in the Sunbird-1 core (Appendix 10) using the calibration of Bemis et al. (1998) (Equation 6.2). An uncertainty of  $\pm 0.091\text{‰}$  due to any potential influence of salinity. Seawater  $\delta^{18}\text{O}$  ( $\delta^{18}\text{O}_{\text{sw}}$ ) is from Cramer et al. (2011), with a 90% confidence envelope (Figure 6.3). This  $\delta^{18}\text{O}_{\text{sw}}$  was converted from VSMOW to VPDB by incorporating a  $-0.27\text{‰}$  correction (Hut, 1987). Maximum and Minimum temperatures refer to the full range of absolute temperatures derived incorporating the analytical and calibration uncertainty. Spl Error Only Maximum and Minimum temperatures refer to the range of temperatures derived from the analytical uncertainty only. Shaded samples are discounted. See text for details.

### Bottom Water Temperature

Depth (MBSL)	Age (Ma)	$\delta^{18}\text{O}$ (‰ VPDB)	$\delta^{18}\text{O}$ 1 SD	Seawater $\delta^{18}\text{O}$ (‰)	Temperature (°C)	Maximum Temperature (°C)	Minimum Temperature (°C)	Spl Error Only Max Temperature (°C)	Spl Error Only Min Temperature (°C)
1356	9.44	0.633	0.039	0.276	14.4	16.9	11.8	14.8	14.0
1359	9.48	0.763	0.057	0.271	13.8	16.6	11.2	14.3	13.2
1362	9.52	0.383	0.031	0.271	15.6	18.1	13.0	15.9	15.3
1365	9.57	0.437	0.019	0.28	15.4	17.9	12.5	15.5	15.2
1368	9.61	0.807	0.027	0.28	13.6	16.2	10.8	13.8	13.3
1371	9.65	0.550	0.03	0.288	14.9	17.5	12.0	15.1	14.6

1374	9.69	1.012	0.054	0.288	12.7	15.5	9.8	13.2	12.1
1377	9.73	0.301	0.014	0.288	16.0	18.6	13.2	16.2	15.9
1380	9.78	0.545	0.017	0.281	14.8	17.3	12.0	15.0	14.7
1383	9.82	1.238	0.034	0.281	11.5	14.2	8.8	11.9	11.2
1386	9.86	0.558	0.024	0.256	14.7	17.2	11.9	14.9	14.4
1389	9.90	1.779	0.053	0.256	8.9	11.7	6.1	9.4	8.3
1392	9.94	N/A	N/A	0.256					
1395	9.99	1.114	0.024	0.22	11.8	14.5	9.3	12.1	11.6
1398	10.03	0.166	0.027	0.22	16.4	19.0	13.8	16.6	16.1
1401	10.07	0.969	0.062	0.19	12.4	15.4	9.9	13.0	11.8
1404	10.11	0.567	0.018	0.19	14.3	16.9	11.8	14.5	14.1
1407	10.15	-0.101	0.041	0.169	17.4	20.2	14.9	17.8	17.0
1410	10.20	1.421	0.049	0.169	10.1	13.1	7.6	10.6	9.7
1413	10.24	N/A	N/A	0.169					
1416	10.28	0.358	0.026	0.152	15.1	17.7	12.6	15.4	14.9
1419	10.32	0.400	0.051	0.152	14.9	17.7	12.4	15.4	14.4
1422	10.36	0.903	0.021	0.141	12.5	14.8	9.9	12.7	12.3
1425	10.41	0.988	0.041	0.141	12.1	14.6	9.5	12.5	11.7
1428	10.45	0.241	0.03	0.141	15.6	18.1	13.1	15.9	15.3
1431	10.49	0.540	0.049	0.127	14.1	16.6	11.8	14.6	13.7
1434	10.54	0.572	0.046	0.127	14.0	16.4	11.6	14.4	13.5
1437	10.59	1.128	0.041	0.108	11.2	13.3	9.0	11.6	10.9
1440	10.64	0.376	0.024	0.108	14.8	16.8	12.6	15.1	14.6
1443	10.69	1.158	0.03	0.087	11.0	12.8	8.9	11.3	10.7

1446	10.74	0.862	0.041	0.087	12.4	14.3	10.3	12.8	12.0
1449	10.79	0.375	0.038	0.063	14.6	16.4	12.7	15.0	14.3
1452	10.82	0.595	0.051	0.063	13.6	15.4	11.7	14.1	13.1
1455	10.86	0.588	0.036	0.039	13.5	15.2	11.7	13.8	13.1
1458	10.89	0.742	0.028	0.039	12.8	14.4	10.9	13.0	12.5
1461	10.93	-0.335	0.032	0.039	17.9	19.6	16.1	18.2	17.6
1464	10.96	1.712	0.065	0.01					
1467	10.99	0.614	0.028	0.01	13.2	15.0	11.4	13.5	13.0
1470	11.03	-0.475	0.021	0.01	18.4	20.1	16.6	18.6	18.2
1473	11.06	-0.171	0.029	-0.018	16.8	18.7	15.1	17.1	16.6
1476	11.09	2.737	0.06	-0.018	14.2	16.4	12.4	14.8	13.6
1476	11.13	0.377	0.026	-0.018	22.8	24.7	21.1	23.1	22.6
1479	11.16	-1.432	0.018	-0.034	12.9	14.7	11.3	13.1	12.7
1482	11.20	0.637	0.045	-0.034					
1488	11.23	-0.052	0.027	-0.034	16.2	18.0	14.6	16.4	15.9
1491	11.26	-1.089	0.037	-0.042	21.1	22.9	19.7	21.4	20.7
1494	11.30	-0.723	0.028	-0.042	19.3	21.1	17.9	19.6	19.1
1497	11.33	0.843	0.036	-0.042	11.9	13.7	10.5	12.2	11.5
1500	11.36	0.370	0.04	-0.047	14.1	15.9	12.9	14.5	13.7
1503	11.40	-0.987	0.041	-0.047	20.6	22.4	19.3	21.0	20.2
1506	11.43	-0.765	0.018	-0.047	19.5	21.1	18.3	19.7	19.3
1509	11.47	0.629	0.035	-0.045	12.9	14.6	11.8	13.2	12.6
1512	11.50	0.538	0.037	-0.045	13.3	15.0	12.2	13.7	13.0
1515	11.53	0.092	0.021	-0.045	15.4	17.0	14.3	15.6	15.2

1518	11.57	0.424	0.015	-0.046	13.9	15.3	12.8	14.0	13.7
1521	11.60	-0.681	0.022	-0.046	19.1	20.7	18.1	19.3	18.9
1524	11.60	0.280	0.022	-0.046	14.5	16.1	13.5	14.8	14.3
1527	11.61	0.466	0.047	-0.046	13.7	15.4	12.6	14.1	13.2
1530	11.61	-1.317	0.03	-0.046	22.1	23.8	21.1	22.4	21.9
1533	11.62	1.095	0.03	-0.046	10.7	12.3	9.6	11.0	10.4
1536	11.62	0.717	0.051	-0.046	12.5	14.3	11.4	13.0	12.0
1539	11.63	-0.697	0.014	-0.046	19.2	20.7	18.1	19.3	19.1
1542	11.63	0.682	0.039	-0.046	12.6	14.3	11.6	13.0	12.3
1545	11.66	1.124	0.04	-0.049	10.5	12.2	9.4	10.9	10.1
1548	11.69	1.107	0.046	-0.049	10.6	12.3	9.5	11.0	10.2
1551	11.71	-0.436	0.036	-0.049	17.9	19.6	16.9	18.3	17.6
1554	11.74	0.935	0.017	-0.049	11.4	12.9	10.3	11.6	11.3
1557	11.77	-0.747	0.03	-0.051	19.4	20.9	18.3	19.7	19.1
1560	11.80	-0.699	0.015	-0.051	19.2	20.6	18.0	19.3	19.0
1563	11.82	-0.112	0.034	-0.051	16.4	18.0	15.2	16.7	16.1
1566	11.85	-0.318	0.044	-0.067	17.3	18.9	16.1	17.7	16.9
1569	11.88	-1.618	0.011	-0.067	23.5	24.8	22.3	23.6	23.4
1572	12.02	0.935	0.051	-0.095					
1575	12.16	-1.522	0.034	-0.119	22.8	24.1	21.5	23.1	22.5
1578	12.29	-0.435	0.046	-0.071	17.8	19.3	16.5	18.3	17.4
1581	12.43	-0.672	0.036	-0.032	19.1	20.5	17.8	19.5	18.8
1584	12.57	-1.073	0.046	-0.092	20.8	22.1	19.4	21.2	20.3
1587	12.66	-1.028	0.023	-0.182	20.1	21.3	18.9	20.3	19.9

1590	12.76	-1.106	0.032	-0.267	20.1	21.4	18.9	20.4	19.8
1593	12.85	-0.791	0.031	-0.322	18.3	19.7	17.3	18.6	18.0
1596	12.94	-1.669	0.03	-0.322	22.5	23.9	21.4	22.8	22.2
1599	13.04	-0.886	0.029	-0.341	18.7	20.0	17.7	19.0	18.4
1602	13.13	-1.051	0.046	-0.339	19.5	21.1	18.5	19.9	19.1
1605	13.20	-1.353	0.022	-0.322	21.0	22.4	20.0	21.2	20.8
1608	13.27	-1.255	0.033	-0.285	20.7	22.1	19.7	21.0	20.4
1611	13.34	-0.347	0.041	-0.285	16.4	17.9	15.4	16.8	16.0
1614	13.41	-1.550	0.019	-0.233	22.4	23.6	21.4	22.5	22.2
1617	13.48	-1.563	0.017	-0.188	22.6	23.8	21.6	22.8	22.5
1620	13.55	-1.682	0.024	-0.174	23.3	24.4	22.2	23.5	23.0
1623	13.62	-1.132	0.026	-0.174	20.7	21.9	19.5	20.9	20.4
1626	13.69	-1.487	0.03	-0.209	22.2	23.4	21.1	22.5	21.9

### Sea Surface Temperature

Depth (MBSL)	Age (Ma)	$\delta^{18}\text{O}$ (‰ VPDB)	$\delta^{18}\text{O}$ 1 SD	Seawater $\delta^{18}\text{O}$ (‰)	Temperature (°C)	Maximum Temperature (°C)	Minimum Temperature (°C)	Spl Error Only Max Temperature (°C)	Spl Error Only Min Temperature (°C)
1356	9.44	-2.546	0.034	0.276	28.4	31.6	25.2	28.8	28.1
1359	9.48	-3.045	0.038	0.271	30.8	34.1	27.2	31.2	30.5
1362	9.52	-2.697	0.029	0.271	29.1	32.4	25.6	29.4	28.9
1365	9.57	N/A	N/A	0.28					
1368	9.61	-2.630	0.019	0.28	28.9	32.1	25.2	29.1	28.7

1371	9.65	N/A	N/A	0.288						
1374	9.69	-2.863	0.025	0.288	30.0	33.3	26.3	30.3	29.8	
1377	9.73	-2.768	0.041	0.288	29.6	33.0	25.7	30.0	29.2	
1380	9.78	-2.752	0.029	0.281	29.5	32.7	25.7	29.7	29.2	
1383	9.82	-2.828	0.039	0.281	29.8	33.2	26.0	30.2	29.4	
1386	9.86	-2.858	0.053	0.256	29.8	33.4	25.9	30.4	29.3	
1389	9.90	-2.822	0.049	0.256	29.7	33.2	25.8	30.1	29.2	
1392	9.94	N/A	N/A	0.256						
1395	9.99	-2.878	0.021	0.22	29.8	33.0	26.3	30.0	29.6	
1398	10.03	-2.860	0.028	0.22	29.7	33.0	26.2	30.0	29.4	
1401	10.07	-2.657	0.011	0.19	28.6	31.7	25.3	28.7	28.5	
1404	10.11	-2.572	0.042	0.19	28.2	31.6	24.6	28.6	27.8	
1407	10.15	-2.829	0.027	0.169	29.3	32.7	25.8	29.5	29.0	
1410	10.20	N/A	N/A	0.169						
1413	10.24	-2.757	0.019	0.169	28.9	32.3	25.6	29.1	28.8	
1416	10.28	-2.809	0.033	0.152	29.1	32.4	25.6	29.4	28.8	
1419	10.32	-2.852	0.035	0.152	29.3	32.6	25.8	29.7	29.0	
1422	10.36	-2.860	0.032	0.141	29.3	32.4	25.8	29.6	29.0	
1425	10.41	-2.887	0.047	0.141	29.4	32.7	25.8	29.9	29.0	
1428	10.45	-2.754	0.038	0.141	28.8	32.0	25.2	29.2	28.4	
1431	10.49	-2.886	0.029	0.127	29.4	32.3	26.1	29.6	29.1	
1434	10.54	-3.034	0.021	0.127	30.1	32.9	26.8	30.3	29.9	
1437	10.59	N/A	N/A	0.108						
1440	10.64	-3.037	0.026	0.108	30.0	32.6	26.9	30.2	29.7	

1443	10.69	-2.944	0.037	0.087	29.4	32.0	26.3	29.8	29.1
1446	10.74	-2.604	0.03	0.087	27.8	30.3	24.8	28.1	27.5
1449	10.79	-2.958	0.032	0.063	29.4	31.8	26.5	29.7	29.1
1452	10.82	-3.060	0.043	0.063	29.9	32.3	26.9	30.3	29.5
1455	10.86	N/A	N/A	0.039					
1458	10.89	-2.906	0.039	0.039	29.0	31.4	26.2	29.4	28.7
1461	10.93	-2.893	0.042	0.039	29.0	31.4	26.1	29.4	28.6
1464	10.96	N/A	N/A	0.01					
1467	10.99	-2.748	0.035	0.01	28.1	30.6	25.3	28.5	27.8
1470	11.03	-2.564	0.026	0.01	27.3	29.6	24.5	27.5	27.0
1473	11.06	N/A	N/A	-0.018					
1476	11.09	-3.201	0.016	-0.018	30.2	32.6	27.6	30.3	30.0
1476	11.13	-2.793	0.024	-0.018	28.2	30.7	25.6	28.5	28.0
1479	11.16	-2.892	0.038	-0.034	28.6	31.2	26.0	29.0	28.3
1482	11.20	-2.900	0.012	-0.034	28.7	31.0	26.2	28.8	28.5
1488	11.23	-2.852	0.027	-0.034	28.4	30.9	25.9	28.7	28.2
1491	11.26	N/A	N/A	-0.042					
1494	11.30	-2.854	0.03	-0.042	28.4	30.8	26.1	28.7	28.1
1497	11.33	-2.918	0.026	-0.042	28.7	31.1	26.4	29.0	28.5
1500	11.36	-3.018	0.024	-0.047	29.2	31.5	27.0	29.4	28.9
1503	11.40	-2.825	0.025	-0.047	28.2	30.6	26.1	28.5	28.0
1506	11.43	N/A	N/A	-0.047					
1509	11.47	-2.808	0.035	-0.045	28.2	30.5	26.1	28.5	27.8
1512	11.50	-2.797	0.027	-0.045	28.1	30.4	26.1	28.4	27.9

1515	11.53	-2.764	0.032	-0.045	28.0	30.3	25.9	28.3	27.6
1518	11.57	-3.100	0.02	-0.046	29.6	31.7	27.7	29.8	29.4
1521	11.60	-2.838	0.029	-0.046	28.3	30.6	26.3	28.6	28.0
1524	11.60	-2.815	0.032	-0.046	28.2	30.5	26.2	28.5	27.9
1527	11.61	-2.800	0.028	-0.046	28.1	30.4	26.1	28.4	27.9
1530	11.61	-2.629	0.041	-0.046	27.3	29.7	25.2	27.7	26.9
1533	11.62	-2.669	0.011	-0.046	27.5	29.6	25.7	27.6	27.4
1536	11.62	-2.850	0.032	-0.046	28.4	30.7	26.3	28.7	28.1
1539	11.63	-2.782	0.029	-0.046	28.0	30.3	26.0	28.3	27.8
1542	11.63	N/A	N/A	-0.046					
1545	11.66	-2.883	0.034	-0.049	28.5	30.8	26.4	28.8	28.2
1548	11.69	N/A	N/A	-0.049					
1551	11.71	-2.786	0.038	-0.049	28.0	30.4	25.9	28.4	27.7
1554	11.74	-2.737	0.024	-0.049	27.8	30.0	25.8	28.0	27.6
1557	11.77	-3.133	0.024	-0.051	29.7	31.8	27.6	29.9	29.5
1560	11.80	-2.830	0.02	-0.051	28.2	30.3	26.2	28.4	28.0
1563	11.82	N/A	N/A	-0.051					
1566	11.85	N/A	N/A	-0.067					
1569	11.88	-2.764	0.025	-0.067	27.8	29.9	25.7	28.1	27.6
1572	12.02	-2.668	0.022	-0.095	27.3	29.2	25.1	27.5	27.0
1575	12.16	-2.718	0.03	-0.119	27.4	29.4	25.1	27.7	27.1
1578	12.29	-2.857	0.031	-0.071	28.3	30.2	26.0	28.6	28.0
1581	12.43	-2.959	0.024	-0.032	28.9	30.8	26.7	29.2	28.7
1584	12.57	-2.338	0.072	-0.092					

1587	12.66	-3.340	0.026	-0.182	30.1	31.9	27.9	30.3	29.8
1590	12.76	-3.395	0.027	-0.267	29.9	31.8	27.8	30.2	29.7
1593	12.85	-3.258	0.033	-0.322	29.0	31.0	26.9	29.3	28.7
1596	12.94	-3.229	0.019	-0.322	28.9	30.8	26.9	29.0	28.7
1599	13.04	-3.396	0.046	-0.341	29.6	31.7	27.4	30.0	29.1
1602	13.13	-3.450	0.02	-0.339	29.8	31.8	28.0	30.0	29.6
1605	13.20	-3.197	0.024	-0.322	28.7	30.8	26.8	28.9	28.5
1608	13.27	-3.470	0.023	-0.285	30.2	32.2	28.3	30.4	30.0
1611	13.34	-3.629	0.017	-0.285	31.0	32.9	29.1	31.1	30.8
1614	13.41	-3.202	0.024	-0.233	29.2	31.1	27.3	29.4	28.9
1617	13.48	-3.254	0.026	-0.188	29.6	31.5	27.6	29.9	29.4
1620	13.55	-3.446	0.037	-0.174	30.6	32.6	28.5	31.0	30.3
1623	13.62	-3.395	0.029	-0.174	30.4	32.2	28.3	30.6	30.1
1626	13.69	-3.468	0.031	-0.209	30.5	32.4	28.5	30.8	30.2

**Appendix 12:** Benthic and planktic foraminiferal seawater  $\delta^{18}\text{O}$  ( $\delta^{18}\text{O}_{\text{sw}}$ ) records at Sunbird-1. Planktic foraminiferal  $\delta^{18}\text{O}_{\text{sw}}$  (‰) is calculated using the equation of Bemis et al. (1998) (Equation 6.1), and benthic foraminiferal  $\delta^{18}\text{O}_{\text{sw}}$  (‰) is calculated using the equation of Lynch-Stieglitz et al. (1999) (Equation 6.2). Temperature values used are given in Appendix 8, and  $\delta^{18}\text{O}$  values are given in Appendix 10. For Mg/Ca paleotemperatures where adjacent samples have been combined to ensure the mean Mg/Ca of the sample is representative, the same has been done with the corresponding  $\delta^{18}\text{O}$  samples.

**Planktic foraminiferal  $\delta^{18}\text{O}_{\text{sw}}$**

Depth (MBSL)	Age (Ma)	Minimum Age (Ma)	Maximum Age (Ma)	Mean $\delta^{18}\text{O}_{\text{sw}}$	Maximum $\delta^{18}\text{O}_{\text{sw}}$	Minimum $\delta^{18}\text{O}_{\text{sw}}$	Sample Error Only Maximum $\delta^{18}\text{O}_{\text{sw}}$	Sample Error Only Minimum $\delta^{18}\text{O}_{\text{sw}}$
1365	9.57	9.65	9.48	0.16	1.14	-0.69	0.34	-0.02
1386	9.86	9.86	9.86	0.20	1.34	-0.81	0.53	-0.14
1407	10.15	10.28	10.03	0.51	1.69	-0.55	0.83	0.16
1422	10.36	10.36	10.36	-0.23	0.87	-1.21	0.07	-0.54
1425	10.41	10.41	10.41	0.05	1.13	-0.90	0.30	-0.21
1431	10.49	10.49	10.49	-0.04	1.05	-1.01	0.22	-0.32
1444.5	10.72	10.79	10.64	0.23	1.35	-0.76	0.48	-0.03
1452	10.82	10.82	10.82	0.04	1.23	-1.02	0.36	-0.30
1463	11.06	11.23	10.89	0.08	1.30	-1.01	0.43	-0.30
1500	11.36	11.36	11.36	-0.09	0.94	-0.99	0.08	-0.26
1510.5	11.48	11.53	11.43	0.45	1.55	-0.53	0.66	0.23
1521	11.60	11.60	11.60	-0.32	0.77	-1.29	-0.06	-0.59

1524	11.61	11.61	11.61	-0.33	0.77	-1.33	-0.05	-0.64
1531.5	11.62	11.62	11.62	0.54	1.69	-0.49	0.79	0.26
1548	11.70	11.72	11.67	-0.08	1.04	-1.07	0.19	-0.36
1554	11.75	11.75	11.75	-0.36	0.58	-1.19	-0.21	-0.51
1560	11.80	11.80	11.80	-0.46	0.50	-1.32	-0.29	-0.64
1572	12.02	12.02	12.02	0.26	1.33	-0.70	0.48	0.02
1588.5	12.71	12.85	12.57	-0.08	1.09	-1.11	0.17	-0.34
1606.5	13.24	13.34	13.13	-0.37	0.85	-1.38	-0.13	-0.62

### Benthic Foraminiferal $\delta^{18}\text{O}_{\text{sw}}$

Depth (MBSL)	Age (Ma)	Minimum Age (Ma)	Maximum Age (Ma)	Mean $\delta^{18}\text{O}_{\text{sw}}$	Maximum $\delta^{18}\text{O}_{\text{sw}}$	Minimum $\delta^{18}\text{O}_{\text{sw}}$	Sample Error Only Maximum $\delta^{18}\text{O}_{\text{sw}}$	Sample Error Only Minimum $\delta^{18}\text{O}_{\text{sw}}$
1401	10.07	9.86	10.28	-0.07	0.75	-0.80	0.26	-0.41
1440	10.64	10.49	10.79	0.43	1.43	-0.47	0.92	-0.06
1459	10.91	10.82	10.99	0.13	0.82	-0.49	0.34	-0.09
1476	11.09	11.09	11.09	-0.07	0.62	-0.68	0.13	-0.28
1479	11.13	11.13	11.13	-1.94	-1.27	-2.52	-1.76	-2.12
1500	11.36	11.36	11.36	-0.19	0.51	-0.80	0.02	-0.41
1506	11.43	11.43	11.43	-1.35	-0.71	-1.90	-1.19	-1.51
1512	11.50	11.50	11.50	0.20	0.96	-0.46	0.45	-0.06
1521	11.60	11.60	11.60	-1.24	-0.61	-1.77	-1.10	-1.38
1524	11.61	11.61	11.61	-0.18	0.52	-0.79	0.02	-0.40
1530	11.62	11.62	11.62	-1.85	-1.17	-2.43	-1.66	-2.04
1533	11.62	11.62	11.62	0.61	1.32	-0.01	0.82	0.38

1542	11.64	11.64	11.64	0.13	0.79	-0.43	0.30	-0.04
1545	11.67	11.67	11.67	0.50	1.19	-0.09	0.70	0.29
1551	11.72	11.72	11.72	-1.25	-0.58	-1.82	-1.05	-1.45
1554	11.75	11.75	11.75	0.15	0.73	-0.33	0.26	0.05
1560	11.80	11.80	11.80	-0.98	-0.27	-1.60	-0.78	-1.19
1566	11.85	11.85	11.85	-0.67	0.07	-1.32	-0.43	-0.92
1570.5	11.95	11.88	12.02	-0.72	2.45	-3.81	1.95	-3.41
1585.5	12.62	12.57	12.66	-1.78	-1.16	-2.31	-1.64	-1.93
1600	13.03	12.85	13.20	-1.45	-0.38	-2.43	-0.89	-2.02